Characterizing the Ce^{3+}/Ce^{4+} Chemistry for Use in Redox Flow Battery Applications

by

Cailin Anne Buchanan

A dissertation submitted in partial fulfillment
of the requirements for the degree of
Doctor of Philosophy
(Chemical Engineering)
in the University of Michigan
2022

Doctoral Committee:

Assistant Professor Nirala Singh, Chair
Assistant Professor Bryan R. Goldsmith
Professor Suljo Linic
Professor Melanie Sanford

Cailin Anne Buchanan

cailinab@umich.edu

ORCID iD: 0000-0001-9978-2687

Dedication

To my parents, my sister, and Nick, who have all supported and encouraged me endlessly.

Acknowledgements

I would like to thank my PhD advisor, Prof. Nirala Singh, and committee members, Professors Bryan Goldsmith, Suljo Linic, and Melanie Sanford for lending their time and expertise to my dissertation. I was very fortunate to have weekly meetings with Prof. Singh, during which I learned how to think more critically about my research topics. His research and professional mentorship have been extremely beneficial to me, and I know the skills I have learned from him on experimental design, troubleshooting, TEA, and scientific communication will benefit me in my future research career. Through Prof. Goldsmith, I learned how powerful first principles modeling can be, and I am grateful for his support of me in many applications over the years. Prof. Suljo Linic's electrochemistry class was illuminating (you can never beat thermodynamics) and he has offered many helpful suggestions to my dissertation. I appreciate Prof. Melanie Sanford's big picture questions, and her electrolyte engineering insights have been hugely helpful.

I would also like to acknowledge my scientific collaborators and funding sources. To my Singh Group lab mates: thank you for your scientific advice and friendship. I would like to specifically acknowledge Harsh Agarwal, who trained me on the energy storage electrochemistry techniques when I first joined the group and who was always willing to puzzle through scientific questions with me. To Danielle Richards and Zixuan Wang, I enjoyed our lab bench chats and appreciated your assistance with my numerous HUPD troubleshooting attempts. To James Akinola, your enthusiasm is a wonderful addition to the group, and I enjoyed our experience GSI-ing together. To Claire, Jared, and Wendy, it has been a privilege to watch you all develop as scientists and learn from you along the way. To the undergraduate and master's students I worked

with (Spencer Cira, Dana Suchara, Alyssa Rorie, and Dasol Jun), I thank you all for your assistance on the cerium projects. Learning how to mentor students was a highlight of my time as a PhD student. I would also like to thank Dr. Mahalingam Balasubramanian and Dr. John Fulton for offering their expertise during my EXAFS fitting attempts. Eunbyeol Ko's and Dylan Herrera's computational work on the cerium ion structures and kinetics were critical to my dissertation. I also would like to express gratitude to the UM Dow Doctoral Sustainability Fellowship program and the Momental Foundation for the Mistletoe Research Fellowship that helped to fund my PhD.

Lastly, I would like to thank my family and friends for their support throughout my PhD. I have met so many wonderful people who made Ann Arbor feel like home, including Elizabeth Wilson, Hunter Wilson, Emma Purcell, Kaylee Smith, Pete Alsip, Abbey Alsip, Krutarth Jhaveri, Kirstie Hostetter and so many more from my time at SNRE/SEAS. To Kendra Walter, Lisa Gustafson, Gia Rich, and Chris Chang, thank you for always being there for a phone call. I would like to thank the entire Boucher/Weill family for being so supportive of my research, asking for updates and always managing to stump me with tough battery questions! I am so grateful to be joining such an encouraging family. To Nick, who has been with me every step of this journey, I don't know what I would do without you. Your constant support, like helping me practice all my research talks, cooking us dinner almost every day these past four years, and always making me laugh and feel loved, is so appreciated. I am excited for our next chapter. Finally, to my sister and my parents, thank you for your unending support. Erin, you inspire me endlessly with your work ethic, humor, and grit. To my dad, thank you for teaching me calculus, instilling a love of learning in me, and always being willing to chat about that new climate technology you just read about. To my mom, thank you for being my biggest advocate and for showing Erin and me that women can do anything. I am so grateful for you all.

Table of Contents

List of Tables

List of Figures

List of Schemes

List of Appendices

Abstract

Energy storage technologies will be crucial to meeting rising renewable electricity demand in the U.S., but there is currently not enough storage capacity to meet this demand. As described in **Chapter 1**, redox flow batteries (RFBs) are a favorable energy storage technology for large scale, long-duration energy storage, but the state-of-the-art all-vanadium RFB (VRFB) is too expensive. Cerium is promising in RFBs because of its higher voltage and cheaper precursor. The economic and environmental performance of a Ce RFB compared to the VRFB has not been assessed in detail, however, and the fundamental processes that control the Ce^{3+}/Ce^{4+} thermodynamics and kinetics are not understood. To address this, we compare the VRFB and Ce-V RFB storage cost and greenhouse gas (GHG) emissions and study the Ce^{3+}/Ce^{4+} structures, thermodynamics, and kinetics. The theory behind the economic and environmental modeling and spectroscopy and kinetic measurements is discussed in **Chapter 2**.

In **Chapter 3**, we develop technoeconomic assessment (TEA) and life cycle inventory (LCI) models and determine that the Ce-V RFB minimum levelized cost of electricity (LCOE) is lower and the two RFBs' levelized GHG (LGHG) emissions are similar, suggesting Ce should be considered further in RFB applications. The redox potential and exchange current density are identified through a sensitivity analysis to be highly influential to the Ce-V RFB cost and emissions, motivating the need for further work into the fundamental phenomena that control thermodynamics and kinetics. A 194 mV increase in redox potential is equivalent to an increase in kinetics by a factor of two, providing electrolyte and electrode engineering guidance.

The Ce^{3+}/Ce^{4+} redox potential is highly dependent on the electrolyte anion. To determine the link between anions and thermodynamics in **Chapter 4**, we study the Ce^{3+} and Ce^{4+} ionic structures in acids relevant for battery applications. Using UV-Vis spectroscopy, extended X-ray absorption fine structure spectroscopy (EXAFS), and density functional theory calculations, we find that Ce^{3+} is coordinated by nine water molecules and Ce^{4+} is complexed by at least one anion. The decrease in redox potential is driven by stronger anion complexation of Ce^{4+}. Thus, to maximize thermodynamics for RFB applications, electrolytes with weaker complexing anions should be selected.

The cerium electron transfer kinetics must be increased for RFB applications by optimizing the factors that control kinetics, but the Ce^{3+}/Ce^{4+} charge transfer mechanism is not known. We couple EXAFS and kinetics measurements to propose a two-step mechanism in H_2SO_4 (**Chapter 5**). The first step of the mechanism is a chemical step, and the second step is a rate-determining electron transfer described through Marcus theory. We find the electrolyte controls the kinetics and hypothesize that the Ce^{3+}/Ce^{4+} kinetics will be fastest in weaker complexing electrolytes, e.g., $HClO_4$. Assuming the same mechanism holds in $HClO_4$ and the preexponential factor does not change, we expect the kinetics can increase by a factor of 10,000 in $HClO_4$, whereas the electrode would affect the kinetics up to a factor of nine through electrostatic effects. To control the kinetics in an RFB, a weaker Ce^{4+}-anion complexing electrolyte like HNO_3 should be selected, and the electrode surface area should be increased until the increase in electrode costs outweighs the kinetic savings. Since the electrolyte is expected to control both the Ce RFB's thermodynamics and kinetics future work should optimize the electrolyte for thermodynamics and kinetics through electrolyte engineering (**Chapter 6**).

Chapter 1 Introduction

1.1 Summary

This chapter provides context for the use of the cerium (Ce^{3+}/Ce^{4+}) chemistry in redox flow battery (RFB) applications, as well as the challenges and open questions associated with its use, which motivates the research completed in this thesis. The motivation for RFBs is first introduced as a strategy to promote the use of renewable energy in the U.S. electricity grid. A review of RFBs is provided, including the basic principles, the state-of-the-art inorganic, aqueous technology (the all-vanadium RFB, or VRFB), and ongoing challenges with market deployment of RFBs, which are primarily related to the cost of energy storage. Cerium is presented as a promising alternative to the positive electrolyte of the VRFB because of the high Ce^{3+}/Ce^{4+} redox potential and lower precursor cost, and so a review of the applications of the Ce^{3+}/Ce^{4+} chemistry, including energy storage, and relevant research studies into the ionic structures and kinetics is provided. It is found that while Ce has been proposed as an active species in RFBs, there have been very few technoeconomic or life cycle assessment studies of Ce RFBs conducted to understand the impact that switching to Ce will have on cost and greenhouse gas (GHG) emissions of energy storage. Additionally, the structures of the Ce^{3+} and Ce^{4+} ions are not well understood, and the charge transfer mechanism of the Ce^{3+}/Ce^{4+} redox reaction has not been determined, which limits any efforts to control the Ce^{3+}/Ce^{4+} thermodynamics and kinetics. Controlling both the thermodynamics and kinetics is important to improving the performance of the Ce^{3+}/Ce^{4+} redox reaction in RFB applications. Addressing these outlined challenges was the goal of this

dissertation. The chapter concludes by providing a description of the thesis objective and scope, as well as a brief summary of each of the dissertation chapters.

1.2 Motivation for energy storage and redox flow batteries

This section will discuss motivation for the use of redox flow batteries in large-scale, electricity grid energy storage applications. In **Section 1.2.1**, current and future renewable electricity trends for the U.S. are described, highlighting the need for energy storage. In **Section 1.2.2**, a review of relevant energy storage technologies is provided. Of the possible technologies, redox flow batteries are particularly well-suited for grid scale electricity storage.

1.2.1 Trends in renewable electricity in the U.S.

As of 2021, renewable sources make up 21% of the electricity grid profile in the U.S.,[1] and their share of the grid is projected to grow substantially in the next several decades. The EIA projects based on current economic trends and laws and regulations that 60% of cumulative capacity additions in the U.S. through 2050 will be renewable electric generating technologies.[1] The share of electricity from renewable sources is increasing due to both economic drivers (falling costs of photovoltaic and wind[1]) and policy drivers that are related to greenhouse gas (GHG) emissions mitigation strategies (increasing renewable portfolio standards and tax credits[1]). The EIA prediction that renewable energy will account for 42% of electricity sources by 2050 is based on current economic trends and policies,[1] but the International Renewable Energy Agency (IRENA) indicates that 78% of the U.S. electricity grid needs to be powered by renewable sources by 2050 to meet the Paris Agreement goal of limiting the rise in global temperatures to 2 ℃.[2] The IRENA estimate highlights the significant need for renewable energy integration into the electricity grid.

Energy storage is needed for stable and useful integration of renewable energy into the electricity grid. While there are many types of renewable energy, solar and wind sources currently account for 57% of the renewable energy supply in the U.S., and by 2050, they are projected to account for 81%.[1] Both wind and solar sources are intermittent in nature, meaning that the supply is often not predictable or aligned with customer demand on the electricity grid. The electricity grid must be able to balance demand and supply. Currently, electricity grid operators balance the grid by using a combination of conventional baseload power plants, e.g., nuclear, coal-fired, or combined cycle gas turbines,[3] which are relatively inflexible (ramp up and down rates on the order of several hours[3]), and peaking plants, e.g., natural gas-fired internal combustion engines (ICE) or oil-fired ICE,[3,4] which are used to adjust supply on the time scale of minutes.[3] As intermittent renewable energy sources become increasingly integrated into the grid, however, challenges in scheduling, system frequency, and regulation and grid stabilization are expected.[5] There are reports that if the electricity grid has more than 60% of its energy derived from renewable sources, the grid will become destabilized.[6–8] The supply of renewable energy does not typically align with customer demand on the electricity grid, motivating the advancement of energy storage to promote renewable electricity.

New types of energy storage technologies will need to be advanced and implemented to make up the difference between the current energy storage capacity and what is needed by 2050 to meet the aggressive renewable electricity targets required to drive down GHG emissions. Researchers at the National Renewable Energy Lab used the Regional Energy Deployment System (ReEDS) model to estimate the amount of storage capacity that would be needed to achieve different levels of renewable energy penetration into the grid by 2050 (**Fig. 1.1**).[9] It was found that to achieve 80% of electricity in the U.S. from renewable energy by 2050, which is approximately

the proportion identified by IRENA necessary to keep global temperatures rising above 2 ℃, 123 GW of energy storage would be needed.[9] As of 2020, however, the U.S. had only 24 GW of storage capacity.[10] Of this 24 GW of storage capacity, 93% is completed with pumped storage hydropower (PSH).[11] Siting completely new PSH facilities is challenging, however, because PSH is geographically limited due to the need for large elevation changes. Additional PSH capacity is being met primarily through upgrades to existing plants.[11] Thus, the types of energy storage technologies used to store energy in the U.S. will need to be diversified. A review of the possible energy storage technologies is provided next.

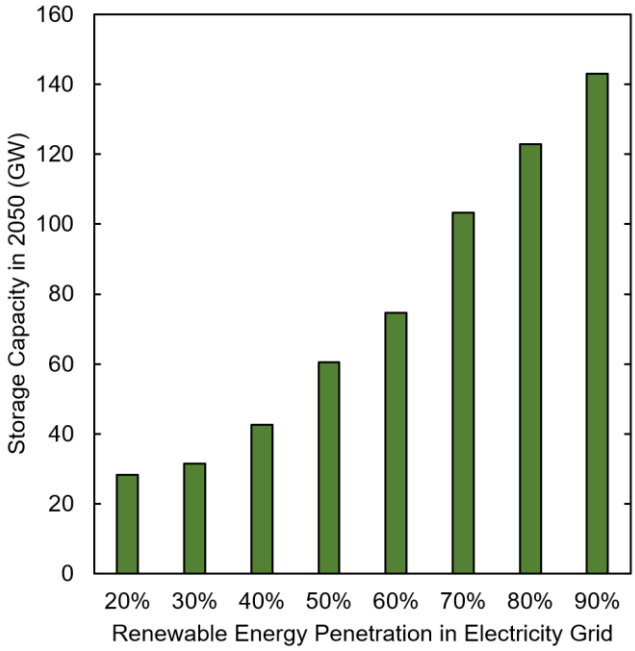

Figure 1.1. Predicted storage capacity requirements for different renewable energy penetration scenarios in the U.S. electricity grid in 2050. Image adapted from Mai et al. (2012).[9]

1.2.2 A review of energy storage technologies

The main categories of energy storage technologies are PSH, thermal, electromechanical, and electrochemical,[10] and the technologies' different power ratings and discharge times make them well-suited for different applications. As mentioned above, PSH provides the dominant source of energy storage, but will not be able to supply the additional storage capacity required to

decarbonize the electricity grid in the coming decades. Thermal storage technologies include ice and chilled water storage, which is commonly used for displacing compressor and chiller motor electric loads during peak cooling hours in buildings, and systems that use large solar collectors to heat salts or organics to generate steam when necessary to drive generators.[12] Notable electromechanical technologies include compressed air energy storage (CAES) and flywheel energy storage.[13] Electrochemical technologies consist of supercapacitors and batteries, of which there are many different types. Notable battery technologies include lead-acid, lithium (Li)-ion, sodium-sulfur (NaS), nickel-cadmium (NiCd), and flow batteries.[13] The discharge times and power ratings for many types of energy storage technologies are included in **Fig. 1.2**, where bulk power management refers to services like electric energy time-shift, T&D Grid Support and Load Shifting refer to Transmission & Distribution and ancillary services, and UPS (uninterruptible power supply) and Power Quality refer to supply in the event of shortages.[12] Comparing the different energy storage applications in **Fig. 1.2**, PSH and CAES are both well-suited for bulk power management because of their large power ratings and long discharge times (8-10 hours),[12] but they both are constrained by geological and geographic requirements.[14] Many battery technologies have been developed for mobile and transportation[15] due to their high energy densities and shorter discharge time scales. There are several batteries, however, that are being considered for grid scale electricity storage applications, primarily for UPS, T&D Grid Support, and Load Shifting applications, including the advanced lead-acid battery, the NaS battery, the Li−ion battery, and the redox flow battery (RFB).[13]

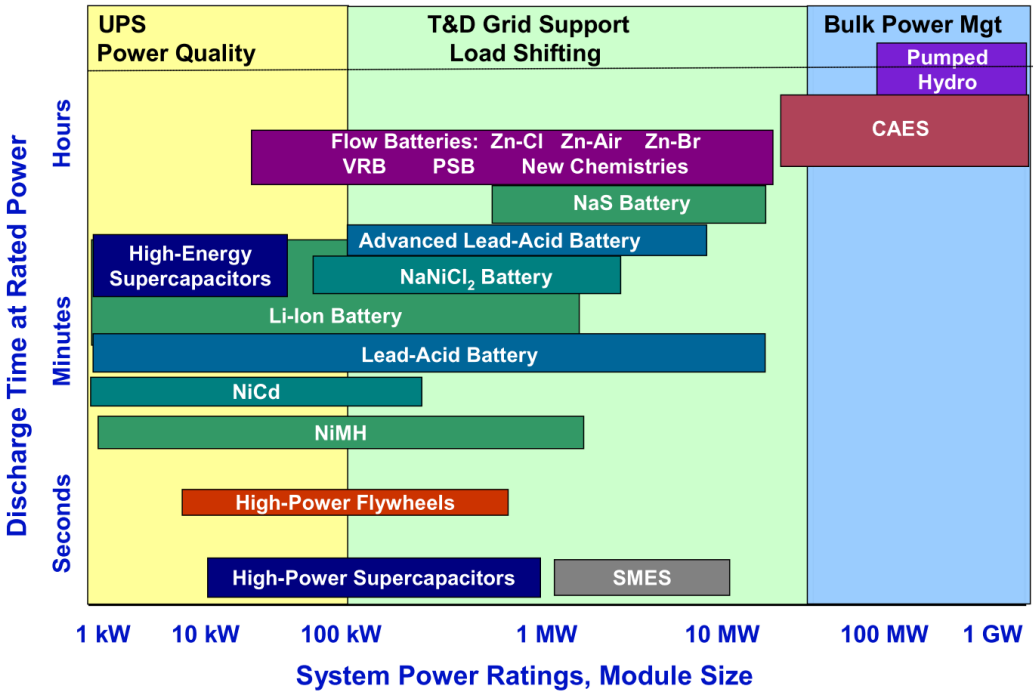

Figure 1.2. Energy storage technologies as a function of their discharge time and system power ratings. Image reproduced from Akhil et al. (2015).[12]

Considering the possible batteries, each have advantages and disadvantages that make them better suited for certain applications over others. The lead-acid battery is used for a number of energy storage applications, including microgrids, spinning reserve, and bulk energy storage, and has a efficiency ranging between 70%−80%, but it requires significant maintenance, has a short lifetime[13] and the potential for hydrogen explosions.[14] Advanced valve-regulated lead acid batteries have been shown to have significantly longer lifetimes.[13] The NaS battery is noted for its high energy density, low maintenance requirements, and long lifetime,[13] but there are safety concerns due to the required high operation temperature and it has poor thermal cycling.[14] The Li−ion battery makes up the majority of implemented battery projects, and it has a high efficiency and high power density,[13] but it has a high cost and significant safety[14] concerns related to the formation of dendrites which can lead to fires and explosions. Compared to the other batteries, RFBs have longer discharge times, significantly longer lifetimes (>10,000 cycles compared to

<5,000 cycles),[13] fewer safety concerns, and have the unique feature of the separation of energy and power components, which make RFBs suitable for many different energy storage applications.[15] RFBs will be described in more detail in the next section to motivate the research conducted in this dissertation.

1.3 Redox flow battery background

This section introduces the RFB technology, describing how it functions in **Section 1.3.1**, before providing information on the state-of-the-art aqueous inorganic RFB, the VRFB, in **Section 1.3.2**. Information on nascent RFB technologies, including a brief discussion of organic RFBs, is included in **Section 1.3.3**. Finally, a discussion of one of the primary challenges associated with the state-of-the-art RFB, which is its cost of energy storage, is provided in **Section 1.3.4**. The motivation for investigating the Ce^{3+}/Ce^{4+} chemistry in RFB applications is introduced in **Section 1.3.4** as well.

1.3.1 Introduction to redox flow batteries

Unlike other batteries, the active species of RFBs are stored in external tanks of electrolyte, which are typically comprised of acid solutions for aqueous systems, in which the active redox species is dissolved. As shown in **Fig. 1.3** for a generic chemistry for discharging, the pumps are used to flow the positive and negative electrolyte past the respective electrode. There are two compartments separated by an ion-exchange membrane. In each compartment, there is an electrode at which a half-cell reaction occurs, which means that an electron is either accepted (reduction) or released (oxidation) during the reaction. A fully charged battery is considered to be at 100% State of Charge (SoC), where SoC refers to the amount of charge available in the battery relative to its total capacity.[16] At 100% SoC, the active species at the negative electrode is in its fully reduced

state, i.e., C^{m+} in **Fig. 1.3**, and the positive electrode active species is in its fully oxidized state, i.e., A^{n+} in **Fig. 1.3**. During discharge, at the negative electrode, the active species (C^{m+}) is oxidized as it flows past, releasing an electron, while on the positive electrode, the active species (A^{n+}) is reduced, accepting an electron. The difference between the standard redox potentials of the active species at the negative and positive electrodes is the open circuit voltage (OCV), which represents the thermodynamic amount of voltage that can be extracted from the battery. The ion-exchange membrane allows an ion, typically protons in aqueous RFBs, to pass from the positive electrode compartment to the negative electrode compartment, but the electron is not allowed through. Instead, the electron is forced through the external circuit to complete the half-cell reaction at the positive electrode during discharge.[15]

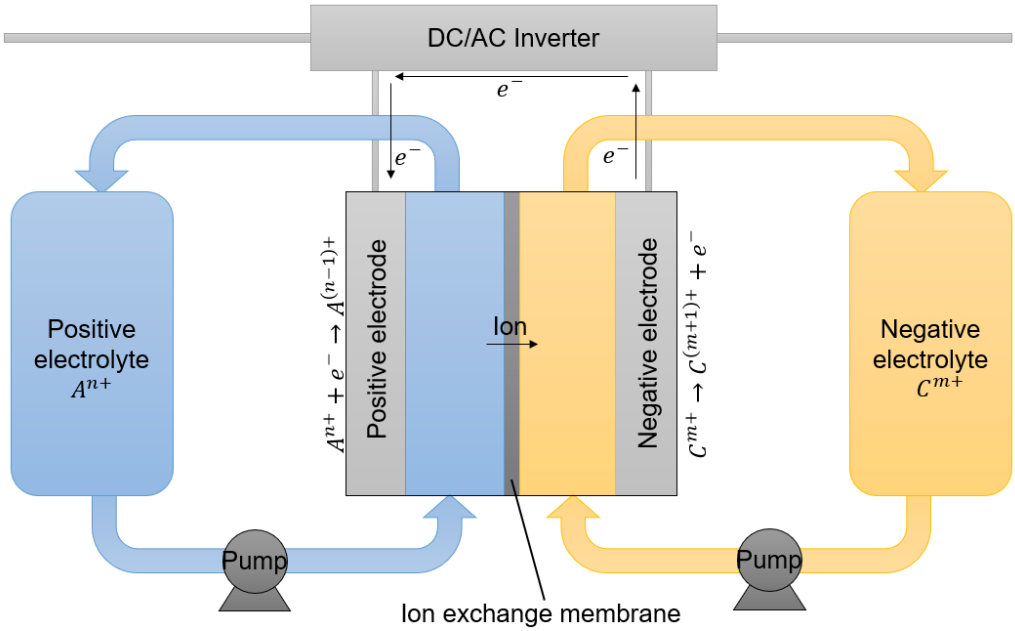

Figure 1.3. Diagram of redox flow battery in discharge mode, with generic positive electrolyte A^{n+} accepting an electron and negative electrolyte C^{m+} releasing an electron. The electron is forced to travel through the external circuit to complete the half-cell redox reactions, while an ion such as H^+ travels through the ion exchange membrane.

A fully discharged battery is at 0% SoC, meaning that at the negative electrode, the active species is in its oxidized state, e.g., $C^{(m+1)+}$, and at the positive electrode, the active species is initially entirely reduced, e.g., $A^{(n-1)+}$. As a result of the oxidation states of the active species being

changed, when these electrolytes are flowed past the electrodes during charging, the reverse reactions occur, and so the active species at the positive electrode is oxidized, and the active species at the negative electrode is reduced.

An RFB is comprised of a stack of multiple cells that each contain the two half-cell compartments described above as well as the ion exchange membrane. In addition to the positive electrode, ion exchange membrane, and negative electrode, the RFB stack also includes any assembly components necessary to combine the elements, such as gaskets, bipolar plates, and flow fields. An example of this stack configuration is demonstrated in **Fig. 1.4**.

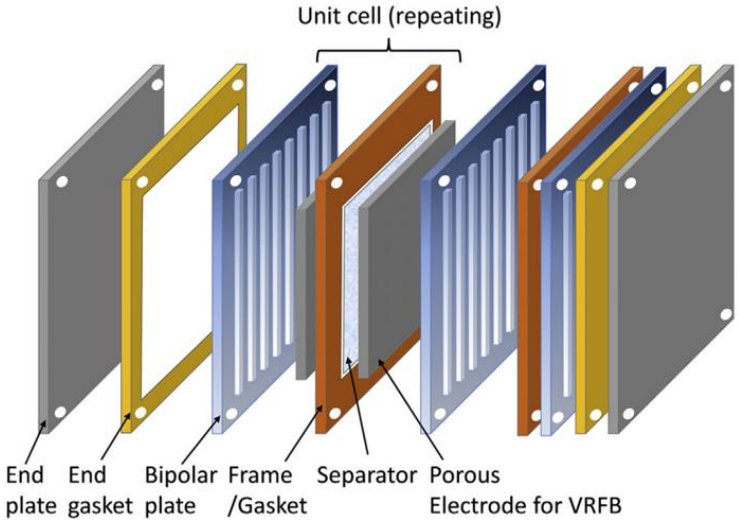

Figure 1.4. Representation of a RFB stack, with a repeating unit cell that consists of the bipolar plate, electrode, frame, and separator (ion exchange membrane) highlighted. For a VRFB, the electrode is generally porous. Image reproduced from Ha and Gallagher (2015).[17]

The set up described above results in the key advantages of the RFB. First, the RFB has enhanced delivery of the reactants to the electrode surface because the pumps can be used to control the flow rate of the active species. Additionally, there is less degradation of the RFB electrode material over time, because the active species is not a part of the electrode itself, which leads to a greater number of discharge cycles. Finally, the RFB has separation of power and energy components, because the power delivery of the RFB scales with the cell area, e.g., area of

membrane-electrode assembly. The energy storage capacity, however, scales with the availability of active species, which is related to the concentration and volume of the electrolyte. The separation of power and energy is unique to RFBs and is especially beneficial because the design of the RFB can be tuned to the specific energy storage needs of the application. Power-dependent components are generally noted to be expensive,[15] and so in applications where high rates of power delivery are not the priority, the cost of energy storage can be reduced. RFBs are also being considered for long-term energy storage applications (>10 hours[8,18]) because they become more economical at longer discharge times.

1.3.2 State-of-the-art aqueous redox flow battery

The most commercialized RFB is the VRFB, which has the two half-cell reactions shown in **Eq. 1.1a−b**, with the standard equilibrium redox potentials listed. While the thermodynamic potential of the VRFB would be 1.26 V based on the standard equilibrium redox potentials, the OCV has been observed experimentally to be 1.4 V at 50% SoC due to non-idealities, such as the Donnan potential at the membrane surfaces.[19] During charge, VO^{2+} is oxidized to VO_2^+ at the positive electrode and V^{3+} is reduced to V^{2+} at the negative electrode, while during discharge, VO_2^+ is reduced to VO^{2+} and V^{2+} is oxidized to V^{3+}. The VO_2^+/VO^{2+} redox couple is often referred to as the V^{4+}/V^{5+} redox reaction.

$$VO_2^+ + 2H^+ + e^- \rightleftarrows VO^{2+} + H_2O \qquad E^\circ = 1.00\ \text{V vs. SHE} \quad \textbf{(1.1a)}$$

$$V^{3+} + e^- \rightleftarrows V^{2+} \qquad E^\circ = -0.26\ \text{V vs. SHE} \quad \textbf{(1.1b)}$$

There are examples of pilot-scale VRFB projects,[6,19–21] and the largest VRFB energy storage project as of 2021 was a 200 MW/800 MWh VRFB in Dalian, China.[13,19] The VRFB has been so heavily developed because it is symmetric, meaning that the same active species is used

at both electrode compartments. This reduces the challenges associated with crossover of active species ions through the ion exchange membrane,[14] although it is noted that capacity fade due to crossover is still a technical challenge for VRFBs.[6] The energy density for VRFBs is reported to be approximately 25-35 Wh/L, and the roundtrip efficiency ranges between 85-90% in small single cells.[19] Typical current densities for the VRFB range between 80-100 mA/cm^2, but lab scale tests have reported current densities up to 1.5 A/cm^2.[19] Active areas of research for the VRFB include enhancing electrode kinetics through treatment of the carbon felt,[22] increasing active species concentrations through electrolyte research, and improved membranes that prevent crossover and increase conductivity.[19] A challenge identified with further integration of the VRFB into the electricity grid is its cost,[14] as will be discussed further below.

1.3.3 Other redox flow battery technologies of note

In this section, a brief description of other notable RFB technologies is given to provide a broader context of the research field of RFBs. In addition to the VRFB, other inorganic redox flow battery technologies (either pure or hybrid) that have been significantly developed include the iron (Fe)-chromium (Cr), zinc (Zn)-bromine (Br), and bromine-polysulphide chemistries.[14] The Fe-Cr system was first developed in the 1970s, and uses the Fe^{2+}/Fe^{3+} redox couple at the positive electrode (0.77 V vs. SHE) and the Cr^{2+}/Cr^{3+} redox couple at the negative electrode (−0.41 V vs. SHE).[15] The primary advantage of the Fe-Cr system is that the costs of its active species precursors are very low, on the order of \$0.1-\$1/kg.[23] It has a relatively low open circuit voltage, however, and the Cr^{2+}/Cr^{3+} kinetics are slow, requiring electrocatalysts.[15] The Zn-Br is considered a hybrid flow battery, because the Zn/Zn^{2+} redox reaction involves plating solid Zn onto the electrode, which means that power and energy will not scale independently. The Zn-Br system is considered the state-of-the-art hybrid RFB,[19] with demonstrations of MW sized Zn-Br systems.[13,15] The

Br^-/Br_2 redox reaction at the positive electrode occurs at 1.09 V vs. SHE, while the Zn/Zn^{2+} reaction occurs at −0.76 V vs. SHE, leading to a high open circuit voltage of 1.85 V and a theoretical specific energy of 440 Wh/kg.[19] Limitations of the Zn-Br RFB include the toxicity of the Br_2 electrolyte, the corrosive nature of HBr, and the tendency for dendrite formation.[15] In bromine-polysulphide systems, sodium bromine is the positive electrolyte (1.09 V vs. SHE), sodium polysulfide is the negative electrolyte (−0.265 V vs. SHE), and the charge carrier is the sodium ion.[15] While there are large scale demonstration projects on the order of 10 MWh/MW,[15] several challenges limit broader use of bromine-polysulphide RFBs. Crossover of both electrolyte solutions can lead to precipitation of sulfur species on the membrane as well as the formation of gases such as H_2S and Br_2.[14,15]

In addition to inorganic RFBs, which have dominated the market, both aqueous and non-aqueous organic redox flow batteries are being considered for energy storage applications,[24] although their successful scale-up and deployment has not been demonstrated.[25] Organic redox couples are a promising alternative to inorganic RFBs because of the natural abundance of their elemental components[19] and lower active species cost,[23] as well as their potential for molecular engineering, multiple electron transfer capability, and wider voltage windows.[24] Organic RFBs can be aqueous or non-aqueous, and non-aqueous organic RFBs specifically can have voltage windows significantly wider than the water stability limit.[25] Examples of aqueous organic redox couples include anthraquinone and benzoquinone which are estimated to cost between $1-$3/kg.[23] Examples of non-aqueous organic redox couples include 2,2,6,6-tetramethylpiperidine-1-oxyl (TEMPO), 2,1,3-benzothiadiazole (BzNSN), and quinoxaline.[24] A significant issue for both aqueous and non-aqueous organic RFBs is stability during cycling due to degradation reactions. For instance, the dihydroxyanthraquinone redox couple has been explored for use at the negative

electrode in aqueous organic RFBs and was found to undergo a disproportionation reaction which led to capacity fade.[23] A study of BzNSN in acetonitrile found that cycling resulted in increased viscosity and crossover, with the ultimate result of poor voltage and current efficiency of the BzNSN RFB.[24] While the study of organic RFBs is an active area of research, the focus of this thesis was to explore a chemistry that could be used in an aqueous, inorganic RFB application, given their proven capability to be scaled up and implemented in the market.

1.3.4 An ongoing challenge in aqueous redox flow batteries: Cost of energy storage

The U.S. Department of Energy (DOE) has established a target capital cost for stationary energy storage technologies of 150 $/kWh[26] for 5-hour storage. The capital costs of VRFBs, however, have been estimated to range between 300-600 $/kWh for discharge times ranging between 4 and 12 hours.[6,27–31] Additionally, the DOE has established a levelized cost of electricity (LCOE) target of 0.05 $/kWh for energy storage for the energy-dependent and power-dependent material, where LCOE is the average net present cost of electricity supplied over a product's lifetime.[32] The VRFB LCOE ranges between 0.16-0.50 $/kWh,[8,29,30,33,34] underscoring how uneconomical the VRFB currently is. The vanadium precursor salt V_2O_5 is identified as a significant contributor to total cost and is noted to be volatile in both price and supply.[7,19,35]

Given the pressing need for increased energy storage capacity and the promising attributes for RFBs for long duration energy storage applications, it is imperative that the cost of RFB energy storage be driven down relative to the state-of-the-art VRFB's costs. Strategies for reducing RFB capital costs and LCOE include decreasing overvoltages associated with kinetics,[28] mass transport, and ohmic losses[28] and exploring chemistries alternative to V^{2+}/V^{3+} and VO^{2+}/VO_2^{+} with less costly precursors[23,28] and larger voltage windows.[25,36] Perry at al. recently highlighted that OCVs greater than 1.5 V are possible even for aqueous RFBs through electrolyte maintenance and

electrode selection, and they demonstrated that for a generic RFB system with active species costs of $10/kg, an OCV greater than 2.5 V would result in 6-hour storage that met the $150/kWh DOE target.[25] If the active species cost were reduced to $5/kg, then an OCV of 2 V would be needed to achieve 4-hour $150/kWh storage.[25] Chemistries that demonstrate either more negative redox potentials than V^{2+}/V^{3+} or more positive redox potentials than VO^{2+}/VO_2^+ must be explored for RFB applications.

The cerium chemistry is a promising alternative to the VO^{2+}/VO_2^+ chemistry at the positive electrode of an RFB because it has a significantly higher redox potential, and its precursor cost is a fraction of the cost of V_2O_5. The Ce^{3+}/Ce^{4+} redox potential ranges between 1.44-1.74 V vs. SHE[37] depending on the acid used in the electrolyte, compared to VO^{2+}/VO_2^+ redox potential of 1 V. Thus, a battery that uses Ce as the positive electrolyte instead of V would have an extra 0.44-0.74 V of theoretical voltage, depending on the electrolyte selected. Additionally, the Ce precursor (CeO_2, ~1.9 $/kg[38]) is significantly less expensive than V_2O_5 (~22 $/kg[39]), satisfying the strategy to replace V_2O_5 with less expensive alternatives.

Despite these advantages to using Ce in RFB applications, there are several challenges that must be addressed before Ce could be implemented in RFBs, as will be described in more detail in the following section. Although the replacement of the VO^{2+}/VO_2^+ chemistry at the positive electrode of a VRFB with the Ce^{3+}/Ce^{4+} chemistry would result in an increased theoretical voltage, it is unclear how the overall cost of energy storage would be affected, because an in-depth study of how roundtrip efficiency would change has not been completed. A technoeconomic assessment based on the expected thermodynamic and kinetic performance of a Ce-based RFB that compares the Ce-based RFB's LCOE to a VRFB's is needed to determine whether additional research into Ce for RFB applications is warranted. The GHG emissions associated with the production and use

of a Ce-based RFB compared to a VRFB are also not well known and given the goal of using RFBs to decarbonize electricity, the life cycle GHGs for each RFB should be quantified. Additionally, the influence of the acid on the Ce^{3+}/Ce^{4+} redox potential is not well understood, limiting any efforts at tuning the Ce redox potential for optimal RFB performance. It is expected that the anions in the acid interact with the Ce^{3+} and Ce^{4+} ions, but the exact structures of the Ce ions are not well known in many acids relevant to RFB applications, motivating additional study to isolate the link between Ce^{3+} and Ce^{4+} structures in relevant acids and the observed shift in redox potential. Finally, the Ce^{3+}/Ce^{4+} kinetics are reported to be slow, and the charge transfer mechanism is not known, meaning that the factors that control the Ce^{3+}/Ce^{4+} electron transfer, e.g., electrolyte or electrode properties, are also not known. Carefully controlled kinetic measurements of the Ce^{3+}/Ce^{4+} electron transfer in relevant acidic media are needed to elucidate the charge transfer mechanism, which can be used to make predictions about the best performing electrolyte and electrode materials for Ce-based RFB applications. Background on the Ce^{3+}/Ce^{4+} is provided in the next section to provide context on the previous and current uses of Ce, as well as highlight the gaps in the relevant structural and kinetic literature that motivate the work conducted in this dissertation.

1.4 Ce^{3+}/Ce^{4+} chemistry background

Given the promising nature of the cerium chemistry for redox flow battery applications, the Ce^{3+}/Ce^{4+} redox couple should be seriously considered as a candidate for the positive electrolyte active species. A background on the Ce^{3+}/Ce^{4+} redox couple is provided in this section. Applications of the cerium chemistry, including energy storage, are discussed in **Section 1.4.1**, and previous studies of Ce-based RFBs as well as studies of the Ce^{3+}/Ce^{4+} redox potential, the structures of the Ce^{3+} and Ce^{4+} ions, and the Ce^{3+}/Ce^{4+} redox kinetics are all highlighted in **Section**

1.4.2. The remaining challenges with using Ce in RFBs, which motivate the work in this dissertation, are discussed in **Section 1.4.3**.

1.4.1 Applications of the Ce^{3+}/Ce^{4+} chemistry

As shown in **Fig. 1.5**, the cerium redox reaction between Ce^{3+} and Ce^{4+} (**Eq. 1.2**) has a myriad of applications, which stems primarily from its high redox potential (1.28-1.74 V vs. SHE, depending on the electrolyte).[37,40,41] Below, common uses of the cerium chemistry are described, and the concept of cerium in energy storage applications is introduced.

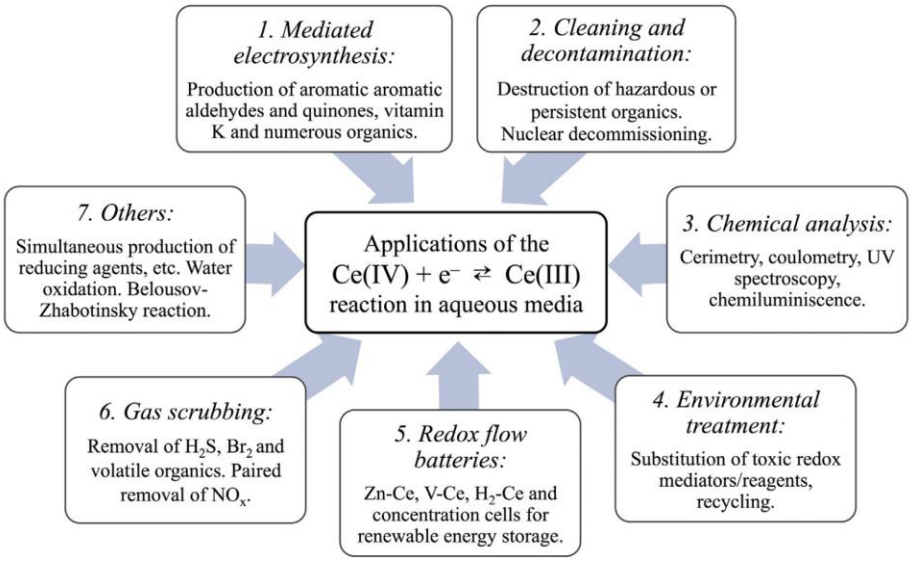

Figure 1.5. Applications of Ce^{3+}/Ce^{4+} redox couple. Image reproduced from Arenas et al. (2016).[37]

$$Ce^{4+} + e^- \rightleftarrows Ce^{3+} \qquad E^\circ = 1.28 - 1.74\ \text{V vs. SHE} \qquad \textbf{(1.2)}$$

The high redox potential of the Ce^{3+}/Ce^{4+} couple enables Ce^{4+} to be used in mediated electrosynthesis processes, in which Ce^{4+} indirectly oxidizes a range of organic molecules, e.g., anthracene oxidized to anthraquinone,[42] toluene or xylenes oxidized to benzaldehydes,[43] or naphthalene to naphthoquinone.[44] A benefit of the mediated electrosynthesis process is that Ce^{4+}

can be regenerated electrochemically.[37] This property also makes it useful in waste remediation applications,[37] including the destruction of organic contaminants such as methylene blue,[45] dichlorobenzene, xylene, and cyclohexanone.[46] Ce^{4+} has also been used in nuclear decontamination and decommissioning applications, because it can be used to strip radionuclides from steel vessels and pipelines used in a nuclear facility, as well as oxidize radionuclide-contaminated organics.[37] The ability to oxidize hazardous organics with Ce^{4+} also has important implications for use in the field of environmental treatment, including soil remediation and replacement of more toxic redox mediators and oxidants, e.g., chromium.[37] Similarly, Ce^{4+} has been used in gas scrubbers to oxidize noxious substances such as SO_2, NO_x, and H_2S,[37] and the cerium oxide, CeO_2, is used in automotive catalytic converters to convert CO to CO_2.[47,48] Other industrial uses for CeO_2 include acting as a glass additive,[49] in glass polishing applications,[49] and in casting alloys.[47]

Ce^{4+} has also been used in a number of chemical analyses, including volumetric[50] and potentiometric titration and chemiluminescence.[37] As will be described in more detail in **Chapter 2**, Ce^{4+} can be used to titrate Fe^{2+} directly, among other metals and organics. Additionally, Ce^{4+} redox titration can be used to complete volumetric analysis of a number of inorganic compounds that contain copper, molybdate, nitrate, and persulfate, and hydrogen peroxide.[37] Chemiluminescence methods for drugs such as acetaminophen, quinine, and chlorpromazine have been promoted through Ce^{4+} reduction.[37]

If the cerium chemistry is used in a positive electrolyte of a RFB, its high redox potential is expected to result in an increased difference in the positive and negative electrode potentials and therefore increase energy storage and power output relative to the state-of-the-art VRFB. As will be described in **Section 1.4.2**, a variety of Ce RFBs have been studied at the laboratory scale,

highlighting the potential chemistry combinations that could work for a Ce RFB as well as underscoring the need for additional economic, environmental, thermodynamic, and kinetic assessments. The uses of cerium described above highlight that cerium is relevant to a number of different fields. While this dissertation is focused on assessing the economic and environmental feasibility of a Ce-based RFB, which motivates the need for a greater understanding of the Ce^{3+} and Ce^{4+} structures in aqueous solutions and the Ce^{3+}/Ce^{4+} redox kinetics, a better fundamental understanding of the way Ce ions interact with their aqueous surroundings and behave during redox reactions will help to advance the use of Ce in a number of different industries.

1.4.2 Previous studies of the Ce^{3+}/Ce^{4+} chemistry relevant for RFB applications

In this section, relevant previous studies of the cerium chemistry are detailed, which will motivate the objectives of the thesis. Specifically, this section first focuses on the various Ce RFBs that have been studied at the laboratory scale and the Ce^{3+}/Ce^{4+} redox potential. We identify that a better understanding of what controls the Ce^{3+}/Ce^{4+} redox potential and charge transfer mechanism are needed to advance RFBs, which motivates our review of studies on the structure of Ce^{3+} and Ce^{4+} ions and the Ce^{3+}/Ce^{4+} kinetics.

Studies of the Ce^{3+}/Ce^{4+} redox flow batteries. Ce RFBs that have been studied at the laboratory scale include Zn-Ce, vanadium (V)-Ce, hydrogen (H_2)-Ce, and Ce concentration cell RFBs. The Zn-Ce cell was first patented by Plurion Inc,[51,52] and is noted to have one of the highest reported open circuit voltage values (>2.4 V) of any RFB, because of the very negative redox potential of the Zn/Zn^{2+} electrolyte and the high positive redox potential of Ce^{3+}/Ce^{4+}.[53] While this is promising thermodynamically, because the Zn-Cell RFB is a hybrid flow battery, the power and energy will not scale independently. The Zn-Ce cell has been studied primarily with the use of methanesulfonic acid (CH_3SO_3H, MSA) as the electrolyte,[53–56] but mixed H_2SO_4-MSA

electrolytes[57] and sulfamic acid[41] have also been researched. MSA has been the primary electrolyte studied because Ce is noted to have higher solubility in MSA than the more common RFB electrolyte H_2SO_4.[58] These lab-scale Zn-Ce cells have been operated at current densities ranging from 5-50 mA/cm^2,[54,55] and coulombic efficiencies and voltage efficiencies have been reported to range between 63%[54]-94%[55] and 47.5%[41]-84.5%,[57] respectively, depending on operating conditions. There have been fewer studies of V-Ce cells, but a study of a V-Ce cell in H_2SO_4 reported 87% coulombic efficiency and an open-circuit voltage after charging of 1.87 V,[59] and for a V-Ce cell with MSA as the positive electrolyte, a discharge current density of 14.3 mA/cm^2 and charge current density of 85.7 mA/cm^2 were achieved, and separately, a voltage efficiency of 46.5% was achieved.[60] Finally, the H_2-Ce cell has been explored using MSA as the positive electrolyte, and an energy efficiency of 90% and power density of 895 mW/cm^2 were reported.[61] While these lab scale studies demonstrate the feasibility of Ce-based RFBs, the kinetics of the Ce^{3+}/Ce^{4+} have been noted to be slow[55,62] which limits RFB performance.[61] To improve the Ce^{3+}/Ce^{4+} kinetics, the charge transfer mechanism must be determined, which will allow us to determine what parameters, e.g., the electrolyte or electrode, control the rate of reaction. Identification of the Ce^{3+} and Ce^{4+} structures in aqueous solutions will also aid efforts to identify the charge transfer mechanism. Thus, additional fundamental studies of the Ce^{3+}/Ce^{4+} structures and kinetics are needed. We provide a review of the work that has previously been done in the areas of Ce^{3+}/Ce^{4+} redox potentials, structures, and kinetics next.

Studies of the Ce^{3+} and Ce^{4+} redox potential. **Table 1.1** includes the redox potentials that have been reported for the Ce^{3+}/Ce^{4+} redox couple in literature. 1.28 V vs. SHE is the historically reported redox potential for Ce^{3+}/Ce^{4+} in 1 M HCl,[40] however, this value has been called into question[63,64] because of the Cl^-/Cl_2 redox reaction that will occur at similar potentials, which will

interfere with the measurement of the Ce^{3+}/Ce^{4+} redox potential. $HClO_4$ is known to be non-complexing, and so the value of 1.74 V vs. SHE can be taken to be the standard redox potential.[65]

Table 1.1. List of experimental redox potentials measured at 1 M acid. The redox potential for HCl is marked with an asterisk (*) due to the high degree of uncertainty in the value, as described in the text.

Acid	Standard redox potential, $E°$ (V vs. SHE)
$HClO_4$	1.74[66]
HNO_3	1.61[67]
MSA	1.61[37]
H_3NSO_3	1.52[41]
H_2SO_4	1.44[40,68]
HCl	1.28*[40,66]

The large shift in redox potential from the standard value of 1.74 V vs. SHE with acid suggests that the anions in solution are interacting with the Ce^{3+} and Ce^{4+} ions to influence the thermodynamics. If it were known whether Ce^{3+} or Ce^{4+} or both ions were complexing with anions in solution, then predictions about the effect of complexation strength on redox potential could be made for additional electrolytes, offering a unique opportunity to tune the Ce^{3+}/Ce^{4+} redox potential and thus the voltage window of the RFB with electrolyte choice. Thus, understanding the structure of the Ce ions in aqueous solutions that are relevant for battery applications is a crucial step towards increasing the thermodynamic performance of Ce-based RFBs. We discuss the previous studies that have investigated the Ce^{3+} and Ce^{4+} ionic structures next and highlight the gaps in which more work is needed next.

Studies of the Ce^{3+} and Ce^{4+} ion structures. The data in **Table 1.2** summarize the Ce^{3+} structures reported in literature, with mixed reports about whether Ce^{3+} complexes with anions. Although an early EXAFS study of L_1, L_2, and L_3 edges of rare earth metals indicates that Ce^{3+} is coordinated by 12 water molecules,[69] this finding was later discounted because of the use of chloride rare-earth salts,[70] which likely distorted the EXAFS data. Density functional theory (DFT)

calculations using the B3LYP functional predict that Ce^{3+} is hydrated by eight or nine water molecules in the first coordination shell, with a water exchange free energy from eight to nine being downhill by –16.7 kJ mol^{-1}.[71] Quantum mechanical charge field molecular dynamics predictions of Ce^{3+} in pure water find an average first shell coordination number of 9.1 waters with the first shell maxima located at 2.61 Å.[72]

A kinetic photolysis study indicates that up to five nitrate anions would complex to each Ce^{3+} ion in solutions ranging from 0.1 to 15 M HNO_3,[73] and Raman spectroscopy of Ce^{3+}-nitrate in the glassy state at high [NO_3^-] indicates that $Ce(NO_3)^{2+}$ and $Ce(NO_3)_2^+$ complexes are present.[74] A cation-exchange resin experiment suggests the presence of two Ce^{3+}-$(SO_4^{2-})_y$ (y = 1 or 2) complexes.[75] UV-Vis data collected in the 1950s suggest that Ce^{3+} complexes with one sulfate ion at low sulfuric acid concentrations.[76] More recent spectroscopy studies have also been used to study the Ce^{3+} structure in aqueous solutions. Fourier Transforms of EXAFS data of the Ce^{3+} L_3-edge indicate that at higher chloride concentrations (14 M LiCl), Ce^{3+} complexes with chloride (coordination number ~1.8),[77] but at lower concentrations (0.2 M), Ce^{3+} has an average coordination number of 9.3 water molecules. Raman spectroscopy verifies that 1 or 2 chloride ions could complex with Ce^{3+} (in concentration range of 0.27 M–2.17 M $CeCl_3$), but that Ce^{3+} is fully hydrated at lower concentrations (0.1 M Cl^-).[78] Raman spectroscopy of the Ce^{3+} ion in 0.202 M perchloric acid shows that Ce^{3+} is fully hydrated by nine water molecules, but at higher concentrations of perchloric acid (> 1.5 M), outer-sphere ion and contact ion pairs between Ce and perchlorate ions form.[78] EXAFS of the Ce^{3+} K- and L_3-edge in 0.1 M trifluoromethanesulfonic (triflic acid, TFSA) also suggest that Ce^{3+} is hydrated by nine water molecules.[79]

Table 1.2. Summary of Ce^{3+} complexes reported in various aqueous media, along with experimental conditions, methods, and references.

Electro-lyte/anion	Anion Concentration	Structure	Ce^{3+} Concentration	Method & Reference
Water	NA	$Ce(H_2O)_x^{3+}$, x = 8 or 9; square antiprism or tricapped trigonal bipyramid	NA	DFT and complete active space self-consistent field (CASSCF)[71]
	NA	$Ce(H_2O)_x^{3+}$, $x \approx 9.1$; Ce-O bond length: 2.61 Å; tricapped trigonal prism or capped square antiprism	One Ce^{3+} ion, 1000 water molecules	Quantum mechanical charge field molecular dynamics[72]
ClO_4^-	0.202 M	$Ce(H_2O)_9^{3+}$; Ce–O bond length: 2.57 Å	202 mM	Raman[78]
	>1.5 M	$Ce(H_2O)_9^{3+}$; outer-sphere-ion pairs and contact-ion pairs present	1678 mM	
NO_3^-	0.1 M–15 M	$Ce(NO_3)^{2+}$, $Ce(NO_3)_2^+$, $Ce(NO_3)_3$, $Ce(NO_3)_4^-$, $Ce(NO_3)_5^{2-}$	~4 mM	Kinetic photolysis study; chemical model[73]
	20 mol H_2O/mol salt	$Ce(NO_3)^{2+}$ and $Ce(NO_3)_2^+$	Solid glassy state; 20 mol H_2O/mol salt	Raman[74]
SO_4^{2-}	0.004 M–0.3 M	$Ce(SO_4)^+$	2 mM to 10 mM	UV-Vis[76]
	< 0.05 M	$Ce(SO_4)^+$ and $Ce(SO_4)_2^-$	> 100 mM	Cation-exchange resin experiment[75]
Cl^-	0.05, 0.10, 0.20 M	$Ce(H_2O)_{12}^{3+}$	50, 100, 200 mM	EXAFS of Ce L_3-edge[69]
	0.2 M	$Ce(H_2O)_x$, $x \approx 9.3$	100 mM	EXAFS of Ce L_3-edge[77]
	14 M	$Ce(H_2O)_{9-x}Cl_x$, $x \approx 1.8$; Ce-Cl bond length: 2.89 Å	100 mM	
	0.5 M NaCl, 0.1 M extractant (dodecylphenyl-methyl-β-diketone or LIX 54)	No Cl complexes formed	> 500 mM	Extraction from NaCl solution with LIX 54 in n-heptane[80]
	0.81 M–6.5 M	$Ce(H_2O)_{9-x}Cl_x$, x = 1 or 2	270 mM to 2167 mM	Raman[78]
$CF_3SO_3^-$	0.1 M	$Ce(H_2O)_9(CF_3SO_3)_3$; Ce–O bond length: 2.541 Å; tricapped trigonal-prism	200 mM	EXAFS of Ce L_3-edge[79]

The data in **Table 1.3** summarizes the structures of Ce^{4+} reported in literature and shows that Ce^{4+} complexes with anions in most acids. Like Ce^{3+}, Ce^{4+} is also hydrated by nine water molecules in pure water based on Quantum mechanical charge field molecular dynamics simulations.[70] The $Ce(H_2O)_9^{4+}$ is predicted to adopt a tricapped trigonal prismatic or capped square antiprismatic geometry.[70] The average Ce^{4+}-O bond length is calculated to be 2.44 Å.[70]

In 6 M $HClO_4$, Ce^{4+} prepared from ammonium nitrate salts is shown through EXAFS measurements of the Ce^{4+} L_2 and L_3 edges[81] to also have a Ce-O coordination number of approximately nine, with an average Ce^{4+}-O bond length of 2.42 Å.[81] Other studies in perchloric acid, however, suggest the presence of Ce^{4+} dimers. UV-Vis studies indicate that Ce^{4+} forms dimers in perchloric acid (possibly $[Ce\text{-}O\text{-}Ce]^{6+}$, $[HOCe\text{-}O\text{-}CeOH]^{4+}$, or $[Ce\text{-}O\text{-}CeOH]^{5+}$), based on the fact that extinction coefficients are not linear with increasing ceric ion concentrations, as predicted by Beer's Law.[82,83] The presence of Ce^{4+} dimers is also suggested in a kinetic study of the Ce^{3+}/Ce^{4+} redox couple in 0.5 M $HClO_4$, which finds that the heterogeneous rate of electron transfer between Ce^{3+} and Ce^{4+} is proportional to the square of the ceric ion concentration.[84] EXAFS measurements of the Ce^{4+} K-edge in 2 M $HClO_4$ suggest that dimers are present based on the presence of a secondary peak of the Fourier Transform of the EXAFS data around 4 Å.[85] DFT-based free energy calculations predict that a mixture of three dimers (single OH-bridging, double OH-bridging, or single oxo-bridging) is energetically possible.[85] Although complexes between the Ce^{4+} ion and perchlorate anions do not form, the presence of dimers in perchloric acid could be indicative of the structure of Ce^{4+} ion other electrolytes. XRD studies of both solution-based and crystal ceric ammonium nitrate conducted in the 1960s indicate the structure of Ce^{4+} in nitric acid to be monomeric ($[Ce(NO_3)_6]^{2-}$),[86,87] but more recent EXAFS studies of the Ce^{4+} L_1- and L_3-edges find that dimeric forms of Ce^{4+} in nitric acid are possible,[88,89] which is confirmed with Raman

spectroscopy.[88] Unlike in perchloric acid and nitric acid, transference measurements of ceric sulfate[90] and UV-Vis measurements of Ce^{4+} ions in various concentrations of H_2SO_4 indicate that Ce^{4+} is complexed sulfate, with reports ranging between 1, 2, or 3 sulfate ions, depending on the concentration of H_2SO_4.[91,92] A study using DFT to understand the competitive complexation of Ce^{4+} with chloride as compared to pyridine reports an exothermic free energy when Ce^{4+} is complexed by six Cl^- ions, with a Ce^{4+}-Cl bond of 2.68 Å.[93]

Table 1.3. Summary of the Ce^{4+} complexes reported in various aqueous media, along with experimental conditions, methods, and references.

Electro-lyte/anion	Anion Concentration	Structure	Ce^{4+} Concentration	Method & Reference
Water	NA	$Ce(H_2O)_9^{4+}$; Ce^{4+}-O bond distance: 2.44 Å; tricapped trigonal prism, capped square antiprism	50 mM	QMCF-MD[70]
ClO_4^-	~1 M	$(Ce\text{-}O\text{-}Ce)^{6+}$, $(HOCe\text{-}O\text{-}CeOH)^{4+}$, or $(Ce\text{-}O\text{-}CeOH)^{5+}$	12 mM	UV-Vis[82]
	4 M	Ce^{4+}, $CeOH^{3+}$, $(Ce\text{-}O\text{-}Ce)^{6+}$	1.3 mM–13.6 mM	UV-Vis[83]
	0.5 M	Dimer possible	> 0.4 mM	Kinetic study[84]
	2 M	Dimers (single OH-bridging, double OH-bridging, single oxo-bridging)	50 mM	EXAFS of Ce K-edge[85]
NO_3^-	6 M $HClO_4$, 0.01−0.1 M NO_3	$Ce(H_2O)_x^{4+}$, $x \approx 9.1$; Ce^{4+}-O bond length: 2.42 Å	10, 20, 50, 100 mM	EXAFS (Ce L_3- and L_2-edges)[81]
	53.7% weight ceric ammonium nitrate (CAN)	$Ce(NO_3)_6^{2-}$	53.7% weight CAN	XRD of solution based CAN[86]
	3 M	Mixture (e.g., Ce^{4+}, $Ce(NO_3)^{3+}$, $Ce(NO_3)_2^{2+}$, $[(H_2O)_{6\text{-}7}Ce\text{-}O\text{-}Ce(OH_2)_{6\text{-}7}]^{6+}$)	40 mM	EXAFS (Ce L_1, L_3 edges), Raman[88,89]
SO_4^{2-}	0.123-0.663 M	$HCe(OH)_3SO_4$, $Ce(SO_4)_2$-$4H_2O$	5.1-94 mM	Transference[90]
	> 0.01 M	$Ce(SO_4)^{2+}$	2 mM–30 mM	UV-Vis [91]
	> 0.7 M	$Ce(SO_4)^{2+}$, $Ce(SO_4)_2$, $Ce(SO_4)_3^{2-}$	0.16 mM–5.2 mM	UV-Vis [92]
Cl^-	0.5 M–12 M	$CeCl_6^{2-}$; Ce-Cl bond length: 2.68 Å	Not reported	DFT modelling[93]

From the reviewed studies, there are uncertainties in the structures of both Ce^{3+} and Ce^{4+} in the acidic media that are relevant for RFBs. Specifically, while much of the literature points to Ce^{3+} being coordinated by only water molecules, there are some studies that suggest Ce^{3+} will complex with sulfate and nitrate anions in sulfuric acid and nitric acid, respectively, especially at higher anion concentrations. It is recognized that Ce^{4+} will be complexed by anions in acids other than perchloric acid, but the exact number of anions complexing is unclear. Additionally, some studies suggest dimers will form. A clearer understanding of the structures of Ce^{3+} and Ce^{4+} in acids will be necessary to understanding the influence of the acid on the Ce^{3+}/Ce^{4+} redox couple, and structural information will also be important when studying the charge transfer mechanism. A stronger fundamental understanding of the Ce ionic structures will thus provide guidance on how best to control a Ce-based RFB's thermodynamic and kinetic performance. In addition to knowing the structures, it is also important to have a clear picture of how the Ce^{3+}/Ce^{4+} kinetics behave as a function of electrolyte and electrode to determine the charge transfer mechanism. Previous Ce^{3+}/Ce^{4+} kinetic studies will therefore be discussed next.

Studies of the Ce^{3+}/Ce^{4+} redox kinetics. **Table 1.4** shows the kinetic activities reported previously for the Ce^{3+}/Ce^{4+} redox couple for many different electrode-electrolyte combinations. Although many electrode materials have been studied for the Ce^{3+}/Ce^{4+} redox reaction, including metals (Au, Pt, Ir, Pt/Ti, Pt/Nb), alloys (Pt-Ir, RuO_x-IrO_x-TiO_x), metal oxides (SnO_2, WO_3/C, TiO_2, PbO_2, SnO_2/Ti, IrO_x-Ti, RuO_x-Ti) and carbon materials (diamond, glassy carbon, graphite rods and felts),[37,42,61,94–101] the reported kinetic parameters vary widely depending on the type of surface (mesh, rotating disk electrode, wire), temperature, electrolyte, and SoC. For the Ce^{3+}/Ce^{4+} redox chemistry, SoC refers to the amount of Ce^{4+} relative to the total cerium concentration. The lack of consistent conditions under which the kinetic parameters are measured and reported makes it

difficult to directly compare different electrode surfaces. Understanding the influence of the electrode on kinetics is an important step to determining whether the charge transfer mechanism is inner- or outer-sphere. When an electron transfer is inner-sphere, the active species has to interact directly with the electrode surface for the electron transfer to occur, whereas for an outer-sphere mechanism, the active species is always separated by a layer of solvent.[102] Additionally, literature values are often not reported normalized to surface area with standard experimental conditions, making it impossible to compare intrinsic rates. From **Table 1.4**, there are conflicting reports of activity, for example, in one work reported standard rate constants vary from 2.0×10^{-6} to 4.0×10^{-2} cm/s depending on the electrode in the order of glassy carbon >> graphite > iridium > platinum > gold > diamond,[95] and in another, Ir was reported to have a larger rate constant (4.0×10^{-4}) than Au (2.0×10^{-4}).[101] Thus, the inconsistent values in current literature make it difficult to ascertain the influence of electrode on the redox reaction kinetics. There is a need for a more controlled kinetic study of the Ce^{3+}/Ce^{4+} redox kinetics, so that the effect of the electrode can be more clearly obtained and the charge transfer mechanism can be ascertained. Knowledge of the Ce^{3+}/Ce^{4+} charge transfer mechanism will help to inform the design of future Ce-based RFBs for enhanced kinetic performance by indicating what factors control the kinetics.

Table 1.4. Kinetics parameters for Ce^{3+}/Ce^{4+} charge transfer for different electrodes and electrolytes, through different measurement methods. Kinetic parameters reported include standard rate constant, k_0, exchange current density, i_0, the split between reduction and oxidation peaks, ΔE_p, and anodic and cathodic charge transfer coefficients, α_a and α_c. In the main text we are referring to cathodic charge transfer when we report the charge transfer coefficient.

Electrode	Electrolyte		$[Ce^{3+}]$ (M)	$[Ce^{4+}]$ (M)	Method	Kinetic Parameters					Ref
	Acid	[Acid] (M)				$k_0 \times 10^4$ (cm s^{-1})	$i_0 \times 10^2$ (mA cm^{-2})	ΔE_p (mV)	α_a	α_c	
Au	$HClO_4$	1	0.01[b]	0.001–0.01[b]	Polarization resistance; Ce^{4+} reduction	3.0	2–4	–	0.65±0.1	–	[100]
	H_2SO_4	1	–	0.010	Radiochemical & Cyclic Voltammetry (CV); Ce^{4+} reduction	1.8-2.1[a]	–	–	–	0.33	[101]
		1	0.01[b]	0.0001–0.001[b]	Polarization resistance; Ce^{4+} reduction	3.8	9–29	–	0.65±0.1	–	[100]
		1	–	0.001 – 0.01	Tafel; Ce^{4+} reduction	39	–	–	–	0.16	[103]
		0.5	0.02	–	Current-Overpotential curve; Rotating Disk Electrode (RDE); Ce^{3+} oxidation	0.73	–	–	–	0.16	[104]
		0.5	0.0013	0.0013	CV; Koutecký-Levich; Tafel	6.2-14.2[c]	–	–	0.12-0.13[c]	–	[105]
Boron-doped Diamond	$HClO_4$	0.1	0.01	–	CV; Current-Overpotential curve; Ce^{3+} oxidation	0.16	1.5	–	0.29	–	[106]
	HNO_3	0.1	0.01	–	CV; Current-Overpotential curve; Ce^{3+} oxidation	0.14	1.4	–	0.27	–	[106]
	H_2SO_4	0.1	0.01	–	CV; Current-Overpotential curve; Ce^{3+} oxidation	0.02	0.19	–	0.28	–	[106]
Graphite	H_2SO_4/MSA	1:1	0.2	0.2	CV; Linear Sweep Voltammetry (LSV); Current-Overpotential curve	4.17	810	–	–	–	[57]
	MSA	2	0.25	0.25	CV; LSV; Current-Overpotential curve; Chronoamperometry	4.06	980	–	–	–	[56]
		1	0.05	–	CV	0.992	–	410	–	–	[99]
Glassy Carbon	$HClO_4$	1	–	0.167	CV	–	–	290	–	–	[107]
	HNO_3	1	0.02	–	CV	20	–	–	–	–	[108]
		1	–	0.167	CV	–	–	260	–	–	[107]
		4	0.02	–	CV; LSV; Ce^{3+} oxidation	–	0.5	200	0.91	–	[109]
	H_2SO_4	1	–	0.010	Radiochemical & CV; Ce^{4+} reduction	2.4-4.0[a]	–	–	–	0.25	[101]
		1	0.01	–	CV	–	–	261	–	–	[59]
		1	–	0.167	CV	–	–	220	–	–	[107]
		0.5	0.02	–	Current-Overpotential curve; RDE; Ce^{3+} oxidation	0.87	–	–	–	0.49	[104]
		1	0.012	–	CV	–	–	1200	–	–	[62]

Table 1.4. Continued											
Glassy Carbon	MSA	1	0.034	–	CV	35.2-36.8[(d)]	–	–	–	–	[42]
		4	0.034	–	CV	58.0-85.4[(d)]	–	–	–	–	[42]
		1	–	0.167	CV	–	–	290	–	–	[107]
Ir	H_2SO_4	1	–	0.010	Radiochemical & CV; Ce^{4+} reduction	3.2-4.3[(a)]	–	–	–	0.26	[101]
Pt	H_2SO_4	0.5	0.019	0.003–0.044	Current-Overpotential curve; Butler Volmer (BV) formulism; Ce^{4+} reduction	0.75-1.21	–	–	–	0.12-0.13	[94]
		0.5	0.004–0.058	0.007	Current-Overpotential curve; BV formulism; Ce^{3+} oxidation	0.35-1.01	–	–	0.59-0.87	–	[94]
		1.25	0.2	0.2	CV	2.96	–	–	0.197	0.16	[110]
		2	0.0013	0.0013	CV; Koutecký-Levich; Tafel	8.2	–	–	0.17	–	[105]
		0.5	0.02	–	Current-Overpotential curve; RDE; Ce^{3+} oxidation	0.35	–	–	–	0.3	[104]
		0.5	0.01	–	RDE; Levich equation	3.7	–	–	–	0.21	[111]
		1	0.0001	0.001	Koutecký-Levich; RDE; Ce^{4+} reduction	–	13×10^5	–	–	0.3	[112]
		0.5	0.16	0.012	RDE; Tafel	3.7	–	–	0.4-0.6	0.2	[113]
		1	–	0.1	CV; Electrochemical Impedance Spectroscopy (EIS)	1.6	–	–	–	–	[114]
		1	–	0.1	CV; Levich plot	1.6	–	270	–	0.31	[115]
	H_2SO_4/ $C_7H_6O_6S$	1:0.5	0.0005	0.0005	CV; Current-Overpotential curve	3.2	310	97	–	–	[116]
	H_2SO_4/ DTPA[(e)]	1:0.03	–	0.1	CV; Levich plot	3.1	–	270	–	0.42	[115]
	H_2SO_4/ MSA	1:1	0.02	–	CV; LSV; Current-Overpotential curve	–	–	103	–	–	[57]
	MSA	2	0.25	0.25	CV; LSV; Current-Overpotential curve; Chronoamperometry	0.55	130	–	–	–	[56]
		4	0.8	–	CV	–	–	738	–	–	[55]
		4.5	0.02	0.2	CV; LSV; EIS	–	37×10^5 (Tafel), 24×10^5(EIS)	–	–	–	[117]
		4.5	0.2	0.6	Tafel method, Linear polarization, EIS	–	24-67[(g)]	–	–	–	[96]
	NH_2SO_3H	1	0.3	0.1	CV; LSV; Current-Overpotential curve; Tafel	0.5	60	–	–	–	[41]

Table 1.4. Continued											
SnO_2 on graphite felt	MSA	1	0.05	–	CV	499	–	199	–	–	[99]
VCE[f]	HNO_3	1	0.015	–	CV	20	–	–	–	–	[118]

(a) A range of rate constants is provided for electrodes studied by Keikens et al.[101] because several independent methods of calculating the rate constant were compared.
(b) Reported in Normality (N), converted to Molarity (M).
(c) In study by Sacchetto et al.,[105] the electrochemical behavior on a gold electrode was reportedly irreproducible, so kinetic parameters of the two extreme cases of behavior are reported here.
(d) A range of rate constants is provided by Devadoss et al.[42] based on scan rate used in CV.
(e) Diethylenetriaminepentaacetic acid.[115]
(f) Vitreous carbon electrode.[118]
(g) In study by Nikiforidis et al.,[96] three different exchange current densities were reported because of different methods of collecting exchange current density.

1.4.3 Ongoing challenges with using the Ce^{3+}/Ce^{4+} chemistry in redox flow battery systems

As described above, the redox potential of the Ce^{3+}/Ce^{4+} couple is higher than many other redox couples, ranging between 1.28-1.44 V vs. SHE in aqueous media, which makes it very promising for use in RFB applications. While some laboratory scale studies of Ce RFBs have been conducted which highlight its technical feasibility, no detailed study of the expected cost and emissions of a Ce RFB throughout its lifetime compared to the state-of-the-art VRFB has been conducted. Only one preliminary cost assessment of a Ce RFB exists,[119] but it is lacking in detail and does not consider the impact of the electricity grid mix on overall cost of storage. This study also compares the production phase GHG emissions of a Ce-Zinc (Zn) RFB to the VRFB,[119] and it shows that the Ce-Zn electrolyte has higher GHG emissions than the VRFB in the production phase. Given the goal of using energy storage to integrate renewable energy into the electricity grid to drive down GHG emissions from energy production, we need to confirm that the use of a Ce RFB will not result in increased GHG emissions. In the aforementioned study, however, the use phase is not considered, limiting our understanding of the relative environmental impacts of Ce and V-based RFBs. A detailed comparison of the Ce RFB's cost and GHG emissions to the VRFB's on a normalized basis, i.e., 1 kWh delivered electricity, is needed to quantify the savings (or consequences) expected for switching to a Ce RFB. Without a technoeconomic and life cycle assessment study of Ce-based RFBs, the field of Ce RFBs will remain relatively nascent, because the magnitude of cost and emissions savings relative to the VRFB are unknown. It will only be with a detailed economic and environmental assessment proving the feasibility of using Ce^{3+}/Ce^{4+} at the positive electrode that the Ce RFB can be advanced significantly.

In addition to confirming the economic and environmental feasibility of a Ce RFB compared to the state-of-the-art VRFB, it is important to gain a better fundamental understanding

of the behavior of the Ce^{3+} and Ce^{4+} ions during the electron transfer so that the thermodynamic and kinetic performance of the Ce RFB can be optimized. The large shift in redox potential with acid suggests that the anions in the acid are interacting with the Ce ions and controlling the thermodynamics. The structures of the Ce^{3+} and Ce^{4+} ions are not well understood, however, which limits our understanding of why the redox potential shifts so dramatically and also our ability to control Ce-based RFB thermodynamics. Ideally, if the structures of Ce^{3+} and Ce^{4+} are known for a variety of aqueous media, then the redox potential can be tuned by manipulating those structures through electrolyte engineering. Thus, there is a need for a better understanding of how the Ce^{3+} and Ce^{4+} ions interact with their surrounding aqueous environment to advance the thermodynamic performance of Ce RFBs. Additionally, the kinetics of the Ce^{3+}/Ce^{4+} redox reaction have been noted to be slow in Ce RFBs. To improve the kinetics, the charge transfer mechanism, which will indicate the rate limiting step and demonstrate the relative effect of the electrolyte and electrode on the kinetics, must be identified. Currently, the Ce^{3+}/Ce^{4+} the charge transfer mechanism is not well understood. To enhance the overall performance of a Ce-based RFB, the kinetics should be increased as much as possible, and so the charge transfer mechanism must be identified. There is thus a need to better understand the fundamental phenomena that are controlling the Ce^{3+}/Ce^{4+} thermodynamics and kinetics, so that the application of using Ce in RFBs can be advanced, which is needed to meet the growing demand for energy storage in the U.S.

1.5 Research objectives and scope

The overall goal of the dissertation was to characterize the Ce^{3+}/Ce^{4+} chemistry for RFB applications in terms of its economic impact, environmental performance, thermodynamics, and kinetics. To achieve this goal, the following main objectives were developed:

1. Assess the economic and environmental performance of the Ce-V RFB compared to the VRFB for current and future low-carbon energy storage applications.

2. Identify the structure of Ce^{3+} and Ce^{4+} ions in acids relevant to RFB applications and identify how the ion structures and interaction with surrounding anions influence thermodynamics.

3. Conduct carefully controlled kinetic measurements of the Ce^{3+}/Ce^{4+} redox couple on two different electrode surfaces to ascertain the effect of the electrode on kinetics.

4. Identify possible charge transfer mechanisms, and by comparing the derived rate laws' modeled performance to observed structural and kinetics information, identify which charge transfer mechanism is most consistent.

5. Make recommendations based on modeling and experimental results about further research and optimization efforts for the Ce RFB.

The dissertation consists of six chapters and is structured as outlined below:

Chapter 1 motivates the need for redox flow batteries to address the gap between the current available stationary energy storage capacity in the U.S. and the needed amount for increased integration of renewable energy into the electricity grid. This Chapter overviwed the redox flow battery technology as well as the state-of-the-art aqueous inorganic RFB, the VRFB, which is currently too costly for widescale market deployment. I proposed the Ce^{3+}/Ce^{4+} redox couple as a possible alternative to the active species in the positive electrolyte of the RFB and provide a background on the applications and research studies of the Ce^{3+}/Ce^{4+} chemistry. I motivated the need for additional study of the economic and environmental impact of a Ce RFB relative to the VRFB, as well as the structure, kinetics, and charge transfer mechanism of the Ce^{3+}/Ce^{4+} chemistry to optimize the Ce RFB.

Chapter 2 overviews the methods and theory behind the techniques used in the dissertation. Specifically, the concepts of technoeconomic and life cycle assessment techniques are introduced, and the theories of UV-Vis and Extended X-ray Absorption Fine Structure spectroscopy are discussed. Additionally, methods to determine the concentration of Ce ions in solution are presented, as are electrochemical techniques used to measure the kinetics of the Ce^{3+}/Ce^{4+} reaction. Finally, methods to model the kinetic behavior are discussed.

Chapter 3 presents the results of our technoeconomic and life cycle inventory model comparing the levelized cost of electricity (LCOE) and levelized GHG emissions (LGHG) of a Ce-V and VRFB battery. We find that the Ce-V RFB has lower LCOE than the VRFB and comparable LGHG assuming the current average U.S. electricity mix, and that as the grid becomes more renewable, the Ce-V RFB will continue to be more economical than the VRFB. Because Ce has higher production emissions than V, however, we find that in a 100% renewable grid scenario, while the GHG emissions are still drastically reduced compared to the present-day average U.S. electricity mix, the Ce-V RFB has a higher LGHG than the VRFB. Finally, we find that both the Ce-V RFB LCOE and LGHG are most sensitive to redox potential, and we demonstrate the tradeoff between material cost and thermodynamic and kinetic performance.

Chapter 4 discusses the structures and free energies of the Ce^{3+} and Ce^{4+} ions in aqueous media ($HClO_4$, HNO_3, CH_3SO_3H, CF_3SO_3H, H_3NSO_3, H_2SO_4, and HCl) that are relevant for RFB applications. We use Extended X-ray Absorption Fine Structure (EXAFS), UV-Vis, and Density Functional Theory (DFT) calculations to identify the structures and calculate the free energies. We find that Ce^{3+} coordinates with nine water molecules as $[Ce(H_2O)_9]^{3+}$ in all studied electrolytes. However, Ce^{4+} complexes with anions in all electrolytes except $HClO_4$. Thus, our results suggest that Ce^{4+}-anion complexation leads to the large shifts in standard redox potential.

Chapter 5 studies the structure, kinetics, and charge transfer mechanism of the Ce^{3+}/Ce^{4+} redox couple in sulfuric acid. We confirm the Ce^{3+} and Ce^{4+} structures and identify the charge transfer mechanism in sulfuric acid via EXAFS, kinetic measurements, and DFT calculations. We show EXAFS evidence that confirms the Ce^{3+} is coordinated by nine waters and suggests Ce^{4+} is complexed by water and three bisulfates in sulfuric acid. Despite the change in complexation within the first coordination shell between Ce^{3+} and Ce^{4+}, we show the kinetics are independent of the electrode (studied on platinum and glassy carbon), suggesting outer-sphere electron transfer behavior. We identify a two-step mechanism where Ce^{4+} exchanges the bisulfate anions with water in a chemical step followed by a rate-determining electron transfer step that follows Marcus theory, which we call the *CE* mechanism. This mechanism is consistent with all experimentally observed structural and kinetic data. The asymmetry of the Ce^{3+}/Ce^{4+} charge transfer and the observed shift in the redox potential with acid is explained by the addition of the chemical step in the charge transfer mechanism. The fitted parameters from this rate law qualitatively agree with DFT-predicted free energies and the reorganization energy.

Chapter 6 summarizes the major findings of the thesis and presents an outlook for the use of the Ce^{3+}/Ce^{4+} chemistry in RFB applications. Specifically, given our findings on the sensitivity of the Ce-V RFB LCOE and GHG emissions to the redox potential, and the effect of complexation on redox potential and the kinetics (for a *CE* mechanism), I propose that the Ce^{3+}/Ce^{4+} redox couple be studied in additional acids with weaker complexation than sulfuric acid to optimize both the thermodynamics and kinetics for RFB applications. Limitations of the work are also highlighted, and future work is proposed to address them.

1.6 References

1. U.S. Energy Information Administration. *Annual Energy Outlook 2021*. (2021).
2. International Renewable Energy Agency. *Global energy transformation: A roadmap to 2050*. (2018).
3. IRENA. *Innovation landscape brief: Flexibility in conventional power plants*. (2019).
4. Heshmati, A. Demand, customer base-line and demand response in the electricity market: A survey. *J. Econ. Surv.* **28**, 862–888 (2014).
5. Dwyer, C. O., Member, S., Flynn, D. & Member, S. Using energy storage to manage high net load variability at sub-hourly time-scales. *IEEE Trans. Power Syst.* **30**, 2139–2148 (2015).
6. Rodby, K. E. *et al.* Assessing the levelized cost of vanadium redox flow batteries with capacity fade and rebalancing. *J. Power Sources* **460**, 227958 (2020).
7. Rodby, K. E., Perry, M. L. & Brushett, F. R. Assessing capacity loss remediation methods for asymmetric redox flow battery chemistries using levelized cost of storage. *J. Power Sources* **506**, 230085 (2021).
8. Hunter, C. A. *et al.* Techno-economic analysis of long-duration energy storage and flexible power generation technologies to support high-variable renewable energy grids. *Joule* **5**, 2077–2101 (2021).
9. Mai, T. *et al. Renewable Electricity Futures Study. Volume 1: Exploration of High-Penetration Renewable Electricity Futures*. vol. 1 (2012).
10. Center for Sustainable Systems University of Michigan. *U. S. Grid Energy Storage Factsheet*. (2021).
11. U.S. DOE Water Technologies Office. *U.S. Hydropower Market Report*. (2021).
12. Akhil, Abbas AHuff, G. *et al. DOE/EPRI Electricity Storage Handbook in Collaboration with NRECA*. (2015).
13. Rahman, M., Oni, A. O., Gemechu, E. & Kumar, A. Assessment of energy storage technologies: A review. *Energy Convers. Manag.* **223**, 113295 (2020).
14. Skyllas-Kazacos, M., Chakrabarti, M. H., Hajimolana, S. A., Mjalli, F. S. & Saleem, M. Progress in flow battery research and development. *J. Electrochem. Soc.* **158**, R55–R79 (2011).
15. Weber, A. Z. *et al.* Redox flow batteries: A review. *J. Appl. Electrochem.* **41**, 1137–1164 (2011).
16. Sauer, D. U. *et al.* State of charge- What do we really speak about? *21st Int. Telecommun. Energy Conf.* (1999).
17. Ha, S. & Gallagher, K. G. Estimating the system price of redox flow batteries for grid storage. *J. Power Sources* **296**, 122–132 (2015).
18. Albertus, P., Manser, J. S. & Litzelman, S. Long-duration electricity storage applications, economics, and technologies. *Joule* **4**, 21–32 (2020).
19. Sanchez-Díez, E. *et al.* Redox flow batteries: Status and perspective towards sustainable stationary energy storage. *J. Power Sources* **481**, 228804 (2021).
20. Guarnieri, M., Trovo, A., Marini, G., Sutto, A. & Alotto, P. High current polarization tests on a 9 kW vanadium redox flow battery. *J. Power Sources* **431**, 239–249 (2019).
21. Darling, R. M. & Perry, M. L. Method of maintaining health of a flow battery, U.S. Patent 20160056487. (2013).
22. He, Z. *et al.* Electrode materials for vanadium redox flow batteries: Intrinsic treatment and

introducing catalyst. *Chem. Eng. J.* **427**, 131680 (2022).
23. Narayan, S. R. *et al.* Next-generation aqueous flow battery chemistries. *Curr. Opin. Electrochem.* **18**, 72–80 (2019).
24. Li, M., Rhodes, Z., Minteer, S. D. & Cabrera-Pardo, J. R. Recent advancements in rational design of non-aqueous organic redox flow batteries. *Sustain. Energy* **4**, 4370–4389 (2020).
25. Perry, M. L., Rodby, K. E. & Brushett, F. R. Untapped potential: The need and opportunity for high-voltage aqueous redox flow batteries. *ACS Energy Lett.* 659–667 (2022) doi:10.1021/acsenergylett.1c02225.
26. U.S. DOE. *Energy Storage Program Planning Document*. (2011).
27. Zhang, M., Moore, M., Watson, J. S., Zawodzinski, T. A. & Counce, R. M. Capital cost sensitivity analysis of an all-vanadium redox-flow battery. *J. Electrochem. Soc.* **159**, A1183–A1188 (2012).
28. Darling, R. M., Gallagher, K. G., Kowalski, J. A., Ha, S. & Brushett, F. R. Pathways to low-cost electrochemical energy storage: A comparison of aqueous and nonaqueous flow batteries. *Energy Environ. Sci.* **7**, 3459–3477 (2014).
29. Viswanathan, V. *et al.* Cost and performance model for redox flow batteries. *J. Power Sources* **247**, 1040–1051 (2014).
30. Crawford, A. *et al.* Comparative analysis for various redox flow batteries chemistries using a cost performance model. *J. Power Sources* **293**, 388–399 (2015).
31. Mongird, K. *et al. 2020 Grid Energy Storage Technology Cost and Performance Assessment*. (2020).
32. Pawel, I. The cost of storage- how to calculate the levelized cost of stored energy (LCOE) and applications to renewable energy generation. *Energy Procedia* **46**, 68–77 (2014).
33. Schmidt, O., Melchior, S., Hawkes, A. & Staffell, I. Projecting the future levelized cost of electricity storage technologies. *Joule* **3**, 81–100 (2019).
34. Lai, C. S. & Mcculloch, M. D. Levelized cost of electricity for solar photovoltaic and electrical energy storage. *Appl. Energy* **190**, 191–203 (2017).
35. Dieterle, M., Fischer, P., Blume, N., Minke, C. & Bischi, A. Life cycle assessment (LCA) for flow batteries: A review of methodological decisions. *Sustain. Energy Technol. Assessments* **53**, 102457 (2022).
36. Noack, J., Wietschel, L., Roznyatovskaya, N., Pinkwart, K. & Tübke, J. Techno-economic modeling and analysis of redox flow battery systems. *Energies* **9**, 627 (2016).
37. Arenas, L. F., Ponce De León, C. & Walsh, F. C. Electrochemical redox processes involving soluble cerium species. *Electrochim. Acta* **205**, 226–247 (2016).
38. Stormcrow. Cerium oxide price worldwide from 2009 to 2020 with a forecast from 2021 to 2030 (in U.S. dollars per metric ton). (2021).
39. LIVE Vanadium Price. vanadiumprice.com.
40. Smith, G. F. & Getz, C. A. Cerate oxidimetry: Theoretical considerations and determination of approximate electrode reference potentials. *Ind. Eng. Chem. Res.* **10**, 191–195 (1938).
41. Xiong, F., Zhou, D., Xie, Z. & Chen, Y. A study of the Ce3+/Ce4+ redox couple in sulfamic acid for redox battery application. *Appl. Energy* **99**, 291–296 (2012).
42. Devadoss, V., Ahmed Basha, C. & Jayaraman, K. Indirect electrochemical oxidation of p-methoxy-toluene to p-methoxy-benzaldehyde using ceric methanesulphonate: A scale-up study. *Ind. Eng. Chem. Res.* **47**, 4607–4616 (2008).
43. Kreh, R. P., Spotnitz, R. M. & Lundquist, J. T. Mediated electrochemical synthesis of aromatic aldehydes, ketones, and quinones using ceric methanesulfonate. *J. Org. Chem.* **54**,

1526–1531 (1989).
44. Binnemans, K. Chapter 229. Applications of Tetravalent Cerium Compounds. in *Handbook on the Physics and Chemistry of Rare Earths* vol. 36 281–392 (2006).
45. Katafias, A., Kita, P. & Wrzeszcz, G. Kinetics of the methylene blue oxidation by cerium (IV) in sulphuric acid solutions. *Transit. Met. Chem.* 1–7 (2006) doi:10.1007/s11243-006-0120-3.
46. Varela, J. A., Oberg, S. G., Neustedter, T. M. & Nelson, N. Non-thermal organic waste destruction: Characterization of the CerOx System 4. *Environ. Prog.* **20**, 261–271 (2001).
47. Minor Metals Trade Association. Cerium. https://mmta.co.uk/metals/ce/ (2022).
48. Bleiwas, D. I. *Potential for recovery of cerium contained in automotive catalytic converters*. *U.S. Geological Survey* (2013).
49. Borra, C. R., Vlugt, T. J. H., Yang, Y. & Offerman, S. E. Recovery of cerium from glass polishing waste: A critical review. *Metals (Basel).* **8**, (2018).
50. Furman, N. H. Applications of ceric sulfate in volumetric analysis. I. The preparation and stability of solutions of ceric sulfate (containing free sulfuric acid). II. Potentiometric study of the reactions between ceric and ferrous or oxalate ion. Application to the st. *J. Am. Chem. Soc.* **50**, 755–764 (1928).
51. Clarke, R. L., Dougherty, B. J., Harrison, S., Millington, P. J. & Mohanta, S. A1, Cerium Batteries. (2004).
52. Clarke, R. L., Dougherty, B. J., Harrison, S., Millington, P. J. & Mohanta, S. A1, Battery with bifunctional electrolyte. (2005).
53. Walsh, F. C. *et al.* The development of Zn-Ce hybrid redox flow batteries for energy storage and their continuing challenges. *Chempluschem* **80**, 288–311 (2015).
54. Leung, P. K., Ponce-De-León, C., Low, C. T. J., Shah, A. A. & Walsh, F. C. Characterization of a zinc-cerium flow battery. *J. Power Sources* **196**, 5174–5185 (2011).
55. Leung, P. K., Ponce De León, C., Low, C. T. J. & Walsh, F. C. Ce(III)/Ce(IV) in methanesulfonic acid as the positive half cell of a redox flow battery. *Electrochim. Acta* **56**, 2145–2153 (2011).
56. Xie, Z., Zhou, D., Xiong, F., Zhang, S. & Huang, K. Cerium-zinc redox flow battery: Positive half-cell electrolyte studies. *J. Rare Earths* **29**, 567–573 (2011).
57. Xie, Z., Xiong, F. & Zhou, D. Study of the Ce3+/Ce4+ redox couple in mixed-acid media (CH3SO3H and H2SO4) for redox flow battery application. *Energy and Fuels* **25**, 2399–2404 (2011).
58. Spotnitz, R. M., Kreh, R. P., Lundquist, J. T. & Press, P. J. Mediated electrosynthesis with cerium (IV) in methanesulphonic acid. *J. Appl. Electrochem.* **20**, 209–215 (1990).
59. Fang, B., Iwasa, S., Wei, Y., Arai, T. & Kumagai, M. A study of the Ce(III)/Ce(IV) redox couple for redox flow battery application. *Electrochim. Acta* **47**, 3971–3976 (2002).
60. Govindan, M., He, K. & Moon, I. Evaluation of dual electrochemical cell design for cerium-vanadium redox flow battery to use different combination of electrodes. *Int. J. Electrochem. Sci.* **8**, 10265–10279 (2013).
61. Tucker, M. C., Weiss, A. & Weber, A. Z. Improvement and analysis of the hydrogen-cerium redox flow cell. *J. Power Sources* **327**, 591–598 (2016).
62. Paulenova, A., Creager, S. E., Navratil, J. D. & Wei, Y. Redox potentials and kinetics of the Ce3+/Ce4+redox reaction and solubility of cerium sulfates in sulfuric acid solutions. *J. Power Sources* **109**, 431–438 (2002).
63. Wadsworth, E., Duke, F. R. & Goetz, C. A. Present status of cerium (IV)-cerium(III)

potentials. *Anal. Chem.* 1824–1825 (1957) doi:10.1021/ac60132a046.
64. Maverick, A. W. & Yao, Q. The cerium(IV)/cerium(III) electrode potential in hydrochloric acid solution. *Inorg. Chem.* **32**, 5626–5628 (1993).
65. Piro, N. A., Robinson, J. R., Walsh, P. J. & Schelter, E. J. The electrochemical behavior of cerium(III/IV) complexes: Thermodynamics, kinetics and applications in synthesis. *Coord. Chem. Rev.* **260**, 21–36 (2014).
66. Morss, L. R. Yttrium, Lanthanum, and the Lanthanide Elements. in *Standard Potentials in Aqueous Solution* (eds. Bard, A. J., Parsons, R. & Jordan, J.) 619–621 (Marcel Dekker, Inc., 1985).
67. Noyes, A. A. & Garner, C. S. Strong oxidizing agents in nitric acid solution. I. Oxidation potential of cerous-ceric salts. *J. Am. Chem. Soc.* **58**, 1265–1268 (1936).
68. Kunz, A. H. The reduction potential of the ceric-cerous electrode. *J. Am. Chem. Soc.* **53**, 98–102 (1931).
69. Solera, J. A., García, J. & Proietti, M. G. Multielectron excitations at the L edges in rare-earth ionic aqueous solutions. *Phys. Rev. B* **51**, 2678–2686 (1995).
70. Lutz, O. M. D., Hofer, T. S., Randolf, B. R., Weiss, A. K. H. & Rode, B. M. A QMCF-MD investigation of the structure and dynamics of Ce 4+ in aqueous solution. *Inorg. Chem.* **51**, 6746–6752 (2012).
71. Dinescu, A. & Clark, A. E. Thermodynamic and structural features of aqueous Ce(III). *J. Phys. Chem. A* **112**, 11198–11206 (2008).
72. Lutz, O. M. D., Hofer, T. S., Randolf, B. R. & Rode, B. M. Computational study of the cerium(III) ion in aqueous environment. *Chem. Phys. Lett.* **539**–**540**, 50–53 (2012).
73. Martin, T. W. & Glass, R. W. Competitive electron transfer. Activity-defined formation constants of cerium(III) nitrate complexes based on reaction with the nitrate free radical. *J. Am. Chem. Soc.* **92**, 5075–5083 (1970).
74. Kanno, H. & Hiraishi, J. Raman study of aqueous rare-earth nitrate solutions in liquid and glassy states. *J. Phys. Chem.* **88**, 2787–2792 (1984).
75. Blatz, L. A. The use of a cation-exchange resin to study the cerous and sulfate ion complexes. *J. Phys. Chem.* **66**, 160–164 (1962).
76. Newton, T. W. & Arcand, G. M. A spectrophotometric study of the complex formed between cerous and sulfate ions. *J. Am. Chem. Soc.* **75**, 2449–2453 (1953).
77. Allen, P. G., Bucher, J. J., Shuh, D. K., Edelstein, N. M. & Craig, I. Coordination chemistry of trivalent lanthanide and actinide ions in dilute and concentrated chloride solutions. *Inorg. Chem.* **39**, 595–601 (2000).
78. Rudolph, W. W. & Irmer, G. Raman spectroscopic characterization of light rare earth ions: La3+, Ce3+, Pr3+, Nd3+and Sm3+- hydration and ion pair formation. *Dalt. Trans.* **46**, 4235–4244 (2017).
79. Persson, I., D'Angelo, P., De Panfilis, S., Sandström, M. & Eriksson, L. Hydration of lanthanoid(III) ions in aqueous solution and crystalline hydrates studied by EXAFS spectroscopy and crystallography: The myth of the 'gadolinium break'. *Chem. - A Eur. J.* **14**, 3056–3066 (2008).
80. Urbanski, T. S., Fornari, P. & Abbruzzese, C. The extraction of cerium(III) and lanthanum(III) from chloride solutions with LIX 54. *Hydrometallurgy* **40**, 169–179 (1996).
81. Sham, T. K. Electronic structure of hydrated Ce4+ ions in solution: An X-ray absorption study. *Phys. Rev. B* **40**, 6045–6051 (1989).
82. Heidt, L. J. & Smith, M. E. Quantum yields of the photochemical reduction of ceric ions by

water and evidence for the dimerization of ceric ions. *J. Am. Chem. Soc.* **70**, 2476–2481 (1948).
83. Hardwick, T. J. & Robertson, E. Ionic species in ceric perchlorate solutions. *Can. J. Chem.* **29**, 818–827 (1951).
84. Fronaeus, S. & Ostman, C. O. The mechanism of the exchange reaction between cerium(III) and cerium(IV) at platinum surfaces. *Acta Chem. Scand.* **10**, 769–778 (1956).
85. Ikeda-Ohno, A., Tsushima, S., Hennig, C., Yaita, T. & Bernhard, G. Dinuclear complexes of tetravalent cerium in an aqueous perchloric acid solution. *Dalt. Trans.* **41**, 7190–7192 (2012).
86. Larsen, R. D. & Brown, G. H. The structure of ammonium hexanitratocerate(IV) in solution. *J. Phys. Chem.* **68**, 3060–3062 (1964).
87. Beineke, T. A. & Delgaudio, J. The crystal structure of ceric ammonium nitrate. *Inorg. Chem.* **7**, 715–721 (1968).
88. Demars, T. J., Bera, M. K., Seifert, S., Antonio, M. R. & Ellis, R. J. Revisiting the solution structure of ceric ammonium nitrate. *Angew. Chem. Int. Ed. Engl.* **54**, 7534–8 (2015).
89. Antonio, M. R., Ellis, R. J., Estes, S. L. & Bera, M. K. Structural insights into the multinuclear speciation of tetravalent cerium in the tri-n-butyl phosphate-n-dodecane solvent extraction system. *Phys. Chem. Chem. Phys.* **19**, 21304–21316 (2017).
90. Jones, E. G. & Soper, F. G. The nature of the ceric sulphates. *J. Chem. Soc.* 802–805 (1935).
91. Moore, R. L. & Anderson, R. C. Spectrophotometric studies on cerium(IV) sulfate complex ions. *J. Am. Chem. Soc.* **67**, 167–171 (1945).
92. Hardwick, T. J. & Robertson, E. Association of ceric ions with sulphate (a spectral study). *Can. J. Chem.* **29**, 828–837 (1951).
93. Wang, Z., Chu, T., Chai, Z. & Wang, D. A density functional theory study of the competitive complexation of pyridine against H2O and Cl- to Cm3+ and Ce4+. *Radiochim. Acta* **102**, 101–109 (2014).
94. Randle, T. H. & Kuhn, A. T. Kinetics and mechanism of the cerium(III)/cerium(IV) redox reaction on a platinum electrode. *J. Chem. Soc., Faraday Trans. 1* **79**, 1741–1756 (1983).
95. Xie, Z., Liu, Q., Chang, Z. & Zhang, X. The developments and challenges of cerium half-cell in zinc-cerium redox flow battery for energy storage. *Electrochim. Acta* **90**, 695–704 (2013).
96. Nikiforidis, G., Berlouis, L., Hall, D. & Hodgson, D. An electrochemical study on the positive electrode side of the zinc-cerium hybrid redox flow battery. *Electrochim. Acta* **115**, 621–629 (2014).
97. Nikiforidis, G., Berlouis, L., Hall, D. & Hodgson, D. Charge/discharge cycles on Pt and Pt-Ir based electrodes for the positive side of the Zinc-Cerium hybrid redox flow battery. *Electrochim. Acta* **125**, 176–182 (2014).
98. Na, Z., Wang, X., Yin, D. & Wang, L. Graphite felts modified by vertical two-dimensional WO3nanowall arrays: High-performance electrode materials for cerium-based redox flow batteries. *Nanoscale* **10**, 10705–10712 (2018).
99. Na, Z., Wang, X., Yin, D. & Wang, L. Tin dioxide as a high-performance catalyst towards Ce(VI)/Ce(III) redox reactions for redox flow battery applications. *J. Mater. Chem. A* **5**, 5036–5043 (2017).
100. Bonewitz, R. A. & Schmid, G. M. Oxygen adsorption on gold and the Ce(III)/Ce(IV) reaction. *J. Electroanal. Chem.* **117**, 1367–1372 (1970).
101. Kiekens, P., Steen, L., Donche, H. & Temmerman, E. Kinetics of Ce(IV) reduction at gold,

carbon and iridium electrodes. *Electrochim. Acta* **26**, 841–845 (1981).
102. Bard, A. J. & Faulkner, L. R. *Electrochemical Methods: Fundamentals and Applications*. (John Wiley & Sons, Inc., 2001). doi:10.1016/B978-0-08-098353-0.00003-8.
103. Heinritz, A., Binninger, T., Patru, A. & Schmidt, T. J. Asymmetric Butler−Volmer kinetics of the electrochemical Ce(III)/Ce(IV) redox couple on polycrystalline Au electrodes in sulfuric acid and the dissociation field effect. *ACS Catal.* **11**, 8140–8154 (2021).
104. Bishop, E. & Cofre, P. Anodic generation of cerium(IV). Charge-transfer kinetic parameters and conditional potentials at platinum, gold and glassy Carbon. *Analyst* **106**, 316–322 (1981).
105. Sacchetto, G. A., Pastore, P., Favaro, G. & Fiorani, M. Liquid chromatographic determination of non-volatile nitrosamines by post-column redox reactions and voltammetric detection at solid electrodes. Study of a flow reactor system based on Ce(IV) reagent. *Anal. Chim. Acta* **258**, 99–108 (1992).
106. Maeda, Y. *et al.* The electrochemical response of highly boron-doped conductive diamond electrodes to Ce3+ ions in aqueous solution. **44**, 3441–3449 (1999).
107. Vijayabarathi, T., Velayutham, D. & Noel, M. Influence of aromatic reactants and products involved in the two stage electro- chemical oxidation on the voltammetric behaviour of Ce(IV)/Ce(III) redox couple. *J. Appl. Electrochem.* **31**, 979–986 (2001).
108. Wei, Y., Fang, B., Arai, T. & Kumagai, M. Electrolytic oxidation of Ce(III) in nitric acid and sulfuric acid media using a flow type cell. *J. Appl. Electrochem.* **35**, 561–566 (2005).
109. Chen, T. S., Yeh, K. J. C. & Huang, K. L. Anion effects on the electrochemical regeneration of Ce(IV) in nitric acid used for etching chromium. *J. Hazard. Mater.* **152**, 922–928 (2008).
110. Liu, Y., Xia, X. & Liu, H. Studies on cerium (Ce4+/Ce3+)-vanadium (V2+/V3+) redox flow cell- cyclic voltammogram response of Ce4+/Ce3+redox couple in H2SO4 solution. *J. Power Sources* **130**, 299–305 (2004).
111. Galus, Z. & Adams, R. N. The investigation of the kinetics of moderately rapid electrode reactions using rotating disk electrodes. *J. Phys. Chem.* **67**, 866–871 (1963).
112. Greef, R. & Aulich, H. The kinetics of the cerous-ceric redox reaction at a platinum electrode. *J. Electroanal. Chem. Interfacial Electrochem.* **18**, 295–307 (1968).
113. Kuhn, T. & Randle, H. Effect of oxide thickness on the rates of some redox reactions on a platinum electrode. *J. Chem. Soc., Faraday Trans. 1* **81**, 403–419 (1985).
114. Modiba, P., Matoetoe, M. & Crouch, A. M. Electrochemical impedance spectroscopy study of Ce (IV) with aminopolycarboxylate ligands for redox flow batteries applications. *J. Power Sources* **205**, 1–9 (2012).
115. Modiba, P. & Crouch, A. M. Electrochemical study of cerium(IV) in the presence of ethylenediaminetetraacetic acid (EDTA) and diethylenetriaminepentaacetate (DTPA) ligands. *J Appl Electrochem* **38**, 1293–1299 (2008).
116. Xie, Z. P., Xiong, F. J. & Zhou, D. B. Effect of sulfosalicylic acid on kinetics of Ce3+/Ce4+ electrode reaction. *Adv. Mater. Res.* **279**, 451–455 (2011).
117. Nikiforidis, G., Berlouis, L., Hall, D. & Hodgson, D. A study of different carbon composite materials for the negative half-cell reaction of the zinc cerium hybrid redox flow cell. *Electrochim. Acta* **113**, 412–423 (2013).
118. Pletcher, D. & Valdes, E. M. Studies of the Ce(III)/Ce(IV) couple in multiphase systems containing a phase transfer reagent- I. Conditions for the extraction of Ce(IV) and electrode kinetics. *Electrochim. Acta* **33**, 499–507 (1988).
119. Fernandez-Marchante, C. M., Millán, M., Medina-Santos, J. I. & Lobato, J. Environmental

and preliminary cost assessments of redox flow batteries for renewable energy storage. *Energy Technol.* **1900914**, 1–10 (2019).

Chapter 2 Methods and Background on Modeling and Experimental Techniques

2.1 Introduction

In this chapter, the methods and theory behind the techniques used throughout the dissertation are described. In **Section 2.2**, background information on technoeconomic and life cycle inventory modeling is provided. **Section 2.3** introduces the spectroscopic techniques used to identify the structures of the Ce^{3+} and Ce^{4+} ions, specifically UV-Vis spectroscopy and extended X-ray absorption fine structure (EXAFS). Methods to determine the concentration of Ce ions in solution are highlighted in **Section 2.4**. The electrochemistry techniques and methods used to evaluate and extract kinetic parameters are discussed in **Section 2.5**. Further information on modeling observed kinetic behavior that is relevant for the Ce^{3+}/Ce^{4+} redox reaction is provided in **Section 2.6**.

2.2 Cost and emissions modeling techniques

To compare the cost and intensity of greenhouse gas (GHG) emissions of a redox flow battery (RFB) that uses the Ce^{3+}/Ce^{4+} redox chemistry at the positive electrode to the state-of-the-art all-vanadium RFB in **Chapter 3**, technoeconomic assessment and life cycle inventory modeling tools are used. Background information on technoeconomic assessment modeling is included in **Section 2.2.1** and the life cycle inventory modeling is discussed in more detail in **Section 2.2.2**.

2.2.1 Technoeconomic assessment modeling

A technoeconomic assessment (TEA) model estimates the technical performance of a product or technology, and based on this performance, calculates the economic costs associated with the production and operation of that technology.[1] The general process of conducting a TEA includes: building a process model and sizing equipment, calculating the capital and operating costs associated with the technology, and developing a user interface.[2] The process model should consider all material and energy inputs to the technology, as well as all equipment needed. Based on the functional unit of the TEA, which is the amount of product, material, or service that the technology performance is being referenced against,[1,3] the necessary size of equipment, e.g., electrolyte tanks or reactors, can be determined. Capital costs are expenses that are incurred only once per product (barring replacement costs), and are considered investments from which economic benefits are expected to generated.[2] Capital costs often refer to the equipment used in the delivery of a product or service, such as pumps, reactors, and heat exchangers.[2] Operating costs can include variable and fixed, where variable costs scale with operation and fixed costs do not.[2] The levelized cost of electricity (LCOE) is the average net present cost of electricity generated over a product's lifetime.[4] In order to calculate the LCOE, assumptions related to the rate of use of the technology, service life of the technology, and total discount factor are needed.[5] The total discount factor estimates the net present value of future costs. In TEAs, sensitivity analysis is conducted to determine how the individual components built into the model impact cost.[2] Information on capital and operating costs are typically pulled from literature or directly from vendors.

In **Chapter 3**, a TEA of two redox flow battery chemistries, the all-vanadium (VRFB) and a cerium (Ce)-vanadium battery, is conducted. There have been a number of TEAs of VRFBs

which estimate the capital cost to range between 300-600 $/kWh (2012-2020 USD) for discharge times ranging between 4 and 12 hours,[6–11] and other redox flow battery technologies have been considered as well, including iron-vanadium,[7] iron-chromium,[8,12] zinc-bromine,[12] polysulfide-bromine,[12] and hydrogen-bromine.[5] These studies have primarily modeled the effect of individual components like membrane,[13] bipolar plates,[14] and electrolyte cost,[11] as well as operating conditions like current density[7,11,15] and discharge time,[7,8,11,12] on overall systems cost. These TEAs highlight the influence that both components and operating conditions can have on redox flow battery costs and motivate the use of TEA to compare the well-studied VRFB to the Ce-V RFB, which has not been studied thoroughly, in this dissertation.

2.2.2 Life cycle inventory modeling

To assess the GHG emissions associated with RFBs, we develop a life cycle inventory model based on life cycle assessment (LCA) techniques. An LCA is defined as the examination, identification, and evaluation of a product or system's environmental implications, including the material and energy consumption and emissions into the environment.[3] LCA should incorporate the production, use, and end-of-life (EoL) stages of a product or system. The production phase consists of burdens associated with material production, i.e., resource extraction and processing, availability/scarcity, and recyclability, as well as manufacturing, which could include the energy and environmental impact of individual manufacturing steps as well as operational burdens (e.g., facility lighting, climate control). Use phase burdens typically include operational energy consumption, carbon emissions and other environmental burdens of the fuel source (both upstream and during use), maintenance burdens, and transportation burdens. Lastly, the EoL impacts of a product can typically be split into two categories: the burdens (energy and environmental) associated with processing or storing the waste (i.e., sending to landfill) and recycling the product.

The full LCA framework consists of four stages: goal and scope definition, inventory analysis, impact analysis, and interpretation of results.[3] Goal and scope definition includes identification of the boundaries of the impact assessment, e.g., boundaries in processes considered, as well as space and time boundaries, and the functional unit, which is the amount of product, material, or service to which the LCA is applied.[3] The first step to inventory analysis is establishing a material inventory, in which the amount of material and energy needed in each life cycle stage of the product or system is quantified. The amount of material is then normalized by the functional unit. Then, the environmental burdens associated with each of those materials can be calculated on a functional unit basis using LCA databases, which include SimaPro,[16] GaBi,[17] or the GREET (Greenhouse gases, Regulated Emissions, and Energy use in Technologies) model.[18] These databases contain information on energy use and environmental burdens such as global warming potential, eutrophication potential, and acidification potential for different materials and processes. Impact analysis evaluates the magnitude and significance of inventory analysis results, and impact analysis can be a technical, quantitative or qualitative process to characterize and assess the environmental burdens associated that were identified in the inventory analysis phase. Stages of impact assessment include classification, characterization, localization, and valuation.[3] Interpretation of the results includes conducting sensitivity analyses to understand what parameters/variables can be used to promote the biggest change as well as proposing policy or design changes to drive down environmental burdens identified in the impact assessment as the most influential. Impact assessment has been identified as highly subjective and dependent on the specific goals of an LCA, and so in this thesis (**Chapter 3**), a life cycle inventory (LCI) is completed, in which only the goal and scope definition, inventory analysis, and interpretation stages are completed.

LCAs for electrochemical systems like batteries have been completed previously which can lend insight into what factors are expected to control environmental burdens. The most relevant production burdens for a battery relate to the energy burden per unit of material production as well as materials' scarcity and toxicity.[19] For many systems including electrochemical systems, the use phase typically accounts for the largest portion of energy consumption and environmental burden.[20,21] For a static system like a battery, the transportation burdens of the material to the final site would most likely be negligible, and instead, electricity consumption and delivery will dominate. Operational characteristics that will influence the magnitude of the environmental burdens of the use phase include service life, charge/discharge degradation, round-trip efficiency, faradaic efficiency, and discharge duration. When conducting a comparative LCA for a battery, it is important to consider what energy source the battery is displacing. While there are burdens associated with recycling, these burdens are typically outweighed by the benefits of reducing material production demands.[22] LCAs of energy storage technologies[23,24] including RFBs[21,25–31] have been conducted. The production phase GHG emissions of the all-vanadium RFB is dominated by the electrolyte, primarily due to the emissions associated with the production of V_2O_5.[29–31] Regarding the use phase, the roundtrip efficiency has been shown to have a significant impact on life cycle emissions,[25] with the bulk of emissions stemming from losses incurred during the electricity delivery phase, assuming an electricity mix which still relies on fossil fuels. Finally, increasing all-vanadium redox flow batteries capacity results in lower GHG emissions when reducing high wind curtailment,[26] which highlights the importance of the electricity grid application on the LCA results. In **Chapter 3**, an LCI of two RFBs is conducted and many of the trends discussed above are found to hold in our study.

2.3 Spectroscopy techniques

To determine the structure of the Ce^{3+} and Ce^{4+} ions in a variety of acidic media, as described in **Chapters 4** and **5**, Ultraviolet (UV)-Visible (Vis) spectroscopy and extended X-ray absorption fine structure (EXAFS) spectroscopy were used. A discussion of the different possible characterization techniques is included below to motivate the use of UV-Vis and EXAFS techniques. The theories behind the UV-Vis and EXAFS spectroscopy techniques are described in detail below. Additionally, the characteristics of UV-Vis and EXAFS spectra of Ce^{3+} and Ce^{4+} ions are described.

2.3.1 The utility of UV-Vis and EXAFS spectroscopies for cerium bulk structure studies

There exist many types of characterization techniques that can be used to study the bulk composition, structure, and surface structures of a system. For cerium, it is important to study the structures of the bulk aqueous solution, because the structures of the ionic species are expected to control both the thermodynamics and kinetics (see **Chapter 1** for more discussion). Bulk structure characterization techniques include UV-Vis spectroscopy, X-ray absorption spectroscopy (XAS), Raman spectroscopy, and X-ray diffraction (XRD). Of these available techniques, we relied on UV-Vis spectroscopy and X-ray absorption, of which EXAFS is a subset. UV-Vis spectroscopy is a relatively simple technique that provides information on the bonding behavior of an atom's valence electrons. We relied on UV-Vis to determine whether the Ce^{3+} and Ce^{4+} coordination environment was changing with acid because it was a convenient way to quickly screen a number of different acids and cerium and acid concentrations. To obtain a more detailed understanding of the cerium ions in solution, including their coordination and complexation structures, we relied on XAS. XAS uses X-rays to probe the geometric and electronic structure of a central atom, as will be described in more detail in **Section 2.3.3**. EXAFS is particularly powerful because it is sensitive

to the oxidation state, distances to neighboring atoms, coordination number of neighboring atoms, and the elemental composition of neighboring atoms.[32] Additionally, the EXAFS equation allows for fitting of experimental spectra to obtain quantitative information on coordination number and scattering distances. The use of a synchrotron to generate the high energies of the X-rays is generally needed, however, which makes using XAS a more logistically challenging technique to use. Raman spectroscopy is another useful technique that has been used to study cerium in solution,[33–36] and it works by passing UV and visible light through a sample and observing the light that is scattered in the direction that is perpendicular to the incident beam.[37] The scattered light is categorized between strong and weak frequencies compared to the incident beam, where the weak frequencies comprise the Raman scattering and contains information related to the vibrational frequencies of a molecule.[37] The vibrational frequency is measured as a shift from the incident beam frequency. Compared to EXAFS, identification of unknown structures with Raman spectroscopy can be more challenging, as it is often based on empirical evidence of previously collected solutions with similar spectra. XRD is generally used to study the structures of crystals, where the crystalline structure diffracts the X-rays and the angle of diffraction is used to determine interplanar spacings of crystallographic phases and identify chemical bonds and crystallographic disorder.[38] While XRD of solutions can be collected, the width of the peaks is severely widened, which can make structural determination of ions in solution difficult. Techniques that focus on surface adsorbate characterization like infrared (IR) spectroscopy are not as useful for studying the cerium kinetics in aqueous systems because there is no evidence of Ce^{3+} and Ce^{4+} ions adsorbing to the electrode surface during electron transfer (see **Chapter 5**). Given the ease of use of UV-Vis and the detailed information that can be obtained from the powerful EXAFS technique, we used

these two techniques to obtain information on the cerium structures in bulk solution. The theory of these spectroscopy techniques is described in detail next.

2.3.2 UV-Vis spectroscopy

UV-Vis spectroscopy is a type of electronic spectroscopy and is the measurement of the transition of electrons between energy levels.[39] Specifically, UV-Vis spectroscopy is an electromagnetic absorption technique, in which the absorption is caused by the excitation of an electron from one molecular orbital to a higher orbital.[40] In this section, we first describe theories of electronic transitions, then describe selectivity rules of transition moments, before introducing UV-Vis instrumentation and information on UV-Vis of cerium solutions.

Theories to describe electronic transitions. Electronic transitions can be described through crystal field theory (CFT), molecular orbital (MO) theory, or the more realistic ligand field theory (LFT), which is the combination of CFT and MO.[40] CFT was originally developed to describe electronic transitions in transition metal ions and asserts that the interaction between transition metals and surrounding ligands stems from the attraction between the positively charged metal cation and negatively charged non-binding electron of the ligand.[40] CFT was developed for the case of the five degenerate *d* orbitals of a transition metal (**Fig. 2.1**). When a static electric field is produced by a surrounding charge distribution (modeled by an array of point charges), the degeneracy of the electronic *d* orbital is broken. This is demonstrated by the progression shown in **Fig. 2.1** for the common octahedral geometry, which starts with a metal cation *M* with charge *n*. If an electron is inserted into the orbital set, coulombic repulsion causes the energy of all the orbitals to be raised equally, which is referred to as a spherical field situation.[40] The ligand electrons are closer to some of the *d* orbitals than others, which results in a loss in degeneracy. As a result, the *d* orbitals that are closer to the ligand have higher energy than the *d* orbitals that are

farther from the ligand. In **Fig. 2.1**, Δ_o is the difference in the energies of the *d* orbitals and is affected by the nature of the metal and ligands, the oxidation state of *M*, and the geometry of the complex. The splitting of the d_{xy}, d_{xz}, d_{yz}, d_z^2 and $d_{x^2-y^2}$ orbitals demonstrated in **Fig. 2.1** is specifically for the transition metal ion complex with octahedral geometry. CFT breaks down when there is strong interaction between *M* and the ligand, for which MO theory is a better descriptor of electronic transitions.[41]

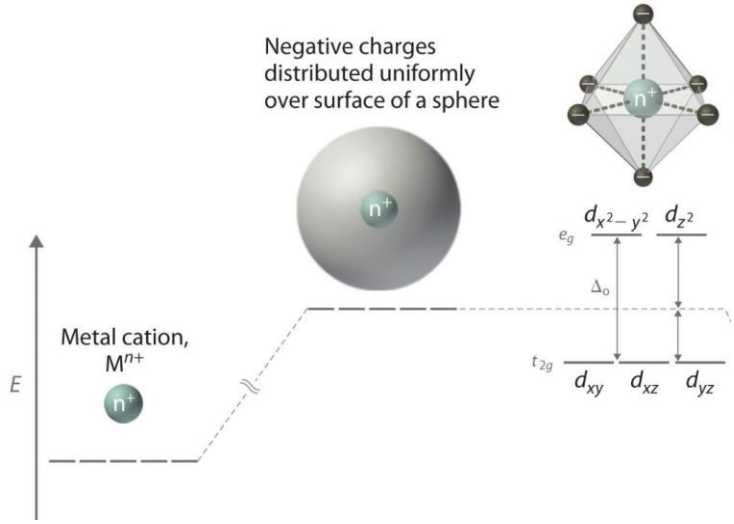

Figure 2.1. Demonstration of CFT. Going from left to right in diagram: the *d* orbitals of a transition metal ion M^{n+} are all raised equally when a charge of −6 is spread uniformly around M^{n+}. When ligands approach M^{n+} in an octahedral complex geometry, a charge of −1 is assigned to each vertex of the octahedron. While the average energy of the d orbitals is the same as the case in which a charge of −6 is uniformly spread around the cation, the degeneracy of the d orbitals is split, with the e_g orbitals being raised in energy and the t_{2g} orbitals being lowered. Reproduced from Awan et al. (2021).[42]

LFT is an extension of CFT, because it is a freely parameterized model and is not localized to point charge ligands like CFT.[39] LFT can be used in conjunction with MO theory, which models covalent interactions between metals and ligands.[40] As shown in **Fig. 2.2** for an octahedral complex, neglecting π electron interaction, MO theory combines orbitals from *M* and the ligand which results in new orbitals that are of different energies than the individual components.[43] This approach results in different types of orbitals: bonding, antibonding, and non-bonding. Bonding orbitals are stabilized by electrons, while antibonding orbitals are destabilized by electrons. In the

octahedral complex, 12 electrons from 6 ligand lone pairs occupy σ-bonding orbitals.[40] The t_{2g} remain as σ non-bonding orbitals, and participate in π-bonding, as described next. *d* electrons of *M* are then inserted into the next highest orbitals, and some of the interactions between *s* and *p* orbitals of *M* also lead to bonding and anti-bonding orbitals. If the ligand has *p* or π orbitals that are orthogonal to the *M* bond direction, then further interaction between the t_{2g} *d* orbital of *M* and *p* or π orbitals of the ligand can occur.

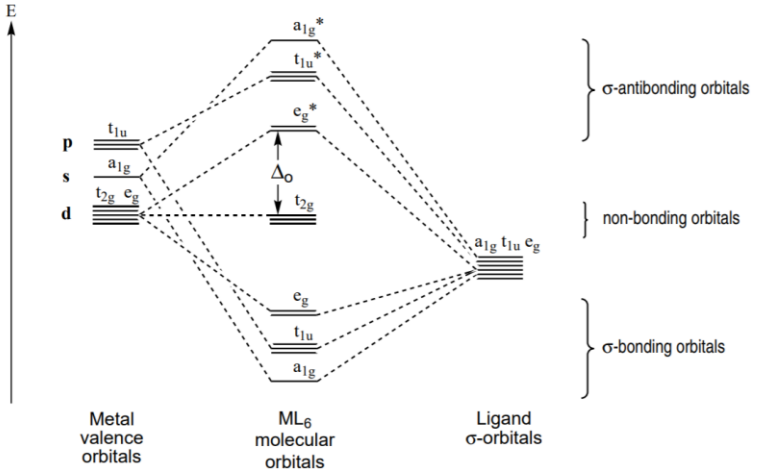

Figure 2.2. MO diagram of an octahedral transition metal complex, neglecting π electron interaction. On the lefthand side of the image are the metal valence orbitals (t_{2g} and e_g correspond to the *d* orbitals, a_{1g} corresponds to the *s* orbital, and t_{1u} corresponds to the *p* orbitals). On the righthand side are the ligand σ orbitals with designations a_{1g}, t_{1u}, and e_g. In the middle of the image are the octahedral complex ML_6 orbitals, with the σ-bonding orbitals filled by the lone pairs of the ligand and the *d* electrons of the metal filling the t_{2g} and e_g^* orbitals of the complex. Δ_o is the difference in the energies of the *d* orbitals in the ML_6 complex. Image reproduced from Lawrance (2010).[43]

When *p* orbitals of the ligand are not used in σ-bonding, or when ligands have any π or π^* molecular orbitals, then π-bonding can occur. There are two important π bonds that can form, which are called 1) ligand-to-metal and 2) metal-to-ligand bonds and are shown in **Fig. 2.3**. In ligand-to-metal bonding (**Fig. 2.3a**), the t_{2g} orbital of M interacts with the π orbitals of the filled ligand, and as a result, the bonding and antibonding energy levels are similar to the initial metal and ligand energy levels. Thus, Δ_o is decreased and the π antibonding orbitals are lower in energy than the σ antibonding orbitals. In metal-to-ligand bonding (**Fig. 2.3b**), the ligand π antibonding

orbital energy levels are higher than the M t_{2g} orbital energy levels, and so the t_{2g} orbital is lowered and Δ_o is increased.

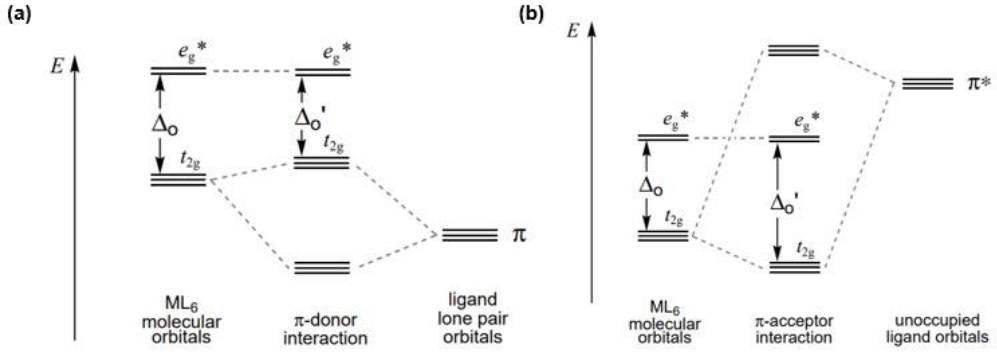

Figure 2.3. MO diagram for an octahedral transition metal complex, with the influence of π interactions for **(a)** ligand-to-metal bonding, and **(b)** metal-to-ligand bonding. Δ_o is the difference in the energies of the t_{2g} and e_g^* orbitals of the ML_6 complex and Δ_o' is the difference in orbitals that has been affected by the π donor or π acceptor interaction. Image adapted from Lawrance (2010).[43]

Intensity and selectivity rules of electronic transitions. Electronic spectroscopy is the measurement of the interaction between electromagnetic radiation and matter. Radiation energy, frequency, wavenumber, and wavelength are all used to define electronic spectroscopy.[40] When an electron absorbs the energy of electromagnetic radiation and is excited to a higher molecular orbital with a very short half-life, a transition moment is said to occur.[40] Because molecular orbitals are quantized, the electronic transition is associated with a specific energy, ΔE.[39] This is typically followed by relaxation to the ground state. Absorption measures the transition moment, and the intensity of the absorption is indicative of the probability of the transition to occur. Unlike atomic absorption spectra, which are sharp, molecular electronic absorption spectra are usually broad bands because molecules experience vibrational and rotational motions which are slower than photon absorption.[39] The Franck-Condon approximation asserts that electronic transitions occur on a much faster time scale than nuclear motion,[39] and so the electronic transition represents a

certain vibrational and rotational state of the molecule. Thus, electronic transitions occur over a range of ΔE values.

The intensity of the electromagnetic radiation, I_0, is compared to the intensity of the electromagnetic radiation passed through the sample, I, to calculate the absorbance of the sample, A, through **Eq. 2.1**. Transmittance, T, is defined as the ratio of I_0 to I.

$$A = \log(T) = \log\left(\frac{I_0}{I}\right) \quad \textbf{(2.1)}$$

The Beer-Lambert law[39,44] (**Eq. 2.2**) states that absorbance is proportional to the sample concentration (c), the light pathlength (l), and the sample's molar extinction coefficient (ε), an intrinsic property that indicates how strongly the chemical absorbs light. Typical values of ε range between 0-10,000 $M^{-1}cm^{-1}$, with higher values indicating stronger absorption.[39]

$$A = \varepsilon \times c \times l \quad \textbf{(2.2)}$$

The probability of intensity of a transition depends on the allowed nature of a transition. As shown in **Eq. 2.3**, the intensity of the transition is proportional to the square of the transition moment, $\boldsymbol{M}$.[40] If only the electric oscillating field is involved in the transition moment, then $\boldsymbol{M}$ is defined as shown in **Eq. 2.4**, with ϕ_{ground} and $\phi_{excited}$ representing the ground and excited state wave functions, and û being the electric dipole operator.[40] **Eq. 2.4** can be further modified to **Eq. 2.5**, separating $\boldsymbol{M}$ to three components: the Frank-Condon factor ($\langle\phi_v^*\phi_v\rangle$), which is the vibrational integral which is non-zero, the orbital selection rule ($\langle\phi_{orbital}|\hat{u}|\phi_{orbital}^*\rangle$), and the spin selection rule ($\langle\phi_{spin}|\phi_{spin}^*\rangle$).[40] The orbital selection rule and spin selection rule may or may not be zero. If one of the two is zero, then the total integral will be zero and no absorption will occur. Considering

the orbital selection rule, also referred to as the Laporte selection rule, a transition is not allowed if electrons are only redistributed within the same type of orbitals.[40] Regarding the spin selection rule, the spin multiplicity of the ground and excited states must be the same, i.e., $\phi_{spin} = \phi^*_{spin}$, for a transition to be allowed, because light has no spin properties and will not change the spin.[40]

$$I \propto \boldsymbol{M}^2 \tag{2.3}$$

$$\boldsymbol{M} = \langle \phi_{ground} | \hat{u} | \phi_{excited} \rangle \tag{2.4}$$

$$\boldsymbol{M} = \langle \phi_v^* \phi_v \rangle \langle \phi_{orbital} | \hat{u} | \phi^*_{orbital} \rangle \langle \phi_{spin} | \phi^*_{spin} \rangle \tag{2.5}$$

There are exceptions to these selectivity rules, however, which can result in an increase in the allowed nature of a transition. One major exception is the mixing of *d* and *p* orbitals, which is caused by a noncentrosymmetric point group[40] and results in *d*(*p*)→*p*(*d*) transitions, meaning the orbital selection rule is satisfied. Vibronic coupling[40] can also lead to the mixing of orbitals by destroying the symmetry of a complex. Finally, spin-orbit coupling can also result in mixing orbital and spin parts, leading to exceptions to the selectivity rules.[40]

Absorption spectral lines are associated with either the central ion, the ligand, or an electron transfer between the central ion and ligand (charge transfer spectra). Central ion spectra such as *d*→*d* are forbidden by the orbital selection rule, and are therefore weak.[40] They are characterized by wider band widths caused by vibrational structure breathing, spin-orbit coupling, and temperature.[40] Additionally, they are prone to band splitting due to the presence of multiple ligands or the Jahn-Teller effect, in which an unstable degenerate ground electronic configuration is stabilized by the distortion of octahedral symmetries to lower symmetries, e.g., tetragonal or square planar, and additional transitions become possible.[40,41] Charge transfer spectra are typically intense bands, representing a much more significant displacement of charge between the metal or ligand

than central ion spectra, and are either metal-to-ligand or ligand-to-metal transitions, which were described above. In ligand-to-metal transitions, the more oxidizing the metal is and the more reducing the ligand is, the less energy a charge transfer will have, which corresponds with a higher wavelength. The greater the metal's oxidation state, the greater its oxidizing nature and lower its charge transfer energy.[40] Ligand spectra are typically associated with organic molecules which posses π electron systems that result in intense $\pi^* - \pi$ bands.[40]

UV-Vis instrumentation and operation. UV-Vis spectrophotometers work by passing UV and visible light (typical range between 200-800 nm[39], but the Thermo Scientific instruments we used in this dissertation, Evolution^{TM} 300 and 350, had a wider range of 190-1100 nm) through a solution sample that is typically held in a quartz cuvette. To operate the Evolution^{TM} series of UV-Vis instruments, the transmittance T of light through a "blank" sample, which contains only the relevant solvent, is measured. This is referred to as the baseline measurement and the measurement is calibrated so that the baseline $T = 1$ across measured wavelengths. Then, the T of light through the sample is collected and corrected against the baseline T. From **Eq. 2.2**, absorbance can be calculated from the value of the corrected$T$ for the sample.

UV-Vis of lanthanides. The above discussion of electronic transitions was focused primarily on transition metals, but the theory can be applied to lanthanides, and the intensity of the absorption spectra can be described through Judd-Ofelt theory.[45] Lanthanide ions have the electronic configuration shown in **Fig. 2.4** and are characterized by the shielded 4*f* shell, in which the electronic transitions take place. The UV-Vis spectra of lanthanides have been noted to be sharp, suggesting the transitions were occurring between levels inside the electronic shell.[45] This does not align with the orbital selection (Laporte) rule, which asserts that *f*→*f* transitions are forbidden.[45] It was determined that lanthanides experience such intense spectra because the

transitions are actually electric dipole radiation, which can be forced if opposite parity states from higher energy orbitals outside the 4*f* shell, e.g., the 5*d* shell, are mixed into the upper state.[45] Spin-orbit coupling has been noted to be more important than crystal field splitting for lanthanides.[39] Electric dipole radiation is possible when the atom is placed in a noncentrosymmetric perturbing field like the crystal field of a lattice.[45]

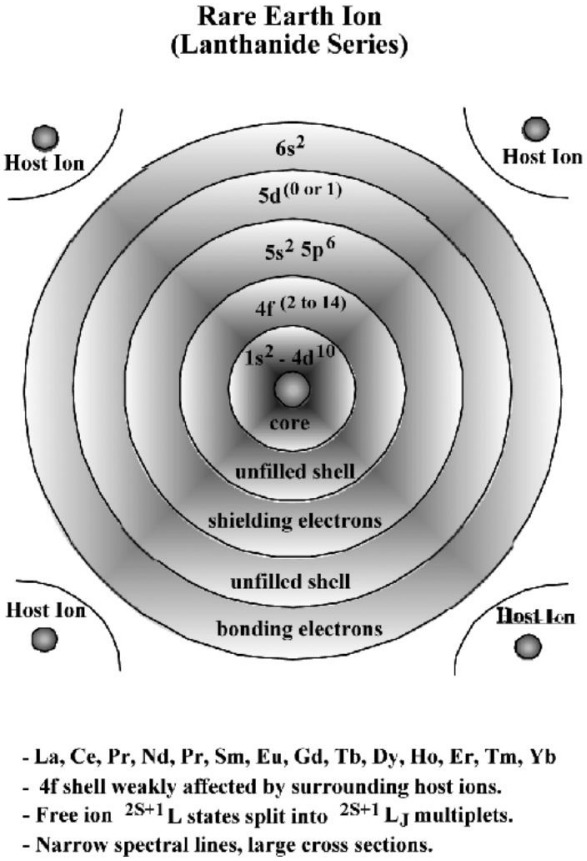

Figure 2.4. Electronic configuration of the lanthanide series. Image reproduced from Walsh (2006).[45]

The line strength of lanthanide transitions, $S_{ED}(J;J')$, where J and J' refer to the total angular momentum quantum number before and after the electronic transition,[39] can be described through Judd-Ofelt theory, from which **Eq. 2.6** is derived.[45] Here, S is the total spin angular momentum and L is the total angular orbital momentum.[39] Ω_2, Ω_4, and Ω_6 are the Judd-Ofelt intensity parameters, and they are the square of the charge displacement caused by electric dipole

transition.[46] The intensity parameters are typically determined empirically for different lanthanides, and Görrler-Walrand et al. (1998) report an extensive compilation of these parameters.[46] The terms in the brackets in **Eq. 2.6** represent the intermediate coupled wavefunctions before and after the electronic transition.[45,47] Obtaining J from S and L in this way is based on LS or Russell-Saunders coupling.[39] The irreducible tensor form of the dipole operator are represented by $\boldsymbol{U}^{(\lambda)}$.[45]

$$S_{ED}(J;J') = \sum_{\lambda=2,4,6} \Omega_\lambda \left| \langle f^n[SL]J || \boldsymbol{U}^{(\lambda)} || f^n[S'L']J' \rangle \right| \quad \textbf{(2.6)}$$

The Ce^{3+} exhibits narrow absorbance peaks in the wavelength range of 190 nm to 500 nm in glasses,[48,49] sulfuric acid,[50,51] and a mixture of MSA and sulfuric acid.[52] These peaks are attributed to 4*f*→5*d* transitions and indicate a loss of degeneracy of the 5*d* orbitals when a 4*f* electron is excited to a 5*d* orbital.[48,53] In contrast, Ce^{4+} has a wider absorption band that is characteristic of charge transfer transitions from the first-coordination-sphere ligand to the 4*f* orbital of cerium.[48] The peak locations of Ce^{3+} and Ce^{4+} shift depending on the first-coordination-sphere of the cerium ion[49] and signify changing covalency between the metal ion and the ligands. The 4*f*→5*d* transition energies decrease as covalency increases because the partly filled 4*f* shell expands due to a nephelauxetic effect, which decreases the interelectronic repulsion between the 5*d* and ligand orbitals. This phenomenon is reflected in Judd-Ofelt theory by the dependence of one of its parameters, Ω_2, on the energy difference between the 4*f* and 5*d* orbitals.[54,55] The weaker repulsion results in shorter cation-ligand distances and lower energies required for electronic transitions.[48,49] Therefore, altered line intensities, spectra lines shifts, and the splitting and broadening of spectral lines[49] are evidence of ligand complexation with cerium ions.

2.3.3 X-ray absorption fine structure spectroscopy

General Background on EXAFS. X-ray absorption fine structure spectroscopy (XAFS) can be used to study the chemical nature of an atom as well as its structure in relation to its surrounding environment, e.g., coordination number, distances to neighboring atoms, and neighboring atom composition. We refer to the atom being studied by XAFS as the central, absorbing atom, because XAFS measures the change in X-ray absorption probability of the atom at or above a core electron of the atom.[32] XAFS is a type of X-ray absorption spectroscopy, which relies on the photoelectric effect, which is shown in **Fig. 2.5a**. The photoelectric effect occurs when an X-ray of a specific energy that matches the energy of a core electron of the central atom is passed into a sample.[32] The energy of the core electrons correspond to orbitals such as the 1*s* or 2*p* levels. When this occurs, the X-ray is absorbed by the central atom, which causes the core electron to be ejected as a photoelectron into the continuum and creates a core hole. Then, a decaying event occurs within a few femtoseconds of the excitation event.[56] There are two decaying methods: X-ray fluorescence (**Fig. 2.5b**) and the Auger effect (**Fig. 2.5c**). In X-ray fluorescence, a higher energy core electron will drop down to fill the core-hole, and this process results in the ejection of an X-ray of well-defined energy.[56] K_α refers to the fluorescence line that occurs when a core electron of the L shell drops into the K shell, and K_β refers to the fluorescence that occurs when a core electron from the M shell drops into the K level. In the Auger effect, a higher energy electron drops down to fill the core-hole, and an additional electron is ejected into the continuum. When X-rays have energies greater than 2 keV, fluorescence will be more prevalent than the Auger effect, but at lower energies, the Auger effect dominates.[56]

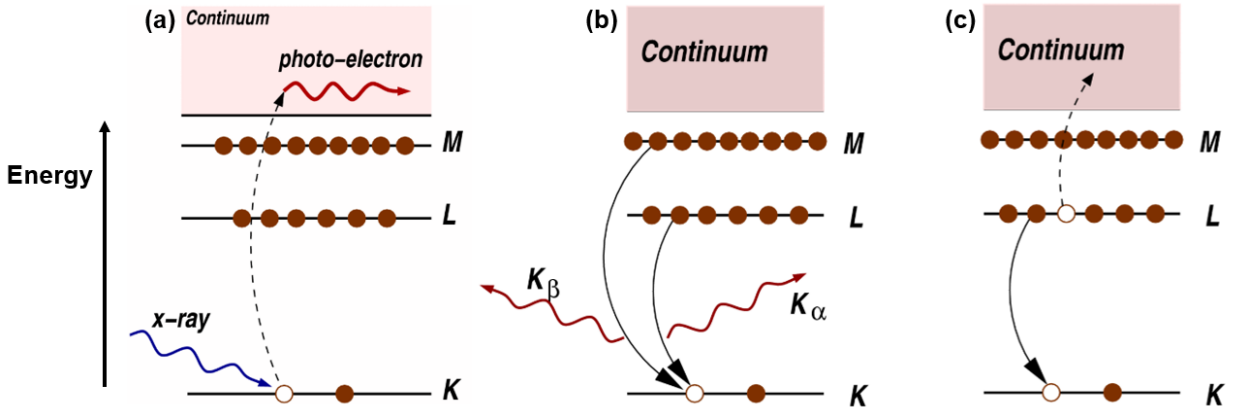

Figure 2.5. (a) Photoelectric effect, in which the X-ray with the same energy as the core electron is absorbed and the core electron is ejected as a photo-electron into the continuum of the sample. **(b)** X-ray fluorescence, in which the core hole is filled by a higher level core electron, which in turn ejects an X-ray of well-defined energy (K_α or K_β) depending on the level of the higher level core electron. **(c)** Auger effect, in which a higher energy electron fills the core hole and another photo-electron is ejected into the continuum. The K, L, and M labels refer to different absorption edges, which align with energies of the core electron of the central atom. Image adapted from Newville (2004).[56]

Regardless of the decay event that takes place, the absorption of the X-ray can be measured, although it is noted that fluorescence is more common to measure than the Auger effect.[56] The probability of the absorption of the X-ray is described by the Beer-Lambert Law,[32] which was defined previously in **Eq. 2.2**. XAFS is often displayed as the absorption coefficient, $\mu(E)$, measured against the X-ray energy, where $\mu(E)$ is distinct from the electric dipole operator $\hat{u}$ described earlier. $\mu(E)$ can be calculated from the Beer-Lambert law as shown below in **Eq. 2.7**, where l is the thickness of the sample, A is the absorbance defined in **Eq. 2.1**-**2.2**, I_0 is the intensity of the incident X-ray, I is the intensity of the X-ray passed through the sample, ε is the sample's molar extinction coefficient, and c is the concentration of the sample.

$$\mu(E) = \frac{1}{l}\ln(10)A = \frac{1}{l}\ln\left(\frac{I_0}{I}\right) = \ln(10)\,\varepsilon \times c \qquad \textbf{(2.7)}$$

As shown in **Fig. 2.6a** for a FeO sample,[56] the absorption of the X-ray can be directly measured. The large jump in absorption is called the absorption edge, and it occurs at the energy

at which the incoming X-ray has the same energy as the core electron, which is called the threshold energy, E_0. Thus the absorption edges, which are labeled K, L_1, L_2, L_3, etc. (see **Fig. 2.5**), correspond to core electron orbitals including $1s_{1/2}$, $2s_{1/2}$, $2p_{1/2}$, $2p_{3/2}$, etc.[57] Because the core-level electron energies are specific to the atom, XAS is an element-specific method of measurement.[56] X-ray absorption can be measured in two geometries: transmission (**Eq. 2.8**) or fluorescence (**Eq. 2.9**), where I_f is the measured intensity of the fluorescence line.[56]

$$\mu(E) = \log(I_0/I) \tag{2.8}$$

$$\mu(E) \approx I_f/I_0 \tag{2.9}$$

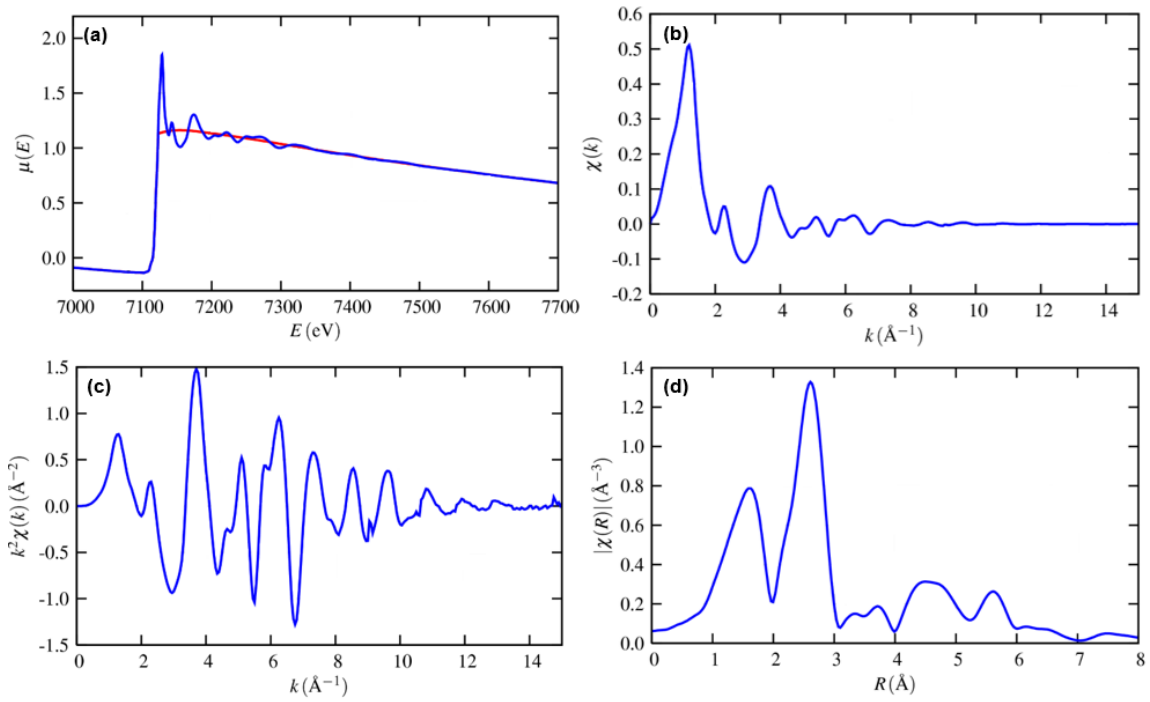

Figure 2.6. (a) XAS absorption spectrum of the FeO crystal, **(b)** EXAFS data of the FeO crystal in the k space, **(c)** k^2 weighted EXAFS data of the FeO crystal in the k space, and **(d)** EXAFS data of the FeO crystal in the R space (magnitude). Image adapted from Newville (2004).[56]

XAFS refers to the absorption region near and above the absorption edge and is shown in **Fig. 2.6a** by the oscillations in the absorption coefficient as a function of X-ray energy that occur

at higher energies than the absorption edge. The XAFS can be split into two regions: the X-ray absorption near edge spectra (XANES) and the extended X-ray absorption fine structure (EXAFS) spectra. XANES is generally considered to be within 30 eV of the absorption edge.[56] The oscillations in the absorption spectrum occur because the emitted photo-electron of the central atom can scatter between the central atom and any neighboring atoms before returning to the absorbing atom, which alters the absorption coefficient.[32] The EXAFS region of the absorption spectrum can be related to the EXAFS fine-structure function $\chi(E)$ through **Eq. 2.10**, where $\mu_0(E)$ is a smooth background function that represents the absorption of an isolated atom (demonstrated in **Fig. 2.6a** by the red line), and $\Delta\mu_0(E)$ is the jump in the absorption at the threshold energy E_0.[32] The EXAFS can be treated as wavelike, and so it is helpful to redefine **Eq. 2.10** in terms of the wave number of the photo-electron k, which is defined in **Eq. 2.11**.[32] Here, m is the electron mass and $\hbar$ is Planck's constant. Thus, the EXAFS spectrum can be redefined as a function of k, as shown in **Fig. 2.6b**.

$$\chi(E) = \frac{\mu(E) - \mu_0(E)}{\Delta\mu_0(E)} \tag{2.10}$$

$$k = \sqrt{\frac{2m(E - E_0)}{\hbar^2}} \tag{2.11}$$

Because the EXAFS oscillations decay quickly with increasing k, the EXAFS spectrum is multiplied by powers of k as shown in **Fig. 2.6c** for a k^2 weighted case, i.e., $k^2 \cdot \chi(k)$. The EXAFS equation (**Eq. 2.12**) describes the oscillations observed in the $\chi(k)$ spectra, which each correspond to near-neighbor coordination shells of the central atom. In **Eq. 2.12**, $f_j(k)$ and $\delta_j(k)$ are scattering properties of neighboring atom j, N_j is the number of neighboring atom j, R_j is the distance to the

neighboring atom j, and σ_j^2 is the Debye-Waller factor[58] for the neighboring atom j, which is a measure of the disorder in the neighbor distance.[32] The EXAFS equation allows us to determine the coordination number and scattering distance between the central atom and any neighboring atoms by fitting it to experimental spectra. It also allows us to determine the specific elemental composition of the neighboring atom because the scattering properties are dependent on the neighboring atom's number, Z.[32]

$$\chi(k) = \sum_j \frac{N_j f_j(k) e^{-2k^2\sigma_j^2}}{kR_j^2} sin\left[2kR_j + \delta_j(k)\right] \quad \textbf{(2.12)}$$

The EXAFS equation is based on Fermi's golden rule (**Eq. 2.13**), where $\langle i|$ is the initial state and $|f\rangle$ is the final state of the sample before and after X-ray absorption, and H is the interaction term, which represents going from the initial energy and momentum state to the final energy and momentum state during the electronic transition,[56] and can be defined as the product of the polarization vector and electron coordinate.[59] The interaction term simplifies to a term that is proportional to e^{jkr},[32] where j is the imaginary number, k is the wavenumber, and r is the distance between the central atom and a neighboring atom. Additionally, the change in the final state can be described by the scattered photoelectron wave-function $\psi_{scatter}(r)$.[32] Thus, EXAFS will be proportional to the wavefunction of the scattered photo-electron,[32,57] and through manipulation of **Eq. 2.13**, the EXAFS equation (**Eq. 2.12**) can be obtained.

$$\mu(E) \propto |\langle i|\mathrm{H}|f\rangle|^2 \quad \textbf{(2.13)}$$

Another common method of presenting EXAFS data is shown in **Fig. 2.6d**, in which the Fourier transform of the EXAFS is taken, converting $\chi(k)$ to $\chi(R)$.[32] While a Fourier transform

results in both imaginary and real components, it is common to present the magnitude of the Fourier transform, as is shown in **Fig. 2.6d**. This is done because the peaks of the magnitude component correspond to significant scattering events of the X-ray between the central atom and its neighbors.[32] It can be considered similar to a radial distribution function, $g(R)$, in which the probability of an atom being a distance R away from the absorbing atom is given, but the EXAFS gives additional information regarding the elemental composition of the surrounding environment.[32] EXAFS can provide information on the types of atoms surrounding the central atom because the scattering properties in the EXAFS equation, $f_j(k)$ and $\delta_j(k)$, are dependent on the atomic weight of the neighboring atom.[32] Thus, if we obtain a satisfactory fit of the EXAFS using scattering properties of a particular atom, then we can conclude that that atom is a neighbor to the central atom. Although the magnitude of the EXAFS presents a relatively intuitive way to study the EXAFS, it can hide important oscillations in the complex $\chi(R)$,[32] and so it is best practice to report either the imaginary or real component of the EXAFS data in addition to the magnitude. Another important aspect of the $\chi(R)$ spectrum is that it is shifted by approximately -0.5 Å[32] because of the scattering phase shift $\delta(k)$.

The software ATHENA[60] can be used to perform EXAFS data reduction and normalization, and ARTEMIS[60] can be used to fit the normalized EXAFS data with possible scattering pathways. The expected scattering pathways can be generated using FEFF9 if the xyz-coordinates of a structure (typically, geometrically optimized using density functional theory) are fed into JFEFF.[61] By fitting the expected scattering pathways to the experimental data, the relevant scattering events can be identified, as can the coordination number, N_j, and scattering distance, R_j, from the EXAFS equation.

EXAFS of Ce^{3+} and Ce^{4+} ions. At the L_3-edge, the threshold energy E_0 for Ce^{3+} is 5723.4 eV,[62] while at the K-edge, it is 40443 eV.[62] There is more uncertainty in the exact value of the E_0 value for Ce^{4+}, especially at the L_3-edge because it displays a unique doublet feature,[63,64] but it is expected that the Ce^{4+} E_0 value will be higher than the Ce^{3+} E_0 value because higher oxidation states have higher core electron energies. The structures of Ce^{3+} and Ce^{4+} in aqueous media are analyzed using EXAFS in both **Chapter 4** and **Chapter 5**, and the experimental details related to the collection, normalization, and fitting of the EXAFS spectra are given in more detail in those chapters.

2.4 Cerium concentration determination

To accurately compare kinetic parameters extracted from different experimental conditions (e.g., electrolyte, acid concentration, electrode material), it is necessary to ensure that the cerium ion concentrations at which the parameters are being compared is accurate. These are important because of the role of the ion concentration on observed kinetics for many charge transfer mechanisms. The cerium ion concentrations are often reported for RFBs in terms of the total cerium ion concentration and the state of charge (SoC). SoC indicates the relative oxidation state of cerium ions in solution, with 0% SoC representing a sample that is comprised entirely of Ce^{3+}, and 100% SoC a sample that is entirely Ce^{4+} (**Eq. 2.14**).

$$\text{SoC} = \frac{[Ce^{4+}]}{[Ce^{3+}] + [Ce^{4+}]} \quad (\mathbf{2.14})$$

There are multiple methods of determining SoC, such as using open circuit voltage (OCV) to extract SoC from the Nernst equation, comparing UV-Vis peaks of unknown samples to calibrated UV-Vis peaks of samples with known SoC, and using titration to determine the amount

of Ce^{4+} present in solution. The titration method is the most accurate way to measure SoC. Each method is described below.

2.4.1 Determining Ce concentration through open circuit voltage

In the OCV method, the Nernst equation (**Eq. 2.15**, written for generic oxidized O and reduced R species), is used to compare the open circuit voltage (OCV, E_{cell}) of the cerium-acid solution to the standard OCV (E°_{cell}) of the cerium redox couple in the acid (i.e., when equilibrium is achieved and $[Ce^{4+}] = [Ce^{3+}]$). In **Eq. 2.15**, R is the ideal gas constant, T is the temperature, n is the number of electrons in the electron transfer, assumed to be 1 for Ce^{3+}/Ce^{4+}, and F is the Faraday constant. Since the standard redox potential is the point at which Ce^{3+} and Ce^{4+} concentrations are equal, the change in cell potential from the standard potential can be used to extract the amount of Ce^{4+} present relative to Ce^{3+}, and thus the SoC. The OCV method is prone to error, however, as it assumes that the OCV is a reflection of only the reaction of interest (Ce^{3+}/Ce^{4+}), which may not be the case. For instance, the oxygen evolution reaction (OER) has a similar redox potential (1.23 V vs. SHE)[65] to Ce^{3+}/Ce^{4+} in H_2SO_4 (1.44 V vs. SHE), and is known to be competitive with the Ce^{3+}/Ce^{4+} redox reaction in aqueous solutions. If OER is occurring in addition to the Ce^{3+}/Ce^{4+} reaction, then the OCV of the system would be decreased relative to the OCV for a system which just had the Ce^{3+}/Ce^{4+} redox reaction occurring. Thus, when not taking into account competitive OER, the calculated SoCs would be calculated to be lower than they actually are.

$$E_{cell} = E^{\circ}_{cell} + \frac{RT}{nF}\ln\frac{[O]}{[R]} \qquad \textbf{(2.15)}$$

2.4.2 Determining Ce concentration through UV-Vis spectroscopy

In the UV-Vis method, UV-Vis absorption spectra of samples of known concentrations of Ce^{3+} and Ce^{4+} are collected as a function of wavelength. Gaussian curves of these spectra are then constructed to extract fitting parameters that are independent of cerium concentration. Then, these Gaussian equations are fitted to UV-Vis spectra of samples with unknown concentrations of Ce^{3+} and Ce^{4+} using least-squares regression to extract cerium concentration. The UV-Vis method, however, can be inaccurate as it is difficult to deconvolute the contributions of Ce^{3+} and Ce^{4+} to peak intensities as the two oxidation states are active at similar wavelengths.

2.4.3 Determining Ce concentration through titration

In titration, the cerium solution is used to titrate a sample of ammonium iron(II) sulfate of known concentration to determine the concentration of Ce^{4+}.[66–68] To determine the concentration of Ce^{4+} in a solution, we prepare 5 mL of a known concentration of ammonium iron(II) sulfate (Acros Organics, 99+%, for analysis) in 2 M H_2SO_4, add a drop of Ferroin Oxidation-Reduction Indicator (LabChem), and then titrate the cerium solution in until the solution changes from a red/burnt orange color to a pale blue. The amount of cerium solution it takes to completely oxidize Fe^{2+} to Fe^{3+} can then be used to calculate the concentration of Ce^{4+} in the original cerium solution. If the total concentration of cerium ions is known, then the state of charge (SoC) can be estimated from **Eq. 2.14**. A potential disadvantage of the titration method is that the total concentration of the cerium ions could be decreasing with time due to crossover in the electrochemical cell, which would not be detected through titration of the working electrode sample. If we did not correct for crossover, then the calculated SoC would be lower than the actual SoC.

Each of the three methods described above have advantages and disadvantages. The appropriate technique for estimating SoC will depend on the circumstances of the solution being

studied, e.g., are there possible competitive side reactions that could impact the OCV or do the different oxidation states have distinct UV-Vis peaks that can be deconvoluted from each other. For the Ce^{3+}/Ce^{4+} kinetic studies conducted in this dissertation, a combination of these techniques is used. The SoCs are calculated using both titration and OCV, and the corresponding kinetic activity that is measured for that solution is only reported if the SoC from both methods is within 10% of each other. The UV-Vis of the solution is also used qualitatively to confirm that the solution spectrum is in agreement with other spectra collected at the same SoC.

2.5 Electrochemical techniques

In this section, we describe the techniques used to study the electrochemical behavior of the Ce^{3+}/Ce^{4+} redox reaction in **Chapter 5**. Specifically, we introduce cyclic voltammetry, electrochemical impedance spectroscopy, and electrochemical active surface area (ECSA) characterization techniques. Finally, we describe how kinetic parameters can be extracted from experimental electrochemical measurements.

2.5.1 Cyclic voltammetry

In cyclic voltammetry, a linearly varying potential E is applied to the electrode or "swept" at a certain speed, called the scan rate. The response current I of the electrode is measured as a function of potential applied to create a cyclic voltammogram (CV).[69] A sample CV is included in **Fig. 2.7** below. The cathodic trace refers to when the potential is swept negatively from a starting potential to the switching potential,[70] after which the scan is reversed and the anodic trace is completed (i.e., potential is swept positively back to starting potential). Cathodic and anodic peaks occur in the CV as reduction and oxidation rates of reaction start to decrease, respectively.

As the potential is swept negatively, e.g., the cathodic trace, both oxidation and reduction can be occurring, which results in the current measured in the CV. As the cathodic trace becomes significantly more negative than the equilibrium redox potential of the system, the reduction reaction will begin to dominate, where the oxidized species O is reduced to the reduced species R near the electrode surface. At the point at which the cathodic current is a maximum (peak labeled $I_{p,c}$ in **Fig. 2.7**), called the cathodic peak, the current is controlled by the amount of additional O that can be delivered to the electrode surface, since O is continuously being converted to R locally.[70] As more negative potentials are applied, the diffusion layer, which is the thickness of the solution to the electrode surface where the local concentration O differs from the bulk O concentration, increases. Thus, mass transfer becomes slower and the current associated with O reduction decreases until the switching potential is met. At the switching point, the potential begins to be swept in the positive direction, e.g., the anodic trace, and the current is related to the oxidation and reduction reactions that are possible at the potential applied relative to the OCV. As the applied potential becomes larger than the equilibrium redox potential of the system, R oxidation begins to dominate until the anodic peak (peak labeled $I_{p,a}$ in **Fig. 2.7**) is reached.

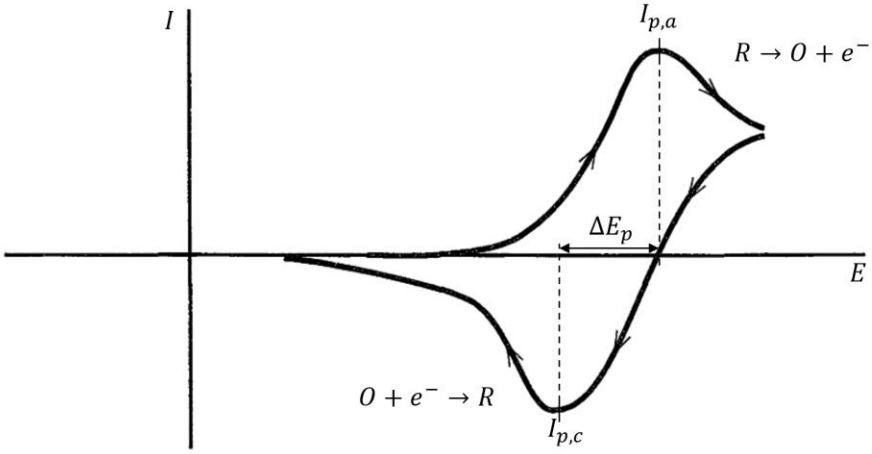

Figure 2.7. Example CV for generic species O and R, with $I_{p,c}$, $I_{p,a}$, and ΔE_p labeled. Image adapted from Bard and Faulkner (2001).[71]

CVs are a useful tool to characterize electrochemical processes and have been used for a variety of applications, including identification of oxidation and reduction steps, electrochemical cleaning (through repeated plating and stripping of an electrode surface), double layer capacitance measurements, and extraction of kinetic parameters (as will be described in **Section 2.5.4**, the potential difference in cathodic and anodic peak currents, ΔE_p, is a useful indicator of kinetic reversibility).

2.5.2 Electrochemical impedance spectroscopy

EIS is used to measure the impedance of an electrochemical cell, where impedance, Z in **Eq. 2.16** below, is the frequency dependent resistance to current flow. When using EIS, a sinusoidal oscillating perturbation with fixed frequency is applied to the voltage, E_t in **Eq. 2.16**, and the resulting frequency-dependent current is measured, I_t in **Eq. 2.16**. I_t will be sinusoidal with the same frequency as E_t, but it may have a phase shift, ϕ, relative to the E_t function.[71,72] E_t and I_t can be defined in terms of sine or cosine waves, or as a superposition of cosine and sine waves, as was done in **Eq. 2.16**.[72] Here, $E_{t,0}$ is the amplitude of the excitation signal, $I_{t,0}$ is the amplitude of the response signal, ω is the radial frequency, , and j is the imaginary unit $\sqrt{-1}$.

$$Z = \frac{E_t}{I_t} = \frac{E_{t,0}\cos(\omega t) + jE_{t,0}\sin(\omega t)}{I_{t,0}\cos(\omega t - \phi) + jI_{t,0}\sin(\omega t - \phi)} = \frac{E_{t,0}(\cos(\omega t) + j\sin(\omega t))}{I_{t,0}(\cos(\omega t - \phi) + j\sin(\omega t - \phi))} \quad \textbf{(2.16)}$$

Using Euler's relationship $(\exp(jx) = \cos(x) + j\sin(x))$, impedance can be expressed as a complex number, as shown in **Eq. 2.17** below.

$$Z(\omega) = Z_0 \frac{\exp(j\omega t)}{\exp(j(\omega t - \phi))} = Z_0 \exp(j\phi) = Z_0(\cos\phi + j\sin\phi) \quad \textbf{(2.17)}$$

In an experiment, since E_t is set and I_t is measured, these values can be compared and divided into imaginary and real components, as shown in **Eq. 2.17**. By plotting the imaginary component of the impedance against the real component, a Nyquist plot can be obtained, where each point on the Nyquist plot corresponds to the impedance at one frequency. As shown by the sample Nyquist plot below in **Figure 2.8**, obtained for a Pt rotating disk electrode (RDE) in a 2 M H_2SO_4 solution with 50 mM of total cerium, the solution resistance, R_s, and charge transfer resistance, R_{ct}, can be determined by fitting an equivalent electrical circuit (e.g., Randles circuit) and finding the *x*-intercepts of the semi-circle. The Randles circuit is a simple equivalent circuit that can be used to model the electrode response and is shown as an inset in **Fig. 2.8**. The Randles circuit is composed of the solution resistance, R_s, the charge transfer resistance, R_{ct}, and the double layer capacitance, C_{dl}, and can also include the Warburg impedance, W, which can be used to model linear diffusion. For Randles circuit, **Eq. 2.18** can be used to determine the C_{dl} by determining the radial frequency, ω, at the peak of the semi-circle.

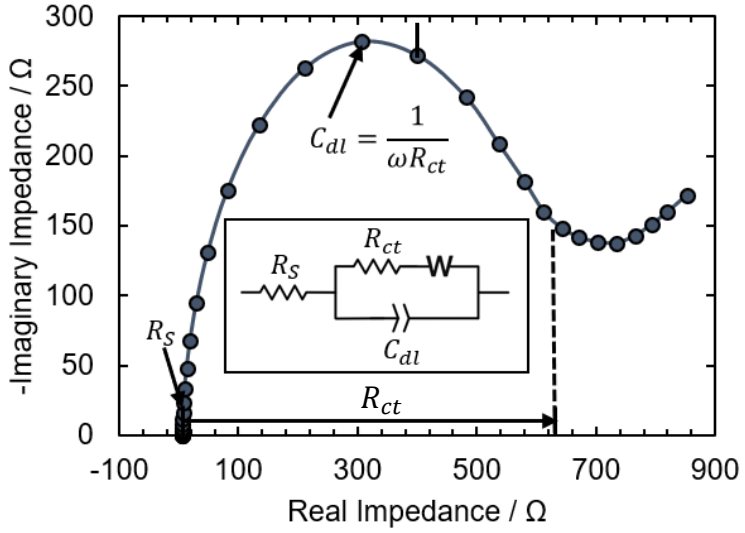

Figure 2.8. Nyquist plot for Pt RDE in 2 M H_2SO_4 solution with 50 mM total cerium ions, at open circuit voltage (OCV), frequency range: 500 kHz to 100 mHz. The inset demonstrates a Randles circuit with Warburg impedance, W. Image of Randles circuit adapted from Lacey (2020).[73]

$$C_{dl} = \frac{1}{\omega R_{ct}} \quad \textbf{(2.18)}$$

2.5.3 ECSA characterization techniques

To measure the catalytic activity of an electrode, it is important to normalize by the electrode's electrochemical surface area (ECSA).[74,75] There are several methods available for obtaining the ECSA of an electrode,[76] broadly divided into methods related to capacitance, coulometric, and geometric. Each of the methods are described in more detail below.

Capacitance. In capacitance-based methods, the double layer capacitance is used to extract the ECSA based on an estimation of the specific capacitance of the electrode/electrolyte interface. To obtain the double layer capacitance, either CVs or EIS can be used. CVs and EIS are described in detail in **Section 2.5.1** and **Section 2.5.2**, respectively. When using a CV, the potential is cycled so that only the non-Faradaic region is captured for a series of scan rates, as demonstrated in **Fig. 2.9a** for a polycrystalline Pt electrode.[77] Then the difference between the anodic and cathodic currents in the middle of the potential window are plotted against the corresponding scan rate (see **Fig. 2.9b**). The difference in currents should display a linear dependence with the scan rate if double layer charging is the only process occurring,[77] and half of the slope of the line is the double layer capacitance value. Alternatively, as described in **Section 2.5.2**, EIS can be used to determine the double layer capacitance directly from the Nyquist plot through **Eq. 2.18**. Then, the ECSA can be calculated by dividing the double layer capacitance (in units of μF) by the specific capacitance of the electrode/electrolyte interface (μF cm^{-2}). The specific capacitance of the electrode/electrolyte is not always well known, with reported values ranging typically between 20 and 40 μF cm^{-2}.[77] It has been noted that this uncertainty in specific capacitance can lead to large errors in ECSA calculated through capacitance.[77]

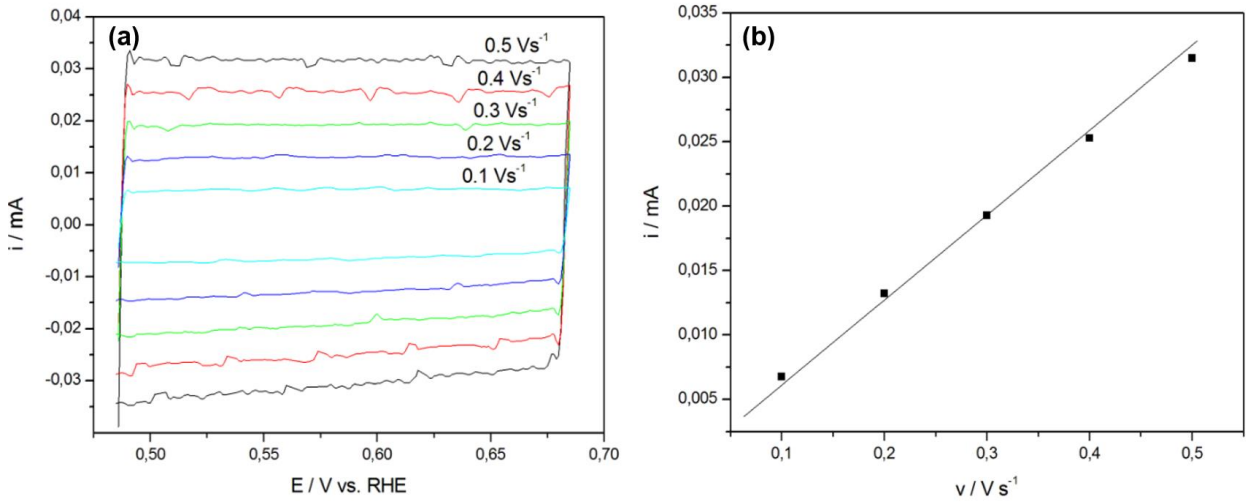

Figure 2.9. For a polycrystalline Pt electrode in 0.5 M H_2SO_4, **(a)** CV of the non-Faradaic region for a series of scan rates, and **(b)** the difference in anodic and cathodic current in the middle of the potential range as a function of scan rate, from which the double layer capacitance can be extracted. Images adapted from Lukaszewski et al. (2016).[77]

Coulometric. Coulometric methods involve directly counting the charge associated with reactions limited to the surface of the electrode. For Pt-metal group electrodes a common coulometric method is to use Hydrogen Underpotential Deposition (HUPD),[78] which is based on the capability of Pt-group metals to adsorb a monolayer of hydrogen at reducing potentials slightly more positive than reducing potentials that would result in bulk hydrogen evolution.[76] To perform HUPD on Pt, as was done for the Pt electrode studied in **Chapter 5**, either a CV or chronopotentiometry[76] (fixed current steps are applied and the resulting potential is monitored) is used to determine the potential at which the switch from the adsorption of the hydrogen monolayer to bulk hydrogen evolution will occur. A limiting assumption of the HUPD technique is that the onset of hydrogen evolution after hydrogen adsorption can be exactly identified.[76] After this point is identified, additional CVs are completed with the potential range set so that the most negative potential reached is at the edge of the hydrogen adsorption range, and the most positive potential applied results in Pt oxidation, as demonstrated in **Fig. 2.10**. The characteristic features of the Pt HUPD region (**Fig. 2.10**) include the two peaks associated with hydrogen adsorption and hydrogen desorption.

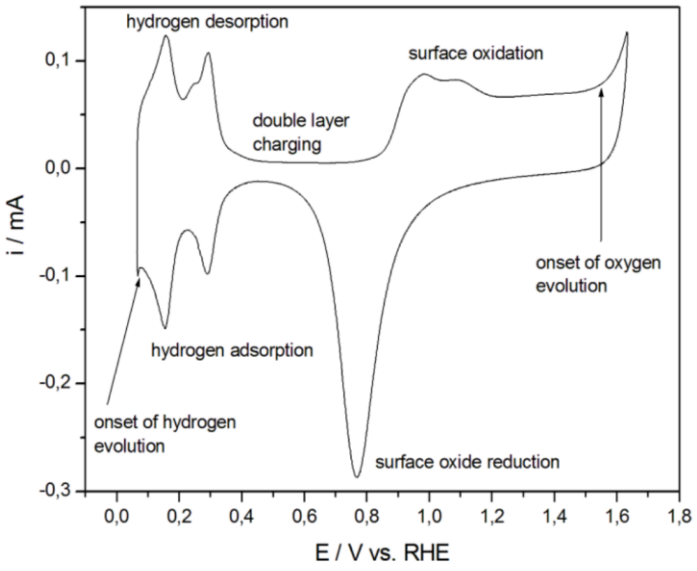

Figure 2.10. Example of a CV in which the HUPD region is clearly shown between 0.05 V vs. RHE and 0.3 V vs. RHE for a polycrystalline Pt electrode in 0.5 M H_2SO_4. Image adapted from Lukaszewski et al. (2016).[77]

To determine the ECSA using the HUPD technique, the amount of charge associated with the desorption of a monolayer of adsorbed hydrogen on the Pt-group electrode is divided by the specific charge of the electrode material (in units of μC cm^{-2}) to obtain the ECSA. The desorption charge is usually used because the adsorption charge is difficult to deconvolute because of the contributions from the onset of hydrogen evolution.[77] Each metal atom on the surface is assumed to adsorb one hydrogen atom.[76] The specific charge of Pt was assumed to be 210 μC cm^{-2} in **Chapter 5**, based on reported specific charge values for polycrystalline Pt.[76] Before dividing the desorption charge by the specific charge, the amount of charge associated with the non-Faradaic region, which is associated with double layer charging, must be subtracted out.[77] Coulometric methods such as HUPD are generally considered to be more accurate than capacitance based techniques, because HUPD physically measures how much hydrogen adsorbs, however it can underestimate true surface area for surfaces that have modified electronic structures.[79]

Geometric. In the geometric method, an estimate of the surface area is made based on the geometry of the electrode. For instance, for the standard 5 mm rotating disk electrode (RDE), the geometric

surface area is 0.196 cm^2. The geometric method is a simple method of approximating the current density if capacitance or coulometric methods cannot be used, but it is typically the least accurate. Simply approximating the ECSA as the exposed area (assuming a uniformly flat surface) typically leads to large errors due to roughness of the electrode surface.

2.5.4 Methods of extracting kinetic parameters

Here we discuss methods (Butler-Volmer, Tafel, charge transfer resistance, Koutecký-Levich, and CV) used for extracting kinetic parameters, including the exchange current density, Tafel slope, standard rate constant, and diffusion coefficient. To obtain the kinetic parameters included in **Chapter 5** for the Ce^{3+}/Ce^{4+} redox reaction on Pt and glassy carbon, we primarily used the Butler-Volmer method coupled with the Tafel and charge transfer resistance methods. The Koutecký-Levich method was used to confirm that the measured currents are kinetically controlled. Here, we also include a discussion of the CV method, which is a common method but is not appropriate for the Ce^{3+}/Ce^{4+} system, as will be described below.

Butler-Volmer method. In the Butler-Volmer formulation of kinetics, the current density i is described as a function of overpotential, η, as shown in **Eq. 2.19**. In **Eq. 2.19**, α is the cathodic charge transfer coefficient, which indicates the symmetry of the redox reaction, and i_0 is the exchange current density, which represents the "background" current that flows at equilibrium conditions and indicates how fast the kinetics are.[71] η is defined as the difference between the applied electrode potential and the equilibrium potential of the system. With some simplifying assumptions, the Butler-Volmer formulation can be reduced to a form in which the i_0 is related to the standard rate constant (k_0), as shown in **Eq. 2.20**. In **Eq. 2.20**, C_O^* and C_R^* are the bulk concentrations of the oxidized (O) and reduced (R) species, respectively. Since the i_0 can be

extracted experimentally either through the Tafel equation or the charge transfer resistance, as will be described next, this provides a convenient means to obtain a k_0.

$$i = i_0 \left(e^{-\alpha\left(\frac{F}{RT}\right)\eta} - e^{(1-\alpha)\left(\frac{F}{RT}\right)\eta} \right) \quad \textbf{(2.19)}$$

$$i_0 = nFk_0 C_O^{*(1-\alpha)} C_R^{*\alpha} \quad \textbf{(2.20)}$$

Once experimental exchange current densities are obtained, **Eq. 2.20** can be fit to the i_0 as a function of C_O^* and C_R^* to obtain k_0 and α. This method is used in **Chapter 5** as a simple way to compare the kinetic parameters of the Pt and glassy carbon electrodes for the Ce^{3+}/Ce^{4+} redox reaction. Derivation of the Butler-Volmer equation is described in more detail in **Section 2.6**.

Tafel method. To obtain i_0, as well as the Tafel slope, the Tafel method can be used. If the applied overvoltage η is large enough that one exponential term in **Eq. 2.19** becomes negligible, i.e., >118 mV at 25 ℃,[71] then **Eq. 2.19** can be further simplified. For instance, for a large negative η, **Eq. 2.19** reduces to **Eq. 2.21**.

$$i = i_0 e^{-\alpha\left(\frac{F}{RT}\right)\eta} \quad \textbf{(2.21)}$$

Rearranging **Eq. 2.21** results in the Tafel equation, **Eq. 2.22**, where the expression $2.3RT/\alpha F$ is the Tafel slope, b, and the *y*-intercept of **Eq. 2.22** is the log of i_0. The factor of 2.3 in the Tafel slope accounts for the conversion from the natural logarithm to the base-10 logarithm. A plot of current versus overvoltage, referred to as the Tafel plot, allows one to obtain both the Tafel slope and i_0.

$$\eta = \frac{2.3RT}{\alpha F}\log i_0 - \frac{2.3RT}{\alpha F}\log i \qquad \textbf{(2.22)}$$

To obtain a Tafel plot, a series of fixed potentials is applied to the electrochemical solution for a certain amount of time that results in steady state currents (**Fig. 2.11a**). For the 0.05 M Ce^{3+}/Ce^{4+} in 2 M H_2SO_4 solution studied in **Chapter 5**, two minutes was sufficient to achieve steady state currents. The steady state currents are then normalized by the ECSA (see **Section 2.5.4**) and plotted as a function of η (**Fig. 2.11b**). As shown in **Fig. 2.11b**, the *y*-intercept of the plot can be used to obtain i_0 and the Tafel slope can be calculated by inverting the slope of the Tafel plot.

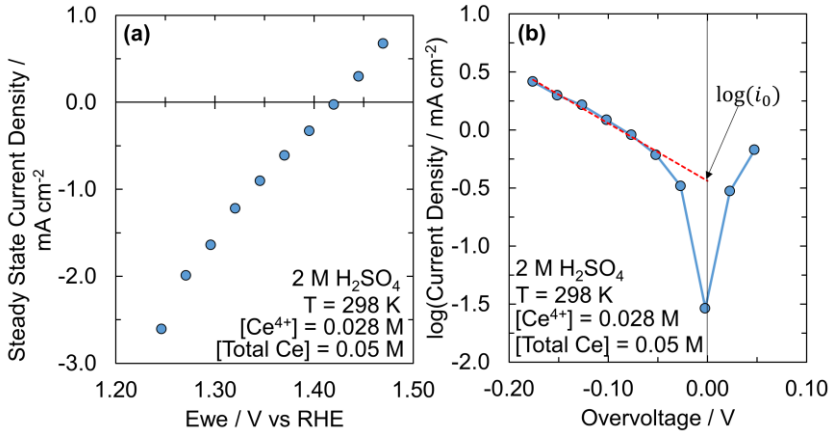

Figure 2.11. For the Pt electrode, 0.05 M total cerium concentration, **(a)** steady state current densities measured as a function of fixed potential, and **(b)** resulting Tafel plot. Red line represents linear fit of Tafel plot in appropriate potential region to obtain i_0.

Charge transfer resistance method. If η is close to zero, then **Eq. 2.19** reduces to **Eq. 2.23** below.[71]

$$i = -i_0\left(\frac{F}{RT}\right)\eta \qquad \textbf{(2.23)}$$

Rearranging **Eq. 2.23** to obtain an expression for $\eta/_i$, which is often referred to as the charge transfer resistance R_{ct} due to its units of Ωcm^2, **Eq. 2.24** is obtained, which allows one to calculate the i_o if R_{ct} is known. EIS is used to determine R_{ct} as discussed in more detail in **Section 2.5.2**.

$$i_0 = \frac{RT}{FR_{ct}} \quad \textbf{(2.24)}$$

Koutecký-Levich approach. The Koutecký-Levich approach allows for deconvolution of the contributions of the mass transport of the oxidized and reduced species and the kinetic activity to the observed current of an electrochemical system. Hydrodynamic and convective-diffusion equations have been developed rigorously for the rotating disk electrode (RDE) at steady-state,[71] and the Koutecký-Levich equation was derived for this electrochemical set-up. In solving the hydrodynamic equations for the RDE, it is assumed that gravitational forces are absent, and that there are no special flow effects at the edge of the disk. An RDE consists of a disk of an electrode material embedded in an insulated material,[71] such that the rotation of the RDE can be controlled to manipulate electrochemical activity. **Eq. 2.25** is the Koutecký-Levich equation, where i_K represents the current that flows under kinetic limitation (i.e., mass transfer is fast enough to keep concentration at surface equal to the bulk concentration),[71] and $i_{l,c}$ is the limiting current and defined in **Eq. 2.26** for the RDE configuration. The limiting current is defined as the maximum rate of electron transfer possible for a given set of mass transport conditions.[71] In **Eq. 2.26**, ω is the angular velocity in s^{-1}.

$$\frac{1}{i} = \frac{1}{i_K} + \frac{1}{i_{l,c}} \quad \textbf{(2.25)}$$

$$i_{l,c} = 0.62nFAD_O^{2/3}\omega^{1/2}\nu^{-1/6}C_O^* \quad \textbf{(2.26)}$$

Plotting $1/i$ versus $1/\omega^{1/2}$ results in a straight line that can be extrapolated to $1/\omega^{1/2} = 0$ to obtain $1/i_K$. The i_K is measured at different E and can be used to evaluate kinetic parameters of k_0 and α.

Because the Koutecký-Levich approach is useful for differentiating between kinetic and mass transport contributions to observed current as a function of potential, we use it to confirm that the Ce^{3+}/Ce^{4+} currents reported in **Chapter 5** are kinetically controlled instead of mass transport controlled.

CV method. The k_0 can be extracted from a CV of a simple one step electron transfer step by manipulating the governing diffusion equations under a set of simplifying assumptions. It is common to assume a uniform electrode surface, a planar electrode with diffusion acting as the only form of mass transport (i.e., no convection, including natural convection),[80] and that the electron transfer at the surface is so rapid that the redox species concentrations immediately adjust to those predicted by the Nernst equation.[71] The ratio of the anodic and cathodic peak currents, $i_{p,a}/i_{p,c}$, provides an indication of chemical reversibility. $i_{p,a}/i_{p,c}$ will be equal to 1 for a system with a stable product,[71] e.g., chemically reversible. Deviations of $i_{p,a}/i_{p,c}$ from 1 indicate complications in the electrode process.[71] The difference between the cathodic and anodic peaks of the CV, or peak-to-peak separation (ΔE_p) can be used to assess electrochemical reversibility as well as to extract k_0. Electrochemical reversibility refers to the rate of electron transfer between the electrode and electrolyte and is also related to the symmetry of the reaction, with electrochemically reversible reactions having values of α close to 0.5. An electrochemically reversible one-electron reaction, i.e., a reaction with a low barrier to electron transfer, will have a ΔE_p of 57 mV at room temperature once steady state CVs are reached,[70,71] whereas sluggish

electron transfer reactions will have a larger ΔE_p. For quasireversible systems, ΔE_p is function of scan rate (v), k_0, α, and E_λ. E_λ is the potential at which the scan rate is reversed.[71] The k_0 is identified from a parameter ψ, which is defined in **Eq. 2.27** and tabulated for different values of ΔE_p,[71,80,81] provided the reaction is a one electron-transfer ($n = 1$) and $\alpha = 0.5$. Bard and Faulkner note, however, that ΔE_p is nearly independent of α when $0.3 < \alpha < 0.7$.[71] Therefore, after conducting a CV, ΔE_p can be used to identify ψ, which can then be used to calculate k_0 from **Eq. 2.27**. To use **Eq. 2.27** to determine k_0, the diffusion coefficient of the oxidized species, D_O, must also be determined, either from the Randles-Sevcik equation (**Eq. 2.28**) or another method. Assumptions for **Eq. 2.28** are that the electron transfer is reversible and that it occurs between freely diffusing redox species.[70] This equation can be used to determine the diffusion constant D_O by plotting the peak of the cathodic current $i_{p,c}$ vs. $v^{1/2}$ of the reduction scan (i.e., one direction of the CV) and extracting the slope. Additionally, if the species are thought to be freely diffusing, but the plot of $i_{p,c}$ vs. $v^{1/2}$ is non-linear, this is an indication of electrochemical quasi-reversibility or a surface-adsorbed redox species.

$$\psi = \frac{\xi^{\alpha} k_0}{[\pi \sigma D_o]^{1/2}} \tag{2.27}$$

$$i_{p,c} = 0.4463 nFAC_O^* \left(\frac{nFvD_O}{RT}\right)^{1/2} \tag{2.28}$$

While using CVs is an efficient 'diagnostic' method to study new redox systems, it is not ideal for extracting quantitative kinetic values because of the uncertainty in peak separations and heights.[71] Extracting kinetics from CV also relies on operating in a diffusion-limited regime, which can be experimentally difficult to control and also requires that the charge transfer rate law obeys

a predetermined mechanism. The CV method is also unable to distinguish between multiple reactions that may be occurring in the same potential, such as the Ce^{3+}/Ce^{4+} redox reaction and the oxygen evolution reaction (OER). Lastly, uncompensated resistance must be considered small relative to the size ΔE_p for the CV approach of extracting kinetic parameters to be appropriate, because the effect of uncompensated resistance on the behavior of ΔE_p is comparable to that of ψ.[71] This limitation becomes especially significant at higher currents and as k_0 approaches the reversible limit. If the effect of solution resistance on applied potential is compensated for appropriately, however, this specific concern can be rectified.

2.6 Modeling electrode kinetics

As described by Bard and Faulkner (2001),[71] theories to describe electrode kinetics can either be macroscopic or microscopic. The first approach, of which the Butler-Volmer formulism is one, can capture the observed kinetic behavior as a function of potential through a group of empirical parameters like k_0 or α. It cannot, however, be used to make more sophisticated predictions about the influence of the broader electrochemical environment, i.e., the electrode and the electrolyte, on the rate of reaction. For this, a microscopic approach is needed, in which the molecular structure and environment are incorporated into the electrode kinetic model.[71] One such model can be derived from Marcus theory. In this section, the derivation of kinetic models is discussed, first for the Butler-Volmer approach, and then for the Marcus theory. Finally, the general approach to microkinetic modeling is described, which will be used in **Chapter 5** to identify the appropriate mechanism for the Ce^{3+}/Ce^{4+} redox reaction.

2.6.1 Macroscopic approach: Butler-Volmer formulism

To develop the Butler-Volmer formulation, it is first necessary to assume a certain electron transfer model, for instance a reversible, one-electron transfer (**Eq. 2.29**). In **Eq. 2.29**, O is the oxidized species and R is the reduced species. Additionally, it must be assumed that there are no other chemical steps occurring.[71] Current can then be related to the concentrations of the oxidized and reduced species as well as cathodic and anodic rate constants, k_c and k_a, via **Eq. 2.30** below. $C_O(0,t)$ and $C_R(0,t)$ are the concentrations of O and R at the electrode surface as a function of time t.

$$O + e^- \rightleftarrows R \quad \textbf{(2.29)}$$

$$i/A = nF(k_c C_O(0,t) - k_a C_R(0,t)) \quad \textbf{(2.30)}$$

To ascertain expressions for the rate constants, it is useful to relate free energies of the cathodic and anodic reactions, $\Delta G_c^{\ddagger}$ and $\Delta G_a^{\ddagger}$, respectively, to electrode potential, via **Eq. 2.31** and **2.32**, where $\Delta G_{0c}^{\ddagger}$ and $\Delta G_{0a}^{\ddagger}$ are the standard free energies, and α is the cathodic charge transfer coefficient.

$$\Delta G_c^{\ddagger} = \Delta G_{0c}^{\ddagger} + \alpha F(E - E^{\circ}) \quad \textbf{(2.31)}$$

$$\Delta G_a^{\ddagger} = \Delta G_{0a}^{\ddagger} - (1-\alpha) F(E - E^{\circ}) \quad \textbf{(2.32)}$$

If it is assumed that the cathodic and anodic rate constants have an Arrhenius behavior, then they can be related to the cathodic and anodic free energies, and after simplification, the rate constants can be defined as **Eq. 2.33** and **2.34** below.

$$k_c = k_0 \exp\left(\alpha\left(\frac{F}{RT}\right)(E - E^\circ)\right) \quad \textbf{(2.33)}$$

$$k_a = k_0 \exp\left((1-\alpha)\left(\frac{F}{RT}\right)(E - E^\circ)\right) \quad \textbf{(2.34)}$$

Plugging these expressions into **Eq. 2.30**, the Butler-Volmer formulation is obtained as **Eq. 2.35**, which relates to current as a function of potential.

$$i/A = nFk_0\left(C_O(0,t)e^{-\alpha\left(\frac{F}{RT}\right)(E-E^\circ)} - C_R(0,t)e^{(1-\alpha)\left(\frac{F}{RT}\right)(E-E^\circ)}\right) \quad \textbf{(2.35)}$$

If it is assumed that the system is at equilibrium, such that bulk concentrations are also at the electrode surface,[71] then **Eq. 2.35** can be redefined as **Eq. 2.36** below.

$$i_0/A = nFk_0C_O^* e^{-\alpha\left(\frac{F}{RT}\right)(E-E^\circ)} \quad \textbf{(2.36)}$$

Using the Nernst equation to relate bulk concentration to the potential, **Eq. 2.36** can be further simplified to **Eq. 2.37**.[71]

$$i_0/A = nFk_0C_O^{*(1-\alpha)}C_R^{*\alpha} \quad \textbf{(2.37)}$$

From **Eq. 2.37**, i_0 can be directly related to k_0 if the bulk concentrations are known, provided there are no other chemical steps. To relate experimentally determined i_0 to an overall k_0 of an electrode in a specific electrolyte solution, it is first necessary to obtain i_0 from experiment. To do this, **Eq. 2.35** should be divided by **Eq. 2.36** to obtain an expression (**Eq. 2.38**) linking i to i_0.

$$i = i_0\left(\frac{C_O(0,t)}{C_O^*}e^{-\alpha\left(\frac{F}{RT}\right)\eta} - \frac{C_R(0,t)}{C_R^*}e^{(1-\alpha)\left(\frac{F}{RT}\right)\eta}\right) \quad \textbf{(2.38)}$$

If it is further assumed that mass transfer is not limiting, e.g., through efficient stirring and sufficiently low currents,[71] then **Eq. 2.38** can be simplified to the Butler-Volmer equation which was introduced in **Section 2.5.5** as **Eq. 2.19** and reproduced below.

$$i = i_0 \left(e^{-\alpha\left(\frac{F}{RT}\right)\eta} - e^{(1-\alpha)\left(\frac{F}{RT}\right)\eta} \right) \quad \textbf{(2.19)}$$

While the Butler-Volmer formulism of kinetics is a very common method of describing electrode kinetics, it does not allow for a deeper understanding of the electrochemical environment's effect on kinetics. The Marcus theory of electrode kinetics allows for a more nuanced view of the electrode kinetics and is described next.

2.6.2 Microscopic approach: Marcus theory

The Marcus theory of electron transfer kinetics was developed originally for homogeneous electron transfers,[82] which are electron transfers that occur between two metal ions.[71] Its use was eventually extended to heterogeneous electron transfers, which refers to electron transfers between an ionic species and an electrode.[83] There are two main types of electron transfer mechanisms: inner-sphere and outer-sphere. In inner-sphere heterogeneous electron transfers, the active species has to interact directly with the electrode surface, typically through a ligand bridge, for the electron transfer to take place, and so the properties of the electrode control the rate of reaction.[84] This is in contrast to outer-sphere heterogeneous electron transfers, in which the active species does not interact directly with the electrode for the electron transfer to occur.[71] Instead, the electron typically tunnels between at least one monolayer of solvent.[84] As a result, the reaction rate for outer-sphere kinetics are controlled by the properties of the electrolyte, including the reorganization energy, which refers to the energy needed to transform the configuration of the reactant to that of the

product.[71] Marcus theory is specifically used for outer-sphere electron transfers, which is relevant for the Ce^{3+}/Ce^{4+} charge transfer mechanism (see **Chapter 5**).

For a single electron transfer step as shown in **Eq. 2.29** for which Marcus theory is being applied, the kinetic current would still be described through **Eq. 2.30**. The reduction and oxidation rate constants k_c and k_a, however, would not be defined using a constant α, as is done in the Butler-Volmer formulism, but rather they would be described through **Eq. 2.39** and **2.40**.[71]

$$k_{c,MT} = \kappa_{el} K_{p,O} \upsilon_n \exp\left(\frac{-\Delta G^{\ddagger}_{c,MT}}{RT}\right) \quad \textbf{(2.39)}$$

$$k_{a,MT} = \kappa_{el} K_{p,R} \upsilon_n \exp\left(\frac{-\Delta G^{\ddagger}_{a,MT}}{RT}\right) \quad \textbf{(2.40)}$$

In **Eq. 2.39–2.40**, κ_{el} is the electronic transmission coefficient, which is related to the probability of electron tunneling, $K_{p,O}$ and $K_{p,R}$ are the precursor equilibrium constants for the O and R species, respectively, and υ_n is the nuclear frequency factor.[71] $\Delta G^{\ddagger}_{c,MT}$ and $\Delta G^{\ddagger}_{a,MT}$ are the free energies of the transition state for the reduction and oxidation rate constants defined using Marcus theory, as shown in **Eq. 2.41–2.42**, where $\lambda_{MT,j}$ is the reorganization energy of reaction j and ΔG_{MT} represents the free energy of the electron transfer reaction. ΔG_{MT} is related to the electrode potential through **Eq. 2.43**, where E is the electrode potential and E° is the equilibrium potential.

$$\Delta G^{\ddagger}_{c,MT} = \frac{\lambda_{MT.c}}{4}\left(1 + \frac{\Delta G_{MT}}{\lambda_{MT}}\right)^2 \quad \textbf{(2.41)}$$

$$\Delta G^{\ddagger}_{a,MT} = \frac{\lambda_{MT,a}}{4}\left(1 - \frac{\Delta G_{MT}}{\lambda_{MT}}\right)^2 \quad \textbf{(2.42)}$$

$$\Delta G_{MT} = nF(E - E^{\circ}) \quad \textbf{(2.43)}$$

Fig. 2.12 demonstrates that the Gibbs free energy of the oxidized and reduced species are still quadratically dependent on reaction coordinate in Marcus theory. The transition state ($\Delta G^{\ddagger}_{c,MT} = \Delta G^{\ddagger}_{a,MT}$) is represented by the intersection of the two free energy parabolas and is the point at which the oxidized and reduced species have the same configuration.[71] This indicates that that Franck-Condon principle, which indicates that the nuclear momenta and positions of the species involved in the electron transfer do not change at the same time scale as the electron transfer, holds in Marcus theory.[71] The reorganization energies for the cathodic and anodic reactions ($\lambda_{MT,c}$ and $\lambda_{MT,a}$), which are the energy needed to go from the configuration of the reactant to the product without an electron transfer taking place,[85] can be obtained from the free energy curves, as demonstrated in **Fig. 2.12**.

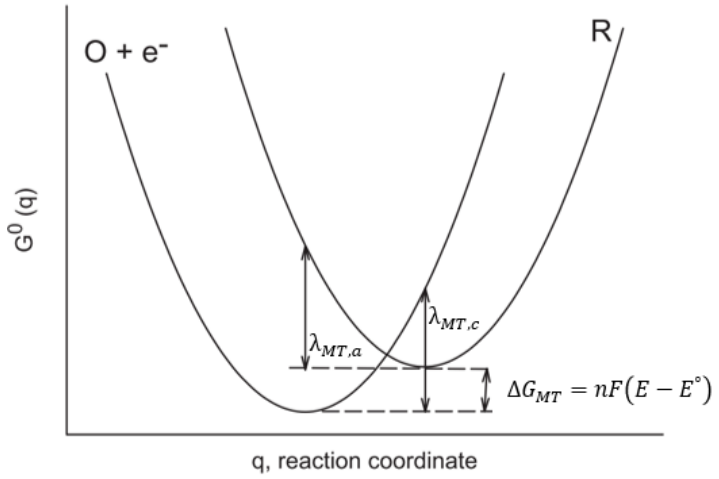

Figure 2.12. Free energy curves G^0 as a function of reaction coordinate q from Marcus theory for a generic oxidation reaction. The reorganization energies for the cathodic ($\lambda_{MT,c}$) and anodic ($\lambda_{MT,a}$) reactions are labeled on the plot, as is the reaction Gibbs free energy ΔG_{MT}. Image adapted from Henstridge et al. (2012).[85]

Several physical insights of Marcus theory are notable. First, the analogous cathodic charge transfer coefficient for Marcus theory is not predicted to be constant with potential, as it is for Butler-Volmer. Instead, it varies with potential, as demonstrated in **Eq. 2.44**.[71] Additionally, Marcus theory offers useful predictions about the rate of kinetics. Because $\Delta G^{\ddagger}_{c,MT} \approx \frac{\lambda_{MT,c}}{4}$ when

$E = E^{\circ}$ and $k_{c,MT} = k_{a,MT} = k_0$, k_0 will be larger when reorganization energies are smaller.[71] Reorganization energy is comprised of two components: the inner- and outer-reorganization energies (**Eq. 2.45**), where the inner-reorganization energy relates to changes in metal-ligand bond lengths and the outer-reorganization energy relates to solvation changes.[71] When the oxidized and reduced species have similar structures, λ_i will be lower, leading to faster kinetics. Solvation impacts both λ_O (larger molecules have lower solvation energies and smaller changes in solvation with electron transfer, meaning larger molecules will result in lower reorganization energies) and the pre-exponential factor through the nuclear frequency factor υ_n (as solution viscosity increases, kinetics become slower).[71]

$$\alpha = \frac{1}{F}\frac{\partial G_{c,MT}^{\ddagger}}{\partial E} = \frac{1}{2} + \frac{F(E - E^{\circ})}{2\lambda_{MT,c}} \quad \textbf{(2.44)}$$

$$\lambda = \lambda_i + \lambda_o \quad \textbf{(2.45)}$$

2.6.3 Microkinetic modeling

The process of microkinetic modeling refers to the development of rate laws from possible mechanisms that can be compared to experimental or computational kinetic data, where each step of the mechanism is an elementary step.[86] While microkinetic modeling is generally applied to catalytic systems, the same basic principles can be applied to heterogeneous outer-sphere mechanisms, in which no adsorption to an electrode surface will occur. Below, the general process for microkinetic modeling is described.

The first step to microkinetic modeling is to establish a possible reaction mechanism, which consists of a series of elementary reactions that include the reactant, product, and any proposed intermediates.[86] Next, stoichiometric consistency must be established, so that each elementary step

is repeated the number of times necessary to obtain the overall stoichiometric reaction.[86] This is typically done by establishing stoichiometric coefficients for each elementary step, σ_i. At steady state conditions, for a single reaction pathway, the overall rate of reaction $r_{overall}$ can be related to the individual reaction step rates, r_i, as well as the forward and backward rates, $r_{i,f}$ and $r_{i,b}$, through **Eq. 2.46**.[86]

$$r_{overall} = \frac{r_i}{\sigma_i} = \frac{r_{i,f} - r_{i,b}}{\sigma_i} \quad \textbf{(2.46)}$$

It is important to note that the series of elementary steps should be consistent with the overall reaction thermodynamics, which leads to **Eq. 2.47**, in which the product of the equilibrium constants for each of the elementary steps $K_{i,eq}$ is equal to the overall equilibrium constant $K_{overall}$.[86] $K_{i,eq}$ is defined by the Gibbs free energy of elementary step, ΔG_i°, as shown in **Eq. 2.48**.

$$K_{overall} = \prod_i K_{i,eq}^{\sigma_i} \quad \textbf{(2.47)}$$

$$K_{i,eq} = \exp\left(\frac{-\Delta G_i^\circ}{RT}\right) \quad \textbf{(2.48)}$$

Next, rate laws for each elementary step should be written using the law of mass action[86] in terms of the rate constant k_i and concentrations (or pressures) of the reactants (C_A and C_B), as shown in **Eq. 2.50** for the generic elementary reaction **Eq. 2.49**, in which reactants A and B react to form intermediates C and D.

$$A + B \rightarrow C + D \quad \textbf{(2.49)}$$

$$r_i = k_i C_A C_B \quad \textbf{(2.50)}$$

The rate constant k_i can then be described using general theories like transition state theory or collision theory,[86] or Marcus theory for electron transfers, as shown in **Chapter 5**. Once rate laws are established for each elementary step in the mechanism, simplifying assumptions can be made to establish a rate law for the overall reaction. The modeled behavior of the kinetics based on this rate law can then be compared to the observed kinetic behavior to determine whether the developed rate law is appropriate. Assumptions that can be made include the pseudo-steady state hypothesis (PSSH) or the quasi-equilibrium approximation. In the PSSH approach, the net rate of formation of an intermediate is assumed to be zero, since the intermediate will react almost as fast as it forms.[87] In this approximation, r_C, the rate of intermediate species C is equal to zero, as shown in **Eq. 2.51**, where $r_{C,i}$ refers to the rate of species C for elementary step i. The PSSH approximation is useful because the overall reaction rate, which would be defined as the formation rate of the product, will most likely include the concentration of the intermediate species C in its equation. **Eq. 2.51** can be used to determine an expression for the concentration of the intermediate species C in terms of known concentrations of the reactants and products.

$$r_C = \sum_{i=1}^{n} r_{C,i} = 0 \qquad (\mathbf{2.51})$$

Another approximation that can be used is the quasi-equilibrium approach,[88] in which one of the elementary steps is assumed to be rate-determining. As a result, all other steps are assumed to be in quasi-equilibrium, and so the rates of reaction for all steps other than the rate-determining step can be approximated as zero for the time-scale of the reaction. This is again useful because it can be used to redefine the concentration of unknown intermediates in terms of known reactant and product concentrations that can be measured experimentally for the resulting rate law. The

quasi-equilibrium approach was employed in **Chapter 5**. In **Chapter 5**, a series of two-step mechanisms are explored for the Ce^{3+}/Ce^{4+} redox reaction in sulfuric acid. The process of microkinetic modeling is used to determine a rate law for each of the considered mechanisms. The rate law modeled kinetic behavior as a function of Ce^{4+} concentration and temperature was then compared to the observed experimental kinetics to determine which mechanism was most consistent with the Ce^{3+}/Ce^{4+} charge transfer.

2.7 References

1. Zimmermann, A. W. *et al.* Techno-economic assessment guidelines for CO2 utilization. *Front. Energy Res.* **8**, 1–23 (2020).
2. Burk, C. Techno-economic modeling for new technology development. *Chem. Eng. Prog.* **114**, 43–52 (2018).
3. Graedel, T. E. *Streamlined Life-Cycle Assessment*. (Prentice-Hall, Inc., 1998).
4. Pawel, I. The cost of storage- how to calculate the levelized cost of stored energy (LCOE) and applications to renewable energy generation. *Energy Procedia* **46**, 68–77 (2014).
5. Singh, N. & McFarland, E. W. Levelized cost of energy and sensitivity analysis for the hydrogen-bromine flow battery. *J. Power Sources* **288**, 187–198 (2015).
6. Darling, R. M., Gallagher, K. G., Kowalski, J. A., Ha, S. & Brushett, F. R. Pathways to low-cost electrochemical energy storage: A comparison of aqueous and nonaqueous flow batteries. *Energy Environ. Sci.* **7**, 3459–3477 (2014).
7. Viswanathan, V. *et al.* Cost and performance model for redox flow batteries. *J. Power Sources* **247**, 1040–1051 (2014).
8. Crawford, A. *et al.* Comparative analysis for various redox flow batteries chemistries using a cost performance model. *J. Power Sources* **293**, 388–399 (2015).
9. Mongird, K. *et al. 2020 Grid Energy Storage Technology Cost and Performance Assessment*. (2020).
10. Rodby, K. E. *et al.* Assessing the levelized cost of vanadium redox flow batteries with capacity fade and rebalancing. *J. Power Sources* **460**, 227958 (2020).
11. Zhang, M., Moore, M., Watson, J. S., Zawodzinski, T. A. & Counce, R. M. Capital cost sensitivity analysis of an all-vanadium redox-flow battery. *J. Electrochem. Soc.* **159**, A1183–A1188 (2012).
12. Zheng, M., Sun, J., Meinrenken, C. J. & Wang, T. Pathways toward enhanced techno-economic performance of flow battery systems in energy system applications. *J. Electrochem. Energy Convers. Storage* **16**, 021001 (2019).
13. Minke, C. & Turek, T. Economics of vanadium redox flow battery membranes. *J. Power Sources* **286**, 247–257 (2015).
14. Minke, C., Hickmann, T., Antonio, R., Kunz, U. & Turek, T. Cost and performance prospects for composite bipolar plates in fuel cells and redox fl ow batteries. *J. Power Sources* **305**, 182–190 (2016).
15. Noack, J., Wietschel, L., Roznyatovskaya, N., Pinkwart, K. & Tübke, J. Techno-economic modeling and analysis of redox flow battery systems. *Energies* **9**, 627 (2016).
16. SimaPro. SimaPro | The World's Leading LCA Software. https://simapro.com/ (2019).
17. GaBi. Life Cycle Assessment: GaBi Software. (2017).
18. UChicago Argonne LLC. GREET 1, Version 2021. (2021).
19. Arbabzadeh, M., Johnson, J. X., Keoleian, G. A., Rasmussen, P. G. & Thompson, L. T. Twelve principles for green energy storage in grid applications. *Environ. Sci. Technol.* **50**, 1046–1055 (2016).
20. Bhandari, R., Trudewind, C. A. & Zapp, P. Life cycle assessment of hydrogen production via electrolysis - A review. *J. Clean. Prod.* **85**, 151–163 (2014).
21. Rydh, C. J. Environmental assessment of vanadium redox and lead-acid batteries for stationary energy storage. *J. Power Sources* **80**, 21–29 (1999).
22. Dieterle, M., Fischer, P., Blume, N., Minke, C. & Bischi, A. Life cycle assessment (LCA)

for flow batteries: A review of methodological decisions. *Sustain. Energy Technol. Assessments* **53**, 102457 (2022).
23. Brown, P. D., Peças Lopes, J. A. & Matos, M. A. Optimization of pumped storage capacity in an isolated power system with large renewable penetration. *IEEE Trans. Power Syst.* **23**, 523–531 (2008).
24. Ibrahim, H., Younès, R., Ilinca, A., Dimitrova, M. & Perron, J. Study and design of a hybrid wind-diesel-compressed air energy storage system for remote areas. *Appl. Energy* **87**, 1749–1762 (2010).
25. Hiremath, M., Derendorf, K. & Vogt, T. Comparative life cycle assessment of battery storage systems for stationary applications. *Environ. Sci. Technol.* **49**, 4825–4833 (2015).
26. Arbabzadeh, M., Johnson, J. X., De Kleine, R. & Keoleian, G. A. Vanadium redox flow batteries to reach greenhouse gas emissions targets in an off-grid configuration. *Appl. Energy* **146**, 397–408 (2015).
27. Denholm, P. & Kulcinski, G. L. Life cycle energy requirements and greenhouse gas emissions from large scale energy storage systems. *Energy Convers. Manag.* **45**, 2153–2172 (2004).
28. Jones, C., Gilbert, P. & Stamford, L. Assessing the climate change mitigation potential of stationary energy storage for electricity grid services. *Environ. Sci. Technol.* **54**, 67–75 (2020).
29. Fernandez-Marchante, C. M., Millán, M., Medina-Santos, J. I. & Lobato, J. Environmental and preliminary cost assessments of redox flow batteries for renewable energy storage. *Energy Technol.* **1900914**, 1–10 (2019).
30. He, H. *et al.* Flow battery production: Materials selection and environmental impact. *J. Clean. Prod.* **269**, 121740 (2020).
31. Weber, S., Peters, J. F., Baumann, M. & Weil, M. Life cycle assessment of a vanadium redox flow battery. *Environ. Sci. Technol.* **52**, 10864–10873 (2018).
32. Newville, M. Fundamentals of XAFS. *Rev. Mineral. Geochemistry* **78**, 33–74 (2014).
33. Rudolph, W. W. & Irmer, G. Raman spectroscopic characterization of light rare earth ions: La3+, Ce3+, Pr3+, Nd3+and Sm3+- hydration and ion pair formation. *Dalt. Trans.* **46**, 4235–4244 (2017).
34. Kanno, H. & Hiraishi, J. Raman study of aqueous rare-earth nitrate solutions in liquid and glassy states. *J. Phys. Chem.* **88**, 2787–2792 (1984).
35. Antonio, M. R., Ellis, R. J., Estes, S. L. & Bera, M. K. Structural insights into the multinuclear speciation of tetravalent cerium in the tri-n-butyl phosphate-n-dodecane solvent extraction system. *Phys. Chem. Chem. Phys.* **19**, 21304–21316 (2017).
36. Demars, T. J., Bera, M. K., Seifert, S., Antonio, M. R. & Ellis, R. J. Revisiting the solution structure of ceric ammonium nitrate. *Angew. Chem. Int. Ed. Engl.* **54**, 7534–8 (2015).
37. Ferraro, J. R., Nakamoto, K. & Brown, C. W. *Introductory Raman Spectroscopy*. (2003).
38. Chatterjee, A. K. X-ray Diffraction. in *Handbook of Analytical Techniques in Concrete Science and Technology* (eds. Ramachandran, V. S. & Beaudoin, J. J.) (William Andrew Publishing/Noyes Publications, 2001).
39. Housecroft, C. E. & Sharpe, A. G. *Inorganic Chemistry, Fifth Edition*. (2018).
40. Gispert, J. R. *Coordination Chemistry*. (Wiley-VCH, 2008).
41. Förster, H. UV/VIS Spectroscopy. in *Mol. Sieves* vol. 4 337–426 (2004).
42. Awan, A., Truong, H. & Lancashire, R. J. Crystal Field Theory. *LibreTexts* 1–6 (2021).
43. Lawrance, G. A. *Introduction to Coordination Chemistry*. (2010).

44. Hughes, H. K. Beer's Law and the optimum transmittance in absorption measurements. *Appl. Opt.* **2**, 937–945 (1963).
45. Walsh, B. M. Judd-Ofelt theory: Principles and practices. *Advances in Spectroscopy for Lasers and Sensing* 403–433 (2006) doi:10.1007/1-4020-4789-4_21.
46. Görller-Walrand, C. & Binnemans, K. Spectral Intensities of f-f Transitions. in *Handbook on the Physics and Chemistry of Rare Earths* vol. 25 101–264 (1998).
47. Hehlen, M. P., Brik, M. G. & Krämer, K. W. 50th anniversary of the Judd-Ofelt theory: An experimentalist's view of the formalism and its application. *J. Lumin.* **136**, 221–239 (2013).
48. Ebendorff-Heidepriem, H. & Ehrt, D. Formation and UV absorption of cerium, europium and terbium ions in different valencies in glasses. *Opt. Mater. (Amst).* **15**, 7–25 (2000).
49. Reisfeld, R. Spectra and energy transfer of rare earths in inorganic glasses. *Rare Earths* 53–98 (1973) doi:10.1007/3-540-06125-8.
50. Greenhaus, H. L., Feibush, A. M. & Gordon, L. Ultraviolet spectrophotometric determination of cerium(III). *Anal. Chem.* **29**, 1531–1534 (1957).
51. Medalia, A. I. & Byrne, B. J. Spectrophotometric determination of cerium(IV). *Anal. Chem.* **23**, 453–456 (1951).
52. Yu, X. & Manthiram, A. A zinc-cerium cell for energy storage using a sodium-ion exchange membrane. *Adv. Sustain. Syst.* **1**, 1–6 (2017).
53. Reisfeld, R., Patra, A., Panczer, G. & Gaft, M. Spectroscopic properties of cerium in sol-gel glasses. *Opt. Mater. (Amst).* **13**, 81–88 (1999).
54. Ebendorff-Heidepriem, H. & Ehrt, D. Tb3+ f-d absorption as indicator of the effect of covalency on the Judd-Ofelt Ω2 parameter in glasses. *J. Non. Cryst. Solids* **248**, 247–252 (1999).
55. Jørgensen, C. K. & Reisfeld, R. Judd-Ofelt parameters and chemical bonding. *J. Less-Common Met.* **93**, 107–112 (1983).
56. Newville, M. *Fundamentals of XAFS*. *Consortium for Advanced Radiation Sources* (2004).
57. Gaur, A., Shrivastava, B. D. & Nigam, H. L. X-ray absorption fine structure (XAFS) spectroscopy– A review. *Proc Indian Natn Sci Acad* **79**, 921–966 (2013).
58. Rehr, J. J., Kas, J. J., Vila, F. D. & Newville, M. Theory and Analysis of XAFS. in *XAFS Techniques for Catalysts, Nanomaterials, and Surfaces* (eds. Iwasawa, Y., Asakura, K. & Tada, M.) (Springer International Publishing, 2017). doi:10.1007/978-3-319-43866-5.
59. Woo, J. W., Forrey, R. C. & Cho, K. Astrophysical extended X-ray absorption fine-structure analysis. *Astrophys. J.* **477**, 235–240 (1997).
60. Ravel, B. & Newville, M. ATHENA, ARTEMIS, HEPHAESTUS: Data analysis for X-ray absorption spectroscopy using IFEFFIT. *J. Synchrotron Radiat.* **12**, 537–541 (2005).
61. Rehr, J. J., Kas, J. J., Vila, F. D., Prange, M. P. & Jorissen, K. Parameter-free calculations of X-ray spectra with FEFF9. *Phys. Chem. Chem. Phys.* **12**, 5503–5513 (2010).
62. Merritt, E. A. X-ray absorption edges. (2010).
63. Sham, T. K. L edge chemical shift and bond length difference of the mixed oxidation Ce3+/Ce4+ redox couple in solution. *J. Chem. Phys.* **79**, 1116–1121 (1983).
64. Sham, T. K. Electronic structure of hydrated Ce4+ ions in solution: An X-ray absorption study. *Phys. Rev. B* **40**, 6045–6051 (1989).
65. Vanýsek, P. Electrochemical Series. in *CRC Handbook of Chemistry and Physics* 1–10 (2000).
66. Arenas, L. F., Ponce De León, C. & Walsh, F. C. Electrochemical redox processes involving soluble cerium species. *Electrochim. Acta* **205**, 226–247 (2016).

67. Spotnitz, R. M., Kreh, R. P., Lundquist, J. T. & Press, P. J. Mediated electrosynthesis with cerium (IV) in methanesulphonic acid. *J. Appl. Electrochem.* **20**, 209–215 (1990).
68. Xie, Z., Xiong, F. & Zhou, D. Study of the Ce3+/Ce4+ redox couple in mixed-acid media (CH3SO3H and H2SO4) for redox flow battery application. *Energy and Fuels* **25**, 2399–2404 (2011).
69. Nicholson, R. S. & Shain, I. Theory of stationary electrode polarography: Single scan and cyclic methods applied to reversible, irreversible, and kinetic Systems. *Anal. Chem.* **36**, 706–723 (1964).
70. Elgrishi, N. *et al.* A practical beginner's guide to cyclic voltammetry. *J. Chem. Educ.* **95**, 197–206 (2018).
71. Bard, A. J. & Faulkner, L. R. *Electrochemical Methods: Fundamentals and Applications*. (John Wiley & Sons, Inc., 2001). doi:10.1016/B978-0-08-098353-0.00003-8.
72. Fuller, T. F. & Harb, J. N. *Electrochemical Engineering*. (John Wiley & Sons, Inc., 2018).
73. Lacey, M. Simulation- the Randles circuit. (2020).
74. Voiry, D. *et al.* Best practices for reporting electrocatalytic performance of nanomaterials. *ACS Nano* **12**, 9635–9638 (2018).
75. Moniri, S., Van Cleve, T. & Linic, S. Pitfalls and best practices in measurements of the electrochemical surface area of platinum-based nanostructured electro-catalysts. *J. Catal.* **345**, 1–10 (2017).
76. Trasatti, S. & Petrii, O. A. Real Surface Area Measurements in Electrochemistry. *Pure Appl. Chem.* **63**, 711–734 (1991).
77. Lukaszewski, M., Soszko, M. & Czerwiński, A. Electrochemical methods of real surface area determination of noble metal electrodes - an overview. *Int. J. Electrochem. Sci.* **11**, 4442–4469 (2016).
78. Rudi, S., Cui, C., Gan, L. & Strasser, P. Comparative study of the electrocatalytically active surface areas (ECSAs) of Pt alloy nanoparticles evaluated by Hupd and CO-stripping voltammetry. *Electrocatalysis* **5**, 408–418 (2014).
79. Van Cleve, T. B. Development of cathodic electrocatalysts for low temperature H2 fuel cell applications: Improving oxygen reduction activity through the manipulation of size, shape, and composition. (University of Michigan, 2016).
80. Nicholson, R. S. Theory and application of cyclic voltammetry for measurement of electrode reaction kinetics. *Anal. Chem.* **37**, 1351–1355 (1965).
81. Tanimoto, S. & Ichimura, A. Discrimination of inner- and outer-sphere electrode reactions by cyclic voltammetry experiments. *J. Chem. Educ.* **90**, 778–781 (2013).
82. Marcus, R. A. Electron transfer reactions in chemistry. Theory and experiment. *Rev. Mod. Phys.* **65**, 599–610 (1993).
83. Weaver, M. J. & Anson, F. C. Distinguishing between inner- and outer-sphere electrode reactions. Reactivity Ppatterns for some chromium(III)-chromium(II) electron-transfer reactions at mercury electrodes. *Inorg. Chem.* **15**, 1871–1881 (1976).
84. Bard, A. J. Inner-sphere heterogeneous electrode reactions. Electrocatalysis and photocatalysis: The challenge. *J. Am. Chem. Soc.* **132**, 7559–7567 (2010).
85. Henstridge, M. C., Laborda, E., Rees, N. V & Compton, R. G. Marcus – Hush – Chidsey theory of electron transfer applied to voltammetry: A review. *Electrochim. Acta* **84**, 12–20 (2012).
86. Motagamwala, A. H. & Dumesic, J. A. Microkinetic modeling: A tool for rational catalyst design. *Chem. Rev.* **121**, 1049–1076 (2021).

87. Fogler, H. S. *Elements of Chemical Reaction Engineering*. (2020).
88. Filot, I. A. W. *Introduction to microkinetic modeling*. (2018).

Chapter 3 Comparing the Levelized Cost of Electricity and Life Cycle Emissions of Ce- and V-Based Redox Flow Batteries

3.1 Introduction

To reduce reliance on fossil fuels that emit greenhouse gases (GHG),[1] renewable energy sources such as wind and solar are being integrated into electricity grids, with estimates that the share of renewable electricity in the U.S. will double by 2050.[2] As the fraction of intermittent renewables increase there will be an estimated need of 4-120 GW of additional energy storage by 2050.[3–6] A majority of this is expected to be long duration (>10 hours[5,7]) storage to meet electricity demand with variable renewable energy supply.[5] Currently, 93% of U.S. energy storage capacity comes from pumped storage hydropower,[8] which is geographically limited and so cannot be increased to match the projected additional storage needs. Redox flow batteries (RFBs) are promising for increasing stationary storage capacity because energy and power delivery scale separately,[9] making them suitable for long duration storage. However, RFB energy storage costs need to be reduced through increases in open circuit voltage, decreases in overvoltages, and the use of lower-cost materials. With a goal of using RFBs to integrate renewable electricity, it is also important to consider how RFB's construction and use contributes to GHG emissions. Here we compare the economic and environmental performance of the state-of-the-art all-vanadium RFB (VRFB) and a higher voltage RFB that uses Ce at the positive electrode (Ce-V RFB) under conditions ranging from the current U.S. electricity mix to a 100% renewable electricity supply.

Unlike other batteries, RFBs operate by storing active species in external electrolyte tanks, and flowing the electrolyte past the electrodes during charging and discharging.[9] Because the

electrodes themselves are not the active species, RFB electrodes experience less degradation than conventional batteries like lithium-ion. The external storage of the active species means that the RFB energy (electrolyte tank volume) and power (electrode area) are decoupled, which is a significant advantage of RFBs compared to other batteries,[9,10] especially for long duration storage. As the battery discharge time is increased, RFBs will become more economical compared to conventional batteries because the RFB power-dependent capital costs do not increase with discharge time.[11] The state-of-the-art RFB technology is the VRFB (V^{2+}/V^{3+} and VO^{2+}/VO_2^{+}), which has the advantage of using the same active species at each electrode, reducing crossover effects.[3] Although there are examples of pilot-scale VRFB projects,[3,12–14] VRFBs have not been widely integrated into the U.S. electricity grid because they are currently too costly.

Technoeconomic assessments (TEAs) on VRFB capital cost and levelized cost of electricity (LCOE) demonstrate that the VRFB is too expensive, but considerations for optimizing operation for long durations (>10 hours) with different electricity sources are needed. For 4-12 hour discharge times, the VRFB capital cost and LCOE range between 300-600 \$/kWh [3,11,15–18] and 0.16-0.50 \$/kWh_d,[5,16,17,19,20] respectively, where LCOE is the average net present cost of electricity delivered over a product's lifetime.[21] These values are currently above the U.S. DOE energy storage capital cost (150 \$/kWh) and LCOE (0.05 \$/kWh_d) targets.[22] To minimize cost, current density and discharge time variations are often considered. Increasing from 15 minute discharge time to 4 hours incentivizes lower current densities to promote more efficient operation.[17] For 12-hour discharge, power-dependent costs decrease with increasing current density, but energy-dependent costs increase.[11,23] Electricity costs and comparisons to shorter discharge times were not included, however, making it difficult to understand how optimal current densities will change either as electricity source is changed or discharge time is increased to 12

hours and beyond. There is a need for further TEA studies of RFB current density optimization that include the electricity delivery phase at longer discharge times (> 10 hours), given the need for longer discharge times (10-100 hours[7]) and the shift towards more renewable energy electricity sources.

TEA studies of specific aqueous RFB chemistries with known wider voltage windows are also needed, because most aqueous RFB TEAs of non-VRFB chemistries only consider voltage windows less than the stability limit of water.[10] Recently, Perry et al. showed that a generic aqueous RFB with a voltage of 2.3 V or greater could reach the 150 $/kWh capital cost target.[10] We investigate the Ce^{3+}/Ce^{4+} redox chemistry as a promising positive RFB electrolyte. The Ce^{3+}/Ce^{4+} redox potential is higher than VO^{2+}/VO_2^+ and ranges as a function of acid between 1.44 – 1.74 V vs. SHE.[24] The Ce precursor (CeO_2, ~1.9 $/kg[25]) is also less expensive than the V precursor (V_2O_5, ~22 $/kg[26]). Replacing the V^{2+}/V^{3+} and VO^{2+}/VO_2^+ chemistries with less costly precursors is another strategy for reducing energy storage costs,[15,27] because V_2O_5 is volatile in both price and supply.[4,12,28] Despite the advantages of Ce, it is unclear how the overall cost of energy storage would compare to that of the VRFB, because an in-depth study of how roundtrip efficiency would change has not been completed. Only one preliminary cost estimate of a Ce RFB exists,[29] but it does not consider the impact of the electricity grid mix on overall cost, motivating additional study.

Since RFB production and electricity delivery result in GHG emissions, a model comparing the cost of an alternative RFB to the state-of-the-art VRFB for the purpose of decarbonizing electricity should also consider how the RFBs' life cycle GHG emissions compare. Life cycle assessment (LCA) can be used to quantify the RFBs' emissions throughout the production, use, and end-of-life (EoL) phases.[29] Previous RFB LCAs showed the EoL phase GHG emissions are

negligible,[28,30] the electrolyte dominates production emissions,[29,31,32] and use phase emissions are controlled by the RFB roundtrip efficiency.[33] The production emissions of a Ce-Zn RFB were higher than those of a VRFB,[29] but the two RFBs' use phase emissions were not considered, and so more analysis is needed to ensure that a Ce-based RFB does not result in significantly increased life cycle emissions compared to the VRFB. RFB life cycle GHG emissions decrease significantly as the share of renewable energy increases,[32–35] and so comparing the VRFB to Ce-based RFB under different energy mixes may be valuable. Wind energy stored through VRFBs was found to be cost-effective only when very stringent CO_2 emission targets were implemented, meaning that the model was constrained so that GHG emissions calculated through LCA could not exceed that limit.[36] At less stringent emissions targets, wind curtailment was more economical, emphasizing the importance of coupling LCA methods with economic analysis to determine optimal operating conditions and using economic instruments like carbon taxes to promote energy storage. No RFB modeling studies yet compare the different optimal current densities for an RFB in which cost versus emissions are minimized. Additionally, the influences of a carbon tax on optimal operating current density have not been studied. Identification of the optimal operating parameters for these scenarios, as well as identification of the key RFB parameters that control cost and emissions, will help energy storage researchers target future areas of work and operators to select appropriate operating discharge times and current densities to minimize cost and emissions.

In this work we develop a TEA model and life cycle inventory (LCI) model to quantify the levelized costs and GHG emissions of a Ce-V RFB and VRFB. An LCI uses LCA techniques but does not incorporate the impact assessment stage, because weighting techniques are noted to be subjective.[37] We find that significantly lower current densities are needed to minimize GHG emissions than to minimize LCOE, because the use phase emissions dominate life cycle emissions,

whereas production costs make up a more significant portion of the LCOE. The optimal current density for 12-hour storage is lower relative to the 4-hour storage case. The Ce-V RFB has lower energy storage costs and similar GHG emissions to the VRFB with the current U.S. electricity mix at current densities between 25-140 mA/cm^2, while for a 100% renewable grid, the GHG emissions drop dramatically, but the Ce-V RFB emissions become significantly higher than the VRFB. Even with a stringent carbon tax, however, the Ce-V RFB is cheaper than the VRFB. We show that the most important factors on the LCOE of both RFBs are the electrolyte redox potential, faradaic efficiency, and cost of the V_2O_5 precursor, but the Ce-V RFB is also influenced by Ce^{3+}/Ce^{4+} kinetics. RFB emissions are similarly controlled by the redox potentials, faradaic efficiency, and kinetics of both the positive and negative redox couples, but the Ce-V RFB is more impacted by the emissions rate of CeO_2 production than the VRFB is by the V_2O_5 production emissions. The LCOE sensitivity trends do not change for different electricity mixes, but the emissions associated with the production phase become more influential while parameters that control the use phase become less significant for a 100% renewable grid relative to the average grid mix. Given the lowered cost of the Ce-V RFB compared to VRFB, our study motivates further consideration of using Ce in RFB applications to achieve more affordable energy storage.

3.2 Methods

The technoeconomic assessment (TEA) cost model and life cycle inventory (LCI) emissions model reported in this study were developed using a component level approach and coupled with a performance (charge-discharge voltage) model for two different redox flow battery (RFB) systems. Briefly, as shown by the process depicted in **Scheme 3.1**, the charge-discharge performance model incorporates kinetics, ohmic losses, and mass transport to determine the voltage during charge or discharge as a function of current density i_m for the RFBs. The TEA cost

model gives the levelized cost of electricity (LCOE) at a particular operating i_m, using the performance model to calculate the voltage. The LCI emissions model gives the levelized GHG emissions (LGHG) at the same operating i_m and voltages from the performance model. The LCOE or LGHG was minimized by iteratively varying the i_m to minimize the LCOE and LGHG while accounting for any changes in the RFB roundtrip efficiency (RTE) through our performance model. Below, the system boundaries and functional unit are defined in **Section 3.2.1**. The performance model parameters and charge-discharge calculations are described in **Section 3.2.2**. In **Section 3.2.3** the energy dependent components and power dependent components are described as well as details on the electricity mixes. In **Section 3.2.4**, the TEA cost model is described, and the LCI emissions model is detailed in **Section 3.2.5**. Finally, the optimization method and sensitivity analysis are described in **Section 3.2.6**.

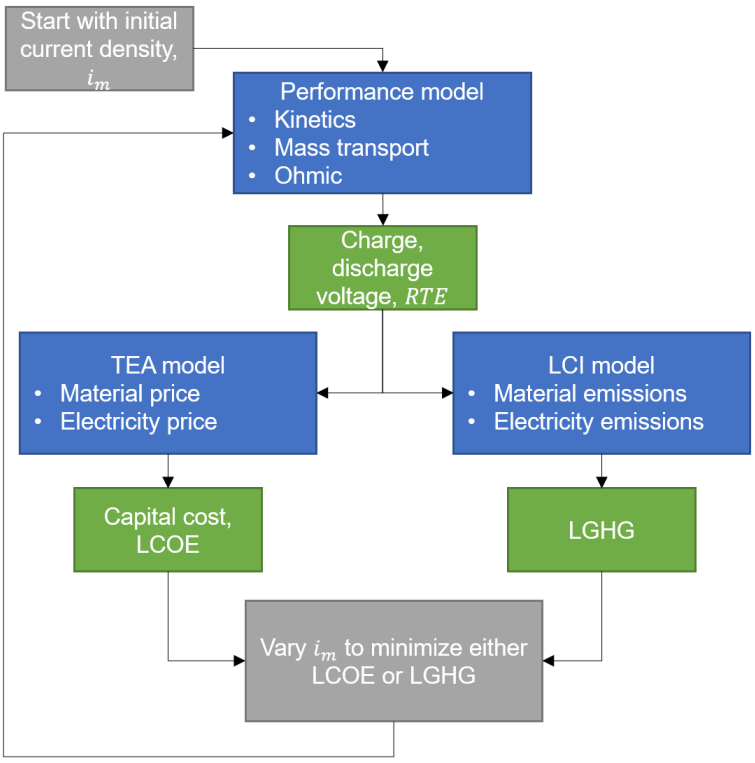

Scheme 3.1. Flow chart for optimization process to minimize either LCOE or LGHG using the performance and TEA-LCI models by varying current density i_m. RTE refers to roundtrip efficiency.

3.2.1 System definition

In life cycle assessment studies, the functional unit (FU) is a reference unit and represents the amount of product, material, or service that the technology performance is referenced against.[38] Herein, the FU was defined as the delivery of 1 kWh of electricity by the RFB over an assumed lifetime of 20 years. Only the impacts of the production and use phases were incorporated in the TEA-LCI models, e.g., the end-of-life costs and environmental burdens were not considered. Upstream processes such as material mining, processing, and manufacturing were included in the production phase. The use phase was defined as the storage and delivery of electricity and included the impacts of the battery roundtrip efficiency, which was related to the loss in electricity that occurs during charging and discharging.

3.2.2 Charge-discharge performance model for RFBs

RFB chemistry and operation. The two RFB systems considered were the all-vanadium RFB (VRFB) and the Ce-V RFB. The VRFB consists of the two half-cell reactions shown in **Eq. 3.1a-b**, with **Eq. 3.1a** occurring at the positive electrode and **Eq. 3.1b** occurring at the negative electrode, and their respective standard redox potentials, E°, listed.[9] Based on the E° values at the positive and negative electrodes, the theoretical voltage expected for the VRFB is 1.26 V. Experimentally, however, the open circuit voltage (OCV) of the VRFB is generally found to be 1.4 V at 50% state of charge (SoC),[12] where SoC refers to the ratio between the available amount of charge of a battery and its total capacity.[39] At 50% SoC, 50% of the positive electrolyte is in the V^{5+} (or VO_2^+) state and 50% of the negative electrolyte is in the V^{2+} state. This difference between theoretical and actual OCV has been ascribed to the effect of the proton concentration at the positive electrolyte on potential as well as the charged double layers at each side of the ion-

exchange membrane, which are caused by a concentration gradient of protons between the membrane and the electrolyte, which is called the Donnan potential.[40] Thus, we assumed that the redox potential of the positive electrolyte for the VRFB was $V_{pos,thermo} = 1.0875$ V and the redox potential of the negative electrolyte was $V_{neg,thermo} = -0.3125$ V, so that the overall OCV would be 1.4 V. During charge, VO^{2+} is oxidized to VO_2^+ at the positive electrode and V^{3+} is reduced to V^{2+} at the negative electrode, while during discharge, VO_2^+ is reduced to VO^{2+} and V^{2+} is oxidized to V^{3+}. The VO^{2+}/ VO_2^+ redox couple is often referred to as the V^{4+}/V^{5+} reaction, which is how we will refer to it.

$$VO_2^+ + 2H^+ + e^- \rightleftarrows VO^{2+} + H_2O \qquad E^\circ = 1.00 \text{ V vs. RHE} \qquad \textbf{(3.1a)}$$

$$V^{3+} + e^- \rightleftarrows V^{2+} \qquad E^\circ = -0.26 \text{ V vs. RHE} \qquad \textbf{(3.1b)}$$

The Ce-V RFB has the same half-cell reaction at the negative electrode as the VRFB (**Eq. 3.1b**), but at the positive electrode, **Eq. 3.2** occurs. The redox potential of the Ce^{3+}/Ce^{4+} redox couple is highly dependent on electrolyte, varying from 1.44 V vs. RHE in 1 M H_2SO_4 to 1.74 V vs. RHE in 1 M $HClO_4$.[24] In this study, we assume the electrolyte used for the Ce^{3+}/Ce^{4+} redox couple is H_2SO_4, so $V_{pos,thermo}$ = 1.44 V for the Ce-V RFB. As discussed for the VRFB we treat the V^{2+}/V^{3+} redox potential to be −0.3125 V. Thus, the OCV for the Ce-V RFB used in the performance model is 1.7525 V. During charge, at the positive electrode, Ce^{3+} is oxidized to Ce^{4+}, and at the negative electrode, V^{3+} is reduced to V^{2+}. During discharge, Ce^{4+} is reduced to Ce^{3+} while V^{2+} is oxidized to V^{3+}.

$$Ce^{4+} + e^- \rightleftarrows Ce^{3+} \qquad E^\circ = 1.44 \text{ V vs. RHE} \qquad \textbf{(3.2)}$$

The kinetic, mass transport, and ohmic performance parameters for the redox couples for both charge and discharge were based on literature values and are included in **Table 3.1**. To represent the state-of-the-art performance of the VRFB, the V^{4+}/V^{5+} exchange current density (i_0) and V^{2+}/V^{3+} exchange current density and Tafel slopes were extracted from a recent study of the kinetic performance of graphite electrodes with Co_3O_4 catalysts.[41] The V^{4+}/V^{5+} Tafel slopes (b_{dis} and b_{charge}) on graphite varied significantly in the literature,[42–44] so standard values of approximately 0.12 V/decade were selected. The limiting current densities ($i_{L,dis}$ and $i_{L,charge}$) for both V^{4+}/V^{5+} and V^{2+}/V^{3+} were based on reports of VRFBs reaching current densities of 1 A/cm^2.[45,46] A platinized titanium mesh was assumed for the Ce^{3+}/Ce^{4+} electrode, because carbon-based materials are not stable at the higher oxidizing materials.[12] Information on the kinetics of the Ce^{3+}/Ce^{4+} redox reaction in Ce-V RFBs is limited, and so the exchange current density on platinum was extracted from a study of a cerium-zinc battery,[47] and the limiting current densities were obtained from a cerium-hydrogen RFB study.[48] The Ce^{3+}/Ce^{4+} discharge Tafel slope is an estimate from experimental measurements on a platinum disk in our laboratory (see **Chapter 5**), and the charge Tafel slope is from literature, albeit for a different electrolyte.[49] The faradaic efficiency values were based on average values from RFB literature,[10,15,50] and the effect of faradaic efficiency was studied in the sensitivity analysis.

Table 3.1. Kinetic, mass transport, ohmic, and solubility parameters as well as depth of discharge (SoC_{usable}) and faradaic efficiency ($FE_{discharge}$, FE_{charge}) assumptions used in the charge-discharge performance model. Exchange current densities are normalized to geometric area of the battery.

Performance Model Parameters	Value	Ref.
VO_2^+/VO^{2+} i_0 (mA/cm^2)	43.5	[41]
VO_2^+/VO^{2+} $i_{L,dis}$ (mA/cm^2)	1000	[45,46]
VO_2^+/VO^{2+} $i_{L,charge}$ (mA/cm^2)	1000	[45,46]
VO_2^+/VO^{2+} b_{dis} (mV/dec)	117	[42–44]
VO_2^+/VO^{2+} b_{charge} (mV/dec)	120	[44]
VO_2^+/VO^{2+} solubility (M)	1.75	[51]
V^{2+}/V^{3+} i_0 (mA/cm^2)	16.8	[41]
V^{2+}/V^{3+} $i_{L,dis}$ (mA/cm^2)	1000	[45,46]
V^{2+}/V^{3+} $i_{L,charge}$ (mA/cm^2)	1000	[45,46]
V^{2+}/V^{3+} b_{dis} (mV/dec)	71.9	[41]
V^{2+}/V^{3+} b_{charge} (mV/dec)	84.9	[41]
V^{2+}/V^{3+} solubility (M)	1.6	[52]
Ce^{3+}/Ce^{4+} i_0 (mA/cm^2)	24.2	[47]
Ce^{3+}/Ce^{4+} $i_{L.dis}$ (mA/cm^2)	750	[48]
Ce^{3+}/Ce^{4+} $i_{L,charge}$ (mA/cm^2)	200	[48]
Ce^{3+}/Ce^{4+} b_{dis} (mV/dec)	250	See **Chapter 5**
Ce^{3+}/Ce^{4+} b_{charge} (mV/dec)	300	[49]
Ce^{3+}/Ce^{4+} solubility in 2 M H_2SO_4 (M)	0.35	[53]
$FE_{discharge}$	0.985	[10,15,50]
FE_{charge}	0.985	[10,15,50]
SoC_{usable}	0.85	[18]
R_{area} (Ωcm^2)	0.843	[54]
$loss_{pump}$	2%	[55]

The assumptions related to the operation of the battery, such as lifetime and cycles per year, are included in **Table 3.2**. Based on reports that the VRFB calendar life falls between 10−20 years,[18] we assumed the VRFB has a lifetime of 20 years. We assumed that all stack components and electrolyte would remain stable for the entire 20-year lifetime. This represents a limitation of the current work which should be addressed in future iterations. We assumed that the battery was operated once per day, for a total of 365 cycles per year, and that it delivered 1 kWh per cycle.

Table 3.2. RFB operation assumptions used in charge-discharge performance model.

Operation Parameter	Value	Ref.
Operating lifetime, $n_{lifetime}$ (yr)	20	[18]
Cycles per year (cycles/yr)	365	–
Electricity rate per cycle (kWh_d/cycle)	1	–

Charge-discharge calculations. To calculate the charge ($V_{actual,charge}$) and discharge ($V_{actual,dis}$) voltages at a given current density, i_m, **Eq. 3.3a** and **Eq. 3.3b** were used. As seen in **Eq. 3.3a-b**, the charge and discharge voltages are comprised of the thermodynamic voltages for the chemistry at positive and negative electrodes, $V_{pos,thermo}$ and $V_{neg,thermo}$, respectively, as well as the kinetic, mass transport, and ohmic overvoltages η, described in more detail below.

$$V_{actual,charge} = \left(V_{pos,thermo} + \eta_{MT,pos,charge} + \eta_{k,pos,charge}\right) - \left(V_{neg,thermo} + \eta_{MT,neg,charge} + \eta_{k,neg,charge}\right) + \eta_{O,total} \quad \textbf{(3.3a)}$$

$$V_{actual,dis} = \left(V_{pos,thermo} - \eta_{MT,pos,dis} - \eta_{k,pos,dis}\right) - \left(V_{neg,thermo} + \eta_{MT,neg,dis} + \eta_{k,neg,dis}\right) - \eta_{O,total} \quad \textbf{(3.3b)}$$

The kinetic ($\eta_{k,pos,charge}$, $\eta_{k,neg,charge}$, $\eta_{k,pos,dis}$, $\eta_{k,neg,dis}$) and mass transport ($\eta_{MT,pos,charge}$, $\eta_{MT,neg,charge}$, $\eta_{MT,pos,dis}$, $\eta_{MT,neg,dis}$) overvoltages are broken down between discharge and charge for both the positive and negative chemistries and $\eta_{O,total}$ is the overvoltage from all ohmic losses. The Butler-Volmer (BV) formulism of kinetics was used to relate current density i_m to kinetic overvoltages,[56] as shown in **Eq. 3.4**, where i_0 is the exchange current density, α is the charge transfer coefficient which can be related to the Tafel slope, η_k is a generic kinetic overvoltage, and F, R, and T have their usual meanings.

$$i_m = i_0\left(\exp\left(\frac{\alpha F \eta_k}{RT}\right) - \exp\left(\frac{-(1-\alpha)F\eta_k}{RT}\right)\right) \quad \textbf{(3.4)}$$

Because each of the overvoltages are a function of i_m, we selected to make current density the independent variable and each overvoltage was a dependent variable. In the non-simplified BV form, however, there is not a simple analytical method to calculate the individual kinetic overvoltages in the RFB ($\eta_{k,pos,charge}$, $\eta_{k,neg,charge}$, $\eta_{k,pos,dis}$, $\eta_{k,neg,dis}$) at a given current density using their relevant Tafel slopes and exchange current density extracted from literature. Thus, we simplify the BV equation so that there is an analytical solution for each kinetic overvoltage based on the current density i_m. As shown in **Eq. 3.5a**, at low kinetic overvoltages ($\eta_k < \eta_{low}$), i_m can be approximated to be linearly dependent on overvoltage and the different kinetic overvoltages were calculated from i_m using the parameters in **Table 3.1**.[56] At large overvoltages ($\eta_k > \eta_{high}$), i_m will display an exponential dependence on overvoltage (**Eq. 3.5b**), where b is the Tafel slope for charge or discharge, because either the anodic or cathodic branch of the Butler-Volmer expression dominates (i.e., Tafel equation).[56] To estimate the relationship between measured current and overvoltage at intermediate overvoltages, a "linearization" approach was taken, in which the slope of the line formed between the points at the low overvoltage and high overvoltage ranges was used to calculate the approximate value of the current, as shown in **Eq. 3.5c**, where $slope$ represents the slope and $intercept$ refers to the y-intercept of the line formed between the low and high overvoltage points. This approach resulted in reasonable approximations of current in the intermediate overvoltage range compared to the full BV equation. For the Ce^{3+}/Ce^{4+} reaction, η_{low} and η_{high} were found to be 0.03 V and 0.1 V, respectively, while for the V^{2+}/V^{3+}, η_{low} and η_{high} values of 0.03 V and 0.06 V resulted in the best approximation of the full Butler-Volmer expression. For V^{4+}/V^{5+}, the best approximating values of η_{low} and η_{high} were 0.03 V and 0.073 V.

$$when\ \eta_k < \eta_{low}, \eta_k = \frac{i_m RT}{i_0 F} \quad \textbf{(3.5a)}$$

$$when\ \eta_k > \eta_{high}, \eta_k = b \log\left(\frac{i_m}{i_o}\right) \quad \textbf{(3.5b)}$$

$$when\ \eta_{low} \leq \eta_k \leq \eta_{high}, \eta_k = i_m \times slope + intercept \quad \textbf{(3.5c)}$$

To calculate the mass transport overvoltages ($\eta_{MT,pos,charge}$, $\eta_{MT,neg,charge}$, $\eta_{MT,pos,dis}$, $\eta_{MT,neg,dis}$) at a given current density, **Eq. 3.6a-b** were used if $i_m > 0.1 i_L$. Here, i_k is the kinetically-limited current and i_L is the limiting current for the particular redox couple and direction (e.g., for the positive electrolyte and during charging) from **Table 3.1**. The i_k was calculated with **Eq. 3.6a** and represents the current density achievable if there were no mass transport limitations. The mass transport overvoltage is calculated using **Eq. 3.6b** with the kinetic overvoltage from **Eq. 3.5**. If $i_m \leq 0.1 i_L$, then it was assumed that the mass transport overvoltage was negligible. $\eta_{O,total}$ is the ohmic overvoltage and defined in **Eq. 3.6c**, where R_{area} is the area specific resistance.

$$when\ i_m > 0.1 i_L, i_k = \frac{i_L i_m}{i_L - i_m} \quad \textbf{(3.6a)}$$

$$when\ i_m > 0.1 i_L, \eta_{MT} = b \log\left(\frac{i_k}{i_o}\right) - \eta_k \quad \textbf{(3.6b)}$$

$$\eta_{O,total} = R_{area} \times i_m \quad \textbf{(3.6c)}$$

Combining the overvoltages from **Eq. 3.5** and **Eq. 3.6** with **Eq. 3.3**, the charge and discharge voltage curves were determined as a function of current density.

3.2.3 Components and electricity sources

Energy-dependent material. The components of the RFB that scale with energy, i.e., the energy-dependent material, include the electrolyte and the electrolyte tanks. The pumps and flow meters associated with flowing the electrolyte past the electrodes were also assumed to be energy-dependent, because the sizing of the pumps would be dependent on the volume of electrolyte being moved. The electrolyte consists of the active species, i.e., VO_2^+/VO^{2+}, V^{2+}/V^{3+}, or Ce^{3+}/Ce^{4+}, and the acid, which was assumed to be 2 M H_2SO_4 for both positive and negative electrodes in both the VRFB and Ce-V RFB. This concentration was selected because in VRFB systems, 2-3 M is typically used.[51] In future iterations, the influence of acid concentration should be studied on the Ce-V RFB system.

To calculate the concentration of active species, [*Active species*], to deliver 1 kWh of electricity to inform the TEA-LCI calculations, **Eq. 3.7** was used. The volume of H_2SO_4 needed was based on the concentration of active species and solubility of the active species in H_2SO_4. The electrolyte tanks were assumed to be cylindrical in shape and made of corrosion resistant polyethylene[55] and were sized according to the volume of H_2SO_4 calculated, assuming an inner radius of 0.15 m and a thickness of 2.5 cm. The pumps used to flow the electrolyte in the RFB were assumed to be DC magnetic drive pumps with a flow rate of 2.5 L/min.[55] $V_{actual,dis}$ is the discharge voltage from **Eq. 3.3a**. $FE_{discharge}$ is the discharge faradaic efficiency, SoC_{usable} accounts for the depth of discharge, and $loss_{pump}$ accounts for the loss in efficiency from operating the RFB pumps. These parameters are also included in **Table 3.1**.

$$[Active\ species] = \left(V_{actual,dis} \times \left(1 \times FE_{discharge} \times F \times SoC_{usable}\right) \times (1 - loss_{pump})\right)^{-1} \quad \textbf{(3.7)}$$

Power-dependent material. The cell stack components are power-dependent, meaning that the cell area scales with the power required, as dictated by the efficiency of the RFB and current density. The stack includes the end plates, current collectors, bipolar plates, membrane electrode assembly, which consists of a frame, the negative and positive electrodes, the ion-exchange membrane, and gaskets. To determine the area of the cell components needed to deliver the specified current density, i_m, **Eq. 3.8** was used. While it is recognized that an actual RFB would have multiple cells of a smaller area, it was assumed in this model that only one stack would be used, and so the area reported is the total area of cell needed.

$$Cell\ area = \left(i_m \times FE_{discharge} \times V_{actual,dis} \times (1 - loss_{pump})\right)^{-1} \quad \textbf{(3.8)}$$

The end plates and bipolar plates were assumed to be stainless steel and the current collectors were assumed to be made from copper. The cell stack was assumed to have two end plates, bipolar plates, and current collectors each, and each of these components were assumed to be 0.25 cm thick. The ion-exchange membrane was assumed to be Nafion 117, and the membrane electrode assembly was assumed to be a high-density polymer that was 0.25 cm thick. The gaskets were assumed to be rubber of thickness of 0.25 cm. Graphite felt was modeled as the electrode used for both VO_2^+/VO^{2+} and V^{2+}/V^{3+} redox reactions and was assumed to be 0.25 cm thick. For the Ce^{3+}/Ce^{4+} redox reaction, a platinized titanium mesh was assumed to be the electrode, with a platinum loading of 2 g/m^2, which was an estimate based on typical platinum loadings used in proton exchange membrane fuel cells.[57] We assumed that this electrode had the same kinetic performance as reported for a cerium-zinc battery.[47] We discuss the impact of higher surface area electrodes in the sensitivity analysis in **Section 3.3.4**. Another possible positive electrode option is a pure platinum mesh but given the high cost of platinum, we did not model this electrode. In

addition to the area-scaled cell stack components, another power-dependent component is the power conversion system (PCS), which is used to convert DC electricity generated by the battery to AC. It was sized on a kW basis, as discussed further below.

Electricity grid. Four electricity grid scenarios were included in the model: average U.S. electricity mix, 100% coal, 100% natural gas, and 100% renewables. The average U.S. electricity mix is based on the EIA 2021 electricity generation source profile,[58] as shown in **Table 3.3**. The 100% renewables case includes wind (46.0%), hydropower (31.5%), solar (14.0%), biomass (6.5%), and geothermal (2.0%) at the same proportions as assumed in the average U.S. electricity mix.

Table 3.3. Distribution of 2021 U.S. electricity generation sources used for the average U.S. electricity mix scenario.[58]

Electricity Generation Source	Share of Generation
Natural gas	38.0%
Coal	22.0%
Nuclear	19.0%
Wind	9.2%
Hydropower	6.3%
Solar	2.8%
Biomass	1.3%
Geothermal	0.4%

Other considerations. Balance of System (BOS) costs were incorporated on a kWh basis. PCS was modeled separately, so herein, BOS was assumed to include factors such safety equipment and meters and instrumentation and modeled after Mongird et al.[18] Other factors like operating costs, installation costs, tax rates, inflation were not included.

3.2.4 Technoeconomic assessment (TEA) model

The technoeconomic assessment (TEA) cost model calculated the economic cost of the energy- dependent and power-dependent material as well as the electricity use phase in U.S.

dollars. Both the capital cost and LCOE are calculated. Below, the economic assumptions that went into the TEA model, as well as the calculation of the LCOE, and the carbon tax scenarios are described. All costs are reported in $USD in 2021.

Economic assumptions. The component costs used in the TEA are included in **Table 3.4**. The price of CeO_2, V_2O_5, and H_2SO_4 were obtained from vendors or market analyses on a mass basis. The price of the electrolyte tanks, pumps, flow meters, end plates, current collectors, bipolar plates, membrane electrode assembly, graphite felt electrode, platinized titanium electrode and gaskets were obtained from literature. There was a large range in possible prices to use for the platinized titanium electrode based on costs of titanium and Pt-group metal coated titanium electrodes available in the literature,[59–61] depending on the Pt-group metal loading. We based our value of the titanium mesh off of an NREL report that a titanium anode porous transport layer for a proton exchange membrane water electrolyzer would cost 435 $/m^2 (15 $/kW at large production scale for electrolyzers with a power density of 28.9 kW/m^2).[59] We then added the cost of platinum (39 $/g)[62] assuming a 2 g/m^2 loading, to obtain a total cost of 511 $/m^2 for the platinized titanium mesh electrode. Given the large uncertainty in this price, we explore the effect of the cost of the platinized titanium electrode on the Ce-V RFB cost in the sensitivity analysis. Reports of the Nafion 117 cost varied between 250-350 $/m^2,[17,55,63] and the lower limit was assumed in this analysis. The BOS and PCS costs were pulled from a DOE report of VRFB costs.[18] The cost of charging the electricity grid was based on the levelized cost of electricity calculations from Lazard,[64] with the average U.S. electricity grid and 100% renewables costs consisting of weighted sums of each of the different energy sources that make these mixes up, based on the distribution shown in **Table 3.3**. The costs for each energy source were pulled from Lazard[64] except hydropower, which was based on an EIA report.[65]

Table 3.4. Components' costs for VRFB and Ce-V RFB systems.

Component	Cost	$/unit	Ref.
Energy-dependent capital			
CeO_2	0.30	$/mol	[25]
V_2O_5	1.96	$/mol	[26]
H_2SO_4	0.032	$/mol	[66]
Electrolyte tank (polyethylene)	500	$/m^3	[55]
Electrolyte pump	4.76	$/(L/min)	[16]
Electrolyte pump flow meter	1	$/(L/min)	[55]
BOS	44	kWh	[18]
Power-dependent capital			
End plate (stainless steel)	10	$/m^2	[55]
Current collector (copper)	10	$/m^2	[55]
Bipolar plate (stainless steel)	55	$/m^2	[67]
V^{2+}/V^{3+} and VO_2^+/VO^{2+} electrode (graphite felt)	90	$/m^2	[55]
Ce^{3+}/Ce^{4+} electrode (platinized titanium mesh)	511	$/m^2	[59,62]
Membrane (Nafion 117)	250	$/m^2	[17,55,63]
Membrane electrode assembly frame (high-density polymer)	50	$/m^2	[55]
Gaskets (rubber)	28	$/m^2	[55]
PCS	133	$/kW	[18]
Electricity			
Average U.S. electricity mix	0.064	$/kWh	[64]
100% coal	0.071	$/kWh	[64]
100% natural gas	0.056	$/kWh	[64]
100% renewable	0.075	$/kWh	[64]

Calculation of LCOE. To calculate the LCOE of the battery, **Eqs. 3.9a-3.9j** were used. In **Eq. 3.9a**, the LCOE is split between the LCOE of the production and use phases, $LCOE_{production}$ and $LCOE_{use}$ and has units of $/kWh$_d$, where kWh$_d$ refers to delivered electricity. As seen in **Eq. 3.9b**, $LCOE_{production}$ is a function of the energy-dependent and power-dependent capital, as well as the annual energy discharged, and total discount factor, TDF. The energy-dependent and power-dependent capital costs were calculated using **Eq. 3.9c** and **Eq. 3.9d**, respectively, where there are m energy-dependent components and l power-dependent components. The total discount factor,

TDF, was dependent on the assumed discount rate, $i_{discount}$, which was assumed to be 10%, and the operating lifetime in years, $n_{lifetime}$ (**Eq. 3.9f**). $LCOE_{use}$ was calculated using **Eq. 3.9g** and is a function of the price of electricity, which is dependent on the electricity grid source, and the roundtrip efficiency RTE. RTE is defined in **Eq. 3.9h** as the product of the charge and discharge voltage efficiencies and roundtrip faradaic efficiency (**Eq. 3.9i**), where charge voltage efficiency is defined in **Eq. 3.9j** and discharge voltage efficiency is defined in **Eq. 3.9k**.

$$LCOE = LCOE_{production} + LCOE_{use} \quad \textbf{(3.9a)}$$

$$LCOE_{production} = \frac{energy\ dep.capital + power\ dep.capital}{annual\ energy\ discharged \times TDF} \quad \textbf{(3.9b)}$$

$$energy\ dep.capital = \sum_{n=1}^{m} unit_{energy-dep.component,n} \times cost \quad \textbf{(3.9c)}$$

$$power\ dep.capital = \left(\sum_{n=1}^{l} unit_{power-dep.component,n} \times cost\right) \times \frac{1}{discharge\ time} \quad \textbf{(3.9d)}$$

$$annual\ energy\ discharged = \frac{energy}{discharge\ cycle} \times \frac{number\ of\ cycle\ discharges}{yr} \quad \textbf{(3.9e)}$$

$$TDF = \frac{1 - (1 + i_{discount})^{-n_{lifetime}}}{i_{discount}} \quad \textbf{(3.9f)}$$

$$LCOE_{use} = \frac{electricity\ price}{RTE} \quad \textbf{(3.9g)}$$

$$RTE = charge\ efficiency \times discharge\ efficiency \times FE_{roundtrip} \quad \textbf{(3.9h)}$$

$$FE_{roundtrip} = FE_{discharge} \times FE_{charge} \quad \textbf{(3.9i)}$$

$$charge\ voltage\ efficiency = \frac{\left(V_{pos,thermo} - V_{neg,thermo}\right)}{V_{actual,charge} \times (1 + loss_{pump})} \quad \textbf{(3.9j)}$$

$$discharge\ voltage\ efficiency = \frac{V_{actual,dis} \times (1 - loss_{pump})}{\left(V_{pos,thermo} - V_{neg,thermo}\right)} \quad \textbf{(3.9k)}$$

When reporting *LCOE* in the **Results and Discussion**, we identify the contributions from energy-dependent capital (Capital_E), power-dependent capital (Capital_P), and electricity (Elec.). The Capital_E, Capital_P, and Elec. contributions are defined in **Eq. 3.10a-c**.

$$\text{Capital}_\text{E} = \frac{energy\ dep.capital}{annual\ energy\ discharged \times TDF} \quad \textbf{(3.10a)}$$

$$\text{Capital}_\text{P} = \frac{power\ dep.capital}{annual\ energy\ discharged \times TDF} \quad \textbf{(3.10b)}$$

$$\text{Elec.} = LCOE_{use} \quad \textbf{(3.10c)}$$

Carbon tax scenarios. Three carbon tax scenarios were incorporated into the LCOE calculation: no carbon tax ($0/tonne CO_2e), moderate ($50/tonne CO_2e), and extreme ($150/tonne CO_2e). The carbon tax was added to the total LCOE as shown in **Eq. 3.11**, where $LCOE_{base}$ is calculated from **Eq. 3.9a**. The levelized amount of carbon emitted from the production and use phases, $LGHG$, was calculated using methods described in the next section.

$$LCOE_{with\ CO_2e\ tax} = LCOE_{base} + LGHG \times carbon\ tax \quad \textbf{(3.11)}$$

3.2.5 Life cycle inventory (LCI) model

The life cycle inventory (LCI) emissions model used attributional life cycle assessment (LCA) methods to quantify the greenhouse gas emissions of the production and use phases of the RFBs per kWh of electricity delivered. LCA principles and framework are defined by the International Organization for Standardization.[68] The greenhouse gas emissions were defined in terms of equivalent CO_2 on a 100 year basis (kg CO_2e). The production phase included the mining of materials, material production, and manufacturing. Wherever possible, the GHG emissions

intensity per RFB component was sourced from GREET 2 Version 2020,[69] as shown in **Table 3.5**. For CeO_2, GREET 2 reported the emissions intensity of all rare earth metals as an aggregate number, and so we assumed that value to be representative of the emissions for CeO_2. The electrolyte pumps were assumed to be made of polypropylene and weigh 6 kg each, and the emissions of the pump were calculated on a mass basis using the emissions intensity of polypropylene from GREET 2.[69] The flow meters were assumed to consist of an acrylic body (0.2 kg) and stainless steel fittings (0.05 kg) and the emissions were also calculated on a mass basis. GHG emissions for acrylic were not available from GREET 2, so the average plastic product emissions were used.[69] The electrolyte tanks were assumed to be polypropylene and the average of the LDPE and HDPE emissions from GREET 2 were used.[69] Emissions associated with the BOS were assumed to be negligible. For the membrane electrode assembly frame, high-density polymer emissions were assumed to be the same as polyethylene emissions from GREET 2.[69] The gasket was assumed to be rubber, and the average rubber product emissions from GREET 2[69] were used to model it. The PCS was estimated to weigh 0.345 kg according to vendor supply lists, and as an upper limit estimate of the emissions associated with producing the PCS, it was assumed that the entire weight of the system was silicon material. Using the emissions intensity of silicon from GREET 2,[69] the emissions associated with the PCS were calculated on a mass basis. The emissions of the V_2O_5 precursor were not available through GREET 2, and so instead, a report on the emissions of several metal oxides including vanadium pentoxide was used.[70] The emissions associated with titanium were not available through GREET 2, and so literature reports of the carbon intensity of titanium on a mass basis were used.[71] To estimate the emissions intensity of the platinized titanium mesh on a m^2 basis, the titanium carbon intensity was converted first to a volume basis using the density of titanium and then to a m^2 basis assuming a thickness of the

titanium layer of 0.0025 m. The emissions of the platinum were added to this titanium value by taking the emissions intensity of platinum on a mass basis available from GREET 2 and multiplying it by the assumed loading of 2 g/m^2.

The use phase accounted for the roundtrip efficiency of the RFB to deliver 1 kWh of electricity and the emissions associated with the energy source of the electricity. The emissions associated with each energy source are included in **Table 3.5** and are based off GREET 1 reported emissions.[72] Specifically, the stationary use: U.S. mix emissions were used for the average U.S. electricity mix, the coal-fired power plant emissions were used for the 100% coal case, the NG-fired power plant emissions were used for the 100% natural gas case, and the 100% renewables case was based on the average of the wind and photovoltaic power plant emissions, which were both zero. Because of the share of coal in the average U.S. electricity grid (22%), the average U.S. electricity grid mix results in slightly higher emissions than the 100% natural gas case, which has lower emissions associated with it than coal.

To calculate the levelized greenhouse gas emissions (LGHG) of the production phase, which has units of kg CO_2e/kWh_d, the GHG of the energy-dependent material and power-dependent material were summed and then normalized by the total amount of electricity delivered throughout the RFB lifetime, as shown in **Eq. 3.12a**. The energy-dependent and power-dependent GHGs were calculated in **Eq. 3.12b** and **Eq. 3.12c**, respectively, where there are m energy-dependent components and l power-dependent components and GHG_n refers to the greenhouse gases associated with producing a particular unit. The total amount of energy delivered by a battery in its lifetime was calculated using **Eq. 3.12d**, where $n_{lifetime}$ is the lifetime of the battery in years and $annual\ energy\ discharged$ was equal to the assumed number of cycles per year (see **Table 3.2**) multiplied by the energy delivered per cycle, which was set to 1 kWh.

Table 3.5. Component GHG emissions for VRFB and Ce-V RFB systems with references for all emissions listed.

Component	GHG_n	kg CO_2e/unit	Ref.
Energy-dependent material			
CeO_2	2.3	kg CO_2e/mol	[69]
V_2O_5	0.31	kg CO_2e/mol	[70]
H_2SO_4	0.011	kg CO_2e/mol	[69]
Electrolyte tank (polyethylene)	2865	kg CO_2e/m^3	[69]
Electrolyte pumps (polypropylene)	2.4	kg CO_2e/kg	[69]
Electrolyte pump flow meters (80% acrylic, 20% stainless steel)	3.3	kg CO_2e/kg	[69]
BOS	NA	NA	NA
Power-dependent material			
End plate (stainless steel)	38	kg CO_2e/m^2	[69]
Current collector (copper)	68	kg CO_2e/m^2	[69]
Bipolar plate (stainless steel)	38	kg CO_2e/m^2	[69]
V^{2+}/V^{3+} and VO_2^+/VO^{2+} electrode (graphite felt)	27	kg CO_2e/m^2	[69]
Ce^{3+}/Ce^{4+} electrode (platinized titanium mesh)	402	kg CO_2e/m^2	[69,71]
Membrane (Nafion 117)	0.47	kg CO_2e/m^2	[69]
Membrane electrode assembly frame (high-density polymer)	7.2	kg CO_2e/m^2	[69]
Gaskets (rubber)	15	kg CO_2e/m^2	[69]
PCS (silicon)	463	kg CO_2e/kg	[69]
Electricity			
Average U.S. electricity mix	0.435	kg CO_2e/kWh	[72]
100% coal	0.996	kg CO_2e/kWh	[72]
100% natural gas	0.425	kg CO_2e/kWh	[72]
100% renewable	0.0	kg CO_2e/kWh	[72]

$$LGHG_{production} = \frac{energy\ dep.GHG + power\ dep.GHG}{lifetime\ energy\ delivered} \quad \textbf{(3.12a)}$$

$$energy\ dep.GHG = \sum_{n=1}^{m} unit_{energy-dep.component,n} \times GHG_n \quad \textbf{(3.12b)}$$

$$power\ dep.GHG = \left(\sum_{n=1}^{l} unit_{power-dep.component,n} \times GHG_n\right) \times \frac{1}{discharge\ time} \quad \textbf{(3.12c)}$$

$$lifetime\ energy\ delivered = annual\ energy\ discharged \times n_{lifetime} \quad \textbf{(3.12d)}$$

The use phase GHG, $LGHG_{use}$, was calculated using the roundtrip efficiency, RTE, as well as the electricity mix GHG intensity, as shown in **Eq. 3.13**. The electricity GHG values were those shown in **Table 3.5**. The RTE was calculated using **Eq. 3.9h**. The total LGHG was calculated by summing the production and use phase LGHGs (**Eq. 3.14**), and it has units of kg CO_2e/kWh$_d$.

$$LGHG_{use} = \frac{electricity\ GHG}{RTE} \quad \textbf{(3.13)}$$

$$LGHG = LGHG_{production} + LGHG_{use} \quad \textbf{(3.14)}$$

When we report the LGHG in **Section 3.3**, we identify the contributions from energy-dependent material, power-dependent material, and electricity, which are all defined below in **Eq. 3.15a-c**.

$$\mathrm{GHG_{En.}} = \frac{energy\ dep.GHG}{lifetime\ energy\ delivered} \quad \textbf{(3.15a)}$$

$$\mathrm{GHG_{Pow.}} = \frac{power\ dep.GHG}{lifetime\ energy\ delivered} \quad \textbf{(3.15b)}$$

$$\mathrm{GHG_{Elec.}} = LGHG_{use} \quad \textbf{(3.15c)}$$

3.2.6 Optimization and sensitivity analysis

Current density optimization. In the TEA-LCI models, the performance of the RFB, e.g., the charge and discharge voltage, was dependent on the specified current density. As a result, the amount of material needed for the energy- and power-dependent capital and the cost and emissions of the RFB were all controlled by the current density input into the models (**Eq. 3.4-3.5** and **Scheme 3.1**). In addition to reporting the expected performance of the RFB as a function of current density, the models were used to optimize the current density to minimize either levelized cost of electricity (LCOE) or levelized greenhouse gas (LGHG) emissions. The methods to calculate

LCOE and LGHGs are included above in their respective sections. The Solver function within Excel (Microsoft 365) was used for optimization.[73] The Solver method used was GRG Nonlinear, and the optimization was run until the current density selected to minimize either LGHG or LCOE converged no matter the starting current density. The constraint precision of the Solver was 1×10^{-6} and the convergence was set to 1×10^{-4}.

Sensitivity analysis. Parameters considered in the sensitivity analysis of the VRFB and Ce-V RFB include those associated with the thermodynamics, kinetics, solubility, faradaic efficiency, and precursor costs and emissions on a mass basis. Specifically, each of the redox couple's redox potentials were included in the sensitivity analysis, as were each redox couple's exchange current density and charge and discharge Tafel slopes. The effect of each of these parameters except redox potentials and faradaic efficiency on the minimum LCOE and LGHG results was tested by changing the base values and varying the current density to minimize either the LCOE or LGHG in the cases when the parameter is (1) increased by 20% and (2) decreased by 20%, while holding all other parameters values constant. The redox potentials were varied by +/− 200 mV and the roundtrip faradaic efficiency was varied by approximately +/− 2%, i.e., both the charge and discharge faradaic efficiency were either increased or decreased by 1%. The base values for each of the performance parameters are included in **Table 3.1** and the base values for the cost and emissions parameters are included in **Table 3.4** and **Table 3.5**, respectively.

3.3 Results and Discussion

Here, we present the results of our TEA-LCI models. In **Section 3.3.1**, we determine the charge and discharge voltages, LCOE, and LGHG for a 1 MW sized VRFB as a function of current density and discharge time to validate our models against previously reported literature values. In **Section 3.3.2**, we compare the LCOE and LGHG of a Ce-V RFB to the VRFB for a longer

discharge time of 12 hours assuming the average U.S. electricity grid. We consider the effects of future, low carbon scenarios on LCOE and LGHG such as 100% renewables and carbon taxes in **Section 3.3.3** and explore the sensitivity of the results to different performance and cost parameters in **Section 3.3.4**.

3.3.1 Effect of current density and discharge time on LCOE and LGHG for all-vanadium redox flow battery

Our TEA-LCI models determine the minimum levelized cost of electricity (LCOE) or minimum levelized greenhouse gas emissions (LGHG) by varying the operating current density using our charge-discharge performance model. For a VRFB, we show in **Fig. 3.1a** that increasing current density causes the discharge voltage to decrease and the charge voltage to increase due to kinetic, mass transport, and ohmic overvoltages. As a result, the roundtrip efficiency, RTE, decreases with increasing current density. We show how current density affects LCOE and LGHG for the VRFB with a discharge time of 4 hours in **Fig. 3.1b**. As the current density is increased from zero, both LCOE and LGHG drop significantly, because a higher current density means a smaller battery area is needed, and power-dependent, e.g., materials related to the battery stack, capital costs and production emissions decrease. As the current density is further increased the LCOE and LGHG reach minima then start to increase, because the decrease in RTE increases electricity costs and emissions as well as energy-dependent, e.g., electrolyte, capital costs and emissions. We denote the current densities at which the VRFB LCOE and LGHG are minimized for 4-hour discharge in **Fig. 3.1b** with a blue circle and green triangle, respectively, demonstrating the different current densities needed to minimize LCOE and LGHG.

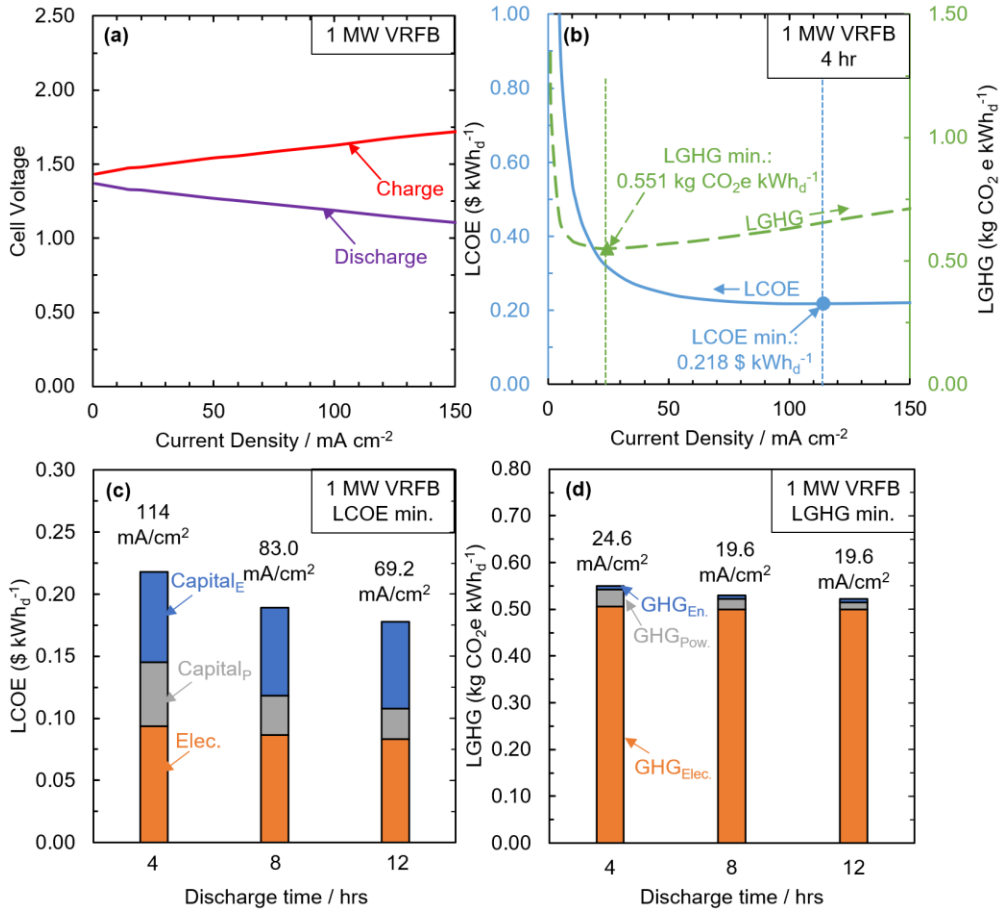

Figure 3.1. For a 1 MW VRFB: **(a)** discharge and charge voltage as a function of current density. **(b)** LCOE (light blue solid line) and levelized GHGs (green dashed line) as a function of current density for 4-hour discharge time, with minima for both LCOE and LGHG indicated. **(c)** Minimized LCOE and **(d)** minimized levelized GHGs for 4-, 8-, 12-hour discharge time. Current densities for each minimized value are indicated. LCOE and LGHG contributions from energy dependent material ($Capital_E$ and $GHG_{En.}$, blue), power dependent material ($Capital_P$ and $GHG_{Pow.}$, gray), and electricity (Elec. and $GHG_{Elec.}$, orange) indicated. LGHG and LCOE values are calculated assuming average U.S. electricity grid mix.

The LGHG minimum occurs at a lower current density than the LCOE minimum because LGHG is more dominated by the use phase of the VRFB, and so LGHG and LCOE cannot be minimized simultaneously. From **Fig. 3.1b**, the minimum LCOE for the 4-hour discharge VRFB of 0.218 $/kWh$_d$ occurs at a current density of 114 mA/cm^2, while the minimum LGHG of 0.551 kg CO_2e/kWh$_d$ occurs at a lower current density of 24.6 mA/cm^2. Typically, only LCOE minimization is considered in RFB modeling studies, but it is useful to determine how operating conditions would differ when minimizing LGHG, to understand if there is a regime in which both

LCOE and LGHG can be minimized. We show in **Fig. 3.1c** that the shares of LCOE for 4-hour discharge related to energy-dependent capital ($Capital_E$, 33%) and electricity costs (Elec., 43%) are slightly larger than power-dependent capital costs ($Capital_P$, 24%). With increasing current density, the battery area decreases, so power-dependent costs decrease, but the discharge voltage also decreases, meaning that more electrolyte is needed to deliver 1 kWh, so energy-dependent capital costs increase. Additionally, as previously noted, the RTE decreases with increasing current density, meaning the electricity costs increase. In **Fig. 3.1d**, the minimum LGHG is not split evenly between the three types of costs. Instead, 92% of the minimum LGHG for 4-hour discharge is driven by electricity ($GHG_{Elec.}$). As a result, LGHG is impacted more by losses in the electricity delivery phase than LCOE. Thus, to minimize LGHG, a lower current density is incentivized compared to the LCOE, which is influenced by the trade-off between decreasing power-dependent costs and increasing electricity costs and energy-dependent capital costs with increased current density. We show the full results of minimizing LCOE and LGHG in **Table 3.6**. The trend between energy-dependent and power-dependent capital costs with current density has been identified previously,[11,23] and the tradeoff between the power-dependent costs with electricity costs underscores why the LCOE and LGHG cannot be minimized simultaneously.

Table 3.6. Current density, RTE, capital cost, LCOE, and LGHG for LCOE and LGHG minimization cases for different discharge times for 1 kWh VRFB. Round trip faradaic efficiency was assumed to be 97%.

	LCOE minimized			**LGHG minimized**		
	4-hour	**8-hour**	**12-hour**	**4-hour**	**8-hour**	**12-hour**
Current density (mA/cm^2)	114	83.0	69.2	24.6	19.6	19.6
RTE (%)	67.9	73.8	76.4	85.9	87.1	87.1
Capital cost ($/kWh)	386	319	293	757	545	432
LCOE ($/$kWh_d$)	0.218	0.189	0.178	0.318	0.248	0.212
LGHG (kg CO_2e/kWh_d)	0.657	0.603	0.581	0.551	0.530	0.522

The capital costs, LCOE, and LGHG values we obtain for a 4-hour 1 MW VRFB agree with previously reported values and trends, validating our TEA-LCI models. For a 4-hour VRFB

with high discharge voltage efficiency (92%), a capital cost of approximately 555 $/kWh in 2014 USD was calculated including contributions such as depreciation and overhead.[15] Crawford et al. reported a capital cost of approximately 400 $/kWh in 2015 USD at a current density of 100 mA/cm^2,[2,17] and Mongird et al. reported more recently a capital cost of $391/kWh in 2020 USD, but the current density assumed was not clearly stated.[18] Our capital cost at 100 mA/cm^2 is $397/kWh, which falls in the previously reported range. The reported LCOE for VRFBs range between 0.16 $/kWh$_d$ (in 2015 USD),[17] for which the cost of electricity was not incorporated, and 0.47 $/kWh$_d$ (in 2018 USD).[74] Our LCOE for 4-hour discharge 0.218 $/kWh$_d$, falls within this range. Importantly, our TEA model indicates that the capital costs and LCOE (**Fig. 3.1b**) decrease with increasing current density up to approximately 115 mA/cm^2, which agrees with literature that shows increasing current density decreases VRFB storage costs until energy-dependent costs begin to dominate.[11,17,23] A wide range in VRFB LGHG has been reported, from 0.279 kg CO_2e/kWh$_d$[32] to 0.95 kg CO_2e/kWh$_d$,[33] and our LGHG for the case when LCOE is minimized for the 4-hour VRFB of 0.657 kg CO_2e/kWh$_d$ falls within this range. As will be discussed in more detail below, we show that the LGHG is dominated by the use phase emissions, which is a trend that has been noted in literature.[33] The VRFB capital costs, LCOE, and LGHG results of our TEA-LCI models fall within the ranges reported in literature, substantiating the models and lending confidence to our results.

When minimizing either cost or emissions, the optimal current density for the VRFB decreases with discharge time (**Fig. 3.1c,d**), because the power-dependent costs and emissions become less impactful and energy-dependent material and electricity dominate, which are improved with increased round trip efficiency. The decrease in LCOE from 0.218 $/kWh$_d$ for 4 hours to 0.178 $/kWh$_d$ for 12 hours in **Fig. 3.1c** occurs because the power-dependent capital costs

do not change with increasing discharge time, and so when normalized by discharge time, they become less costly on a kWh basis. Thus, the power-dependent capital costs become less influential to the overall cost, and a lower current density can be tolerated, which has the benefit of decreasing the energy-dependent capital costs and electricity costs. We demonstrate the decrease in optimal current densities in **Fig. 3.1c**. When minimizing for LCOE, the LGHG for the VRFB also decreases with increasing discharge time (**Table 3.6**), because the emissions associated with electricity decrease with decreased current density. **Fig. 3.1c,d** and **Table 3.6** highlight the utility of increasing discharge time to be both more economical and less emissions-intensive. Regarding the effect of discharge time on minimum LGHG (**Fig. 3.1d**), as discharge time increases from 4 hours to 12 hours, the current density decreases, and the minimum LGHG decreases from 0.551 kg CO_2e/kWh_d to 0.522 kg CO_2e/kWh_d, primarily due to the decrease in emissions of the power-dependent material. The result that the optimal current density decreases with increasing discharge time indicates that as long duration (>10 hours[5,7]) energy storage becomes more relevant, battery efficiency will become even more crucial. This has important implications for the broader field of battery operation as well as for what parameters will control battery performance. For example, kinetics losses dominate at lower current densities rather than mass transport or ohmic losses, and so improvements in kinetics (e.g., using catalysts) will become increasingly important. While we modeled 4-hour discharge here to compare to literature, we consider 12-hour discharge moving forward as we compare the VRFB and Ce-V RFB performance given the utility of RFBs for long-duration energy storage applications.

3.3.2 Minimized LCOE and LGHG for Ce-V RFB compared to VRFB assuming average U.S. electricity mix

In **Fig. 3.2** we compare the LCOE and LGHG as a function of current density for a 1 MW sized VRFB and Ce-V RFB and show that the Ce-V RFB has slightly lower LCOE at intermediate current densities, but higher LGHG compared to the VRFB even at low current densities meant for minimizing LGHG. We compare the Ce-V RFB and VRFB LCOE across a range of current densities in **Fig. 3.2a** for 12-hour discharge, assuming the average U.S. electricity grid. Above 25 mA/cm^2 and below 150 mA/cm^2, the Ce-V RFB LCOE is lower than the VRFB LCOE, and the minimum LCOE for the Ce-V RFB (0.170 $\$/kWh_d$) is lower than for the VRFB (0.178 $\$/kWh_d$) and occurs at a lower current density. The large increase in the Ce-V RFB LCOE at 200 mA/cm^2 is due to the limiting current density of the Ce^{3+}/Ce^{4+} redox couple during charging. Comparing the LGHG as a function of current density in **Fig. 3.2b**, at current densities less than 25 mA/cm^2, we show the emissions are similar between the Ce-V RFB and the VRFB, but as current densities increase, the Ce-V RFB LGHG increases more than the VRFB. The LGHG minima for both the VRFB and the Ce-V RFB occur at 19.6 mA/cm^2. The Ce-V RFB LGHG of 0.539 kg CO_2e/kWh_d is 3% higher than the VRFB LGHG of 0.522 kg CO_2e/kWh_d. It is useful to understand what operating conditions are necessary to minimize GHG emissions, given the goal of using RFBs to promote renewable energy sources to decrease GHG emissions. An analysis of the effect of current density on each of the cost and emissions components can lend insight to why the Ce-V RFB performs better in terms of cost but worse in terms of emissions than the VRFB.

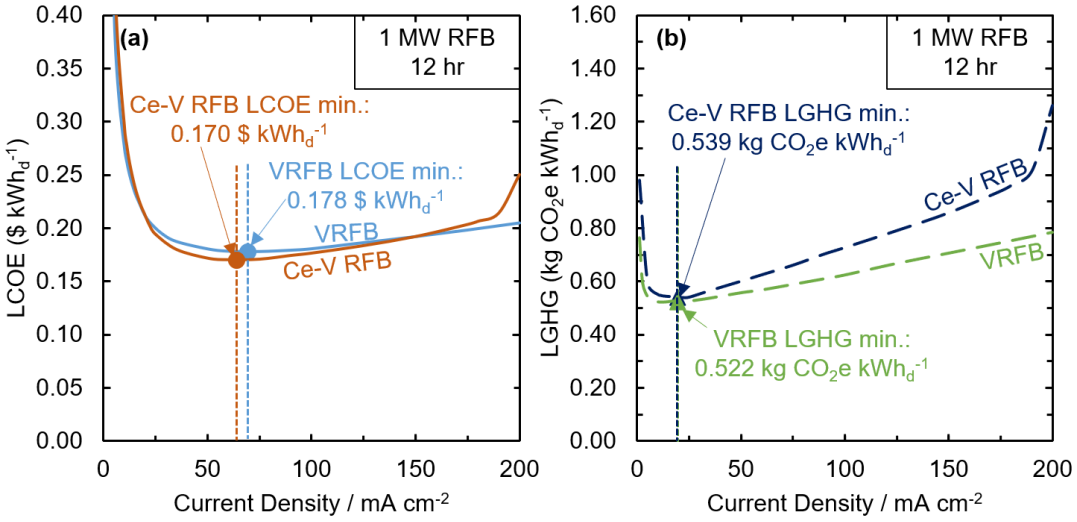

Figure 3.2. For 12-hour discharge: **(a)** LCOE for VRFB (light blue solid line) and Ce-V RFB (dark orange solid line), and **(b)** levelized GHGs for VRFB (green dashed line) and Ce-V RFB (indigo dashed line) as a function of current density, with minima for LCOE in **(a)** and LGHG in **(b)** indicated with circle and triangle markers, respectively.

Compared to the VRFB, the Ce-V RFB has a slightly lower minimum LCOE because of its lower electrolyte cost, larger thermodynamic voltage, and lower corresponding current density, which is incentivized because of the slower Ce^{3+}/Ce^{4+} kinetics. When LCOE is minimized, the VRFB LCOE is 0.178 $/kWh$_d$ and the Ce-V RFB is 0.170 $/kWh$_d$ (**Fig. 3.3a**) and the optimal current density for VRFB is higher at 69 mA/cm^2 than the Ce-V RFB (64 mA/cm^2). Comparing the breakdown of costs in **Fig. 3.3a**, the Ce-V RFB energy-dependent costs are lower than the VRFB's, but the Ce-V RFB's power-dependent capital and electricity costs are higher. The lower energy-dependent costs are due to three factors: 1) the lower cost of CeO_2 compared to V_2O_5, 2) the larger open circuit voltage (OCV), and 3) the lower current density. Comparing the breakdown of costs into their individual components for the VRFB (**Fig. 3.3b**) and Ce-V RFB (**Fig. 3.3c**), the share of the cost of the positive electrolyte drops significantly for Ce-V RFB because of the lower cost of CeO_2 than V_2O_5. Additionally, the Ce-V RFB's higher thermodynamic voltage and lower current density means the operating discharge voltage is higher, resulting in less electrolyte required to deliver 1 kWh. The VRFB has a higher current density compared to the Ce-V RFB

because it has a lower thermodynamic voltage, meaning that if the batteries had the same area, the VRFB would need a higher current density to deliver the same amount of power. Additionally, the VRFB has faster kinetics, and so a higher current density for the VRFB results in lower overvoltages relative to the Ce-V RFB. Thus, a higher current density is incentivized to drive the power-dependent costs down for the VRFB. The Ce-V RFB optimized power-dependent capital costs are higher than for the VRFB (**Fig. 3.3a**) because the current density is low enough to require more area for the Ce-V RFB system, despite the larger thermodynamic voltage. The Ce-V RFB LCOE is still close to the VRFB LCOE because of the higher cost of the Ce^{3+}/Ce^{4+} electrode (platinized titanium, needed for stability at higher potentials) than the V^{4+}/V^{5+} electrode (graphite). The higher cost is evident in the electrodes cost for the Ce-V RFB in **Fig. 3.3c** compared to the VRFB Electrodes cost in **Fig. 3.3b**. A higher current density is not incentivized for the Ce-V RFB despite its larger power-dependent capital costs because the Ce^{3+}/Ce^{4+} redox system has slower kinetics than V^{4+}/V^{5+}. The slower kinetics of the Ce-V RFB result in its lower RTE (71.4%) than the VRFB RTE (76.4%), despite the larger OCV of the Ce-V RFB. The lower RTE results in the larger electricity costs of the Ce-V RFB compared to the VRFB (**Fig. 3.3a**). This analysis demonstrates why the minimum Ce-V RFB LCOE is lower than the VRFB under current grid assumptions, and a similar analysis is conducted next to understand why the LGHG for Ce-V RFB and VRFB are similar.

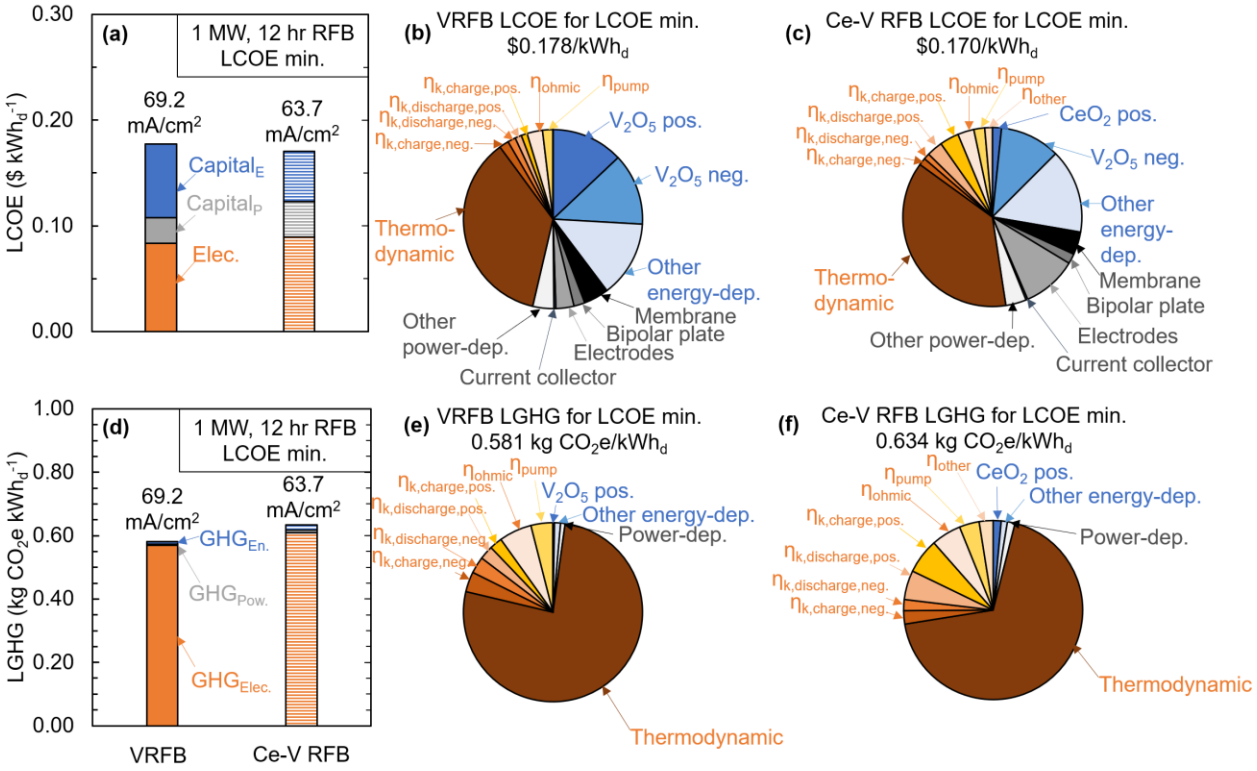

Figure 3.3. When minimizing LCOE: **(a)** 1 MW, 12-hour discharge VRFB (solid) and Ce-VRBs (dashed) LCOE, with contributions from energy-dependent capital ($Capital_E$, blue), power-dependent capital ($Capital_P$, gray), and electricity (Elec., orange) costs. Component breakdown of LCOE for **(b)** VRFB and **(c)** Ce-V RFB. Other energy-dependent components include: acids for positive and negative electrolyte, electrolyte tanks, pumps, and flow meters. Other power-dependent components include: end plates, membrane electrode assembly, gaskets, and PCS. Other electricity components include the overvoltages associated with the charge and discharge mass transport for both the positive and negative electrodes. **(d)** 1 MW, 12-hour discharge VRFB and Ce-V RFB LGHG with contributions from energy-dependent material ($GHG_{En.}$, blue), power-dependent material ($GHG_{Pow.}$, gray), and electricity emissions ($GHG_{Elec.}$, orange). Component breakdown of LGHG for **(e)** VRFB and **(f)** Ce-V RFB. All values calculated assuming average U.S. electricity grid mix.

When minimizing for LCOE, the Ce-V RFB LGHG is higher than the VRFB LGHG, because of the Ce-V RFB's lower RTE, which results in increased use phase emissions. The LGHG values for the VRFB and Ce-V RFB when LCOE is optimized are 0.581 kg CO_2e/kWh$_d$ (VRFB) and 0.634 kg CO_2e/kWh$_d$ (**Fig. 3.3d**), respectively. From **Fig. 3.3d**, we show that the LGHG for both RFBs is dominated by the use phase (98% and 96% of the LGHG are from electricity for VRFB and Ce-V, respectively). The use phase LGHG for the VRFB is 0.569 kg CO_2e/kWh$_d$ and 0.609 kg CO_2e/kWh$_d$ for the Ce-V RFB, and the larger Ce-V RFB electricity LGHG is due to the lower RTE, which occurs despite the larger thermodynamic voltage and lower current density of

the Ce-V RFB because of its larger kinetic overvoltages. Additionally, the Ce-V RFB has a larger share of electrolyte-related production emissions due to the use of CeO_2 (CeO_2 pos. in **Fig. 3.3f** compared to V_2O_5 pos. in **Fig. 3.3e**). The Ce-V RFB LGHG is dominated by the electricity grid emissions, however, not the production emissions, suggesting that in future decarbonized electricity grid scenarios, the Ce-V RFB may be a more environmentally friendly option than it is for the average U.S. electricity grid scenario. This analysis highlights that for the average U.S. electricity grid, the Ce-V RFB will result in a 9% increase in GHG emissions compared to the VRFB when operating conditions are chosen to minimize cost, and so it is useful to consider how the Ce-V RFB LGHG will compare to the VRFB's when operating conditions are selected to minimize LGHG.

When minimizing for LGHG, the Ce-V RFB LCOE and VRFB LCOE values are similar, because the power-dependent capital of the Ce-V RFB is more costly than the VRFB power-dependent capital, but the Ce-V RFB's energy-dependent capital costs are less than the VRFB's. We include the comparison of VRFB and Ce-V RFB LCOEs when LGHG is minimized in **Fig. 3.4a**. The VRFB and Ce-V LCOEs in this case are both 0.212 $/kWh$_d$. The current densities for minimizing emissions are significantly lower for both the VRFB and Ce-V RFB than in the case for minimizing cost because the use phase dominates LGHG, incentivizing high roundtrip efficiencies. The current densities are the same for the VRFB and Ce-V RFB (19.6 mA/cm^2) because the current densities are incentivized to be as low as possible before power-dependent material emissions start to dominate, as seen in **Fig. 3.2** at current densities lower than 19.6 mA/cm^2. These similar current densities result in similar RTEs and therefore similar electricity costs (**Fig. 3.4a**). At conditions to minimize LGHG, the Ce-V RFB power-dependent capital costs are larger because the platinized titanium mesh electrode for the Ce^{3+}/Ce^{4+} positive electrolyte is

significantly more expensive than the graphite felts assumed for the VRFB (see smaller Electrodes cost for VRFB in **Fig. 3.4b** and larger Ce-V RFB Electrodes in **Fig. 3.4c**). Comparing the energy-dependent costs, the Ce-V RFB's are lower, primarily due to the higher thermodynamic voltage, meaning less material is required to deliver the same amount of electricity, and the lower cost of CeO_2 compared to V_2O_5. This lower cost is visible in the comparison of the share of positive electrolyte cost for the VRFB in **Fig. 3.4b** (V_2O_5 pos.) compared to the Ce-V RFB positive electrolyte cost in **Fig. 3.4c** (CeO_2 pos.). Compared to the minimum LCOE, the LCOE when LGHG is minimized is 19% higher for the VRFB and 25% higher for the Ce-V RFB. This increase in cost suggests that the operating conditions will not be varied to minimize emissions unless incentives like carbon taxes are incorporated to penalize higher emissions. Nonetheless, it is useful to understand what the minimum possible emissions are for each system, given the goal of using energy storage to decrease GHG emissions through renewable energy integration.

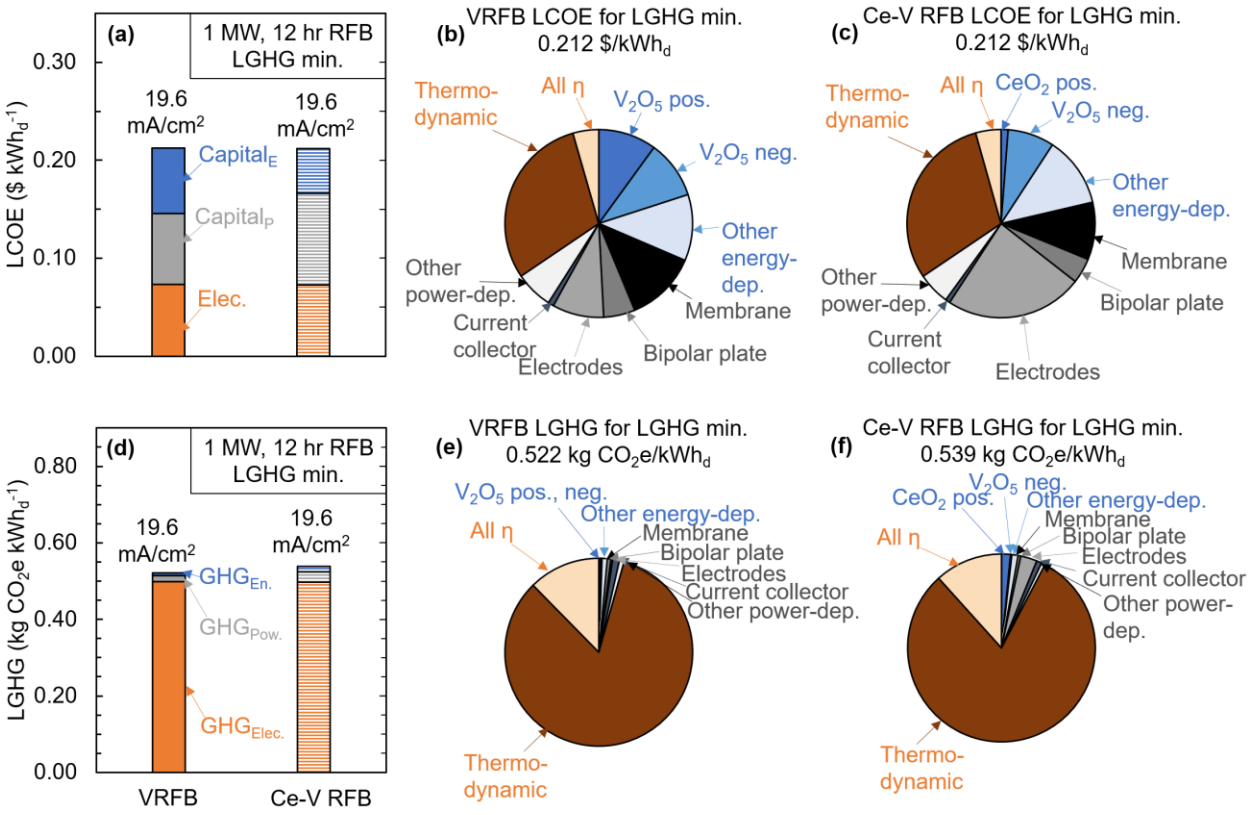

Figure 3.4. When minimizing LGHG: **(a)** 1 MW, 12-hour discharge VRFB (solid) and Ce-V RFBs (dashed) LCOE with contributions from energy-dependent capital ($Capital_E$, blue), power-dependent capital ($Capital_P$, gray), and electricity costs (Elec., orange). Component breakdown of LCOE for **(b)** VRFB and **(c)** Ce-V RFB. **(d)** 1 MW, 12-hour discharge VRFB and Ce-V RFB LGHG with contributions from energy-dependent material ($GHG_{En.}$, blue), power-dependent material ($GHG_{Pow.}$, gray), and electricity emissions ($GHG_{Elec.}$, orange). Component breakdown of LGHG for **(e)** VRFB and **(f)** Ce-V RFB. All values calculated assuming average U.S. electricity grid mix.

The VRFB and Ce-V RFB LGHG minima and corresponding current densities are within 4% of each other, with the Ce-V RFB performing slightly worse due to the higher emissions of the energy-dependent material. When LGHG is minimized, VRFB LGHG is 0.522 kg CO_2e/kWh$_d$ while Ce-V RFB LGHG is 0.539 kg CO_2e/kWh$_d$, as seen in **Fig. 3.4d**. The VRFB *RTE* is 87.0% and the Ce-V RFB *RTE* is 87.3%, and so the emissions for use phase of the Ce-V RFB are lower than for the VRFB. The energy-dependent material emissions are greater for the Ce-V RFB because of the larger positive electrolyte emissions (in **Fig. 3.4e**, V_2O_5 pos. contribution is very small compared to CeO_2 pos. contribution in **Fig. 3.4f**). The power-dependent material emissions are also greater for the Ce-V RFB because of the larger emissions associated with the production

of the platinized titanium electrode (**Fig. 3.4f**) than the graphite electrode (**Fig. 3.4e**). The larger material emissions are what drive the larger LGHG for the Ce-V RFB than the VRFB. While it is unlikely that RFBs will be operated to minimize GHG emissions at the expense of increased LCOE, this analysis demonstrates that when minimizing for emissions, switching from the VRFB to the Ce-V RFB results in only a 4% increase in LGHG and a 0.3% increase in LCOE for the case in which the average U.S. electricity grid is assumed to be charging the battery. Overall, the exploration of the Ce-V RFB performance compared to the VRFB assuming the average U.S. electricity grid demonstrates that there are operating conditions at which the Ce-V RFB is more economical and does not result in a significant increase in GHG emissions when the battery is operated to minimize either LGHG or LCOE. Next, we conduct an analysis to understand how the Ce-V RFB and VRFB compare assuming a 100% renewable grid and the addition of a carbon tax to indicate how selection between and operation of these batteries may change in future, low carbon scenarios.

3.3.3 Minimized LCOE and LGHG for Ce-V RFB compared to VRFB for future, low-carbon scenarios

As the electricity grid mix becomes more renewable, although both RFBs LGHG decrease, the Ce-V RFB LGHG becomes increasingly larger than the VRFB LGHG because the production phase begins to dominate LGHG. In **Fig. 3.5a** we show the LGHG when LCOE is minimized for four different electricity grid scenarios for both the VRFB and Ce-V RFB: a 100% coal case, the average U.S. electricity grid, 100% natural gas case, and a 100% renewables case. As expected, the LGHG trends roughly match the emissions associated with the electricity source listed in **Table 3.5**. Because coal-based electricity emissions are twice as high as any of the other cases and the use phase dominates emissions, the 100% coal case results in the largest LGHG for both the VRFB

and Ce-V RFB. Because the average U.S. electricity grid mix results in slightly higher emissions than the 100% natural gas case, the RFBs have higher LGHGs for the U.S. mix than the natural gas. For these three electricity grid scenarios, the Ce-V RFB results in higher emissions than the VRFB because of the larger positive electrolyte production emissions and larger use phase emissions. In the 100% renewables case, the use phase emissions are 0 kg CO_2e/kWh$_d$, and so the overall emissions for both the VRFB and Ce-V RFB drop by over 96% to 0.013 kg CO_2e/kWh$_d$ and 0.026 kg CO_2e/kWh$_d$, respectively. As we show in the inset in **Fig. 3.5a**, when 100% renewables are used, the RFB production emissions associated with both the energy-dependent and power-dependent materials play more important roles. The Ce-V RFB has a significantly higher LGHG than the VRFB in the 100% renewables case primarily due to the larger emissions intensity of CeO_2 than V_2O_5, although the power-dependent material emissions are also increased for the Ce-V RFB compared to the VRFB due to the increased production emissions of the platinized titanium electrode compared to the graphite felt. For RFBs, the 100% coal and 100% renewables cases are optimized at lower current density than the average U.S. electricity grid, because coal and renewable electricity are more expensive than the average U.S. grid, incentivizing higher RTE. The 100% natural gas cases are optimized at a higher current density, because natural gas is cheaper than the average U.S. grid, meaning that a lower RTE can be tolerated.

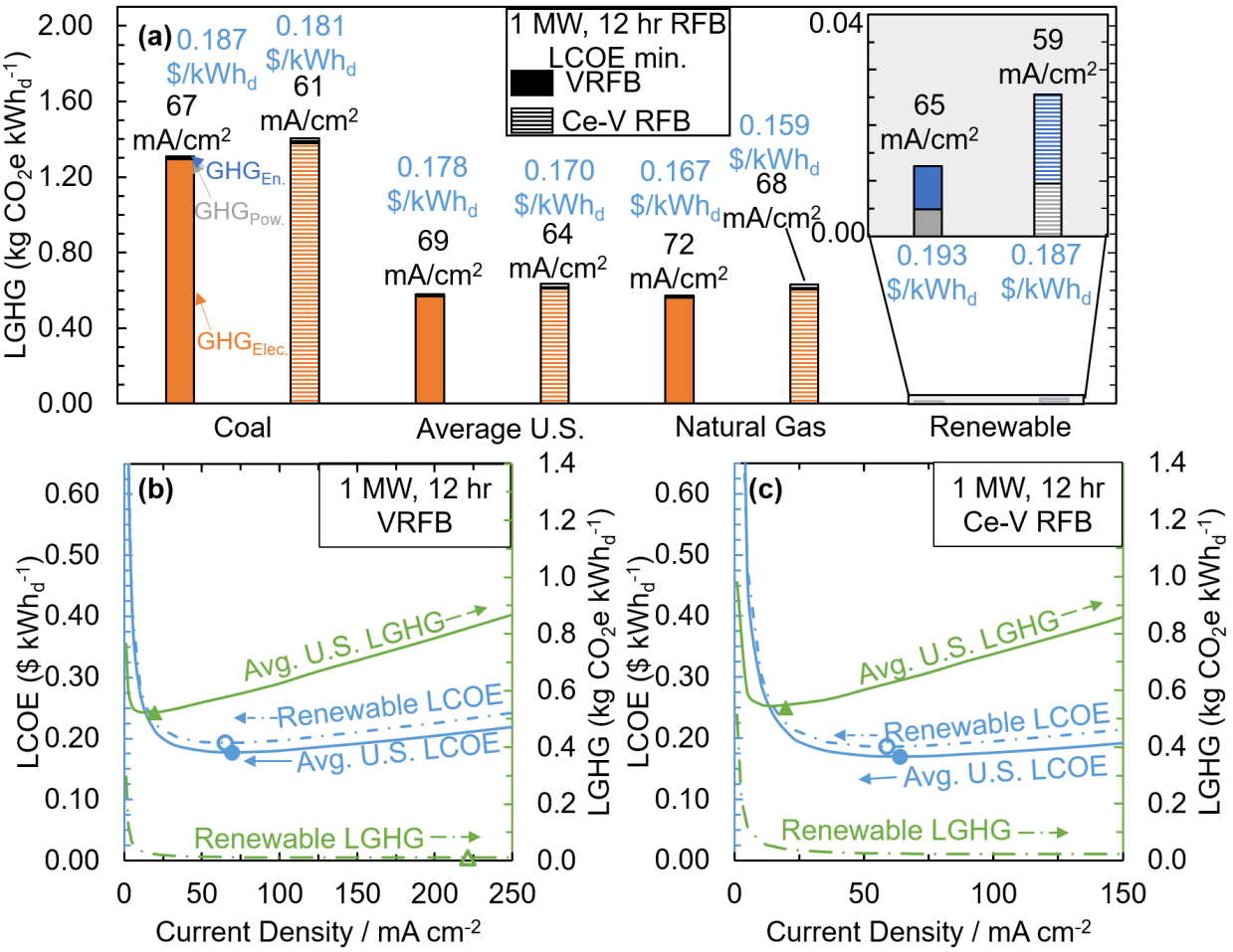

Figure 3.5. (a) LGHG when LCOE is minimized for 1 MW delivery power for 12 hours for coal, U.S. mix, natural gas, pure renewable for VRFB (solid) and Ce-V (dashed) batteries. Emissions broken down between energy dependent material ($GHG_{En.}$, blue), power dependent material ($GHG_{Pow.}$, gray), and electricity emissions ($GHG_{Elec.}$, orange). Optimal current densities to achieve minimum LCOE included in panel, and minimum LCOE for each scenario is listed in blue. For 1 MW, 12-hour **(b)** VRFB and **(c)** Ce-V RFB, LCOE (light blue) and LGHG (green) as a function of current density for average U.S. electricity grid and 100% renewable electricity grid. LCOE (circle) and LGHG (triangle) minima are included in (b) and (c) for average U.S. grid (filled) and 100% renewables (unfilled) cases.

The optimal current densities for minimum LGHG increase significantly for the 100% renewable case for both the VRFB (**Fig. 3.5b**) and Ce-V RFB (**Fig. 3.5c**), while the current densities for the RFB LCOE minima decrease slightly. **Fig. 3.5b** shows the LCOE and LGHG as a function of current density for a 1 MW VRFB with a 12-hour discharge time for both the average U.S. electricity grid case and the 100% renewable grid case, and we show the same analysis for the Ce-V RFB in **Fig. 3.5c**. The LCOE for the renewables case is larger for both RFBs than the average U.S. electricity grid, because the cost of the electricity source is higher. The minimum

LCOEs for all four electricity grid scenarios are included in **Fig. 3.5a**, and the average U.S. electricity grid and 100% renewables grid are marked by the filled and unfilled blue markers, respectively, in **Fig. 3.5b** (VRFB) and **Fig. 3.5c** (Ce-V RFB). The optimal current density to minimize LCOE decreases slightly with the 100% renewables grid, which is driven by the need to increase RTE to decrease the cost of electricity delivery. Compared to the LGHGs for both RFBs for the average U.S. electricity grid case, the LGHGs for the 100% renewables grid drops dramatically across the entire range of current density. The LGHG minima are marked in **Fig. 3.5b-c** by the green triangles. The minimum LGHG for the 100% renewables case (unfilled triangle) occurs at significantly higher current densities (221 mA/cm^2 for VRFB and 155 mA/cm^2 for Ce-V RFB) than for the average U.S. electricity grid case because the RTE does not need to be as high, since the use phase does not control the emissions for the 100% renewables case. The VRFB optimal current density is higher than the Ce-V RFB because the Ce-V RFB is still incentivized to keep current densities low enough to minimize the emissions of the CeO_2 electrolyte. With higher current densities, the discharge voltage decreases, and more energy-dependent material is needed. The power-dependent material emissions are higher for the Ce-V RFB than the VRFB as a result of this lower current density and the larger production emissions of the platinized titanium electrode. As the grid shifts closer to a renewables-dominated supply, as is needed to drive down GHG emissions, the Ce-V RFB will remain cost competitive but will become increasingly emissions intensive relative to the VRFB. In addition to understanding the influence of an increasingly renewable grid on performance results, it is useful to consider the impacts of a carbon tax, which can be used to quantify the penalty for the increased emissions of the Ce-V RFB compared to the VRFB.

With the incorporation of a carbon tax assuming the average U.S. electricity grid, the optimal current density to minimize LCOE decreases for both the VRFB and Ce-V RFB, and the corresponding LCOE increases. We show the minimized LCOE ranging from no carbon tax to a stringent carbon tax of \$150/tonne CO_2e for the VRFB and Ce-V RFB in **Fig. 3.6a** and **Fig. 3.6b**, respectively. The LCOEs for both the VRFB and Ce-V RFB increase with increasing carbon tax. The effect of decreasing current density with increasing carbon tax is demonstrated for the VRFB in **Fig. 3.6a** and Ce-V RFB in **Fig. 3.6b** by the decrease in the LGHG (triangles). We include the LCOE for each carbon tax scenario as a function of current density for the VRFB and Ce-V RFB in **3.6c** and **3.6d**. The LCOE minima denoted by circle markers in **Fig. 3.6c-d** occur at lower current densities as the carbon tax increases. The decrease in current density with higher LGHG penalty occurs because LGHG is dominated by the use phase for the average U.S. electricity grid, motivating higher RTE when carbon is penalized. For a 100% renewables case, the optimized current density would not decrease as significantly, because the LGHG is no longer dominated by the use phase and RTE. The carbon tax analysis can be used to understand whether the VRFB or Ce-V RFB would be better suited to a future scenario where emissions were penalized.

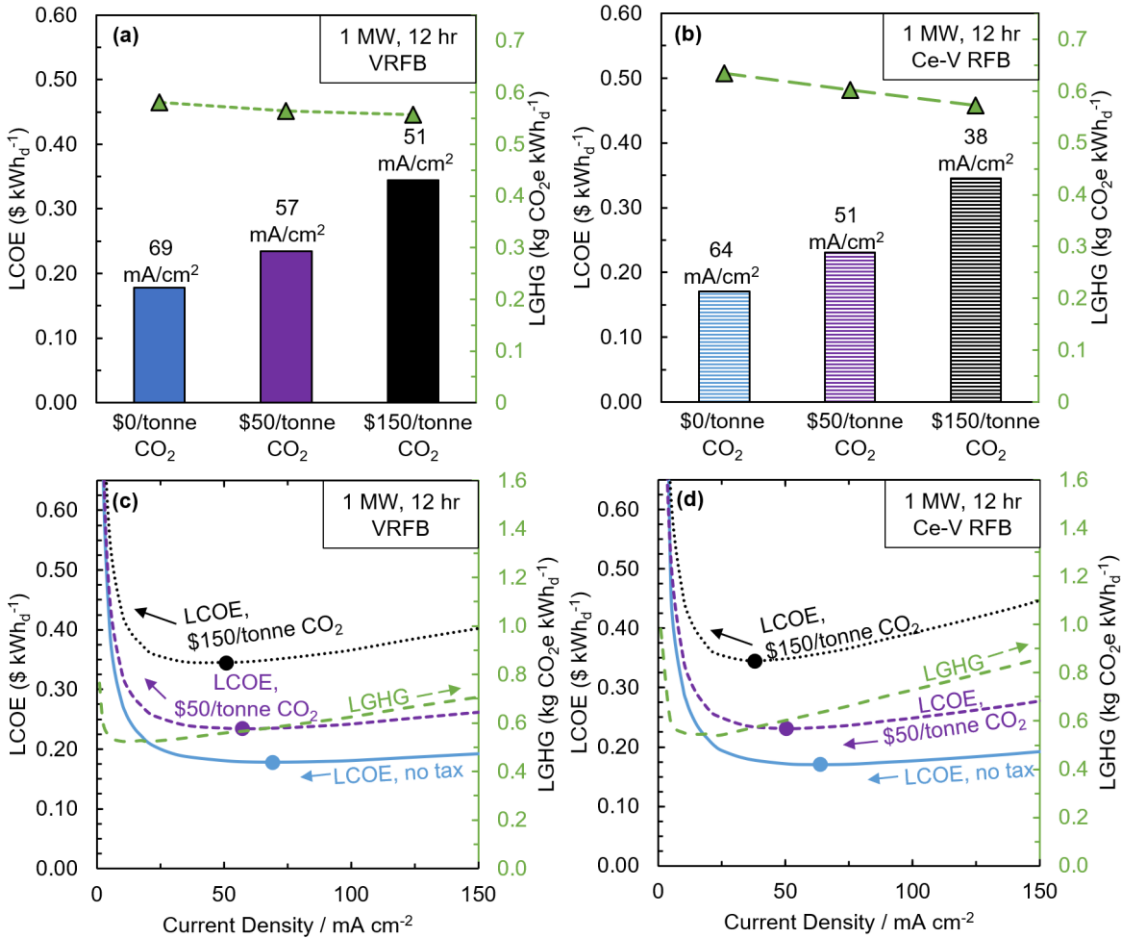

Figure 3.6. Minimized LCOE and corresponding LGHGs (green triangles) for different carbon tax scenarios, with optimal current densities indicated, for **(a)** VRFB and **(b)** Ce-V RFB with 12-hour discharge. LCOE and LGHGs (dashed green line) as a function of current density for: no carbon tax (solid light blue line), \$50/tonne CO_2 carbon tax (dashed purple line), and \$150/tonne CO_2 carbon tax (dotted black line) scenarios, for **(c)** VRFB and **(d)** Ce-V RFB with 12-hour discharge. The dots in **(c)** and **(d)** represent LCOE minima for each carbon tax scenario.

Up to a large carbon tax of \$150/tonne CO_2e, the Ce-V RFB LCOE is lower than the VRFB at current densities less than 50 mA/cm^2, despite the larger Ce-V RFB emissions. For a \$50/tonne CO_2e carbon tax, the minimum VRFB LCOE is 0.234 \$/kWh$_d$ (**Fig. 3.6c**) and the minimum Ce-V RFB LCOE is 0.231 \$/kWh$_d$ (**Fig. 3.6d**). As the carbon tax is increased to \$150/tonne CO_2e, the minimum LCOE for the VRFB becomes 0.344 \$/kWh$_d$ and the Ce-V RFB becomes 0.345 \$/kWh$_d$. This indicates that at carbon taxes less stringent than \$150/tonne CO_2, the Ce-V RFB is more economical than the VRFB.

3.3.4 Thermodynamic, kinetic, selectivity, and material properties are important to the performance of the Ce-V RFB and VRFB

For both RFBs the redox potential has the biggest impact on cost and second biggest impact on emissions, which motivates further investigation into controlling the redox potential through electrolyte preparation and selection. As an example, from **Fig. 3.7a**, a 200 mV increase in V^{4+}/V^{5+} redox potential causes the minimum VRFB LCOE to decrease from 0.178 \$/kWh$_d$ to 0.166 \$/kWh$_d$. The effect of redox potential on VRFB LGHG is shown in **Fig. 3.7b**, and effects of redox potential on the Ce-V RFB LCOE and LGHG are shown in **Fig. 3.7c** and **Fig. 3.7d**, respectively. The electrolyte redox potential changes the overall voltage of the battery, which controls the amount of energy-dependent material needed, the total area of the battery required, i.e., the power-dependent material, and the roundtrip efficiency. While kinetic parameters affect the overall voltage of the battery through the kinetic overvoltages, the change in overvoltage is smaller than the change in redox potential. The finding that redox potential has the largest influence on an RFB's cost is in line with literature reports that OCV has a significant impact on cost.[10] The electrolyte can be manipulated to increase the RFBs' redox potentials. Both increasing the concentration of V_2O_5 from its solubility limit of 0.5 M to 1.6 M through chemical or electrochemical reduction[52] and controlling the Donnan potential through changing the relative positive and negative electrolyte proton concentrations have an impact on VRFB OCV.[10,40] For the Ce-V RFB, the Ce^{3+}/Ce^{4+} redox potential can be varied significantly by changing the electrolyte, for instance changing the electrolyte from H_2SO_4 to CH_3SO_3H (MSA) causes the Ce^{3+}/Ce^{4+} redox potential to increase from 1.44 V vs. SHE to 1.61 V vs. SHE.[24] We explore the tradeoff between the effect of electrolyte selection on thermodynamics and other parameters like kinetics below.

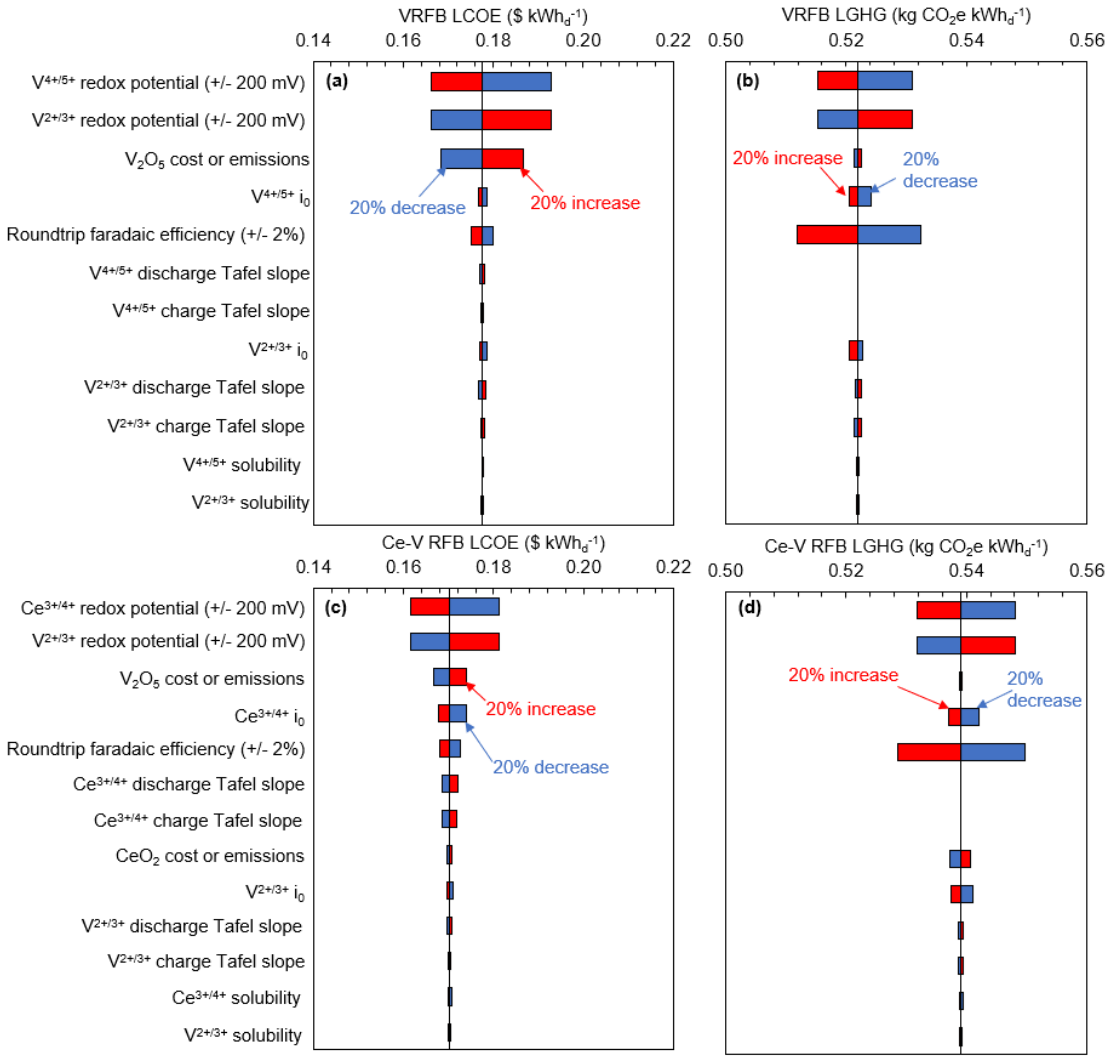

Figure 3.7. For 1 MW delivery power with 12-hour delivery and average U.S. electricity mix, sensitivity of **(a)** VRFB LCOE, **(b)** VRFB LGHG, **(c)** Ce-V RFB LCOE, and **(d)** Ce-V RFB LGHG to a 20% increase (red) or 20% decrease (blue) change in parameter, unless otherwise noted. Parameters include V^{4+}/V^{5+} redox potential, V^{4+}/V^{5+} charge Tafel slope, V^{4+}/V^{5+} discharge Tafel slope, V^{4+}/V^{5+} exchange current density, V^{4+}/V^{5+} solubility, V^{2+}/V^{3+} redox potential, V^{2+}/V^{3+} charge Tafel slope, V^{2+}/V^{3+} discharge Tafel slope, V^{2+}/V^{3+} exchange current density, V^{2+}/V^{3+} solubility, V_2O_5 cost and CO_2 intensity, Ce^{3+}/Ce^{4+} redox potential, roundtrip faradaic efficiency, Ce^{3+}/Ce^{4+} charge Tafel slope, Ce^{3+}/Ce^{4+} discharge Tafel slope, Ce^{3+}/Ce^{4+} exchange current density, Ce^{3+}/Ce^{4+} solubility, and CeO_2 cost and CO_2 intensity.

The kinetic rates and roundtrip faradaic efficiency are significant drivers of both RFBs' LCOE and LGHG as we show in **Fig. 3.7**, and the cost of the V_2O_5 impacts the LCOE for both RFBs, while only the Ce-V RFB LGHG is affected substantially by precursor production emissions. An increase in faradaic efficiency results in a decreased active species concentration and decreased battery area, driving down their related costs and emissions, and an increase in *RTE*.

The large impact of faradaic efficiency on *RTE* is why the faradaic efficiency has such a large impact on LGHG, which is controlled by the *RTE* for the average U.S. electricity grid. Thus, factors that control faradaic efficiency such as an electrode's selectivity should be prioritized in RFB development. Exchange current density, i_0, and Tafel slopes have an impact on the RFB's LCOE and LGHG by changing the kinetic overvoltages as a function of current density. The Ce^{3+}/Ce^{4+} i_0 has a larger impact on minimum Ce-V RFB LCOE than the V^{2+}/V^{3+} i_0 because an increase in the V^{2+}/V^{3+} i_0 does not reduce kinetic overvoltages as significantly as an increase in the Ce^{3+}/Ce^{4+} i_0. For the case of minimizing LGHG, where the current densities are optimized to be lower relative to the case of minimizing LCOE, the BV equation is simplified to show a linear dependence between Tafel slope and current density and so Tafel slopes have less of an influence, but i_0 still has an influence on the minimum LGHG. The V_2O_5 precursor cost also has a significant effect on both RFB's minimum LCOE and is more significant for the VRFB (**Fig. 3.7a**) because it uses V_2O_5 in both electrolytes. The influence of V_2O_5 precursor cost underscores why it is so important to identify alternatives to the V chemistry for RFB applications. The CeO_2 production emissions are more influential to the Ce-V RFB minimum LGHG than V_2O_5 production emissions are to either the Ce-V RFB or VRFB LGHG because the CeO_2 production emissions are an order of magnitude larger than the V_2O_5 production emissions. In developing new systems, it is important to maximize the thermodynamic potential of the RFB, kinetic rates, and faradaic efficiency while taking into account possible changes in electrolyte or electrode cost.

The sensitivity analysis can be used to quantify the allowable increase in material costs for a 200 mV increase in thermodynamics or a doubling in the exchange current density as well as indicate what the equivalent changes in thermodynamics and kinetics are for the same cost savings. For instance, for the Ce-V RFB, a 200 mV increase in redox potential is worth an increase in

electrolyte cost of up to 1.83 $/kg, assuming no significant changes in solubility or molecular weight with electrolyte. Here we mean that a 200 mV increase in redox potential with a corresponding 1.83 $/kg increase in electrolyte cost would keep the overall LCOE the same, and if the electrolyte cost increase was <1.83 $/kg, the LCOE would decrease. For reference, the cost of H_2SO_4 used in this study is 0.32 $/kg. An increase in roundtrip faradaic efficiency to 99.98% from 97.02% is worth an increase in electrolyte cost of 0.66 $/kg. A doubling of the Ce^{3+}/Ce^{4+} i_0 justifies a 333 $/m^2 increase in electrode price, assuming the area of the battery remains the same, due to the corresponding decrease in overvoltage. As a reminder, the amount of platinum that is assumed to be deposited on the titanium mesh used for the electrode costs 77 $/m^2, which suggests that an effective strategy for reducing cost would be to use twice as much Pt to double the electrode active surface area because the increase in i_0 would save more than the cost of the additional Pt. We note that the i_0 used is normalized to the geometric surface area, and so for our model a doubling of the active surface area per geometric area would effectively double i_0. If the Ce^{3+}/Ce^{4+} i_0 is increased by more than a factor of 7, however, the cost savings from increased performance no longer outweigh the increased cost of Pt (assuming the Pt cost is also increased by a factor of 7). Another strategy to increase the surface area would be to change the geometric configuration of the titanium mesh underlayer, which would be expected to have an increased manufacturing cost that would need to be compared to the overvoltage savings. Alternatively, an increase in the Ce^{3+}/Ce^{4+} i_0 by a factor of 2 is approximately equivalent to a 194 mV increase in redox potential, demonstrating the significance of Ce^{3+}/Ce^{4+} kinetics on performance. For the VRFB, to keep the LCOE at its current minimum of 0.178 $/kWh$_d$, the electrolyte cost could be increased by 10.03 $/kg for a 200 mV increase in redox potential. This much larger window for the electrolyte cost for the same increase in redox potential between VRFB and the Ce-V RFB (10.03 $/kg and 1.83

$/kg, respectively), is because of the much higher total amount of electrolyte needed for Ce, due to its lower solubility than V. For an increase in roundtrip faradaic efficiency from 97.02% up to 99.98%, the electrolyte could increase by 2.71 $/kg. An increase in electrode cost from 90 $/m^2 to 166 $/m^2 could be tolerated to double the V^{4+}/V^{5+} i_0. A 37 mV increase in the V^{4+}/V^{5+} redox potential is approximately equivalent to the effect on cost of doubling the V^{4+}/V^{5+} i_0. Compared to the equivalent change in Ce^{3+}/Ce^{4+} redox potential to achieve a doubled i_0 for the Ce-V RFB of 200 mV, the equivalent V^{4+}/V^{5+} redox potential increase is quite low, indicating that the Ce^{3+}/Ce^{4+} kinetics are more influential to the Ce-V RFB cost than the V^{4+}/V^{5+} kinetics are to the VRFB cost. These analyses help quantify how important a certain improvement in thermodynamic and kinetic performance is to a system, e.g., for a Ce-V RFB, if an electrolyte that increases the Ce^{3+}/Ce^{4+} redox potential by 200 mV and does not increase electrolyte costs more than 1.83 $/kg above the H_2SO_4 price, then the electrolyte is a viable alternative to H_2SO_4. A summary of the allowable electrolyte and electrode cost increases for different thermodynamic and kinetic improvements of the redox couples is included in **Table 3.7**.

Table 3.7. Reference values and equivalent effects on costs for U.S. grid electricity mixture.

Cerium-Vanadium Redox Flow Battery (Ce-V RFB)					
	Ce^{3+}/Ce^{4+} Redox Potential	**Electrolyte Cost**	**Roundtrip Faradaic Efficiency**	**Ce^{3+}/Ce^{4+} i_0**	**Positive Electrode Cost**
Reference Value	1.44 V vs. SHE	0.32 \$/kg (H_2SO_4 only)	97.02%	24.2 mA/cm^2 (geometric area)	511 \$/m^2 (76 \$/m^2 for Pt)
	+200 mV	+1.83 \$/kg			
		+0.66 \$/kg	+2.96%		
		+\$1.77 \$/kg		×2	+333 \$/m^2
				×7	+574 \$/m^2
	+194 mV			×2	
	V^{2+}/V^{3+} Redox Potential	**Electrolyte Cost**	**Roundtrip Faradaic Efficiency**	**V^{2+}/V^{3+} i_0**	**Negative Electrode Cost**
Reference Value	−0.3125 V vs. SHE	0.32 \$/kg (H_2SO_4 only)	97.02%	16.8 mA/cm^2 (geometric area)	90 \$/m^2
	−200 mV	+16.72 \$/kg			
		+6.06 \$/kg	+2.96%		
		+3.05 \$kg		×2	+63 \$/m^2
	−36.5 mV			×2	
All Vanadium Redox Flow Battery (VRFB)					
	V^{4+}/V^{5+} Redox Potential	**Electrolyte Cost**	**Roundtrip Faradaic Efficiency**	**V^{4+}/V^{5+} i_0**	**Positive Electrode Cost**
Reference Value	1.0875 V vs. SHE	0.32 \$/kg (H_2SO_4 only)	97.02%	43.5 mA/cm^2	90 \$/m^2
	+200 mV	+10.03 \$/kg			
		+2.71 \$/kg	+2.96%		
		+1.86 \$/kg		×2	+76 \$/m^2
	+37 mV			×2	
	V^{2+}/V^{3+} Redox Potential	**Electrolyte Cost**	**Roundtrip Faradaic Efficiency**	**V^{2+}/V^{3+} i_0**	**Negative Electrode Cost**
Reference Value	−0.3125 V vs. SHE	0.32 \$/kg (H_2SO_4 only)	97.02%	16.8 mA/cm^2 (geometric area)	90 \$/m^2
	−200 mV	+18.35 \$/kg			
		+4.96 \$/kg	+2.96%		
		+3.30 \$kg		×2	+74 \$/m^2
	−36 mV			×2	

Comparing the sensitivity of the Ce-V RFB and VRFB LCOE and LGHG values in **Fig. 3.7a-d**, there are cases in which the Ce-V RFB has lower LGHG than the VRFB, or the minimum VRFB LCOE is lower than the minimum Ce-V RFB, assuming the average U.S. electricity grid mix. For instance, if the Ce^{3+}/Ce^{4+} redox potential was decreased by 20%, the Ce-V RFB minimum LCOE would be 0.181 $/kWh$_d$, which is higher than the baseline VRFB minimum LCOE. If the Ce-V RFB roundtrip faradaic efficiency was increased to 99%, its minimum LGHG would be 0.529 kg CO_2e/kWh$_d$, which is lower than the VRFB minimum LGHG if its faradaic efficiency were decreased to 95% (0.532 kg CO_2e/kWh$_d$). The large influence of the faradaic efficiency demonstrates that more certainty in VRFB and Ce-V RFB faradaic efficiencies is important to further quantify the relative LCOEs and LGHGs for the two systems, since in the TEA-LCI models we assumed the roundtrip faradaic efficiencies were both equal to approximately 97% due to a lack of information on the Ce-V RFB. Additionally, if the Ce^{3+}/Ce^{4+} redox potential were increased by 200 mV to 1.64 V vs. SHE, the minimum LGHG would be 0.517 kg CO_2e/kWh$_d$. The sensitivity analysis in **Fig. 3.7** demonstrates that there are opportunities for reducing the LGHG of the Ce-V RFB further to align with or even surpass the performance of the state-of-the-art VRFB, and also highlights parameters used in the TEA-LCI models such as faradaic efficiency that should be further verified to confirm that the Ce-V RFB minimum LCOE is lower than the VRFB LCOE.

Given the large uncertainty in the price of the platinized titanium electrode assumed for the Ce-V RFB positive electrode, we conduct an additional sensitivity analysis to understand its effect on the minimum Ce-V RFB LCOE. Our baseline price of the platinized titanium electrode was 511 $/m^2, but both platinum and titanium are expensive, and it is possible that the actual price is significantly higher. We find that for a positive electrode price of 1500 $/m^2,[61] the minimum Ce-V RFB LCOE is 0.195 $/kWh$_d$, which is significantly larger than the minimum VRFB LCOE of

0.178 \$/kWh$_d$, and the positive electrode accounts for 19% of the total Ce-V RFB LCOE. The large impact of the positive electrode price on minimum LCOE highlights the need for greater certainty in its value through additional studies. Additionally, there is a need for the development of an inexpensive positive electrode for the Ce-V RFB, for instance, if the positive electrode cost were reduced to 100 \$/m^2 to be more comparable to the VRFB positive electrode, the Ce-V RFB minimum LCOE would decrease to 0.158 \$/m^2.

For the case of 100% renewable electricity, the trends in sensitivity for both RFBs remain approximately the same for LCOE, as do the tolerated materials cost for increasing thermodynamic and kinetic performance, but the LGHG for both batteries becomes more sensitive to the factors that control the production phase emissions relative to the U.S. average electricity grid mix case. As seen in **Fig. 3.8a** for the VRFB minimum LCOE, the redox potentials, V_2O_5 cost, and faradaic efficiency remain the most influential parameters for the 100% renewables case, with the baseline minimum LCOE increasing to 0.193 \$/kWh$_d$. In **Fig. 3.8b**, the relative influence of the V_2O_5 production emissions on the VRFB minimum LGHG is greater compared to the kinetics and faradaic efficiency because the production phase emissions now dominate emissions. In **Fig. 3.8c**, the Ce-V RFB minimum LCOE is similarly most impacted by redox potential, V_2O_5 cost, and kinetics, which is consistent with the trends observed in **Fig. 3.7c** for the average U.S. grid case. Like the 100% renewables case for the VRFB, the minimum LGHG for the Ce-V RFB (**Fig. 3.8d**) is influenced by the redox potentials, and the CeO_2 production emissions and solubility, which are both strongly related to the energy-dependent material emissions, also become important. Considering the tradeoffs between material cost and thermodynamic and kinetic performance (**Table 3.8**), a 200 mV increase in V^{4+}/V^{5+} would be worth a 10.36 \$/kg increase in electrolyte cost, and an increase in electrode cost of up to 78 \$/m^2 would be justified to double the V^{4+}/V^{5+} i_0

for the 100% renewables case. For the Ce-V RFB assuming a 100% renewable grid, a 200 mV increase in the Ce^{3+}/Ce^{4+} redox couple would be worthwhile for an increase in electrolyte cost up to 1.92 \$/kg, and to double the Ce^{3+}/Ce^{4+} i_0, an increase in electrode cost of 336 \$/m^2 could be tolerated. The results of the sensitivity analysis for the 100% renewables case help to illustrate how RFB performance is expected to change as the electricity grid becomes increasingly decarbonized through renewable energy sources.

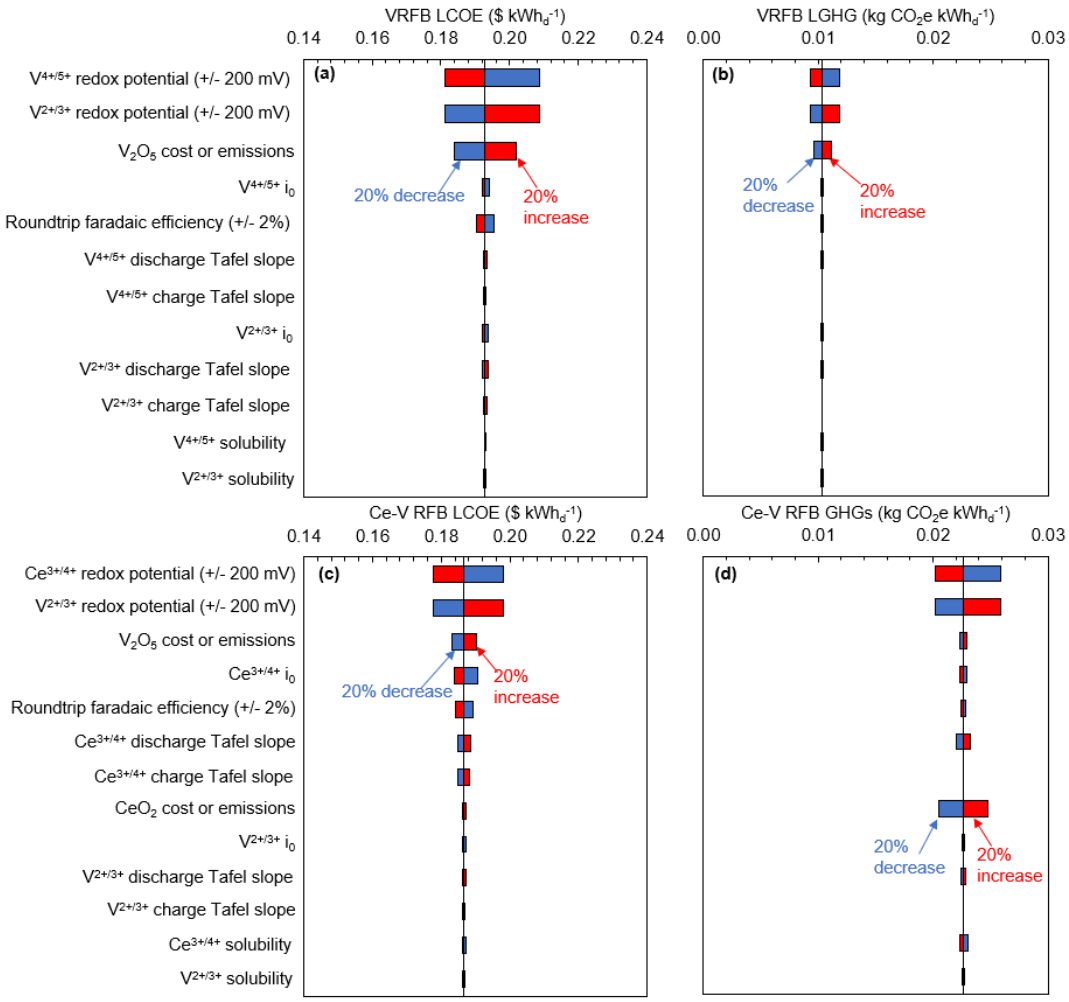

Figure 3.8. For 1 MW delivery power with 12-hour delivery and 100% renewables, sensitivity of **(a)** VRFB LCOE, **(b)** VRFB LGHG, **(c)** Ce-V RFB LCOE, and **(d)** Ce-V RFB LGHG to a 20% increase (red) or 20% decrease (blue) change in parameter, unless otherwise noted. Parameters include V^{4+}/V^{5+} redox potential, V^{4+}/V^{5+} charge Tafel slope, V^{4+}/V^{5+} discharge Tafel slope, V^{4+}/V^{5+} exchange current density, V^{4+}/V^{5+} solubility, V^{2+}/V^{3+} redox potential, V^{2+}/V^{3+} charge Tafel slope, V^{2+}/V^{3+} discharge Tafel slope, V^{2+}/V^{3+} exchange current density, V^{2+}/V^{3+} solubility, V_2O_5 cost and CO_2 intensity, Ce^{3+}/Ce^{4+} redox potential, roundtrip faradaic efficiency, Ce^{3+}/Ce^{4+} charge Tafel slope, Ce^{3+}/Ce^{4+} discharge Tafel slope, Ce^{3+}/Ce^{4+} exchange current density, Ce^{3+}/Ce^{4+} solubility, and CeO_2 cost and CO_2 intensity.

Table 3.8. Reference values and equivalent effects on costs for 100% renewable electricity.

Cerium-Vanadium Redox Flow Battery (Ce-V RFB)					
	Ce^{3+}/Ce^{4+} Redox Potential	**Electrolyte Cost**	**Roundtrip Faradaic Efficiency**	**Ce^{3+}/Ce^{4+} i_0**	**Positive Electrode Cost**
Reference Value	1.44 V vs. SHE	0.32 \$/kg (H_2SO_4 only)	97.02%	24.2 mA/cm^2 (geometric area)	511 \$/m^2 (76 \$/m^2 for Pt)
	+200 mV	+1.92 \$/kg			
		+0.76 \$/kg	+2.96%		
		+1.94 \$/kg		×2	+336 \$/m^2
	+202 mV			×2	
	V^{2+}/V^{3+} Redox Potential	**Electrolyte Cost**	**Roundtrip Faradaic Efficiency**	**V^{2+}/V^{3+} i_0**	**Negative Electrode Cost**
Reference Value	−0.3125 V vs. SHE	0.32 \$/kg (H_2SO_4 only)	97.02%	16.8 mA/cm^2 (geometric area)	90 \$/m^2
	−200 mV	+17.55 \$/kg			
		+6.92 \$/kg	+2.96%		
		+3.33 \$/kg		×2	+63 \$/m^2
	−38 mV			×2	
All Vanadium Redox Flow Battery (VRFB)					
	V^{4+}/V^{5+} Redox Potential	**Electrolyte Cost**	**Roundtrip Faradaic Efficiency**	**V^{4+}/V^{5+} i_0**	**Positive Electrode Cost**
Reference Value	1.0875 V vs. SHE	0.32 \$/kg (H_2SO_4 only)	97.02%	43.5 mA/cm^2	90 \$/m^2
	+200 mV	+10.36 \$/kg			
		+3.07 \$/kg	+2.96%		
		+2.04 \$/kg		×2	+78 \$/m^2
	+0.39 mV			×2	
	V^{2+}/V^{3+} Redox Potential	**Electrolyte Cost**	**Roundtrip Faradaic Efficiency**	**V^{2+}/V^{3+} i_0**	**Negative Electrode Cost**
Reference Value	−0.3125 V vs. SHE	0.32 \$/kg (H_2SO_4 only)	97.02%	16.8 mA/cm^2 (geometric area)	90 \$/m^2
	−200 mV	+18.95 \$/kg			
		+5.62 \$/kg	+2.96%		
		+3.61 \$/kg		×2	+76 \$/m^2
	−38 mV			×2	

3.4 Conclusion

Here we investigate the levelized cost of electricity (LCOE) and the levelized greenhouse gas emissions (LGHG) associated with that delivered electricity for an all-vanadium redox flow battery (VRFB) and a $V^{2+}/V^{3+}//Ce^{3+}/Ce^{4+}$ redox flow battery (Ce-V RFB) using a performance

model that allows us to optimize the operating current density to minimize cost or emissions. Although both redox flow batteries have more emissions than directly produced electricity, this is primarily due to the inherent inefficiency in storing electricity, and only a small contribution of the LGHGs are from the production of the batteries (<10% for 12-hour operation with the current US electricity mix). Based on our assumptions, which include similar roundtrip faradaic efficiency between the two RFBs, the Ce-V RFB is a promising alternative to the VRFB because it can result in reduced energy storage cost, which is the major challenge for the VRFB system. For the Ce-V RFB to be seriously considered as an alternative RFB, the Ce-V RFB technical performance should be confirmed at larger scale than benchtop studies, and substitutes for the positive electrode that are significantly cheaper than the platinized titanium mesh are needed given the low abundance of Pt and high costs of Pt and titanium and their large effect on minimum LCOE. Our findings are promising for use of RFBs as a long-duration renewable energy storage system and implies that as electricity sources shift to sources with less greenhouse gas emissions and energy storage shifts to longer time scales (e.g., from 4 to 12 hours), RFB emissions will also decrease. Despite having a higher amount of greenhouse gases emitted during its production, the Ce-V RFB emits a similar amount of LGHG during its lifetime as the VRFB, because the higher redox potential of the Ce-V RFB allows it to be operated at lower current densities (higher round trip efficiency) than the VRFB without an economic penalty.

3.5 References

1. U.S. Energy Information Administration. *June 2022 Monthly Energy Review*. vol. June (2022).
2. U.S. Energy Information Administration. *Annual Energy Outlook 2021*. (2021).
3. Rodby, K. E. *et al.* Assessing the levelized cost of vanadium redox flow batteries with capacity fade and rebalancing. *J. Power Sources* **460**, 227958 (2020).
4. Rodby, K. E., Perry, M. L. & Brushett, F. R. Assessing capacity loss remediation methods for asymmetric redox flow battery chemistries using levelized cost of storage. *J. Power Sources* **506**, 230085 (2021).
5. Hunter, C. A. *et al.* Techno-economic analysis of long-duration energy storage and flexible power generation technologies to support high-variable renewable energy grids. *Joule* **5**, 2077–2101 (2021).
6. Mai, T. *et al. Renewable Electricity Futures Study. Volume 1: Exploration of High-Penetration Renewable Electricity Futures*. vol. 1 (2012).
7. Albertus, P., Manser, J. S. & Litzelman, S. Long-duration electricity storage applications, economics, and technologies. *Joule* **4**, 21–32 (2020).
8. U.S. DOE Water Technologies Office. *U.S. Hydropower Market Report*. (2021).
9. Weber, A. Z. *et al.* Redox flow batteries: A review. *J. Appl. Electrochem.* **41**, 1137–1164 (2011).
10. Perry, M. L., Rodby, K. E. & Brushett, F. R. Untapped potential: The need and opportunity for high-voltage aqueous redox flow batteries. *ACS Energy Lett.* 659–667 (2022) doi:10.1021/acsenergylett.1c02225.
11. Zhang, M., Moore, M., Watson, J. S., Zawodzinski, T. A. & Counce, R. M. Capital cost sensitivity analysis of an all-vanadium redox-flow battery. *J. Electrochem. Soc.* **159**, A1183–A1188 (2012).
12. Sanchez-Díez, E. *et al.* Redox flow batteries: Status and perspective towards sustainable stationary energy storage. *J. Power Sources* **481**, 228804 (2021).
13. Guarnieri, M., Trovo, A., Marini, G., Sutto, A. & Alotto, P. High current polarization tests on a 9 kW vanadium redox flow battery. *J. Power Sources* **431**, 239–249 (2019).
14. Darling, R. M. & Perry, M. L. Method of maintaining health of a flow battery, U.S. Patent 20160056487. (2013).
15. Darling, R. M., Gallagher, K. G., Kowalski, J. A., Ha, S. & Brushett, F. R. Pathways to low-cost electrochemical energy storage: A comparison of aqueous and nonaqueous flow batteries. *Energy Environ. Sci.* **7**, 3459–3477 (2014).
16. Viswanathan, V. *et al.* Cost and performance model for redox flow batteries. *J. Power Sources* **247**, 1040–1051 (2014).
17. Crawford, A. *et al.* Comparative analysis for various redox flow batteries chemistries using a cost performance model. *J. Power Sources* **293**, 388–399 (2015).
18. Mongird, K. *et al. 2020 Grid Energy Storage Technology Cost and Performance Assessment*. (2020).
19. Schmidt, O., Melchior, S., Hawkes, A. & Staffell, I. Projecting the future levelized cost of electricity storage technologies. *Joule* **3**, 81–100 (2019).
20. Lai, C. S. & Mcculloch, M. D. Levelized cost of electricity for solar photovoltaic and electrical energy storage. *Appl. Energy* **190**, 191–203 (2017).
21. Pawel, I. The cost of storage- how to calculate the levelized cost of stored energy (LCOE)

and applications to renewable energy generation. *Energy Procedia* **46**, 68–77 (2014).
22. U.S. DOE. *Energy Storage Program Planning Document*. (2011).
23. Noack, J., Wietschel, L., Roznyatovskaya, N., Pinkwart, K. & Tübke, J. Techno-economic modeling and analysis of redox flow battery systems. *Energies* **9**, 627 (2016).
24. Arenas, L. F., Ponce De León, C. & Walsh, F. C. Electrochemical redox processes involving soluble cerium species. *Electrochim. Acta* **205**, 226–247 (2016).
25. Stormcrow. Cerium oxide price worldwide from 2009 to 2020 with a forecast from 2021 to 2030 (in U.S. dollars per metric ton). (2021).
26. Live vanadium price. vanadiumprice.com.
27. Narayan, S. R. *et al.* Next-generation aqueous flow battery chemistries. *Curr. Opin. Electrochem.* **18**, 72–80 (2019).
28. Dieterle, M., Fischer, P., Blume, N., Minke, C. & Bischi, A. Life cycle assessment (LCA) for flow batteries: A review of methodological decisions. *Sustain. Energy Technol. Assessments* **53**, 102457 (2022).
29. Fernandez-Marchante, C. M., Millán, M., Medina-Santos, J. I. & Lobato, J. Environmental and preliminary cost assessments of redox flow batteries for renewable energy storage. *Energy Technol.* **1900914**, 1–10 (2019).
30. Morales-mora, M. A., Pijpers, J. J. H. & Castillo, A. Life cycle assessment of a novel bipolar electrodialysis-based flow battery concept and its potential use to mitigate the intermittency of renewable energy generation. *J. Energy Storage* **35**, 102339 (2021).
31. He, H. *et al.* Flow battery production: Materials selection and environmental impact. *J. Clean. Prod.* **269**, 121740 (2020).
32. Weber, S., Peters, J. F., Baumann, M. & Weil, M. Life cycle assessment of a vanadium redox flow battery. *Environ. Sci. Technol.* **52**, 10864–10873 (2018).
33. Hiremath, M., Derendorf, K. & Vogt, T. Comparative life cycle assessment of battery storage systems for stationary applications. *Environ. Sci. Technol.* **49**, 4825–4833 (2015).
34. Jones, C., Gilbert, P. & Stamford, L. Assessing the climate change mitigation potential of stationary energy storage for electricity grid services. *Environ. Sci. Technol.* **54**, 67–75 (2020).
35. Denholm, P. & Kulcinski, G. L. Life cycle energy requirements and greenhouse gas emissions from large scale energy storage systems. *Energy Convers. Manag.* **45**, 2153–2172 (2004).
36. Arbabzadeh, M., Johnson, J. X., De Kleine, R. & Keoleian, G. A. Vanadium redox flow batteries to reach greenhouse gas emissions targets in an off-grid configuration. *Appl. Energy* **146**, 397–408 (2015).
37. Pennington, D. W. *et al.* Life cycle assessment part 2: Current impact assessment practice. *Environ. Int.* **30**, 721–739 (2004).
38. Graedel, T. E. *Streamlined Life-Cycle Assessment*. (Prentice-Hall, Inc., 1998).
39. Sauer, D. U. *et al.* State of charge- What do we really speak about? *21st Int. Telecommun. Energy Conf.* (1999).
40. Knehr, K. W. & Kumbur, E. C. Open circuit voltage of vanadium redox flow batteries: Discrepancy between models and experiments. *Electrochem. commun.* **13**, 342–345 (2011).
41. You, D. *et al.* Investigation of advanced catalytic effect of Co3O4 nanosheets modified carbon felts as vanadium flow battery electrodes. *J. Power Sources* **494**, 229775 (2021).
42. Yamamura, T., Watanabe, N., Yano, T. & Shiokawa, Y. Electron-Transfer Kinetics of Np3+/Np4+, NpO2+/NpO22+, V2+/V3+, and VO2+/VO2+ at Carbon Electrodes. *J.*

Electrochem. Soc. **152**, A830 (2005).
43. Wang, W. *et al.* The reduction reaction kinetics of vanadium(V) in acidic solutions on a platinum electrode with unusual difference compared to carbon electrodes. *Electrochim. Acta* **283**, 1313–1322 (2018).
44. Xiang, Y. & Daoud, W. A. Cr2O3-modified graphite felt as a novel positive electrode for vanadium redox flow battery. *Electrochim. Acta* **290**, 176–184 (2018).
45. Guarnieri, M., Mattavelli, P., Petrone, G. & Spagnuolo, G. Vanadium redox flow batteries: Potentials and challenges of an emerging storage technology. *IEEE Ind. Electron. Mag.* **10**, 20–31 (2016).
46. Granieri, S. F. *et al.* An high performance carbon-nano onion electrode for vanadium redox flow battery. in *2022 ECS Meeting Abstract* (2022).
47. Amini, K. & Pritzker, M. D. In situ polarization study of zinc – cerium redox flow batteries. *J. Power Sources* **471**, 228463 (2020).
48. Tucker, M. C., Weiss, A. & Weber, A. Z. Improvement and analysis of the hydrogen-cerium redox flow cell. *J. Power Sources* **327**, 591–598 (2016).
49. Nikiforidis, G., Berlouis, L., Hall, D. & Hodgson, D. Charge/discharge cycles on Pt and Pt-Ir based electrodes for the positive side of the Zinc-Cerium hybrid redox flow battery. *Electrochim. Acta* **125**, 176–182 (2014).
50. Ghimire, P. C. *et al.* Optimization of thermal oxidation of electrodes for the performance enhancement in all-vanadium redox flow betteries. *Carbon N. Y.* **155**, 176–185 (2019).
51. El Hage, R. *et al.* Kinetic study of the dissolution of vanadyl sulfate and vanadium pentoxide in sulfuric acid aqueous solution. *Chem. Eng. Sci.* **199**, 123–136 (2019).
52. Martin, J., Schafner, K. & Turek, T. Preparation of electrolyte for vanadium redox-flow batteries based on vanadium pentoxide. *Energy Technol.* **8**, (2020).
53. Paulenova, A., Creager, S. E., Navratil, J. D. & Wei, Y. Redox potentials and kinetics of the Ce3+/Ce4+redox reaction and solubility of cerium sulfates in sulfuric acid solutions. *J. Power Sources* **109**, 431–438 (2002).
54. Kim, J. & Park, H. Electrokinetic parameters of a vanadium redox flow battery with varying temperature and electrolyte flow rate. *Renew. Energy* **138**, 284–291 (2019).
55. Singh, N. & McFarland, E. W. Levelized cost of energy and sensitivity analysis for the hydrogen-bromine flow battery. *J. Power Sources* **288**, 187–198 (2015).
56. Bard, A. J. & Faulkner, L. R. *Electrochemical Methods: Fundamentals and Applications*. (John Wiley & Sons, Inc., 2001). doi:10.1016/B978-0-08-098353-0.00003-8.
57. Banham, D. *et al.* Ultralow platinum loading proton exchange membrane fuel cells: Performance losses and solutions. *J. Power Sources* **490**, 229515 (2021).
58. U.S. Energy Information Administration. *Electric Power Monthly, February 2021*. (2021).
59. Mayyas, A., Ruth, M., Pivovar, B., Bender, G. & Wipke, K. *Manufacturing Cost Analysis for Proton Exchange Membrane Water Electrolyzers*. *National Renewable Energy Laboratory* (2019).
60. Metalary. Titanium price. https://www.metalary.com/titanium-price/.
61. Jourdin, L., Sousa, J., Stralen, N. van & Strik, D. P. B. T. B. Techno-economic assessment of microbial electrosynthesis from CO2 and/or organics: An interdisciplinary roadmap towards future research and application. *Appl. Energy* **279**, 115775 (2020).
62. JM Bullion. Platinum spot price & charts. https://www.jmbullion.com/charts/platinum-price/ (2021).
63. Taleb, A., Kjeang, E. & Maine, E. Cost analysis for durable proton exchange membrane in

PEM fuel cells. in *2012 Proceedings of PICMET '12: Technology Management for Emerging Technologies* 2943–2950 (IEEE, 2012).
64. Lazard. *Lazard's levelized cost of energy analysis— version 13.0*. (2019).
65. U.S. Energy Information Administration. *Levelized costs of new generation resources in the annual energy outlook 2022*. (2022).
66. YCharts. US producer price index: Chemicals and allied products: Sulfuric acid. https://ycharts.com/indicators/us_producer_price_index_chemicals_and_allied_products_sulfuric_acid (2022).
67. Duan, Z., Qu, Z., Ren, Q. & Zhang, J. Review of bipolar plate in redox flow batteries: Materials, structures, and manufacturing. *Electrochem. Energy Rev.* **4**, 718–756 (2021).
68. International Organization for Standardization. International Standard ISO 14040 Environmental Management- Life Cycle Assessment- Principle and Framework. (2006).
69. UChicago Argonne LLC. The Greenhouse gases, Regulated Emissions, and Energy use in Techonolgies (GREET) model: GREET 2, Version 2020. (2020).
70. AMG Advanced Meallurgical Group N.V. *Methodology for reduction in GHG emissions from metal production using metal bearing wastes*. www.amg-nv.com (2021).
71. Norgate, T. E. & Wellwood, G. The potential applications for titanium metal powder and their life cycle impacts. *Jom* **58**, 58–63 (2006).
72. UChicago Argonne LLC. The Greenhouse gases, Regulated Emissions, and Energy use in Technologies (GREET) Model: GREET 1, 2019. (2019).
73. Microsoft Corporation. Microsoft Excel. (2022).
74. Lazard. Lazard's Levelized Cost of Storage Analysis- Version 4.0. (2018).

Chapter 4 Structures and Free Energies of Cerium Ions in Acidic Electrolytes

This chapter was adapted from Buchanan, C. A. et al. (2020). "Structures and Free Energies of Cerium Ions in Acidic Electrolytes." *Inorganic Chemistry*, *59*(17), 12552-12563.

4.1 Introduction

The Ce^{3+}/Ce^{4+} redox couple is used in many fields, including organic synthesis,[1] materials chemistry,[2] waste remediation,[3] and energy storage.[4–7] The potential of the Ce^{3+}/Ce^{4+} redox couple is important for its utility as an intermediate for indirect oxidation[8] and for high voltage flow batteries, and is tunable by changing the electrolyte to fit the desired application.[1] The redox potential ranges between 1.44 V vs. SHE in H_2SO_4 and 1.74 V vs. SHE in $HClO_4$ for aqueous systems,[4,9,10] with even lower redox potentials reported with significant uncertainty in HCl,[9,11,12] as shown in **Scheme 4.1**. The solubility of cerium ions also varies with electrolyte. Methanesulfonic acid (MSA) has been explored in research because of its ability to solvate high cerium ion concentrations,[13] which is necessary to increase electrolyte energy density and current areal density for energy storage applications.

The different redox potentials in **Scheme 4.1** arise from the different Gibbs free energies of cerium ions in the electrolytes, as described by the Nernst equation. A less positive redox potential corresponds to Ce^{4+} having lower free energy than Ce^{3+} as compared to other electrolytes. This lower free energy is a result of anion complexation with the cerium ions, or differences in screening of long range electrostatic interactions for Ce^{3+} as compared to Ce^{4+}. Electrostatic interactions include ion pairing such as outer-sphere ion pairs or solvent sharing ions. As expected from known trends in the cerium ion radii[14] and Lewis acid strength,[1] our experimental and

computational findings here show the shift in redox potential is primarily from the differences in anion complexation of Ce^{3+} and Ce^{4+}. The electrostatic effects are hypothesized to be partially responsible for differences in solubility of Ce^{3+} and Ce^{4+} in different acids, in addition to different free energies of the cerium precursor salts used in the different acids. Whether the redox potential shift is caused by anions complexing with Ce^{4+} only or both Ce^{3+} and Ce^{4+} is uncertain because whether Ce^{3+} complexes with anions is unclear in the literature. In this study, we use the term *complex* to refer to the Ce ion and its first coordination sphere (or inner sphere) involving an anion, where anion complexation corresponds to a covalent bond formed between Ce and an anion.[15]

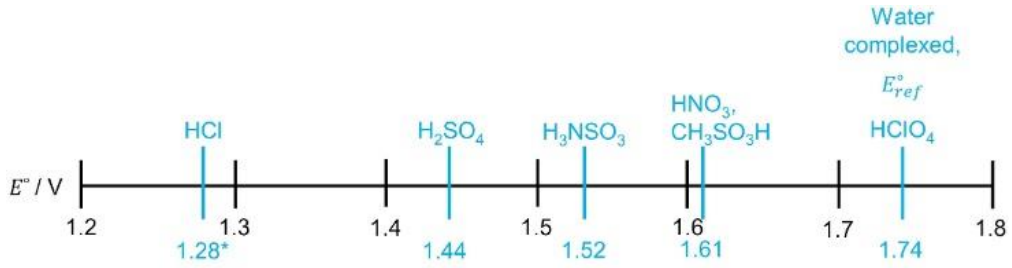

Scheme 4.1. Standard redox potentials (E°) vs. SHE for the Ce^{3+}/Ce^{4+} redox couple in different 1 M acidic aqueous electrolytes. The redox potential of Ce^{3+}/Ce^{4+} without anion complexation (i.e., $[Ce(H_2O)_9]^{3+}/[Ce(H_2O)_9]^{4+}$), E°_{ref}, at 1.74 V vs. SHE is determined in perchloric acid and is used as a reference because of the noncomplexing nature of the perchlorate anion.[16] *The reported redox potential for Ce^{3+}/Ce^{4+} in HCl[9] is included here for completeness, but has a high value of uncertainty due to the interference of the Cl^-/Cl_2 redox couple.[11,12]

We refer to Ce ions with only water in the first coordination sphere as hydrated, to distinguish from anion complexation. We show that Ce^{3+} is hydrated in all studied electrolytes, while Ce^{4+} is complexed by anions, which agrees with previous reports of stronger stabilization of Ce^{4+} through ligand coordination in aqueous solutions than Ce^{3+}.[1,4,17,18] Furthermore, we explain the shift in redox potential in **Scheme 4.1** semi-quantitatively using ab initio calculations.

Knowledge of the structures and free energies of cerium ions in acidic electrolytes would clarify trends in solubility, redox potentials and redox kinetics,[1,8,19] as well as enable better control over the Ce^{3+}/Ce^{4+} redox potential for target applications. For example, understanding whether the Ce^{3+}/Ce^{4+} redox reaction involves a change in the inner sphere is important for discerning the

charge transfer mechanism and kinetics. Therefore, herein we calculate the structures and free energies of the Ce^{3+} and Ce^{4+} ions in seven different acidic electrolytes, namely, HCl, H_2SO_4, H_3NSO_3, CH_3SO_3H, HNO_3, CF_3SO_3H, and $HClO_4$. We also use spectroscopy to probe the structure experimentally in five of the acids (HCl, H_2SO_4, CH_3SO_3H, HNO_3, and CF_3SO_3H). These acids were selected because they span a range of redox potentials and are commonly used. Besides clarifying the redox potential shift, this work provides benchmarks of predicted free energies of cerium-anion complexes from quantum mechanical calculations.

The Ce^{3+} and Ce^{4+} structures have been studied in H_2O, CF_3SO_3H, $HClO_4$, HCl, H_2SO_4, and HNO_3, but information on Ce^{3+} anion complexation is inconsistent, and free energies of complexation for either Ce^{3+} or Ce^{4+} are rarely reported. In pure water, Ce^{3+} and Ce^{4+} are hydrated by nine water molecules as $[Ce(H_2O)_9]^{3+/4+}$.[20–22] $[Ce(H_2O)_9]^{3+}$ is the dominant species in trifluoromethanesulfonic acid (also known as triflic acid or TFSA),[23] and low concentrations of hydrochloric acid[24,25] and perchloric acid.[26] Outer-sphere ion pairs (i.e., solvent sharing ion pairs[15]) are reported to occur at concentrations greater than 1.5 M in perchloric acid,[26] with contact ion pairs (i.e., long range, non-directional electrostatic forces[15]) occurring at concentrations higher than 3.1 M $HClO_4$. Evidence of Ce^{3+} complexation with anions has been reported for nitrate,[27,28] sulfate,[29,30] and systems with high concentrations of chloride (14 M),[25] but its structure in MSA has not been studied. The structure of the Ce^{4+} complex is unknown in MSA and TFSA, but Ce^{4+} is expected to complex with anions in all acids studied here[31–37] except perchloric acid,[38] where evidence of dimerization has been reported.[39–42] The structures of Ce^{3+} and Ce^{4+} are rarely studied in more than one electrolyte per study. Additionally, the methods and conditions at which the cerium ions are studied are varied, which limits the ability to compare structures across acids and

extract trends in free energy. Previous structural studies of Ce^{3+} and Ce^{4+} in acidic electrolytes are summarized in **Section 1.4.2** of the **Introduction**.

The inconsistencies and heterogeneity of the Ce^{3+}-anion complexation literature motivate this study to characterize Ce^{3+} and Ce^{4+} complexation using the same methods across multiple acidic electrolytes. We show that the dominant Ce^{3+} structure is with water only in all electrolytes, whereas Ce^{4+} complexes with anions in all electrolytes except perchloric acid. We obtain electronic information of the Ce^{3+} ion from X-ray Absorption Near Edge Spectroscopy (XANES) and UV-Vis, and structural information from Extended X-ray Absorption Fine Structure (EXAFS) in electrolytes that span a range of Ce^{3+}/Ce^{4+} redox potentials (**Scheme 4.1**), including HCl, H_2SO_4, MSA, and HNO_3. We also include TFSA as a standard, due to recent reports of its structure via EXAFS,[23] despite not having a measured redox potential. UV-Vis of Ce^{4+} in three of the acids (HCl, H_2SO_4, MSA) is used to provide evidence of Ce^{4+} complexation. From EXAFS, we find both Ce^{3+} and Ce^{4+} are coordinated by nine waters or anions.

We compute free energies using Density Functional Theory (DFT) of both Ce^{3+} and Ce^{4+} ions in the seven considered acidic electrolytes. These DFT calculations predict the most stable structures of Ce^{3+} and Ce^{4+} in each electrolyte are tricapped trigonal pyramid $[Ce(H_2O)_9]^{3+}$ and $[Ce(H_2O)_x(anion)_y^{\alpha-}]^{4-y\alpha}$, respectively. This finding from DFT is consistent with the experimentally determined coordination numbers and bond lengths. Therefore the large shift in redox potential manifests from the anion-stabilization of the Ce^{4+} ion, not the Ce^{3+} ion. This observation allows us to extract free energies of complexation for the Ce^{4+} ion in the electrolytes from experimentally reported redox potentials, which agree with DFT-predicted free energies of Ce^{4+} complexes. The structures, coordination numbers, and the Ce-water distances from DFT are consistent with our EXAFS measurements. We also determine the structures of Ce^{3+} and Ce^{4+} in

MSA, which have not been previously reported. Our free energy calculations also lend insight to the existing Ce^{3+} and Ce^{4+} solubility trends, indicating that complexation is not responsible for the high solubility of Ce^{3+} or Ce^{4+} in MSA.[13] Ultimately, these findings clarify the solvation structures and free energies of Ce^{3+} and Ce^{4+} in acidic electrolytes, which have implications for electrolyte and electrocatalyst design for energy storage, organic synthesis, and waste remediation.

4.2 Experimental and computational methods

4.2.1 Experimental methods

Preparation of electrolyte solutions. Electrolytes prepared included H_2SO_4 (Aldrich Chemistry, 99.999% purity), MSA (Sigma-Aldrich, ≥ 99.0% purity), TFSA (Acros Organics, 99% extra pure), HCl (Sigma-Aldrich, 37%), and HNO_3 (Fisher Chemical, 67–70%), ranging in concentration from 0.001 M to 2 M. All acids were prepared by diluting the commercially available acid with water purified through the MilliporeSigma™ Synergy™ UltrapureWater Purification System (18.2 MΩ cm resistivity). To prepare Ce^{3+} acidic solutions, a cerium(III) carbonate hydrate salt ($Ce_2(CO_3)_3$, Aldrich Chemistry, 99.9% trace metals basis) was added to the acid at room temperature while stirring for no more than 1 hour. Cerium(III) carbonate was used as the primary cerium precursor because of its common use as a precursor for cerium flow batteries.[43] It should be noted, however, that lanthanides complex with carbonate,[44] so if carbonate remains in solution, cerium could be complexed by carbonate instead of either being hydrated by water or complexed by anions. During the addition of cerium(III) carbonate to acidic media, carbon dioxide is vented away and does not remain in solution, according to the balanced series of chemical reactions below (**R1-R5**). The reaction series **R1-R5** is written for the dissolution of cerium(III) carbonate into HCl, but it would hold similarly for the other acids studied experimentally here (HNO_3, H_2SO_4, MSA, TFSA). Based on the large equilibrium constants for the series of reactions (**R2-R5**) to

convert CO_3^{2-} to $CO_{2(aq)}$,[45] it is assumed that most of the CO_3^{2-} is converted to $CO_{2(aq)}$. Using Henry's law, the vapor pressure of CO_2 for a starting concentration of 1.5 mM $Ce_2(CO_3)_3$ is 0.13 atm, which is high enough such that sparging with nitrogen at a rate of 10 mL/min is sufficient to remove any $CO_{2(aq)}$ from solution within 20 minutes.

$$Ce_2(CO_3)_3 + 6HCl \rightleftharpoons 2Ce^{3+} + 3CO_3^{2-} + 6H^+ + 6Cl^- \quad \textbf{(R1)}$$

$$CO_3^{2-} + H^+ \rightleftharpoons HCO_3^- \quad \textbf{(R2)}$$

$$HCO_3^- + H^+ \rightleftharpoons H_2CO_3 \quad \textbf{(R3)}$$

$$H_2CO_3 \rightleftharpoons CO_{2\,(aq)} + H_2O_{(l)} \quad \textbf{(R4)}$$

$$CO_{2\,(aq)} \rightleftharpoons CO_{2\,(g)} \quad \textbf{(R5)}$$

While lanthanides have been reported to complex with carbonate,[44] this study was conducted in basic media, in which reactions **R2-R5** would be less likely to occur due to the lack of protons, meaning carbonate would remain in solution and be available for complexation. Additionally, we have monitored the redox potential while adding the cerium(III) carbonate salt to sulfuric acid and have observed that the redox potential stays at approximately 1.2 V vs. SHE throughout the addition. If Ce^{3+} were being complexed by carbonate, we would expect the redox potential to drop to approximately 0.45 V vs. SHE.[1] The matching UV-Vis spectra of Ce^{3+} in TFSA and H_2SO_4 prepared from different non-carbonate precursors to the spectra from the carbonate precursor, also indicates no carbonate remained in the solutions studied here (see **Appendix A**).

To prepare Ce^{4+} in H_2SO_4 solutions, a cerium(IV) sulfate salt ($Ce(SO_4)_2$, Acros Organics, 99%) was added to H_2SO_4 and stirred for 24 hours to ensure complete dissolution. In MSA and HCl, a cerium(III) carbonate salt was added to the acid and then electrochemically oxidized using a two compartment electrochemical cell with a Nafion® N117 (Fuel Cell Store) proton conducting membrane until the Ce^{3+} ions were fully converted to Ce^{4+}. Anodes for solution preparation were

either a 5.0 cm height by 0.615 cm in diameter graphite rod (Alfa Aesar™, 99.9995% metals basis) fed through a 6.35 cm thick carbon felt (Alfa Aesar™, 99.0%), or a mesh titanium-based anode supplied by De Nora, coating type DN-240. The counter electrode was a coiled 0.127 mm diameter Pt wire (Alfa Aesar™, 99.9% metals basis), and the reference electrode was a double junction Ag/AgCl electrode (saturated KCl, Pine Research).

Determining the State of Charge. State of charge (SoC) refers to the amount of Ce^{4+} ions present in solution relative to the total cerium ion concentration, with 100% SoC indicating a solution comprised entirely of Ce^{4+}. To determine SoC of a solution, UV-Vis was used to verify that the spectrum did not change with additional oxidation, and confirmed using titration with ammonium iron(II) sulfate. For more details on titration, see **Chapter 2**.

UV-Vis spectroscopy. The Evolution™ 300, Thermo Scientific double-slit UV-Vis Spectrophotometer was used to collect absorption spectra as a function of wavelength from 190 to 1100 nm at a scan rate of 600 nm/min. The absorbance values were automatically corrected against a baseline sample, which consisted of the supporting electrolyte solution without cerium. A quartz cuvette with a pathlength of either 10 mm or 1 mm (for high Ce concentrations) was used to hold the samples during measurements. UV-Vis spectroscopy is described in more detail in **Chapter 2**.

X-ray absorption fine structure (XAFS) spectroscopy of solid CeO_2 and aqueous Ce^{3+} and Ce^{4+}. To extract electronic and structural information on Ce^{3+} in HCl, H_2SO_4, HNO_3, MSA, and TFSA and Ce^{4+} in H_2SO_4, both X-ray absorption near edge spectroscopy (XANES) and extended X-ray absorption fine structure (EXAFS) were collected at the sector 20 BM beamline at the Advanced Photon Source in Argonne National Laboratory. A polyacrylate electrochemical flow cell that was previously designed[46] for use in the beamline was used to pump aqueous solutions continuously during data collection. To maintain the oxidation state of Ce^{4+} in H_2SO_4, a potential

of 1.57 V vs. RHE was applied to the working electrode of the flow cell. Deaerated and degassed electrolyte was flowed past a carbon felt working electrode separated from the carbon felt counter electrode by a Nafion membrane through the electrochemical cell at 0.5 mL min^{-1} using a syringe pump. XAFS measurements were performed at the Ce L_3 X-ray absorption edge. A Si(111) double-crystal monochromator was used to monochromatize the incidental beam. Harmonic contamination was suppressed using a Rh coated harmonic mirror set to a cut off energy of 5.8 keV and by detuning the incident beam intensity to 85% of its maximum value. An appropriate combination of helium and nitrogen gases was used to measure the incident beam intensity. Energy reproducibility was verified by measuring the XANES of a vanadium foil several times throughout the data collection process. The vanadium foil was used because a Ce foil was unavailable, and the vanadium K-edge energy (5465 eV) is close to the L_3-edge energy of Ce (5723 eV). Data collection was performed in fluorescence mode, using a 13-element germanium fluorescence detector. Five scans were collected for each solution-based Ce ion sample, and then the cell was flushed with the next Ce ion sample for 20 minutes at a flow rate of 0.5 mL min^{-1} before scans for the next solution sample were collected. XAFS spectra of CeO_2 were also collected to serve as a standard. A pellet was made by mixing 20 mg CeO_2 (Alfa Aesar™, 99.99%) and 132 mg boron nitride (Sigma Aldrich) then adding into a die and forming a pellet using a pellet press with a pressure of 15,000 psi. The pellet was then measured using fluorescence, because a stable pellet could not be made thin enough to conduct a transmission measurement.

XAFS data normalization. Background subtraction and calibration of the XAFS data collected for the CeO_2 solid pellet and aqueous Ce^{3+} and Ce^{4+} samples was conducted in the software ATHENA.[47] The threshold energy (E_0) was set to 5724.5 eV for Ce^{3+}, based on the inflection point in the absorption energy spectrum, which agrees with the theoretical value of the

Ce^{3+} L_3-edge energy.[48–52] For Ce^{4+} and CeO_2, E_0 was set to 5729 eV which aligns with previous reports[53] of the difference between aqueous Ce^{3+} and Ce^{4+} edge energies. The pre-edge range for both the aqueous Ce^{3+} and Ce^{4+} samples and the solid CeO_2 sample were all set to be -150 eV to -50 eV. The normalized range was 27 eV to 400 eV for Ce^{3+}, 37 eV to 400 eV for Ce^{4+}, and 150 eV to 400 eV for CeO_2, while the spline k ranges for all samples were set to be 0 to 10.2 $Å^{-1}$. Due to self-absorption, the white line intensity of the CeO_2 sample was very low, and so the CeO_2 sample was corrected for self-absorption in ATHENA. After this correction, the absorption intensity was comparable to the intensity values of the Ce^{4+} solution-based sample as well as previous CeO_2 L_3-edge XAFS.[54] Only the corrected spectra for CeO_2 are shown here. No other samples were corrected for self-absorption. The R_{bkg} parameter for all Fourier transformed EXAFS data were set to 1.2 Å. All plotted EXAFS data have unadjusted R space values.

Double-electron excitation correction. Solution-based lanthanides are known to exhibit anomalies in the EXAFS spectra (typically between 5−6 $Å^{-1}$ of k range) that have been attributed to multi-electron excitation (MEE).[55,56] There are multiple methods that have been proposed to remove multi-electron excitation (MEE) effects,[57,58] including using a damped sine wave to isolate the EXAFS signal of a single excitation,[59] or using arctangent and Lorentzian functions to represent peaks associated with the single and double excitations, and then subtracting the functions associated with MEE effect from the raw data.[55–57] In this work to determine the effect of a MEE correction, we used the option in ATHENA to use an arctangent function and specify a broadening term (similar to using a Lorentzian function), as well as set an "energy shift" and a "scale by" parameter. "Energy shift" specifies the edge energy at which the MEE effect starts to occur relative to the absorption edge energy and "scale by" is the amplitude of the correction as a fraction of the edge step. For the Ce^{3+} solution EXAFS MEE correction, the energy shift was set

to 122 eV, scale by was set to 0.015, and broadening was set to 2 eV, based on previous reports for corrections and because these values resulted in the most clear removal of MEE features. However, for both Ce^{3+} and Ce^{4+} solutions in this study, we chose not to include a MEE correction in the presented data because this correction did not affect the coordination numbers for Ce^{3+} and distances of the first coordination sphere for both Ce^{3+} and Ce^{4+}. Instead, the MEE correction method introduced inaccuracies in the spectra and more uncertainty in the fitting results. See **Appendix A** for comparisons of fitting Ce^{3+} in MSA with and without MEE correction.

Extended X-ray absorption fine structure (EXAFS) fitting. The EXAFS data of the normalized aqueous Ce^{3+} and Ce^{4+} samples were fit using the software program ARTEMIS[47] with paths generated from DFT-predicted structures using FEFF9 with self-consistency in JFEFF.[60] For Ce^{3+}, the R range of the fit was 1.4 Å to 3.0 Å, the k range was 1.5 $Å^{-1}$ to 9.7 $Å^{-1}$, and the data were k^2 weighted, because k^2 weighting places emphasis on the scattering of lighter atoms, such as oxygen, and it avoids overemphasis of higher energy k data, where the L_2 edge will start to interfere with the L_3 edge k data. The Ce^{3+} EXAFS data in all acids were fit using one Ce-O shell from water scattering, although additional water and anion scattering shells were considered, as discussed in **Section 4.3.1**. Three parameters were obtained by fitting: coordination number (CN), the change in the path distance from the FEFF9-predicted path length (ΔR), and the Debye-Waller factor (σ^2). The amplitude reduction factor (S_0^2, 0.970) and shift in threshold energy (ΔE_0, 0.954 eV) were obtained by fitting the Ce^{3+} EXAFS data in TFSA, and then these values were set as fixed global parameters for the fits of Ce^{3+} in the four other acids.

To fit the EXAFS data of Ce^{4+} in H_2SO_4, the standard CeO_2 EXAFS data were first fit in ARTEMIS using paths generated in JFEFF with FEFF9 from the known structure[61–67] to obtain appropriate values of S_0^2 and ΔE_0. Three shells were included in the fit of CeO_2: two Ce-O shells

and one Ce-Ce shell. The R range of the CeO_2 fit was 1.5 Å to 4.6 Å, while the k range was 3.0 $Å^{-1}$ to 9.7 $Å^{-1}$, and the data were k^3 weighted because higher k data is affected less by the choice of the E_0 value, which is less certain for Ce^{4+} samples.[38,68] The CN of each shell was set to the expected value,[54] and S_0^2 and ΔE_0 were found to be 0.687 and 2.918 eV, respectively. These values were then set as fixed global parameters for the fit of the EXAFS data of Ce^{4+} in H_2SO_4. Because we were primarily interested in finding the Ce-O distance of Ce^{4+} as compared to Ce^{3+}, the final fit of the k^3 weighted Ce^{4+} data included only a Ce-O shell, generated from the DFT-predicted structure for Ce^{4+} with a bisulfate anion attached. The R range of the fit was 1.4 Å to 2.2 Å, with a k range of 3.0 $Å^{-1}$ to 9.7 $Å^{-1}$. The CN, ΔR, and σ^2 of the Ce-O shell were obtained by fitting.

4.2.2 Computational methods

Density functional theory (DFT) modeling of ligand exchange reactions. The NWChem software package[69] was used to perform all the DFT calculations. The B3LYP-D3 hybrid functional was employed for modeling the structures and ligand exchange reaction energies of Ce^{3+} and Ce^{4+} complexes in solution.[70,71] There were no symmetry constraints included during geometry optimization of cerium complexes, and the energy convergence cut-off was set to 5×10^{-5} Hartree. The mixed basis set that was used comprised of the Stuttgart RSC ECP for the cerium ion[72] and the 6-31+g* split-valence basis set for all other atoms.[73,74] The spin states of the Ce^{3+} and Ce^{4+} complexes were 2 and 1, respectively. The Conductor-like Screening Model (COSMO) solvation model was used to implicitly compute the solvation free energy of all reactants and products during geometry optimization, with the dielectric constant of 78.4 for water used and all other settings set to default.[75,76]

The Gibbs free energy of complexation ($\Delta G_{complex}$) in the aqueous phase was computed as

$$\Delta G_{complex}(T) = \sum_{products}^{i} v_i \, G_i - \sum_{reactants}^{j} v_j \, G_j \quad \textbf{(4.1)}$$

where G_i is the aqueous-phase Gibbs free energy of species *i* at temperature *T* and v_i is the corresponding stoichiometric coefficient of species *i* for the reaction. Entropic and enthalpic contributions were evaluated at 298.15 K. The free energy for each species in the aqueous phase was approximated as[77,78]

$$G_i = E_{i,gas} + \Delta G_{i,solv} + \Delta H_{i,gas} - T(S_{i,liq}) \quad \textbf{(4.2)}$$

where $E_{i,gas}$ is the DFT-computed electronic energy of species *i* in the gas phase, $G_{i,solv}$ is the solvation free energy of species *i* via COSMO, $\Delta H_{i,gas}$ is the ideal gas thermal correction to enthalpy of species *i* (including zero-point, translational, rotational, and harmonic vibrational enthalpy contributions), and $S_{i,liq}$ is the liquid phase entropy of species *i*. The Wertz correction was used to correct the ideal gas phase entropy ($S_{i,gas}$) of each species for solvation induced structural ordering in the aqueous electrolyte to obtain $S_{i,liq}$ (i.e., $S_{i,liq} = 0.54 S_{i,gas} + 0.006578$ kJ mol^{-1} at 1 M).[79] Free energy calculations assumed a concentration of 1 M for all species except H_2O, which was 55 M.

When modeling the free energy of water complexation with cerium to form $[Ce(H_2O)_x]^{3+}$ or $[Ce(H_2O)_x]^{4+}$ in pure water

$$Ce^{3+}_{(aq)} + x\, H_2O_{(l)} \rightleftarrows [Ce(H_2O)_x]^{3+}_{(aq)} \quad \textbf{(4.3)}$$

$$Ce^{4+}_{(aq)} + x\, H_2O_{(l)} \rightleftarrows [Ce(H_2O)_x]^{4+}_{(aq)} \quad \textbf{(4.4)}$$

we use a single water molecule in COSMO implicit solvent to calculate G_{H_2O}. However, when computing the free energy of Ce-anion (i.e., ClO_4^-, NO_3^-, $CH_3O_3S^-$, $CF_3SO_3^-$, $H_2NO_3S^-$, SO_4^{2-}, HSO_4^-, or Cl^-) ligand exchange reactions for Ce^{3+} and Ce^{4+}:

$$[Ce(H_2O)_9]^{3+}{}_{(aq)} + [anion]^{\alpha-}{}_{(aq)} \rightleftharpoons [Ce(H_2O)_8(anion)]^{3-\alpha}{}_{(aq)} + H_2O_{(l)} \quad \textbf{(4.5)}$$

$$[Ce(H_2O)_9]^{4+}{}_{(aq)} + [anion]^{\alpha-}{}_{(aq)} \rightleftharpoons [Ce(H_2O)_8(anion)]^{4-\alpha}{}_{(aq)} + H_2O_{(l)} \quad \textbf{(4.6)}$$

we use another procedure. Specifically, we solvate the anions with 12 explicit water molecules in addition to implicit COSMO solvation to improve the accuracy for modeling anions in solution.[80,81] Ligand exchange reactions without explicit water solvation of the anion greatly overpredict complexation strength with cerium ions (see **Appendix B**). The free energy of an anion was computed as

$$G_{[anion]^{\alpha-}} = G_{[anion(H_2O)_{12}]^{\alpha-}} - G_{(H_2O)_{12}} \quad \textbf{(4.7)}$$

and in **Eq. 4.5**, **4.6**, $\boldsymbol{G_{H_2O}}$ is approximated as $\frac{\mathbf{1}}{\mathbf{12}}\boldsymbol{G_{(H_2O)_{12}}}$. The initial geometries for the $[anion(H_2O)_{12}]^{\alpha-}$ species were generated by placing 12 explicit water molecules around each anion. The initial 12 explicit water structure was the same starting configuration for all anions. The $[anion(H_2O)_{12}]^{\alpha-}$ structure was first equilibrated for 1 ps then sampled for 10 ps with a 0.12 fs time step using Car Parrinello Molecular Dynamics in the NVT ensemble at 298.15 K with the Berendsen thermostat.[82] Next, DFT-based geometry optimization of multiple selected $[anion(H_2O)_{12}]^{\alpha-}$ structures from the 10 ps simulation were performed and the lowest energy structure identified was chosen. The geometry of $(H_2O)_{12}$ was created by removing the anion from the lowest-energy optimized $[anion(H_2O)_{12}]^{\alpha-}$ structure (i.e., a different $(H_2O)_{12}$ for each anion

was used) and a single point calculation of $(H_2O)_{12}$ was done to compute $\boldsymbol{G_{(H_2O)_{12}}}$ (all vibrational frequencies were confirmed to be positive). The cerium-anion complexes were not explicitly solvated by the 12 additional water molecules and were only modelled with implicit COSMO solvation. All computational data has been uploaded to the Novel Materials Discovery (NOMAD) Repository and is accessible via https://dx.doi.org/10.17172/NOMAD/2020.05.22-1.

4.3 Results and discussion

4.3.1 Determining the structure and free energies of Ce^{3+} in aqueous acidic electrolytes

In this section, we use XANES, UV-Vis, EXAFS, and DFT calculations to gain information about the structure of Ce^{3+} in aqueous solutions. We find that the dominant Ce^{3+} structure is Ce^{3+} only hydrated by water as $[Ce(H_2O)_9]^{3+}$, based on the similar EXAFS data and fitting results in all electrolytes. Our XANES and UV-Vis measurements support these EXAFS findings of Ce^{3+} because there is no significant shift in energy of the absorption peaks as the acid is changed, whereas anion complexation in the first coordination shell causes the L_3-edge white line of other lanthanides in XANES to shift by 1 eV,[83] and the UV-Vis absorption spectra of Ce^{3+} glasses to shift ~20 nm.[84–87] DFT-predicted free energies from models of Ce^{3+} in pure water and acidic solutions corroborate that Ce^{3+} preferentially coordinates only with nine water molecules. The first coordination shell of aqueous Ce^{3+} is the same in TFSA, HCl, and MSA based on the similar Ce L_3-edge EXAFS peaks and intensities, as shown in **Figure 4.1a**. The EXAFS data in k space for Ce^{3+} in all five acids is in **Appendix A**, to give information on the data's signal to noise ratio. The similar local structure in these three acids implies the dominant Ce^{3+} structure has only water in its first coordination shell. The structural evidence from EXAFS of hydrated Ce^{3+} is supported by the lack of peak shifts in XANES (**Figure 4.2**) and UV-Vis (absorption peak at 255

nm in **Figure 4.3a**) in these acids, showing an absence of anion complexation that would otherwise influence the electronic properties of Ce^{3+}.[83–87]

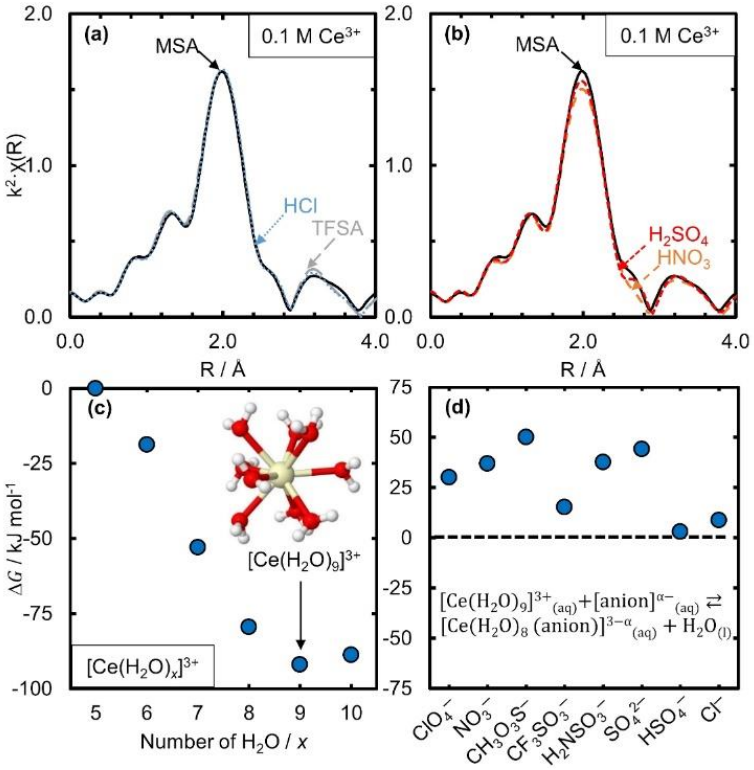

Figure 4.1. The magnitude component of $k^2 \cdot \chi(R)$ Fourier transformed EXAFS spectra of the L_3-edge of Ce for **(a)** 0.1 M Ce^{3+} in TFSA (0.05 M $Ce_2(CO_3)_3$ + 2 M TFSA), HCl (0.05 M $Ce_2(CO_3)_3$ + 2 M HCl), and MSA (0.05 M $Ce_2(CO_3)_3$ + 2 M MSA) and **(b)** 0.1 M Ce^{3+} in H_2SO_4 (0.05 M $Ce_2(CO_3)_3$ + 2 M H_2SO_4), HNO_3 (0.05 M $Ce_2(CO_3)_3$ + 2 M HNO_3), and Ce^{3+} in MSA. Plots of the k^2 weighted EXAFS data in the k space for Ce^{3+} in all five experimentally considered acids are included in **Appendix A**. **(c)** DFT-predicted Gibbs free energy of $[Ce(H_2O)_x]^{3+}$ structures containing different numbers of water molecules (x) in their first-coordination shell (x = 5−10) in pure water. Inset: structure of Ce^{3+} surrounded by nine water molecules in a tricapped trigonal prismatic geometry. Atom color legend: oxygen = red; cerium = beige; hydrogen = white. **(d)** Predicted change in Gibbs free energy of $[Ce(H_2O)_9]^{3+}$ due to anion complexation in seven different acids. For sulfuric acid, two anions are considered (HSO_4^- and SO_4^{2-}). Each species was set to have a concentration of 1 M, except water was set to 55 M. Positive values correspond to unfavorable complexation at standard conditions.

The normalized XANES spectra of the aqueous cerium solutions in **Figure 4.2** all exhibit the same white line centered at 5726 eV, albeit with slightly different intensities. The single-peaked white line situated immediately above the absorption threshold is characteristic of Ce^{3+} XANES, and is associated with the $2p^6 4f^1(5d,6s)^3 \rightarrow 2p^5 4f^1(5d,6s)^4$ electron transition,[88] whereas Ce^{4+} solutions are known to exhibit two peaks in XANES, which are associated with the mixing of two electronic configurations that are possible for Ce^{4+}: $4f^0$ and $4f^1\underline{L}$, where $\underline{L}$ indicates a ligand

hole.[38,68] Thus, the oxidation state of all cerium ions in the 0.1 M Ce solutions tested was Ce^{3+}, as two peaks are not present for any of the solutions. Differences in white line intensities could be attributed to differences in the local environment or covalency, but it is possible that self-absorption, or the attenuation of the fluorescence signal as the depth that the incident beam can penetrate changes,[89] could also be contributing to the intensity difference observed in **Figure 4.2**.

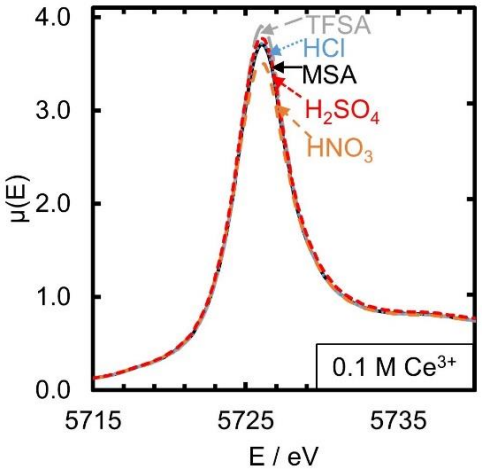

Figure 4.2. XANES of the Ce L_3-edge of Ce^{3+} (0.05 M $Ce_2(CO_3)_3$) in 2 M TFSA, 2 M HCl, 2 M MSA, 2 M H_2SO_4, and 2 M HNO_3.

The UV-Vis peak locations of Ce^{3+} in 2 M MSA, 0.5 M HCl, and 2 M TFSA all nearly overlap (**Figure 4.3a**), implying that the dominant species is the same in these three electrolytes. Ce^{3+} exhibits narrow UV-Vis absorbance peaks in acids[90–92] and glasses,[84,86] which can shift on the order of 20 nm[84] depending on the first-coordination sphere of the cerium ion[86] because of changing covalency between the metal ion and the ligands.[85,87] UV-Vis shows that the dominant structure contains only water in the first-coordination sphere (i.e., $[Ce(H_2O)_9]^{3+}$). The amplitude of the peaks located at 202 nm and 212 nm are affected by oxidation state and nitrogen sparging (**Appendix A**), so we do not attribute these small differences between the acids to anion complexation. Thus, we can confirm our findings from DFT and EXAFS that $[Ce(H_2O)_9]^{3+}$ is the dominant Ce^{3+} structure in MSA, HCl, and TFSA.

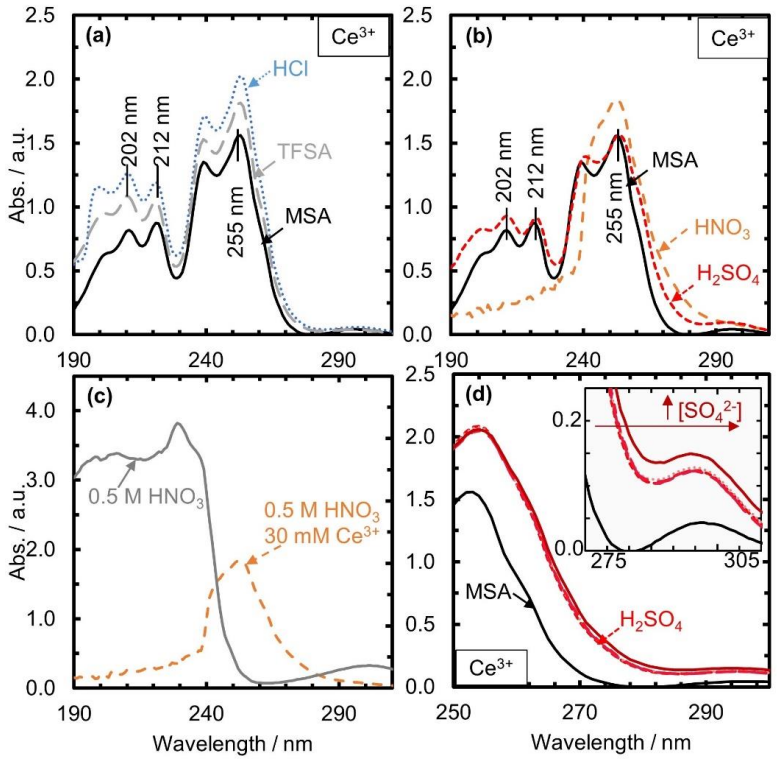

Figure 4.3. UV-Vis absorbance as a function of wavelength at room temperature (T = 23 ± 1 °C) of **(a)** Ce^{3+} spectra for MSA (3 mM Ce^{3+} + 2 M MSA) and TFSA (3 mM Ce^{3+} + 2 M TFSA) using both a 10 mm cuvette, and HCl (30 mM Ce^{3+} + 0.5 M HCl) using a 1 mm cuvette—the higher concentration of 30 mM Ce^{3+} was used to increase the signal to noise in 0.5 M HCl because the chloride ion absorbs strongly at the low wavelength regions of light; **(b)** Ce^{3+} spectra for MSA and H_2SO_4 (3 mM Ce^{3+} + 2 M H_2SO_4) using a 10 mm cuvette, and HNO_3 (30 mM Ce^{3+} + 0.5 M HNO_3) using a 1 mm cuvette; **(c)** Ce^{3+} in HNO_3 spectrum (30 mM Ce^{3+} + 0.5 M HNO_3) as well as 0.5 M HNO_3 spectrum both using a 1 mm cuvette; and **(d)** Ce^{3+} spectrum for MSA (3 mM Ce^{3+} + 2 M MSA) as well as Ce^{3+} spectra for H_2SO_4 (3 mM Ce^{3+} + 2 M H_2SO_4) with increasing sulfate concentration (0 to 0.4 M Na_2SO_4) in wavelength region of 250 to 310 nm, using a 10 mm cuvette. Inset in (d) shows magnified portion between 280 and 310 nm. All spectra were obtained by adding $Ce_2(CO_3)_3$ to acid and venting CO_2 out of the electrolyte.

In apparent contrast to Ce^{3+} in TFSA, HCl and MSA, the EXAFS spectra in **Figure 4.1b** of Ce^{3+} in H_2SO_4 and HNO_3 display differences between 2.4 Å and 3.0 Å (unadjusted). Additionally, the UV-Vis of Ce^{3+} in H_2SO_4 and HNO_3 (**Figure 4.3b**) exhibit slight differences. The higher Ce^{3+} concentration of 30 mM was used in HNO_3 because of the strong absorbance of nitrate (**Figure 4.3c**), which blocks any meaningful information for Ce^{3+} in nitric acid below 240 nm. The peak locations are the same for H_2SO_4 and HNO_3 in **Figure 4.3b** as they were for the other acids studied, suggesting that the dominant structure is still $[Ce(H_2O)_9]^{3+}$. However, H_2SO_4 and HNO_3 have wider shoulders to the right of the peak at 255 nm compared to MSA, which could

be attributed to a small fraction of the Ce^{3+} species being complexed by anions. **Figure 4.3d** supports this assignment for H_2SO_4 because the widening of the 255 nm peak increases with increasing sulfuric acid concentration. Although this evidence of minor anion complexation occurring in H_2SO_4 and HNO_3 from UV-Vis is consistent with some prior UV-Vis[30] and Raman spectroscopy[27] studies, our DFT calculations and EXAFS fits do not support the assignment of sulfate or nitrate complexation of Ce^{3+}. Additionally, the XANES are not shifted (**Figure 4.2**). Although these slight differences in the EXAFS and UV-Vis may suggest structural differences of Ce^{3+} in H_2SO_4 and HNO_3 compared to the other acids, DFT calculations and EXAFS fitting, discussed next, indicate they are not due to anion complexation.

The DFT-predicted free energies for Ce^{3+} structures in pure water shown in **Figure 4.1c** indicate the most stable species is hydrated by nine water molecules. The free energies were computed for $[Ce(H_2O)_x]^{3+}$, with x varied from 5 to 10 (all structures included in **Appendix B**). The lowest energy structure, $[Ce(H_2O)_9]^{3+}$, has a tricapped trigonal prismatic geometry as shown in **Figure 4.1c**. This structure in pure water agrees with previous quantum mechanical predictions,[20,21] previous EXAFS studies of 0.2 M Ce^{3+} in 0.1 M TFSA,[23,93] and the EXAFS we report here (see below for fitting to determine coordination numbers). The average bond distances for Ce^{3+}-O from our DFT calculations match within 0.04 Å of those reported from experimental EXAFS.[21]

For the five acids we experimentally study and H_3NSO_3 and $HClO_4$, we calculate via DFT the free energy of anion-complexation of $[Ce(H_2O)_9]^{3+}$ at standard conditions to be endergonic as shown in **Figure 4.1d**. Further information on the computed Ce^{3+}-anion structures and bond lengths is given in **Appendix B**. Two methods of computing the free energy of Ce^{3+}-anion ligand exchange were used: implicit COSMO (COnductor-like Screening MOdel) solvation[75] with and

without explicit solvation using 12 water molecules. As discussed in **Section 4.2.2**, the implicit water solvent only calculations for Ce^{4+} led to large errors when compared to experiment, so we report only the explicit+implicit water values in the main text for both Ce^{3+} and Ce^{4+}. Even for the three most strongly complexing anions (i.e., bisulfate, sulfate, and chloride), complexing with two anions is less favorable compared with one anion at 1 M (**Figure 4.4a**). A prior EXAFS study found that the 1.8 chloride ions are bound to the Ce^{3+} in 14 M LiCl,[25] but we do not predict via DFT that two chloride ions prefer to complex to Ce^{3+} at 1 M Cl^- nor is it observed in our experimental EXAFS spectra at 2 M Cl^-.

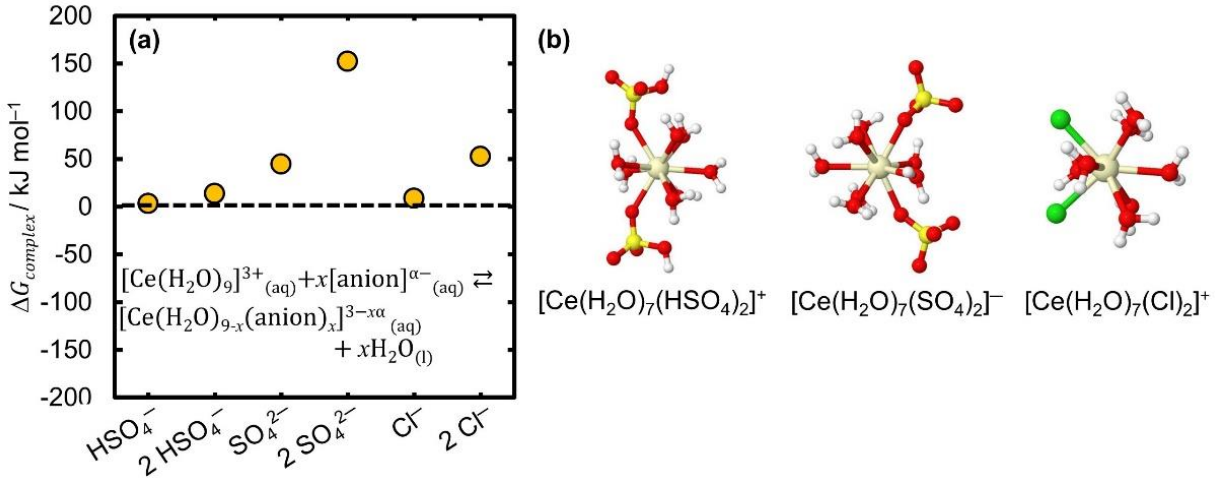

Figure 4.4. (a) DFT-predicted $\Delta G_{complex}$ of Ce^{3+} to form $[Ce(H_2O)_{9-x}(anion)_x]^{3-x\alpha}$ with x = 1 or 2. **(b)** DFT-predicted structures for $[Ce(H_2O)_7(anion)_2]^{3-2\alpha}$, where α is the charge of the anion.

Our DFT prediction that $[Ce(H_2O)_9]^{3+}$ is the dominant (lowest energy) species in the different acids is consistent with the majority of previous reports, and consistent with our experimental results here. $[Ce(H_2O)_9]^{3+}$ is shown to be the dominant species by prior EXAFS measurements in TFSA[23] and low concentrations of HCl (0.2 M).[25] $[Ce(H_2O)_9]^{3+}$ is also the dominant species in TFSA, MSA, and HCl based on our XANES (**Figure 4.2**), UV-Vis (**Figure 4.3a**) and EXAFS (**Figure 4.1a**). Although Ce^{3+}-Cl complexation has been reported to occur in solutions with high Cl^- activity such as 14 M LiCl,[25] this is because of the large activity coefficient

for concentrated LiCl (e.g., activity of 12 M LiCl is 620)[25]. If we adjust our DFT calculated free energies to represent a concentration of 12 M LiCl instead of 1 M Cl^-, the free energy of complexation of Ce^{3+} with Cl^- would shift from an unfavorable 8.5 kJ mol^{-1} to a favorable free energy of −7.6 kJ mol^{-1}, in agreement with the previous work showing Ce^{3+} does not complex with Cl^- in 0.2 M HCl, but it does complex with Cl^- in 14 M LiCl.[25] For sulfuric acid and nitric acid, where there are uncertainties in the structure from our experimental results, we turn to EXAFS fitting analysis to confirm the structures.

As expected from the visual inspection of the EXAFS data in **Figure 4.1a**, the best fit of the EXAFS data of Ce^{3+} in MSA shown in **Figures 4.5a,b** only included scattering from water molecules in the first coordination shell (i.e., Ce-O scattering). EXAFS fitting was conducted using ARTEMIS[47] with FEFF9 for generating paths, as described in **Section 4.2.1**. The best fit was determined by which set of included paths/shells gave the lowest reduced χ^2 values and uncertainty in fitting parameters.

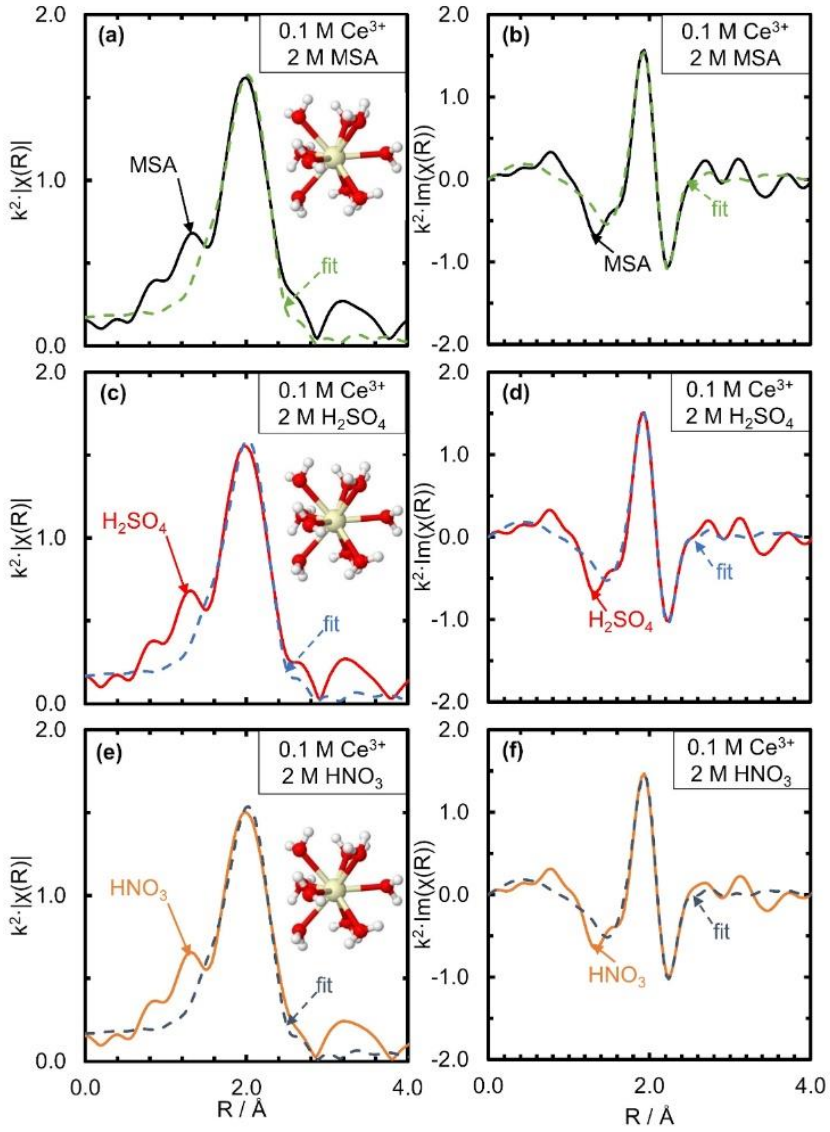

Figure 4.5. EXAFS spectra of the Ce L_3-edge for 0.1 M Ce^{3+} in 2 M MSA and a fit with a Ce-O shell plotted in **(a)** $k^2 \cdot \chi(R)$ Fourier transformed space (magnitude), and **(b)** Fourier transformed space (imaginary). EXAFS spectra of the Ce L_3-edge for 0.1 M Ce^{3+} in 2 M H_2SO_4 and fit with a Ce-O shell in the **(c)** Fourier transformed space (magnitude) and **(d)** $k^2 \cdot \chi(R)$ Fourier transformed space (imaginary). EXAFS spectra of the Ce L_3-edge for 0.1 M Ce^{3+} in 2 M HNO_3 and fit with a Ce-O shell in the **(e)** $k^2 \cdot \chi(R)$ Fourier transformed space (magnitude) and **(f)** $k^2 \cdot \chi(R)$ Fourier transformed space (imaginary). All Ce sources were $Ce_2(CO_3)_3$. Inset geometries are the optimized structure of $[Ce(H_2O)_9]^{3+}$ from DFT, that were also used to generate paths using FEFF9. The fitting window in the R space was 1.4 to 3.0 Å, and 1.5 to 9.7 $Å^{-1}$ in the k space.

The real component of the MSA fit is included in **Appendix A**. As discussed in **Section 4.2.1**, although the multi-electron excitation (MEE) 2p,4d→5d,5d is known to occur in the L_3 EXAFS spectra of Ce^{3+},[55,58,94] MEE corrections introduced more uncertainty in the fitting parameters and resulted in larger reduced χ^2 values of the Ce-O shell fit and therefore were not

used. The inset structure in **Figure 4.5a** shows the DFT-predicted structure of Ce^{3+} in MSA ($[Ce(H_2O)_9]^{3+}$) from which the Ce-O shell scattering path that gave the best fit was generated. The same scattering path used for MSA also gave the best fit for the Ce^{3+} L_3-edge spectra in TFSA and HCl, and the similar fitted parameters imply Ce^{3+} has the same structure in all three acids. **Table 4.1** gives the details of the EXAFS fits with one Ce-O shell for Ce^{3+} in MSA, TFSA, and HCl. The coordination numbers for the Ce-O shell in these three acids were between 8.7 and 9.0, substantiating our DFT prediction of $[Ce(H_2O)_9]^{3+}$ and previous literature findings that Ce^{3+} is hydrated by nine water molecules in 0.1 M triflic acid.[23]

Table 4.1. EXAFS fitting results for Ce^{3+} in TFSA, MSA, HCl, HNO_3, and H_2SO_4 from ARTEMIS, fitting with one Ce-O shell. Three parameters were varied: CN (coordination number), ΔR (to obtain the scattering distance), and σ^2 (Debye-Waller factor). S_0^2 (amplitude reduction factor) and ΔE_0 were obtained by fitting the Ce^{3+} in triflic acid data, and then these same values were set as fixed global parameters for the fits of Ce^{3+} in the other four acids. S_0^2 was 0.970 and ΔE_0 was 0.954 eV. All the other parameters for the Ce-O shell were obtained by fitting. Data for other fits using different combinations of shells that all resulted in higher reduced χ^2 are in **Appendix A**.

Acid	Ce-O shell			Reduced χ^2
	R (Å)	σ^2 (Å^2)	CN	
TFSA	2.543±0.007	0.010±0.002	9.0±0.9	27.7
MSA	2.542±0.007	0.010±0.002	8.7±0.9	55.5
HCl	2.543±0.007	0.010±0.002	8.8±0.9	33.2
HNO_3	2.550±0.007	0.010±0.002	8.4±0.8	40.9
H_2SO_4	2.541±0.006	0.010±0.002	8.5±0.8	32.9

The Ce-O bond distances for these three acids are all 2.54±0.01 Å, which is within 0.06 Å of our DFT predicted Ce-O bond lengths, and within 0.07 Å of previously reported Ce^{3+}-O bond lengths.[21,23,25,26] A fit with a Ce-H shell in addition to the Ce-O shell was also made, but it resulted in higher reduced χ^2 and uncertainty values in the fitted parameters. A fit with a combination of one Ce-O shell and one multiple scattering Ce-O-O shell was also attempted, but resulted in physically unrealistic values. EXAFS fitting using a Ce-Cl path provides no evidence that Ce^{3+} is complexed by Cl^- in 2 M in HCl. Consequently, the EXAFS analysis implies Ce^{3+} is hydrated by nine water molecules in MSA, HCl, and TFSA, as expected by our DFT predictions.

To study the apparent differences in the EXAFS spectra between 2.4 and 3.0 Å in **Figure 4.1b** for H_2SO_4 and HNO_3 compared to the other three acids, we performed several fits with various possible scattering shells associated with anions in HNO_3 and H_2SO_4. However, we were unable to obtain reasonable fitting parameters when fitting the EXAFS data of Ce^{3+} in HNO_3 with scattering shells associated with the nitrate anion. The best fits of the EXAFS data of Ce^{3+} in H_2SO_4 and HNO_3 were again achieved by including only a Ce-O shell (**Figures 4.5c–f**), the same shell used in MSA, HCl, and TFSA. It should be noted, however, that it is not possible to resolve from Ce L_3-edge EXAFS data the source of the O atom (i.e., whether it arises from a H_2O or NO_3^- molecule), and previous EXAFS studies of Ce^{3+} in 3 M HNO_3 suggest monodentate complexation of Ce^{3+} with nitrate,[31] while other experimental methods have led to the conclusion that upwards of five nitrate anions can complex with Ce^{3+}.[28] Nevertheless, based on our EXAFS fitting results here, along with our DFT predictions and findings from UV-Vis, we include the DFT-predicted structures of Ce^{3+} in H_2SO_4 and HNO_3 (i.e., $[Ce(H_2O)_9]^{3+}$) as inset structures in **Figures 4.5c** and **4.5e**. The real components of the H_2SO_4 and HNO_3 fits are included in **Appendix A**, as are all attempted anion-scattering EXAFS fits discussed herein.

From **Table 4.1**, the Ce-O coordination numbers of Ce^{3+} in H_2SO_4 and HNO_3 are similar to those determined in MSA, HCl, and TFSA. The length of the Ce-O bond reported in H_2SO_4 and HNO_3 are both within error of the distances reported for Ce^{3+} in MSA, HCl, and TFSA. Our DFT calculations predict that the Ce-O bond distance would be shorter if there was a change in Ce coordination, for example, if the O was part of a nitrate anion (e.g., Ce-ONO_2 for HNO_3) instead of a water molecule (**Appendix A**). We thus conclude that there is no clear evidence of anion complexation of Ce^{3+} in H_2SO_4 or HNO_3 based on the EXAFS fits, which aligns with our DFT calculations, despite prior literature's assertion that Ce^{3+} can complex with nitrate.[28,31] We attribute

the slight differences of the spectra in **Figure 4.1b** to other effects, such as minor differences in the extent of self-absorption.[89] Differences in self-absorption may also be the cause of the slightly different XANES intensities in **Figure 4.2**.

Ultimately, the UV-Vis, XANES, and EXAFS spectra of Ce^{3+} and the DFT-predicted free energies of Ce^{3+}-anion complexes, show that Ce^{3+} does not readily complex with perchlorate, methanesulfonate, triflate, or chloride. $Ce[(H_2O)_9]^{3+}$, the dominant structure of Ce^{3+}, had not been determined previously in MSA. Slight visual discrepancies in EXAFS and UV-Vis could indicate minor complexation with nitrate and either bisulfate or sulfate, which agrees with previous studies that suggest Ce^{3+} complexes with anions in HNO_3[27,28,31] and H_2SO_4.[29,30] There is no evidence of significant Ce^{3+}-anion complexation in either of these acids, however, from either our EXAFS fitting or DFT calculations.

The finding that Ce^{3+} does not complex with anions in MSA suggests that the high solubility of Ce^{3+} in MSA[13,95] relative to other acids is caused by an effect other than anion complexation in the first coordination sphere, such as the free energy of the solid Ce^{3+} salt used, or a high permittivity of the MSA solvent. In a study analyzing the solubility Ce^{3+} from $Ce_2(CO_3)_{3(s)}$ in H_2SO_4, the solubility equilibrium constant is found to increase when MSA is included,[95] using the same Ce^{3+} salt. We thus hypothesize that the high solubility of Ce^{3+} in MSA is at least partially due to a higher permittivity of MSA, which results in higher electrostatic screening in MSA, which dampens long-range Coulombic interactions between ions. This strong screening in MSA would lower the cerium ion activity coefficient compared to other acids based on Debye-Hückel theory.[96–100] A higher permittivity in MSA is consistent with the high solubility of other metal ions in MSA.[101–103] However, this would likely stabilize both Ce^{3+} and Ce^{4+} similarly, and so may not be responsible for the redox potential shift in **Scheme 4.1**. Because Ce^{3+}

is predominantly only hydrated by water, we hypothesize that anion complexation with Ce^{4+} is responsible for the shift in redox potential with electrolyte. The results shown in the next section corroborate this hypothesis.

4.3.2 Determining the structure of Ce^{4+} in aqueous acidic electrolytes

In this section, we first present the XAFS of Ce^{4+} in H_2SO_4 as compared to Ce^{3+} in H_2SO_4 and find that the bond lengths for Ce^{4+}-O are shorter than Ce^{3+}-O from fitting the Ce^{4+} EXAFS with a Ce-O shell. Next, we discuss the DFT-predicted structure of Ce^{4+} in pure water, then clarify the structure of Ce^{4+} in different electrolytes and the complexation strength of the different anions using both DFT and UV-Vis. Unlike Ce^{3+}, our cumulative findings show that Ce^{4+} readily complexes with anions in aqueous acidic electrolytes, and the free energy of Ce^{4+} complexation is responsible for the change in Ce^{3+}/Ce^{4+} redox potential, which is consistent with previous reports of stronger anion complexation for Ce^{4+} than Ce^{3+}.[1,4,17] These findings also indicate that the Ce^{3+}/Ce^{4+} redox reaction involves a change in the inner sphere, which may help to understand the kinetics of this reaction.

The XANES and EXAFS spectra of 0.1 M Ce^{4+} in 2 M H_2SO_4 (**Figure 4.6**) are different than 0.1 M Ce^{3+} in 2 M H_2SO_4 and solid CeO_2 due to electronic and structural differences. The core electrons of CeO_2 and Ce^{4+} have less electrostatic screening than Ce^{3+}, which results in the higher L_3-edge energy observed in **Figure 4.6a**. The matching XANES L_3-edge energy between CeO_2 and Ce^{4+} in H_2SO_4 proves that the Ce^{4+} sample has no Ce^{3+} present. The first EXAFS peaks for each sample in **Figure 4.6b** are attributed to a Ce-O shell, and thus the Ce-O distance is shorter for Ce^{4+} than for Ce^{3+}, as expected.[38] See **Appendix A** for the EXAFS data of Ce^{4+} in H_2SO_4 plotted in the k space (k^3 weighted).

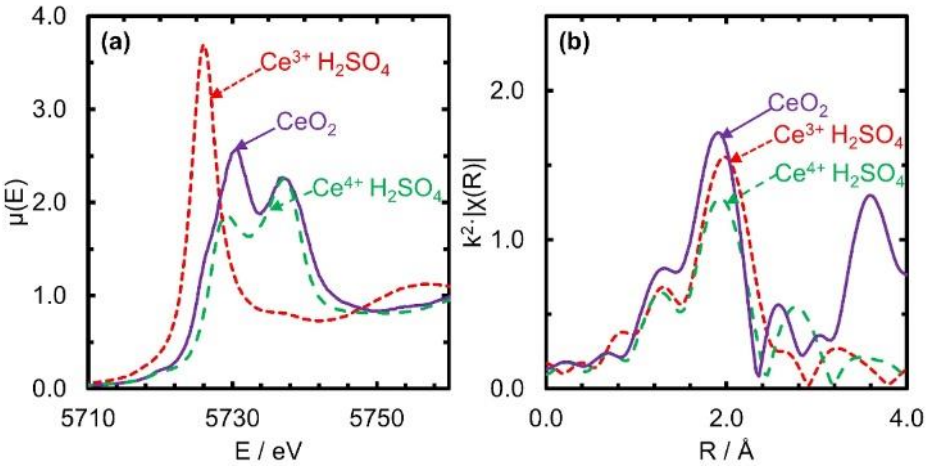

Figure 4.6. (a) XANES of the L_3-edge of Ce for 0.1 M Ce^{4+} in H_2SO_4 (0.1 M $Ce(SO_4)_2$ + 2 M H_2SO_4), 0.1 M Ce^{3+} in H_2SO_4 (0.05 M $Ce_2(CO_3)_3$ + 2 M H_2SO_4), and a solid CeO_2 standard. **(b)** The magnitude component of $k^2 \cdot \chi(R)$ Fourier transformed EXAFS spectra of the L_3-edge of Ce for 0.1 M Ce^{4+} in H_2SO_4, 0.1 M Ce^{3+} in H_2SO_4, and a CeO_2 standard. The CeO_2 standard has been corrected for self-absorption. The CeO_2 and Ce^{4+} EXAFS data is k^3 weighted before being fit due to uncertainty in the value of Ce^{4+} E_0. Plots of the k^3 weighted EXAFS data in the k space for Ce^{4+} in H_2SO_4 as well as the CeO_2 standard are included in **Appendix A**.

To quantify the difference in the Ce-O distance between Ce^{4+} and Ce^{3+}, we fit the experimental EXAFS of Ce^{4+} in H_2SO_4 using ARTEMIS with a single Ce-O path. The shift in edge energy (ΔE_0) and the amplitude reduction factor (S_0^2) values were obtained from fitting the CeO_2 standard (**Figure 4.7**). The experimental EXAFS data of Ce^{4+} in H_2SO_4 and the fits are included in **Figure 4.8**, and the fitting results are included in **Table 4.2**. The Ce^{4+}-O coordination number was set to 9 for the reported fits, chosen because of previous EXAFS reports of Ce^{4+} oxygen coordination in other electrolytes,[38] as well as our own DFT calculations, reported next. The Ce^{4+}-O distance is 2.40 $\pm$ 0.01 Å for Ce^{4+} in H_2SO_4, which is 0.14 Å shorter than the Ce^{3+}-O distance in H_2SO_4 obtained through EXAFS fitting. As discussed previously for Ce^{3+}, MEE effects were not removed before fitting the Ce^{4+} EXAFS data. While we attempted fits that included further shells, such as Ce-S (potentially due to anion complexation), we could not obtain clear fits to the experimental data that distinguish between water or sulfate/bisulfate coordination. Thus, we rely on DFT calculations and UV-Vis to obtain a greater understanding of the structure of Ce^{4+} in acidic electrolytes.

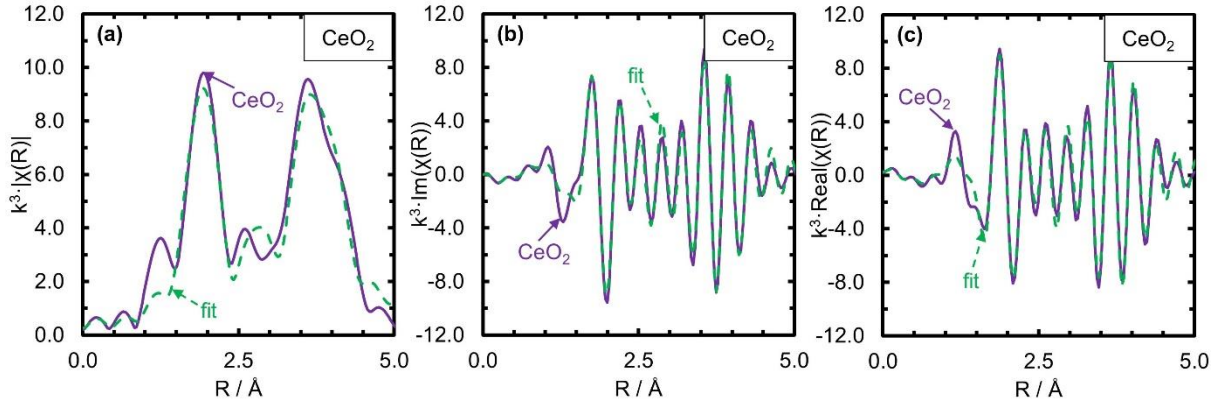

Figure 4.7. EXAFS spectra of the Ce L_3-edge for CeO_2 along with a fit using two Ce-O shells and a Ce-Ce shell plotted in **(a)** $k^3 \cdot \chi(R)$ Fourier transformed space (magnitude), **(b)** $k^3 \cdot \chi(R)$ Fourier transformed space (imaginary), and **(c)** $k^3 \cdot \chi(R)$ Fourier transformed space (real). The fitting window in the R space was 1.5 to 4.6 Å, and 3.0 to 9.7 $Å^{-1}$ in the k space. The CeO_2 standard has been corrected for self-absorption.

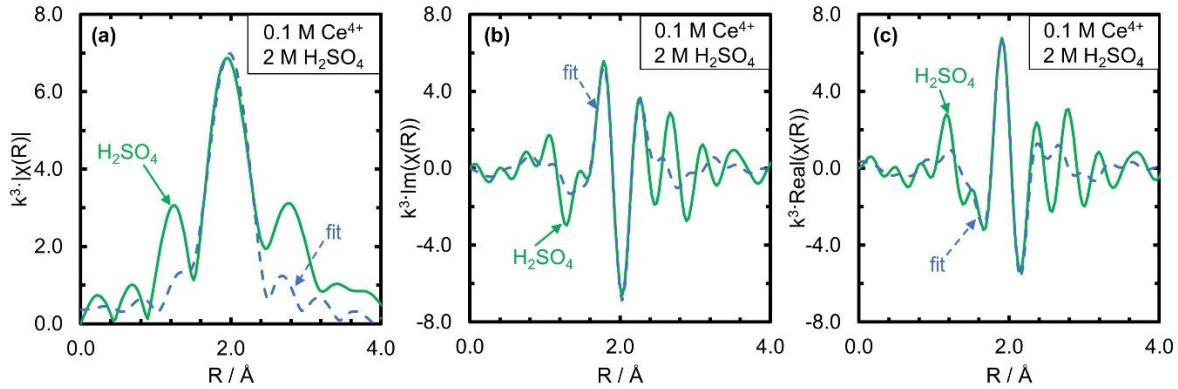

Figure 4.8. EXAFS spectra of the L_3 edge of Ce for 0.1 M Ce^{4+} in 2 M H_2SO_4, as well as a fit with a Ce-O shell, both plotted in the k^3 weighted **(a)** Fourier transformed space (magnitude), **(b)** Fourier transformed space (imaginary), and the **(c)** Fourier transformed space (real).The fitting window in the R space was 1.4 to 2.2 Å, and 3.0 to 9.7 $Å^{-1}$ in the k space.

Table 4.2. EXAFS fitting results for Ce^{4+} in H_2SO_4 from ARTEMIS, fitting with one Ce-O shell. Five parameters were used in the fit: CN (coordination number), ΔR (scattering distance), σ^2 (Debye-Waller factor), S_0^2 (amplitude reduction factor) and ΔE_0. S_0^2 and ΔE_0 were both obtained by fitting the CeO_2 data (**Figure 4.7**), discussed in **Section 4.2.1**, and then set as fixed parameters in the fit of Ce^{4+}, with a value of 0.687 and 2.918 eV, respectively. The CN for the Ce-O shell was set to 9. All of the other parameters for the Ce-O shell were obtained by fitting.

Ce^{4+} H_2SO_4 EXAFS Fit			
Ce-O shell			**Reduced χ^2**
R (Å)	**CN (set)**	**σ^2 ($Å^2$)**	
2.402±0.012	9	0.007±0.002	29.2

The DFT-predicted free energies of Ce^{4+} in **Figure 4.9a** show Ce^{4+} prefers to coordinate with nine water molecules in pure water, i.e., $[Ce(H_2O)_9]^{4+}$. All the predicted $[Ce(H_2O)_x]^{4+}$

structures (x = 5−10) are included in **Appendix B**. Like $[Ce(H_2O)_9]^{3+}$, the $[Ce(H_2O)_9]^{4+}$ structure has a tricapped trigonal prismatic geometry with C_1 symmetry. From our DFT calculations, the average bond length for Ce^{4+}-O (2.44 Å) is 0.13 Å shorter than Ce^{3+}-O (2.57 Å), agreeing with our EXAFS data. The prediction that Ce^{4+} prefers to coordinate with nine water molecules in water matches previous first-principles predictions of Ce^{4+} in water,[22] experimental EXAFS of Ce^{4+} (L_2 and L_3 edges) in $HClO_4$,[38] and our EXAFS data in H_2SO_4 reported in **Table 4.2**. While our DFT prediction of $[Ce(H_2O)_9]^{4+}$ being the lowest energy structure in pure water aligns with previous Ce^{4+} literature, it should be noted that the last element in the lanthanide series, Lu^{3+}, has a similar ionic radius to Ce^{4+},[104] but is only coordinated by eight water molecules.[23] This difference suggests that although ionic radius is an important indicator of water coordination number, other factors such as oxidation state may play a role as well. The bond distances for Ce^{4+}-O from our DFT calculations match within 0.02 Å of those reported from experimental EXAFS.[38]

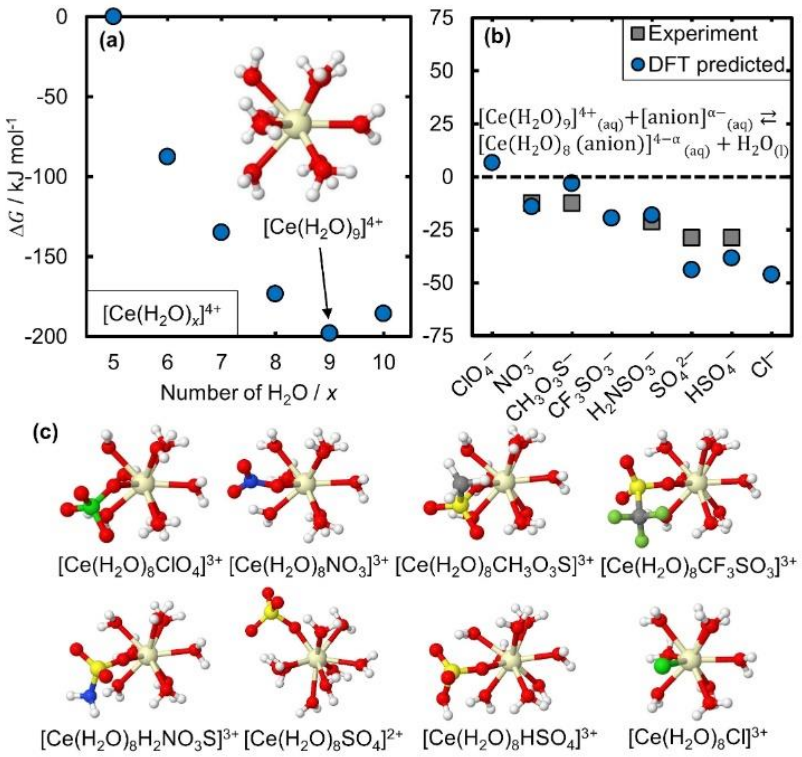

Figure 4.9. (a) DFT-predicted Gibbs free energy of $[Ce(H_2O)_x]^{4+}$ structures containing different numbers of water molecules (x) in their first-coordination shell (x = 5–10) in pure water. Inset is the structure of the $[Ce(H_2O)_9]^{4+}$ from DFT. **(b)** Predicted change in Gibbs free energy of $[Ce(H_2O)_9]^{4+}$ due to anion complexation ($\Delta G_{complex}$) in different acids. The change in Gibbs free energy reported for the exchange of one water molecule with one anion was calculated using DFT assuming an anion concentration of 1 M and water at 55 M (circles). Experimental Gibbs free energies (squares) were calculated from standard redox potentials reported in literature (**Appendix C**) using the Nernst equation (**Eq. 4.9**). Note that the experimental free energy of sulfuric acid includes both sulfate and bisulfate anions, which are at equilibrium concentrations of 0.01 M and 0.99 M, respectively. **(c)** Predicted structures of various Ce^{4+} complexes with anions corresponding to the anion exchange free energies in (b). Atom color legend: beige = cerium, red = oxygen, white = hydrogen, yellow = sulfur, gray = carbon, pear-green = fluorine, blue = nitrogen.

Unlike Ce^{3+}, the complexation energy from DFT shows a negative (favorable) complexation energy of Ce^{4+} for all acids apart from perchloric. The data in **Figure 4.9b** shows semiquantitative agreement between the Gibbs free energy of Ce^{4+} complexation ($\Delta G_{complex}$) with anions from DFT calculations ($\Delta G_{complex,DFT}$) and those derived from experimental redox potentials ($\Delta G_{complex,E^\circ}$). The DFT-predicted free energies were calculated by modeling the exchange of one water molecule with an anion (i.e., $[Ce(H_2O)_9]^{4+}$ becomes $[Ce(H_2O)_8(anion)]^{4-\alpha}$, where α is the magnitude of the anion's charge), shown in **Eq. 4.8**.

$$\Delta G_{f,Ce^{4+}\,complex} + y\Delta G_{f,H_2O} - \Delta G_{f,Ce^{4+}} - y\Delta G_{f,anion} = \Delta G_{complex} \quad \textbf{(4.8)}$$

Here, y is the number of complexing anions, and $\Delta G_{f,i}$ is the Gibbs free energy of formation for species i, (i.e., $\Delta G_{f,Ce^{4+}}$ is the Gibbs free energy of formation of $[Ce(H_2O)_9]^{4+}$, and $\Delta G_{f,Ce^{4+}\,complex}$ is the Gibbs free energy of formation of $[Ce(H_2O)_{9-y}(anion)_y]^{4-\alpha y}$). We use explicit water solvation in addition to COSMO implicit solvation to determine the Ce^{4+} free energies from DFT (i.e., $\Delta G_{complex,DFT}$ in **Figure 4.9b**), similar to the Ce^{3+} calculations. We also tested whether Ce^{4+} preferably complexed with one or two anions for the three strongest binding anions (chloride, sulfate, and bisulfate). Ce^{4+} is predicted to complex with one anion (y = 1) for chloride and sulfate, whereas the free energies of Ce^{4+} with one and two bisulfate anions are comparable (**Figure 4.10a**). The DFT-predicted average distances between Ce and atoms in the first coordination sphere are reported in **Table 4.3**. The weighted average Ce-O distances from DFT are 2.44 Å, 2.45 Å, and 2.43 Å for $[Ce(H_2O)_9]^{4+}$, $[Ce(H_2O)_8SO_4]^{2+}$, and $[Ce(H_2O)_8HSO_4]^{3+}$, respectively, which are three possible structures of Ce^{4+} in H_2SO_4. All these values are within 0.05 Å of the Ce-O distance of Ce^{4+} in H_2SO_4 from EXAFS (2.40 Å), so we cannot identify the structure solely based on the Ce-O distance.

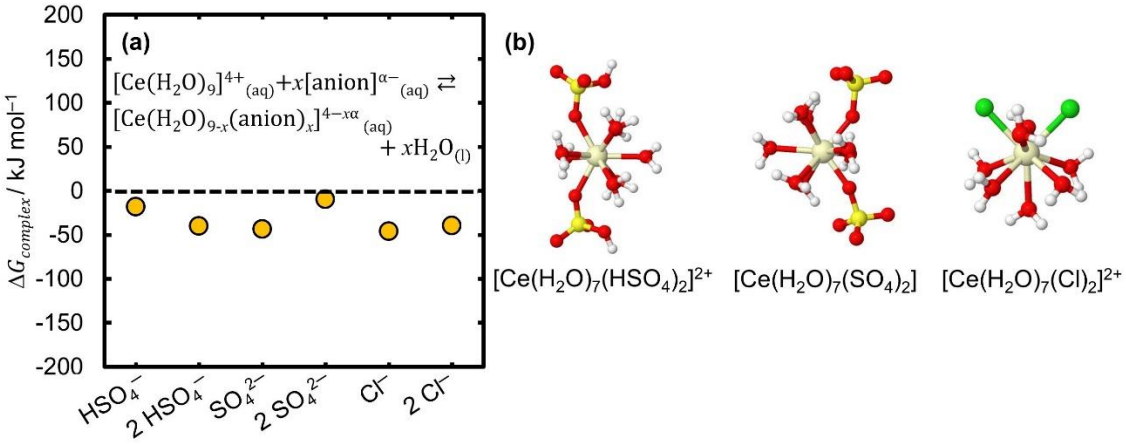

Figure 4.10. (a) DFT-predicted complexation free energy ($\Delta G_{complex,DFT}$) for $[Ce(H_2O)_{9-x}(anion)_x]^{4-x\alpha}$ with x = 1 or 2. **(b)** DFT-predicted structures for $[Ce(H_2O)_7(anion)_2]^{4-2\alpha}$, where α is the charge of the anion.

Table 4.3. DFT-calculated bond length of Ce^{4+}-anion complexes from this work, literature values from either experimental EXAFS or computational methods, and from EXAFS measurements in this work. Connections are written to denote the atom in the anion that is closest to the Ce cation. All distances are in Å.

Electrolyte	Literature references	DFT-predicted average distances	DFT-predicted weighted average	EXAFS Ce-O distances
H_2O	Ce-O: 2.44[22]	Ce-OH_2: 2.44	Ce-O: 2.44	N/A
$HClO_4$	Ce-O: 2.42[38]	Ce-OH_2: 2.43, Ce-$OClO_3$: 2.40	Ce-O: 2.43	N/A
HNO_3	N/A	Ce-OH_2: 2.46, Ce-ONO_2: 2.24	Ce-O: 2.44	N/A
MSA	N/A	Ce-OH_2: 2.47, Ce-OCH_3SO_2: 2.19	Ce-O: 2.44	N/A
TFSA	N/A	Ce-OH_2: 2.45, Ce-OCF_3SO_2: 2.25	Ce-O: 2.43	N/A
H_3NSO_3	N/A	Ce-OH_2: 2.47, Ce-OH_2NSO_2: 2.21	Ce-O: 2.44	N/A
H_2SO_4	N/A	Ce-OH_2: 2.49, Ce-OSO_3: 2.13	Ce-O: 2.45	N/A
HSO_4	N/A	Ce-OH_2: 2.45, Ce-$OHSO_3$: 2.27	Ce-O: 2.43	Ce-OH_2: 2.40
HCl	Ce-Cl: 2.68 ($CeCl_6^{2-}$)[37]	Ce-OH_2: 2.47, Ce-Cl: 2.60	N/A	N/A

The experimental free energy values for Ce^{4+} complexation ($\Delta G_{complex,E^\circ}$) were derived from the shift in the measured redox potentials reported in literature (**Scheme 4.1**) using the Nernst

equation (**Eq. 4.9**), assuming Ce^{3+} does not complex with anions and thus has the same Gibbs free energy in all electrolytes. The assumption that the dominant Ce^{3+} structure is $[Ce(H_2O)_9]^{3+}$ is supported by our results from **Section 4.3.1**.

$$-nF\left(E^{\circ}_{ref} - E^{\circ}\right) = \Delta G_{complex,E^{\circ}} \quad (\mathbf{4.9})$$

Here n is the number of electrons transferred (n = 1 for Ce^{3+}/Ce^{4+}), F is Faraday's constant, E° is the standard redox potential of Ce^{3+}/Ce^{4+} in an electrolyte, and E°_{ref} is the standard redox potential in perchloric acid (does not complex with either Ce^{3+} or Ce^{4+}). See **Appendix C** for additional details. TFSA does not have a reported E° for Ce^{3+}/Ce^{4+}, so we were unable to report a $\Delta G_{complex,E^{\circ}}$. Based on our $\Delta G_{complex,DFT}$ calculations we would estimate the E° in TFSA as 1.54 V vs. RHE. It should be noted that the experimental redox potential used to calculate the free energy of Ce^{4+} anion complexation in 1 M HCl (1.28 V vs. SHE[9]) is considered to have a high level of uncertainty[11,12] due to the possible contribution of the Cl^-/Cl_2 redox couple, which occurs at similar potentials to the measured Ce^{3+}/Ce^{4+} redox potential. Thus, $\Delta G_{complex,E^{\circ}}$ for Ce^{3+}/Ce^{4+} in HCl is not reported in **Figure 4.9b**.

The $\Delta G_{complex}$ from both DFT and redox potentials shown in **Figure 4.9b** are all favorable, except for perchloric acid. The agreement between DFT-predicted and experimental $\Delta G_{complex}$ supports our finding that the dominant Ce^{3+} structure is $[Ce(H_2O)_9]^{3+}$ and therefore, the shift in reported redox potentials (**Scheme 4.1**) is caused by the free energy of Ce^{4+}-anion complexation. Importantly, $\Delta G_{complex}$ is related to the equilibrium constant of the Ce^{4+} complexation reaction, allowing us to obtain the expected concentration of complexed Ce^{4+} (**Appendix C**). As discussed previously, we ascribe electrostatic differences in the acids as a possible cause of the high solubility

of Ce^{3+} in MSA. Although these electrostatic differences may impact the Ce ion activity coefficients, good agreement is neverthless achieved between experiment and DFT free energies in **Figure 4.9b** when electrostatic differences between acids are neglected for the DFT calculations. This agreement suggests that the difference in these electrostatics for Ce^{3+} and Ce^{4+} is small compared to the energy associated with complexation.

The UV-Vis spectra of Ce^{4+} in 2 M MSA, 2 M H_2SO_4, and 2 M HCl are noticeably different from one another (**Figure 4.11a**), corroborating our findings from DFT-calculations that Ce^{4+} complexes with anions. The absorption peak is at 210 nm, 237 nm, and 320 nm in MSA, HCl, and H_2SO_4, respectively. Because the electronic configuration of Ce^{4+} is $[Xe]4f^0$, there are no valence electrons available for metal-to-ligand interactions (i.e., Ce^{4+} electron donation).

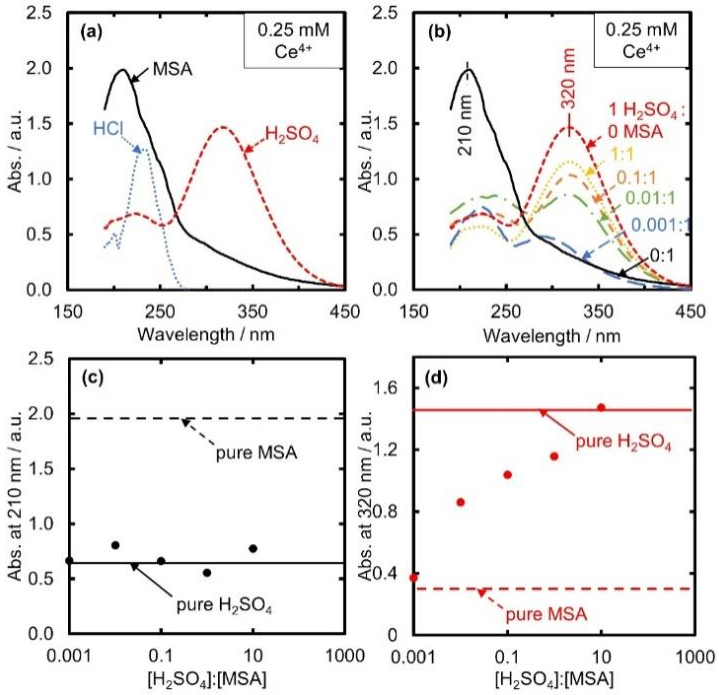

Figure 4.11. UV-Vis absorbance as a function of wavelength at room temperature (23 ± 1 °C) for **(a)** Ce^{4+} spectra for MSA, H_2SO_4, and HCl, obtained by adding specified cerium salt to acid and, for MSA and HCl solutions, venting CO_2 and oxidizing Ce^{3+} fully to Ce^{4+}; **(b)** Ce^{4+} spectra (0.25 mM $Ce_2(CO_3)_3$) for a series of MSA/H_2SO_4 solutions, with X:Y indicating X M H_2SO_4 and Y M MSA. **(c)** Absorbance intensity at a wavelength of 210 nm of 0.25 mM Ce^{4+} spectra for a series of MSA/H_2SO_4 solutions including those in **(b)**, as a function of the ratio of H_2SO_4:MSA concentration. The absorbance intensity in pure H_2SO_4 and pure MSA are shown by solid and dashed lines, respectively. **(d)** Absorbance at wavelength 320 nm of 0.25 mM Ce^{4+} spectra for a series of MSA/H_2SO_4 solutions including those in **(b)**, as a function of the ratio of H_2SO_4:MSA concentration.

Thus, all these absorptions manifest from a ligand-to-metal (i.e., ligand electron donation) electronic interaction, corroborating that Ce^{4+} is complexed by anions. The magnitude of the shifts in UV-Vis peak locations with electrolyte for Ce^{4+} in **Figure 4.11a** are much greater than the negligible shifts observed in **Figures 4.3a,b** for Ce^{3+} in the same electrolytes. Because the shift in UV-Vis peaks of Ce^{3+} and Ce^{4+} are similarly sensitive to ligand environment for the same anion,[84] our UV-Vis results suggest that anion complexation is much more prevalent for Ce^{4+} than Ce^{3+} in the electrolytes studied. There is evidence that Ce^{4+} forms dimers in perchloric and nitric acid,[31,33,39–42] but no evidence for dimerization of Ce^{4+} in H_2SO_4 (up to 10 mM Ce^{4+}) is observed from our UV-Vis measurements. In **Figure 4.12**, when the concentration is increased to 10 mM, the peak locations do not change, suggesting that there is either no change in the Ce^{4+} structure in 2 M H_2SO_4 as concentration increases (either no dimers or only dimers present at all concentrations), or that the Ce^{4+}-Ce^{4+} and Ce^{4+}-O bonds have the same absorption spectra. Thus, we observe no definitive evidence of Ce^{4+} dimerization in sulfuric acid.

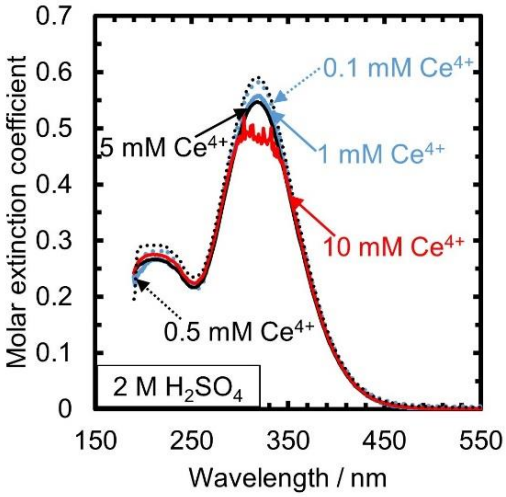

Figure 4.12. Molar extinction coefficient (absorbance normalized by cuvette pathlength and concentration) as function of wavelength at room temperature (23.3 °C) from UV-Vis spectra for Ce^{4+} at several concentrations of $Ce(SO_4)_2$ in 2 M H_2SO_4: 0.1 mM, 0.5 mM, 1 mM, 5 mM, and 10 mM $Ce(SO_4)_2$, obtained by adding cerium sulfate to acid and stirring 24 hours to dissolve all particles. Spectra collected in cuvette with a pathlength of either 1 mm or 10 mm cuvette (1 mm pathlength used for concentrations higher than 5 mM Ce^{4+}).

To qualitatively compare anion complexation strength, UV-Vis spectra of Ce^{4+} in mixed acids are used to determine the dominant complexed species. From the DFT-predicted free energies and experimental free energies in **Figure 4.9b**, we find that bisulfate and sulfate complex with Ce^{4+} stronger than methanesulfonate, such that in a mixture of MSA and H_2SO_4, the dominant complex would be Ce^{4+} with bisulfate or sulfate. In fact, Ce^{4+} will be complexed more weakly by anions in MSA than in any other acids, excluding $HClO_4$. This finding that Ce^{4+} is complexed more strongly by bisulfate/sulfate than methanesulfonate is supported by the UV-Vis data in **Figures 4.11b−d**. The UV-Vis peak at 210 nm (MSA) and at 320 nm (H_2SO_4) are visible in mixed MSA/H_2SO_4 solutions, shown ranging from 0.001 M H_2SO_4:1 M MSA to 1 M H_2SO_4:1 M MSA in **Figure 4.11b**. The data in **Figures 4.11c,d** show the change in peak intensity at 210 nm (MSA) and 320 nm (H_2SO_4), respectively, as the ratio of H_2SO_4 to MSA concentration increases, with the peak intensities in the pure acids added as lines for reference. Even at the lowest concentration of H_2SO_4 in MSA, the intensity of the peak at 210 nm (**Figure 4.11c**) decreases to near that of pure H_2SO_4. The peak at 320 nm (**Figure 4.11d**) increases at low concentrations of H_2SO_4 such that at a 1:1 ratio of H_2SO_4:MSA the peak intensity is nearly the same as in pure H_2SO_4. The UV-Vis spectra in mixed MSA/H_2SO_4 matches more closely to H_2SO_4, suggesting the dominant species is a Ce^{4+}-sulfate complex rather than a Ce^{4+}-methanesulfonate complex. The finding that Ce^{4+} is complexed more strongly by sulfate or bisulfate than by methanesulfonate is consistent with our DFT calculations, as well as the larger redox potential shift observed from $HClO_4$ to H_2SO_4 than to MSA.

The result that methanesulfonate complexes weaker with Ce^{4+} than sulfate/bisulfate is opposite to what one would expect based on the reported solubility trends in MSA and H_2SO_4 electrolytes. The solubility of Ce^{4+} in H_2SO_4 prepared from $Ce(SO_4)_{2(s)}$ is 0.75 M at room

temperature in 0.1 M H_2SO_4,[17] and decreases with increasing H_2SO_4 concentration. In contrast, the solubility of Ce^{4+} in MSA, prepared from $Ce_2(CO_3)_{3(s)}$ followed by oxidation, increases with increasing acid concentration, achieving a solubility limit of approximately 1 M at 4 M MSA.[13] Because sulfate complexes with Ce^{4+} stronger than methanesulfonate, the higher solubility of Ce^{4+} in MSA is hypothesized to arise from the higher free energy of $Ce(SO_4)_{2(s)}$ compared to $Ce_2(CO_3)_{3(s)}$ (and the Ce-MSA salt), perhaps stemming from differences in the enthalpy or entropy of the cerium salts in the two acids (shown to occur for other lanthanides depending on the anions present),[105] or better screening of long range cation interactions in MSA than H_2SO_4. Better screening of cations in MSA than H_2SO_4 aligns with reports of other metal ions′ improved solubility in MSA compared to H_2SO_4,[102] and would occur if MSA has a higher permittivity than H_2SO_4. This hypothesis is also consistent with the higher solubility of Ce^{3+} in MSA than in other acids, despite the lack of anion complexation by Ce^{3+}, as discussed in **Section 4.3.1**.

4.4 Conclusion

We find that the dominant Ce^{3+} structure is hydrated only by water in all considered electrolytes as $[Ce(H_2O)_9]^{3+}$ in a tricapped trigonal prismatic geometry. Unlike Ce^{3+}, Ce^{4+} complexes with at least one anion in all acids other than perchloric acid. The Ce^{4+} free energies we predict from calculations match experiment, suggesting we have obtained accurate cerium ion structures. The free energies from calculations explain the large shift of the Ce^{3+}/Ce^{4+} redox potential with electrolyte and indicate that anion complexation is not solely responsible for the trends observed in cerium ion solubility. In principle we can also predict redox potentials for new electrolytes.

The major factor in the large shift in the Ce^{3+}/Ce^{4+} redox potential is the Ce^{4+}-anion complexation energy, with differences in the long range screening of different acids having a much

smaller effect on the free energy differences of Ce^{3+} and Ce^{4+}. That is, even ignoring differences in relative permitttivities for different acids, the Ce^{3+}/Ce^{4+} redox potential trends observed experimentally match those predicted here from DFT-predicted anion complexation energies. However, in terms of solubility these long range screening effects may play a larger role. For Ce^{3+}, which does not complex with anions, the long range screening differences could be responsible for the high solubility of Ce^{3+} in MSA. Nevertheless, to have a complete understanding of the solubility of cerium ions in different electrolytes we would need the complexation energies (reported here), as well as accurate values of the acidic electrolytes' permittivity and free energies, enthalpies, and entropies of the dissolution of the solid cerium salts.

The structure and thermodynamics of cerium complexes is known to affect the kinetics of Ce^{3+}/Ce^{4+} electron transfer,[8,17] and previous work on other redox chemistries[106,107] have shown that reorganizational energy requirements can be used to predict charge transfer. Therefore, the information gained here can be used to predict charge transfer of the Ce^{3+}/Ce^{4+} redox couple using theoretical models such as Marcus theory. Additionally, analyzing the EXAFS of Ce^{4+} in a series of acids, similar to the analysis conducted here for Ce^{3+}, should be done to obtain more experimental evidence of Ce^{4+} anion complexation. Lastly, mixed acids are becoming increasingly important as they are shown to improve cerium redox kinetics.[95] Future studies should expand on mixed H_2SO_4-MSA studies included here to understand the structure of metal ions and the effect of those structures' thermodynamics on kinetics.

4.5 References

1. Piro, N. A., Robinson, J. R., Walsh, P. J. & Schelter, E. J. The electrochemical behavior of cerium(III/IV) complexes: Thermodynamics, kinetics and applications in synthesis. *Coord. Chem. Rev.* **260**, 21–36 (2014).
2. Robinson, J. R. *et al.* Tuning reactivity and electronic properties through ligand reorganization within a cerium heterobimetallic framework. *J. Am. Chem. Soc.* **135**, 19016–19024 (2013).
3. Suwa, T., Kuribayashi, N. & Tachikawa, E. Development of chemical decontamination process with sulfuric acid-cerium (Iv) for decommissioning. *J. Nucl. Sci. Technol.* **25**, 574–585 (1988).
4. Arenas, L. F., Ponce De León, C. & Walsh, F. C. Electrochemical redox processes involving soluble cerium species. *Electrochim. Acta* **205**, 226–247 (2016).
5. Arenas, L. F., León, C. P. De & Walsh, F. C. Mass transport and active area of porous Pt/Ti electrodes for the Zn-Ce redox flow battery determined from limiting current measurements. *Electrochim. Acta* **221**, 154–166 (2016).
6. Weber, A. Z. *et al.* Redox flow batteries: A review. *J. Appl. Electrochem.* **41**, 1137–1164 (2011).
7. Ke, X. *et al.* Rechargeable redox flow batteries: Flow fields, stacks and design considerations. *Chem. Soc. Rev.* **47**, 8721–8743 (2018).
8. Robinson, J. R., Carroll, P. J., Walsh, P. J. & Schelter, E. J. The impact of ligand reorganization on cerium(III) oxidation chemistry. *Angew. Chemie - Int. Ed.* **51**, 10159–10163 (2012).
9. Smith, G. F. & Getz, C. A. Cerate oxidimetry: Theoretical considerations and determination of approximate electrode reference potentials. *Ind. Eng. Chem. Res.* **10**, 191–195 (1938).
10. Xiong, F., Zhou, D., Xie, Z. & Chen, Y. A study of the Ce3+/Ce4+ redox couple in sulfamic acid for redox battery application. *Appl. Energy* **99**, 291–296 (2012).
11. Wadsworth, E., Duke, F. R. & Goetz, C. A. Present status of cerium (IV)-cerium (lll) potentials. *Anal. Chem.* 1824–1825 (1957) doi:10.1021/ac60132a046.
12. Maverick, A. W. & Yao, Q. The cerium(IV)/cerium(III) electrode potential in hydrochloric acid solution. *Inorg. Chem.* **32**, 5626–5628 (1993).
13. Kreh, R. P., Spotnitz, R. M. & Lundquist, J. T. Mediated electrochemical synthesis of aromatic aldehydes, ketones, and quinones using ceric methanesulfonate. *J. Org. Chem.* **54**, 1526–1531 (1989).
14. Kilbourn, B. T. *Cerium and Cerium*. *Kirk-Othmer Encyclopedia of Chemical Technology* (Wiley, 2011). doi:10.1002/0471238961.030518091109120.
15. Marcus, Y. & Hefter, G. Ion pairing. *Chem. Rev.* **106**, 4585–4621 (2006).
16. Baes, C. F. J. & Mesmer, R. E. Yttrium, Lanthanides, Actinium. in *The Hydrolysis of Cations* 138–146 (Krieger Publishing Company, 1986).
17. Paulenova, A., Creager, S. E., Navratil, J. D. & Wei, Y. Redox potentials and kinetics of the Ce3+/Ce4+redox reaction and solubility of cerium sulfates in sulfuric acid solutions. *J. Power Sources* **109**, 431–438 (2002).
18. Sridharan, V. & Menéndez, J. C. Cerium(IV) ammonium nitrate as a catalyst in organic synthesis. *Chem. Rev.* **110**, 3805–3849 (2010).
19. Bard, A. J. & Faulkner, L. R. *Electrochemical Methods: Fundamentals and Applications*. (John Wiley & Sons, Inc., 2001). doi:10.1016/B978-0-08-098353-0.00003-8.

20. Dinescu, A. & Clark, A. E. Thermodynamic and structural features of aqueous Ce(III). *J. Phys. Chem. A* **112**, 11198–11206 (2008).
21. Lutz, O. M. D., Hofer, T. S., Randolf, B. R. & Rode, B. M. Computational study of the cerium(III) ion in aqueous environment. *Chem. Phys. Lett.* **539**–**540**, 50–53 (2012).
22. Lutz, O. M. D., Hofer, T. S., Randolf, B. R., Weiss, A. K. H. & Rode, B. M. A QMCF-MD investigation of the structure and dynamics of Ce4+ in aqueous solution. *Inorg. Chem.* **51**, 6746–6752 (2012).
23. Persson, I., D'Angelo, P., De Panfilis, S., Sandström, M. & Eriksson, L. Hydration of lanthanoid(III) ions in aqueous solution and crystalline hydrates studied by EXAFS spectroscopy and crystallography: The myth of the 'gadolinium break'. *Chem. - A Eur. J.* **14**, 3056–3066 (2008).
24. Urbanski, T. S., Fornari, P. & Abbruzzese, C. The extraction of cerium(III) and lanthanum(III) from chloride solutions with LIX 54. *Hydrometallurgy* **40**, 169–179 (1996).
25. Allen, P. G., Bucher, J. J., Shuh, D. K., Edelstein, N. M. & Craig, I. Coordination chemistry of trivalent lanthanide and actinide ions in dilute and concentrated chloride solutions. *Inorg. Chem.* **39**, 595–601 (2000).
26. Rudolph, W. W. & Irmer, G. Raman spectroscopic characterization of light rare earth ions: La3+, Ce3+, Pr3+, Nd3+and Sm3+- hydration and ion pair formation. *Dalt. Trans.* **46**, 4235–4244 (2017).
27. Kanno, H. & Hiraishi, J. Raman study of aqueous rare-earth nitrate solutions in liquid and glassy states. *J. Phys. Chem.* **88**, 2787–2792 (1984).
28. Martin, T. W. & Glass, R. W. Competitive electron transfer. Activity-defined formation constants of cerium(III) nitrate complexes based on reaction with the nitrate free radical. *J. Am. Chem. Soc.* **92**, 5075–5083 (1970).
29. Blatz, L. A. The use of a cation-exchange resin to study the cerous and sulfate ion complexes. *J. Phys. Chem.* **66**, 160–164 (1962).
30. Newton, T. W. & Arcand, G. M. A spectrophotometric study of the complex formed between cerous and sulfate ions. *J. Am. Chem. Soc.* **75**, 2449–2453 (1953).
31. Antonio, M. R., Ellis, R. J., Estes, S. L. & Bera, M. K. Structural insights into the multinuclear speciation of tetravalent cerium in the tri-n-butyl phosphate-n-dodecane solvent extraction system. *Phys. Chem. Chem. Phys.* **19**, 21304–21316 (2017).
32. Beineke, T. A. & Delgaudio, J. The crystal structure of ceric ammonium nitrate. *Inorg. Chem.* **7**, 715–721 (1968).
33. Demars, T. J., Bera, M. K., Seifert, S., Antonio, M. R. & Ellis, R. J. Revisiting the solution structure of ceric ammonium nitrate. *Angew. Chem. Int. Ed. Engl.* **54**, 7534–8 (2015).
34. Larsen, R. D. & Brown, G. H. The structure of ammonium hexanitratocerate(IV) in solution. *J. Phys. Chem.* **68**, 3060–3062 (1964).
35. Hardwick, T. J. & Robertson, E. Association of ceric ions with sulphate (a spectral study). *Can. J. Chem.* **29**, 828–837 (1951).
36. Moore, R. L. & Anderson, R. C. Spectrophotometric studies on cerium(IV) sulfate complex ions. *J. Am. Chem. Soc.* **67**, 167–171 (1945).
37. Wang, Z., Chu, T., Chai, Z. & Wang, D. A density functional theory study of the competitive complexation of pyridine against H2O and Cl- to Cm3+ and Ce4+. *Radiochim. Acta* **102**, 101–109 (2014).
38. Sham, T. K. Electronic structure of hydrated Ce4+ ions in solution: An x-ray absorption study. *Phys. Rev. B* **40**, 6045–6051 (1989).

39. Fronaeus, S. & Ostman, C. O. The mechanism of the exchange reaction between cerium(III) and cerium(IV) at platinum surfaces. *Acta Chem. Scand.* **10**, 769–778 (1956).
40. Hardwick, T. J. & Robertson, E. Ionic species in ceric perchlorate solutions. *Can. J. Chem.* **29**, 818–827 (1951).
41. Heidt, L. J. & Smith, M. E. Quantum yields of the photochemical reduction of ceric ions by water and evidence for the dimerization of ceric ions. *J. Am. Chem. Soc.* **70**, 2476–2481 (1948).
42. Ikeda-Ohno, A., Tsushima, S., Hennig, C., Yaita, T. & Bernhard, G. Dinuclear complexes of tetravalent cerium in an aqueous perchloric acid solution. *Dalt. Trans.* **41**, 7190–7192 (2012).
43. Tucker, M. C., Weiss, A. & Weber, A. Z. Improvement and analysis of the hydrogen-cerium redox flow cell. *J. Power Sources* **327**, 591–598 (2016).
44. Janicki, R., Starynowicz, P. & Mondry, A. Lanthanide carbonates. *Eur. J. Inorg. Chem.* 3601–3616 (2011) doi:10.1002/ejic.201100184.
45. Harned, H. S. & Davis Jr., R. The ionization constant of carbonic acid in water and the solubility of carbon dioxide in water and aqueous salt solutions from 0 to 50°. *J. Am. Chem. Soc.* **65**, 2030–2037 (1943).
46. Singh, N. *et al.* Carbon-supported Pt during aqueous phenol hydrogenation with and without applied electrical potential: X-ray absorption and theoretical studies of structure and adsorbates. *J. Catal.* **368**, 8–19 (2018).
47. Ravel, B. & Newville, M. ATHENA, ARTEMIS, HEPHAESTUS: Data analysis for X-ray absorption spectroscopy using IFEFFIT. *J. Synchrotron Radiat.* **12**, 537–541 (2005).
48. Brennan, S. & Cowan, P. L. A suite of programs for calculating X-ray absorption, reflection and diffraction performance for a variety of materials at arbitrary wavelengths. *Rev. Sci. Instrum.* **63**, (1992).
49. Cromer, D. T. Anomalous dispersion corrections computed from self-consistent field relativistic Dirac–Slater wave functions. *Acta Crystallogr.* **18**, 17–23 (1965).
50. Cromer, D. T. & Liberman, D. Relativistic calculation of anomalous scattering factors for X rays. *J. Chem. Phys.* **53**, 1891–1898 (1970).
51. Cromer, D. T. & Liberman, D. A. Anomalous dispersion calculations near to and on the long-wavelength side of an absorption edge. *Acta Crystallogr. Sect. A* **37**, 267–268 (1981).
52. Merritt, E. A. X-ray absorption edges. (2010).
53. Sham, T. K. L edge chemical shift and bond length difference of the mixed oxidation Ce3+/Ce4+ redox couple in solution. *J. Chem. Phys.* **79**, 1116–1121 (1983).
54. Fonda, E., Andreatta, D., Colavita, P. E. & Vlaic, G. EXAFS analysis of the L3 edge of Ce in CeO2: Effects of multielectron excitations and final-state mixed valence. *J. Synchrotron Radiat.* **6**, 34–42 (1999).
55. Chaboy, J., Marcelli, A. & Tyson, T. A. Influence of double-electron transitions on the EXAFS L edges of rare-earth systems. *Phys. Rev. B* **49**, 11652–11661 (1994).
56. Solera, J. A., García, J. & Proietti, M. G. Multielectron excitations at the L edges in rare-earth ionic aqueous solutions. *Phys. Rev. B* **51**, 2678–2686 (1995).
57. Ohta, A., Kagi, H., Tsuno, H., Nomura, M. & Kawabe, I. Influence of multi-electron excitation on EXAFS spectroscopy of trivalent rare-earth ions and elucidation of change in hydration number through the series. *Am. Mineral.* **93**, 1384–1392 (2008).
58. Chaboy, J. & Tyson, T. A. Relative cross sections for bound-state double-electron LN4,5-edge transitions. *Phys. Rev. B* **49**, 5869–5875 (1994).

59. Kodre, A. *et al.* Double photoexcitation [2(s,p)4(p,d)] in the Xe-isoelectronic series Cs+, Ba2+, La3+. *J. Phys.* **C9**, 397–400 (1994).
60. Rehr, J. J., Kas, J. J., Vila, F. D., Prange, M. P. & Jorissen, K. Parameter-free calculations of X-ray spectra with FEFF9. *Phys. Chem. Chem. Phys.* **12**, 5503–5513 (2010).
61. Bradlyn, B. *et al.* Topological quantum chemistry. *Nature* **547**, 298–305 (2017).
62. Vergniory, M. G. *et al.* A complete catalogue of high-quality topological materials. *Nature* **566**, 480–485 (2019).
63. Bilbao Crystallographic Server.
64. Topological Materials Database.
65. Aroyo, M. I. *et al.* Crystallography online: Bilbao crystallographic server. *Bulg. Chem. Commun.* **43**, 183–197 (2011).
66. Aroyo, M. I., Kirov, A., Capillas, C., Perez-Mato, J. M. & Wondratschek, H. Bilbao Crystallographic Server. II. Representations of crystallographic point groups and space groups. *Acta Crystallogr. Sect. A Found. Crystallogr.* **62**, 115–128 (2006).
67. Aroyo, M. I. *et al.* Bilbao Crystallographic Server: I. Databases and crystallographic computing programs. *Zeitschrift fur Krist.* **221**, 15–27 (2006).
68. Bianconi, A. *et al.* Specific intermediate-valence state of insulating 4f compounds detected by L3 x-ray absorption. *Phys. Rev. B* **35**, 806–812 (1987).
69. Valiev, M. *et al.* NWChem: A comprehensive and scalable open-source solution for large scale molecular simulations. *Comput. Phys. Commun.* **181**, 1477–1489 (2010).
70. Becke, A. D. Density-functional thermochemistry. III. The role of exact exchange. *J. Chem. Phys.* **98**, 5648–5652 (1993).
71. Lee, C., Yang, W. & Parr, R. G. Development of the Colic-Salvetti correlation-energy formula into a functional of the electron density. *Phys. Rev. B 8* **37**, 785–789 (1988).
72. Dolg, M., Stoll, H., Preuss, H. & Pitzer, R. M. Relativistic and correlation effects for element 105 (hahnium, Ha). A comparative study of M and MO (M = Nb, Ta, Ha) using energy-adjusted ab initio pseudopotentials. *J. Phys. Chem.* **97**, 5852–5859 (1993).
73. Ditchfield, R., Hehre, W. J. & Pople, J. A. Self-consistent molecular-orbital methods. IX. An extended Gaussian-type basis for molecular-orbital studies of organic molecules. *J. Chem. Phys.* **54**, 724–728 (2004).
74. Spitznagel, G. W., Clark, T., von Ragué Schleyer, P. & Hehre, W. J. An evaluation of the performance of diffuse function-augmented basis sets for second row elements, Na-Cl. *J. Comput. Chem.* **8**, 1109–1116 (1987).
75. Klamt, A. & Schuurmann, G. COSMO: A new approach to dielectric screening in solvents with explicit. *J. Chem. Soc. Perkin Trans* **2**, 799–805 (1993).
76. York, D. M. & Karplus, M. A smooth solvation potential based on the conductor-like screening model. *J. Phys. Chem. A* **103**, 11060–11079 (1999).
77. Goldsmith, B. R., Hwang, T., Seritan, S., Peters, B. & Scott, S. L. Rate-enhancing roles of water molecules in methyltrioxorhenium-catalyzed olefin epoxidation by hydrogen peroxide. *J. Am. Chem. Soc.* **137**, 9604–9616 (2015).
78. Kuznetsov, M. L. & Pombeiro, A. J. L. Radical formation in the [MeReO3]-catalyzed aqueous peroxidative oxidation of alkanes: A theoretical mechanistic study. *Inorg. Chem.* **48**, 307–318 (2009).
79. Wertz, D. H. Relationship between the gas-phase entropies of molecules and their entropies of solvation in water and 1-octanol. *J. Am. Chem. Soc.* **102**, 5316–5322 (1980).
80. Jinnouchi, R., Hatanaka, T., Morimoto, Y. & Osawa, M. First principles study of sulfuric

acid anion adsorption on a Pt(111) electrode. *Phys. Chem. Chem. Phys* **14**, 3208–3218 (2012).
81. Tawa, G. J., Topol, I. A., Burt, S. K., Caldwell, R. A. & Rashin, A. A. Calculation of the aqueous solvation free energy of the proton. *J. Chem. Phys.* **109**, 4852–4863 (1998).
82. Car, R. & Parrinello, M. Unified approach for molecular dynamics and density-functional theory. *Phys. Rev. Lett.* **55**, 2471–2474 (1985).
83. Hu, Z., Kaindl, G. & Meyer, G. X-ray absorption near-edge structure at the LI-III thresholds of Pr, Nd, Sm, and Dy compounds with unusual valences. *J. Alloys Compd.* **246**, 186–192 (1997).
84. Ebendorff-Heidepriem, H. & Ehrt, D. Formation and UV absorption of cerium, europium and terbium ions in different valencies in glasses. *Opt. Mater. (Amst).* **15**, 7–25 (2000).
85. Ebendorff-Heidepriem, H. & Ehrt, D. Tb3+ f-d absorption as indicator of the effect of covalency on the Judd-Ofelt Ω2 parameter in glasses. *J. Non. Cryst. Solids* **248**, 247–252 (1999).
86. Reisfeld, R. Spectra and energy transfer of rare earths in inorganic glasses. *Rare Earths* 53–98 (1973) doi:10.1007/3-540-06125-8.
87. Jørgensen, C. K. & Reisfeld, R. Judd-Ofelt parameters and chemical bonding. *J. Less-Common Met.* **93**, 107–112 (1983).
88. Hennig, C. *et al.* Crystal structure and solution species of Ce(III) and Ce(IV) formates: From mononuclear to hexanuclear complexes. *Inorg. Chem.* **52**, 11734–11743 (2013).
89. Tröger, L. *et al.* Full correction of the self-absorption in soft-fluorescence extended x-ray-absorption fine structure. *Phys. Rev. B* **46**, 3283–3289 (1992).
90. Greenhaus, H. L., Feibush, A. M. & Gordon, L. Ultraviolet spectrophotometric determination of cerium(III). *Anal. Chem.* **29**, 1531–1534 (1957).
91. Medalia, A. I. & Byrne, B. J. Spectrophotometric setermination of cerium(IV). *Anal. Chem.* **23**, 453–456 (1951).
92. Yu, X. & Manthiram, A. A zinc-cerium cell for energy storage using a sodium-ion exchange membrane. *Adv. Sustain. Syst.* **1**, 1–6 (2017).
93. D'Angelo, P. & Spezia, R. Hydration of lanthanoids(III) and actinoids(III): An experimental/ theoretical saga. *Chem. - A Eur. J.* **18**, 11162–11178 (2012).
94. Filipponi, A., Bernieri, E. & Mobilio, S. Multielectron excitations in x-ray-absorption spectra of a-Si:H. *Phys. Rev. B* **38**, 3298–3304 (1988).
95. Xie, Z., Xiong, F. & Zhou, D. Study of the Ce3+/Ce4+ redox couple in mixed-acid media (CH3SO3H and H2SO4) for redox flow battery application. *Energy and Fuels* **25**, 2399–2404 (2011).
96. Debye, P. & Hückel, E. The theory of electrolytes I. Freezing point depression and related occurrences. *Phys. Zeitschrift* **24**, 185–206 (1923).
97. Valiskó, M. & Boda, D. Activity coefficients of individual ions in LaCl3 from the II+IW theory. *Mol. Phys.* **115**, 1245–1252 (2017).
98. Tikanen, A. C. & Fawcett, W. R. The role of solvent permittivity in estimation of electrolyte activity coefficients for systems with ion pairing on the basis of the mean spherical approximation. *Berichte der Bunsengesellschaft für Phys. Chemie* **640**, 634–640 (1996).
99. Abraham, M. H. & Danil de Namor, A. F. Solubility of electrolytes in 1,2-dichloroethane and 1,1-dichloroethane, and derived free energies of transfer. *J. Chem. Soc. Faraday Trans. 1 Phys. Chem. Condens. Phases* **72**, 955–962 (1976).
100. Monk, C. B. Electrolytes in solutions of amino acids. Part V.—The solubilities of calcium,

barium and lanthanum iodates in glycine, alanine and glycyl-glycine. *Trans. Faraday Soc.* **47**, 1233–1240 (1951).
101. Roitman, D. B., McAlister, J. & Oaks, F. L. Composition characterization of methanesulfonic acid. *J. Chem. Eng. Data* **39**, 56–60 (1994).
102. Gernon, M. D., Wu, M., Buszta, T. & Janney, P. Environmental benefits of methanesulfonic acid: Comparative properties and advantages. *Green Chem.* **1**, 127–140 (1999).
103. Hazza, A., Pletcher, D. & Wills, R. A novel flow battery: A lead acid battery based on an electrolyte with soluble lead(II). *Phys. Chem. Chem. Phys.* **6**, 1773–1778 (2004).
104. Taylor, S. R. & McLennan, S. M. The Significance of the Rare Earths in Geochemistry and Cosmochemistry. in *Handbook on the Physics and Chemistry of Rare Earths* vol. 11 485–578 (1988).
105. Danil de Namor, A. F., Ritt, M. C., Schwing-Weill, M. J. & Arnaud-Neu, F. Solution thermodynamics of lanthanide(III) cations (La3+, Pr3+ and Nd3+) and cryptands in propylene carbonate and in acetonitrile. *J. Chem. Soc. Faraday Trans.* **86**, 89–93 (1990).
106. Alexandrov, V. & Rosso, K. M. Ab initio modeling of Fe(II) adsorption and interfacial electron transfer at goethite (α-FeOOH) surfaces. *Phys. Chem. Chem. Phys.* **17**, 14518–14531 (2015).
107. Marcus, R. A. Electron transfer reactions in chemistry. Theory and experiment. *Rev. Mod. Phys.* **65**, 599–610 (1993).

Chapter 5 Unveiling the Ce^{3+}/Ce^{4+} Structures and Charge Transfer Mechanism in Sulfuric Acid

5.1 Introduction

Charge transfer (CT) is integral to many processes such as energy storage, chemical conversion, and biological reactions.[1] Theories of CT are crucial to interpret experiments and to predict rates and trends. The Marcus theory (MT) of electron transfer (*E*) was developed to describe homogeneous self-exchange *E* reactions.[1–3] Marcus theory and its extensions rationalize *E* for biological systems,[1,4,5] across liquid-liquid interfaces,[1,6] and for reactions at electrode interfaces.[7–10] In this work we use MT to understand a heterogeneous *E* reaction that initially seems to have discrepancies between the observed kinetics and aqueous ionic structure. Specifically, we study the Ce^{3+}/Ce^{4+} redox couple in sulfuric acid on different electrodes because sulfuric acid is a common electrolyte used in RFB applications. We find notable differences in electrolyte complexation[11] between the Ce^{3+} and Ce^{4+} oxidation states and extreme asymmetry in the observed redox kinetics. A system is considered asymmetric when the charge transfer coefficient (α) is far from 0.5,[12] and Ce^{3+}/Ce^{4+} is reported to have α <0.3.[13–20] The high voltage and tunable redox potentials achievable by Ce^{3+}/Ce^{4+} lead to its myriad of applications, such as organic oxidation and energy storage,[21–26] thus understanding the Ce^{3+}/Ce^{4+} reaction mechanism is important to rationally improve redox kinetics. The work herein highlights the necessity of understanding the cerium ion structure and ligand exchange with the electrolyte to explain the Ce^{3+}/Ce^{4+} redox kinetics and mechanism. Furthermore, the methodology established to study the cerium CT

mechanism is applicable to other redox couples that so far have not been adequately described, like the V^{4+}/V^{5+} redox reaction.[27,28]

The Ce^{3+}/Ce^{4+} charge transfer mechanism has not been satisfactorily determined, leading to unresolved questions about structure-kinetic relationships and the origin of the highly asymmetric α of Ce^{3+}/Ce^{4+} in common electrolytes. We have previously shown that a structural change in the first coordination shell occurs between the Ce^{3+} and Ce^{4+} oxidation states,[11] in agreement with literature showing that Ce^{3+} is preferentially coordinated by water in most acids[29–32] and Ce^{4+} is complexed by anions in acids.[33–38] The density functional theory (DFT)-calculated energy of this complexation explains the shift in the Ce^{3+}/Ce^{4+} redox potential with acid.[21] However, we identified small differences in the extended X-ray absorption fine structure spectroscopy (EXAFS) of Ce^{3+} in sulfuric acid compared to other acids. We were unable to identify the exact structure of Ce^{4+} in sulfuric acid through EXAFS motivating additional EXAFS studies.

The Ce^{3+}/Ce^{4+} charge transfer has typically been studied as a single outer-sphere *E* step despite this evidence of uneven complexation. A recent study of Ce^{3+}/Ce^{4+} kinetics on a gold electrode in sulfuric acid corroborated reports of asymmetry.[13] However, this asymmetric behavior could not be accounted for even with an asymmetric model of MT. Electrostatic effects in the region beyond the outer Helmholtz plane were proposed to control the observed kinetics through a rate-determining step (RDS) involving ligand dissociation. Although this finding highlights the importance of considering chemical steps in the overall mechanism, the derived rate law is inconsistent with the experimentally observed exchange current densities as a function of Ce^{4+} concentration that we report here.

We hypothesize that the Ce^{3+}/Ce^{4+} CT can be explained by considering ligand exchange and electron transfer steps in series. This type of mechanism is an example of a mechanism with

chemical (*C*) and *E* steps (e.g., *CE*, *EC*, or *CEC* mechanisms).[39,40] The *CE* reaction mechanism is shown in **Scheme 5.1a**, where M is a metal ion undergoing an electron transfer and X^- is a complexing ligand. From **Scheme 5.1a**, the first step is a ligand exchange with free energy ΔG_1. We define ligand exchange or complexation as the replacement of a water molecule with a complexing ligand in the first solvation shell of M.[41] Then, an electron transfer occurs with free energy ΔG_2, where the species before and after the *E* are complexed by the same molecules. When the electrode potential U is equal to the standard redox potential of the overall reaction, U°, ΔG_1 is equal to the negative of ΔG_2.

Multiple studies have developed mathematical models for the kinetics and current-potential responses of coupled electron transfer-chemical reactions,[7,39,40,42–47] as well as tested the validity of these mechanisms by fitting them to experimental data of organic compounds[39,43,48] and heterogeneous metal ion complexes.[7,46] MT has been used to understand the *E* step in coupled *E* and *C* systems such as organic compounds,[43,49] transition metal ions,[7,50] transition metal oxides,[47] and coupled redox inactive metal ion-organic electron acceptor pairs.[51] **Scheme 5.1b** shows how the free energy parabolas derived from standard MT can be used to describe the free energies of the species involved in a *CE* mechanism. The difference in values of the free energy curves at the reaction coordinate value of 1 gives information about the reorganization energy of the *E* step, λ_2. Importantly, several of these studies note that an ongoing challenge in identifying CT mechanisms is obtaining accurate structural information of reactants and products[50] as well as the intermediate species[43] undergoing charge transfer.

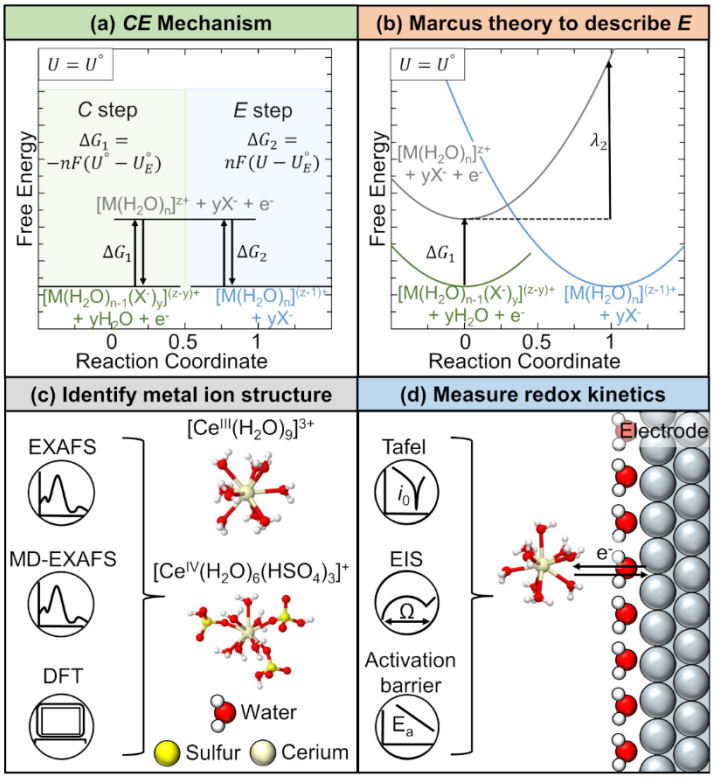

Scheme 5.1. (a) Steps for a *CE* mechanism, and **(b)** free energy curves for the species involved in the mechanism. The metal ion, M, undergoes a *CE* mechanism between oxidation states of M^{z+} and $M^{(z-1)+}$, with M^{z+} undergoing a ligand exchange (*C* step) before the *E* step. System free energy is depicted at electrode potential $U = U^{\circ}$. The redox potential of the overall reaction is U°, and the redox potential of the electron transfer step is U_E°. The free energy of the *E* step is $\Delta G_2 = nF(U - U_E^{\circ})$. This difference is related to the *C* step energy, ΔG_1, through the Nernst equation. The reorganization energy, λ_2, is defined as the energy required to change the reactant and solvent nuclear configuration to the configurations of the product. To inform the Ce^{3+}/Ce^{4+} charge transfer mechanism, we identify the **(c)** Ce^{3+} and Ce^{4+} structures using EXAFS, Molecular-dynamics EXAFS (MD-EXAFS), and DFT calculations, and the **(d)** Ce^{3+}/Ce^{4+} kinetics (exchange current density, i_0, and activation barrier, E_a) in sulfuric acid using Tafel plots and Electrochemical Impedance Spectroscopy (EIS) to extract charge transfer resistances (Ω) at different temperatures.

Herein, we confirm the Ce^{3+} and Ce^{4+} structures and present a new charge transfer mechanism in sulfuric acid. We use EXAFS and molecular dynamics-EXAFS (MD-EXAFS) of the Ce L_3-edge and K-edge to address unresolved uncertainties about the structure of Ce^{3+} and Ce^{4+} in sulfuric acid (**Scheme 5.1c**) and confirm the favorability of these structures through DFT modeling. Ce^{3+} coordinates with nine waters as $[Ce^{III}(H_2O)_9]^{3+}$ and Ce^{4+} likely complexes with six waters and three bisulfates as $[Ce^{IV}(H_2O)_6(HSO_4)_3]^{+}$. Despite the change in the inner-sphere ligand coordination between Ce^{3+} and Ce^{4+}, we show the Ce^{3+}/Ce^{4+} charge transfer kinetics are similar as a function of Ce^{4+} concentration and temperature on platinum (Pt) and glassy carbon (GC). We

use two independent methods to obtain standard rate constants and CT coefficients for the Pt and GC rotating disk electrodes (RDEs), namely the Tafel method and the charge transfer resistance method (**Scheme 5.1d**). The similar rate constants, CT coefficients, and activation energies on two different electrode surfaces implies an outer-sphere charge transfer mechanism. We measure a low cathodic CT coefficient of $\alpha = 0.23$, in qualitative agreement with prior reports of an asymmetric CT reaction (see **Chapter 1.3.2**). We explain this behavior through a mechanism where the anion-complexed Ce^{4+} species rapidly undergoes a ligand exchange to form $[Ce^{IV}(H_2O)_9]^{4+}$, which is then followed by a rate-determining outer-sphere *E* between $[Ce^{IV}(H_2O)_9]^{4+}$ and $[Ce^{III}(H_2O)_9]^{3+}$. We derive a rate law based on this *CE* mechanism that results in a better fit to the experimentally observed kinetic data than a Butler-Volmer (BV) rate law. Using this *CE* rate law, we extract parameters such as reorganization energy and Gibbs free energy of the ligand exchange step. We find agreement between the experimentally fitted and DFT-predicted reorganization energies and ligand exchange free energies. We show that the fitted ligand exchange free energy agrees qualitatively with the shift in redox potential observed for the Ce^{3+}/Ce^{4+} redox couple between $HClO_4$ (a non-complexing acid) and H_2SO_4.[21] These findings demonstrate the necessity of considering ligand exchange energetics to rationalize CT kinetics and shed light on the Ce^{3+}/Ce^{4+} charge transfer reaction, which will aid various electrochemical applications.

5.2 Experimental and computational methods

5.2.1 Experimental methods

Solution preparation. The Ce^{3+} solution preparation methods and chemical sources are described in detail elsewhere.[11] To prepare solutions of mixed oxidation state, i.e., some Ce^{3+} and some Ce^{4+} present, or entirely Ce^{4+}, cerium(III) carbonate hydrate (same source as used for Ce^{3+} solutions) was added to 2 M H_2SO_4 and stirred until all cerium had dissolved and a clear solution

had formed. Then, using a two-compartment glass electrochemical cell discussed in more detail elsewhere,[11] Ce^{3+} ions were electrochemically oxidized to Ce^{4+} until the desired ratio of Ce^{4+} to Ce^{3+} was achieved using a titanium-based anode from De Nora (coating type DN-240 or DN-300) as the working electrode, a graphite rod (Alfa Aesar™, 99.9995% metals basis) as the counter electrode, and a double junction Ag/AgCl electrode (saturated KCl, Pine Research) as the reference electrode. The concentrations of Ce^{3+} and Ce^{4+} were measured using titration, as described in detail elsewhere.[11]

Electrochemistry cell setup. For room temperature kinetic measurements on either the Pt or GC working electrodes, the same electrochemical cell was used that was used for solution preparation, with the same reference and counter electrodes. For activation barrier measurements, a jacketed two-compartment electrochemical cell (Adams & Chittenden Scientific Glass) was used and a refrigerated/heated bath circulator (Fisher Scientific) controlled the temperature of the water. The temperature of the solution was measured before kinetic measurements. A VSP potentiostat (Biologic Science Instruments USA) was used to supply voltage and measure kinetics. Before kinetic measurements, the working electrode compartment solution was sparged for at least 15 minutes with nitrogen (Metro Welding Supply Corp, pure compressed nitrogen) to minimize oxygen contamination, and the solution was continuously blanketed with nitrogen. A Modulated Speed Rotator (Model AFMSRCE, Pine Research) was used to control the rotation rate of the RDEs, which were inserted into the E5TQ ChangeDisk Tip (Pine Research). To eliminate the effect of cerium crossover, no kinetic measurements were taken beyond 48 hours from when the solution had been added to the cell.

Experimental XAFS data collection, normalization, and fitting. X-ray absorption fine structure (XAFS) measurements consisting of both X-ray near edge spectroscopy (XANES) and

extended X-ray absorption structure (EXAFS) were collected at the Advanced Photon Source at Argonne National Laboratory (L_3-edge collected at 20 BM, K-edge collected at 20 ID-B,C). Data analyzed in this paper included EXAFS of a CeO_2 standard and 0.1 M Ce^{4+} in 2 M H_2SO_4 at the Ce L_3-edge from our previous work[11] (newly normalized) and additional EXAFS of cerium species at the Ce L_3- and K-edges.

The Ce^{3+} and Ce^{4+} solutions used in the additional XAFS measurements were shipped to the beamline in either glass vials or capillary tubes. To ensure the solutions of Ce^{4+} maintained their oxidation state, they were shipped in dry ice and stored in a freezer with temperatures less than 0 °C. The frozen solutions were thawed and syringed into solution holders immediately before the EXAFS measurements. The XANES of the Ce^{4+} solutions were compared to CeO_2 XANES to confirm 100% Ce^{4+} oxidation state. The $CeCl_3$-$7H_2O$ and CeO_2 standards were prepared by mixing $CeCl_3$ (Strem Chemicals, Inc., 99.9% pure) and CeO_2 (Alfa Aesar™, 99.99%), respectively, with boron nitride (BN, Sigma Aldrich) in air, grinding using a mortar and pestle, and then forming a pellet using a pellet press with a pressure of 10,000 psi. The ratios of either $CeCl_3$ or CeO_2 to BN for each edge were as follows: 3.3 mg $CeCl_3$:166 mg BN for $CeCl_3$-$7H_2O$ standard at the L_3-edge; 50 mg $CeCl_3$:250 mg BN for $CeCl_3$-$7H_2O$ standard at the K-edge; 4.78 mg CeO_2:139 mg BN for CeO_2 standard at the L_3-edge; and 50 mg CeO_2:250 mg BN for CeO_2 standard at the K-edge.

For the Ce L_3-edge XAFS measurements, the same monochromator was used as previously described,[11] as were the processes for harmonic contamination suppression and incident beam intensity measurement. For all Ce L_3-edge XAFS except the 0.05 M Ce^{4+}/2M H_2SO_4 solution XAFS in **Fig. 5.4f**, data collection was performed in transmission mode. A chromium (Cr) foil was used as a reference to verify energy reproducibility, because its K-edge energy (5989 eV) is close to the Ce L_3-edge energy (5723 eV). The Ce L_3-edge XAFS of the 0.05 M Ce^{4+}/2M H_2SO_4

solution in **Fig. 5.4f** was collected in fluorescence mode due to low transmission signal, using a 13-element germanium fluorescence detector. The Ce K-edge XAFS studies were carried out at 295 K. The incident beam was monochromatized using a pair of Si(311) crystals. Higher order harmonics were suppressed by detuning the monochromator to reduce the incident X-ray intensity by approximately 15%. Argon-filled ion chambers were used for the I_0, I_t, *and* I_{ref} detectors. All Ce K-edge XAFS were collected in transmission mode, and the XANES of a CeO_2 standard was used to confirm energy reproducibility several times throughout the data collection. At least two scans were collected for each sample. For the Pt L_3-edge XAFS data discussed in the SI, the XAFS measurements were collected in a polyacrylate electrochemical cell designed for beamline measurements described in more detail elsewhere.[52]

The XAFS data were normalized using the software ATHENA,[53] and all normalization parameters used are listed in **Appendix A**. The repeating scans for each sample were merged after energy alignment and normalization. The Fourier transformed EXAFS data used an R_{bkg} parameter of 1.4 Å for all K-edge samples and 1.2 Å for all L_3-edge samples. All plotted EXAFS data have unadjusted R space values. No attempt was made to correct for multi-electron excitation (MEE) effects in the L_3-edge data based on our previous findings that correcting for MEE did not improve fitting results.[11]

The normalized and k^2 weighted EXAFS were analyzed using the software ARTEMIS,[53] with R and k ranges specified in **Appendix A**. FEFF9 was used to generate paths from the known structures of $CeCl_3$-$7H_2O$ (sourced from the Cambridge Structural Database[54,55]) and CeO_2 (source included in our previous work[11]) to fit the standards for Ce^{3+} and Ce^{4+}. For the $CeCl_3$-$7H_2O$ standard, the Ce-O and Ce-Cl were used in the fit. The amplitude reduction factor (S_0^2) was first fixed at a value of 1.0 while the value of shift in threshold energy (ΔE_0) and path specific values

(the shift in scattering distance (ΔR), the Debye-Waller factor (σ^2), and the coordination numbers (*CN*) were obtained by fitting. The *CN* were fixed to sum to 9, and these fitted results were then set as fixed parameters to obtain S_0^2. Fits of the $CeCl_3$-$7H_2O$ data for the K- and L_3-edges are shown in **Appendix A**, as are the fitted parameter values. For CeO_2, two Ce-O shells (Ce-O_1 and Ce-O_2) and one Ce-Ce shell were included in the fit. The S_0^2, ΔE_0, and path specific ΔR and σ^2 were obtained by fitting, but *CN* of Ce-O_1 was set to 8, *CN* of Ce-Ce was set to 12, and *CN* of Ce-O_2 was set to 24. Fits of the CeO_2 data and the fitted parameter values are included in **Appendix A**.

To fit the k^2 weighted EXAFS data of cerium solutions, FEFF9 was used to generate paths with self-consistency in JFEFF from DFT-predicted cerium structures. The final fit of Ce^{3+} in H_2SO_4 was a Ce-O scattering shell co-fit to Ce L_3-edge EXAFS of 0.1 M Ce^{3+}/2 M H_2SO_4 and Ce K-edge EXAFS of 0.05 M Ce^{3+}/2 M H_2SO_4. The values of S_0^2 and ΔE_0 were set as fixed global parameters and were obtained from the fits of the $CeCl_3$-$7H_2O$ standard. The *CN*, ΔR, and σ^2 were all obtained by co-fitting. Ce K-edge data of 0.05 M Ce^{3+} in 2 M MSA, 2 M TFSA, and 2 M H_2SO_4 were fit with a Ce-O scattering shell with the same R range and k range as used for the K-edge data in the co-fit. The final fit of Ce^{4+} in H_2SO_4 was a co-fit using Ce L_3-edge EXAFS of 0.1 M Ce^{4+}/2 M H_2SO_4 and Ce K-edge EXAFS of 0.05 M Ce^{4+}/2 M H_2SO_4, with Ce-O and Ce-S shells. Four path-specific parameters (*CN*, ΔR, σ^2, and the third cumulant, σ^3) were obtained by co-fitting, and values for S_0^2 and ΔE_0, which were set as fixed global parameters, were obtained from the fit of the CeO_2 standard. See **Appendix A** for R and k ranges.

Electrode pretreatment. To prepare the rotating disk electrodes (RDEs) for kinetic measurements, a polishing, sonication, and electrochemical cleaning procedure was followed for each electrode material. For GC, the RDE was polished for three minutes using a 0.3 μm alumina

slurry (Allied High Tech Products, Inc., DeAgglomerated), and then sonicated (Fisher Scientific, 2.8 L Ultrasonic Bath) in water purified with the MilliporeSigma™ Synergy™ UltrapureWater Purification System (18.2 MΩ cm resistivity) for 45 minutes. Electrochemical Impedance Spectroscopy (EIS) was used to measure the solution resistance, and then a series of cyclic voltammograms (CVs) were conducted in the range 0.36 V vs. RHE to 1.16 V vs. RHE, i.e., the non-Faradaic region, as a function of scan rate in 2 M H_2SO_4. If no impurities were detected from the CVs, the double layer capacitance could be calculated and the GC was ready for kinetic measurements of the cerium redox couple. For Pt, which was more sensitive to oxidation and thus required a more rigorous cleaning procedure, the RDE was first polished for three minutes using a 0.3 μm alumina slurry, and then sonicated in Millipore water for 45 minutes. Then the RDE was dried and polished for three minutes using a 0.05 μm alumina slurry (Allied High Tech Products, Inc., DeAgglomerated) before being sonicated again in Millipore water for 45 minutes. The Pt RDE was subjected to 50 electrochemical cleaning cycles in 2 M H_2SO_4 (CV with a potential range of −0.35 V vs. RHE to 1.56 V vs. RHE and a scan rate of 100 mV/s) to remove any contaminants on the Pt surface. Following the cleaning cycles, the Pt RDE Hydrogen Underpotential Deposition (HUPD) peaks were characterized, and the electrochemically active surface area (ECSA) was calculated by dividing the amount of charge associated with the desorption of a monolayer of adsorbed hydrogen on the Pt-surface by the specific charge of Pt (210 μC cm^{-2}). If the HUPD peaks demonstrated any oxygen contamination or contamination on the Pt surface, e.g., extremely low or misshapen hydrogen desorption peaks, then the cleaning cycles were repeated with additional N_2 sparging and blanketing at higher flow rates until HUPD peaks were stable. Pt kinetic data was only used if the ECSA calculated from the HUPD peaks was greater than or equal to the

geometric surface area of the Pt RDE (0.196 cm^2) and had a corresponding roughness factor that was less than 2.5.

Kinetic measurements. To measure the kinetic activity of the Pt and GC electrodes, the exchange current density of the reaction, i_0, the Tafel slope, b, and the activation energy, E_a, were extracted. Two independent methods of obtaining the exchange current density were used: the Tafel method and the charge transfer resistance method. In the Tafel method, a series of fixed potentials were applied to the working electrode and the resulting steady state currents were measured to achieve a polarization curve. The applied potentials were compensated for solution resistance using EIS measurements. The steady state currents were then normalized by surface area to obtain steady state current densities. For Pt measurements, the ECSA from HUPD measurements were used to normalize the currents, whereas the GC kinetic activity was normalized by its geometric surface area of 0.196 cm^2. From the steady state current densities, a Tafel plot was constructed from the Tafel equation (see **Chapter 2**). The Tafel slope was extracted from the Tafel plot by fitting a linear trendline in the overpotential range of −0.250 to −0.118 V[12] and extrapolating to $\eta = 0$ to obtain i_0.

In the charge transfer resistance method, the charge transfer resistance, R_{ct}, was extracted from a Nyquist plot using EIS. The solution resistance, R_s, and charge transfer resistance, R_{ct}, was found by fitting an electrical circuit, assumed here to be the Randles circuit, and finding the intercepts of the x-axis of the semi-circle, which is the real portion of the impedance. R_s is the left-most x-intercept (i.e., high frequencies), and R_{ct} is the x-intercept at the right-most side of the semi-circle (i.e., low frequencies). See **Chapter 2** for more details.

Obtaining similar exchange current density values from the Tafel method and the charge transfer method lends confidence in the kinetic values reported, and so the exchange current densities were measured using both methods for all values reported in this study.

A competitive redox reaction that will occur at similar potentials as the Ce^{3+}/Ce^{4+} electron transfer is the oxygen evolution reaction (OER).[56] To avoid measuring OER activity, only the reduction currents of Ce^{4+} to Ce^{3+}, which occur at potentials at which OER is negligible, were used to determine i_0 from the Tafel method. As noted, oxygen reduction contributions are mitigated by purging the electrolyte with nitrogen.

To ensure the data reported herein were kinetically controlled, all activity measurements were collected using RDEs. The observed activity for the GC and Pt RDEs was no longer dependent on rotation rate at 2000 rpm, so all reported kinetic activity was collected at a rotation speed of 2000 rpm. Additionally, a Koutecký-Levich analysis was conducted for the Pt RDE (**Fig. 5.1**) at a 0.02 M Ce^{4+} concentration (total Ce concentration of 0.05 M), and it was found that using the kinetically limited current from the Koutecký-Levich analysis resulted in an exchange current density that was less than 1% different than the exchange current density extracted from the Tafel method.

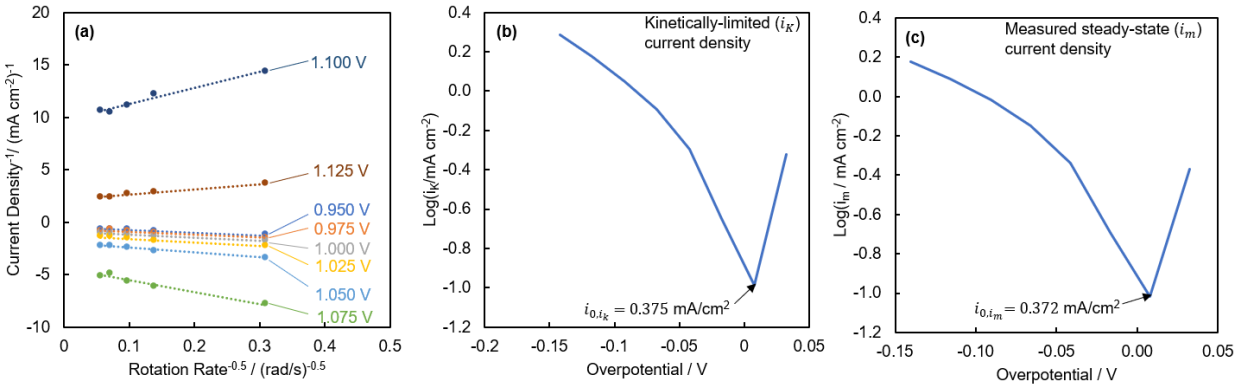

Figure 5.1. Koutecký-Levich analysis of Ce^{3+}/Ce^{4+} kinetics on Pt RDE. (a) Koutecký-Levich plot for Pt RDE in 2 M H_2SO_4/0.05 M Ce solution (0.02 M Ce^{4+}), **(b)** Tafel plot for Pt RDE in 2 M H_2SO_4/0.05 M Ce solution (0.02 M Ce^{4+}) using kinetically limited current densities, extracted from the Koutecký-Levich plot in **(a)**, and **(c)** Tafel plot for Pt RDE in 2 M H_2SO_4/0.05 M Ce solution (0.02 M Ce^{4+}) using measured steady state current densities.

Several precautions were taken to ensure the kinetic data were accurate and reproducible and the concentrations of Ce^{3+} and Ce^{4+} were accurate. As mentioned, only electrode surfaces with no indication of impurities from the CV were used for analysis. To ensure that the kinetic measurements were reproducible, the reported i_0 and Tafel slope values were determined from the average of three measurement runs at a specific experimental condition (either Ce^{4+} concentration or temperature), with uncertainty represented by one standard deviation. The accuracy of the concentration of Ce^{4+} relative to the total amount of cerium was determined from three methods for each data point: (1) titration, (2) using the open circuit voltage (OCV) and obtaining concentrations from the Nernst equation, and (3) the UV-Vis spectrum of the solution in the working electrode compartment of the electrochemical cell compared to other UV-Vis spectra at similar Ce^{4+} concentrations. Only data points that had Ce^{4+} concentrations results that were less than 10% different between titration and OCV, and with UV-Vis spectrum in qualitative agreement with the expected peak intensity from Ce^{4+}, were used for analysis. The UV-Vis spectra of Ce^{3+} and Ce^{4+} are discussed in more detail in our previous work.[11]

Kinetic data fitting. To fit the kinetic rate laws to the experimentally collected kinetic data, the normalized mean square error (NMSE) was calculated for each data set ($i_0[Ce^{4+}]$, $i_0[T]$, $b[Ce^{4+}]$, $b[T]$) using **Eq. 5.1**, where $y_{obs,i}$ is the experimentally observed data point i, $y_{mod,i}$ is the modeled data point i, $\overline{y_{obs}}$, is the mean of the experimentally observed data points, $\overline{y_{mod}}$ is the mean of the modeled data points, and N is the number of i data points.

$$NMSE = \frac{\sum_{i=1}^{N}\left(y_{obs,i} - y_{mod,i}\right)^2}{N\overline{y_{obs}}\,\overline{y_{mod}}} \quad \textbf{(5.1)}$$

The modeled data points were calculated using the rate laws discussed below by using the Tafel method to extract exchange current densities and cathodic Tafel slopes from modeled kinetic currents as a function of overvoltage. The NMSE for each set of data was then weighted equally and summed together, and a solver function was used to minimize the total summed error by varying relevant fitting parameters. For the BV rate law, the fitting parameters were standard rate constant, k_0, charge transfer coefficient, α, and activation energy, E_a. For the two-step *EC* and *CE* mechanisms, the fitting parameters were the reorganization energy, a preexponential factor, and the equilibrium constant of the *C* step. The uncertainty in the fitted parameters was the standard error of the value, estimated using the jackknife method.[57]

5.2.2 Computational methods

MD-EXAFS spectra calculations. Molecular dynamics EXAFS (MD-EXAFS) spectra of $[Ce^{III}(H_2O)_9]^{3+}$, $[Ce^{IV}(H_2O)_9]^{4+}$, $[Ce^{III}(H_2O)_8SO_4]^{+}$, and $[Ce^{IV}(H_2O)_8SO_4]^{2+}$ complexes were generated by averaging the EXAFS signals of geometry snapshots of the complex in solution over a molecular dynamics trajectory. Carr-Parrinello molecular dynamics (CPMD) were performed in the NWChem software[58] to generate structures of the complexes in solution, which were then used as inputs to the FEFF9 code[59] to calculate EXAFS signals due to scattering paths. The CPMD simulations were performed in an 8×8×8 $Å^3$ periodic box using the PBE functional in the canonical ensemble. Simulations of each cerium complex were run for 50 ps post-equilibration, and one snapshot was taken each ps to generate 50 geometry snapshots. The cerium complexes were explicitly solvated with 15 water molecules (to give a solution density of ≈ 1.0 g/cm^3). All hydrogen atoms were given a fictitious mass of 2 amu to decrease the frequency of O-H bond vibrations, allowing a larger time step of 5.0 au to be used for computational tractability. The Nosé-Hoover thermostat[60] was used to maintain the temperature of the system at 300 K throughout the

simulation, and the periods of the ionic and electronic thermostats were set to 1200 a.u. All non-cerium atoms were treated with the Hamann pseudopotential,[61] and the cerium ion was treated with the Troullier-Martins pseuodopotential.[62]

Each sampled geometry snapshot was fed into the FEFF9 code to calculate an EXAFS spectrum. Each spectrum was calculated using a cluster radius of 6 Å centered on the cerium ion. The 50 geometries were averaged to produce a final EXAFS spectrum of the complex in solution. To generate spectra without sulfate scattering pathways, those paths were omitted during FEFF9 runs.

Reorganization energy and anion complexation free energy calculations. Reorganization energies were calculated for the $[Ce^{III}(H_2O)_9]^{3+}/[Ce^{IV}(H_2O)_9]^{4+}$ CT. All calculations were performed in the NWChem software unless otherwise noted. DFT-optimized structures of the cerium ion and its first coordination shell (nine water molecules) were used at each step in the process. For all geometry optimizations and calculations, a mixed basis set was used with the Stuttgart RSC 1997 ECP basis set[63] for the cerium ion, and the 6-31+G* basis set[64] for all non-cerium atoms. This basis set was used to maintain computational tractability and accuracy. The calculated reorganization energy was shown to converge with this basis set (see converged outer-sphere reorganization energies in **Appendix B**). Implicit solvation was included using COnductor-like Screening MOdel (COSMO) with default parameters.[65] The B3LYP functional with Grimme's D3 dispersion correction[66] was employed for all electron transfer calculations.[66–68]

The reorganization energy λ includes inner- (λ_i) and outer-sphere (λ_o) contributions (see **Chapter 2.6.2**), which were calculated separately. λ_i was approximated by Nelsen's four-point method (**Eq. 5.2**),[69] in which single-point energy calculations of the oxidized and reduced species

geometries (with COSMO) at both the oxidized and reduced charge states were used to estimate the energetics of inner sphere reorganization.

$$\lambda_i = [E_{ox}(R^{red}) - E_{ox}(R^{ox}) + E_{red}(R^{ox}) - E_{red}(R^{red})]/2 \quad \textbf{(5.2)}$$

where R^{ox} and R^{red} are the optimized geometries of the oxidized and reduced species, respectively, and E_{ox} and E_{red} are the energies of the oxidized and reduced states, respectively, evaluated at the given geometry. Energies of each species were evaluated at each state using the computational settings described above.

The outer-sphere reorganization energy, λ_o, was obtained within the PCM framework[70] in the GAMESS[71] software. The PCM framework was employed to calculate solvation free energy at different polarization potentials (**Eq. 5.3**).

$$\lambda_o = \left[G_{ox}^{neq} - G_{ox}^{eq} + G_{red}^{neq} - G_{red}^{eq}\right]/2 \quad \textbf{(5.3)}$$

where G_{ox}^{eq} and G_{ox}^{neq} are the free energy of the oxidized geometry evaluated at the oxidized and reduced polarization potentials, respectively. G_{red}^{eq} and G_{red}^{neq} are the free energy of the reduced geometry evaluated at the reduced and oxidized polarization potentials, respectively.

In this framework, the electrode surface was modeled as a perfect conductor and water was implicitly treated as the solvent, meaning that the dielectric constant assumed in the λ_o calculation was the dielectric constant of water. Cavity surfaces that contain the cerium complex were defined using the Gauss-Bonet tessellation procedure, and cavity sizes for each atom were generated using their Van der Waal radius using the default GAMESS radii, except cerium, which was estimated as twice the covalent radius, 4.08 Å.[72] The outer sphere reorganization energies were calculated in

the Born-Oppenheimer limit using inertial polarization,[73] however the self-consistent limit was shown to yield results less than 1 kJ/mol different for the systems studied. The solvated radius of the water molecules used to define the distance of the cavity from the electrode surface was obtained from experiment[74] to be 3.00 Å. Lastly, the anion complexation free energies for the $[Ce^{IV}(H_2O)_6(SO_4)_3]^{2-}$ and $[Ce^{IV}(H_2O)_6(HSO_4)_3]^{+}$ species were calculated in the same manner as our previous paper.[11]

5.3 Results and discussion

5.3.1 Structures of Ce^{3+} and Ce^{4+} in sulfuric acid from EXAFS

We use Ce K-edge and L_3-edge EXAFS to resolve uncertainties in the Ce^{3+} and Ce^{4+} structures in sulfuric acid from our prior work solely at the L_3-edge.[11] The first uncertainty was the Ce^{3+}-O coordination number of nine, which was previously obtained without using a known solid crystalline standard for calibration.[11] The second uncertainty was whether Ce^{3+} in sulfuric acid had Ce-sulfate or bisulfate complexation. The third uncertainty was in the accuracy of the fit of the EXAFS data of Ce^{4+} in sulfuric acid at the Ce L_3-edge, which did not prove the presence of sulfate or bisulfate in the first coordination shell of Ce^{4+}.[11] Herein, we use $CeCl_3$-$7H_2O$ and CeO_2 standards to confirm our previously reported Ce-O coordination numbers and use Ce K-edge and additional L_3-edge EXAFS data to show evidence that Ce^{3+} coordinates solely with water and Ce^{4+} complexes with three bisulfate anions. The Ce K-edge allows for quality data at higher k values than the L_3-edge, where interference from the L_2-edge occurs for lanthanides between 9 $Å^{-1}$ and 15 $Å^{-1}$. Thus, the K-edge gives more accurate structural information for the coordination numbers and scattering distances between Ce^{4+} and its surrounding atoms.[31] Measuring at an additional edge allows for co-fitting both sets of EXAFS data, which will improve the fit statistics. We also collect EXAFS at the Ce L_3-edge to elucidate the influence of Ce ion concentration and acid

concentration on the cerium structure. Our MD-EXAFS predictions of different possible cerium complexes help to interpret the experimental spectra.

We show the Ce^{3+}-O coordination number in sulfuric acid is nine using co-fits of EXAFS data at the Ce L_3- and K-edges. To obtain accurate coordination numbers for Ce^{3+} solutions we first measure EXAFS of a Ce^{3+} standard, $CeCl_3$-$7H_2O$, at both Ce L_3- and K-edges. We determine an amplitude reduction factor, S_0^2, value of 1.5 for Ce^{3+} at the Ce K-edge by fitting the $CeCl_3$-$7H_2O$ standard using ARTEMIS[53], as shown in **Fig. 5.2a**. The fit of the magnitude component in the R space and the fit in the k space of the $CeCl_3$-$7H_2O$ standard and fitting parameters are included in **Appendix A**, as is the fit of the $CeCl_3$-$7H_2O$ standard at the Ce L_3-edge. The S_0^2 value for the Ce L_3-edge was 1.1. Using these S_0^2 values for the Ce K- and L_3-edges, we co-fit the EXAFS of a 0.05 M Ce^{3+} + 2 M H_2SO_4 solution at the Ce K-edge, as seen in **Fig. 5.2b,** and a 0.1 M Ce^{3+} + 2 M H_2SO_4 solution at the Ce L_3-edge, and we obtain a Ce^{3+}-O coordination number (*CN*) of 8.7 ± 0.6. Different concentrations were necessary at the two Ce edges to optimize signal while avoiding energy attenuation through the sample. The *CN* is consistent with the value of 9 that we previously reported for Ce^{3+} in acidic solutions including sulfuric acid.[11] From the fit, we also obtain a Ce^{3+}-O scattering distance of 2.541 ± 0.004 Å, which agrees within 0.01% of our prior reported Ce^{3+}-O distance in sulfuric acid.[11] The Ce K-edge fits in R and k-space and the Ce L_3-edge fits are in **Appendix A**. By using both K- and L_3-edges and a standard, the fit here gives additional confidence to our previous report on the Ce^{3+}-O coordination number and distance in sulfuric acid.

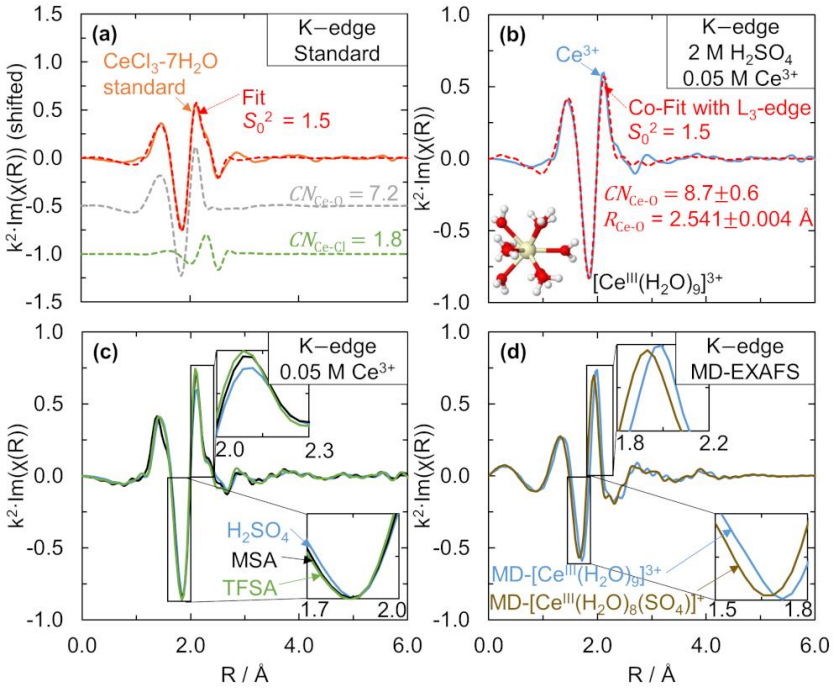

Figure 5.2. Ce K-edge $k^2 \cdot \chi(R)$ EXAFS and fits for different Ce^{3+} species. **(a)** $CeCl_3$-$7H_2O$ standard (orange solid line) with fit (red dashed line), and Ce-O and Ce-Cl path contributions (shifted in y-axis). **(b)** 0.025 M $Ce_2(CO_3)_3$ in 2 M H_2SO_4 (blue solid line) with fit using Ce-O path (red dashed line). Inset structure shows $[Ce^{III}(H_2O)_9]^{3+}$ from a molecular dynamics (MD) snapshot. **(c)** 0.025 M $Ce_2(CO_3)_3$ in 2 M H_2SO_4 (blue solid line), 2 M MSA (black solid line), and in 2 M TFSA (light green solid line). Insets are zoomed in portions of the EXAFS spectra. **(d)** Simulated MD-EXAFS of $[Ce^{III}(H_2O)_9]^{3+}$ (blue solid line) and $[Ce^{III}(H_2O)_8(SO_4)]^{+}$ (brown solid line) for comparison to experimental data in **(a)–(c)**. Insets are zoomed in portions of the EXAFS spectra.

We also confirm the dominant Ce^{3+} structure in sulfuric acid is $[Ce^{III}(H_2O)_9]^{3+}$ by comparing the EXAFS of Ce^{3+} in H_2SO_4 to MD-EXAFS spectra. The co-fit of the EXAFS of Ce^{3+} in 2 M H_2SO_4 did not improve with the addition of a Ce^{3+}-S scattering pathway (**Appendix A**). We compare our experimental Ce K-edge EXAFS of Ce^{3+} in 2 M acids in **Fig. 5.2c**. Ce^{3+} coordinates only with water in triflic acid (TFSA)[31] and methanesulfonic acid (MSA)[11] and so spectra of Ce^{3+} in TFSA and MSA can serve as Ce^{3+}-water coordinated references. We observe no shift in the peak centered at ~1.85 Å and a slight shift to the right in the peak at 2.1 Å in H_2SO_4 compared to MSA or TFSA. From the MD-EXAFS of $[Ce^{III}(H_2O)_9]^{3+}$ and $[Ce^{III}(H_2O)_8(SO_4)]^{+}$ in **Fig. 5.2d**, we see a shift to shorter distances in both peaks when Ce^{3+} is complexed by sulfate because the average Ce^{3+}-O scattering distance is shortened. Because we do not see this shift to the left in our experimental EXAFS of Ce^{3+} in H_2SO_4, as shown qualitatively in **Fig. 5.2c**.

To confirm the observation that the Ce3+-O bond does not decrease quantitatively, we compared the EXAFS of Ce^{3+} at the Ce K-edge and fits with a Ce-O scattering path in three different acids: 2 M H_2SO_4 (**Fig. 5.3a-c**), 2 M CF_3SO_3H (TFSA, **Fig. 5.3d-f**), and 2 M CH_3SO_3H (MSA, **Fig. 5.3g-i**). Although the CN obtained from the Ce-O fit for Ce^{3+} in H_2SO_4 is lower than that obtained from the co-fit, the uncertainty ($\pm$0.6) is large enough to suggest coordination with either 8 or 9 water molecules. Our DFT and EXAFS evidence of Ce^{3+} coordination with 9 water molecules from our previous work[11] resolves this uncertainty from the fit of the EXAFS at just the Ce K-edge. The Ce^{3+}-O scattering distance in H_2SO_4 is slightly larger than the scattering distance in either TFSA or MSA. If Ce^{3+} were complexed by sulfate or bisulfate in H_2SO_4, the Ce^{3+}-O distance would be expected to be smaller than a Ce^{3+}-O scattering distance in which the Ce^{3+} was coordinated only by water, e.g., Ce^{3+} in MSA or TFSA. Based on this evidence that Ce^{3+} does not complex with sulfate or bisulfate, and the evidence that the Ce^{3+}-O coordination number is nine, we conclude that Ce^{3+} exists as $[Ce^{III}(H_2O)_9]^{3+}$, which is consistent with our previous density functional theory (DFT)-predicted free energies.[11]

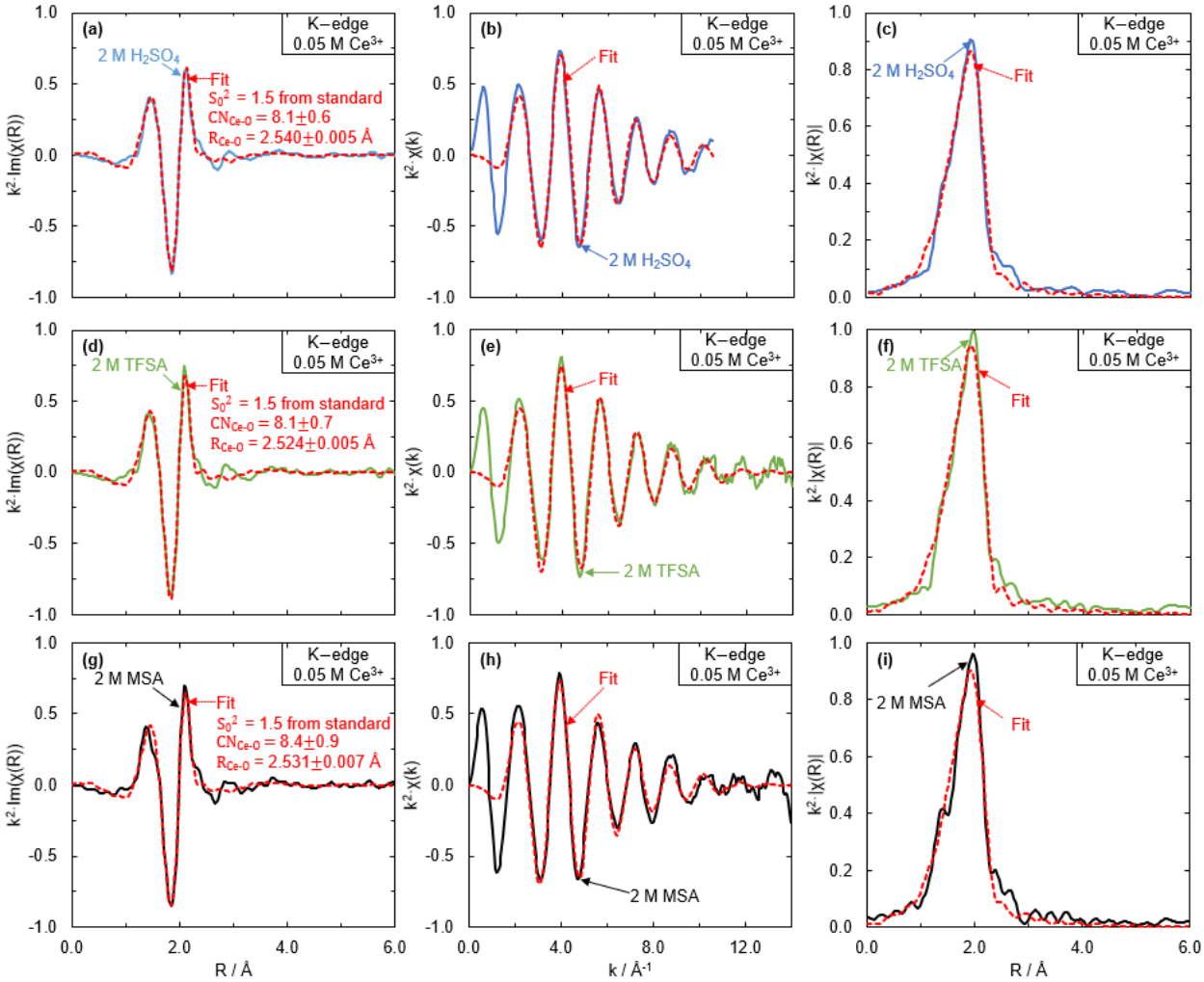

Figure 5.3. Ce K-edge $k^2 \cdot \chi(R)$ EXAFS and fits of Ce^{3+} in H_2SO_4, TFSA, and MSA with Ce-O scattering path. Ce K-edge EXAFS of 0.025 M $Ce_2(CO_3)_3$ in 2 M H_2SO_4 (blue solid line) with fit (red dashed line) using a Ce-O scattering pathway in the **(a)** R space (imaginary), **(b)** k space, and **(c)** R space (magnitude). Ce K-edge EXAFS of 0.025 M $Ce_2(CO_3)_3$ in 2 M TFSA (green solid line) with fit (red dashed line) using a Ce-O scattering pathway in the **(d)** R space (imaginary), **(e)** k space, and **(f)** R space (magnitude). Ce K-edge EXAFS of 0.025 M $Ce_2(CO_3)_3$ in 2 M MSA (black solid line) with fit (red dashed line) using a Ce-O scattering path in the **(g)** R space (imaginary), **(h)** k space, and **(i)** R space (magnitude).

Comparisons between experimental Ce^{4+} EXAFS and MD-EXAFS of possible Ce^{4+} species in H_2SO_4 imply that Ce^{4+} complexes with either sulfate (SO_4^{2-}) or bisulfate (HSO_4^-) anions in sulfuric acid. From **Fig. 5.4a**, we observe a shift in the Ce-O scattering peak as we go from EXAFS of Ce^{3+} to Ce^{4+} in H_2SO_4 at the Ce K-edge (confirmed at the Ce L_3-edge, see **Appendix A**). The shift in Ce-O distance is 0.16 Å based on the co-fits of Ce^{3+} and Ce^{4+} at both edges. We show the MD-EXAFS of $[Ce^{III}(H_2O)_9]^{3+}$ and two possible Ce^{4+} complexes $[Ce^{IV}(H_2O)_8SO_4]^{2+}$ and

$[Ce^{IV}(H_2O)_9]^{4+}$ in **Fig. 5.4b**. Those Ce^{4+} MD-EXAFS complexes were selected to illustrate the expected effect of sulfate complexation in the first coordination shell of Ce^{4+} relative to solely water coordination, since the exact Ce^{4+} anion complex structure was not known. The Ce-O shift of 0.16 Å that we observe experimentally between Ce^{3+} and Ce^{4+} is closer to the 0.13 Å shift between MD-EXAFS $[Ce^{IV}(H_2O)_8SO_4]^{2+}$ and $[Ce^{III}(H_2O)_9]^{3+}$ compared to the 0.11 Å shift between $[Ce^{IV}(H_2O)_9]^{4+}$ and $[Ce^{III}(H_2O)_9]^{3+}$, implying anion complexation of Ce^{4+}. The DFT-predicted shifts in Ce-O from $[Ce^{III}(H_2O)_9]^{3+}$ to bisulfate complexes ($[Ce^{IV}(H_2O)_8HSO_4]^{+}$ and $[Ce^{IV}(H_2O)_6(HSO_4)_3]^{+}$) are 0.14 Å, also close to the experimental shift (**Table 5.1**)**.** Additionally, scattering peaks at ~2.6 Å appear for Ce^{4+} in H_2SO_4 that are not present for Ce^{3+}, as shown in the inset in **Fig. 5.4a**. From the inset in **Fig. 5.4b**, similar peaks appear in the MD-EXAFS of $[Ce^{IV}(H_2O)_8(SO_4)]^{2+}$ that are not observed for $[Ce^{IV}(H_2O)_9]^{4+}$ or $[Ce^{III}(H_2O)_9]^{3+}$. We confirm that the peaks in this region of the MD-EXAFS are due to sulfate scattering by comparing the MD-EXAFS generated spectrum for $[Ce^{IV}(H_2O)_8SO_4]^{2+}$ with and without sulfate scattering pathways included from **Fig. 5.4c**. The S atom in either of the bisulfate complexes also is at the same distance as the S from sulfate. The peaks at ~2.6 Å we see for Ce^{4+} in 2 M H_2SO_4 in the K-edge spectra are also present in the Ce^{4+} EXAFS at the Ce L_3-edge, further suggesting that these peaks are associated with an anion in sulfuric acid, which would be either SO_4^{2-} or HSO_4^{-}. To further probe the anion complexation of Ce^{4+} in sulfuric acid, including the type of anion and coordination number, we next fit the Ce^{4+} EXAFS data.

Table 5.1. Averaged DFT-predicted Ce-O bond distances for different Ce^{3+} and Ce^{4+} species.

Species	DFT Avg Ce-O (Å)
$[Ce^{III}(H_2O)_9]^{3+}$	2.574
$[Ce^{III}(H_2O)_8SO_4]^{+}$	2.576
$[Ce^{IV}(H_2O)_9]^{4+}$	2.436
$[Ce^{IV}(H_2O)_8SO_4]^{2+}$	2.449
$[Ce^{IV}(H_2O)_8HSO_4]^{3+}$	2.432
$[Ce^{IV}(H_2O)_6(HSO_4)_3]^{+}$	2.437

Ce^{4+} likely complexes with three bisulfates in the first coordination shell based on EXAFS fits and DFT-predicted complexation free energies. To fit our experimental Ce^{4+} K- and L_3-edge EXAFS, we measure a CeO_2 standard to determine a value for S_0^2 (**Appendix A**), which gives us confidence in the total coordination number of Ce^{4+}. By co-fitting the 0.05 M Ce^{4+} in 2 M H_2SO_4 EXAFS data at the Ce K-edge and 0.1 M Ce^{4+} in 2 M H_2SO_4 EXAFS data at the Ce L_3-edge with Ce-O and Ce-S scattering pathways, as shown in **Fig. 5.4d**, we confirm evidence of sulfate or bisulfate in the first coordination shell because the Ce-S scattering pathway fits the peaks centered at 2.6 Å (see outlined box). The co-fit with just a Ce-O scattering shell for both edges results in a worse fit. All parameters for Ce^{4+} EXAFS fitting are given in **Appendix A**. From the co-fit with a Ce-S scattering pathway included, the Ce^{4+}-O distance is 2.382 ± 0.006 Å and the Ce^{4+}-S distance is 3.671 ± 0.016 Å. We identify a Ce^{4+}-O coordination number of 8.6 ± 0.5 and a Ce^{4+}-S coordination number of 3.0 ± 0.7.

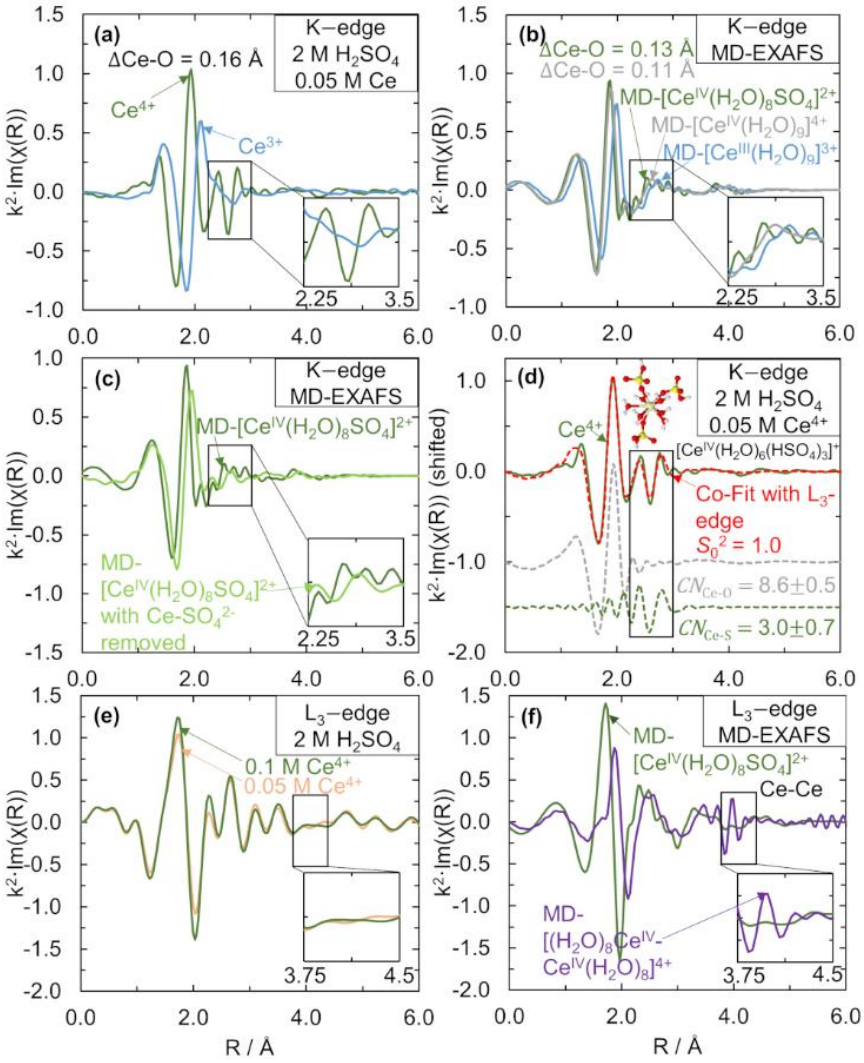

Figure 5.4. Ce K- and L_3-edge $k^2 \cdot \chi(R)$ EXAFS and fits for different Ce^{3+} and Ce^{4+} species. (a) 0.025 M $Ce_2(CO_3)_3$ in 2 M H_2SO_4 (blue solid line) and 0.025 M $Ce_2(CO_3)_3$ oxidized to Ce^{4+} in 2 M H_2SO_4 (dark green solid line), with inset showing zoomed in region of spectra. **(b)** Simulated MD-EXAFS of $[Ce^{III}(H_2O)_9]^{3+}$ (blue solid line), $[Ce^{IV}(H_2O)_9]^{4+}$ (gray solid line), and $[Ce^{IV}(H_2O)_8(SO_4)]^{2+}$ (dark green solid line), with inset showing zoomed in region of spectra, and green-colored ΔCe-O distance representing the shift in Ce-O distance from MD-EXAFS $[Ce^{III}(H_2O)_9]^{3+}$ to $[Ce^{IV}(H_2O)_8(SO_4)]^{2+}$ and gray-colored ΔCe-O distance representing the shift in Ce-O distance from MD-EXAFS $[Ce^{III}(H_2O)_9]^{3+}$ to $[Ce^{IV}(H_2O)_9]^{4+}$. **(c)** Simulated MD-EXAFS of $[Ce^{IV}(H_2O)_8(SO_4)]^{2+}$ (dark green solid line) and $[Ce^{IV}(H_2O)_8(SO_4)]^{2+}$ with paths associated with sulfate scattering removed (light green solid line), with inset showing zoomed in region of spectra. **(d)** 0.025 M $Ce_2(CO_3)_3$ oxidized to Ce^{4+} in 2 M H_2SO_4 (dark green solid line) with best fit (red dashed line), and Ce-O and Ce-S path contributions (shifted in y-axis). Inset is the proposed $[Ce^{IV}(H_2O)_6(HSO_4)_3]^+$ structure. **(e)** 0.025 M $Ce_2(CO_3)_3$ oxidized to Ce^{4+} (orange solid line) and 0.05 M $Ce_2(CO_3)_3$ oxidized to Ce^{4+} (dark green solid line), both in 2 M H_2SO_4, with inset showing zoomed in region of spectra. **(f)** Simulated MD-EXAFS of $[Ce^{IV}(H_2O)_8(SO_4)]^{2+}$ (dark green solid line) and $[(H_2O)_8Ce^{IV}\text{-}Ce^{IV}(H_2O)_8]^{8+}$ (purple solid line), with inset showing zoomed in region of spectra.

It is not possible to distinguish from EXAFS whether the Ce-S path is due to a sulfate or a bisulfate anion in the first coordination shell because the Ce-S scattering distance is so similar for Ce^{4+}-sulfate and Ce^{4+}-bisulfate complexes. Therefore, we turn to DFT modeling to determine

whether sulfate or bisulfate complexation is more favorable. Previously we compared the DFT-predicted ligand exchange free energies for Ce^{4+} complexed with one or two sulfates or one or two bisulfates, and found that of these four options, the $[Ce^{IV}(H_2O)_8SO_4]^{2+}$ species was the most energetically favorable.[11] Here, we extend this analysis to compare the free energies of Ce^{4+} complexed with three sulfates and Ce^{4+} complexed with three bisulfates. We find that the free energy of the $[Ce^{IV}(H_2O)_6(HSO_4)_3]^{+}$ species is the most energetically favorable Ce^{4+}-bisulfate complexed species considered, and its energy is comparable to that of the $[Ce^{IV}(H_2O)_8SO_4]^{2+}$ species (**Fig. 5.5**). Additionally, considering the relative acid dissociation constants of HSO_4^{-} and SO_4^{2-} in sulfuric acid,[75] HSO_4^{-} will be present at 99 times greater concentration than SO_4^{2-}. Although previous studies have proposed a Ce^{4+} structure with three sulfates,[34] this structure is not favorable based on our DFT calculations. The DFT-predicted ligand exchange free energy for $[Ce^{IV}(H_2O)_6(HSO_4)_3]^{+}$ is also in good agreement with the experimentally observed shift in redox potential for the Ce^{3+}/Ce^{4+} redox couple from 1 M $HClO_4$ (a non-complexing acid[76]) to 1 M H_2SO_4 of -28.9 kJ/mol. Because this structure is the most energetically favorable based on DFT and matches our experimental coordination numbers of nine oxygens and three sulfurs for each Ce atom, we conclude the dominant Ce^{4+} species is $[Ce^{IV}(H_2O)_6(HSO_4)_3]^{+}$.

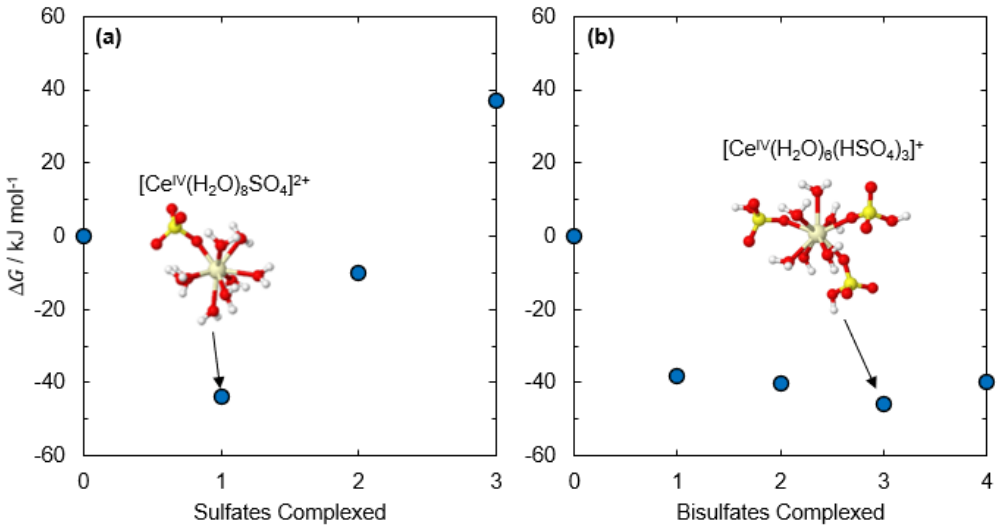

Figure 5.5. DFT-predicted free energies of different Ce^{4+} complexes. Free energy change for Ce^{4+} anion-complexation relative to Ce^{4+} coordination with nine water molecules as a function of **(a)** number of sulfates complexed, and **(b)** number of bisulfates complexed.

We do not detect any evidence of cerium dimers for 0.05–1.0 M Ce^{4+} in 2 M H_2SO_4, unlike what has been proposed for Ce^{4+} in $HClO_4$[77–80] and HNO_3.[37,38] In **Fig. 5.4e**, we see that increasing Ce^{4+} concentration from 0.05 M to 0.1 M does not result in an increase in any features around 4.0 Å, the distance at which the Ce-Ce scattering pathway from dimers are expected to appear based on the MD-EXAFS of a dimer species, as shown in the inset in **Fig. 5.4f**. The lack of dimers in H_2SO_4 may be due to the stronger anion complexation of Ce^{4+} single ions in H_2SO_4 compared to in HNO_3 and $HClO_4$.

Our findings from the Ce K-edge and additional Ce L_3-edge EXAFS in sulfuric acid are consistent with our previous DFT predictions that Ce^{3+} coordinates with nine water molecules while Ce^{4+} complexes with at least one sulfate or bisulfate.[11] Our EXAFS measurements indicate that a structural change occurs within the first coordination shell of Ce between Ce^{3+} and Ce^{4+}. Thus, a CT mechanism for the cerium redox reaction must include the inner-sphere ligand exchange. In the next section, we present kinetic results that show that despite this inner-sphere structural change, the Ce^{3+}/Ce^{4+} redox reaction behaves as if outer-sphere.

5.3.2 Kinetic measurements of the Ce^{3+}/Ce^{4+} charge transfer and modeling with Butler-Volmer

We measure the Ce^{3+}/Ce^{4+} charge transfer coefficient, standard rate constant, and activation energy on two electrode surfaces, Pt and glassy carbon, under identical reaction conditions and show the results are consistent with an outer-sphere electron transfer RDS. Although Ce^{3+}/Ce^{4+} redox kinetics have been measured on multiple electrodes (**Chapter 1.3.2**), the experimental conditions are varied, making it difficult to draw conclusions about the relative rates on different electrodes. Also, methods of extracting information on kinetics often rely on simplifying assumptions that are unsuitable for studying metal ion CTs like the cerium redox couple. For example, cyclic voltammograms (CVs) are a common method to extract a redox couple's standard rate constant based on the anodic and cathodic peak separation. However, the CV method relies on operating under conditions where diffusion is the dominant form of mass transport, which can be experimentally difficult to achieve, and it introduces uncertainty into quantitative kinetic parameters due to the uncertainty in peak separations and heights.[12] Also, the CV method cannot distinguish between multiple reactions occurring in the same potential range, such as the Ce^{3+}/Ce^{4+} redox reaction and the oxygen evolution reaction (OER). Here, we use two independent methods (Tafel method and the charge transfer resistance method) to ensure comparable and accurate steady state kinetic measurements. We study the Ce^{4+} reduction rates to avoid convolution with oxygen evolution or electrode oxidation during Ce^{3+} oxidation and control the mass transport to allow extraction of kinetically limited rates. See **Chapter 2** for more details.

To obtain the Ce^{3+}/Ce^{4+} kinetic parameters and a rate law on a Pt electrode in sulfuric acid, we use the Tafel method to measure exchange current densities, i_0, as a function of Ce^{4+} concentration and temperature, as shown in **Fig. 5.6a** and **Fig. 5.6b**, respectively. The data in **Fig. 5.6c** shows the cathodic Tafel slope as a function of Ce^{4+} concentration. The Ce^{3+}/Ce^{4+} exchange

current densities for Pt extracted from the charge transfer resistance method (**Appendix D**) agree within 31% of the Tafel method. Exchange current densities increase with increasing Ce^{4+} concentration until [Ce^{4+}] = 0.04 M, then decrease. The exchange current densities increase exponentially with temperature.

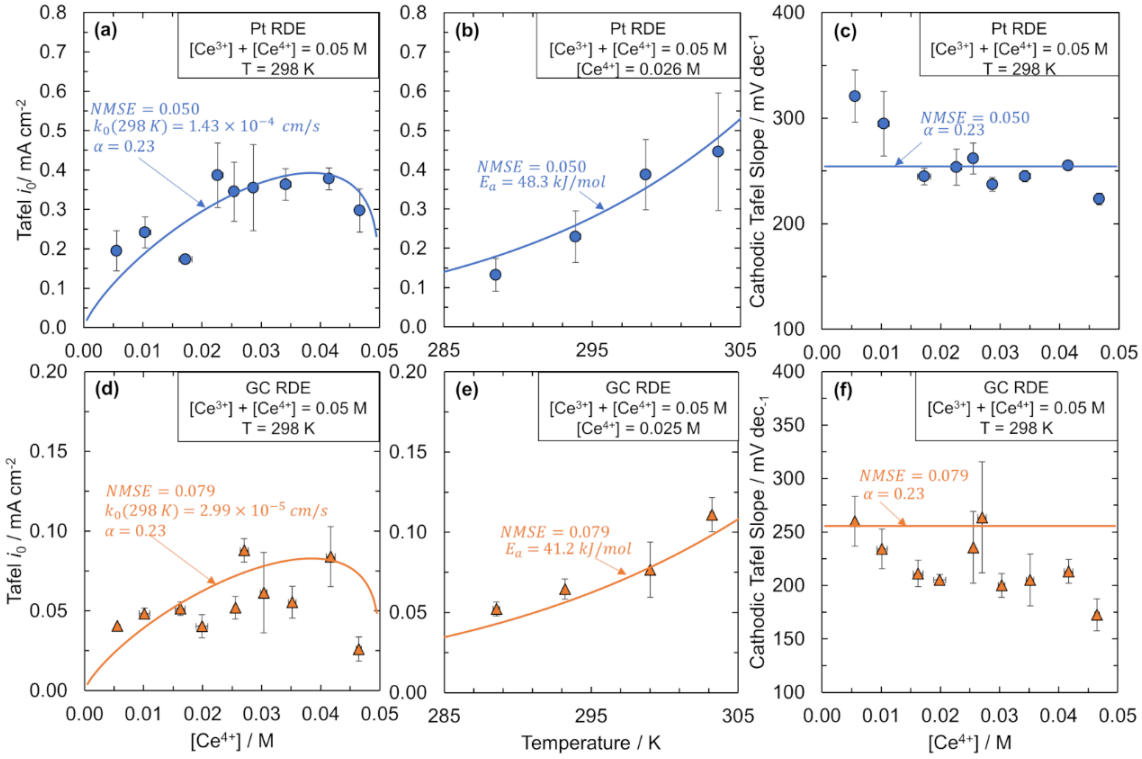

Figure 5.6. Tafel analysis of Ce^{3+}/Ce^{4+} kinetic measurements on Pt and glassy carbon electrode surfaces. Kinetic measurements and fit (solid line) using the Butler-Volmer equation of the Ce^{3+}/Ce^{4+} redox couple. Exchange current densities, i_0, extracted from Tafel plots as a function of Ce^{4+} concentration for **(a)** Pt RDE and **(d)** GC RDE. i_0 extracted from Tafel plots as a function of temperature for **(b)** Pt RDE and **(e)** GC RDE. Cathodic Tafel slopes as a function of Ce^{4+} concentration for **(c)** Pt RDE and **(f)** GC RDE. Ce^{4+} concentrations were determined by titration. Reported values are averaged from three runs, with error bars representing one standard deviation from the average value in both horizontal and vertical directions. Data in **(a)**, **(c)**, **(d)**, and **(f)** collected at room temperature in 2 M H_2SO_4 at total cerium concentration of 0.05 M. Data in **(b)** and **(e)** collected at a total cerium concentration of 0.05 M with a Ce^{4+} concentration of 0.026 M and 0.025 M, respectively. An Ag/AgCl reference electrode and graphite rod counter electrode were used for all measurements. Measurements were done at 2000 rpm of the RDE where mass transport is not limiting. The rate constant k_0, cathodic charge transfer coefficient α, and activation energy E_a were obtained through minimizing the normalized mean square error (NMSE) of the data.

The exchange current densities for Pt reveal that the Ce^{3+}/Ce^{4+} redox reaction is asymmetric, with a low α that is unusual for metal ion CTs and a standard rate constant and activation energy that agree with reported values (**Chapter 1.3.2**). We first attempt to fit our kinetic

data through the BV formulism to describe the kinetic current density, $i_{K,BV}$, (**Eq. 5.4a**), which assumes a one-step *E* and relates exchange current density, $i_{0,BV}$, (**Eq. 5.4b**) to the Ce^{3+} and Ce^{4+} concentrations, where k_0 is the standard rate constant and α is the cathodic charge transfer coefficient.

$$-i_{K,BV} = nFk_0\left[[\mathrm{Ce^{4+}}]\exp\left(-\alpha F(U-U^{\circ})\right) - [\mathrm{Ce^{3+}}]\exp\left((1-\alpha)F(U-U^{\circ})\right)\right]$$
$$= i_{0,BV}\left[\exp\left(-\alpha F\left(U-U_{eq}\right)\right) - \exp\left((1-\alpha)F\left(U-U_{eq}\right)\right)\right] \quad \textbf{(5.4a)}$$

$$i_{0,BV} = nFk_0[Ce^{3+}]^{\alpha}[Ce^{4+}]^{1-\alpha} \quad \textbf{(5.4b)}$$

U is the electrode potential, U° is the standard equilibrium potential (1.44 V vs. SHE), and U_{eq} is the equilibrium potential corresponding to the [Ce^{3+}] and [Ce^{4+}] conditions at which the measurement was taken. The normalized mean square error (NMSE) fit of **Eq. 5.4a** to the exchange current densities using k_0 and α as fitting parameters is shown in **Fig. 5.6a**. The k_0 obtained from the fit is $1.43\times10^{-4}\pm7\times10^{-6}$ cm/s at 298 K, which aligns with many of the standard rate constants reported in literature for Ce^{3+}/Ce^{4+} in sulfuric acid (**Chapter 1.3.2**). The activation energy E_a on Pt from fitting the data in **Fig. 5.6b** is 48.3 ± 21 kJ/mol, which, while having a large degree of uncertainty, agrees within 35% of an activation energy calculated from cerium redox standard rate constants on Pt in sulfuric acid.[81] The value of α obtained from fitting is 0.23 ± 0.005, agreeing with reports for Pt (**Chapter 1.3.2**) and indicating the asymmetric nature of the cerium redox reaction.

The large cathodic Tafel slopes on Pt corroborate the low value of α and therefore the asymmetry of the cerium redox reaction, but the BV equation does not capture the Tafel slopes' dependence on Ce^{4+} concentration. The cathodic Tafel slopes shown in **Fig. 5.6c** are between 220–

320 mV/decade as a function of [Ce^{4+}], which correspond to α values between 0.18–0.27. These α values are similar to those obtained from fitting **Eq. 5.4** to the data in **Fig. 5.6a**, giving further evidence that the Ce^{3+}/Ce^{4+} is highly asymmetric. However, unlike the BV equation where α is constant, here we see a trend in cathodic Tafel slope with concentration. We also measure cathodic Tafel slopes as a function of temperature (**Fig. 5.7a**) and find that the Tafel slope increases with temperature. The BV fit also does not entirely capture the dependence of the Tafel slope on temperature. The inability of the BV equation to capture the cathodic Tafel slopes' dependence on Ce ion concentration suggests that a more accurate rate law than that described through BV kinetics is necessary to describe the Ce^{3+}/Ce^{4+} redox kinetics on Pt.

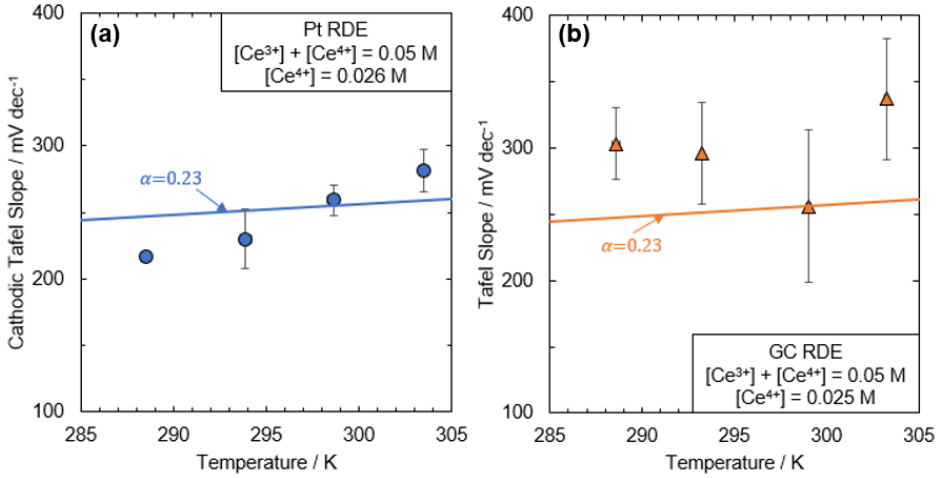

Figure 5.7. Cathodic Tafel slope dependence on temperature for the **(a)** Pt (blue circles) and **(b)** glassy carbon (orange triangles) rotating disk electrode. Cathodic Tafel slopes for the Pt and GC RDE extracted from Tafel plots as a function temperature at Ce^{4+} concentration of 0.025 M and 0.025 M, respectively. Tafel slopes fit using the Butler-Volmer equation (solid line). Reported values are averaged from three runs, with error bars representing one standard deviation from the average value in both horizontal and vertical directions. An Ag/AgCl reference electrode and graphite rod counter electrode were used. The solutions were sparged with nitrogen gas for at least 15 minutes before measurements were collected and blanketing with nitrogen was continued throughout the measurement collection. All data were collected at 2000 rpm of the RDE. Solid line is the fit to the data from the Butler-Volmer equation. The cathodic charge transfer coefficient α was obtained through minimizing the normalized mean square error of the data.

We repeat the same kinetic analysis as Pt for a GC electrode and find that the redox reaction is asymmetric on GC as well. Fitting **Eq. 5.4** to the Tafel exchange current densities as a function of [Ce^{4+}] shown in **Fig. 5.6d**, we determine a k_0 value of $2.99\times10^{-5}\pm1.30\times10^{-6}$ cm/s and an α

value of 0.23±0.008. Exchange current densities derived from charge transfer resistances are given **Appendix D**. The α of GC aligns well with reported values, but the standard rate constant is lower than most of the prior reported values in sulfuric acid (**Chapter 1.3.2**). Based on our Tafel exchange current density vs. temperature data shown in **Fig. 5.6e**, the activation energy on GC is 41.2±14.0 kJ/mol, which is 7.1 kJ/mol smaller than that of Pt. To our knowledge, this is the first time the activation energy of Ce^{3+}/Ce^{4+} has been compared between two electrodes under the same conditions. The magnitude of the cathodic Tafel slopes as a function of Ce^{4+} concentration range from 170–250 mV/decade as shown in **Fig. 5.6f**, which corresponds to α values between 0.24–0.35. Although the fitted value of α qualitatively agrees with the values predicted from the cathodic Tafel slopes, the BV fit is again unable to capture the decrease in Tafel slope with $[Ce^{4+}]$. Also, the BV fit only partially captures the dependence of the cathodic Tafel slopes with temperature (**Fig. 5.7b**). To further probe the CT mechanism of Ce^{3+}/Ce^{4+}, it is beneficial to compare the kinetic behavior on the Pt and GC electrodes.

The similar exchange current densities, charge transfer coefficients, activation energies, and cathodic Tafel slopes for the Pt and GC RDEs in **Fig. 5.6** imply the cerium redox kinetics behave as an outer-sphere reaction. The exchange current densities and rate constants of Pt and GC are within a factor of five of one another, comparable to the differences for various outer-sphere redox couples on different electrode surfaces (**Table 5.2**). Even for well-known outer-sphere redox couples such as $[Fe(CN)_6]^{3-}/[Fe(CN)_6]^{4-}$ in 1.0 M KCl, the electrode materials affect standard rate constants of various outer-sphere redox couples by a factor of 2 to 9.[82–84] These electrode effects are ascribed to a variety of factors, including the Frumkin effect,[85] a metal's electronic properties, e.g., electronic spillover distance, work function, intrinsic electric field,[86] and the interaction of adsorbed water on the electrode surface with electroactive species.[87–89]

Table 5.2. Electrode effect on kinetic activity for outer-sphere redox couples, including this Ce^{3+}/Ce^{4+} work. Factor of difference refers to the ratio of the reported k_0 for the electrode listed first in the Electrodes studied column to the reported k_0 for the electrode listed second. Note that for simplicity, the structure of Ce^{4+} is written as $[Ce^{IV}(H_2O)_8SO_4]^{2+}$, but we show evidence that the Ce^{4+} structure could exist as either $[Ce^{IV}(H_2O)_8SO_4]^{2+}$ or $[Ce^{IV}(H_2O)_6(HSO_4)_3]^{+}$ in sulfuric acid.

Outer-sphere redox couple	Electrodes studied	Supporting electrolyte	Redox species	Ratio of standard rate constants at different electrodes *	Ref
$[Ce^{III}(H_2O)_9]^{3+}$/ $[Ce^{IV}(H_2O)_6(HSO_4)_3]^{+}$	Pt vs. GC	2 M H_2SO_4	0.05 M Ce	4.7	This work
	Pt, reduced vs. oxidized state	0.5 M H_2SO_4	0.016 M Ce^{3+}/ 0.012 M Ce^{4+}	~3[a]	20
$[Fe(CN)_6]^{3-}$/ $[Fe(CN)_6]^{4-}$	Pt, reduced vs. oxidized state	1 M KCl	0.01–0.07 M $[Fe(CN)_6]^{3-}$/ 0.0005–0.01 M$[Fe(CN)_6]^{4-}$	8.6	82
	Pt vs. GC	1 M KCl	0.002 M $[Fe(CN)_6]^{3-}$	3.4	83
	GC, polished vs. laser activation	1 M KCl	0.001 M $[Fe(CN)_6]^{4-}$	3.5	84
$[Cr(H_2O)_6]^{3+}$/ $[Cr(H_2O)_6]^{2+}$	Pb vs. Ga	0.5 M $NaClO_4$ + 0.003 M $HClO_4$	0.001–0.002 M $[Cr(H_2O)_6]^{3+}$	3.8[b]	89
$[Cr(H_2O)_5F]^{2+}$/ $[Cr(H_2O)_5F]^{+}$	Pb vs. Tl	0.5 M $NaClO_4$ + 0.003 M $HClO_4$	0.001–0.002 M $[Cr(H_2O)_5F]^{2+}$	1.3[b]	89
$[Cr(H_2O)_5SO_4]^{+}$/ $[Cr(H_2O)_5\ SO_4]^{0}$	Pb vs. Ga	0.5 M $NaClO_4$ + 0.003 M $HClO_4$	0.001–0.002 M $[Cr(H_2O)_5SO_4]^{+}$	~4.3[b]	89
$[Ru(NH_3)_6]^{3+}$/ $[Ru(NH_3)_6]^{2+}$	GC, polished vs. monolayer adsorption of AQDS,[c] MB,[d] BMB,[e] and chemisorbed nitrophenyl	1 M KCl	0.001 M $[Ru(NH_3)_6]^{3+}$	~2	84
	Ag vs. Hg[f]	1 M KF	Not reported[g]	2.4[h]	90
	Pt vs. Au	1 M KF	0.002 M $[Ru(NH_3)_6]^{3+}$/	1.5	91
$[IrCl_6]^{2-}$/ $[IrCl_6]^{3-}$	GC, polished vs. monolayer adsorption of AQDS,[b] MB,[c] BMB,[d] and chemisorbed nitrophenyl	1 M KCl	5×10^{-4} M $[IrCl_6]^{2-}$	~2	84

a) Ratio calculated using Ce^{4+} reduction data from Fig. 6 in Kuhn and Randle (1985) paper for oxide coverage of 1 relative to oxide coverage of 4.5 for the electrode labeled "Electrode 1," which had been exposed to a longer period of phase oxide formation than other electrodes tested;[20] b) Calculated from reported k_{app} data; c) 2,6-anthraquinonedisulfonate; d) methylene blue; e) bis(4-methylstyryl)benzene; f) Other metal electrodes studied as well,

including Pt, Pd, Au, and Cu, with exchange current densities ranging between 97 A/cm^2 and 116 A/cm^2, while exchange current densities for Ag and Hg were 120 A/cm^2 and 50–79 A/cm^2, respectively; g) Concentrations not reported for experiments on Ag and Hg, but concentrations reported for similar experiments conducted on Pt and Au: 3.3×10^{-4} –8.8×10^{-4} M $[Ru(NH_3)_6]^{3+}$/ 2.8×10^{-4}–8.3×10^{-4} $[Ru(NH_3)_6]^{2+}$; h) Factor calculated using reported exchange current densities, instead of rate constants.
* Ratio is calculated by dividing the reported value of k_0 of the electrode listed first by that of the electrode listed second.

The activation barriers on the Pt and GC RDEs in this work are similar, suggesting a small electrode influence on the kinetics, further underscoring the outer-sphere behavior of the Ce^{3+}/Ce^{4+} electron transfer. Additionally, the Pt and GC RDE cathodic Tafel slopes fall within the same range of 150–320 mV/decade and the α values are both 0.23, highlighting not only the similar kinetic behavior, but also the extreme asymmetry in the CT on both electrodes.

From our structural and kinetic results, the Ce^{3+}/Ce^{4+} reaction is unlikely to be purely a one-step electron transfer reaction. Although adhering to outer-sphere kinetic behavior, the value of α falls far below the expected value of 0.5, suggesting that a rate law based on a one-step electron transfer is inappropriate to model the Ce^{3+}/Ce^{4+} redox kinetics. Additionally, the BV rate law predicts constant cathodic Tafel slopes with $[Ce^{4+}]$, which we do not observe on either Pt or GC. Our structural data from **Fig. 5.2**-**Fig. 5.5** also suggests that solely a one *E* step mechanism cannot adequately describe the cerium redox kinetics, because of the structural change that must occur from $[Ce^{III}(H_2O)_9]^{3+}$ and $[Ce^{IV}(H_2O)_6(HSO_4)_3]^{+}$.

5.3.3 Proposed mechanism for the Ce^{3+}/Ce^{4+} redox reaction in sulfuric acid

We propose a mechanism that aligns with both our structural and kinetic data and discuss the implications of the resulting fit of our experimental data to a rate law derived from the mechanism. The appropriate CT mechanism and rate law for the Ce^{3+}/Ce^{4+} redox reaction must satisfy the following nine *Criteria* observed from our structural and kinetic data:

1. A structural change occurs in addition to an electron transfer.

2. Ce^{3+} preferentially coordinates with water as $[Ce^{III}(H_2O)_9]^{3+}$.

3. Ce^{4+} favorably complexes with three bisulfates as $[Ce^{IV}(H_2O)_6(HSO_4)_3]^{+}$.

4. There is minimal influence of the electrode on kinetic activity.

5. There is a maximum in the exchange current density as a function of Ce^{4+} concentration (with total cerium concentration fixed) occurring between 60−80% $[Ce^{4+}]$ relative to total cerium concentration.

6. The exchange current density increases with increasing temperature.

7. The cathodic Tafel slope is large, with values between 170 mV/decade and 320 mV/decade.

8. The cathodic Tafel slope decreases with increasing ratio of Ce^{4+} concentration to total cerium concentration.

9. The cathodic Tafel slope increases with increasing temperature.

In **Table 5.3**, we summarize six different possible mechanisms and whether each mechanism and its corresponding rate law matches the nine criteria. As has been noted,[92] we cannot prove mechanisms, but instead seek to disprove certain mechanisms and identify ones consistent with the experimental data. We begin with the simplest mechanism and add complexity only when needed to describe the data. We show that a *CE* mechanism where electron transfer is the RDS is the simplest mechanism that satisfies *Criteria* 1–9. The rate law uses MT to describe the electron transfer step. Derivations for all rate laws considered are in **Appendix D**.

Table 5.3. Different possible mechanisms and agreement or disagreement of the mechanism and corresponding rate law to the structural and kinetic data observed experimentally for the Ce^{3+}/Ce^{4+} charge transfer. Mechanisms are separated into one- and two-step. *E* RDS refers to the electron transfer step being the RDS, whereas *C* RDS refers to ligand exchange being the RDS. The numbers in the criteria row correspond with the list of criteria at the beginning of this section. The dashes included for the MT rate law indicate that these criteria are not considered, since they are dependent on *Criterion 1* being met.

Mechanism and rate law		**Criteria: Observed Ce^{3+}/Ce^{4+} Structural and Kinetic Behavior**								
		1	**2**	**3**	**4**	**5**	**6**	**7**	**8**	**9**
One-step *E*	**BV**	Yes	Yes	Yes	Yes	Yes	Yes	Yes	No	Yes
	MT	No	–	–	Yes	No	Yes	Yes	Yes	Yes
Two-step	***CE* Mech, *E* RDS**	Yes	Yes	Yes	Yes	Yes	Yes	Yes	Yes	Yes
	***EC* Mech, *E* RDS**	Yes	No	Yes	Yes	Yes	Yes	Yes	Yes	Yes
	***EC* Mech, *C* RDS**	Yes	Yes	Yes	Yes	No	No	No	No	No
	***CE* Mech, *C* RDS**	Yes	Yes	Yes	Yes	No	No	No	No	No

The BV and the MT rate laws for a one-step electron transfer mechanism do not meet all criteria established from our experimentally observed structural and kinetic data (**Table 5.3**). The BV rate law does not adequately describe the behavior of the cathodic Tafel slope as a function of $[Ce^{4+}]$ concentration (*Criterion 8*), because the Tafel slope from BV is constant with potential. Although the BV rate law describes the Ce^{3+}/Ce^{4+} CT asymmetry through the low value of α, the BV rate law is only an empirical model, and as a result, the fitting parameters are unphysical. The MT rate law better captures the behavior of the cathodic Tafel slopes; however, it does not allow for a structural change to occur between the redox species (*Criterion 1*), and it does not satisfy *Criterion 5* (**Appendix D**). For a symmetric MT rate law, the exchange current density maximum occurs at 50% Ce^{4+}. As has been previously shown,[13] although asymmetric MT can mathematically describe the observed asymmetry in the kinetics, the reorganization energies from fitting the data

are unreasonably large. Additionally, the NMSE of the MT fit is higher for both Pt and GC data than the BV fit (**Appendix D**). Since the rate laws for a one-step *E* mechanism do not satisfy all observed structural and kinetic data, it is necessary to consider mechanisms that include more than a one-step electron transfer.

We next consider different two-step mechanisms, which we refer to as *CE* and *EC* mechanisms. In the *CE* mechanism the Ce^{4+} species, $[Ce^{IV}(H_2O)_6(HSO_4)_3]^+$, undergoes ligand exchanges with water to form $[Ce^{IV}(H_2O)_9]^{4+}$ (**Eq. 5.5a**). The $[Ce^{IV}(H_2O)_9]^{4+}$ is subsequently reduced to form $[Ce^{III}(H_2O)_9]^{3+}$ (**Eq. 5.5b**). Note that the *C* step is unlikely to occur in a single elementary step, as it involves the exchange of three bisulfates with three water molecules. However, we will show below that this *C* step is likely quasi-equilibrated, and thus we can condense the ligand exchange into a single step.

$$[Ce^{IV}(H_2O)_6(HSO_4)_3]^+_{aq} + 3H_2O_{aq} \rightleftarrows [Ce^{IV}(H_2O)_9]^{4+}_{aq} + 3HSO^-_{4\,aq} \quad \textbf{(5.5a)}$$

$$[Ce^{IV}(H_2O)_9]^{4+}_{aq} + e^- \rightleftarrows [Ce^{III}(H_2O)_9]^{3+}_{aq} \quad \textbf{(5.5b)}$$

In the *EC* mechanism the *E* step occurs first between the Ce^{4+} and Ce^{3+} complexes, followed by ligand exchange of the Ce^{3+} (**Appendix D**). For both the *CE* and *EC* mechanisms, we consider two possible rate laws, based on assuming the RDS is either the *E* or *C*. We show the rate law for the kinetic current density ($i_{K,CE,E}$) for the *CE* mechanism when *E* (**Eq. 5.5b**) is the RDS in **Eq. 5.6a**. $[Ce^{4+}]_w$ represents the concentration of the water-coordinated Ce^{4+} (**Eq. 5.6b**), and A, B, and C are defined in **Eq. 5.6c−e**.

$$i_{K,CE,E} = -nFZ_2([Ce^{4+}]_w \exp(A(1+B-C)^2) - [Ce^{3+}]\exp(A(1-B+C)^2)) \quad \textbf{(5.6a)}$$

$$[Ce^{4+}]_w = \frac{[Ce^{4+}][H_2O]^3}{[HSO_4^-]^3} K_1 \quad \textbf{(5.6b)}$$

$$A = \frac{-\lambda_2}{4RT} \quad \textbf{(5.6c)}$$

$$B = \frac{nF\eta}{\lambda_2} \quad \textbf{(5.6d)}$$

$$C = \frac{RT}{\lambda_2} \ln \frac{[Ce^{3+}]}{K_1[Ce^{4+}]} \quad \textbf{(5.6e)}$$

Here K_1 is the equilibrium constant of the *C* step, n is the number of electrons transferred, assumed to be one, F is Faraday's constant, Z_2 is the preexponential factor for the *E* step, $[Ce^{4+}]$ refers to the concentration of the bulk Ce^{4+} species, i.e., $[Ce^{IV}(H_2O)_6(HSO_4)_3]^+$, λ_2 is the reorganization energy of the *E* step, R and T have their usual meanings, η is the overpotential applied ($U - U_{eq}$), and $[Ce^{3+}]$ is the concentration of the bulk Ce^{3+} species, i.e., $[Ce^{III}(H_2O)_9]^{3+}$. **Fig. 5.8a** shows the free energies of the species involved in the *CE* mechanism, as well as the physical meaning of some of the fitting parameters used in the rate law (λ_2, K_1). As shown by the free energy parabolas, standard MT expressions are used to describe the *E* step.

Of the rate laws derived from the two-step mechanisms, the only one that meets all criteria is a *CE* type mechanism with the *E* as the RDS (*CE*, *E* RDS), as summarized in **Table 5.3**. Because the *C* step involves ligand exchange, and the only Ce^{3+} species included in the *CE* mechanism is the $[Ce^{III}(H_2O)_9]^{3+}$ species, *Criteria 1* and *2* are satisfied. The rate law does not incorporate any electrode dependent properties; thus *Criterion 4* is also met. By fitting the exchange current densities and cathodic Tafel slopes for both Pt and GC RDEs to expressions for i_0 and Tafel slopes derived from **Eq. 5.6**, we see the rate law satisfies all observed kinetic criteria. The rate law equation for $i_{K,CE,E}$ indicates that i_0 will be asymmetric with Ce^{4+} concentration and increase with temperature (*Criteria 5* and *6*), as shown in **Fig. 5.8b** and **Fig. 5.8c** for Pt. From **Fig. 5.8d**, the rate law modeled Pt cathodic Tafel slopes agree with observed Tafel slopes (*Criteria 7* and *8*), and the Tafel slopes also increase with increasing temperature (*Criterion 9*, **Appendix D**). The parameters

used in the fit of the Pt experimental data are shown in **Fig. 5.8b−d**. The NMSE of the *CE*, *E* RDS rate law fit to Pt was the lowest for all rate laws at 0.049. The *E* step reorganization energy is reasonable at 100.2 kJ/mol and the equilibrium constant, K_1, is small at 1.1×10^{-7}, indicating that the ligand exchange from $[Ce^{IV}(H_2O)_6(HSO_4)_3]^+$ to $[Ce^{IV}(H_2O)_9]^{4+}$ is unfavorable, as expected from our EXAFS structural data. Additionally, the observed shift in redox potential for the Ce^{3+}/Ce^{4+} redox couple from 1 M $HClO_4$ to 1 M H_2SO_4 is 0.30 V,[21] which corresponds to an equilibrium constant of 8.4×10^{-6}, assuming that the shift is due only to Ce^{4+}-anion complexation in sulfuric acid. Thus, *Criterion 3* is also met. The preexponential factor Z_2 is equal to the product of the electronic transmission coefficient, precursor equilibrium constant, and nuclear frequency factor (see SI),[12] and values for the apparent preexponential factor for metal ions at metal-aqueous interfaces are reported to be on the order of 10^3–10^5 cm/s.[93] Our fitted Z_2 value of 4.22×10^4 cm/s for Pt is within this range. The fit of the *CE*, *E* RDS rate law to the GC data is included in the SI (**Appendix D**), with the lowest NMSE of all rate laws fit to the GC data. The fitted Z_2 and λ_2 values for GC are smaller than those for Pt, and the value of K_1 for GC is two orders of magnitude larger than the Pt equilibrium constant (**Appendix D**). This K_1 value does still correctly predict that Ce^{4+} is complexed by an anion in sulfuric acid and the *CE*, *E* RDS rate law is still the best fitting rate law to the GC data.

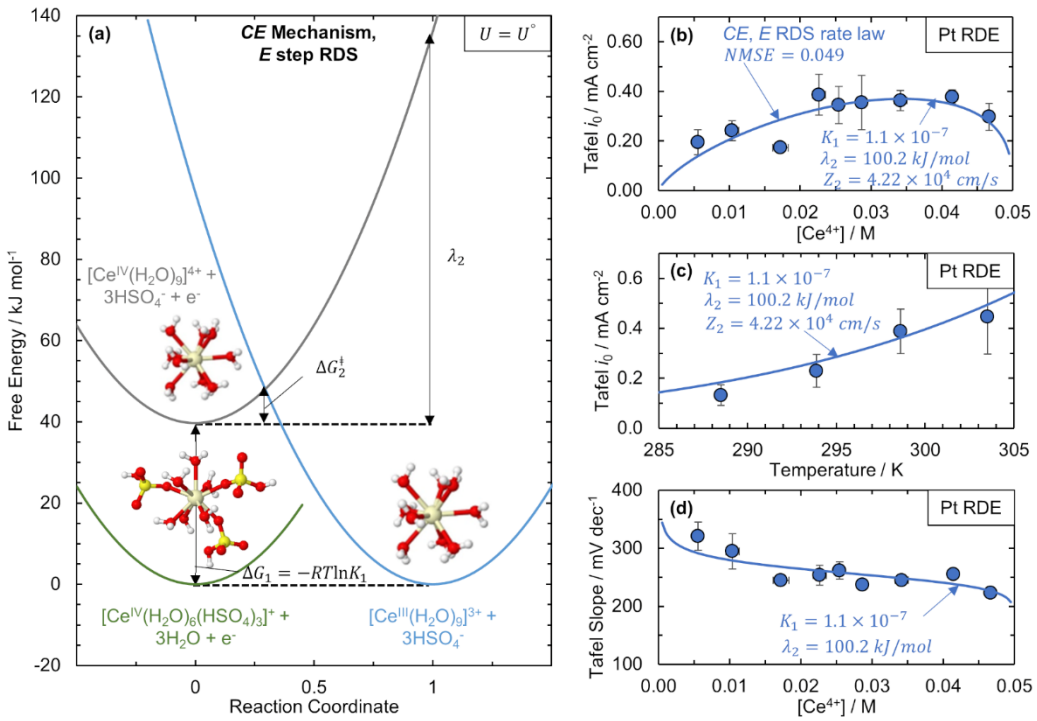

Figure 5.8. Proposed *CE* Mechanism and fit of rate law to kinetic data on Pt assuming the electron transfer step (*E*) is rate-determining. (a) Free energy profiles at the equilibrium Ce^{3+}/Ce^{4+} potential ($U = U^{\circ}$) in H_2SO_4 for the three species involved in the proposed *CE* mechanism for Ce^{3+}/Ce^{4+} charge transfer: $[Ce^{IV}(H_2O)_6(HSO_4)_3]^+$ (green solid line), $[Ce^{IV}(H_2O)_9]^{4+}$ (gray solid line), and $[Ce^{III}(H_2O)_9]^{3+}$ (light blue solid line). Parabolas represent the free energies of the species as a function of reaction coordinate, as defined through Marcus theory. The Ce^{3+}/Ce^{4+} electron transfer is described by the reorganization energy λ_2 and the transition state free energy, $\Delta G_2^{\ddagger}$, and the ligand exchange is described by equilibrium constant K_1. We propose electron transfer between $[Ce^{IV}(H_2O)_9]^{4+}$ and $[Ce^{III}(H_2O)_9]^{3+}$ is the RDS, i.e., $[Ce^{IV}(H_2O)_6(HSO_4)_3]^+$ and $[Ce^{IV}(H_2O)_9]^{4+}$ are quasi-equilibrated. (b)-(c) Fit (dark blue solid line) of the Ce^{3+}/Ce^{4+} exchange current densities (blue circles) in the 0.05 M Ce/2 M H_2SO_4 solution on the Pt RDE using the rate law in **Eq. 5.6** derived for the *CE* mechanism assuming *E* is RDS as a function of (b) Ce^{4+} concentration and (c) temperature. (d) Fit (blue solid line) of the Ce^{3+}/Ce^{4+} cathodic Tafel slopes (blue circles) on the Pt RDE using the rate law in **Eq. 5.6** derived for the *CE* mechanism assuming the *E* is RDS as a function of Ce^{4+} concentration. All fits of the data in (b)–(d) were obtained through minimizing the NMSE of the data.

The rate laws derived from the *CE* and *EC* mechanisms in which the *C* step is the RDS and the rate law for the *EC* mechanism with the *E* step as RDS do not satisfy the observed structural and kinetic behavior (**Table 5.3**), and thus are eliminated as possible mechanisms for the Ce^{3+}/Ce^{4+} charge transfer. Details of the fits of both the Pt and GC data for these rate laws are included in **Appendix D**. The rate laws with the rate-determining *C* step result in a linear dependence of i_0 on $[Ce^{4+}]$, rather than the observed maximum in exchange current density at ~70% Ce^{4+} concentration (*Criterion 5*). If a series of *C* steps were assumed to occur instead of a single *C* step to go from $[Ce^{IV}(H_2O)_6(HSO_4)_3]^+$ to $[Ce^{IV}(H_2O)_9]^{4+}$, and any of these steps were the RDS, then the rate law

would still display a linear dependence of i_0 on [Ce^{4+}]. In recent work that studied the Ce^{3+}/Ce^{4+} kinetics in sulfuric acid on a gold electrode,[13] it was concluded that the *E* step was preceded by a rate-determining ligand dissociation step. From their proposed rate law, exchange current density is linear with Ce^{4+} concentration, as we see for our *C* RDS rate laws. Therefore, we can rule out the rate-determining ligand dissociation step proposed in this prior work based on its failure to meet *Criterion 5*. The *C* RDS rate laws also do not capture the values of the cathodic Tafel slopes, the decrease in Tafel slopes with an increase in Ce^{4+} concentration, or the increase in Tafel slopes with temperature (*Criteria 7–9*). Considering the *EC* mechanism with the *E* step assumed to be the RDS (*EC*, *E* RDS), the fits to the experimental Pt and GC data (**Appendix D**) indicate that Ce^{3+} will favorably complex with an anion, contradicting our experimental EXAFS and thus failing *Criterion 2*. Additionally, the fitted value of the reorganization energy is unreasonably high at 663 kJ/mol (**Appendix D**). Given the poor fits of the *C* RDS rate laws to the observed kinetic data and physically unreasonable values of the fitting parameters of the *EC, E* RDS rate law, we reject these three rate laws and conclude that only the *CE*, *E* RDS rate law is consistent with experimental data. On the principle of Occam's Razor,[94] which asserts that the simplest explanation that satisfies all observed data is preferable, we do not consider more complex mechanisms with additional *C* or *E* steps.

The parameters K_1 and λ_2 extracted from the fit to the experimental data of the *CE*, *E* RDS rate law compare favorably to DFT-predicted values, allowing us to use DFT to gain insight into the contributions to the total reorganization energy and possibly make predictions for different systems. Our DFT-predicted K_1 for the ligand exchange from $[Ce^{IV}(H_2O)_6(HSO_4)_3]^+$ to $[Ce^{IV}(H_2O)_9]^{4+}$ is 9.8×10^{-9} as compared to the fitted value of 1.1×10^{-7} for Pt. These equilibrium constants agree qualitatively with the equilibrium constant derived from the Ce^{3+}/Ce^{4+} redox

potential in H_2SO_4 relative to $HClO_4$. We also calculate the reorganization energy using DFT for the water-coordinated Ce^{3+}/Ce^{4+} CT to be 87.2 kJ/mol (**Appendix D**, and see **Section 5.2.2** for modeling details). This reorganization energy value falls between the experimentally fitted λ_2 values for GC (71.8 kJ/mol) and Pt (100.2 kJ/mol). From DFT, the inner-sphere reorganization energy from the change in the Ce water-coordinated species (e.g., metal-ligand bond length), λ_i, is 40.4 kJ/mol and the outer-sphere reorganization energy related to the reorganization of the solvent,[12,95] λ_o, is 46.8 kJ/mol. Our ability to computationally determine ligand exchange and reorganization energies for the Ce^{3+}/Ce^{4+} CT has implications for future efforts to enhance Ce kinetics. By coupling calculated reorganization energy information with known ligand exchange equilibrium constants (either from DFT calculations or the shift in redox potential), we could use the *CE*, *E* RDS rate law to screen acids to determine which would yield optimal kinetic activities. Assuming the *CE*, *E* RDS rate law holds in other acids, we would expect acids with stronger complexing anions (smaller K_1) to exhibit slower Ce^{3+}/Ce^{4+} kinetics than acids with weaker complexing anions. If the reorganization energies were calculated for Ce-anion complexed species, we could also calculate the expected rates in acids if the dominant mechanism switches to be *EC* (see **Chapter 6** for further discussion).

Although the *CE*, *E* RDS model fits the Pt experimental data and DFT values, we observe discrepancies between the Pt and GC fitted parameters, which could be because we ignore the effect of temperature on Z_2 in all considered rate laws. As noted above, the λ_2 and Z_2 values for GC are smaller than those of Pt (**Appendix D**), whereas the K_1 value for GC is larger. Although we expect a difference in Z_2 between Pt and GC due to factors like the Frumkin effect, the metal's electronic properties, and the effect of water adsorption on the electrode, it is unexpected that there would be different λ_2 and K_1 values. In our model, we captured the temperature dependence of the

kinetic activity through the λ_2 and K_1 parameters and assumed the preexponential value Z_2 to be independent of temperature. However, it has been noted in the case of weak electronic coupling that the nuclear frequency factor has a $T^{1/2}$ dependence on temperature,[2,96] and Z_2 is proportional to the nuclear frequency factor. Thus, it is possible that one reason for the difference in λ_2 and K_1 between Pt and GC is because we ignore the temperature dependence of Z_2. Better treatment of the preexponential factor's dependence on the temperature through more sophisticated treatments[93] as well as kinetic measurements on additional electrodes would be needed in future mechanistic studies of the cerium redox couple.

5.4 Conclusion

We demonstrate how determining the cerium ions' structures and characterizing the kinetic behavior as a function of experimental conditions can be used to identify a charge transfer mechanism that is consistent with both experimentally observed and computationally predicted behavior. We show that a rate law where a chemical step (exchange of bisulfate ligands with water) is followed by a rate determining electron transfer step, described using Marcus theory, successfully captures the extreme asymmetry of the Ce^{3+}/Ce^{4+} kinetics. Additionally, this mechanism is consistent with the differences in complexation observed for the Ce^{3+} and Ce^{4+} oxidation states. The agreement between the rate law-modeled behavior and observed kinetic behavior demonstrates the importance of understanding ion structures, considering possible mechanisms, and the utility of Marcus theory in mechanistic studies. Given the agreement between experimental and computational work, we propose that structural information from either DFT calculations or experiment can be combined with our proposed rate law to predict the activity of the Ce^{3+}/Ce^{4+} redox couple in other electrolytes. The use of Marcus theory coupled with a *CE* or

EC type mechanism informed by detailed structural data could also be applied to understand other redox couples that have seemingly anomalous empirical kinetic parameters such as V^{4+}/V^{5+}.

5.5 References

1. Marcus, R. A. Electron transfer reactions in chemistry. Theory and experiment. *Rev. Mod. Phys.* **65**, 599–610 (1993).
2. Marcus, R. A. & Sutin, N. Electron transfers in chemistry and biology. *Biochim. Biophys. Acta* **811**, 265–322 (1985).
3. Di Giacomo, F. A short account of RRKM Theory of unimolecular reactions and of Marcus Theory of electron transfer in a historical perspective. *J. Chem. Educ.* **92**, 476–481 (2015).
4. Deisenhofer, B. J. & Michel, H. The photosynthetic reaction center from the purple bacterium. *Angew. Chemie - Int. Ed.* **28**, 829–968 (1989).
5. Deisenhofer, J., Epp, O., Miki, K., Huber, R. & Michel, H. X-ray structure analysis of a membrane protein complex. *J. Mol. Bio.* **180**, 385–398 (1984).
6. Osakai, T. & Hotta, H. Electron Transfer at Liquid/Liquid Interfaces. in *International Nanochemistry: Molecular Science and Engineering at Liquid-Liquid Interfaces* (eds. Watarai, H., Teramae, N. & Sawada, T.) 171–188 (Kluwer Academic/ Plenum: New York, 2005).
7. Weaver, M. J. & Anson, F. C. Distinguishing between inner- and outer-sphere electrode reactions. Reactivity patterns for some chromium(III)-chromium(II) electron-transfer reactions at mercury electrodes. *Inorg. Chem.* **15**, 1871–1881 (1976).
8. Weaver, M. J. Correlations between electrochemical and homogeneous redox reactivity. Quantitative comparisons of rate constants and activation parameters for some inorganic outer-sphere reactions. *J. Phys. Chem.* **84**, 568–576 (1980).
9. Bard, A. J. Inner-sphere heterogeneous electrode reactions. Electrocatalysis and photocatalysis: The challenge. *J. Am. Chem. Soc.* **132**, 7559–7567 (2010).
10. Marcus, R. A. On the theory of electron-transfer reactions. VI. Unified treatment for homogeneous and electrode reactions. *J. Chem. Phys.* **43**, 679–701 (1965).
11. Buchanan, C. A. *et al.* Structures and free energies of cerium ions in acidic electrolytes. *Inorg. Chem.* **59**, 12552–12563 (2020).
12. Bard, A. J. & Faulkner, L. R. *Electrochemical Methods: Fundamentals and Applications*. (John Wiley & Sons, Inc., 2001). doi:10.1016/B978-0-08-098353-0.00003-8.
13. Heinritz, A., Binninger, T., Patru, A. & Schmidt, T. J. Asymmetric Butler−Volmer kinetics of the electrochemical Ce(III)/Ce(IV) redox couple on polycrystalline Au electrodes in sulfuric acid and the dissociation field effect. *ACS Catal.* **11**, 8140–8154 (2021).
14. Bishop, E. & Cofre, P. Anodic generation of cerium(IV). Charge-transfer kinetic parameters and confitional potentials at platinum, gold and glassy carbon. *Analyst* **106**, 316–322 (1981).
15. Kiekens, P., Steen, L., Donche, H. & Temmerman, E. Kinetics of Ce(IV) reduction at gold, carbon and iridium electrodes. *Electrochim. Acta* **26**, 841–845 (1981).
16. Randle, H. & Kuhn, T. Kinetics and mechanism of the cerium(IV)/cerium(III) redox reaction on a platinum electrode. *J. Chem. Soc., Faraday Trans. 1* **79**, 1741–1756 (1983).
17. Liu, Y., Xia, X. & Liu, H. Studies on cerium (Ce4+/Ce3+)-vanadium (V2+/V3+) redox flow cell- cyclic voltammogram response of Ce4+/Ce3+redox couple in H2SO4 solution. *J. Power Sources* **130**, 299–305 (2004).
18. Galus, Z. & Adams, R. N. The investigation of the kinetics of moderately rapid electrode reactions using rotating disk electrodes. *J. Phys. Chem.* **67**, 866–871 (1963).
19. Greef, R. & Aulich, H. The kinetics of the cerous-ceric redox reaction at a platinum electrode. *J. Electroanal. Chem. Interfacial Electrochem.* **18**, 295–307 (1968).

20. Kuhn, T. & Randle, H. Effect of oxide thickness on the rates of some redox reactions on a platinum electrode. *J. Chem. Soc., Faraday Trans. 1* **81**, 403–419 (1985).
21. Arenas, L. F., Ponce De León, C. & Walsh, F. C. Electrochemical redox processes involving soluble cerium species. *Electrochim. Acta* **205**, 226–247 (2016).
22. Binnemans, K. Chapter 229. Applications of Tetravalent Cerium Compounds. in *Handbook on the Physics and Chemistry of Rare Earths* vol. 36 281–392 (2006).
23. Kreh, R. P., Spotnitz, R. M. & Lundquist, J. T. Mediated electrochemical synthesis of aromatic aldehydes, ketones, and quinones using ceric methanesulfonate. *J. Org. Chem.* **54**, 1526–1531 (1989).
24. Devadoss, V., Ahmed Basha, C. & Jayaraman, K. Indirect electrochemical oxidation of p-methoxy-toluene to p-methoxy-benzaldehyde using ceric methanesulphonate: A scale-up study. *Ind. Eng. Chem. Res.* **47**, 4607–4616 (2008).
25. Weber, A. Z. *et al.* Redox flow batteries: A review. *J. Appl. Electrochem.* **41**, 1137–1164 (2011).
26. Xie, Z., Liu, Q., Chang, Z. & Zhang, X. The developments and challenges of cerium half-cell in zinc-cerium redox flow battery for energy storage. *Electrochim. Acta* **90**, 695–704 (2013).
27. Roznyatovskaya, N., Noack, J., Pinkwart, K. & Tübke, J. Aspects of electron transfer processes in vanadium redox-flow batteries. *Curr. Opin. Electrochem.* **19**, 42–48 (2020).
28. Gattrell, M. *et al.* Study of the mechanism of the vanadium 4+/5+ redox reaction in acidic solutions. *J. Electrochem. Soc.* **151**, A123–A130 (2004).
29. Solera, J. A., García, J. & Proietti, M. G. Multielectron excitations at the L edges in rare-earth ionic aqueous solutions. *Phys. Rev. B* **51**, 2678–2686 (1995).
30. Allen, P. G., Bucher, J. J., Shuh, D. K., Edelstein, N. M. & Craig, I. Coordination chemistry of trivalent lanthanide and actinide ions in dilute and concentrated chloride solutions. *Inorg. Chem.* **39**, 595–601 (2000).
31. Persson, I., D'Angelo, P., De Panfilis, S., Sandström, M. & Eriksson, L. Hydration of lanthanoid(III) ions in aqueous solution and crystalline hydrates studied by EXAFS spectroscopy and crystallography: The myth of the 'gadolinium break'. *Chem. - A Eur. J.* **14**, 3056–3066 (2008).
32. Urbanski, T. S., Fornari, P. & Abbruzzese, C. The extraction of cerium(III) and lanthanum(III) from chloride solutions with LIX 54. *Hydrometallurgy* **40**, 169–179 (1996).
33. Wang, Z., Chu, T., Chai, Z. & Wang, D. A density functional theory study of the competitive complexation of pyridine against H2O and Cl- to Cm3+ and Ce4+. *Radiochim. Acta* **102**, 101–109 (2014).
34. Hardwick, T. J. & Robertson, E. Association of ceric ions with sulphate (A spectral study). *Can. J. Chem.* **29**, 828–837 (1951).
35. Moore, R. L. & Anderson, R. C. Spectrophotometric studies on cerium(IV) sulfate complex ions. *J. Am. Chem. Soc.* **67**, 167–171 (1945).
36. Larsen, R. D. & Brown, G. H. The structure of ammonium hexanitratocerate(IV) in solution. *J. Phys. Chem.* **68**, 3060–3062 (1964).
37. Antonio, M. R., Ellis, R. J., Estes, S. L. & Bera, M. K. Structural insights into the multinuclear speciation of tetravalent cerium in the tri-n-butyl phosphate-n-dodecane solvent extraction system. *Phys. Chem. Chem. Phys.* **19**, 21304–21316 (2017).
38. Demars, T. J., Bera, M. K., Seifert, S., Antonio, M. R. & Ellis, R. J. Revisiting the solution structure of ceric ammonium nitrate. *Angew. Chemie - Int. Ed.* **54**, 7534–7538 (2015).

39. Rafiee, M., Nematollahi, D. & Salehzadeh, H. CEC mechanism in electrochemical oxidation of nitrocatechol-boric acid complexes. *Electrochim. Acta* **56**, 9946–9952 (2011).
40. Testa, A. C. & Reinmuth, W. H. Stepwise reactions in chronopotentiometry. *Anal. Chem.* **33**, 1320–1324 (1961).
41. Mironov, V. E. Outer-sphere complexes of tervalent cobalt. *Russ. Chem. Rev.* **39**, 319 (1970).
42. Molina, A., López-Tenés, M. & Laborda, E. Unified theoretical treatment of the Eirrev, CE, EC and CEC mechanisms under voltammetric conditions. *Electrochem. commun.* **92**, 48–55 (2018).
43. Costentin, C. & Savéant, J. M. Homogeneous molecular catalysis of electrochemical reactions: Catalyst benchmarking and optimization strategies. *J. Am. Chem. Soc.* **139**, 8245–8250 (2017).
44. Nicholson, R. S. & Shain, I. Theory of stationary electrode polarography: Single scan and cyclic methods applied to reversible, irreversible, and kinetic systems. *Anal. Chem.* **36**, 706–723 (1964).
45. Amatore, C. & Savéant, J. M. Mechanism analysis of electrochemical reactions involving homogeneous chemical steps: The electrodimerization of 4-methoxybiphenyl. *J. Electroanal. Chem.* **144**, 59–67 (1983).
46. Vassiliev, S. Y., Sentyurin, V. V, Levin, E. E. & Nikitina, V. A. Diagnostics of lithium-ion intercalation rate-determining step: Distinguishing between slow desolvation and slow charge transfer. *Electrochim. Acta* **302**, 316–326 (2019).
47. Nikitina, V. A., Vassiliev, S. Y. & Stevenson, K. J. Metal-ion coupled electron transfer kinetics in intercalation-based transition metal oxides. *Adv. Energy Mater.* **10**, 1903933 (2020).
48. Amatore, C., Lexa, D. & Savéant, J. M. ECE reaction pathways in the electrochemical reduction of dicyanocobalamin: Kinetics of ligand substitution in vitamin B12r cyanocob(II)alamin. *J. Electroanal. Chem.* **111**, 81–89 (1980).
49. Schlesener, C. J., Amatore, C. & Kochi, J. K. Kinetics and mechanism of aromatic oxidative substitutions via electron transfer. Application of Marcus theory to organic processes in the endergonic region. *J. Am. Chem. Soc.* **106**, 3567–3577 (1984).
50. Yepes, D., Seidel, R., Winter, B., Blumberger, J. & Jaque, P. Photoemission spectra and density functional theory calculations of 3d transition metal-aqua complexes (Ti-Cu) in aqueous solution. *J. Phys. Chem. B* **118**, 6850–6863 (2014).
51. Fukuzumi, S., Ohkubo, K. & Morimoto, Y. Mechanisms of metal ion-coupled electron transfer. *Phys. Chem. Chem. Phys* **14**, 8472–8484 (2012).
52. Singh, N. *et al.* Carbon-supported Pt during aqueous phenol hydrogenation with and without applied electrical potential: X-ray absorption and theoretical studies of structure and adsorbates. *J. Catal.* **368**, 8–19 (2018).
53. Ravel, B. & Newville, M. ATHENA, ARTEMIS, HEPHAESTUS: Data Analysis for X-Ray Absorption Spectroscopy Using IFEFFIT. *J. Synchrotron Radiat.* **12**, 537–541 (2005).
54. Groom, C. R., Bruno, I. J., Lightfoot, M. P. & Ward, S. C. The Cambridge structural database. *Acta Cryst.* **B72**, 171–179 (2016).
55. Zachariasen, W. H. Crystal chemical studies of the 5f-Series of elements. I . New structure types. *Acta. Cryst.* **1**, 265–268 (1948).
56. Vanýsek, P. Electrochemical Series. in *CRC Handbook of Chemistry and Physics* 1–10 (2000).

57. Efron, B. Nonparametric estimates of standard error: The jackknife , the bootstrap and other methods. *Biometrika* **68**, 589–599 (1981).
58. Aprà, E. *et al.* NWChem: Past, present, and future. *J. Chem. Phys.* **152**, 1–26 (2020).
59. Rehr, J. J., Kas, J. J., Vila, F. D., Prange, M. P. & Jorissen, K. Parameter-free calculations of X-ray spectra with FEFF9. *Phys. Chem. Chem. Phys.* **12**, 5503–5513 (2010).
60. Nosé, S. A unified formulation of the constant temperature molecular dynamics methods. *J. Chem. Phys.* **81**, 511–519 (1984).
61. Hamann, D. R. Optimized norm-conserving Vanderbilt pseudopotentials. *Phys. Rev. B* **88**, 1–10 (2013).
62. Troullier, N. & Martins, J. L. Efficient pseudopotentials for plane-wave calculations. *Phys. Rev. B* **43**, 1993–2006 (1991).
63. Dolg, M., Stoll, H. & Preuss, H. Energy-adjusted ab initio pseudopotentials for the rare earth elements. *J. Chem. Phys.* **3**, 1730–1734 (1989).
64. Ditchfield, R., Hehre, W. J. & Pople, J. A. Self-consistent molecular-orbital methods. IX. An extended Gaussian-type basis for molecular-orbital studies of organic molecules. *J. Chem. Phys.* **54**, 724–728 (1971).
65. Klamt, A. Conductor-like screening model for real solvents: A new approach to the quantitative calculation of solvation phenomena. *J. Phys. Chem.* **99**, 2224–2235 (1995).
66. Grimme, S., Antony, J., Ehrlich, S. & Krieg, H. A consistent and accurate ab initio parametrization of density functional dispersion correction (DFT-D) for the 94 elements H-Pu. *J. Chem. Phys.* **132**, (2010).
67. Becke, A. D. Density-functional exchange-energy approximation with correct asymptotic behavior. *Phys. Rev. A* **38**, 3098–3100 (1988).
68. Lee, C., Yang, W. & Parr, R. G. Development of the Colle-Salvetti correlation-energy formula into a functional of the electron density. *Phys. Rev. B* **37**, 785–789 (1988).
69. Nelsen, S. F., Blackstock, S. C. & Kim, Y. Estimation of inner shell Marcus terms for amino nitrogen compounds by molecular orbital calculations. *J. Am. Chem. Soc.* **109**, 677–682 (1987).
70. Ghosh, S., Horvath, S., Soudackov, A. V & Hammes-Schiffer, S. Electrochemical solvent reorganization energies in the framework of the polarizable continuum model. *J. Chem. Theory Comput.* **10**, 2091–2102 (2014).
71. Barca, G. M. J. *et al.* Recent developments in the general atomic and molecular electronic structure system. *J. Chem. Phys.* **152**, 1–26 (2020).
72. Emsley, J. *The Elements*. (Clarendon Press, 1988).
73. Born, M. Volumen und Hydratationswärme der Ionen. *Zeitschrift für Phys.* **1**, 45–48 (1920).
74. Nightingale, Jr., E. R. Phenomenological theory of ion solvation. Effective radii of hydrated ions. *J. Phys. Chem.* **63**, 1381–1387 (1959).
75. Lower, S. Acid strength and the acid dissociation constant (Ka). in *General Chemistry A Molecular Approach* (2022).
76. Baes, C. F. J. & Mesmer, R. E. Yttrium, Lanthanides, Actinium. in *The Hydrolysis of Cations* 138–146 (Krieger Publishing Company, 1986).
77. Ikeda-Ohno, A., Tsushima, S., Hennig, C., Yaita, T. & Bernhard, G. Dinuclear complexes of tetravalent cerium in an aqueous perchloric acid solution. *Dalt. Trans.* **41**, 7190–7192 (2012).
78. Fronaeus, S. & Ostman, C. O. The mechanism of the exchange reaction between cerium(III) and cerium(IV) at platinum surfaces. *Acta Chem. Scand.* **10**, 769–778 (1956).

79. Hardwick, T. J. & Robertson, E. Ionic species in ceric perchlorate solutions. *Can. J. Chem.* **29**, 818–827 (1951).
80. Heidt, L. J. & Smith, M. E. Quantum yields of the photochemical reduction of ceric ions by water and evidence for the dimerization of ceric ions. *J. Am. Chem. Soc.* **70**, 2476–2481 (1948).
81. Zhao-hua, L., You-qun, C. & Chun-an, M. A comparative study of Ce3+/Ce4+ redox couple on Pt electrode in sulfuric acid and methanesulfonic acid. *J. Electrochem.* **19**, 141–145 (2013).
82. Daum, P. H. & Enke, C. G. Electrochemical kinetics of the ferri—ferrocyanide couple on platinum. *Anal. Chem.* **41**, 653–656 (1969).
83. Tanimoto, S. & Ichimura, A. Discrimination of inner- and outer-sphere electrode reactions by cyclic voltammetry experiments. *J. Chem. Educ.* **90**, 778–781 (2013).
84. Chen, P. & McCreery, R. L. Control of electron transfer kinetics at glassy carbon electrodes by specific surface modification. *Anal. Chem.* **68**, 3958–3965 (1996).
85. Frumkin, A. Hydrogen overvoltage and the structure of the double layer. *Z. Phys. Chem. A-Chem. T.* **164**, 121–133 (1933).
86. Kant, R., Kaur, J. & Mishra, G. K. Theory for influence of the metal electrolyte interface on heterogeneous electron transfer rate constant: Fractional electron transferred transition state approach. *J. Phys. Chem. C* **124**, 2273–2288 (2020).
87. Galizzioli, D. & Trasatti, S. Work function, electronegativity, and electrochemical behavior of metals. IV. Simple electron exchange reactions. Fe2+/Fe3+ redox couple. *Electroanal. Chem. Interfacial Electrochem.* **44**, 367–388 (1973).
88. Barr, S. W., Guyer, K. L. & Weaver, M. J. The dependence of the kinetics of some simple outer-sphere electrode reactions on the nature of the electrode material. *J. Electroanal. Chem.* **111**, 41–59 (1980).
89. Liu, H. Y., Hupp, J. T. & Weaver, M. J. Surface environmental effects in electrochemical kinetics: Outer-sphere chromium(III) reductions at mercury, gallium, lead, and thallium surfaces. *J. Electroanal. Chem.* **179**, 219–238 (1984).
90. Iwasita, T., Schmickler, W. & Schultze, J. W. Influence of the metal on the kinetics of outer sphere redox reactions. *Berichte der Bunsengesellschaft/Physical Chem. Chem. Phys.* **89**, 138–142 (1985).
91. Velmurugan, J., Sun, P. & Mirkin, M. V. Scanning electrochemical microscopy with gold nanotips: The effect of electrode material on electron transfer rates. *J. Phys. Chem. C* **113**, 459–464 (2009).
92. Scott, S. L. The burden of disproof. *ACS Catal.* **9**, 4706–4708 (2019).
93. Hupp, J. T. & Weaver, M. J. The frequency factor for outer-sphere electrochemical reactions. *J. Electroanal. Chem.* **152**, 1–14 (1983).
94. Blumer, A., Ehrenfeucht, D. & Warmuth, M. K. Occam's Razor. *Inf. Process. Lett.* **24**, 377–380 (1987).
95. Chattopadhyay, S. *et al.* Contributions to cytochrome c inner- and outer-sphere reorganization energy. *Chem. Sci.* **12**, 11894–11913 (2021).
96. Clegg, A. D., Rees, N. V., Klymenko, O. V., Coles, B. A. & Compton, R. G. Marcus theory of outer-sphere heterogeneous electron transfer reactions: High precision steady-state measurements of the standard electrochemical rate constant for ferrocene derivatives in alkyl cyanide solvents. *J. Electroanal. Chem.* **580**, 78–86 (2005).

Chapter 6 Conclusions, Future Work, and Outlook

In this chapter, a review of the work completed in this dissertation is first provided, as well as general conclusions that can be drawn from the work. In **Sections 6.2** and **6.3**, limitations of the TEA-LCI model and experimental work are discussed, which help to highlight valuable areas of future work. A discussion of the practical challenges associated with developing a Ce-V RFB is also presented. Finally, the TEA-LCI model, thermodynamic, and kinetic results are synthesized in **Section 6.4** to provide guidelines for future researchers related to the economic feasibility of electrolyte engineering and electrode design strategies. An overall outlook of the current state of Ce RFBs based on the results and limitations of the dissertation is also presented.

6.1 Summary and conclusions

Redox flow batteries (RFBs) are a favorable energy storage technology for integrating renewable energy into the electricity grid given their capability to deliver energy over long discharge times and scale energy storage and power delivery separately. The cost of energy storage for the state-of-the-art RFB, the all-vanadium or VRFB, currently exceeds the targets for capital cost and levelized cost of electricity (LCOE) set by the U.S. DOE.[1] The Ce^{3+}/Ce^{4+} chemistry is a promising alternative for the positive electrolyte in RFBs given its high voltage, relative abundance, and cheaper precursor cost. The Ce^{3+}/Ce^{4+} redox potential is significantly impacted by the acid that it is dissolved in, which suggests that the anions in solution are interacting with the Ce^{3+} and Ce^{4+} ions. The structures of the Ce ions were not well understood, however, which limits any efforts to control the Ce^{3+}/Ce^{4+} thermodynamics for optimal performance in RFB systems.

Additionally, the kinetics of the Ce^{3+}/Ce^{4+} are relatively slow and the charge transfer mechanism is unknown, meaning that the factors that control the rate of reaction are not isolated.

The goal of the dissertation was to assess the economic and environmental viability of a Ce-based RFB compared to the VRFB system, as well as to investigate the structures of the Ce ions in acids relevant for battery applications and the charge transfer mechanism through detailed kinetic studies. We showed that a Ce-V RFB is more cost competitive than the VRFB except at high current densities and does not result in a significant increase in GHG emissions for cost optimization scenarios. The shift in redox potential is driven by anion complexation with Ce^{4+}, whereas Ce^{3+} is coordinated by water in all acids considered. Kinetic measurements suggested outer-sphere like behavior, and a two-step mechanism that aligned with both structural and kinetic data by including a chemical ligand exchange step in addition to an electron transfer step was identified. Given the influence of electrolyte acid on both Ce thermodynamics and kinetics, future efforts to improve a Ce-based RFB should focus on isolating an electrolyte that optimizes thermodynamics and kinetics without resulting in a significant increase in electrolyte cost. After providing more detailed summaries of each of the chapters, we provide suggestions for future work including screening electrolytes further below.

In **Chapter 3**, combined technoeconomic (TEA) and life cycle inventory (LCI) models were used to assess the levelized cost of electricity (LCOE) and levelized greenhouse gas emissions (LGHG) of the Ce-V RFB and VRFB. The TEA-LCI models were bottom-up component models that calculated the cost and emissions based on the charge and discharge voltages of the RFB, which were dependent on the operating current density as well as kinetic, thermodynamic, and ohmic input parameters. For the current average U.S. electricity mix and a discharge time of 12 hours, the minimum LCOE of the Ce-V RFB was found to be 0.170 $/kWh$_d$

at a current density of 63.7 mA/cm^2, compared to the minimum LCOE for the VRFB of 0.178 \$/kWh$_d$ at a current density of 69.2 mA/cm^2. The corresponding LGHGs for the Ce-V RFB and VRFB at these minimized LCOE conditions were 0.634 kg CO_2e/kWh$_d$ and 0.581 kg CO_2e/kWh$_d$, respectively. The lower cost of the Ce-V RFB system was driven primarily by the higher open circuit voltage as well as the lower cost of the positive electrolyte. The emissions are higher for the Ce-V RFB than the VRFB because of the worse roundtrip efficiency which drives up use phase emissions as well as higher emissions associated with the CeO_2 precursor than the V_2O_5 precursor. The most influential parameters on the LCOE for both batteries were the electrolyte redox potential, the cost of the V_2O_5 precursor, kinetics, and faradaic efficiency. The emissions were controlled by the redox potentials, faradaic efficiency, kinetics for both RFBs. The CeO_2 production emissions were more influential to the Ce-V RFB LGHG than the V_2O_5 production emissions were for the VRFB. As the electricity grid becomes more renewable, the LCOE for both RFBs increases, but the LGHG is dramatically reduced because of the dominant influence of the use phase emissions on overall LGHG. This study confirms that the Ce^{3+}/Ce^{4+} chemistry is a viable alternative for the positive electrolyte in RFBs and motivates experimental work to better understand the Ce^{3+} and Ce^{4+} ion structures' influence on thermodynamics as well as the Ce^{3+}/Ce^{4+} kinetics given the fact that Ce^{3+}/Ce^{4+} thermodynamics and kinetics heavily influence LCOE and LGHG.

In **Chapter 4**, we study the structures of the Ce^{3+} and Ce^{4+} ions in seven different acids using a combination of experimental and computational techniques. Specifically, UV-Vis and extended x-ray absorption fine structure (EXAFS) are used to compare the coordination environment of Ce^{3+} in 2 M CH_3SO_3H (MSA), CF_3SO_3H (TFSA), HNO_3, H_2SO_4, and HCl. Both the UV-Vis and Ce L_3-edge EXAFS spectra of Ce^{3+} are similar across all five acids, suggesting a

common coordination environment, i.e., coordination with only water. Through fitting of the EXAFS, we determined a Ce^{3+}-O coordination number of nine. We confirmed through density functional theory (DFT) calculations that the preferred structure of Ce^{3+} in the five acids listed above, as well as $HClO_4$ and H_2NSO_3H, is $[Ce^{III}(H_2O)_9]^{3+}$. The Ce L_3-edge EXAFS of Ce^{4+} in 2 M H_2SO_4 demonstrated that the Ce^{4+}-O scattering distance was shorter than the Ce^{3+}-O scattering distance, and UV-Vis of Ce^{4+} in H_2SO_4, MSA, and HCl all displayed different peak locations and intensities, suggesting ligand-to-metal charge transfer. DFT-predicted Gibbs free energy of anion complexation indicated that Ce^{4+} was preferentially complexed by at least one anion in all seven acids considered, e.g., $[Ce^{IV}(H_2O)_8X^{-n}]^{(4-n)+}$, instead of being coordinated by all waters. The DFT-predicted anion complexation energy was in good agreement with the shift in redox potential observed for the Ce^{3+}/Ce^{4+} redox couple, suggesting that the anion complexation of Ce^{4+} is responsible for the shift in redox potential. This result has useful implications for the use of the Ce^{3+}/Ce^{4+} chemistry in flow battery applications because our findings indicate that the redox potential can be tuned by adjusting the structures of Ce^{3+} and Ce^{4+} in electrolyte solution.

In **Chapter 5**, the structures of the Ce^{3+} and Ce^{4+} ions were confirmed in H_2SO_4 using additional EXAFS and molecular dynamics (MD)-EXAFS techniques, and the Ce^{3+}/Ce^{4+} kinetics were studied on two electrode materials in H_2SO_4 to identify a possible charge transfer mechanism that aligned with both the structure and kinetics information. We co-fit Ce K-edge EXAFS and Ce L_3-edge EXAFS of Ce^{3+} in 2 M H_2SO_4 to resolve remaining uncertainties in the structure of Ce^{3+} in H_2SO_4 from **Chapter 4**, and it was confirmed that the structure of Ce^{3+} was $[Ce^{III}(H_2O)_9]^{3+}$. Evidence of a Ce^{4+}-scattering pathway was observed in the Ce K-edge EXAFS of Ce^{4+} in 2 M H_2SO_4, which was confirmed through the comparison of MD-EXAFS of $[Ce^{IV}(H_2O)_9]^{4+}$ and $[Ce^{IV}(H_2O)_8SO_4]^{2+}$ structures. The co-fit of Ce L_3- and K-edge EXAFS of Ce^{4+} in 2 M H_2SO_4

revealed a Ce^{4+}-S coordination number of three, however. Given the more favorable DFT-predicted Gibbs free energy of $[Ce^{IV}(H_2O)_6(HSO_4)_3]^+$ than $[Ce^{IV}(H_2O)_6(SO_4)_3]^{2-}$, we concluded that Ce^{4+} is complexed by three bisulfate anions in sulfuric acid. To study the kinetics of the Ce^{3+}/Ce^{4+} redox couple, the exchange current densities and Tafel slopes were measured as a function of both Ce^{4+} ion concentration and temperature to extract standard rate constants, charge transfer coefficients, and apparent activation energies on platinum (Pt) and glassy carbon (GC) rotating disk electrodes. The standard rate constants for Pt and GC differed by less than a factor of five, which aligns with other outer-sphere redox couples, and the charge transfer coefficients were both equal to 0.23, demonstrating extreme asymmetry. These findings suggested that the Ce^{3+}/Ce^{4+} electron transfer proceeds through an outer-sphere mechanism, however, standard outer-sphere mechanisms described through the Butler-Volmer formulism of kinetics or Marcus theory do not allow for a chemical step (*C*) in addition to an electron transfer (*E*). We explored two two-step mechanisms (*CE* and *EC*), using Marcus theory to describe the *E* step, and we determined that only the *CE* mechanism in which the *E* step was rate-determining resulted in a satisfactory fit of the kinetic data while also correctly predicting Ce^{4+} was preferentially complexed by anions in solution. The rate law developed for this mechanism can be used to screen the kinetic activity of the Ce^{3+}/Ce^{4+} redox couple in additional acids, assuming the *CE* mechanism holds. Additionally, given the outer-sphere behavior of the kinetics, we know the electrode will not control the kinetics, but rather the electrolyte will.

This work provided valuable information on the Ce^{3+}/Ce^{4+} chemistry which motivates further consideration of Ce-based RFB systems given the cost competitiveness of the Ce-V RFB, tunability of the Ce^{3+}/Ce^{4+} redox potential, and discovery of a potential charge transfer mechanism that can be used to screen the activity in additional electrolytes. We showed that the electrolyte

controls the thermodynamics and kinetics, which has important implications for future efforts to enhance Ce RFB performance, because we showed that the Ce^{3+}/Ce^{4+} redox potential and exchange current density both have a significant impact on LCOE and LGHG. Limitations related to the TEA-LCI study and experimental work of the dissertation are addressed in the sections below with the objective of motivating future avenues of work as well as to provide practical suggestions for using Ce in RFBs.

6.2 Limitations of TEA-LCI study and practical considerations for a Ce-based RFB

The goal of this section is to highlight simplifications that were made in the TEA-LCI study of the Ce-V RFB and VRFB in **Chapter 3** that should be revised in future iterations of the model to provide a more robust analysis of Ce-based RFB economic and environmental costs. Additionally, this discussion provides context on some of the remaining practical challenges associated with Ce-based RFBs related to the omissions and simplifications made in the model. These limiting assumptions are related to the modeled life cycle phases (**Section 6.2.1**), material replacement scenarios throughout the RFB lifetime (**Section 6.2.2**), competitive oxygen and hydrogen evolution reactions (**Section 6.2.3**), capital and operating costs in the LCOE calculation (**Section 6.2.4**), the sensitivity analysis (**Section 6.2.5**), Ce-based RFB chemistries (**Section 6.2.6**), and the availability of active species (**Section 6.2.7**). Each of these limitations is addressed below.

6.2.1 Incorporation of end-of-life phase

Based on previous LCA studies of the VRFB that indicated that the end-of-life (EoL) phase of the battery, which includes the disposal and recycling phases, is negligible compared to the production and use phases,[2,3] the EoL phase emissions or cost was not modeled in our work. While the basis for not including the EoL phase is sound, future technoeconomic and life cycle

assessment studies should incorporate the EoL phase for a more accurate picture of the total costs and emissions associated with the Ce-V RFB and VRFB. The incorporation of recycling rates for the Ce and V actives species could especially impact the results, i.e., by decreasing the required amount of virgin material and thereby driving down the LCOE or LGHG of the RFB when operated at conditions where energy-dependent capital is a significant factor to overall cost or emissions. The recycle rate of vanadium from spent catalysts is 40%,[4] while the recovery rate for rare earths from batteries, permanent magnets, and fluorescent lamps is limited.[4] The significantly higher recycle rate for V than Ce suggests that the production emissions and energy-dependent costs of V_2O_5 could be reduced significantly if the EoL phase were incorporated, while the CeO_2 production costs and emissions would not decrease. Thus, in future TEA-LCI models comparing Ce-based RFBs to the VRFB, the EoL phase should be accounted for.

6.2.2 Replacement scenarios

In this study, it was assumed that all of the components of the cell, e.g., the electrodes, bipolar plates, and membrane, as well as the electrolyte feedstock, would remain stable for the entire RFB lifetime of 20 years. We justified this simplification by assuming that the cell components and electrolyte feedstock would have similar lifetimes in each RFB system, and so any changes to the baseline replacement scenario would affect the Ce-V RFB and VRFB LCOE and LGHG in the same manner. While this assumption most likely holds for many of the cell components, we expect that realistically, the electrolyte replacement scenarios for the Ce-V RFB and VRFB may differ.

We expect crossover of active species to be a more significant issue for the Ce-V RFB system than the VRFB system, and as a result, the Ce-V RFB electrolyte would need to be replaced more frequently. Crossover of active species or solvent across the ion-exchange membrane occurs

due to pressure, potential, and concentration gradients,[5] and results in a concentrated solution on one side of the RFB and a dilute solution on the other,[6] which reduces the storage capacity and is called capacity fade. In our models, we assumed the ion exchange membrane was the standard Nafion membrane, which is a cation-exchange membrane. Although in ideal operation, only protons would be allowed from one compartment of the RFB to the other through Nafion, crossover of the vanadium or cerium cations can also occur. For the VRFB, which is symmetric, the crossover of active species does not result in permanent capacity fade, and the capacity can be recovered through rebalancing, where the positive and negative electrolytes are mixed so that the vanadium ion concentrations reach an equilibrium.[5] Rodby et al. showed that the VRFB storage cost was minimized when rebalancing was conducted after capacity had reached 83% of its initial value.[5] Thus, replacement of the electrolyte would not be necessary in VRFB systems to address capacity fade. Because the Ce-V RFB has different ions in each electrolyte, the crossover of the active species could result in additional problems such as precipitation, membrane fouling, or electrode degradation,[5] which could all result in permanent capacity fade, necessitating complete replacements of electrolyte material. As a result, the LCOE and LGHG of Ce-V RFB would increase relative to the VRFB due to the increased energy-dependent material costs. Future TEA-LCI studies should account for this capacity fade and resulting Ce-V RFB electrolyte replacement. Other strategies to address crossover that could be studied in future modeling work include using anion exchange membranes, which would not allow cations to transport through, or using Nafion with modifications, e.g., charge- or size-exclusion pores,[5] which can be achieved through the sol-gel method and excludes larger cations like vanadium.[6]

6.2.3 Addressing competitive side reactions

The oxygen evolution reaction (OER) and hydrogen evolution reaction (HER) have standard redox potentials at 1.23 V vs. SHE[7] (in acid) and 0 V vs. SHE,[8] respectively, which means that they could be occurring as side reactions for both the VRFB and Ce-V RFB systems. Competitive OER and HER were not explicitly addressed in our TEA-LCI study. Instead, the effect of these competitive reactions was accounted for by the faradaic efficiency, which is the percent of electrons used towards the desired reaction. The baseline roundtrip faradaic efficiency in both models was assumed to be 98%, however, the Ce-V RFB may have a lower faradaic efficiency than the VRFB because of the higher oxidizing potential at the positive electrode that could result in more significant rates of OER. Herein, we considered the effect of varying faradic efficiency on Ce-V RFB and VRFB LCOE and LGHG results in the sensitivity analysis and found that if the Ce-V RFB roundtrip faradaic efficiency were 90.25%, then its LCOE would be larger than the VRFB LCOE assuming a faradaic efficiency of 98%. Future TEA-LCI studies should include strategies for addressing parasitic side reactions.

Practical strategies for addressing OER and HER in other battery systems include electrolyte maintenance, valve regulation, and kinetic stabilization through electrolyte composition and electrode materials, and these strategies should be considered in future TEA-LCI modeling for Ce-based RFBs to determine which are appropriate. Electrolyte maintenance and valve regulation are strategies that help to offset the evolution of hydrogen at the cathode and oxygen at the anode. The lead (Pb)-acid battery has an open circuit voltage (OCV) between 2-2.15 V, which is significantly greater than the water stability window of 1.5 V,[9] and as such, some HER and OER occur, which causes the water content of the battery to decrease overtime and can decrease the lifetime of Pb-acid batteries. In unsealed Pb-acid batteries, water is added periodically

to the battery to make up for this water hydrolysis. Another technique for Pb-acid batteries is to use valve-regulation to capture the H_2 and O_2 that is formed and catalytically react the gases to form water, which eliminates the need for electrolyte maintenance, i.e., the addition of water.[9] These systems use pressure-release valves to control the internal pressure. In RFBs, additional reactors that are separate from the RFB have been used to evolve H_2 and O_2 from the electrolyte in order to control the production of hydrogen and oxygen in the actual RFB.[9] Electrolyte engineering has been used to inhibit HER and OER. For instance, the pH of the electrolyte can be increased to decrease proton concentration, which reduces the rate of HER possible.[9,10] Altering the pH, however, can have adverse effects on electrode stability[12] and redox potential and solubility.[11] Very concentrated electrolytes, also referred to as "water-in-salt" electrolytes, have also been used in aqueous batteries to reduce the amount of water available for HER and OER, and polar protic solvents can be used to change hydrogen bonding networks.[9] These strategies have a potential downside of increased viscosity and higher cost solvents. Another strategy is molecular crowding, in which agents such as polyethylene glycol are used to alter the hydrogen bonds of water in order to suppress water activity.[11] Finally, electrodes that suppress HER and OER have been explored for aqueous energy storage systems, for instance, lead, zinc, and bismuth have all been reported to be "HER anticatalysts," because of their large HER overvoltages, and mixed metal oxides and metal organic frameworks inhibit OER.[12] Mixed metal oxides used at the anode in the chloro-alkali process are a promising anode for Ce-based RFBs which will be discussed in more detail in **Section 6.4.2**. These practical strategies for mitigating the competitive HER and OER should all be considered in a TEA-LCI model for a Ce RFB to determine which are cost-effective and result in the least increase in emissions. Guidelines for assessing the performance versus cost increase of an electrolyte or electrode are addressed further below in **Section 4.6.3**.

6.2.4 Incorporation of additional capital and operating costs

Conventionally, technoeconomic analyses should include fixed and working capital costs, as well as fixed, variable, and general operating costs.[13] Capital costs are one-time expenses, and fixed capital costs refer to all equipment purchases and construction, while working capital cost includes startup costs such as salaries and raw material. Variable operating costs, such as raw materials, waste treatment, utilities, and labor, scale with the operating rate, while fixed and general operating costs do not. Examples of fixed operating costs are insurance and taxes, and marketing, administration, and research and development costs are examples of general operating costs.[13] In this study, we created an economic analysis that paralleled the life cycle inventory, so only costs associated with raw materials (working capital), equipment (fixed capital), and electricity delivery (variable operating) were included. It was assumed that capital costs like construction costs and operating costs like labor and taxes would be the same between a Ce-V RFB and a VRFB and thus could be neglected for the purposes of comparing the costs of the two systems. For a more accurate cost of energy storage value for both RFBs, however, these types of costs should be incorporated. Previous TEAs of the VRFB have included factors such as operating cost and labor, which were estimated to be 40 $/kW/yr and 1 $/kWh, respectively.[14]

Another engineering consideration for the RFB is the balance of plant (BOP). BOP for an RFB generally includes components such as electrolyte storage tanks, recirculation loops for reactants, a power conversion system (PCS), and a system controller.[15] BOP costs can be influential to the overall cost of the RFB, for instance Mongird et al. reported that a VRFB BOP can account for 20% of the total cost of storage.[16] BOP costs are also known to be significant for a similar type of technology, the proton exchange membrane (PEM) fuel cell. In PEM fuel cells, the BOP is a collection of auxiliary systems that are needed for the fuel cell operation, including

air compression, humidification, and cooling, which all take power away from the output.[17] It is important that BOP be appropriately modeled to obtain an accurate assessment of the BOP costs. In our TEA-LCI model, we sized the electrolyte storage tanks based on the amount of active species needed at a specific current density and had a separate line-item cost for the PCS, but the remainder of the BOP costs were lumped into one aggregate number that was not dependent on the size of the system. This is a limitation of the current model that should be revised in future iterations of TEA-LCI models of Ce-based RFBs.

6.2.5 Practical aspects of sensitivity analysis

The purpose of the sensitivity analysis was to determine the relative effect of the kinetic and thermodynamic parameters, as well as the faradaic efficiency and cost, emissions intensity, and solubility of the active species, on overall cost and emissions of the RFB systems. The relative effect of each parameter was studied in **Chapter 3** by individually increasing/decreasing the value of each parameter by 20% to see the resulting impact on either minimum LCOE or LGHG, except for the redox potential and faradaic efficiency, which were changed by 200 mV and 2%, respectively. This type of sensitivity analysis is a simple way to determine which factors are most important and should be focused on in future research efforts as well as to highlight which factors need to have more certainty in their values and for which values large uncertainties can be tolerated.

A downside to this type of sensitivity analysis, however, is that there is no practical consideration as to whether the modeled increase or decrease is realistic, or if the change in one parameter will influence another parameter. For instance, while the Ce^{3+}/Ce^{4+} redox potential has actually been observed to vary by up to 300 mV from the standard redox potential value in $HlCO_4$,[18] the V^{2+}/V^{3+} redox potential and V^{4+}/V^{5+} redox potentials have not been observed to vary

by 200 mV. As discussed in greater detail in **Chapter 3**, the VRFB OCV can be increased from 1.26 V (expected from the V^{2+}/V^{3+} and V^{4+}/V^{5+} standard redox potentials) to 1.4 V by varying the electrolyte proton concentrations as well as through the Donnan potential.[19] Thus, efforts to improve the VRFB LCOE or LGHG should not only focus on trying to improve the thermodynamics of the system, despite the V^{4+}/V^{5+} redox potential being highly influential on LCOE and LGHG. Additionally, many of the factors that were varied individually would not in actuality be independent of each other. As an example, if a catalyst were identified that resulted in increased exchange current density, it is likely that the Tafel slopes equally would be improved, i.e., decrease in value. Additional parameters should be included in the sensitivity analysis that address performance factors other than kinetics and thermodynamics, such as limiting current. Additionally, if an increase in kinetics were obtained through changes to the electrolyte, i.e., through electrolyte engineering, then the thermodynamics would most likely be altered as well, especially for the Ce^{3+}/Ce^{4+} system for which we know the electrolyte controls both the thermodynamics and kinetics. This concept is explored more rigorously in **Section 6.4** for the Ce^{3+}/Ce^{4+} chemistry, but future iterations of a TEA-LCI model of Ce- and V-based RFBs should consider the practical aspects of changing performance parameters in a sensitivity analysis. Finally, we assume that a change in a performance parameter obtained from bench scale experiments will translate to the same change in a flow battery set up, despite no flow battery performance testing. A comparison of the modeled change in performance and the observed change in real flow battery performance with a change in parameter, e.g., through selection of a different electrolyte or electrode material, should be conducted to validate the sensitivity analysis findings.

6.2.6 Other Ce-based RFBs

As mentioned in **Chapter 1**, in addition to Ce-V RFBs, the Ce^{3+}/Ce^{4+} chemistry has been paired with the H_2/H^+ and Zn/Zn^{2+} chemistries at the negative electrode in lab-scale RFB performance tests. These other likely chemistries were not modeled in the TEA-LCI model in **Chapter 3** and should be considered in future Ce-based RFB TEA studies. Hydrogen is considered advantageous as the negative active species in RFBs because it is inexpensive, has fast redox kinetics, and it can be easily separated from positive electrolyte liquid in the event of crossover.[20] Additionally, the infrastructure for a proton-exchange membrane fuel cell, which is a more mature technology that uses hydrogen, can inform the design of a H_2-based RFB.[20] Depending on the acid used for the Ce electrolyte, the Ce-H_2 RFB would have an OCV ranging from 1.44-1.74 V. Lab-scale studies of a Ce-H_2 RFB cell have demonstrated a maximum discharge power of 895 mW/cm^2 and an energy efficiency of 90% at elevated temperatures.[20] Future TEA-LCI models should incorporate this reported performance to determine the expected cost and emissions of the Ce-H_2 RFB compared to the VRFB.

Given the more negative redox potential of the Zn/Zn^{2+} (-0.76 V vs. SHE[21]) redox couple than V^{2+}/V^{3+} (-0.26 V vs. SHE[21]), which would lead to a significantly wider voltage window, it is anticipated that the cost of the Ce-Zn RFB would be further reduced relative to the Ce-V RFB. The cost of zinc (~3 $/kg[22]) is significantly lower than V_2O_5, which would further drive down cost. One previous preliminary economic assessment of the capital costs of a Ce-Zn system relative to a VRFB exists,[23] which indicated that the Ce-Zn RFB was less expensive than the VRFB. The cost of charging the electricity grid was not incorporated in this study, however, and so additional modeling of the Ce-Zn costs is merited.

6.2.7 Availability of active species

Estimates of the global 2021 production rate of Ce range between 24,000[24]-106,000 metric tons.[4,25] Assuming an operating current density of 63.7 mA/cm^2, which was the optimal current density to minimize Ce-V RFB LCOE (**Chapter 3**), the discharge efficiency of the Ce-V RFB is 71.4%. At these conditions, the amount of Ce needed per kWh of electricity delivered is 29.26 mol Ce/kWh$_d$. Thus, according to **Eq. 6.1** below, the total amount of storage capacity possible for Ce-V RFBs if we assume an annual production rate of cerium of 106,000 metric tons and a 12-hour discharge time is 2.15×10^6 kW per year. This means that by 2050, we could supply approximately 60 GW of additional storage capacity through Ce-V RFBs, if all of the global supply of Ce were used in Ce-V RFBs. Given the 24 GW of storage capacity currently available in the U.S.,[26] this amounts to 84 GW of total storage capacity by 2050, which corresponds to a renewable energy electricity grid penetration level between 60% and 70% by 2050.[27]

$$Annual\ Storage\ Capacity(kW) = \frac{Production\ rate\ \left(\frac{g}{yr}\right)}{MW_{Ce}\left(\frac{g}{mol}\right)} \times \frac{1\ kWh_d}{29.26\ mol\ Ce} \times \frac{1}{discharge\ time\ (hr)} \quad \textbf{(6.1)}$$

Additionally, global reserves of rare earth oxides are estimated at approximately 120 million metric tons,[4] where reserves refers to the amount of a resource that could feasibly be extracted. Since Ce makes up approximately 38% of rare earth oxides by mass,[25] if all of the cerium available in reserves were used in Ce-V RFB, we would have a total available storage capacity of ~930 GW. While this calculation provides an indication of the potential storage capacity of Ce in Ce-V RFB, practical considerations related to the current use and availability of Ce remain.

Extraction processes to obtain Ce from rare earth oxides, competition with current uses of Ce for supply, and geographical availability of Ce are all important considerations of using Ce in

RFB applications. Cerium is the most abundant of the rare earth elements and is extracted from rare earth ores such as bastnäsite (REE-CO_3F),[25] monazite (REE-PO_4),[25] and loparite (REE-$(Ti,Nb)O_3$).[28] On average, cerium makes up 38% of rare earth oxides.[25] The 4+ oxidation state of cerium is unique among rare earth elements, providing a convenient means of extracting cerium from the other rare earth elements. To extract Ce, acid leaching and selective oxidation processes are typically employed. For instance, at the Molycorp Mountain Pass, U.S. mine, the bastnäsite is baked at 620 ℃, which causes CO_2 to be emitted and oxidizes Ce^{4+}.[29] Then, this product is exposed to HCl, and the non-cerium components dissolve so that the cerium concentrate can be collected.[29] Ce can also be extracted through sulfuric acid double salt precipitation.[30] We expect that as cerium production rates increase, extraction methods will become more cost and emissions intensive as the rare earth oxides become less abundant, and this effect could be modeled through an increase in productions cost or emissions in a TEA-LCI model. Cerium oxide is currently used in catalytic converters,[24,28] as a glass additive,[28] in glass polishing additives,[28] and in casting alloys.[24] It is estimated that as of 2010, 19,000 metric tons of cerium oxide were used in catalytic converters in the U.S.,[31] and approximately 15,000 metric tons of cerium oxide is used in the glass industry as of 2015.[28] While the glass industry consumption of cerium oxide represents a potential source of competition with using cerium in RFB applications, cerium is considered a low value byproduct of other more valuable REEs that are used in permanent magnet applications. Cerium has been noted to be returned to the mine at additional cost.[25] Recent work has focused on identifying high-volume and high-value applications for Ce so that rare earth mining becomes more economical overall.[25] Thus, by establishing a large market for Ce in RFB applications, the rare earth supply chain would become more economical. Additionally, it is expected that electric vehicles will grow to be 31% of the global vehicle market by 2050,[32] and as electric vehicles become more prevalent

than internal combustion engines, the need for catalytic converts will decrease, representing a significant supply of additional cerium oxide that will become available for RFB applications. Finally, the geographic availability of cerium remains a concern that should be addressed if Ce-based RFBs are to be used in the U.S. The U.S. production of rare earth oxides in 2021 accounted for approximately 15% of the global production, whereas production in China accounted for 60%.[4] Production in Australia and Burma accounted for 8% and 9%, respectively, of global production.[4] Given the volatility of trade relations between the U.S. and China, it will be important to identify a domestic supply of cerium in the U.S.. To this end, in 2021, the U.S. DOE pledged 30 million dollars to advance the rare earth supply chain in the U.S.,[33] underscoring the growing importance of rare earth elements, including cerium.

In addition to having a growing market, cerium is more abundant than vanadium, which is the active species in the state-of-the-art for RFBs. The global annual production of vanadium is 110,000 metric tons,[4] which is comparable to the global annual production of cerium. However, the global reserves of vanadium are 24 million metric tons,[4] compared to cerium's 46 million metric tons. The fact that cerium reserves are approximately double those of vanadium means that significantly more storage capacity could be available from Ce-based RFB systems than from VRFBs. Cerium should be considered a key strategy in future energy storage applications. This section has presented the opportunities for future TEA-LCI modeling work, as well as highlighted the practical considerations such as electrolyte maintenance, electrode selection, and cerium availability that must be accounted for if Ce is to be used in RFB applications. **Section 6.3** will present the limitations of the experimental studies conducted in **Chapters 4** and **5** in order to underscore the additional work that should be completed to better understand the structures, thermodynamics, and kinetics of the Ce^{3+}/Ce^{4+} redox reaction for RFB systems.

6.3 Limitations of experimental work and implications for predicting RFB performance

The goal of this section is to highlight the limitations in the spectroscopy and kinetics measurements of the dissertation as well as to suggest future areas of work that would strengthen the conclusions drawn from the experimental work and allow us to better link the fundamental structural and kinetics information collected here to RFB performance. The difference in cerium concentrations used in the TEA-LCI models and used in spectroscopy and kinetic measurements is addressed in **Section 6.3.1**. In **Section 6.3.2**, the lack of experimental study of the Ce^{4+} structure is addressed and recommendations for techniques to resolve the experimental difficulties we faced are proposed. The limitations of the kinetics studies are highlighted in **Section 6.3.3**, and the implications of these limitations for predicting Ce kinetic activity in RFB systems is discussed.

6.3.1 Experimental concentrations of Ce compared to RFB modeled concentrations

Due to experimental limitations, the cerium concentrations were lower in the spectroscopy and kinetics measurements than were modeled in the TEA-LCI models, which could lead to a difference in the relevant charge transfer mechanism that is prevalent for the RFB. To maximize energy storage capacity, we assumed that the concentration of cerium in the Ce-V RFB would be the solubility limit of Ce^{4+} in 2 M H_2SO_4, which is 0.35 M. The Ce L_3-edge EXAFS spectra collected of Ce^{3+} and Ce^{4+} in **Chapter 4** were collected at cerium concentrations of 0.1 M, however, because higher cerium concentrations would have caused attenuation of the X-ray in the sample. The Ce K-edge EXAFS of Ce^{3+} and Ce^{4+} were conducted at 0.05 M Ce concentration again due to attenuation limitations (**Chapter 5**). We demonstrated that at the conditions tested, there was no evidence of Ce^{3+}-anion complexation, whereas we determined that Ce^{4+} was complexed by three bisulfates in 2 M H_2SO_4. This experimental evidence, coupled with DFT calculations, led us to conclude that the anion complexation of Ce^{4+} was responsible for the shift

in Ce^{3+}/Ce^{4+} redox potential with acid. As discussed in **Section 1.4.2**, however, there has been evidence of Ce^{3+}-anion complexation with sulfate, nitrate, and chloride reported previously, especially at higher concentrations of chloride. This discrepancy could be due to differences in the cerium or acid concentrations selected in our study versus these previous studies. Although we did study the structures of the Ce^{3+} or Ce^{4+} ions in 2 M acids, which was the concentration of H_2SO_4 assumed for the RFB model, it is possible that the cerium ionic structures may differ at conditions used in the RFB. It is also possible that dimeric Ce^{3+} or Ce^{4+} structures could form at higher concentrations of cerium that are relevant for RFBs. A difference in structures could lead to differences in the charge transfer mechanism, e.g., the *CE* mechanism may become less favorable, because the reorganization energy for species with similar solvation structures is typically expected to be lower, and the electron transfer may instead occur between the anion-complexed Ce^{3+} and Ce^{4+} species, precluding the need for a chemical step. We collected UV-Vis of Ce^{3+} at a variety of concentrations in 2 M MSA and 2 M H_2SO_4 and found no evidence of a structural change between 0.5 mM and 5 mM (**Fig. 6.1**), but we could not test at higher concentrations of cerium because the UV-Vis absorption signal became too large. Additionally, in our kinetic measurements, we were not able to obtain reproducible kinetic measurements on Pt with cerium concentrations greater than 0.05 M, which we hypothesized was due to the formation of a Pt oxide in the presence of a large cerium concentration. It is possible that at the higher concentration of cerium assumed in the RFB, the kinetic behavior might change, and the *CE* mechanism may no longer be relevant. To confirm whether our proposed *CE* mechanism determined at lower cerium concentrations in a batch electrochemical cell is relevant for RFB applications, the performance of a Ce-V pilot-scale RFB using H_2SO_4 and a weaker-complexing electrolyte like MSA should be

compared, to see if the hypothesis that a weaker Ce^{4+}-anion complex would result in faster kinetics holds.

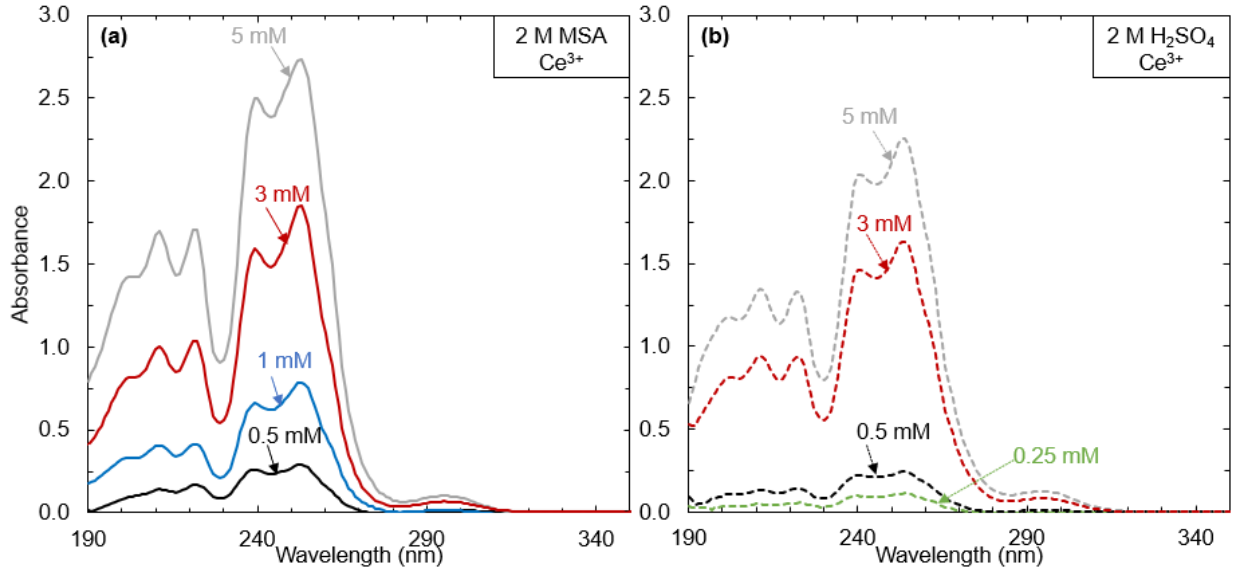

Figure 6.1. UV-Vis spectra of Ce^{3+} prepared from $Ce_2(CO_3)_3$ at a variety of concentrations in **(a)** 2 M MSA, and **(b)** 2 M H_2SO_4.

6.3.2 Experimental evidence of Ce^{4+} structures

Due to difficulties in preparing a stable Ce^{4+} oxidation state in acids other than H_2SO_4 during EXAFS measurements, we were not able to experimentally determine the Ce^{4+} structures in acids other than H_2SO_4, and future work should focus on obtaining experimentally derived Ce^{4+} structural information in acids that are relevant for battery applications. While at the Advanced Photon Source synchrotron facility at Argonne National Laboratory to collect EXAFS measurements, we were not able to prepare 100% Ce^{4+} samples in MSA and HNO_3 through oxidation with a graphite rod inserted into a carbon felt as the working electrode. We attribute this difficulty to the fact that the Ce^{3+}/Ce^{4+} redox potentials in MSA and HNO_3 are higher at 1.61 V vs. SHE than in H_2SO_4 (1.44 V vs. SHE). The higher redox potential means that at the same applied oxidation potential, more of the overvoltage will go towards the competitive OER in MSA and HNO_3 than in H_2SO_4. As a result of this preparation difficulty during EXAFS measurements, we

were only able to measure the EXAFS of Ce^{4+} in H_2SO_4. Previously we had been able to prepare Ce^{4+} in solutions of 2 M HCl, MSA, and H_2SO_4 through oxidation of Ce^{3+} using a combination of a carbon felt and graphite rod, possibly due to longer oxidation periods or less corroded graphite rode. We investigated these Ce^{4+} solutions using UV-Vis (**Chapter 4**), which showed that a change in complexation for Ce^{4+} with acid was occurring, because the peak location and heights changed with acid. While the UV-Vis was experimental evidence of Ce^{4+} anion complexation, it did not elucidate the structure, e.g., coordination number or bond length of the surrounding anions to Ce^{4+}. Instead, we relied on DFT calculations to show the favorable free energy of Ce^{4+} anion complexation relative to water coordination. Using DFT, we proposed a structure of $[Ce^{IV}(H_2O)_8X^-_n]^{(4-n)+}$ for Ce^{4+} in all acids considered except $HClO_4$: H_2SO_4, MSA, TFSA, HNO_3, HCl, H_2NSO_3H. We showed through our EXAFS of Ce^{4+} in H_2SO_4, however, that the Ce^{4+} structure in H_2SO_4 was most likely $[Ce^{IV}(H_2O)_6(HSO_4)_3]^+$, not $[Ce^{IV}(H_2O)_8SO_4]^{2+}$. Since it is difficult to predict which structures should be modeled using DFT, additional work to isolate the structure of Ce^{4+} in other acids relevant to batteries should be undertaken using EXAFS.

Accurate knowledge of the Ce^{4+} structure is integral to determining the Ce^{3+}/Ce^{4+} charge transfer mechanism in an acid, and an understanding of the charge transfer mechanism is necessary to controlling the kinetics for any acid being considered for RFB applications. Given the higher redox potentials of Ce^{3+}/Ce^{4+} in HNO_3 and MSA (1.61 V vs. SHE), which is promising for use in an RFB, we suggest that identification of the Ce^{4+} structures in these two acids be a priority for future research. To address the difficulty of Ce^{4+} preparation in acids with higher redox potentials than H_2SO_4, precursors and OER-sluggish electrodes can be employed. For instance, we determined through titration (see **Chapter 2** for method) that 100% Ce^{4+} can be prepared in HNO_3 by dissolving ceric ammonium nitrate, and if this method were employed at a synchrotron facility,

then EXAFS could be collected immediately after preparation to determine the coordination number and bond distance of the Ce^{4+}-nitrate complex in HNO_3. Additionally, we explored oxidation of Ce^{3+} prepared from $Ce_2(CO_3)_3$ to Ce^{4+} in MSA using a mixed metal oxide from De Nora and found that mixtures of Ce^{3+} and Ce^{4+} can be obtained. The XAFS data processing software ATHENA[34] has linear combination fitting capabilities that could be used to deconvolute the Ce^{3+} and Ce^{4+} spectra to isolate the structure of Ce^{4+} in MSA, since the spectrum of Ce^{3+} in MSA is known (**Chapter 4**). Identification of the Ce^{4+} structure in HNO_3 and MSA would help to inform the charge transfer mechanism in each of these acids, which could then be used to determine how best to optimize the kinetics in each of these acids.

In addition to uncertainty in the structures of Ce^{4+} in acids other than H_2SO_4, we were not able to experimentally prove the existence of the Ce^{4+} intermediate proposed in the *CE* mechanism in **Chapter 5**, $[Ce^{IV}(H_2O)_9]^{4+}$. Experimental determination of intermediates in catalysis and electrochemistry through spectroscopy is notoriously difficult because the reactions are fast.[35] Instead of using spectroscopy to isolate the existence of the $[Ce^{IV}(H_2O)_9]^{4+}$ species, we demonstrated that the Ce^{3+}/Ce^{4+} experimental kinetic measurements could be fit quite well with the rate law derived from the *CE* mechanism in which the $[Ce^{IV}(H_2O)_9]^{4+}$ species was assumed to exist. By demonstrating that the rate law was consistent with experimental kinetics, we provided proof that the $[Ce^{IV}(H_2O)_9]^{4+}$ species existed, but additional spectroscopy evidence would help strengthen this claim. One possible way to investigate the existence of the $[Ce^{IV}(H_2O)_9]^{4+}$ intermediate would be to use X-ray photoelectron (PE) spectroscopy to measure the vertical ionization energy (VIE) of Ce^{4+} in H_2SO_4 versus $HClO_4$, in which Ce^{4+} is known to not be complexed by perchlorate anions.[36–39] X-ray PE spectroscopy works by bombarding a sample with X-rays and measuring the number of emitted photoelectrons over a range of energies.[40] Yepes at

al.[41] showed that PE spectra can be used to obtain the VIE of transition metal ions in aqueous solutions, which is the amount of energy that it takes for the electronic transition to take place in a non-equilibrium state, i.e., without the nuclear relaxation of the solute-solvent interactions. The VIE has been reported to be affected by anion complexation,[41] so if we show that the VIE for the Ce^{3+}/Ce^{4+} charge transfer in H_2SO_4 is the same as the VIE in $HClO_4$, in which we know the Ce ions are not complexed by ClO_4^- anions, that would suggest that the same intermediate Ce^{4+} species is present in both H_2SO_4 and $HClO_4$, suggesting a water coordinated species. Further work would need to be done to determine whether this species is the $[Ce^{IV}(H_2O)_9]^{4+}$ structure we proposed or a Ce^{4+}-hydrolyzed dimer, which is known to occur in $HClO_4$.[36–38] X-ray PE spectroscopy represents an interesting way to further probe the intermediate of the Ce^{3+}/Ce^{4+} charge transfer in H_2SO_4.

6.3.3 Limitations of kinetics measurements for RFB applications

The small number of electrode materials and acidic solutions considered for the Ce^{3+}/Ce^{4+} kinetic studies limit our ability to make predictions about Ce-based RFB performance. To determine the Ce^{3+}/Ce^{4+} charge transfer mechanism in **Chapter 5**, kinetic measurements were collected in H_2SO_4 on two rotating disk electrode (RDE) materials: platinum (Pt) and glassy carbon (GC). While the activity on Pt and GC were similar, suggesting outer-sphere behavior, this trend should be confirmed by studying the Ce^{3+}/Ce^{4+} kinetics on three electrode materials with the same experimental conditions, e.g., acid concentration, electrochemical cell, reference electrode, counter electrode, temperature, and Ce^{3+} and Ce^{4+} ion concentrations. Ce^{3+}/Ce^{4+} kinetic studies have been conducted on gold, iridium, and boron doped diamond previously (see **Chapter 1**), and these materials would all be good candidates for a third electrode. The kinetics should also be studied in additional acids that are relevant for RFB applications such as HNO_3 and MSA. Our

findings in **Chapter 5** indicate that the kinetics will be controlled by complexation strength of the acidic anions if the *CE* mechanism holds for different acids. If the *CE* charge transfer mechanism were found to accurately describe the kinetics in HNO_3 or MSA as well as H_2SO_4, then we could make stronger claims about the expected kinetic activity in additional acids. Being able to make predictions about the expected kinetic activity in additional acids would advance the goal of using Ce in RFB applications by allowing us to screen a large range of acids based on their Ce^{3+}/Ce^{4+} redox potential to determine which would result in increased thermodynamic and kinetic performance. This possibility is discussed in more detail further below. In addition to considering how the number of electrodes and electrolytes considered in the kinetic measurements affect the conclusions we can draw about expected Ce RFB performance, the active species concentration of the kinetics should also be considered.

The kinetic measurements performed in **Chapter 5** to determine the Ce^{3+}/Ce^{4+} charge transfer mechanism were conducted at lower cerium concentrations than would be relevant for RFB applications, which limits our understanding of the Ce^{3+}/Ce^{4+} charge transfer behavior in RFBs. To obtain reproducible Ce^{3+}/Ce^{4+} kinetic measurements in H_2SO_4, we limited the Ce concentration to 0.05 M, because at higher concentrations like 0.15 M, reproducible data at intermediate concentrations of Ce^{4+} on the Pt electrode could not be obtained. We hypothesize that the inconsistent exchange current densities collected at 0.15 M total cerium are because of the effect of cerium on oxide formation on Pt. We collected EXAFS of Pt nanoparticles in sulfuric acid and found that the Pt nanoparticles in the presence of Ce were significantly more oxidized than Pt in the absence of Ce at the same applied potential. We hypothesize that at higher concentrations of total Ce, the Pt is more oxidized, which decreases the activity. Decreased kinetic activity on an oxidized platinum surface have been reported previously for other outer-sphere

redox couples[42] as well as the cerium redox couple.[43,44] Thus, when operating at 0.15 M, more consistent pre-treatment of the Pt RDE such as the scheme suggested by Randle and Kuhn[45] would be required to ensure that the Pt oxide that forms is consistently reproduced. The Ce concentration of 0.05 M is not relevant for RFB applications. In an RFB, we would want to maximize the active species concentration to increase the energy storage capacity, and so we would use the solubility limit of Ce in H_2SO_4, which ranges between 0.225 M and 0.150 M for H_2SO_4 concentrations up to 2 M.[46] We expect that the exchange current density would increase with increased Ce concentration based on the rate law developed in **Chapter 5**, but additional kinetics measurements should be conducted to ensure that the charge transfer mechanism that we developed holds at higher Ce concentrations.

This section has demonstrated the limitations in the experimental work of the dissertation, primarily related to determination of the Ce^{4+} structures in relevant acids for RFBs as well as the kinetics measurements. We have showed that additional work should be completed to confirm the charge transfer mechanism in acids other than H_2SO_4 that would be candidates for RFB electrolytes. The next section serves to provide an outlook for using Ce in RFBs, given the learnings of the TEA-LCI models from **Chapter 3**, the structural and thermodynamic study from **Chapter 4**, and the kinetics study from **Chapter 5**.

6.4 Synthesis of TEA-LCI, thermodynamic, and kinetic studies and outlook for Ce-based RFBs

In this section, we provide recommendations for future areas of research related to the electrolyte (**Section 6.4.1**) and electrode (**Section 6.4.2**) based on the findings of this dissertation. In **Section 6.4.3**, guidelines for material researchers are provided, so that increases in thermodynamics or kinetics can be assessed critically for their economic feasibility. Finally, an

outlook of the current state of Ce-based RFBs as well as areas of future work is presented in **Section 6.4.4**.

6.4.1 Electrolyte recommendations: Screening electrolyte activity through reorganization energy

The reorganization energy, which is the amount of energy it takes for a reactant and its surrounding solvent to transform to a product,[47] is a useful metric of outer-sphere redox kinetics, and so we can use it to make predictions about the rate of Ce^{3+}/Ce^{4+} kinetics in different acids that are relevant for RFB applications. In **Chapter 5**, the rate law for the *CE* mechanism in which the electron transfer step was rate determining (*CE*, *E* RDS) was the only rate law that was consistent with both Ce^{3+}/Ce^{4+} kinetic and structural information in H_2SO_4. It is possible, however, that in other acids, the *EC* mechanism dominates, and thus the *EC*, *E* RDS rate law would be relevant. The rate laws for both the *CE*, *E* RDS and *EC*, *E* RDS mechanisms are functions of a preexponential factor Z, ligand exchange equilibrium constant K, and reorganization energy λ, meaning that if we know these values, then we can make predictions about the expected kinetic rates of the Ce^{3+}/Ce^{4+} redox reaction in acids for which we have not collected experimental measurements. See **Chapter 5** for more information regarding Z, K, and λ. Herein, we conduct a brief analysis of the expected kinetic rates of the Ce^{3+}/Ce^{4+} redox reaction in several acids (H_2SO_4, $HClO_4$, HNO_3, CH_3SO_3H, CF_3SO_3H, HCl) under two different sets of assumptions: (1) the *CE*, *E* RDS mechanism is dominant, and (2) the *EC*, *E* RDS mechanism is dominant.

First, if the *CE* mechanism still holds in other acids, we would expect the reorganization energy to be the same for the Ce^{3+}/Ce^{4+} redox reaction in each of the acids because it is the reorganization energy of the water-coordinated species, and the kinetic rates would depend only on the preexponential factor and ligand exchange equilibrium constant. While we cannot at present

predict how the preexponential factor Z_2 would vary with acid, we do know the trend in ligand exchange equilibrium constant values with acid based on our DFT-predicted anion complexation energies (**Chapter 4**), which agree qualitatively with the trend in redox potential shift from non-complexing $HClO_4$ to other acids. The order in DFT-predicted K_1 is $HClO_4$ > CH_3SO_3H > HNO_3 ~ CF_3SO_3H > H_2SO_4 > HCl, so the Ce^{3+}/Ce^{4+} kinetic rate activity is expected to follow this order as well, with the least complexing acids exhibiting the fastest kinetics. Using the *CE*, *E* RDS rate law developed in **Chapter 5** and assuming Z_2 and λ_2 stay the same in $HClO_4$ as H_2SO_4, the kinetics are expected to increase by a factor of approximately 10,000 from H_2SO_4 to $HClO_4$. With this significant of a change, it is likely another step may become the RDS, or that an entirely different mechanism may dominate. While this is a significantly large factor, and there may be differences based on changes in Z_2, this analysis highlights how influential the complexing behavior is on the kinetics.

It is possible, however, that the *EC* mechanism may be the dominant mechanism for the Ce^{3+}/Ce^{4+} redox reaction in acids other than sulfuric acid. The *EC* mechanism could dominate in other acids if the reorganization energy between the anion-complexed Ce^{3+} and Ce^{4+} species is lower than the water-coordinated species reorganization energy (87.1 kJ/mol) from **Chapter 5**. Using DFT, we calculated the reorganization energies expected for Ce^{3+}/Ce^{4+} anion-complexed species using the same techniques as described in **Chapter 5** for the water-coordinated species, and the reorganization energies for each of the anion complexes is included in **Table 6.1**. We find that the inner-sphere reorganization energy, λ_i, varies widely as the ligand structure of the Ce species changes, while λ_o remains relatively consistent around 50 kJ/mol. Using the reorganization energies of the relevant anion-complexed species in **Table 6.1** along with the ligand exchange equilibrium constant K_4 expected based on our previously reported Ce^{3+} anion complexation free

energies (from **Chapter 4**) we expect the Ce^{3+}/Ce^{4+} kinetic activity to vary in the acids in the following way if the *EC* mechanism is dominant and the preexponential factor is assumed to be independent of acid: HCl ~ CF_3SO_3H > $HClO_4$ > HNO_3 > CH_3SO_3H. We were not able to determine a reorganization energy for the tri-bisulfate complexed Ce species due to computational constraints, so we do not include H_2SO_4 in the acid screening analysis for the *EC* mechanism.

Table 6.1. DFT-predicted reorganization energies for Ce^{3+}/C^{4+} anion complexed species involved in *E* step of *EC* mechanism. Reorganization energies reported in terms of inner-sphere reorganization energy, λ_i, outer-sphere reorganization energy, λ_o, and total reorganization energy, λ. DFT-predicted reorganization energies calculated in same manner as described in **Chapter 5** for water-coordinated Ce^{3+}/C^{4+} species.

Anion-complexed species	λ_i (kJ/mol)	λ_o (kJ/mol)	λ (kJ/mol)
$[Ce(H_2O)_8ClO_4]^{2+/3+}$	56.4	47.3	103.7
$[Ce(H_2O)_8CH_3SO_3]^{2+/3+}$	60.2	50.3	110.5
$[Ce(H_2O)_8NO_3]^{2+/3+}$	63.7	50.2	113.9
$[Ce(H_2O)_8CF_3SO_3]^{2+/3+}$	60.7	48.9	109.6
$[Ce(H_2O)_8Cl]^{2+/3+}$	61.5	49.6	111.1

As seen in **Table 6.1**, the reorganization energies for the anion-complexed Ce species are larger than the water-coordinated reorganization energy value of 87.1 kJ/mol. Thus, based on our hypothesis that the *EC* mechanism would only become relevant for an acid if the anion-complexed reorganization energy was less than the water-coordinated reorganization energy, we predict that the *CE* mechanism will continue to be dominant in the acids considered other than H_2SO_4. Therefore, we recommend that MSA and HNO_3 be used as the acid in the positive electrolyte for Ce-based RFBs, given their predicted faster kinetics and higher redox potentials than H_2SO_4. Future work should confirm that the *CE* mechanism holds in these acids through kinetics measurements. Investigation of other electrolytes that result Ce^{3+} in anion complexation, which would mean that the redox potential would not shift down as dramatically from the standard redox potential value of 1.74 V vs. SHE should also be conducted. Future TEA-LCI models should consider the effects of switching to HNO_3 or MSA or other promising electrolytes in terms of

overall cost, i.e., does the enhanced performance outweigh the increase in electrolyte cost. Electrolyte engineering guidelines will be provided in **Section 6.4.3**.

6.4.2 Electrode recommendations: Dimensionally stable anodes

Although the electrode is not expected to control the Ce^{3+}/Ce^{4+} kinetics because the Ce^{3+}/Ce^{4+} redox reaction is outer-sphere (**Chapter 5**), electrode factors like selectivity, stability, and cost can still have an impact on the overall cost and emissions of a Ce-based RFB. As mentioned in **Section 6.2.3**, OER will occur during oxidation of Ce^{3+} to Ce^{4+}, i.e., charging of a Ce RFB, because its redox potential value of 1.23 V vs. SHE is similar to that of the Ce^{3+}/Ce^{4+} redox potential, e.g., 1.44 V vs. SHE in H_2SO_4. This competition with OER results in a reduced roundtrip electrical efficiency of the system, which will result in higher energy storage costs and emissions. If an electrode that is still conductive but known to be a poor OER catalyst is used as the positive Ce electrode in the RFB, then roundtrip electrical efficiency will be increased. An additional issue for the Ce electrode is stability, because the high operating potentials and acidic solution cause carbon-based electrodes, which are the standard electrode used in VRFBs, to corrode.[48] For this reason, a noble metal like Pt is often used. Noble metals are expensive, however, and so electrode materials that are selective towards the Ce^{3+}/Ce^{4+} redox reaction, stable in the highly corrosive electrolyte environment, and cost-effective are needed for Ce-RFB systems. We demonstrated in **Chapter 3** the significant influence of the positive electrode material cost on the Ce-V RFB minimum LCOE.

Electrodes developed for chlorine evolution in the chloro-alkali industry are promising for Ce-based RFB applications. Dimensionally stable anodes (DSAs), which typically have a Ti base which serves as the conductive substrate with layers of metal oxide coatings overtop, have been shown to be effective in the chloro-alkali industry.[49] In the chloro-alkali process, Cl^- is oxidized to

chlorine at the positive electrode, which occurs at similar potentials to OER. Chlorine evolution therefore has similar constraints when considering electrode selection as the Ce system, i.e., OER competition and corrosive potentials. While the original DSAs consisted of platinum group metals on top of the Ti base, dissolution was known to occur when polarization was reversed.[49] To enhance stability of DSAs, mixed metal oxides that consist of platinum group metals like Pt, Ru, or Ir, and transition metals, like Ti, Ta, or Nb, are used overtop of the Ti base.[49] The state-of-the-art DSAs for chlorine evolution are the family of RuO_2-IrO_2-TiO_2 electrodes. Ru and Ir are also costly precious metals, however, and so efforts to explore precious metal-free chlorine evolution electrocatalysts are ongoing, with tin doping coupled with antimony to enhance conductivity showing promising selectivity.[50] These mixed metal oxides should be considered for the Ce^{3+}/Ce^{4+} redox reaction in RFB systems, given their higher stability and selectivity than typical carbon-based electrodes. The cost of mixed metal oxides, especially Ru- or Ir-based systems, should be accounted for while assessing the overall viability of these electrodes in RFB systems. Guidelines on electrode engineering for Ce-based RFBs are discussed in the next section.

6.4.3 Guidelines for electrolyte and electrode engineering: Thermodynamics, kinetics, and cost tradeoff analysis

Concepts of electrolyte engineering and electrode design have been explored for a number of aqueous batteries and as such represent the relevant next step for enhancing Ce-based RFB systems. As described in **Section 6.2.3**, electrolyte engineering and electrode design have been used to address the competitive HER and OER in aqueous energy storage systems. Electrolyte engineering is also commonly used to enhance performance of aqueous batteries like the zinc ion battery through enhancement of cathode compatibility by adjusting electrolyte concentration or adding organic solvent as well as protection of the anode by increasing the salt concentration or

constructing an artificial solid electrolyte interface.[51] For the Ce^{3+}/Ce^{4+} redox reaction, electrolyte engineering strategies should focus on exploring additives that enhance the kinetics of the redox reaction and also improve the redox potential, possibly through increased Ce^{3+} anion complexation or decreased Ce^{4+} anion complexation strength. Electrocatalysts are a significantly explored area for aqueous batteries with the goal of improving electrochemical activity, for instance, graphene, multi-walled carbon nanotubes, N-doping, and P-doping have all been explored as catalytic strategies for carbon-based electrodes for the VRFB.[52] Electrode design for the Ce^{3+}/Ce^{4+} system should focus on stability, selectivity, and cost, since the Ce^{3+}/Ce^{4+} redox reaction is outer-sphere and therefore will not display a significant dependence of kinetics on electrode material. We showed in **Chapter 3** that the cost of the positive electrode was highly influential to total system cost. We expect that a tradeoff between cost and enhanced performance will occur as new materials are explored for the Ce^{3+}/Ce^{4+} redox system. We provide guidelines for electrolyte engineering and electrode design next, based on the sensitivity analysis of the TEA-LCI model for the Ce-V RFB discussed in **Chapter 3**.

Analyzing the tradeoff between thermodynamic performance, kinetic performance, and material costs for the Ce-V RFB can help provide a roadmap for future electrolyte and electrode development for the Ce^{3+}/Ce^{4+} redox reaction. Because we'd expect that a new electrolyte being explored for its improvement in Ce^{3+}/Ce^{4+} redox potential would be more expensive than H_2SO_4, we calculated the increase in electrolyte cost that could be tolerated for a 200 mV in redox potential. We also calculated the increase in electrode cost that could be tolerated for an increase in Ce^{3+}/Ce^{4+} exchange current density. We found that the electrolyte cost could be increased by \$1.83/kg of electrolyte if the redox potential were improved by 200 mV. For reference, the cost of H_2SO_4 is \$0.32/kg. For a doubling in Ce^{3+}/Ce^{4+} exchange current density, we determined that the

electrode cost could increase by $333/m^2. Additionally, it is possible that an electrolyte that improves thermodynamics may adversely impact kinetics, or vice versa. We determined that a 195 mV increase in redox potential is equivalent to the exchange current density doubling. These numbers can serve as guidelines for researchers as they explore new materials for the Ce-V RFB. For instance, if a new electrolyte is discovered that enhances thermodynamics by 200 mV, but it causes the exchange current density to become 10% of its original value, or the electrolyte is found to cost an additional $2/kg, then it is not currently an economically viable replacement for H_2SO_4.

6.4.4 Overall outlook on Ce-based RFBs

We demonstrated that the Ce^{3+}/Ce^{4+} thermodynamics are controlled by the relative anion complexation of Ce^{3+} and Ce^{4+}, with Ce^{4+} being preferentially complexed by anions in many acids relevant for battery applications. Additionally, we showed that the Ce^{3+}/Ce^{4+} kinetics were outer-sphere, and we identified a possible charge transfer mechanism that suggests that cerium redox activity will be controlled by complexation strength. Our TEA-LCI models highlighted the importance of both thermodynamic and kinetic performance on a Ce-V RFB's LCOE and LGHG. Our identification of the factors that control thermodynamics and kinetics can thus be used to further enhance the performance of Ce for RFB applications. Based on the lower minimum LCOE of the Ce-V RFB relative to the state-of-the-art VRFB, the Ce-V RFB should be seriously considered as an alternative RFB technology. There remain many practical challenges that must be addressed if a Ce-V RFB is to be integrated into the electricity grid, including crossover of cations that can lead to capacity fade, extraction of cerium reserves for large scale energy storage purposes, cost of positive electrode material, and management of the competitive hydrogen and oxygen evolution reactions. Improvements in Ce^{3+}/Ce^{4+} thermodynamics and kinetics through electrolyte engineering and electrode design should be explored, bearing in mind the tradeoff

between performance and cost emphasized in **Section 6.4.3**. Overall, this dissertation demonstrated that the Ce^{3+}/Ce^{4+} chemistry is promising for RFB applications, isolated some of the fundamental mechanisms that control the cerium thermodynamics and kinetics, and highlighted future areas of work that will be needed to see Ce-based RFB technologies become a reality.

6.5 References

1. U.S. DOE. *Energy Storage Program Planning Document*. (2011).
2. Dieterle, M., Fischer, P., Blume, N., Minke, C. & Bischi, A. Life cycle assessment (LCA) for flow batteries: A review of methodological decisions. *Sustain. Energy Technol. Assessments* **53**, 102457 (2022).
3. Morales-mora, M. A., Pijpers, J. J. H. & Castillo, A. Life cycle assessment of a novel bipolar electrodialysis-based flow battery concept and its potential use to mitigate the intermittency of renewable energy generation. *J. Energy Storage* **35**, 102339 (2021).
4. U.S. Geological Survey. *Mineral Commodity Summaries 2022*. *U.S. Geological Survey* (2022) doi:https://doi.org/10.3133/mcs2022.
5. Rodby, K. E. *et al.* Assessing the levelized cost of vanadium redox flow batteries with capacity fade and rebalancing. *J. Power Sources* **460**, 227958 (2020).
6. Lim, T. M., Ulaganathan, M. & Yan, Q. *Advances in membrane and stack design of redox flow batteries (RFBs) for medium- and large-scale energy storage*. *Advances in Batteries for Medium and Large-Scale Energy Storage: Types and Applications* (Elsevier Ltd., 2015). doi:10.1016/B978-1-78242-013-2.00014-5.
7. Hoare, J. P. Oxygen. in *Standard Potentials in Aqueous Solution* (eds. Bard, A. J., Parsons, R. & Jordan, J.) 54 (International Union of Pure and Applied Chemistry, 1985).
8. Ross, P. N. Hydrogen. in *Standard Potentials in Aqueous Solution* (eds. Bard, A. J., Parsons, R. & Jordan, J.) 41 (International Union of Pure and Applied Chemistry, 1985).
9. Perry, M. L., Rodby, K. E. & Brushett, F. R. Untapped potential: The need and opportunity for high-voltage aqueous redox flow batteries. *ACS Energy Lett.* 659–667 (2022) doi:10.1021/acsenergylett.1c02225.
10. Nian, Q. *et al.* Designing electrolyte structure to suppress hydrogen evolution reaction in aqueous batteries. *ACS Energy Lett.* **6**, 2174–2180 (2021).
11. Tan, J. & Liu, J. Electrolyte engineering toward high-voltage aqueous energy storage devices. *Energy Environ. Mater.* **4**, 302–306 (2021).
12. Sui, Y. & Ji, X. Anticatalytic strategies to suppress water electrolysis in aqueous batteries. *Chem. Rev.* **121**, 6654–6695 (2021).
13. Burk, C. Techno-economic modeling for new technology development. *Chem. Eng. Prog.* **114**, 43–52 (2018).
14. Viswanathan, V. *et al.* Cost and performance model for redox flow batteries. *J. Power Sources* **247**, 1040–1051 (2014).
15. Chalamala, B. R. *et al.* Redox flow batteries: An engineering perspective. *Proc. IEEE* **102**, 976–999 (2014).
16. Mongird, K. *et al. 2020 Grid Energy Storage Technology Cost and Performance Assessment*. (2020).
17. Wishart, J., Dong, Z. & Secanell, M. Optimization of a PEM fuel cell system based on empirical data and a generalized electrochemical semi-empirical model. *J. Power Sources* **161**, 1041–1055 (2006).
18. Arenas, L. F., Ponce De León, C. & Walsh, F. C. Electrochemical redox processes involving soluble cerium species. *Electrochim. Acta* **205**, 226–247 (2016).
19. Knehr, K. W. & Kumbur, E. C. Open circuit voltage of vanadium redox flow batteries: Discrepancy between models and experiments. *Electrochem. commun.* **13**, 342–345 (2011).
20. Tucker, M. C., Weiss, A. & Weber, A. Z. Improvement and analysis of the hydrogen-cerium

redox flow cell. *J. Power Sources* **327**, 591–598 (2016).
21. Weber, A. Z. *et al.* Redox flow batteries: A review. *J. Appl. Electrochem.* **41**, 1137–1164 (2011).
22. Statistica. Price of zinc in North America from 2016 to 2021. *Mining, Metals, & Materials* https://www.statista.com/statistics/369252/global-zinc-price-north-america/#:~:text=The zinc price in North,dollars per pound in 2021. (2022).
23. Fernandez-Marchante, C. M., Millán, M., Medina-Santos, J. I. & Lobato, J. Environmental and preliminary cost assessments of redox flow batteries for renewable energy storage. *Energy Technol.* **1900914**, 1–10 (2019).
24. Minor Metals Trade Association. Cerium. https://mmta.co.uk/metals/ce/ (2022).
25. Sims, Z. C. *et al.* How cerium and lanthanum as coproducts promote stable rare earth production and new alloys. *J. Sustain. Metall.* (2022) doi:10.1007/s40831-022-00562-4.
26. Center for Sustainable Systems University of Michigan. *U. S. Grid Energy Storage Factsheet*. (2021).
27. Mai, T. *et al. Renewable Electricity Futures Study. Volume 1: Exploration of High-Penetration Renewable Electricity Futures*. vol. 1 (2012).
28. Borra, C. R., Vlugt, T. J. H., Yang, Y. & Offerman, S. E. Recovery of cerium from glass polishing waste: A critical review. *Metals (Basel).* **8**, (2018).
29. Wall, F. Rare earth elements. in *Encyclopedia of Geology* 680–693 (2014). doi:10.1016/b978-0-08-102908-4.00101-6.
30. Abreu, R. D. & Morais, C. A. Purification of rare earth elements from monazite sulphuric acid leach liquor and the production of high-purity ceric oxide. *Miner. Eng.* **23**, 536–540 (2010).
31. Bleiwas, D. I. *Potential for Recovery of Cerium Contained in Automotive Catalytic Converters*. *U.S. Geological Survey* (2013).
32. Energy Information Administration. *International Energy Outlook*. (2021).
33. Grand View Research. *Cerium market size, share & trends analysis report by application (glass, catalysts, alloys), by region (North America, Europe, Asia Pacific), and segment forecasts, 2021-2028*. (2021).
34. Ravel, B. & Newville, M. ATHENA, ARTEMIS, HEPHAESTUS: Data analysis for X-ray absorption spectroscopy using IFEFFIT. *J. Synchrotron Radiat.* **12**, 537–541 (2005).
35. Costentin, C. & Savéant, J. M. Homogeneous molecular catalysis of electrochemical reactions: Catalyst benchmarking and optimization strategies. *J. Am. Chem. Soc.* **139**, 8245–8250 (2017).
36. Heidt, L. J. & Smith, M. E. Quantum yields of the photochemical reduction of ceric ions by water and evidence for the dimerization of ceric ions. *J. Am. Chem. Soc.* **70**, 2476–2481 (1948).
37. Hardwick, T. J. & Robertson, E. Ionic species in ceric perchlorate solutions. *Can. J. Chem.* **29**, 818–827 (1951).
38. Ikeda-Ohno, A., Tsushima, S., Hennig, C., Yaita, T. & Bernhard, G. Dinuclear complexes of tetravalent cerium in an aqueous perchloric acid solution. *Dalt. Trans.* **41**, 7190–7192 (2012).
39. Fronaeus, S. & Ostman, C. O. The mechanism of the exchange reaction between cerium(III) and cerium(IV) at platinum surfaces. *Acta Chem. Scand.* **10**, 769–778 (1956).
40. Fadley, C. S. X-ray photoelectron spectroscopy: Progress and perspectives. *J. Electron Spectros. Relat. Phenomena* **178**–**179**, 2–32 (2010).

41. Yepes, D., Seidel, R., Winter, B., Blumberger, J. & Jaque, P. Photoemission spectra and density functional theory calculations of 3d transition metal-aqua complexes (Ti-Cu) in aqueous solution. *J. Phys. Chem. B* **118**, 6850–6863 (2014).
42. Daum, P. H. & Enke, C. G. Electrochemical kinetics of the ferri—ferrocyanide couple on platinum. *Anal. Chem.* **41**, 653–656 (1969).
43. Kohl, P. & Schultze, J. Der Einfluß des Tunneleffektes auf die Geschwindigkeit von Redoxreaktionen an oxidbedeckten Platinelektroden. *Berichte der Bunsengesellschaft für Phys. Chemie* **77**, 953–960 (1973).
44. Kuhn, T. & Randle, H. Effect of oxide thickness on the rates of some redox reactions on a platinum electrode. *J. Chem. Soc., Faraday Trans. 1* **81**, 403–419 (1985).
45. Randle, H. & Kuhn, T. Kinetics and mechanism of the cerium(IV)/cerium(III) redox reaction on a platinum electrode. *J. Chem. Soc., Faraday Trans. 1* **79**, 1741–1756 (1983).
46. Paulenova, A., Creager, S. E., Navratil, J. D. & Wei, Y. Redox potentials and kinetics of the Ce3+/Ce4+redox reaction and solubility of cerium sulfates in sulfuric acid solutions. *J. Power Sources* **109**, 431–438 (2002).
47. Bard, A. J. & Faulkner, L. R. *Electrochemical Methods: Fundamentals and Applications*. (John Wiley & Sons, Inc., 2001). doi:10.1016/B978-0-08-098353-0.00003-8.
48. Sanchez-Díez, E. *et al.* Redox flow batteries: Status and perspective towards sustainable stationary energy storage. *J. Power Sources* **481**, 228804 (2021).
49. Dong, H., Yu, W. & Hoffmann, M. R. Mixed metal oxide electrodes and the chlorine evolution reaction. *J. Phys. Chem. C* **125**, 20745–20761 (2021).
50. Alavijeh, M. M. *et al.* A selective and efficient precious metal-free electrocatalyst for chlorine evolution reaction: An experimental and computational study. *Chem. Eng. J.* **421**, 127785 (2021).
51. Wang, Y. *et al.* Electrolyte engineering enables high performance zinc-ion batteries. *Small* **2107033**, 1–20 (2022).
52. Aberoumand, S., Woodfield, P., Shabani, B. & Dao, D. V. Advances in electrode and electrolyte improvements in vanadium redox flow batteries with a focus on the nanofluidic electrolyte approach. *Phys. Rep.* **881**, 1–49 (2020).

Appendices

Appendix A

Spectroscopy characterization

This Appendix contains additional spectroscopy data used to determine the structures of Ce^{3+} and Ce^{4+} in acidic solutions in **Chapters 4** and **5**. Extra UV-Vis spectroscopy data is included in **Appendix A.1**, and additional extended x-ray absorption fine structure (EXAFS) spectra and fitting results are included in **Appendix A.2**.

A.1 UV-Vis spectroscopy

We studied two different, non-carbonate precursors ($Ce(CF_3SO_3)_3$ in TFSA (Alfa Aesar, 98% purity) and reduced $Ce(SO_4)_2$ in H_2SO_4). We found that the UV-Vis absorbance peaks for the reduced $Ce(SO_4)_2$ sample in H_2SO_4 do not change significantly compared to the Ce^{3+} spectrum prepared with cerium(III) carbonate (**Figure A.1b**), which suggests that Ce^{3+} complexation with carbonate is not occurring. While the intensity of the UV-Vis peaks at 190 nm and 210 nm did change for the Ce^{3+} sample prepared in TFSA from $Ce(CF_3SO_3)_3$ as compared to the sample in TFSA from cerium(III) carbonate (**Figure A.1a**), sparging the solution with N_2 gas to remove carbonate as CO_2 did not alter the UV-Vis spectrum significantly (**Figure A.1c**), and a spectrum of Ce^{3+} in TFSA with additional carbonate from Na_2CO_3 also did not differ significantly, again suggesting that Ce^{3+} is not complexed by carbonate.

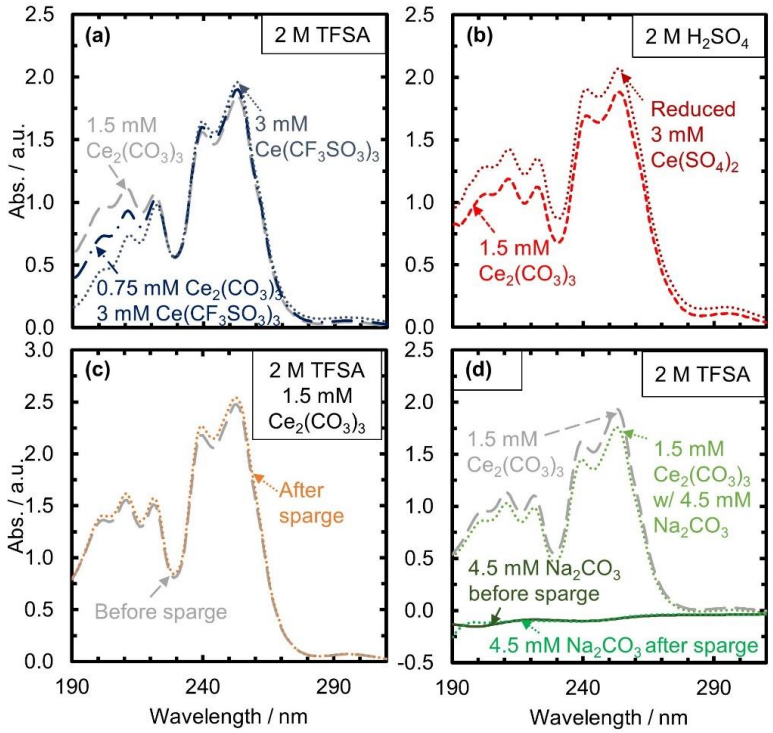

Figure A.1. UV-Vis absorbance as a function of wavelength at room temperature (T = 23 ± 1 °C) of **(a)** Ce^{3+} solutions in 2 M TFSA prepared from a triflate precursor (3 mM $Ce(CF_3SO_3)_3$ + 2 M TFSA), a carbonate precursor (1.5 mM $Ce_2(CO_3)_3$ + 2 M TFSA), and a combined triflate-carbonate precursor (1.5 mM $Ce(CF_3SO_3)_3$ + 0.75 mM $Ce_2(CO_3)_3$ + 2 M TFSA); **(b)** Ce^{3+} solutions in 2 M H_2SO_4 prepared from a carbonate precursor (1.5 mM $Ce_2(CO_3)_3$ + 2 M H_2SO_4) and a sulfate precursor (3 mM $Ce(SO_4)_2$ + 2 M H_2SO_4), which was then reduced electrochemically to Ce^{3+}; **(c)** Ce^{3+} solutions in 2 M TFSA prepared from a carbonate precursor (1.5 mM $Ce_2(CO_3)_3$ + 2 M TFSA) before and after sparging with N_2 gas for 5 hours, and; **(d)** solutions of sodium carbonate in 2 M TFSA (4.5 mM Na_2CO_3 + 2 M TFSA) before and after sparging with N_2 gas for 5 hours as well as a Ce^{3+} solution in 2 M triflic acid prepared from the carbonate precursor (1.5 mM $Ce_2(CO_3)_3$ + 2 M TFSA) and a Ce^{3+} solution in 2 M TFSA prepared with the carbonate precursor with added sodium carbonate (1.5 mM $Ce_2(CO_3)_3$ + 4.5 mM Na_2CO_3 + 2 M TFSA).

A.2 EXAFS spectroscopy

A.2.1 Ce^{3+} EXAFS

Figure A.2 shows the results of fitting the EXAFS of Ce^{3+} in MSA (**Chapter 4**) with and without multi-electron excitation (MEE) correction. The fitting parameters of the MEE corrected EXAFS data of Ce^{3+} in all five acids with one Ce-O shell are included in **Table A.1**. The MEE correction causes an increase in the intensity of an unphysical feature centered at 1.3 Å, which introduces more uncertainty in the fit, as evidenced by the larger uncertainty values in the Ce-O distance, coordination number, and Debye-Waller factor, as well as the larger reduced χ^2 value.

Since we are only fitting shells associated with the first coordination sphere, where MEE effects will not be as significant,[1] we therefore did not correct for MEE effects before fitting the Ce^{3+} EXAFS data.

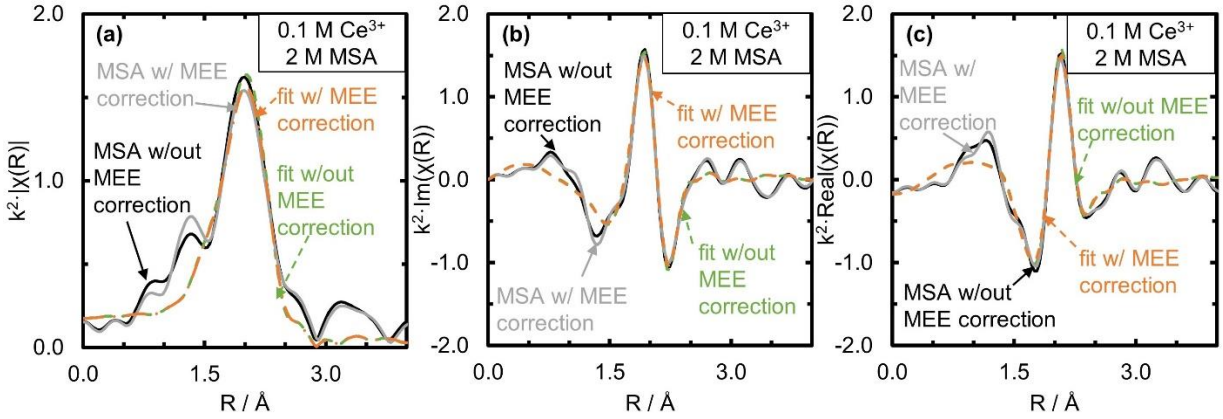

Figure A.2. Comparison of EXAFS spectra of the Ce L_3-edge for 0.1 M Ce^{3+} in 2 M MSA with and without correction for Multi-Electron Excitation (MEE) effects as well as their corresponding EXAFS fits with one Ce-O shell plotted in **(a)** $k^2 \cdot \chi(R)$ Fourier transformed space (magnitude), **(b)** $k^2 \cdot \chi(R)$ Fourier transformed space (imaginary), and **(c)** $k^2 \cdot \chi(R)$ Fourier transformed space (real). The fitting window in the R space was 1.4 to 3.0 Å, and 1.5 to 9.7 $Å^{-1}$ in the k space.

Table A.1. MEE-corrected EXAFS fitting results for Ce^{3+} in TFSA, MSA, HCl, HNO_3, and H_2SO_4 from ARTEMIS, fitting with one Ce-O shell. Three parameters were varied: CN (coordination number), ΔR (to obtain the scattering distance), and σ^2 (Debye-Waller factor). S_0^2 (amplitude reduction factor) and ΔE_0 were obtained by fitting the Ce^{3+} in triflic acid data, and then these same values were set as fixed global parameters for the fits of Ce^{3+} in the other four acids. S_0^2 was 0.982 and ΔE_0 was 1.104 eV. All of the other parameters for the Ce-O shell were obtained by fitting.

Ce^{3+} L_3-edge EXAFS (MEE corrected) Fit				
Acid	**Ce-O shell**			**Reduced χ^2**
	R (Å)	**σ^2 ($Å^2$)**	**CN**	
TFSA	2.546±0.008	0.012±0.003	9.0±1.0	32.1
MSA	2.545±0.009	0.011±0.003	8.7±1.0	63.7
HCl	2.546±0.008	0.011±0.003	8.8±1.0	41.3
HNO_3	2.553±0.008	0.012±0.003	8.4±0.9	45.3
H_2SO_4	2.544±0.008	0.012±0.003	8.5±0.9	44.0

The **Chapter 4** EXAFS data of 0.1 M Ce^{3+} in 2 M MSA, 2 M TFSA, 2 M HCl, 2 M H_2SO_4, and 2 M HNO_3 plotted in the k space (k^2 weighted) are included in **Figure A.3**. EXAFS data in

the k space are especially useful to analyze the quality of the data, as quantified by the signal to noise ratio of the data.

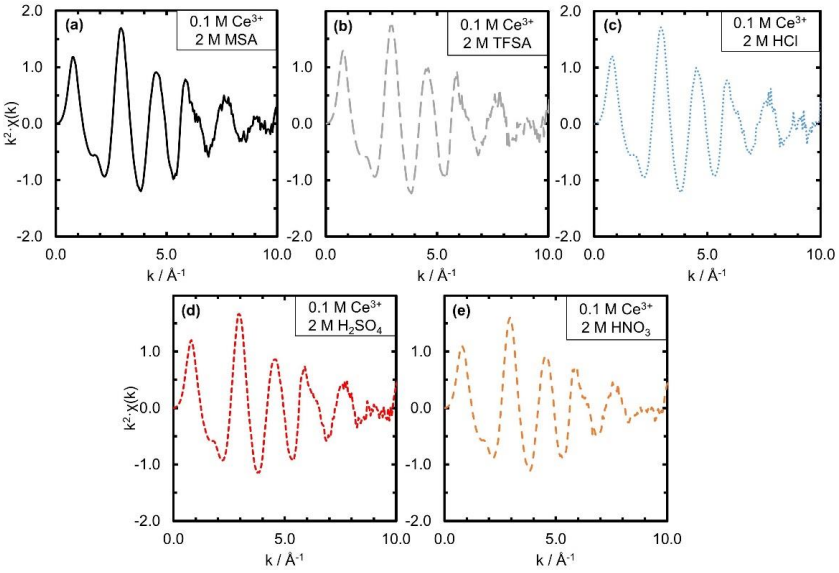

Figure A.3. EXAFS spectra of the Ce L_3-edge plotted in k space (k^2 weighted) for 0.1 Ce^{3+} (0.05 M $Ce_2(CO_3)_3$) in **(a)** 2 M MSA, **(b)** 2 M TFSA, **(c)** 2 M HCl, **(d)** 2 M H_2SO_4, **(e)** HNO_3.

The real components of the Fourier transformed EXAFS spectra of the Ce L_3-edge for 0.1 M Ce^{3+} in 2 M MSA (**Figure A.4a**), 2 M H_2SO_4 (**Figure A.4b**), and 2 M HNO_3 (**Figure A.4c**) are shown along with the real components of their fits with one Ce-O shell. These spectra correspond to the spectra included in **Chapter 4**. The real component of the Fourier transformed EXAFS data is especially useful for providing amplitude and phase information. The good agreement between the real EXAFS spectra and the Ce-O fit within 1.6 and 2.6 Å suggests that Ce^{3+} is complexed solely by water molecules, which aligns with our UV-Vis and DFT results.

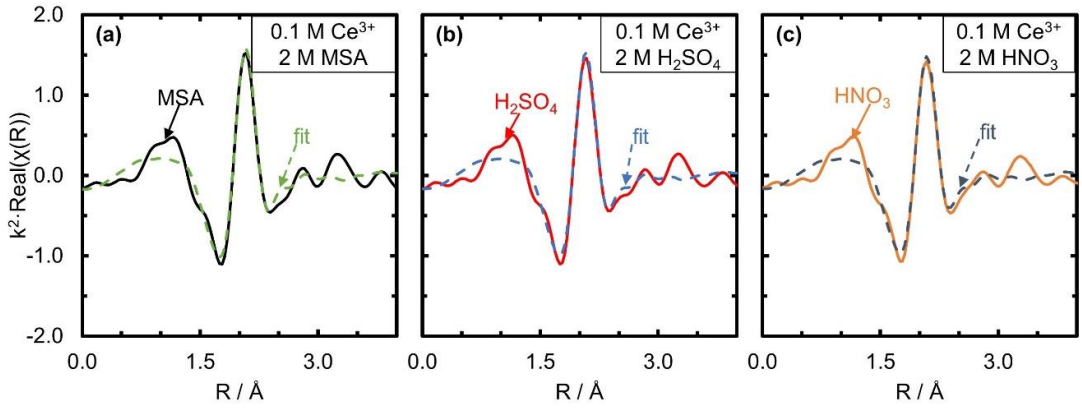

Figure A.4. The real component of $k^2 \cdot \chi(R)$ Fourier transformed EXAFS spectra of the L_3 edge of Ce and a fit with a Ce-O shell for 0.1 M Ce^{3+} in **(a)** 2 M MSA, **(b)** 2 M H_2SO_4, and **(c)** 2 M HNO_3. The fitting window in the R space was 1.4 to 3.0 Å, and 1.5 to 9.7 $Å^{-1}$ in the k space.

While the finalized fits of all of the EXAFS spectra for each Ce^{3+} sample included only a Ce-O shell in **Chapter 4**, several other water scattering paths were attempted that resulted in higher values of uncertainty in the fitting results and a higher reduced χ^2 value, signifying a poorer fit. **Figure A.5** shows the fits of the EXAFS spectra of Ce^{3+} in MSA (**Figure A.5a−c**), H_2SO_4 (**Figure A.5d−f**), and HNO_3 (**Figure A.5g−i**) with one Ce-O shell and one Ce-H shell, because previous studies have shown improved fits of Ce EXAFS with the addition of the Ce-H path.[2] The fits with the Ce-O and Ce-H shells of the EXAFS spectra of Ce^{3+} in TFSA and HCl were comparable to the fit of Ce^{3+} in MSA. **Table A.2** contains the fitting results with one Ce-O shell and one Ce-H shell for all five Ce^{3+}-acid samples. The Ce-O bond distances for all five acids with the two shell fit (i.e., Ce-O and Ce-H shells) are all 2.53±0.009 Å, which is within 0.04 Å of our DFT predicted Ce-O bond lengths. The Ce-H distance is 3.07±0.04 Å in MSA, TFSA, HCl, and H_2SO_4, while it is slightly higher at 3.08 ±0.04 Å in HNO_3. While the feature around 2.9 Å in **Figure A.5** is partially captured by including the Ce-H shell, **Table A.2** demonstrates that while the fitting results for the Ce-O and Ce-H two-shell fit are comparable, the uncertainty values are higher and the goodness of fit is worse than the fit with only the Ce-O shell fit. In addition to testing the fit of the Ce^{3+} EXAFS spectra with one Ce-O shell and one Ce-H shell, the addition of a multiple scattering

path (Ce-O-O) to the fit was also tested. However, the results from fitting including the Ce-O-O path gave physically unrealistic values of the Debye Waller factor (σ^2) for Ce^{3+} in all acids. Therefore, we do not report the results of including the Ce-O-O path here.

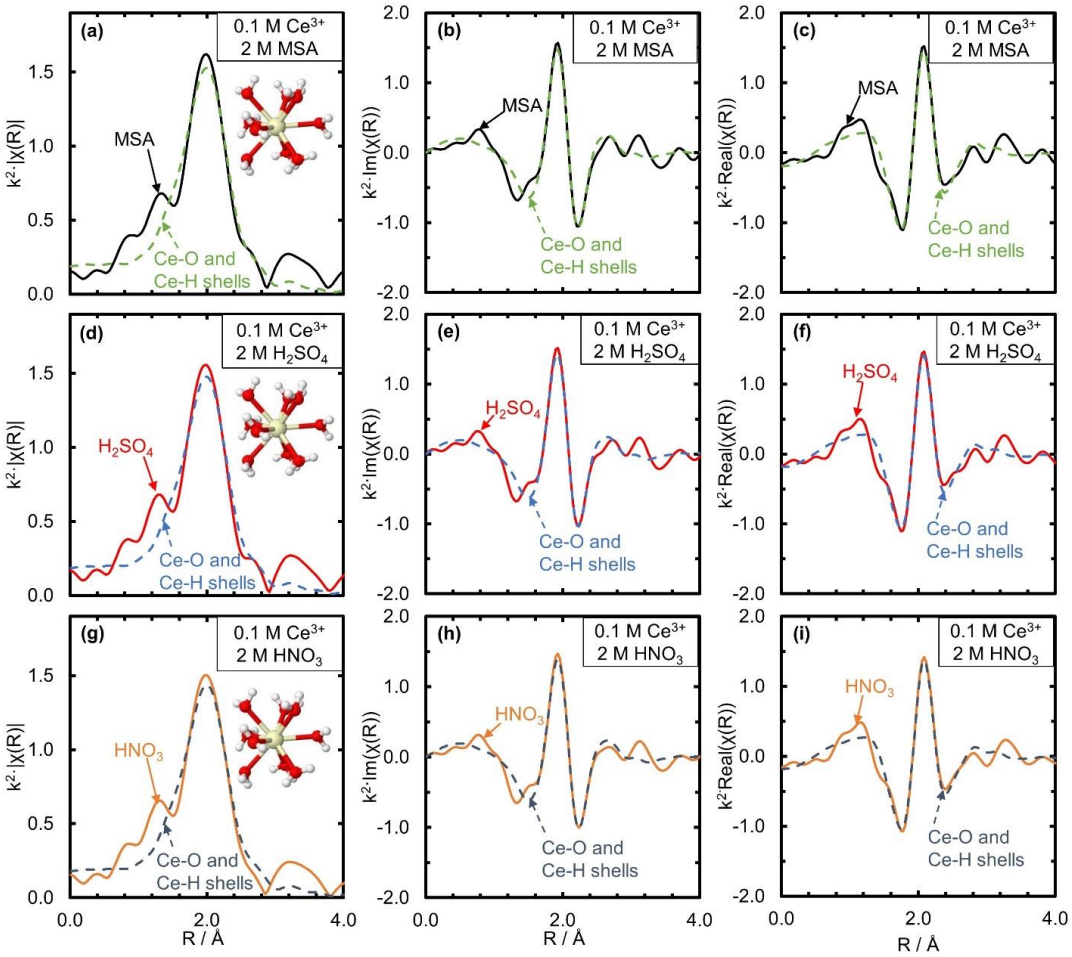

Figure A.5. EXAFS spectra of the Ce L_3-edge for 0.1 M Ce^{3+} in 2 M MSA and a fit with a Ce-O shell and a Ce-H shell plotted in **(a)** $k^2 \cdot \chi(R)$ Fourier transformed space (magnitude), **(b)** $k^2 \cdot \chi(R)$ Fourier transformed space (imaginary), and **(c)** $k^2 \cdot \chi(R)$ Fourier transformed space (real). EXAFS spectra of the Ce L_3-edge for 0.1 M Ce^{3+} in 2 M H_2SO_4 and fit with a Ce-O shell and a Ce-H shell in the **(d)** Fourier transformed space (magnitude), **(e)** $k^2 \cdot \chi(R)$ Fourier transformed space (imaginary), and **(f)** Fourier transformed space (real). EXAFS spectra of the Ce L_3-edge for 0.1 M Ce^{3+} in 2 M HNO_3 and fit with a Ce-O shell and a Ce-H shell in the **(g)** Fourier transformed space (magnitude), **(h)** $k^2 \cdot \chi(R)$ Fourier transformed space (imaginary), and **(i)** Fourier transformed space (real). All Ce sources were $Ce_2(CO_3)_3$. Inset geometries are the optimized structure of $Ce[(H_2O)_9]^{3+}$ from DFT, that were also used to generate paths using FEFF9. The fitting window in the R space was 1.4 to 3.0 Å, and 1.5 to 9.7 $Å^{-1}$ in the k space.

Table A.2. EXAFS fitting results for Ce^{3+} in TFSA, MSA, HCl, HNO_3, and H_2SO_4 from ARTEMIS, fit with one Ce-O shell and one Ce-H shell. Three parameters were varied for each shell: CN (coordination number), ΔR (shell distance), and σ^2 (Debye-Waller factor). The S_0^2 (amplitude reduction factor) and ΔE_0 were obtained by fitting the Ce^{3+} TFSA data with the Ce-O and Ce-H shells, and then these same values were set as fixed global parameters for the fits of Ce^{3+} in the other four acids. S_0^2 was determined to be 1.095, while ΔE_0 was determined to be -0.221 eV. All of the other parameters for the Ce-O shell were obtained by fitting, with CN for the Ce-H shell constrained to 2*CN of the Ce-O shell and σ^2 for Ce-H set to the Ce-O σ^2.

Acid	Ce-O shell			Ce-H shell	Reduced χ^2
	R (Å)	σ^2 (Å^2)	CN	R (Å)	
TFSA	2.533±0.009	0.013±0.003	9.0±1.3	3.073±0.011	40.6
MSA	2.532±0.010	0.012±0.004	8.6±1.3	3.071±0.012	89.8
HCl	2.530±0.010	0.012±0.004	8.7±1.3	3.069±0.012	57.5
HNO_3	2.539±0.010	0.013±0.003	8.3±1.2	3.080±0.011	71.8
H_2SO_4	2.531±0.010	0.013±0.004	8.5±1.3	3.070±0.012	70.1

From **Figure A.6a−c**, it does not appear that including a Ce-Cl scattering path significantly improves the fit for the **Chapter 4** EXAFS of Ce^{3+} in HCl. Although the reduced χ^2 value for the Ce-O and Ce-Cl shell fit of Ce^{3+} in HCl is smaller than the Ce-O shell fit, as can be seen in **Table A.3**, the reduced χ^2 values for the Ce-O and Ce-Cl shell fit of Ce^{3+} in MSA and TFSA (**Figure A.6d−i**) are also smaller than their Ce-O shell fit counterparts, in which there is no physical way for Cl^- to be present in the first coordination shell of Ce^{3+}. Thus, the fit of the EXAFS data of Ce^{3+} in HCl that incorporates a Cl^- ion in the inner shell of Ce^{3+} does not result in a meaningful improvement, and it is concluded that Ce^{3+} is not complexed by Cl^- in at a concentration of 0.1 M in HCl. Although we have tested other possible fits of Ce^{3+} in MSA and TFSA with anion scattering paths, such as Ce-S, we discount these and thus do not report them here on the basis that the electronic information from UV-Vis is so similar between these three acids that the presence of an anion in the first coordination sphere is not realistic.

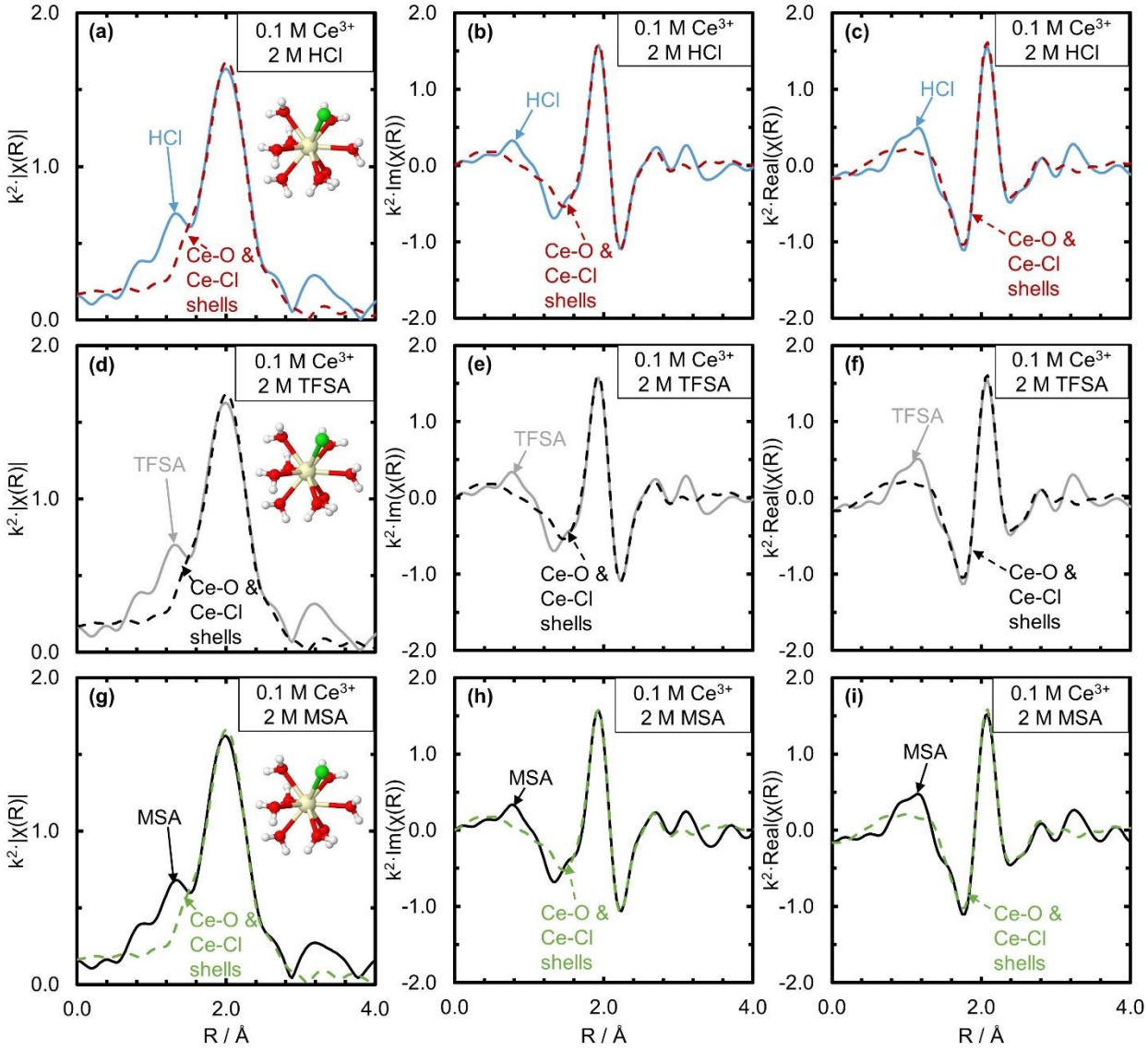

Figure A.6. EXAFS spectra of the Ce L_3-edge for 0.1 M Ce^{3+} in 2 M HCl and a fit with a Ce-O shell and a Ce-Cl shell plotted in **(a)** $k^2 \cdot \chi(R)$ Fourier transformed space (magnitude), **(b)** $k^2 \cdot \chi(R)$ Fourier transformed space (imaginary), and **(c)** $k^2 \cdot \chi(R)$ Fourier transformed space (real). EXAFS spectra of the Ce L_3-edge for 0.1 M Ce^{3+} in 2 M TFSA and fit with a Ce-O shell and a Ce-Cl shell in the **(d)** Fourier transformed space (magnitude), **(e)** $k^2 \cdot \chi(R)$ Fourier transformed space (imaginary), and **(f)** Fourier transformed space (real). EXAFS spectra of the Ce L_3-edge for 0.1 M Ce^{3+} in 2 M MSA and fit with a Ce-O shell and a Ce-Cl shell in the **(g)** Fourier transformed space (magnitude), **(h)** $k^2 \cdot \chi(R)$ Fourier transformed space (imaginary), and **(i)** Fourier transformed space (real). All Ce sources were $Ce_2(CO_3)_3$. Inset geometries are the optimized structure of $Ce[(H_2O)_8Cl]^{2+}$ from DFT, that were also used to generate paths using FEFF9. The fitting window in the R space was 1.4 to 3.0 Å, and 1.5 to 9.7 $Å^{-1}$ in the k space.

Table A.3. EXAFS fitting results for Ce^{3+} in HCl, TFSA, and MSA from ARTEMIS, fit with a Ce-O shell and a Ce-Cl shell. Three parameters were used for each path: CN (coordination number), ΔR (shell distance), and σ^2 (Debye-Waller factor). S_0^2 (amplitude reduction factor) and ΔE_0 were obtained by fitting the Ce^{3+} TFSA data with 1 Ce-O shell, and then these same values were set as fixed global parameters for the fit of Ce^{3+} in the other acids. S_0^2 was determined to be 0.970, while ΔE_0 was determined to be 0.954 eV. The CN of the Ce-Cl shell was set to 1. All of the other parameters were obtained by fitting.

Acid	**Ce-O shell**			**Ce-Cl shell**			**Reduced χ^2**
HCl	**R (Å)**	**CN**	**σ^2 (Å^2)**	**R (Å)**	**CN (set)**	**σ^2 (Å^2)**	
	2.533±0.008	7.8±0.9	0.007±0.002	2.947±0.046	1	0.008±0.008	31.1
TFSA	**Ce-O shell**			**Ce-Cl shell**			**Reduced χ^2**
	R (Å)	**CN**	**σ^2 (Å^2)**	**R (Å)**	**CN (set)**	**σ^2 (Å^2)**	
	2.532±0.007	7.9±0.9	0.008±0.002	2.941±0.039	1	0.006±0.007	23.2
MSA	**Ce-O shell**			**Ce-Cl shell**			**Reduced χ^2**
	R (Å)	**CN**	**σ^2 (Å^2)**	**R (Å)**	**CN (set)**	**σ^2 (Å^2)**	
	2.531±0.007	7.6±0.8	0.007±0.002	2.943±0.039	1	0.006±0.006	46.7

In **Chapter 4**, to determine whether Ce^{3+} was complexed by nitrate anions in HNO_3, the EXAFS data of Ce^{3+} in HNO_3 was fitted with a variety of paths related to scattering off of a nitrate anion. We considered various combinations of scattering paths associated with nitrate along with the Ce-O scattering shell, namely the following combination of scattering shells: Ce-O and Ce-N; Ce-O, Ce-N, and Ce-N-O; Ce-O, Ce-N, and Ce-O-N-O; and Ce-O, Ce-N, Ce-N-O, and Ce-O-N-O. All attempted fits with these scattering paths resulted in unreasonable (i.e., not physically possible) values of either R, CN, or σ^2. Thus, while there are previous studies that suggest Ce^{3+} complexes with nitrate,[3] we conclude there is no evidence of Ce^{3+}-nitrate complexation from our EXAFS data.

We fitted the EXAFS data of Ce^{3+} in H_2SO_4 with a variety of paths related to scattering off of a sulfate anion in **Chapter 4**, to determine whether Ce^{3+} was complexed by bisulfate or sulfate anions in H_2SO_4. We considered various combinations of the following scattering paths with a Ce-O shell: Ce-S, Ce-S-O, Ce-O-S-O. Three fits (**Figure A.7**) resulted in reasonable values of R, CN,

and σ^2, and are included in **Table A.4** below: Ce-O and Ce-S shells, Ce-O, Ce-S, and Ce-S-O shells, and Ce-O, Ce-S, and Ce-O-S-O shells. The other combination of these shells (i.e., Ce-O, Ce-S, Ce-S-O, Ce-O-S-O) resulted in unreasonable values of R and σ^2. The reduced χ^2 values of the fits in **Table A.4** are all larger than the reduced χ^2 value reported for the Ce-O fit of Ce^{3+} in H_2SO_4 (**Table 4.1**), and thus there is no evidence that Ce^{3+} is complexed by a sulfate or bisulfate from our EXAFS data.

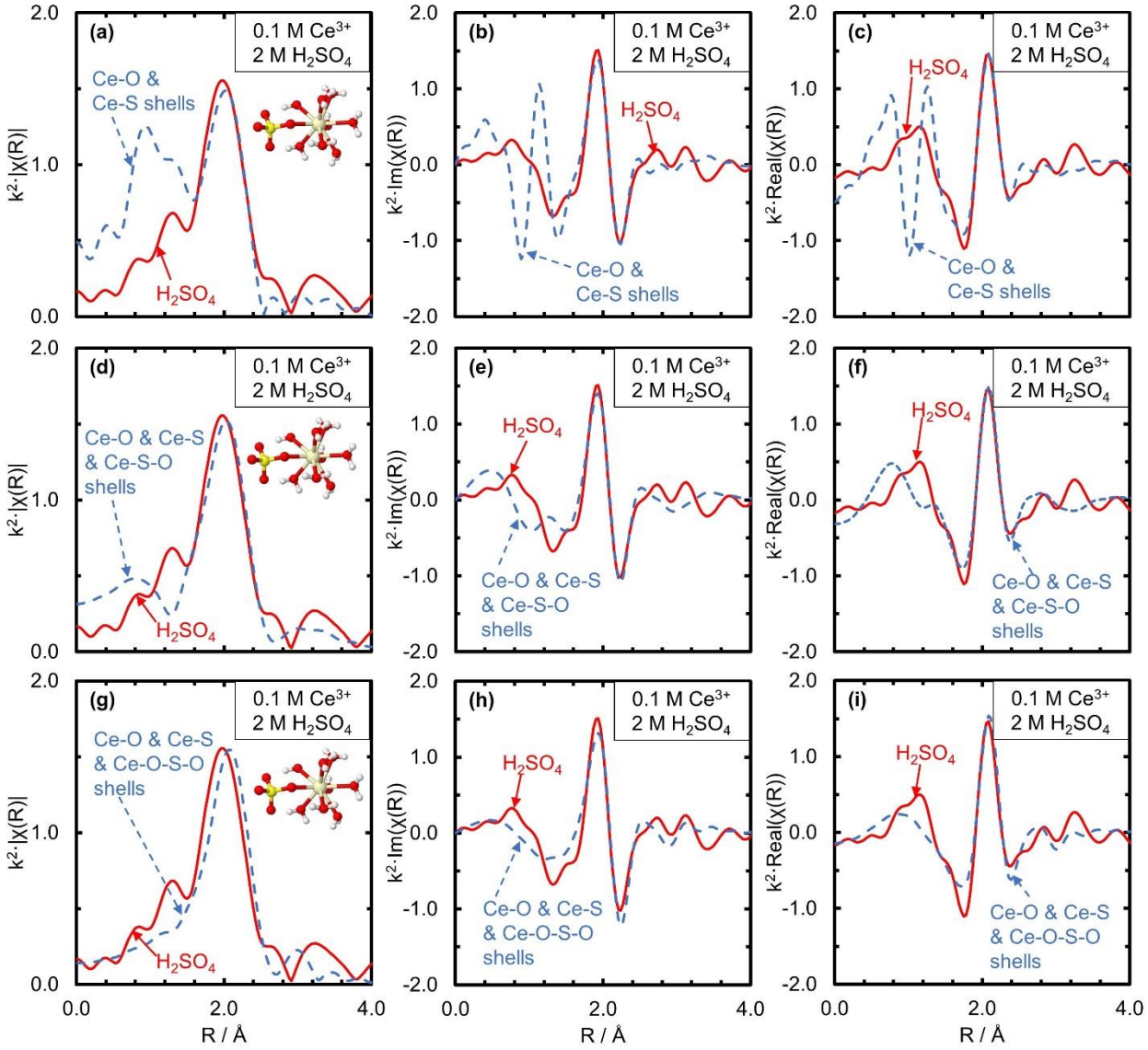

Figure A.7. EXAFS spectra of the Ce L_3-edge for 0.1 M Ce^{3+} in 2 M H_2SO_4 and a fit with a Ce-O shell and a Ce-S shell plotted in **(a)** $k^2 \cdot \chi(R)$ Fourier transformed space (magnitude), **(b)** $k^2 \cdot \chi(R)$ Fourier transformed space (imaginary), and **(c)** $k^2 \cdot \chi(R)$ Fourier transformed space (real). EXAFS spectra of the Ce L_3-edge for 0.1 M Ce^{3+} in 2 M H_2SO_4 and fit with a Ce-O shell, a Ce-S shell, and a Ce-S-O shell in the **(d)** Fourier transformed space (magnitude), **(e)** $k^2 \cdot \chi(R)$ Fourier transformed space (imaginary), and **(f)** Fourier transformed space (real). EXAFS spectra of the Ce L_3-edge for 0.1 M Ce^{3+} in 2 M H_2SO_4 and fit with a Ce-O shell, a Ce-S shell, and a Ce-O-S-O shell in the **(g)** Fourier transformed space (magnitude), **(h)** $k^2 \cdot \chi(R)$ Fourier transformed space (imaginary), and **(i)** Fourier transformed space (real). The Ce source was $Ce_2(CO_3)_3$. Inset geometries are the optimized structure of $Ce[(H_2O)_8SO_4]^+$ from DFT that was also used to generate paths using FEFF9. The fitting window in the R space was 1.4 to 4.0 Å, and 1.5 to 9.7 $Å^{-1}$ in the k space.

Table A.4. EXAFS fitting results for Ce^{3+} in H_2SO_4 from ARTEMIS, fit with (1) a Ce-O shell and a Ce-S shell; (2) a Ce-O shell, a Ce-S shell, and a Ce-S-O multiple scattering shell; and (3) a Ce-O shell, a Ce-S shell, and a Ce-O-S-O multiple scattering shell. Three parameters were used for each path: CN (coordination number), ΔR (shell distance), and σ^2 (Debye-Waller factor). S_0^2 (amplitude reduction factor) and ΔE_0 were obtained by fitting the Ce^{3+} TFSA data with 1 Ce-O shell, and then these same values were set as fixed global parameters for the fit of Ce^{3+} in H_2SO_4. S_0^2 was determined to be 0.970, whereas ΔE_0 was determined to be 0.954 eV. The CN of the Ce-S shell was set to 1, the CN of the Ce-S-O shell was set to 2, and the CN of the Ce-O-S-O shell was set to 1. The σ^2 of the Ce-S-O and Ce-O-S-O shells were both set to the σ^2 of the Ce-S shell. All the other parameters were obtained by fitting.

Ce-O shell			**Ce-S shell**			**Reduced χ^2**		
R (Å)	**CN**	**σ^2 (Å^2)**	**R (Å)**	**Set CN**	**σ^2 (Å^2)**			
2.570± 0.017	5.3± 1.4	0.005± 0.005	1.487± 0.047	1	0.006± 0.007	149.4		
Ce-O shell			**Ce-S shell**			**Ce-S-O shell**		**Reduced χ^2**
R (Å)	**CN**	**σ^2 (Å^2)**	**R (Å)**	**Set CN**	**σ^2 (Å^2)**	**R (Å)**	**Set CN**	
2.578±0.017	7.8±2.8	0.010±0.007	1.636±0.189	1	0.037±0.027	2.751±0.097	2	162.9
Ce-O shell			**Ce-S shell**			**Ce-O-S-O shell**		**Reduced χ^2**
R (Å)	**CN**	**σ^2 (Å^2)**	**R (Å)**	**Set CN**	**σ^2 (Å^2)**	**R (Å)**	**Set CN**	
2.593±0.015	9.0±1.8	0.011±0.005	3.470±0.108	1	0.007±0.015	3.771±0.056	1	180.8

The XAFS normalization parameters used for all Ce^{3+} samples studied in **Chapter 5** are included in **Table A.5**. The EXAFS fitting parameters used for all Ce^{3+} samples in **Chapter 5** are included in **Table A.6**. Whenever possible, the normalization parameters were kept consistent for all Ce^{3+} and all Ce^{4+} samples, and only varied when necessary to obtain appropriate normalization of the spectra.

Table A.5. Normalization parameters for each Ce L_3- and K-edge measurement in **Chapter 5**.

Sample	**Edge**	***E*$_0$ (eV)**	**Pre-edge range**	**Normalization range**	**Spline k range**
$CeCl_3$-$7H_2O$	Ce K	40430	−150 eV to −91.31 eV	45.531 eV to 871.14 eV	0 Å^{-1} to 18.021 Å^{-1}
	Ce L_3	5724.55	−143.61 eV to −9 eV	21 eV to 201 eV	0 Å^{-1} to 10.461 Å^{-1}
Ce^{3+} ion	Ce K	40430	−150 eV to −91.31 eV	45.531 eV to 871.14 eV	0 Å^{-1} to 18.021 Å^{-1}
	Ce L_3	5724.55	−143.61 eV to −9 eV	22 eV to 201 eV	0 Å^{-1} to 10.461 Å^{-1}

Table A.6. Fitting parameters for each Ce L_3- and K-edge measurement in **Chapter 5**.

Sample	Edge	R range	k range
$CeCl_3$-$7H_2O$	Ce K	1.4 Å to 3.0 Å	2.0 $Å^{-1}$ to 14.0 $Å^{-1}$
	Ce L_3	1.2 Å to 3.0 Å	2.0 $Å^{-1}$ to 8.5 $Å^{-1}$
Ce^{3+} ion	Ce K	1.4 Å to 3.0 Å	2.0 $Å^{-1}$ to 14.0 $Å^{-1}$
	Ce L_3	1.4 Å to 3.0 Å	2.0 $Å^{-1}$ to 8.461 $Å^{-1}$

The fits in the k space and the magnitude component in the R space of the $CeCl_3$-$7H_2O$ standard EXAFS from **Chapter 5** at the Ce K-edge are shown in **Fig. A.8a** and **Fig. A.8b**, respectively. The fit of the $CeCl_3$-$7H_2O$ standard EXAFS at the Ce L_3-edge in both the R space and the k space is included in **Fig. A.9**. From the fits of the $CeCl_3$-$7H_2O$ standard at both edges, it is evident that both Ce-O and Ce-Cl scattering paths are necessary in the fit to capture the EXAFS spectra. The fitting results for both edges are included in **Table A.7**. Although typically the amplitude reduction factor, S_0^2, is not larger than 1.0, we see values greater than 1.0 for both edges here. One hypothesis for why we see S_0^2 values >1.0 here is that MEE effects were not corrected for, which are known to be prevalent for Ce samples.[4,5] Having accurate S_0^2 from the $CeCl_3$-$7H_2O$ is necessary to get accurate coordination numbers for our fits of the cerium ions.

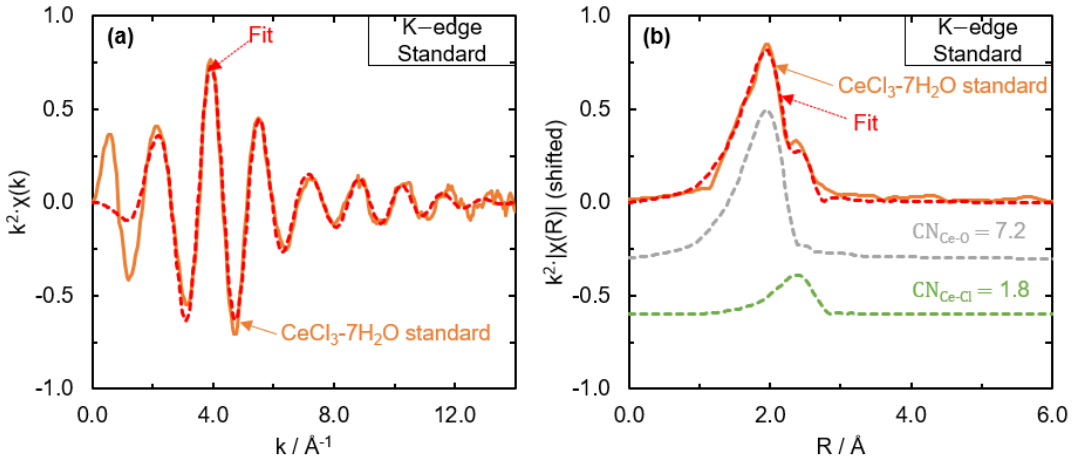

Figure A.8. Ce K-edge $k^2 \cdot \chi(R)$ EXAFS and fit of $CeCl_3$-$7H_2O$ standard. (a) $CeCl_3$-$7H_2O$ standard (orange solid line) with fit (red dashed line) in the k space. **(b)** $CeCl_3$-$7H_2O$ standard (orange solid line) with fit (red dashed line) and Ce-O and Ce-Cl path contributions (shifted in y-axis) in the R space (magnitude).

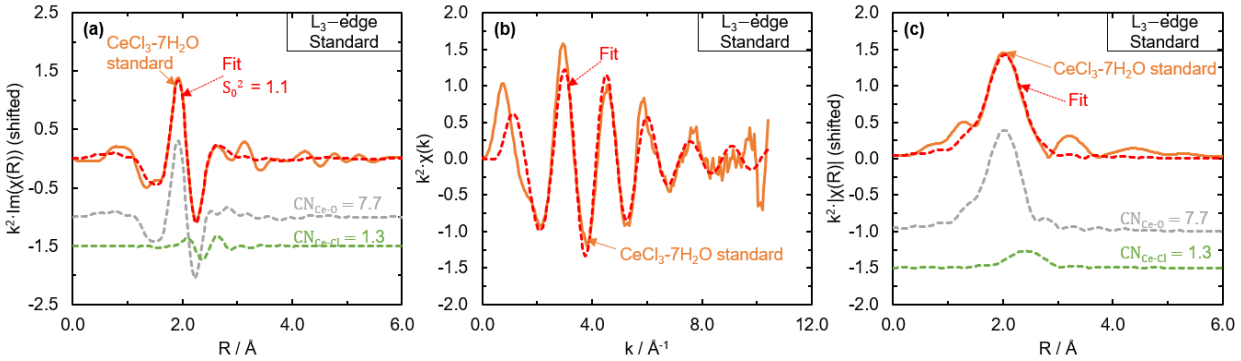

Figure A.9. Ce L_3-edge $k^2 \cdot \chi(R)$ EXAFS and fit of $CeCl_3$-$7H_2O$ standard. (a) Imaginary component of Ce L_3-edge EXAFS in the R space of $CeCl_3$-$7H_2O$ standard (orange solid line) with fit (red dashed line), and Ce-O and Ce-Cl path contributions (shifted in y-axis). **(b)** Ce L_3-edge EXAFS of $CeCl_3$-$7H_2O$ standard (orange solid line) with fit (red dashed line) in the k space. **(c)** Magnitude component of Ce L_3-edge EXAFS in the R space of $CeCl_3$-$7H_2O$ standard (orange solid line) with fit (red dashed line), and Ce-O and Ce-Cl path contributions (shifted in y-axis).

Table A.7. K- and L_3-edge fit parameters of $CeCl_3$-$7H_2O$ standard. Fitting results for $CeCl_3$-$7H_2O$ standard at the Ce L_3- and K-edges from ARTEMIS, fitting with a Ce-O shell and a Ce-Cl shell. The following parameters were varied in the fit: amplitude reduction factor (S_0^2), the shift in threshold energy (ΔE_0), the shift in scattering distance ΔR, and the Debye-Waller factor (σ^2). The coordination number (CN) for each shell was set as a fixed global parameter. The scattering distance R included in the Table is calculated by adding the ΔR fitted value to the expected scattering distance from the FEFF path.

Edge	S_0^2	ΔE_0 (eV)	Ce-O shell		Ce-Cl shell		σ^2 (Å^2)
			R (Å)	CN (set)	R (Å)	CN (set)	
L_3	1.1±0.2	-0.58±1.59	2.556±0.024	7.7	2.942±0.083	1.3	0.009±0.005
K	1.5±0.1	-2.51±0.80	2.5553±0.010	7.2	2.950±0.021	1.8	0.011±0.001

The **Chapter 5** co-fit of the Ce K- and L_3-edge EXAFS of Ce^{3+} in 2 M H_2SO_4 at the Ce K-edge with the Ce-O shell is shown in the k space and the R space (magnitude) in **Fig. A.10a** and **A.10b**. The results of this co-fit at the Ce-L_3 edge are included in **Fig. A.11**. In the fit, we used the edge-specific S_0^2 and shift in threshold energy, ΔE_0, from the $CeCl_3$-$7H_2O$ standard as global fixed parameters. We varied path specific parameters (coordination number, *CN*, shift in scattering distance, ΔR, and the Debye-Waller factor, σ^2) to obtain the best fit of the data. Fitting results are included in **Table A.8**. It should be noted that the fit of the Ce^{3+} EXAFS at the Ce L_3-edge (**Fig. A.11**) does not visually capture the magnitude of the spectrum in the R space. We attribute this to artificial features that were not removed during the background removal and normalization procedure, as evidenced by the strong features occurring between 0 and 0.5 Å, wherein it is known

that no real scattering event can be occurring. Additionally, it can be seen from the k data (**Fig. A.11b**) that the data exhibits poor quality after ~6.0 $Å^{-1}$, most likely due to MEE effects as well as the interference of the L_2-edge.

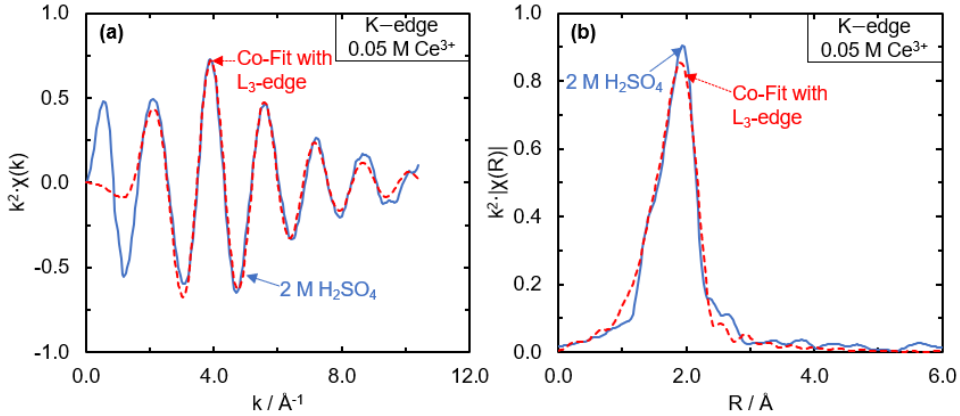

Figure A.10. Ce K-edge $k^2 \cdot \chi(R)$ EXAFS and co-fit of 0.05 M Ce^{3+} in 2 M H_2SO_4 with a Ce-O scattering path. **(a)** Ce K-edge EXAFS in the k space of 0.025 M $Ce_2(CO_3)_3$ in 2 M H_2SO_4 (blue solid line) with co-fit with L_3-edge (red dashed line) using a Ce-O scattering path. **(b)** Magnitude component Ce K-edge EXAFS in the R space of 0.025 M $Ce_2(CO_3)_3$ in 2 M H_2SO_4 (blue solid line) with co-fit (red dashed line) using a Ce-O scattering path. Results of co-fit at Ce L_3-edge are included in **Fig. A.11**.

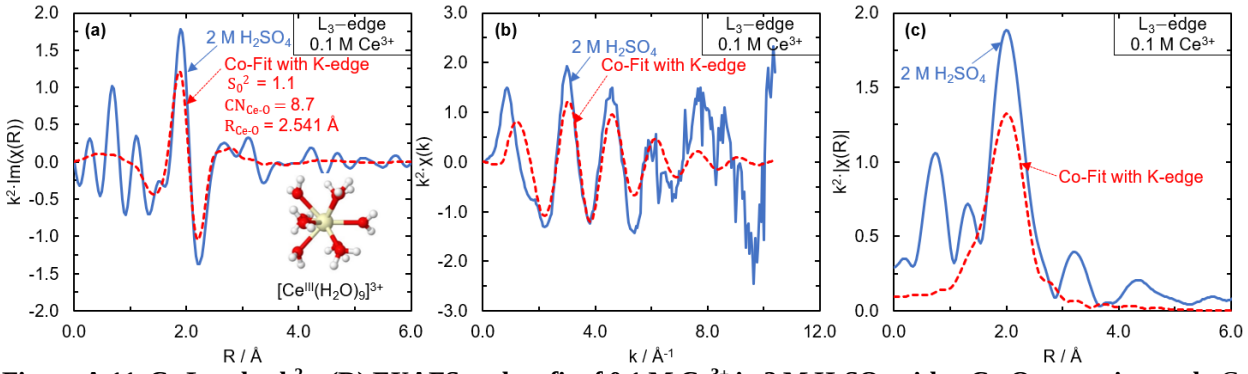

Figure A.11. Ce L_3-edge $k^2 \cdot \chi(R)$ EXAFS and co-fit of 0.1 M Ce^{3+} in 2 M H_2SO_4 with a Ce-O scattering path. Ce L_3-edge EXAFS of 0.05 M $Ce_2(CO_3)_3$ in 2 M H_2SO_4 (blue solid line) with co-fit with K-edge (red dashed line) using a Ce-O scattering path, in the **(a)** R space (imaginary), with inset structure showing $[Ce^{III}(H_2O)_9]^{3+}$ from a MD-EXAFS snapshot, **(b)** k space, and **(c)** R space (magnitude). Results of co-fit at Ce K-edge are included in **Fig. A.10**.

Table A.8. K- and L_3- edge fitting parameters of Ce^{3+}. Fitting results for Ce^{3+} in TFSA, MSA, and H_2SO_4 at the Ce L_3- and K-edges from ARTEMIS, fitting with either a Ce-O shell or a Ce-O shell and a Ce-S shell, and average scattering distances (with standard deviation used as uncertainty) for MD-simulated EXAFS of $[Ce^{III}(H_2O)_9]^{3+}$ and $[Ce^{III}(H_2O)_8(SO_4)]^+$ species. For the fits, S_0^2 (amplitude reduction factor) and ΔE_0 were obtained by fitting the $CeCl_3$-$7H_2O$ standard at the appropriate edge (**Table A.7**), and then were set as fixed global parameters for the fits below. Three parameters were varied in the fits for each scattering shell: the shift in scattering distance (ΔR) to obtain the scattering distance, coordination number (CN), and the Debye-Waller factor (σ^2). The scattering distance R included in the Table is calculated by adding the ΔR fitted value to the expected scattering distance from the FEFF path.

Edge	Electrolyte	Ce-O shell			Ce-S shell			Ref
		***R* (Å)**	***CN***	**σ^2 (Å^2)**	***R* (Å)**	***CN***	**σ^2 (Å^2)**	
L_3	0.1 M Ce^{3+}/ 2 M TFSA	2.543± 0.007	9.0±0.9	0.010± 0.002	–	–	–	**Chapter 4**
	0.1 M Ce^{3+}/ 2 M MSA	2.542± 0.007	8.7±0.9	0.010± 0.002	–	–	–	
	0.1 M Ce^{3+}/ 2 M H_2SO_4	2.541± 0.006	8.5±0.8	0.010± 0.002	–	–	–	
$K + L_3$ (Co-Fit)	K: 0.05 M Ce^{3+}/ 2 M H_2SO_4	2.541± 0.004	8.7±0.6	0.014± 0.001	–	–	–	**Chapter 5**
	L_3: 0.1 M Ce^{3+}/ 2 M H_2SO_4	2.551± 0.003	10.0±0.7	0.014± 0.001	3.690± 0.045	7.3±7.4	0.037± 0.021	
K	0.1 M Ce^{3+}/ 2 M TFSA	2.524± 0.005	8.1±0.7	0.012± 0.001	–	–	–	
	0.1 M Ce^{3+}/ 2 M MSA	2.531± 0.007	8.4±0.9	0.013± 0.002	–	–	–	
	0.1 M Ce^{3+}/ 2 M H_2SO_4	2.540± 0.005	8.1±0.6	0.013± 0.001	–	–	–	
Edge	**Structure**	**Ce-O**			**Ce-S**			**Ref**
		***R* (Å)**	***CN* (set)**		***R* (Å)**	***CN* (set)**		
MD	$[Ce^{III}(H_2O)_9]^{3+}$	2.541± 0.121	9		–	–		**Chapter 5**
	$[Ce^{III}(H_2O)_8SO_4]^+$	2.532± 0.226	9		3.766± 0.115	1		

To confirm the trends that we observed in the co-fit shown above, we used an additional set of Ce L_3-edge Ce^{3+} in H_2SO_4 EXAFS data, which we collected during a different beamline run than that shown in **Chapter 5**. This data set demonstrated fewer quality issues in the k space, and when normalized, exhibited fewer background features. When we co-fit these data with the Ce K-edge data, the resulting *CN*, ΔR, and σ^2 were similar to those reported in **Table A.8**, and the fit was visually in greater agreement with the EXAFS data. We could not use this set of L_3-edge data in the final co-fit, however, because we did not collect EXAFS of a Ce^{3+} standard for that specific run. Instead, to obtain a value for S_0^2 for this data set, we relied on a method similar to our process

from our previous work,[6] in which we fit the Ce^{3+} EXAFS with a *CN* set to 9 while guessing S_0^2. We then fixed the S_0^2 value to the one obtained from the previous fit and allowed *CN* to vary. We acknolwedge that it is preferable to use a Ce^{3+} standard to obtain accurate an S_0^2 value, and so we report the fit of the Ce^{3+} EXAFS at the Ce L_3-edge for which we also collected EXAFS of a standard, despite the poorer quality and resulting worse visual fit.

A.2.2 Ce^{4+} EXAFS

Figure A.12 includes the k^3 weighted Ce L_3-edge EXAFS data used in **Chapter 4**, plotted in the k space for the CeO_2 solid as well as the Ce^{4+} sample in H_2SO_4. The coordination numbers of Ce-O and Ce-Ce scattering paths for CeO_2 were fixed to known values based on its crystal structure, and the ARTEMIS parameters ΔE_0 and S_0^2 were obtained by fitting, which could then be used in fits of experimental EXAFS of Ce^{4+} in H_2SO_4.

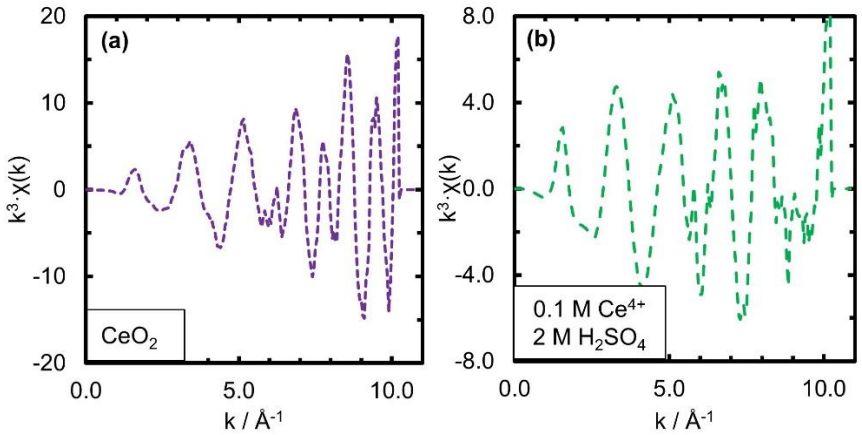

Figure A.12. (a) EXAFS spectra of the Ce L_3-edge for CeO_2 plotted in k space (k^3 weighted). The CeO_2 standard has been corrected for self-absorption. **(b)** EXAFS spectra of the Ce L_3-edge for 0.1 M Ce^{4+} in 2 M H_2SO_4 plotted in k space (k^3 weighted).

The XAFS normalization parameters used for all Ce^{4+} samples studied in **Chapter 5** are included in **Table A.9**. The EXAFS fitting parameters used for all Ce^{4+} samples are included in **Table A.10**. Whenever possible, the normalization parameters were kept consistent for all Ce^{3+} and all Ce^{4+} samples, and only varied when necessary to obtain appropriate normalization of the spectra.

Table A.9. Normalization parameters for each L_3- and K-edge measurement.

Sample	Edge	E_0 (eV)	Pre-edge range	Normalization range	Spline k range
CeO_2	Ce K	40431	−172.298 eV to −91.63 eV	61.995 eV to 1137.247 eV	0 $Å^{-1}$ to 17.977 $Å^{-1}$
	Ce L_3	5727.14	−143.61 eV to −23.12 eV	32 eV to 335 eV	0 $Å^{-1}$ to 10.449 $Å^{-1}$
	New Ce L_3	5727.14	−143.61 eV to −19 eV	33 eV to 330 eV	0 $Å^{-1}$ to 10.449 $Å^{-1}$
Ce^{4+} ion	Ce K	40431	−150 eV to −91.31 eV	58.16 eV to 871.14 eV	0 $Å^{-1}$ to 15.965 $Å^{-1}$
	Ce L_3	5727.14	−143.61 eV to −23.12 eV	32 eV to 330 eV	0 $Å^{-1}$ to 10.449 $Å^{-1}$
	0.05 M Ce L_3 (used in **Fig. 2f**)	5727.14	−143.61 eV to -9 eV	33 eV to 251 eV	0 $Å^{-1}$ to 10.449 $Å^{-1}$
	New Ce L_3	5727.14	−143.61 eV to −9 eV	33 eV to 201 eV	0 $Å^{-1}$ to 10.449 $Å^{-1}$

Table A.10. Fitting parameters for each L_3- and K-edge measurement.

Sample	Edge	R range	k range
CeO_2	Ce K	1.4 Å to 4.6 Å	2.0 $Å^{-1}$ to 15.2 $Å^{-1}$
	Ce L_3	1.4 Å to 4.6 Å	2.0 $Å^{-1}$ to 8.4 $Å^{-1}$
Ce^{4+} ion	Ce K	1.4 Å to 4.6 Å	2.0 $Å^{-1}$ to 14.0 $Å^{-1}$
	Ce L_3	1.4 Å to 4.6 Å	2.0 $Å^{-1}$ to 8.4 $Å^{-1}$

To complement the analysis of Ce^{4+} EXAFS at the Ce K-edge in **Chapter 5**, we completed a similar analysis for Ce^{4+} in H_2SO_4 EXAFS at the Ce L_3-edge, as shown in **Fig. A.13**. In **Fig. A.13a**, we compare the Ce^{3+} EXAFS at the Ce L_3-edge to the EXAFS of Ce^{4+} in H_2SO_4 that we reported in our prior work[6] but renormalized here. It is the co-fit between this L_3-edge data and K edge data that is reported in the main text. In **Fig. A.13b**, we compare additionally collected Ce L_3-edge 0.1 M Ce^{4+} 2 M H_2SO_4 EXAFS (collected as part of a series in which H_2SO_4 concentration was varied, labeled "Ce^{4+} in varied [H_2SO_4]") to the Ce^{3+} EXAFS at the Ce L_3-edge. From both comparisons, the peaks associated with the Ce^{4+}-O scattering are shifted to the left of those associated with Ce^{3+}-O scattering, and there are additional scattering peaks that occur for Ce^{4+} between 2.5 Å and 3.25 Å that do not occur for Ce^{3+}. Compared to the scattering peaks that we

note for Ce^{4+} at the Ce K-edge, these are shifted to the right by ~0.25 Å, which is expected because the χ(k) function of the L_3- and K-edges are shifted 90° from each other, which will be translated into the R space. We see in **Fig. A.13c** that a scattering event occurs in the same range for the Ce L_3-edge MD-EXAFS of $[Ce^{IV}(H_2O)_8(SO_4)]^{2+}$ that is not present for $[Ce^{IV}(H_2O)_9]^{4+}$ or $[Ce^{III}(H_2O)_9]^{3+}$. To further prove that the peaks in this 2.5 Å to 3.25 Å range are due to Ce^{4+}-S scattering, we compare the MD-EXAFS of $[Ce^{IV}(H_2O)_8(SO_4)]^{2+}$ with and without sulfate scattering paths in **Fig. A.13d** and show that peaks in the same 2.5-3.25 Å region disappear when the Ce^{4+}-sulfate scattering path is removed. Finally, we show the results of the co-fit of the Ce^{4+} EXAFS at the Ce K- and L_3-edges for the case when the Ce L_3-edge Ce^{4+} in H_2SO_4 EXAFS data from our previous work[6] is used in **Fig. A.13e**, and for the case when the "Ce^{4+} in varied $[H_2SO_4]$" Ce L_3-edge EXAFS data is used in the co-fit in **Fig. A.13f**. For both co-fits, we fit the EXAFS of a CeO_2 standard collected at the Ce L_3-edge at the same time as the Ce^{4+} in H_2SO_4 data collection to obtain S_0^2 and ΔE_0 values. In both cases, the best fit of the Ce^{4+} in H_2SO_4 EXAFS was achieved with Ce-O and Ce-S scattering shells, with Ce-O *CN* around 9 and the Ce-S *CN* around 3. Fitting parameter results are included farther below in **Table A.12**.

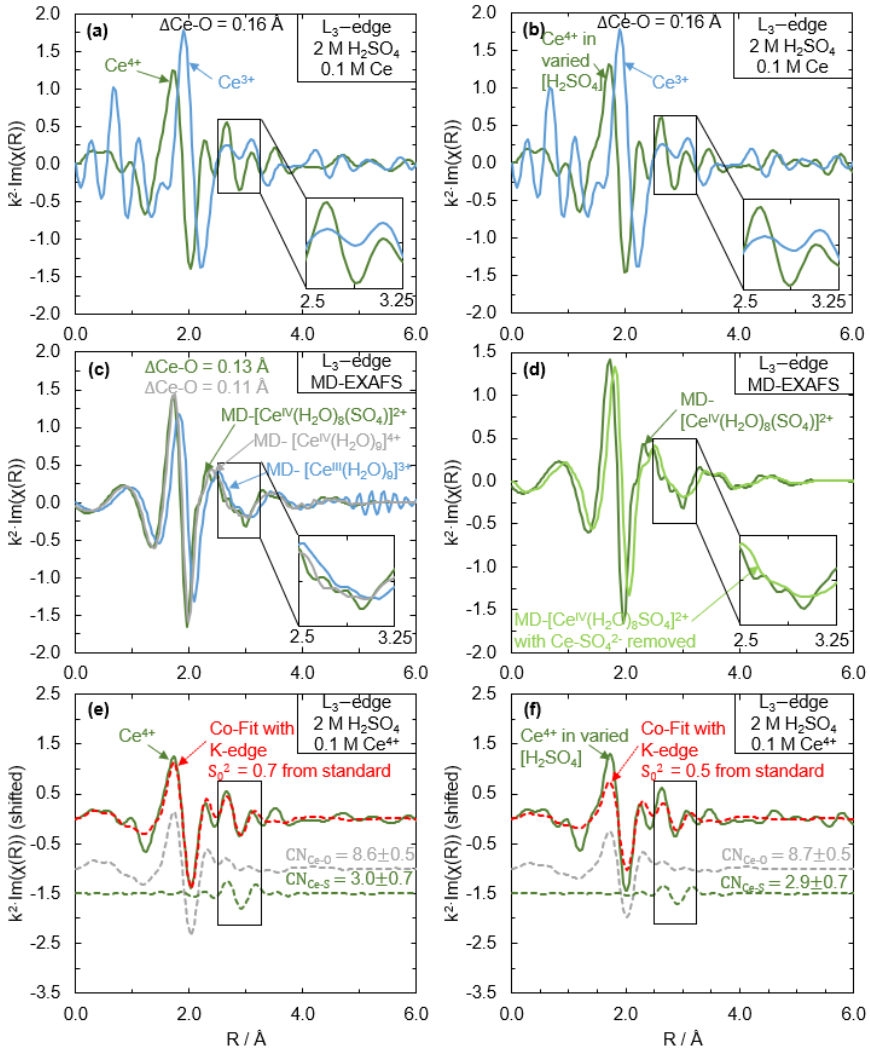

Figure A.13. Ce L_3-edge $k^2 \cdot \chi(R)$ EXAFS and fits for different Ce^{3+} and Ce^{4+} species. (a) 0.05 M $Ce_2(CO_3)_3$ in 2 M H_2SO_4 (blue line) and 0.05 M $Ce_2(CO_3)_3$ oxidized to Ce^{4+} in 2 M H_2SO_4 (dark green solid line), **(b)** 0.05 M $Ce_2(CO_3)_3$ in 2 M H_2SO_4 (blue line) and additional 0.05 M $Ce_2(CO_3)_3$ oxidized to Ce^{4+} in 2 M H_2SO_4 (dark green solid line, "Ce^{4+} in varied $[H_2SO_4]$"), **(c)** simulated MD-EXAFS of $[Ce^{III}(H_2O)_9]^{3+}$ (blue solid line), $[Ce^{IV}(H_2O)_9]^{4+}$ (gray solid line), and $[Ce^{IV}(H_2O)_8(SO_4)]^{2+}$ (dark green solid line), **(d)** simulated MD-EXAFS of $[Ce^{IV}(H_2O)_8(SO_4)]^{2+}$ (dark green solid line) and $[Ce^{IV}(H_2O)_8(SO_4)]^{2+}$ with pathways associated with sulfate scattering removed (light green solid line), **(e)** 0.05 M $Ce_2(CO_3)_3$ oxidized to Ce^{4+} in 2 M H_2SO_4 (dark green solid line) with fit (red dashed line), and Ce-O and Ce-S path contributions (shifted in y-axis), and **(f)** additional 0.05 M $Ce_2(CO_3)_3$ oxidized to Ce^{4+} in 2 M H_2SO_4 (dark green solid line, "Ce^{4+} in varied $[H_2SO_4]$") with fit (red dashed line), and Ce-O and Ce-S path contributions (shifted in y-axis).

The **Chapter 5** fit of the CeO_2 standard EXAFS with three paths (2 Ce-O scattering paths and 1 Ce-Ce scattering path) at the Ce K-edge and L_3-edge is shown in **Fig. A.14a-c** and **Fig. A.14d-f**, respectively. In these fits, we fixed the *CN* values for each path and varied the S_0^2 and ΔE_0 parameters to obtain the best fit. All fitting parameter results are included in **Table A.11**. We

then used the edge-specific values of S_0^2 and ΔE_0 in the co-fit of the Ce^{4+} in H_2SO_4 EXAFS as global fixed parameters.

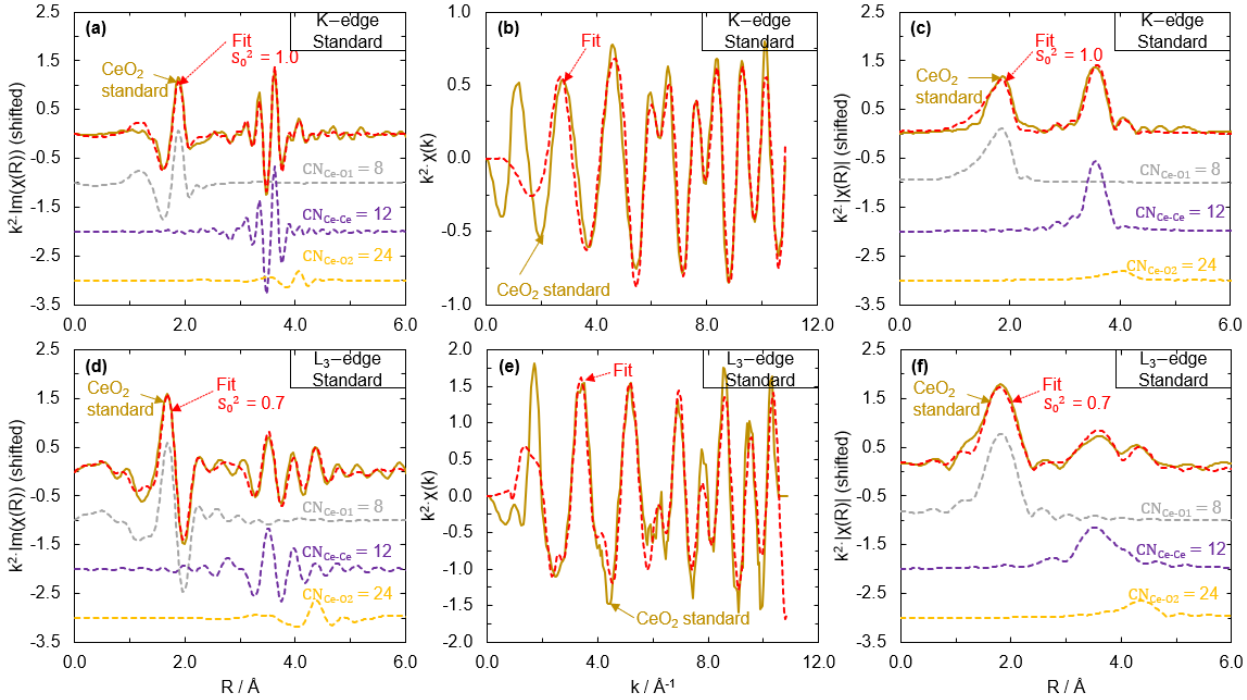

Figure A.14. Ce K- and L_3-edge $k^2 \cdot \chi(R)$ EXAFS and fits of CeO_2 standard. (a) Imaginary component of Ce K-edge EXAFS in the R space of CeO_2 standard (dark yellow solid line) with fit (red dashed line), and two Ce-O and one Ce-Ce path contributions (shifted in y-axis), **(b)** Ce K-edge EXAFS of CeO_2 standard (dark yellow solid line) in the k space, and **(c)** magnitude component of Ce K-edge EXAFS in the R space of CeO_2 standard (dark yellow solid line) with fit (red dashed line), and two Ce-O and one Ce-Ce path contributions (shifted in y-axis). **(d)** Imaginary component of Ce L_3-edge EXAFS in the R space of CeO_2 standard (dark yellow solid line) with fit (red dashed line), and two Ce-O and one Ce-Ce path contributions (shifted in y-axis), **(e)** Ce L_3-edge EXAFS of CeO_2 standard (dark yellow solid line) in the k space, and **(f)** magnitude component of Ce L_3-edge EXAFS in the R space of CeO_2 standard (dark yellow solid line) with fit (red dashed line), and two Ce-O and one Ce-Ce path contributions (shifted in y-axis).

Table A.11. K- and L_3-edge fitting parameters of CeO_2 standard. Fitting results for CeO_2 standard at the Ce L_3- and K-edges from ARTEMIS, fitting with two Ce-O shells and a Ce-Ce shell. The following parameters were varied in the fit: amplitude reduction factor (S_0^2), the shift in threshold energy (ΔE_0), the shift in scattering distance (ΔR), and the Debye-Waller factor (σ^2). The coordination number (CN) for each shell was set as a fixed global parameter. The scattering distance R included in the Table is calculated by adding the ΔR fitted value to the expected scattering distance from the FEFF path.

Edge	S_0^2	ΔE_0 (eV)	Ce-O_1 shell			Ce-Ce shell			Ce-O_2 shell		
			R (Å)	CN (set)	σ^2 (Å^2)	R (Å)	CN (set)	σ^2 (Å^2)	R (Å)	CN (set)	σ^2 (Å^2)
L_3	0.7± 0.2	2.99± 1.61	2.307 ± 0.020	8	0.002 ± 0.004	3.817 ± 0.024	12	0.002 ± 0.004	4.994 ± 0.082	24	0.009 ± 0.013
K	1.0± 0.1	0.82± 0.90	2.359 ±0.009	8	0.006 ±0.001	3.844 ±0.004	12	0.004 ±0.001	4.537 ±0.029	24	0.007 ±0.003

Table A.12. K- and L_3- edge fitting parameters of Ce^{4+}. Fitting results for Ce^{4+} in H_2SO_4 at the Ce L_3- and K-edges from ARTEMIS, fitting with either a Ce-O shell or a Ce-O shell and a Ce-S shell, and average scattering distances (with standard deviation used as uncertainty) for MD-simulated EXAFS of $[Ce^{IV}(H_2O)_9]^{4+}$ and $[Ce^{IV}(H_2O)_8(SO_4)]^{2+}$ species. For the fits, S_0^2 (amplitude reduction factor) and ΔE_0 were obtained by fitting the CeO_2 standard at the appropriate edge (see **Table A.10**), and then were set as fixed global parameters for the fits below. Four parameters were varied in the fits for each scattering shell: the shift in scattering distance (ΔR) to obtain the scattering distance, coordination number (CN), the Debye-Waller factor (σ^2), and the third cumulant (σ^3). The scattering distance R included in the Table is calculated by adding the ΔR fitted value to the expected scattering distance from the FEFF path.

Edge	Electrolyte	Ce-O shell			Ce-S shell			Ref
		R (Å)	CN	σ^2 (Å^2) / σ^3 (Å^3)	R (Å)	CN	σ^2 (Å^2) / σ^3 (Å^3)	
L_3	0.1 M Ce^{4+}/ 2 M H_2SO_4	2.402 ± 0.012	9 (set)	0.007±0.002	–	–	–	Buchanan, et al. (2020)
K + L_3 (Co-Fit)	K: 0.05 M Ce^{4+}/ 2 M H_2SO_4 L_3: 0.1 M Ce^{4+}/ 2 M H_2SO_4	2.395 ± 0.010	9.8±1.0	0.008±0.001 / −0.0002±0.0003	–	–	–	This work
		2.382 ± 0.006	8.6±0.5	0.006±0.001 / −0.0005±0.0002	3.671 ± 0.016	3.0±0.7	0.002±0.001 / 0.0044±0.0002	
Edge	**Structure**	**Ce-O**			**Ce-S**			**Ref**
		R (Å)	**CN (set)**		**R (Å)**	**CN (set)**		
MD	$[Ce^{IV}(H_2O)_9]^{4+}$	2.435 ± 0.092	9		–	–		This work
	$[Ce^{IV}(H_2O)_8SO_4]^{2+}$	2.413 ± 0.098	9		3.719 ± 0.148	1		

A.3 References

1. Ohta, A., Kagi, H., Tsuno, H., Nomura, M. & Kawabe, I. Influence of multi-electron excitation on EXAFS spectroscopy of trivalent rare-earth ions and elucidation of change in hydration number through the series. *Am. Mineral.* **93**, 1384–1392 (2008).
2. Angelo, P. D. *et al.* Revised Ionic Radii of Lanthanoid (III) Ions in Aqueous Solution. 4572–4579 (2011) doi:10.1021/ic200260r.
3. Antonio, M. R., Ellis, R. J., Estes, S. L. & Bera, M. K. Structural insights into the multinuclear speciation of tetravalent cerium in the tri-n-butyl phosphate-n-dodecane solvent extraction system. *Phys. Chem. Chem. Phys.* **19**, 21304–21316 (2017).
4. Chaboy, J., Marcelli, A. & Tyson, T. A. Influence of double-electron transitions on the EXAFS L edges of rare-earth systems. *Phys. Rev. B* **49**, 11652–11661 (1994).
5. Solera, J. A., García, J. & Proietti, M. G. Multielectron excitations at the L edges in rare-earth ionic aqueous solutions. *Phys. Rev. B* **51**, 2678–2686 (1995).
6. Buchanan, C. A. *et al.* Structures and Free Energies of Cerium Ions in Acidic Electrolytes. *Inorg. Chem.* **59**, 12552–12563 (2020).

Appendix B
Computational modeling

This Appendix contains additional information related to density functional theory (DFT) calculations discussed in **Chapters 4** and **5**. The DFT calculations related to **Chapter 4** were completed by Eunbyeol Ko of the Goldsmith Lab, and the DFT calculations related to **Chapter 5** were completed by Dylan Herrera, also of the Goldsmith Lab. The DFT results are included in this dissertation to provide full context on the structural and electron transfer results.

B.1 Additional density functional theory results

To obtain accurate DFT-predicted free energies in **Chapter 4**, explicit water solvation had to be modeled in the Ce-anion ligand exchange free energy calculations. **Figure B.1** shows the DFT-predicted free energies for Ce^{4+}-anion ligand exchanges in seven different acids, when explicit solvation is included, as well as when only implicit COSMO modeling is incorporated into the DFT calculations. Both of these DFT-predicted free energies are compared to the experimental free energies obtained from reported redox potentials. The model that incorporated the explicit solvation was determined to be more accurate based on the large improvement in agreement between the experimentally reported free energies and DFT-predicted free energies of Ce^{4+}.

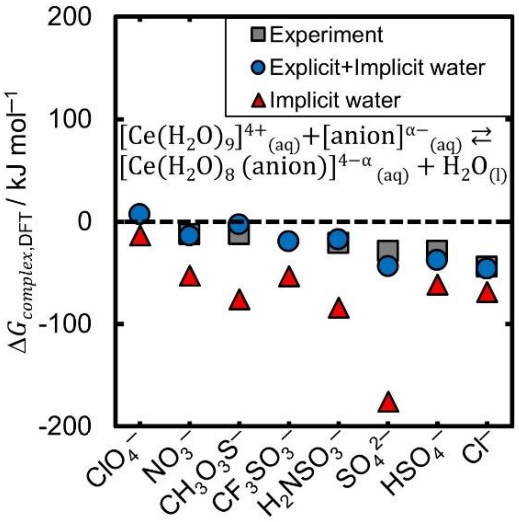

Figure B.1. Effect of solvating the anion with explicit water on the change in Gibbs free energy of $[Ce(H_2O)_9]^{4+}$ due to anion complexation ($\Delta G_{complex}$). DFT-predicted $\Delta G_{complex}$ for $[Ce(H_2O)_9]^{4+}$ in different acids with explicit+implicit or implicit water and compared with experimentally extracted values. The "explicit+implicit water" has the anion surrounded by 12 explicit water molecules and implicit COSMO solvation, whereas the "implicit water" has the anion modeled in only implicit COSMO solvation.

Figure B.2 shows the differences between the model with and without explicit water solvation included for Ce^{3+}-anion ligand exchanges.

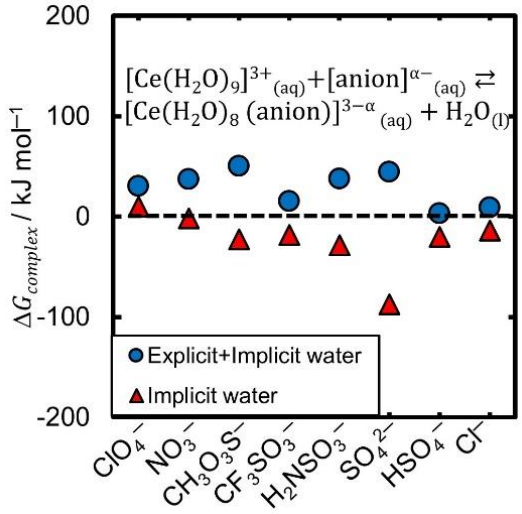

Figure B.2. Effect of solvating the anion with explicit water on the change in Gibbs free energy of $[Ce(H_2O)_9]^{3+}$ due to anion complexation ($\Delta G_{complex,DFT}$). DFT-predicted $\Delta G_{complex,DFT}$ for $[Ce(H_2O)_9]^{3+}$ in different acids with explicit+implicit or implicit water. The "explicit+implicit water" has the anion surrounded by 12 explicit water molecules and implicit COSMO solvation, whereas the "implicit water" has the anion modeled in only implicit COSMO solvation.

To determine the structure of Ce^{3+} in pure water in **Chapter 4**, various $[Ce(H_2O)_x]^{3+}$ hydration complexes are studied (with x varied from 5 to 10), as shown in **Figure B.3a**. These structures correspond to the computed free energies reported in **Figure 4.1c**. The structures of the DFT-predicted Ce^{3+}-anion complexes are shown in **Figure B.3b**, which correspond to the structures used to compute the free energy of anion complexation in **Figure 4.1d.**

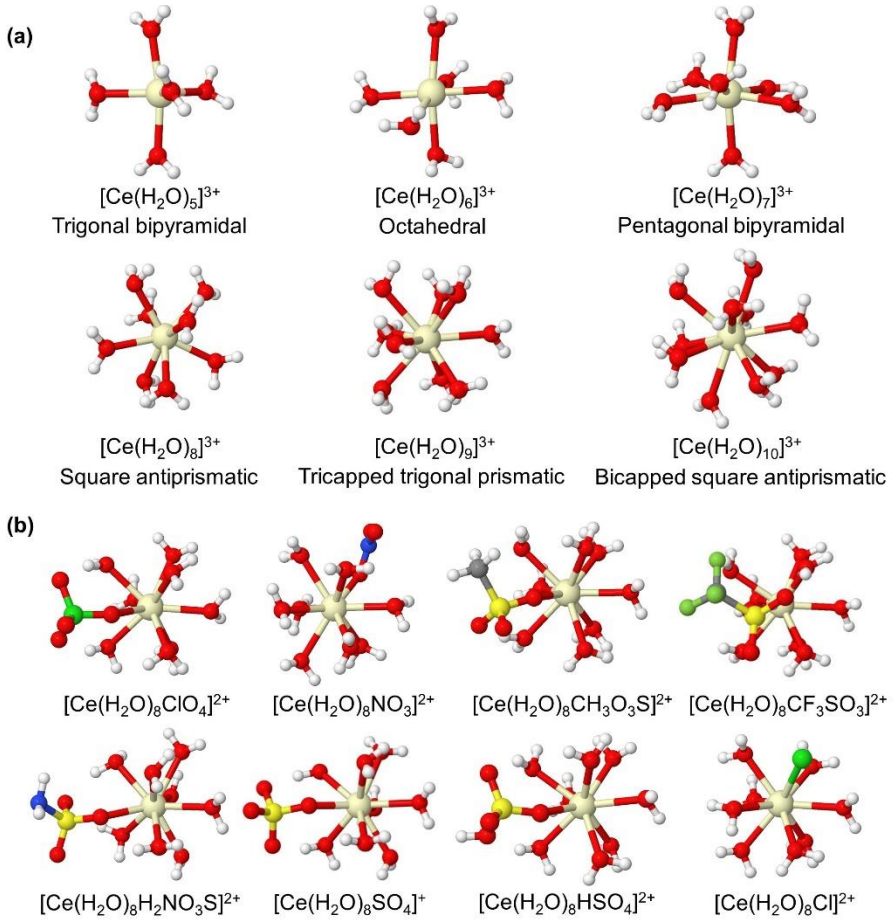

Figure B.3. (a) DFT-predicted structures of the Ce^{3+} ion in pure water corresponding to **Figure 4.1c**. The $[Ce(H_2O)_9]^{3+}$ species is the thermodynamically most stable complex. **(b)** DFT-predicted structures of Ce^{3+} complexes in acidic electrolytes whose anion exchange free energies are reported in **Figure 4.1d**. Atom color legend: beige = cerium, red = oxygen, white = hydrogen, yellow = sulfur, gray = carbon, pear-green = fluorine, blue = nitrogen.

The DFT-predicted average bond lengths in **Chapter 4** are compared with literature references as well as EXAFS fitted values from this work in **Table B.1**. The Ce^{3+}-O distances were reported previously in three electrolytes: pure water, TFSA, and hydrochloric acid. In pure water,

the average bond length for Ce^{3+}-O matches within 0.04 Å compared to experimental EXAFS.[1] In HCl, the bond lengths for Ce^{3+}-O and Ce^{3+}-Cl match within 0.02 Å.[2] The mean reported bond length of Ce^{3+}-O is 2.53 Å in the crystallized structure of $Ce(H_2O)_9(CF_3SO_3)_3$,[3] and the Ce^{3+}-O distance determined from a one shell fit of an EXAFS spectrum of the Ce L_3-edge for Ce^{3+} in TFSA has been reported to be 2.54 Å,[3] agreeing with our DFT-calculated bond length of Ce^{3+}-O in TFSA of 2.58 Å in the aqueous phase.

Table B.1. DFT-calculated bond length of Ce^{3+}–anion complexes compared with literature references as well as the average Ce-OH_2 distances obtained from EXAFS fitting from **Table 4.1** in **Chapter 4**. Note that the DFT-predicted bond lengths are of the complex, but hydrated Ce^{3+} is the most energetically favorable structure in all electrolytes. All distances are in Å.

Electrolyte	Literature references	DFT-predicted average distances from this work	EXAFS Ce-O scattering distances from this work
H_2O	Ce-OH_2: 2.61[1]	Ce-OH_2: 2.57	N/A
$HClO_4$	N/A	Ce-OH_2: 2.57, Ce-$OClO_3$: 2.65	N/A
HNO_3	N/A	Ce-OH_2: 2.58, Ce-ONO_2: 2.52	Ce-OH_2: 2.55
MSA	N/A	Ce-OH_2: 2.60, Ce-OCH_3SO_2: 2.38	Ce-OH_2: 2.54
TFSA	Ce-O: 2.54[3]	Ce-OH_2: 2.58, Ce-OCF_3SO_2: 2.54	Ce-OH_2: 2.54
H_3NSO_3	N/A	Ce-OH_2: 2.58, Ce-OH_2NSO_2: 2.50	N/A
H_2SO_4	N/A	Ce-OH_2: 2.60, Ce-OSO_3: 2.41	Ce-OH_2: 2.54
HSO_4	N/A	Ce-OH_2: 2.59, Ce-$OHSO_3$: 2.52	
HCl	Ce-OH_2: 2.56, Ce-Cl: 2.89[2]	Ce-OH_2: 2.58, Ce-Cl: 2.87	Ce-OH_2: 2.54

To determine the structure of Ce^{4+} in pure water in **Chapter 4**, various $[Ce(H_2O)_x]^{4+}$ species were studied (with *x* varied from 5 to 10), as shown in **Figure B.4**. These structures correspond to the free energies reported in **Figure 4.9a**. The most energetically favorable configuration was the $[Ce(H_2O)_9]^{4+}$ structure, with tricapped trigonal prismatic geometry.

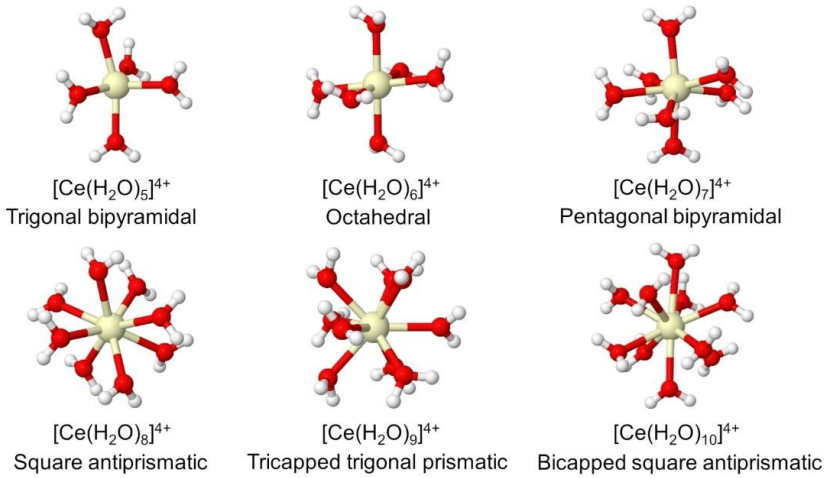

Figure B.4. DFT-predicted structures of the Ce^{4+} ion in pure water corresponding to **Figure 4.9a**. The $[Ce(H_2O)_9]^{4+}$ species is predicted to be the thermodynamically most stable complex in pure water.

B.2 Reorganization energy calculations

We determined in **Chapter 5** that the reorganization energies for the $[Ce^{III}(H_2O)_9]^{3+}/[Ce^{IV}(H_2O)_9]^{4+}$ redox reaction converged with the Stuttgart RSC 1997 ECP basis set[4] for the cerium ion and the 6-31+G* basis set,[5] as seen in **Fig. B.5** for the outer-sphere reorganization energies. The inner-sphere reorganization energies were found to similarly converge in a series of calculations without using COnductor-like Screening MOdel (COSMO). Although the final inner-sphere reorganization energies reported in **Chapter 5** were calculated using COSMO, we expect that the inner-sphere reorganization energies calculated from each basis set would experience a near constant shift (by the energy of the implicit solvent), and so we conclude that the inner-sphere reorganization energies converge with the Stuttgart RSC 1997 ECP and 6-31+G* basis sets as well.

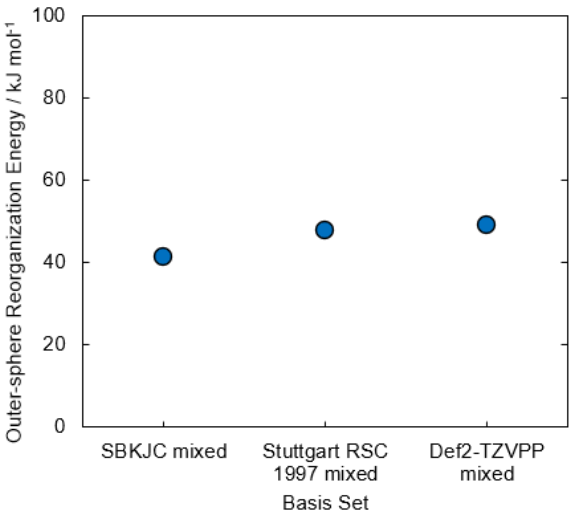

Figure B.5. Outer-sphere reorganization energy converges with increasing basis set size for $[Ce(H_2O)_9]^{3+} \rightleftharpoons Ce(H_2O)_9]^{4+} + e^-$ redox couple. Mixed basis sets utilize the first basis set and its associated ECP on the cerium atom, and the 6-31+G* basis set on all non-cerium atoms.

B.3 References

1. Lutz, O. M. D., Hofer, T. S., Randolf, B. R. & Rode, B. M. Computational study of the cerium(III) ion in aqueous environment. *Chem. Phys. Lett.* **539**–**540**, 50–53 (2012).
2. Allen, P. G., Bucher, J. J., Shuh, D. K., Edelstein, N. M. & Craig, I. Coordination chemistry of trivalent lanthanide and actinide ions in dilute and concentrated chloride solutions. *Inorg. Chem.* **39**, 595–601 (2000).
3. Persson, I., D'Angelo, P., De Panfilis, S., Sandström, M. & Eriksson, L. Hydration of lanthanoid(III) ions in aqueous solution and crystalline hydrates studied by EXAFS spectroscopy and crystallography: The myth of the 'gadolinium break'. *Chem. - A Eur. J.* **14**, 3056–3066 (2008).
4. Dolg, M., Stoll, H. & Preuss, H. Energy-adjusted ab initio pseudopotentials for the rare earth elements. *J. Chem. Phys.* **3**, 1730–1734 (1989).
5. Ditchfield, R., Hehre, W. J. & Pople, J. A. Self-consistent molecular-orbital methods. IX. An extended Gaussian-type basis for molecular-orbital studies of organic molecules. *J. Chem. Phys.* **54**, 724–728 (1971).

Appendix C

Experimental free energies of Ce^{4+} extracted from redox potentials

This Appendix contains detailed information on how the anion complexation free energies of Ce^{4+} were calculated in **Chapter 4**.

C.1 Calculating the experimental Ce^{4+} complexation free energies

Knowledge of the cerium ions' complexation behavior gained from UV-Vis and EXAFS fitting allows us to extract their free energies of complexation in electrolytes using the Ce^{3+}/Ce^{4+} redox potential, which can then be compared to the calculated free energies in **Figure 4.9b** in **Chapter 4**. Neither Ce^{3+} nor Ce^{4+} complex with ClO_4^- in perchloric acid,[1] so the Ce^{3+}/Ce^{4+} electron transfer proceeds via **Eq. C.1a**, in which both Ce^{3+} and Ce^{4+} are hydrated by nine waters.

$$[Ce(H_2O)_9]^{4+} + e^- \rightleftharpoons [Ce(H_2O)_9]^{3+} \quad \textbf{(C.1a)}$$

The redox potential is related to the relative formation energy of the two cerium species through the Nernst equation. **Eq. C.1b** is the Nernst equation corresponding to **Eq. C.1a**, where n is the number of electrons transferred per Ce ion, F is Faraday's constant, E°_{ref} is the standard redox potential in perchloric acid, $\Delta G_{rxn,Ce^{3+}/Ce^{4+}}$ is the Gibbs free energy of reaction, $\Delta G_{f,Ce^{3+}}$ is the Gibbs free energy of formation for $[Ce(H_2O)_9]^{3+}$, and $\Delta G_{f,Ce^{4+}}$ is the Gibbs free energy of formation for $[Ce(H_2O)_9]^{4+}$. Because Ce^{3+} and Ce^{4+} do not complex with anions in perchloric acid, we choose the redox potential in perchloric acid (1.74 V vs. SHE) to serve as a reference value, E°_{ref}.

$$-nFE^{\circ}_{ref} = \Delta G_{rxn,Ce^{3+}/Ce^{4+}} = \Delta G_{f,Ce^{3+}} - \Delta G_{f,Ce^{4+}} \quad \textbf{(C.1b)}$$

As discussed in **Chapter 4**, from UV-Vis (**Figure 4.3**), EXAFS (**Figures 4.1a,b** and **4.5**), and DFT (**Figure 4.1d**), Ce^{3+} coordinates with only water in all the acids studied here. The large change in UV-Vis spectra with anion for Ce^{4+} shown in **Figure 4.11a** and favorable calculated free energy of Ce^{4+}-anion complexation in **Figure 4.9b** indicates Ce^{4+} prefers to complex with anions in all acids here (apart from perchloric). Thus, in acids with stronger complexing behavior than perchloric acid, the electron transfer reaction would proceed via **Eq. C.2a** rather than **Eq. C.1a**.

$$\left[\mathrm{Ce(H_2O)_{9-y}(anion)_y}\right]^{4-\alpha y} + y\mathrm{H_2O} + \mathrm{e^-} \rightleftharpoons \mathrm{[Ce(H_2O)_9]^{3+}} + y\mathrm{[anion]^{\alpha-}} \quad \textbf{(C.2a)}$$

With *y* representing the number of anions that complex with one Ce^{4+} ion and α representing the magnitude of the charge of the anion.

Eq. C.2b is the corresponding Nernst equation for the reaction in **Eq. C.2a**, with standard redox potential E°. Here, $\Delta G_{f,Ce^{3+}}$ is still the Gibbs free energy of formation of $[Ce(H_2O)_9]^{3+}$ in the acid of interest, while $\Delta G_{f,anion}$, $\Delta G_{f,Ce^{4+}\,complex}$, and $\Delta G_{f,H_2O}$ are the Gibbs free energy of formation of $[anion]^{\alpha-}$, $[Ce(H_2O)_{9-y}(anion)_y]^{4-\alpha y}$, and water, respectively.

$$-nFE^{\circ} = \Delta G_{rxn,Ce^{3+}/Ce^{4+}\,complex} = \Delta G_{f,Ce^{3+}} + y\Delta G_{f,anion} - \Delta G_{f,Ce^{4+}\,complex} - y\Delta G_{f,H_2O} \quad \textbf{(C.2b)}$$

Eq. C.3 shows the reaction involved in formation of a Ce^{4+} complex via an anion-water exchange reaction. The free energy of this reaction is the difference in the Gibbs free energy of formation of the reactants ($\Delta G_{f,Ce^{4+}}$ and $\Delta G_{f,anion}$) and products ($\Delta G_{f,Ce^{4+}\,complex}$ and $\Delta G_{f,H_2O}$).

$$[Ce(H_2O)_9]^{4+} + y[\text{anion}]^{\alpha-} \rightleftharpoons [Ce(H_2O)_{9-y}(\text{anion})_y]^{4-\alpha y} + yH_2O \quad \textbf{(C.3)}$$

Eq. C.3 is the same reaction as if we subtracted the reaction in **Eq. C.2a** from the reaction in **Eq. C.1a**, if we neglect any differences in the $[Ce(H_2O)_9]^{3+}$ or $[Ce(H_2O)_9]^{4+}$ energies between the acids, which we show later is a reasonable assumption by the agreement between our DFT-predicted free energies and experimentally-reported free energies. Thus, to calculate the change in Gibbs free energy for the formation of the Ce^{4+}-anion complex shown in **Eq. C.3** from standard redox potentials, we can subtract **Eq. C.2b** from **Eq. C.2b** to obtain **Eq. C.4**. We define $\Delta G_{complex}$ as the reaction energy of Ce^{4+} complexation with anions, because Ce^{3+} does not complex with anions.

$$-nF\left(E^{\circ}_{ref} - E^{\circ}\right) = \Delta G_{f,Ce^{4+}\,complex} + y\Delta G_{f,H_2O} - \Delta G_{f,Ce^{4+}} - y\Delta G_{f,anion} = \Delta G_{complex} \quad \textbf{(C.4)}$$

The $\Delta G_{complex}$ determined from the experimental standard redox potentials was compared to DFT-predicted values in **Figure 4.9b** (using DFT we assumed that y was one). The semi-quantiative agreement supports our assumptions that Ce^{3+} is hydrated fully by water, while Ce^{4+} is complexed by anions. Therefore**,** the shift in redox potential, $E^{\circ}_{ref} - E^{\circ}$, with electrolyte seen in **Scheme 4.1** is from the change in Ce^{4+} free energy due to Ce^{4+}-anion complexation, and not from Ce^{3+} complexation with anions. The change in Gibbs free energy of the Ce^{4+} complex formation was used to calculate the equilibrium constant of the Ce^{4+} complexation reaction, $K_{eq,complex}$ (**Eq. C.5**, where a_i is the activity of species i, and activity coefficients are assumed to be unity, so the activities can be approximated by the concentrations).

$$K_{eq,complex} = \exp\left(-\frac{\Delta G_{complex}}{RT}\right) = \frac{a_{[Ce(H_2O)_{9-y}(anion)_y]^{4-\alpha y}}\, a_{H_2O}^{y}}{a_{Ce(H_2O)_9}^{4+} a_{anion}^{y}}$$
$$\cong \frac{\left[\left[Ce(H_2O)_{9-y}(anion)_y\right]^{4-\alpha y}\right][H_2O]^y}{[[Ce(H_2O)_9]^{4+}][anion]^y} \quad \textbf{(C.5)}$$

Here $\Delta G_{complex}$ and $K_{eq,complex}$ are calculated assuming the redox reaction is a one electron transfer reaction (**Eq. C.6**).

$$[Ce(H_2O)_9]^{3+} + y[anion]^{\alpha-} \rightleftharpoons \left[Ce(H_2O)_{9-y}(anion)_y\right]^{4-\alpha y} + yH_2O + 1e^- \quad \textbf{(C.6)}$$

Table C.1 lists the standard redox potentials, E°, for the Ce^{3+}/Ce^{4+} redox couple that were also listed in **Scheme 4.1** in **Chapter 4**, as well as the difference between the reference redox potential (E°_{ref}) in perchloric acid and the redox potential in the specified electrolyte. This difference enables us to estimate the complexation free energy of Ce^{4+} by using **Eq. C.4**. This calculation is only possible because we know that Ce^{3+} does not readily complex with anions, so that the shift in the redox potential is mostly because of anion complexation with Ce^{4+}. **Table C.1** also includes the DFT-predicted complexation free energies of Ce^{4+}, which agree with the experimental Gibbs free energies from literature values.

Table C.1. The Ce^{3+}/Ce^{4+} standard redox potential (E°) in different acidic electrolytes; the difference between the water-complexed redox potential (E°_{ref}) and the standard redox potential in the listed electrolyte (E°); the Gibbs free energies of reaction for the formation of the Ce^{4+} complex ($\Delta G_{complex,E^{\circ}}$) from **Eq. C.4**; the equilibrium constant of the Ce^{4+} complexation reaction ($K_{eq,complex,E^{\circ}}$) from the experimental $\Delta G_{complex,E^{\circ}}$ using **Eq. C.5**; DFT determined Gibbs free energy of reaction for Ce^{4+} complexes ($\Delta G_{complex,DFT}$); the equilibrium constant of the Ce^{4+} complexation reaction ($K_{eq,complex,DFT}$) from the DFT calculated $\Delta G_{complex,DFT}$. The experimental $\Delta G_{complex,E^{\circ}}$ and $K_{eq,complex,E^{\circ}}$ were calculated assuming: 1) Ce^{3+} does not readily complex with anions based on the UV-Vis and EXAFS experiments, so the shift in redox potential from E°_{ref} (E° in $HClO_4$) is assumed to arise from only complexation of the Ce^{4+} ion, and 2) the redox reaction is a one electron transfer reaction defined as in **Eq. C.2a**.

Electro-lyte	**Standard redox potential, E° (V vs. SHE)**	**$E^{\circ}_{ref} - E^{\circ}$ (V)**	**Experiment[a] $\Delta G_{complex,E^{\circ}}$ (kJ mol^{-1})**	**Experiment[a] $K_{eq,complex,E^{\circ}}$**	**DFT[b] $\Delta G_{complex,DFT}$ (kJ mol^{-1})**	**DFT[b] $K_{eq,complex,DFT}$**
$HClO_4$	1.74[2]	0	> 0	< 1	6.57	0.0705
HNO_3	1.61[3]	0.13	< -13	> 160	−14.26	316.0
MSA	1.61[4]	0.13	−13[c]	160[d]	−3.20	3.64
TFSA	Not available	NA	NA	NA	−19.61	2,738
H_3NSO_3	1.52[5]	0.22	−21	5,300	−18.14	1,513
SO_4^{2-}	1.44[c][6]	0.30	−29	120,000[d]	−43.93	50,180,000
HSO_4^-					−38.31	5,192,000
HCl	1.28[e][2,7]	–	–	–	−46.11	121,000,000

[a] Experimental $\Delta G_{complex}$ and $K_{eq,complex}$ calculated from standard redox potentials reported in literature, with sources for redox potentials included in table; [b] Theory $\Delta G_{complex}$ and $K_{eq,complex}$ calculated using DFT in this work; [c] Based on dissociation constants,[8,9] at a starting concentration of 1 M H_2SO_4, there are approximately 100 times more bisulfate ions present than sulfate ions, and so the shift in redox potential reported for 1 M H_2SO_4 is based on the complexation of Ce^{4+} ions with approximately 0.01 M SO_4^{2-}. A higher concentration of sulfate ions present would results in a greater shift in redox potential; [d] The higher equilibrium constant of complexation for H_2SO_4 than MSA is confirmed by the UV-Vis spectra shown in **Figure 4.11** in **Chapter 4**, where in a mixture of 1:1 H_2SO_4:MSA the Ce^{4+} UV-Vis was most similar to the pure H_2SO_4 spectra, implying those complexes dominated; [e] 1.28 V vs. SHE is the historically reported redox potential for Ce^{3+}/Ce^{4+} in 1 M HCl,[7] however, this value has been called into question[10,11] because of the Cl^-/Cl_2 redox reaction that will occur at similar potentials, which will interfere with the measurement of the Ce^{3+}/Ce^{4+} redox potential. Thus, experimental values of $\Delta G_{complex}$ and $K_{eq,complex}$ were not calculated for the Ce^{3+}/Ce^{4+} redox couple in HCl.

C.2 References

1. Baes, C. F. J. & Mesmer, R. E. Yttrium, Lanthanides, Actinium. in *The Hydrolysis of Cations* 138–146 (Krieger Publishing Company, 1986).
2. Morss, L. R. Yttrium, Lanthanum, and the Lanthanide Elements. in *Standard Potentials in Aqueous Solution* (eds. Bard, A. J., Parsons, R. & Jordan, J.) 619–621 (Marcel Dekker, Inc., 1985).
3. Noyes, A. A. & Garner, C. S. Strong Oxidizing Agents in Nitric Acid Solution. I. Oxidation Potential of Cerous-Ceric Salts. *J. Am. Chem. Soc.* **58**, 1265–1268 (1936).
4. Arenas, L. F., Ponce De León, C. & Walsh, F. C. Electrochemical redox processes involving soluble cerium species. *Electrochim. Acta* **205**, 226–247 (2016).
5. Xiong, F., Zhou, D., Xie, Z. & Chen, Y. A study of the Ce3/Ce4+redox couple in sulfamic acid for redox battery application. *Appl. Energy* **99**, 291–296 (2012).
6. Kunz, A. H. The reduction potential of the ceric-cerous electrode. *J. Am. Chem. Soc.* **53**, 98–102 (1931).
7. Smith, G. F. & Getz, C. A. Cerate Oxidimetry: Theoretical Considerations and Determination of Approximate Electrode Reference Potentials. *Ind. Eng. Chem. Res.* **10**, 191–195 (1938).
8. Young, T. F. & Blatz, L. A. The variation of the properties of electrolytic solutions with degrees of dissociation. *Chem. Rev.* **44**, 93–115 (1949).
9. Lide, D. R. *CRC Handbook of Chemistry and Physics, 84th edition*. (CRC Press LLC, 2004). doi:10.1136/oem.53.7.504.
10. Wadsworth, E., Duke, F. R. & Goetz, C. A. Present Status of Cerium (IV) -Cerium (III) Potentials. *Anal. Chem.* 1824–1825 (1957) doi:10.1021/ac60132a046.
11. Maverick, A. W. & Yao, Q. The Cerium(IV)/Cerium(III) Electrode Potential in Hydrochloric Acid Solution. *Inorg. Chem.* **32**, 5626–5628 (1993).

Appendix D

Kinetics measurements and rate law modeling

This Appendix contains additional Ce^{3+}/Ce^{4+} kinetics measurements on platinum and glassy carbon (**Appendix D.1**), as well as a detailed review of the rate law derivations for each of the one-step and two-step mechanism considered in **Chapter 5** (**Appendix D.2**). In **Appendix D.2**, the fits of each of the rate laws are included as well for both the platinum and glassy carbon data.

D.1 Additional kinetics measurements

The averaged values of the exchange current densities obtained from the charge transfer resistance method on Pt are shown in **Fig. D.1a** as a function of $[Ce^{4+}]$ and in **Fig. D.1b** as a function of temperature. We obtained charge transfer resistances, R_{ct}, using Electrochemical Impedance Spectroscopy (EIS) and collected the charge transfer resistance data either immediately before or after we collected the steady state current responses to complete the Tafel analysis. The magnitudes of the exchange current densities agree within 31% of the values using the Tafel method and demonstrate similar dependence on both $[Ce^{4+}]$ and temperature, providing additional confidence in the reported kinetic activity of Pt.

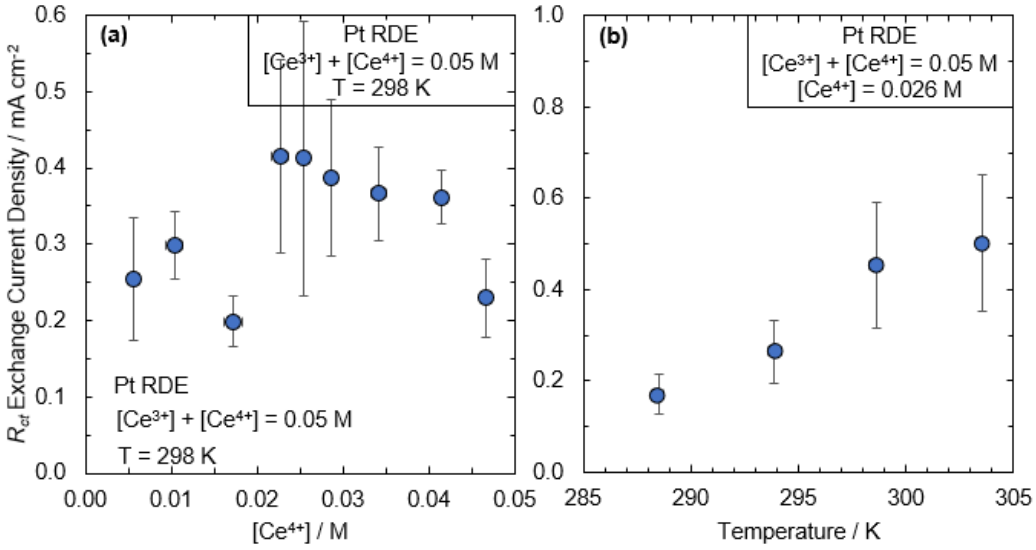

Figure D.1. Exchange current densities for the Pt rotating disk electrode from charge transfer resistance (R_{ct}) method. Exchange current densities as a function of **(a)** Ce^{4+} concentration (based on titration) and **(b)** temperature, in 2 M H_2SO_4 solution with total cerium concentration of 0.05 M. Reported values are averaged from three runs, with error bars representing one standard deviation from the average value in both horizontal and vertical directions. An Ag/AgCl reference electrode and graphite rod counter electrode were used. The solutions were sparged with nitrogen gas for at least 15 minutes before measurements were collected and blanketing with nitrogen was continued throughout the measurement collection. All reported measurements were done at 2000 rpm of the RDE.

The exchange current densities extracted from the charge transfer resistance method for the GC electrode as a function of $[Ce^{4+}]$ and temperature are shown in **Fig. D.2a** and **Fig. D.2b**, respectively. The trends are similar to those observed for exchange current densities extracted from the Tafel method, i.e., exchange current densities demonstrate a maximum in value at intermediate $[Ce^{4+}]$ and they increase with temperature. The magnitude of the exchange current densities is larger for the charge transfer resistance method than the Tafel method, although they are still lower than the kinetic activity observed for the Pt electrode. We use the exchange current densities obtained from the Tafel method in the kinetic activity analysis, given the smaller uncertainty as compared to those observed in the exchange current densities from the charge transfer resistance method.

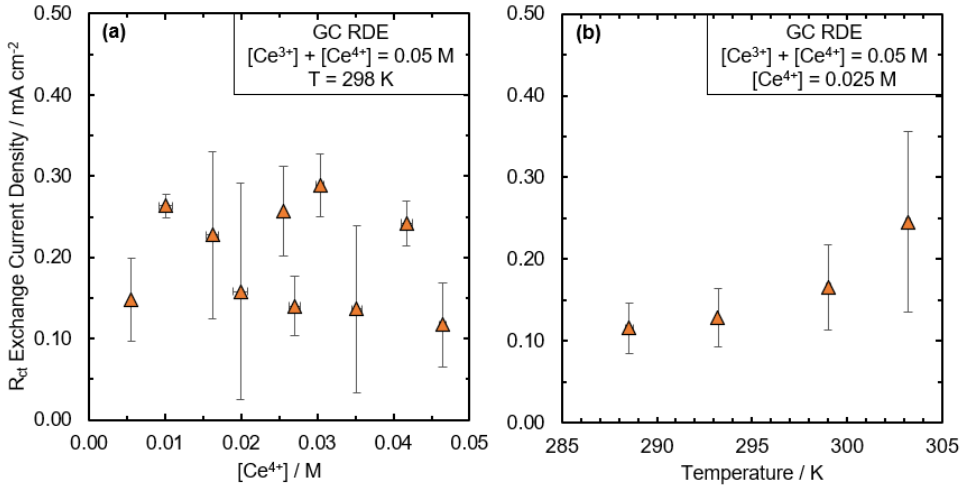

Figure D.2. Exchange current densities for the GC RDE from charge transfer resistance method. Exchange current densities as a function of **(a)** Ce^{4+} concentration (based on titration) and **(b)** temperature in 2 M H_2SO_4 solution with total cerium concentration of 0.05 M. Reported values are averaged from three runs, with error bars representing one standard deviation from the average value in both horizontal and vertical directions. An Ag/AgCl reference electrode and graphite rod counter electrode were used. The solutions were sparged with nitrogen gas for at least 15 minutes before measurements were collected and blanketing with nitrogen was continued throughout the measurement collection. All data were collected at 2000 rpm of the RDE.

D.2 Rate laws considered for cerium charge transfer

A summary of all symbols used in the derivation of the rate laws is in **Table D.1**. Following the list of symbols, the derivation of each relevant rate law is described. The relevant rate laws are the Butler Volmer (BV) and Marcus theory (MT) rate laws, derived for a one-step charge transfer, and the rate laws derived for the *CE* mechanism (*CE*, *E* RDS and *CE*, *C* RDS) and the *EC* mechanism (*EC*, *E* RDS and *EC*, *C* RDS).

Table D.1. Symbols and their definitions used in kinetic rate law derivations.

Symbol	Meaning
General	
$[\mathbf{Ce^{3+}}]$	Concentration of bulk Ce^{3+} species in sulfuric acid, i.e., $[Ce^{III}(H_2O)_9]^{3+}$
$[\mathbf{Ce^{4+}}]$	Concentration of bulk Ce^{4+} species in sulfuric acid, i.e., $[Ce^{IV}(H_2O)_6(HSO_4)_3]^{+}$
$\boldsymbol{n}$	Number of electrons transferred per charge transfer, assumed to be 1
$\boldsymbol{F}$	Faraday's constant
$\boldsymbol{R}$	Ideal gas law constant
$\boldsymbol{T}$	Temperature
$\boldsymbol{U}$	Electrode potential
$\boldsymbol{U_{eq}}$	Equilibrium potential of overall charge transfer mechanism
$\boldsymbol{U^{\circ}}$	Standard equilibrium potential of overall charge transfer mechanism
$\boldsymbol{\eta}$	Overpotential. Defined as the difference between electrode potential and standard equilibrium potential ($\boldsymbol{U - U_{eq}}$)
Definitions for Butler-Volmer	
$\boldsymbol{i_{K,BV}}$	Kinetic current for Butler-Volmer (BV) derived rate law
$\boldsymbol{k_{BV}}$, $\boldsymbol{k_{-BV}}$	Reduction and oxidation rate constants for *E* step in BV derived rate law
$\boldsymbol{A_{BV}}$, $\boldsymbol{A_{-BV}}$	Reduction and oxidation preexponential factors for *E* step in BV derived rate law
$\boldsymbol{\Delta G^{\ddagger}_{BV}}$, $\boldsymbol{\Delta G^{\ddagger}_{-BV}}$	Free energies of the transition state for reduction and oxidation for *E* step in BV derived rate law
$\boldsymbol{\Delta G^{\ddagger}_{0,BV}}$	Redox transition state free energy for *E* step in BV derived rate law when $\boldsymbol{U = U^{\circ}}$
$\boldsymbol{\alpha}$	Cathodic charge transfer coefficient
$\boldsymbol{k_0}$	Standard rate constant
$\boldsymbol{E_a}$	Apparent activation energy in finalized BV derived rate law
Definitions for Marcus Theory	
$\boldsymbol{i_{K,MT}}$	Kinetic current for Marcus Theory (MT) derived rate law
$\boldsymbol{k_{MT}}$, $\boldsymbol{k_{-MT}}$	Reduction and oxidation rate constants for *E* step in MT derived rate law
$\boldsymbol{\kappa_{el}}$	Electronic transmission coefficient
$\boldsymbol{K_{p,Ce^{3+}}}$, $\boldsymbol{K_{p,Ce^{4+}}}$	Precursor equilibrium constants for the Ce^{3+} and Ce^{4+} species
$\boldsymbol{\upsilon_n}$	Nuclear frequency factor
$\boldsymbol{\Delta G^{\ddagger}_{MT}}$, $\boldsymbol{\Delta G^{\ddagger}_{-MT}}$	Free energies of the transition state for reduction and oxidation for *E* step in MT derived rate law
$\boldsymbol{\lambda_{MT}}$	Reorganization energy for *E* step in MT derived rate law
$\boldsymbol{\Delta G_{MT}}$	Free energy of the *E* step in MT derived rate law
Definitions for *CE* mechanism	
$\boldsymbol{i_{K,CE,E}}$	Kinetic current for rate law for *CE* mechanism with *E* RDS

Table D.1 Continued	
k_2, k_{-2}	Reduction and oxidation rate constants for *E* step in *CE* mechanism
$\Delta G_2^{\ddagger}$, $\Delta G_{-2}^{\ddagger}$	Free energies of the transition state for reduction and oxidation reactions for *E* step in *CE* mechanism
λ_2	Reorganization energy for *E* step in *CE* mechanism
ΔG_2	Free energy of the *E* step in *CE* mechanism
$U_{E,2}^{\circ}$	Standard equilibrium potential of species involved in *E* step of *CE* mechanism, i.e., $[Ce^{IV}(H_2O)_9]^{4+}$ and $[Ce^{III}(H_2O)_9]^{3+}$
r_1	Reaction rate of *C* step in *CE* mechanism
k_1, k_{-1}	Forward and backward rate constants for *C* step in *CE* mechanism
K_1	Equilibrium constant for *C* step in *CE* mechanism
ΔG_1	Free energy of *C* step in *CE* mechanism
Z_2	Preexponential factor used in finalized rate law for *CE* mechanism with *E* RDS, equal to factor of κ_{el}, $K_{p,Ce^{3+}}$ or $K_{p,Ce^{4+}}$, and υ_n
$i_{K,CE,C}$	Kinetic current for rate law for *CE* mechanism with *C* RDS
r_2	Reaction rate of *E* step in *CE* mechanism
Definitions for *EC* mechanism	
$i_{K,EC,E}$	Kinetic current for rate law for *EC* mechanism with *E* RDS
k_3, k_{-3}	Reduction and oxidation rate constants for *E* step in *EC* mechanism
$\Delta G_3^{\ddagger}$, $\Delta G_{-3}^{\ddagger}$	Free energies of transition state for reduction and oxidation for *E* step in *EC* mechanism
λ_3	Reorganization energy for *E* step in *EC* mechanism
ΔG_3	Free energy of the *E* step in *EC* mechanism
$U_{E,3}^{\circ}$	Standard equilibrium potential of species involved in *E* step of *EC* mechanism, i.e., $[Ce^{IV}(H_2O)_6(HSO_4)_3]^{+}$ and $[Ce^{III}(H_2O)_6(HSO_4)_3]^{0}$
r_4	Reaction rate of *C* step in *EC* mechanism
k_4, k_{-4}	Forward and backward rate constants for *C* step in *EC* mechanism
K_4	Equilibrium constant for *C* step in *CE* mechanism
ΔG_4	Free energy of *C* step in *CE* mechanism
Z_3	Preexponential factor used in finalized rate law for *EC* mechanism with *E* RDS, equal to factor of κ_{el}, $K_{p,Ce^{3+}}$ or $K_{p,Ce^{4+}}$, and υ_n
$i_{K,EC,C}$	Kinetic current for rate law for *EC* mechanism with *C* RDS
r_3	Reaction rate of *C* step in *EC* mechanism

D.2.1 BV rate law derivation

To derive the BV rate law, the overall reaction mechanism is assumed to be the following (**Eq. D.1**), in which the electron transfer and a chemical step occur in the same step. Including the

chemical step ensures that the Ce^{3+} and Ce^{4+} are in their preferred states in sulfuric acid, i.e., $[Ce^{III}(H_2O)_9]^{3+}$ and $[Ce^{IV}(H_2O)_6(HSO_4)_3]^{+}$, respectively, satisfying *Criteria 1–3* of **Table 5.3** of **Chapter 5**.

$$[Ce^{IV}(H_2O)_6(HSO_4)_3]^{+}_{aq} + 3H_2O_{aq} + e^- \rightleftarrows [Ce^{III}(H_2O)_9]^{3+}_{aq} + 3HSO^-_{4\,aq} \quad \textbf{(D.1)}$$

For this mechanism, the kinetic current would be **Eq. D.2**, where $[Ce^{4+}]$ and $[Ce^{3+}]$ are the bulk Ce^{4+} and Ce^{3+} species. The reduction and oxidation rate constants, k_{BV} and k_{-BV}, are assumed to have an Arrhenius form[1] in **Eq. D.3**–**D.4**, with A_{BV} and A_{-BV} as the preexponential factors, and $\Delta G^{\ddagger}_{BV}$ and $\Delta G^{\ddagger}_{-BV}$ as the free energies of the transition state, of the reduction and oxidation reactions, respectively.

$$-i_{K,BV} = nF(k_{BV}[Ce^{4+}][H_2O]^3 - k_{-BV}[Ce^{3+}][HSO_4^-]^3) \quad \textbf{(D.2)}$$

$$k_{BV} = A_{BV}\exp\left(\frac{-\Delta G^{\ddagger}_{BV}}{RT}\right) \quad \textbf{(D.3)}$$

$$k_{-BV} = A_{-BV}\exp\left(\frac{-\Delta G^{\ddagger}_{-BV}}{RT}\right) \quad \textbf{(D.4)}$$

The transition state energies can be described using **Eq. D.5**–**D.6**, where $\Delta G^{\ddagger}_{0,BV}$ is the redox transition state free energy, for the case in which the electrode potential, U, is equal to the standard equilibrium potential of the redox species, U°, and α is the charge transfer coefficient.[1]

$$\Delta G^{\ddagger}_{BV} = \Delta G^{\ddagger}_{0,BV} + \alpha F(U - U^{\circ}) \quad \textbf{(D.5)}$$

$$\Delta G^{\ddagger}_{-BV} = \Delta G^{\ddagger}_{0,BV} - (1-\alpha)F(U - U^{\circ}) \quad \textbf{(D.6)}$$

Plugging **Eq. D.5–D.6** into **Eq. D.3–D.4**, we obtain the following expressions for the oxidation and reduction rate constants (**Eq. D.7–D.8**).

$$k_{BV} = A_{BV} \exp\left(\frac{-\Delta G_{0,BV}^{\ddagger}}{RT}\right) \exp\left(\frac{-\alpha F}{RT}(U - U^{\circ})\right) \quad \textbf{(D.7)}$$

$$k_{-BV} = A_{-BV} \exp\left(\frac{-\Delta G_{0,BV}^{\ddagger}}{RT}\right) \exp\left(\frac{(1-\alpha)}{RT}F(U - U^{\circ})\right) \quad \textbf{(D.8)}$$

When considering the case when the system is at equilibrium with $[Ce^{4+}] = [Ce^{3+}]$,[1] then $U = U^{\circ}$ and $k_{BV}[H_2O]^3 = k_{-BV}[HSO_4^-]^3$. We then define a standard rate constant, k_0,[1] as $k_0 \equiv A_{BV} \exp\left(\frac{-\Delta G_{0,BV}^{\ddagger}}{RT}\right)[H_2O]^3 = A_{-BV} \exp\left(\frac{-\Delta G_{0,BV}^{\ddagger}}{RT}\right)[HSO_4^-]^3$. Thus **Eq. D.7**–**D.8** can be simplified to

$$k_{BV}[H_2O]^3 = k_0 \exp\left(\frac{-\alpha F}{RT}(U - U^{\circ})\right) \quad \textbf{(D.9)}$$

$$k_{-BV}[HSO_4^-]^3 = k_0 \exp\left(\frac{(1-\alpha)}{RT}F(U - U^{\circ})\right) \quad \textbf{(D.10)}$$

Plugging **Eq. D.9–D.10** into the overall rate law **Eq. D.2** and letting overpotential $\eta = U - U_{eq}$, where U_{eq} is the equilibrium potential of the reaction and defined in **Eq. D.11**, we obtain the final rate law describing the kinetic current as a function of Ce^{3+} and Ce^{4+} bulk species, overpotential, and k_0 and α (**Eq. D.12**). This is the Butler-Volmer equation and is the same as **Eq. 5.4** in **Chapter 5** in the main text. The standard rate constant k_0 is a function of temperature (**Eq. D.13**) through the Arrhenius equation, where E_a is the activation energy.

$$U_{eq} = U^{\circ} - \frac{RT}{nF}\ln\frac{[Ce^{3+}]}{[Ce^{4+}]} \quad \textbf{(D.11)}$$

$$-i_{K,BV} = nFk_0(T)[Ce^{3+}]^{\alpha}[Ce^{4+}]^{1-\alpha}\left(\exp\left(\frac{-\alpha F\eta}{RT}\right) - \exp\left(\frac{(1-\alpha)F\eta}{RT}\right)\right) \quad \textbf{(D.12)}$$

$$k_0(T) = k_0(298\ K)\exp\left(\frac{-E_a}{R}\left(\frac{1}{T} - \frac{1}{298\ K}\right)\right) \quad \textbf{(D.13)}$$

Eq. D.12 can be used to model the exchange current density and cathodic Tafel slopes as a function of both Ce^{4+} concentration and temperature, by applying a Tafel analysis to the modeled current between the overpotential range of −0.250 V and −0.118 V, as was done for the experimentally collected data.

D.2.2 MT rate law derivation

To derive the MT rate law, the possible overall reaction mechanisms are shown in **Eq. D.14**–**D.15**. Note that MT does not allow for an inner-sphere structural change, failing *Criterion 1* in **Table 5.3** in **Chapter 5**, and meaning we must either model the *E* between the bisulfate-complexed (**Eq. D.14**) or water-coordinated Ce species (**Eq. D.15**). For the sake of simplicity, we will derive the rate law assuming **Eq. D.15** is the appropriate reaction mechanism, but the derivation would be analogous for **Eq. D.14**.

$$[Ce^{IV}(H_2O)_6(HSO_4)_3]^{+}_{aq} + e^- \rightleftarrows [Ce^{III}(H_2O)_6(HSO_4)_3]^{0}_{aq} \quad \textbf{(D.14)}$$

$$[Ce^{IV}(H_2O)_9]^{4+}_{aq} + e^- \rightleftarrows [Ce^{III}(H_2O)_9]^{3+}_{aq} \quad \textbf{(D.15)}$$

The kinetic current for **Eq. D.15** would then be **Eq. D.16**, where the reduction and oxidation rate constants k_{MT} and k_{-MT} are described through **Eq. D.17–D.18**, using standard Marcus theory expressions.[1] In **Eq. D.17–D.18**, κ_{el} is the electronic transmission coefficient, which is related to the probability of electron tunneling, $K_{p,Ce^{4+}}$ and $K_{p,Ce^{3+}}$ are the precursor equilibrium constants for the Ce^{4+} and Ce^{3+} species, respectively, and υ_n is the nuclear frequency factor.[1] $\Delta G^{\ddagger}_{MT}$ and $\Delta G^{\ddagger}_{-MT}$ are the free energies of the transition state for the reduction and oxidation rate constants defined using MT, as shown in **Eq. D.19–D.20**, where λ_{MT} is the reorganization energy and ΔG_{MT} represents the free energy of the *E* reaction. ΔG_{MT} is related to the electrode potential through **Eq. D.21**.

$$-i_{K,MT} = nF\left(k_{MT}[\mathrm{Ce^{IV}(H_2O)_9}]^{4+}_{\mathrm{aq}} - k_{-MT}[\mathrm{Ce^{III}(H_2O)_9}]^{3+}_{\mathrm{aq}}\right) \quad \textbf{(D.16)}$$

$$k_{MT} = \kappa_{el} K_{p,Ce^{4+}} \upsilon_n \exp\left(\frac{-\Delta G^{\ddagger}_{MT}}{RT}\right) \quad \textbf{(D.17)}$$

$$k_{-\mathrm{MT}} = \kappa_{el} K_{p,Ce^{3+}} \upsilon_n \exp\left(\frac{-\Delta G^{\ddagger}_{-MT}}{RT}\right) \quad \textbf{(D.18)}$$

$$\Delta G^{\ddagger}_{MT} = \frac{\lambda_{MT}}{4}\left(1 + \frac{\Delta G_{MT}}{\lambda_{MT}}\right)^2 \quad \textbf{(D.19)}$$

$$\Delta G^{\ddagger}_{-MT} = \frac{\lambda_{MT}}{4}\left(1 - \frac{\Delta G_{MT}}{\lambda_{MT}}\right)^2 \quad \textbf{(D.20)}$$

$$\Delta G_{MT} = nF(U - U^{\circ}) \quad \textbf{(D.21)}$$

Plugging these expressions into **Eq. D.16**, and again substituting $\eta = U - U_{eq}$, where U_{eq} is defined in **Eq. D.11**, and letting $Z_{MT} = \kappa_{el} K_{p,Ce^{3+}} \upsilon_n = \kappa_{el} K_{p,Ce^{4+}} \upsilon_n$, we obtain the MT rate law (**Eq. D.22**) that can be used to fit the exchange current densities and cathodic Tafel slopes as a function of [Ce^{4+}] and temperature using Tafel analysis in the same overpotential range as used in the experimental data collection process. Note that in the fitting process of the experimental data with the MT rate law, the concentration of the $[Ce^{IV}(H_2O)_9]^{4+}$ species in **Eq. D.22** was assumed to be equal to the bulk Ce^{4+} species, which we in fact know to be $[Ce^{IV}(H_2O)_6(HSO_4)_3]^{+}$.

$$i_{K,MT} = -nFZ_{MT}\left([\mathrm{Ce^{IV}(H_2O)_9}]^{4+}_{\mathrm{aq}} \exp\left(\frac{-\lambda_{MT}}{4RT}\left(1 + \frac{nF\eta}{\lambda_{MT}} - \frac{RT}{\lambda_{MT}}\ln\frac{[\mathrm{Ce^{3+}}]}{[\mathrm{Ce^{4+}}]}\right)^2\right) - [\mathrm{Ce^{III}(H_2O)_9}]^{3+}_{\mathrm{aq}} \exp\left(\frac{-\lambda_{MT}}{4RT}\left(1 - \frac{nF\eta}{\lambda_{MT}} + \frac{RT}{\lambda_{MT}}\ln\frac{[\mathrm{Ce^{3+}}]}{[\mathrm{Ce^{4+}}]}\right)^2\right)\right) \quad \textbf{(D.22)}$$

D.2.3 CE mechanism, E RDS rate law derivation

The kinetic current for the *CE* mechanism in **Chapter 5** (**Eq. 5.5a–b**), assuming the *E* step is the RDS, is defined in **Eq. D.23**, where the reduction and oxidation rate constants of the *E* step, k_2 and k_{-2}, are defined using MT in **Eq. D.24–S25**. The meanings of κ_{el}, $K_{p,Ce^{3+}}$, $K_{p,Ce^{4+}}$, and

υ_n are all the same as described previously. The free energies of the reduction and oxidation transition states for the *E* step, $\Delta G_2^{\ddagger}$ and $\Delta G_{-2}^{\ddagger}$, are defined using MT in **Eq. D.26–D.27**, with ΔG_2 defined in **Eq. D.28** as the reaction energy of the *E* step, and related to the difference between the potential of the electrode, U, and $U_{E,2}^{\circ}$, the equilibrium electrode potential of the species involved in the *E* step i.e., $[Ce^{IV}(H_2O)_9]^{4+}$ and $[Ce^{III}(H_2O)_9]^{3+}$.

$$-i_{K,CE,E} = nF\left(k_2[\mathrm{Ce^{IV}(H_2O)_9}]_{\mathrm{aq}}^{4+} - k_{-2}[\mathrm{Ce^{III}(H_2O)_9}]_{\mathrm{aq}}^{3+}\right) \quad \textbf{(D.23)}$$

$$k_2 = \kappa_{el} K_{p,Ce^{4+}} \upsilon_n \exp\left(\frac{-\Delta G_2^{\ddagger}}{RT}\right) \quad \textbf{(D.24)}$$

$$k_{-2} = \kappa_{el} K_{p,Ce^{3+}} \upsilon_n \exp\left(\frac{-\Delta G_{-2}^{\ddagger}}{RT}\right) \quad \textbf{(D.25)}$$

$$\Delta G_2^{\ddagger} = \frac{\lambda_2}{4}\left(1 + \frac{\Delta G_2}{\lambda_2}\right)^2 \quad \textbf{(D.26)}$$

$$\Delta G_{-2}^{\ddagger} = \frac{\lambda_2}{4}\left(1 - \frac{\Delta G_2}{\lambda_2}\right)^2 \quad \textbf{(D.27)}$$

$$\Delta G_2 = nF(U - U_{E,2}^{\circ}) \quad \textbf{(D.28)}$$

In the kinetic current rate law, the unknown concentration of the intermediate species $[Ce^{IV}(H_2O)_9]^{4+}$ must be defined in terms of known bulk species concentration, which can be done using the equilibrium constant of the *C* step (**Eq. 5.5a** in **Chapter 5**). As mentioned in the main text, we assume that the ligand exchange occurs in one step rather than a series of *C* steps on the principle of choosing the simplest mechanism that fits the data. Assuming the *C* step is quasi-equilibrated, then the *C* step reaction rate, r_1, would be equal to zero (**Eq. D.29**). k_1 and k_{-1} are the forward and backward rates of the *C* step and are related to the equilibrium constant of the *C* step K_1 through **Eq. D.30**. ΔG_1 in **Eq. D.30** is the reaction energy of the *C* step and is defined in **Eq. D.31**, where U° is the standard equilibrium electrode potential of the overall reaction, as

defined earlier. Thus, in the instance that $U = U^{\circ}$, $\Delta G_1 = \Delta G_2$ as would be expected from **Scheme 5.1** in **Chapter 5**.

$$r_1 = 0 = k_1\left[[\mathrm{Ce^{IV}(H_2O)_6(HSO_4)_3}]^{+}_{aq}\right][\mathrm{H_2O}]^3 - k_{-1}\left[[\mathrm{Ce^{IV}(H_2O)_9}]^{4+}_{aq}\right][\mathrm{HSO_4^-}]^3 \quad \textbf{(D.29)}$$

$$K_1 = \frac{k_1}{k_{-1}} = \exp\left(-\frac{\Delta G_1}{RT}\right) \quad \textbf{(D.30)}$$

$$\Delta G_1 = -nF(U^{\circ} - U^{\circ}_{E,2}) \quad \textbf{(D.31)}$$

Using **Eq. D.29–D.31**, the concentration of $[\mathrm{Ce^{IV}(H_2O)_9}]^{4+}$ is defined as shown in **Eq. D.32**. Plugging in **Eq. D.32** as well as **Eq. D.24–D.25** into **Eq. D.23**, the kinetic current rate law for the *CE* mechanisms with the *E* step as RDS in **Eq. D.33** is determined. In **Eq. D.33**, $Z_2 = \kappa_{el}K_{p,Ce^{3+}}\upsilon_n = \kappa_{el}K_{p,Ce^{4+}}\upsilon_n$ and $[\mathrm{Ce^{4+}}]$ and $[\mathrm{Ce^{3+}}]$ are the concentrations of the bulk Ce^{4+} and Ce^{3+} species.

$$\left[[\mathrm{Ce^{IV}(H_2O)_9}]^{4+}_{aq}\right] = \frac{\left[[\mathrm{Ce^{IV}(H_2O)_6(HSO_4)_3}]^{+}_{aq}\right][\mathrm{H_2O}]^3}{[\mathrm{HSO_4^-}]^3}K_1 = \frac{[\mathrm{Ce^{4+}}][\mathrm{H_2O}]^3}{[\mathrm{HSO_4^-}]^3}K_1 \quad \textbf{(D.32)}$$

$$-i_{K,CE,E} = nFZ_2\left(\frac{[\mathrm{Ce^{4+}}][\mathrm{H_2O}]^3}{[\mathrm{HSO_4^-}]^3}K_1\exp\left(\frac{-\lambda_2}{4RT}\left(1+\frac{nF(U-U^{\circ}_{E,2})}{\lambda_2}\right)^2\right) - [\mathrm{Ce^{3+}}]\exp\left(\frac{-\lambda_2}{4RT}\left(1-\frac{nF(U-U^{\circ}_{E,2})}{\lambda_2}\right)^2\right)\right) \quad \textbf{(D.33)}$$

Eq. D.33 can be further simplified by defining $U^{\circ}_{E,2}$ using **Eq. D.34** and recognizing that $\eta = U - U_{eq}$, to obtain the final rate law in **Eq. D.35** (**Eq. 5.6** in **Chapter 5**). From this kinetic current expression, exchange current densities and cathodic Tafel slopes as a function of $[\mathrm{Ce^{4+}}]$ and temperature can be modeled and compared to experimental values.

$$U^{\circ}_{E,2} = U^{\circ} - \frac{RT}{nF}\ln K_1 \quad \textbf{(D.34)}$$

$$i_{K,CE,E} = -nFZ_2\left(\frac{[\mathrm{Ce^{4+}}][\mathrm{H_2O}]^3}{[\mathrm{HSO_4^-}]^3}K_1\exp\left(\frac{-\lambda_2}{4RT}\left(1+\frac{nF\eta}{\lambda_2}-\frac{RT}{\lambda_2}\ln\frac{[\mathrm{Ce^{3+}}]}{K_1[\mathrm{Ce^{4+}}]}\right)^2\right)\right.$$
$$\left.-[\mathrm{Ce^{3+}}]\exp\left(\frac{-\lambda_2}{4RT}\left(1-\frac{nF\eta}{\lambda_2}+\frac{RT}{\lambda_2}\ln\frac{[\mathrm{Ce^{3+}}]}{K_1[\mathrm{Ce^{4+}}]}\right)^2\right)\right) \quad \textbf{(D.35)}$$

D.2.4 CE mechanism, C RDS rate law derivation

The rate law for the case when the *C* step of the *CE* mechanism is rate-determining is defined below in **Eq. D.36**, where again, the ligand exchange is assumed to occur in one *C* step instead of a series of *C* steps for simplicity.

$$-i_{K,CE,C} = nF\left(k_1\left[[\mathrm{Ce^{IV}(H_2O)_6(HSO_4)_3}]^+_{\mathrm{aq}}\right][\mathrm{H_2O}]^3 - k_{-1}\left[[\mathrm{Ce^{IV}(H_2O)_9}]^{4+}_{\mathrm{aq}}\right][\mathrm{HSO_4^-}]^3\right) \quad \textbf{(D.36)}$$

The concentration of the intermediate species $[\mathrm{Ce^{IV}(H_2O)_9}]^{4+}$ is determined based on the assumption that the *E* step is quasi-equilibrated, and so r_2, the reaction rate of the *E* step, is equal to zero (**Eq. D.37**). The reduction and oxidation rate constants are defined as earlier using MT in **Eq. D.24–D.25**.

$$r_2 = 0 = k_2\left[[\mathrm{Ce^{IV}(H_2O)_9}]^{4+}_{\mathrm{aq}}\right] - k_{-2}\left[[\mathrm{Ce^{III}(H_2O)_9}]^{3+}_{\mathrm{aq}}\right] \quad \textbf{(D.37)}$$

Substituting **Eq. D.24** and **D.25** into **Eq. D.37**, the concentration of the intermediate species $[\mathrm{Ce^{IV}(H_2O)_9}]^{4+}$ is determined (**Eq. D.38**).

$$\left[[\mathrm{Ce^{IV}(H_2O)_9}]^{4+}_{\mathrm{aq}}\right] = \left[[\mathrm{Ce^{III}(H_2O)_9}]^{3+}_{\mathrm{aq}}\right]\exp\left(\frac{nF}{RT}\left(U - U^{\circ}_{E,2}\right)\right) \quad \textbf{(D.38)}$$

Plugging **Eq. D.38** into **Eq. D.36** and using the definition for $U^{\circ}_{E,2}$ from **Eq. D.34**, the definition for K_1 from **Eq. D.30**, and $\eta = U - U_{eq}$, the final rate law for the *CE* mechanism with

the *C* step RDS is found in **Eq. D.39**. Exchange current densities and Tafel slopes can be derived from this rate law to compare to experimental values.

$$i_{K,CE,C} = -nFk_1\left([\mathrm{Ce^{4+}}][\mathrm{H_2O}]^3 - [\mathrm{Ce^{4+}}][\mathrm{HSO_4^-}]^3\exp\left(\frac{nF\eta}{RT}\right)\right) \quad \textbf{(D.39)}$$

Briefly, **Eq. D.39** cannot capture the maximum in exchange current density with [Ce^{4+}] or the cathodic Tafel slopes observed experimentally, and so is not a correct rate law.

D.2.5 EC mechanism, E RDS rate law derivation

For the *EC* mechanism, the Ce^{4+}-anion complex ($[Ce^{IV}(H_2O)_6(HSO_4)_3]^+$) undergoes an endothermic *E* to form the higher energy Ce^{3+} species ($[Ce^{III}(H_2O)_6(HSO_4)_3]^0$) (**Eq. D.40a**), which then undergoes a favorable ligand exchange *C* step with water to form the $[Ce^{III}(H_2O)_9]^{3+}$ species (**Eq. D.40b**). Like the *CE* mechanism, the ligand exchange in the *EC* mechanism is assumed to occur in one *C* step instead of a series of *C* steps.

$$[\mathrm{Ce^{IV}(H_2O)_6(HSO_4)}]^+_{\mathrm{aq}} + \mathrm{e^-} \rightleftarrows [\mathrm{Ce^{III}(H_2O)_6(HSO_4)_3}]^0_{\mathrm{aq}} \quad \textbf{(D.40a)}$$

$$[\mathrm{Ce^{III}(H_2O)_6(HSO_4)_3}]^0_{\mathrm{aq}} + 3\mathrm{H_2O_{aq}} \rightleftarrows [\mathrm{Ce^{III}(H_2O)_9}]^{3+}_{\mathrm{aq}} + 3\mathrm{HSO_4^-}_{\mathrm{aq}} \quad \textbf{(D.40b)}$$

Assuming a rate-determining step exists, the proposed mechanism in **Eq. D.40** has two possible rate laws. Considering the case when the *E* step is the RDS, the kinetic current would be described as in **Eq. D.41** using MT. The reduction and oxidation rate constants of the *E* step are defined in **Eq. D.42–D.43**, where κ_{el}, $K_{p,Ce^{3+}}$, $K_{p,Ce^{4+}}$, and υ_n are all the same as described previously. $\Delta G_3^{\ddagger}$ and $\Delta G_{-3}^{\ddagger}$ are the free energies of the reduction and oxidation transition states of the *E* step, respectively, and are also defined in terms of MT in **Eq. D.44–D.45**, where λ_3 is the reorganization energy of the *E* step and ΔG_3 is the reaction energy of the *E* step, which is related

to electrode potential through **Eq. D.46**. In **Eq. D.46**, $U^{\circ}_{E,3}$ is the standard equilibrium potential of the species involved in the *E* step, i.e., $[Ce^{IV}(H_2O)_6(HSO_4)_3]^+$ and $[Ce^{III}(H_2O)_6(HSO_4)_3]^0$.

$$-i_{K,EC,E} = nF\left(k_3\left[[Ce^{IV}(H_2O)_6(HSO_4)_3]^+_{aq}\right] - k_{-3}\left[[Ce^{III}(H_2O)_6(HSO_4)_3]^0_{aq}\right]\right) \quad \textbf{(D.41)}$$

$$k_3 = \kappa_{el} K_{p,Ce^{4+}} \upsilon_n \exp\left(\frac{-\Delta G^{\ddagger}_3}{RT}\right) \quad \textbf{(D.42)}$$

$$k_{-3} = \kappa_{el} K_{p,Ce^{3+}} \upsilon_n \exp\left(\frac{-\Delta G^{\ddagger}_{-3}}{RT}\right) \quad \textbf{(D.43)}$$

$$\Delta G^{\ddagger}_{f,3} = \frac{\lambda_3}{4}\left(1 + \frac{\Delta G_3}{\lambda_3}\right)^2 \quad \textbf{(D.44)}$$

$$\Delta G^{\ddagger}_{b,3} = \frac{\lambda_3}{4}\left(1 - \frac{\Delta G_3}{\lambda_3}\right)^2 \quad \textbf{(D.45)}$$

$$\Delta G_3 = nF(U - U^{\circ}_{E,3}) \quad \textbf{(D.46)}$$

The unknown concentration of the intermediate $[Ce^{III}(H_2O)_6(HSO_4)_3]^0$ in **Eq. D.41** can be defined in terms of the known concentration of the bulk Ce^{3+} species, $[Ce^{III}(H_2O)_9]^{3+}$, and the equilibrium constant of the *C* step. Assuming the *C* step is quasi-equilibrated, then the reaction rate of the *C* step, r_4, is equal to zero (**Eq. D.47**). In **Eq. D.47**, the forward and backward rates of the *C* step, k_4 and k_{-4}, are related to the equilibrium constant K_4, as shown in **Eq. D.48**. K_4 can also be related to the free energy of the *C* step, ΔG_4, as shown in **Eq. D.48**. ΔG_4 is related to the electrode potential through **Eq. D.49**, where, as defined earlier, U° is the standard equilibrium potential. When $U = U^{\circ}$, $\Delta G_3 = \Delta G_4$.

$$r_4 = 0 = k_4\left[[Ce^{III}(H_2O)_6(HSO_4)_3]^0_{aq}\right][H_2O]^3 - k_{-4}\left[[Ce^{III}(H_2O)_9]^{3+}_{aq}\right][HSO_4^-]^3 \quad \textbf{(D.47)}$$

$$K_4 = \frac{k_4}{k_{-4}} = \exp\left(-\frac{\Delta G_4}{RT}\right) \quad \textbf{(D.48)}$$

$$\Delta G_4 = -nF(U^{\circ} - U^{\circ}_{E,3}) \quad \textbf{(D.49)}$$

Solving **Eq. D.47–D.49** for the concentration of $[Ce^{III}(H_2O)_6(HSO_4)_3]^0$ results in **Eq. D.50**, where $[Ce^{3+}]$ is the concentration of the bulk Ce^{3+} species. Plugging **Eq. D.50** into the kinetic current rate law (**Eq. D.41**), **Eq. D.51** is obtained. In **Eq. D.51**, $Z_3 = \kappa_{el} K_{p,Ce^{3+}} \upsilon_n = \kappa_{el} K_{p,Ce^{4+}} \upsilon_n$ and $[Ce^{4+}]$ is the concentration of the bulk Ce^{4+} species.

$$\left[[Ce^{III}(H_2O)_6(HSO_4)_3]^0_{aq}\right] = \frac{\left[[Ce^{III}(H_2O)_9]^{3+}_{aq}\right][HSO_4^-]^3}{K_4[H_2O]^3} = \frac{[Ce^{3+}][HSO_4^-]^3}{K_4[H_2O]^3} \quad \textbf{(D.50)}$$

$$-i_{K,EC,E} = nFZ_3\left([Ce^{4+}]\exp\left(\frac{-\lambda_3}{4RT}\left(1+\frac{nF\left(U-U^{\circ}_{E,3}\right)}{\lambda_3}\right)^2\right) - \frac{[Ce^{3+}][HSO_4^-]^3}{K_4[H_2O]^3}\exp\left(\frac{-\lambda_3}{4RT}\left(1-\frac{nF(U-U^{\circ}_{E,3})}{\lambda_3}\right)^2\right)\right) \quad \textbf{(D.51)}$$

$E^{\circ}_{E,3}$ is defined in **Eq. D.52**, which, along with $\eta = U - U_{eq}$, can be used to simplify the kinetic current rate law for the *EC* mechanism with the *E* step as the RDS further into **Eq. D.53**. This kinetic current can then be used to derive expressions for exchange current density and cathodic Tafel slopes as a function of $[Ce^{4+}]$ and temperature.

$$U^{\circ}_{E,3} = U^{\circ} - \frac{RT}{nF}\ln K_4 \quad \textbf{(D.52)}$$

$$i_{K,EC,E} = -nFZ_3\left([Ce^{4+}]\exp\left(\frac{-\lambda_3}{4RT}\left(1+\frac{nF\eta}{\lambda_3}-\frac{RT}{\lambda_3}\ln\frac{[Ce^{3+}]}{K_4[Ce^{4+}]}\right)^2\right) - \frac{[Ce^{3+}][HSO_4^-]^3}{K_4[H_2O]^3}\exp\left(\frac{-\lambda_3}{4RT}\left(1-\frac{nF\eta}{\lambda_3}+\frac{RT}{\lambda_3}\ln\frac{[Ce^{3+}]}{K_4[Ce^{4+}]}\right)^2\right)\right) \quad \textbf{(D.53)}$$

Briefly, although **Eq. D.53** does capture the experimentally observed behavior, the parameters from fitting are physically unrealistic as discussed below.

D.2.6 EC mechanism, C RDS rate law derivation

The rate law for the *EC* mechanism when the *C* step is the RDS is shown in **Eq. D.54**. The ligand exchange is assumed to occur as one *C* step.

$$-i_{K,EC,C} = nF\left(k_4\left[\left[\mathrm{Ce^{III}(H_2O)_6(HSO_4)_3}\right]^0_{\mathrm{aq}}\right][\mathrm{H_2O}]^3 - k_{-4}\left[\left[\mathrm{Ce^{III}(H_2O)_9}\right]^{3+}_{\mathrm{aq}}\right][\mathrm{SO_4^{2-}}]^3\right) \quad \textbf{(D.54)}$$

The concentration of the unknown intermediate species, $[\mathrm{Ce^{III}(H_2O)_6(HSO_4)_3}]^0$, can be calculated assuming the *E* step is quasi-equilibrated, meaning the *E* step reaction rate, r_3, is equal to zero, as shown in **Eq. D.55**. In **Eq. D.55**, the reduction and oxidation rate constants of the *E* step are defined using MT, as shown previously in **Eq. D.42–D.43**.

$$r_3 = 0 = k_3\left[\left[\mathrm{Ce^{IV}(H_2O)_6(HSO_4)_3}\right]^+_{\mathrm{aq}}\right] - k_{-3}\left[\left[\mathrm{Ce^{III}(H_2O)_6(HSO_4)_3}\right]^0_{\mathrm{aq}}\right] \quad \textbf{(D.55)}$$

Plugging these expressions for k_3 and k_{-3} into **Eq. D.55**, the concentration of $[\mathrm{Ce^{III}(H_2O)_6(HSO_4)_3}]^0$ is calculated, as shown in **Eq. D.56**.

$$\left[\left[\mathrm{Ce^{III}(H_2O)_6(HSO_4)_3}\right]^0_{\mathrm{aq}}\right] = \left[\left[\mathrm{Ce^{IV}(H_2O)_6(HSO_4)_3}\right]^+_{\mathrm{aq}}\right]\exp\left(\frac{-nF}{RT}\left(U - U^{\circ}_{E,3}\right)\right) \quad \textbf{(D.56)}$$

Substituting **Eq. D.56** in **Eq. D.54** and using the definition for $E^{\circ}_{E,3}$ from **Eq. D.52**, the definition for $K_4 = {k_4}/{k_{-4}}$, and $\eta = U - U_{eq}$, the kinetic current can be simplified further into **Eq. D.57**. This rate law can be used to model exchange current densities and cathodic Tafel slopes as a function of $[\mathrm{Ce^{4+}}]$ and temperature.

$$-i_{K,EC,C} = nFk_{-4}\left(\left[\mathrm{Ce^{3+}}\right][\mathrm{H_2O}]^3\exp\left(\frac{-nF\eta}{RT}\right) - \left[\mathrm{Ce^{3+}}\right][\mathrm{HSO_4^-}]^3\right) \quad \textbf{(D.57)}$$

Briefly, **Eq. D.57** cannot capture the maximum in exchange current density with [Ce^{4+}] observed experimentally, and so it is not a correct rate law.

D.2.7 Kinetic fitting results

Table D.2 includes the optimal fitting parameters used in the fit of each rate law to the Pt and GC data. Fitting parameters were obtained by minimizing the normalized mean square error between the observed and modeled exchange current density and cathodic Tafel slope values. As discussed in **Chapter 5**, the *CE*, *E* RDS rate law was the only rate law that satisfactorily met all nine criteria (**Table 5.3**) and had reasonable results.

Table D.2. Fitted parameters for all considered rate laws. The values of the parameters used in each of the rate law fits to the Pt and GC data are included. The rate laws considered are the BV and MT rate laws, as well as the *CE*, *E* RDS, *CE*, *C* RDS, *EC*, *E* RDS, and the *EC*, *E* RDS rate laws. The corresponding rate law equations are included for reference. For comparison, the DFT-predicted equilibrium constant K_1 and reorganization energy are included. The rate law most consistent with the experimental data is the *CE* mechanism with an *E* RDS.

Rate Law Fitting Results				
BV (Eq. 5.3)				
	$\boldsymbol{E_a}$ (kJ mol^{-1})	$\boldsymbol{\alpha}$	$\boldsymbol{k_0}$ (cm s^{-1})	NMSE
Pt RDE	48.3	0.23	1.43×10^{-4}	0.050
GC RDE	41.2	0.23	2.99×10^{-5}	0.079
MT (Eq. D.22)				
	$\boldsymbol{\lambda_{MT}}$ (kJ mol^{-1})		$\boldsymbol{Z_{MT}}$ (cm s^{-1})	NMSE
Pt RDE	29.7		1.43×10^{-3}	0.097
GC RDE	29.8		2.89×10^{-4}	0.084
***CE* mechanism, *E* RDS (Eq. 5.6)**				
	$\boldsymbol{\lambda_2}$ (kJ mol^{-1})	$\boldsymbol{K_1}$	$\boldsymbol{Z_2}$ (cm s^{-1})	NMSE
Pt RDE	100.2	1.1×10^{-7}	4.22×10^{4}	0.049
GC RDE	71.8	6.5×10^{-5}	8.64	0.065
***CE* mechanism, *C* RDS (Eq. D.39)**				
	$\boldsymbol{k_1}$ (cm s^{-1})			NMSE
Pt RDE	1.29×10^{-4}			46.568
GC RDE	2.61×10^{-5}			49.420
***EC* mechanism, *E* RDS (Eq. D.53)**				
	$\boldsymbol{\lambda_3}$ (kJ mol^{-1})	$\boldsymbol{K_4}$	$\boldsymbol{Z_3}$ (cm s^{-1})	NMSE
Pt RDE	663.4	6.6×10^{-61}	8.22×10^{2}	0.051
GC RDE	56.0	2.4×10^{-3}	4.19×10^{-4}	0.074
***EC* mechanism, *C* RDS (Eq. D.57)**				
	$\boldsymbol{k_{-4}}$ (cm s^{-1})			NMSE
Pt RDE	1.37×10^{-4}			1.514
GC RDE	2.80×10^{-5}			1.562
From density functional theory modeling				
	λ (kJ mol^{-1})		$\boldsymbol{K_1}$	
Ce^{3+}/Ce^{4+} in H_2SO_4*	87.1		9.8×10^{-9}	
*Note, the DFT-predicted λ value is for the $[Ce^{III}(H_2O)_9]^{3+}/[Ce^{IV}(H_2O)_9]^{4+}$ CT, and the DFT-predicted $\boldsymbol{K_1}$ value is for the ligand exchange energy from $[Ce^{IV}(H_2O)_6(HSO_4)_3]^{+}$ to $[Ce^{IV}(H_2O)_9]^{4+}$.				

Fig. D.3 shows the fit of the Pt and GC kinetic data to the MT rate law, with fitting parameters λ_{MT} and Z_{MT} optimized to minimize the mean squared error between the experimental and modeled values. As discussed in the main text, the MT rate law is unable to capture the asymmetry of the observed data points, with the maximum in exchange current density predicted to occur at 50% [Ce^{4+}] instead of the observed ~70% [Ce^{4+}], as shown in **Fig. D.3a** for Pt and **Fig. D.3e** for GC. The modeled cathodic Tafel slope behavior as a function of [Ce^{4+}] for both Pt and GC (**Fig. D.3c**, **Fig. D.3g**) also does not agree with the observed behavior due to the forced symmetry of the MT rate law. The increase in exchange current density and cathodic Tafel slope as a function of temperature is only partially captured for both Pt and GC, most likely due to the low fitted reorganization energy values for both Pt and GC that are approximately equal at 30 kJ/mol (**Fig. D.3b,d** for Pt and **Fig. D.3f,h** for GC).

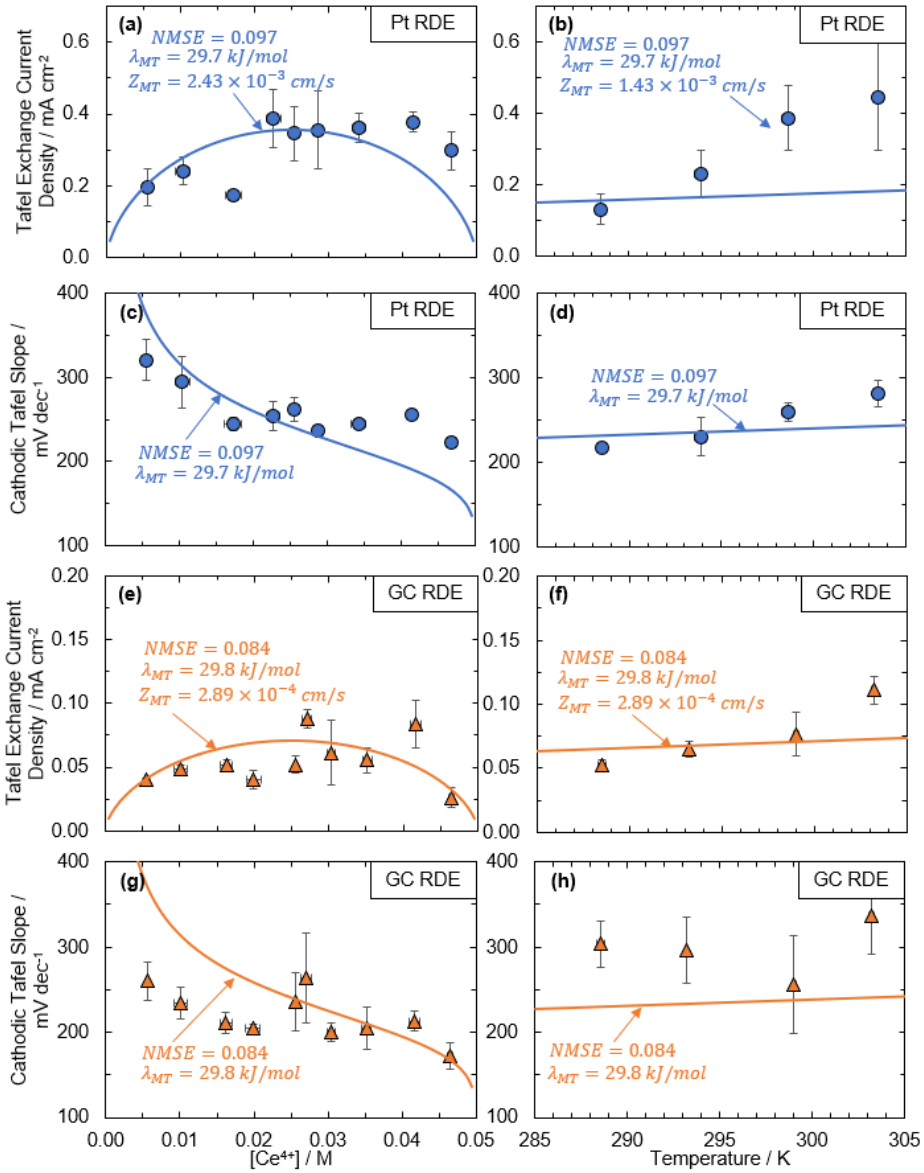

Figure D.3. Fit of Pt and GC data to MT rate law. Fit of the MT rate law to the experimental data for Pt **(a)** exchange current densities as a function of [Ce^{4+}], **(b)** exchange current densities as a function of temperature, **(c)** cathodic Tafel slopes as a function of [Ce^{4+}], and **(d)** cathodic Tafel slopes as a function of temperature. Data in **(a)** and **(c)** collected at room temperature in 2 M H_2SO_4 at total cerium concentration of 0.05 M. Data in **(b)** and **(d)** collected at a total cerium concentration of 0.05 M with a Ce^{4+} concentration of 0.026 M. Solid blue lines are the fit to the data from the MT rate law. The reorganization energy λ_{MT} and preexponential factor Z_{MT} in **(a)-(d)** were obtained through minimizing the NMSE of the Pt data (NMSE = 0.097). Fit of the MT rate law to the experimental data for GC **(e)** exchange current densities as a function of [Ce^{4+}], **(f)** exchange current densities as a function of temperature, **(g)** cathodic Tafel slopes as a function of [Ce^{4+}], and **(h)** cathodic Tafel slopes as a function of temperature. Data in **(e)** and **(g)** collected at room temperature in 2 M H_2SO_4 at total cerium concentration of 0.05 M. Data in **(f)** and **(h)** collected at a total cerium concentration of 0.05 M with a Ce^{4+} concentration of 0.025 M. Solid orange lines are the fit to the data from the MT rate law. The reorganization energy λ_{MT} and preexponential factor Z_{MT} in **(e)-(h)** were obtained through minimizing the NMSE of the GC data (NMSE = 0.084). Reported values are averaged from three runs, with error bars representing one standard deviation from the average value in both horizontal and vertical directions. An Ag/AgCl reference electrode and graphite rod counter electrode were used for all measurements. All measurements were collected at 2000 rpm of the RDE where mass transport is not limiting.

The fit of the *CE*, *E* RDS derived rate law to the cathodic Tafel slope as a function of temperature is shown in **Fig. D.4**. The model successfully predicts an increase in cathodic Tafel slope with increasing temperature, although the slope is not completely captured. This is most likely due to the value of the reorganization energy of the *E* step, λ_2, being lower than what would be required to achieve a faster increase in cathodic Tafel slope with temperature. The fitted value of λ_2 is obtained through the fit of not only the data shown in **Figure D.4**, but also the data in **Figure 5.8b–d** shown in **Chapter 5**. The best fit was found for a value of λ_2 of 100.2 kJ/mol to satisfactorily fit the rest of the data in addition to the Tafel slope data.

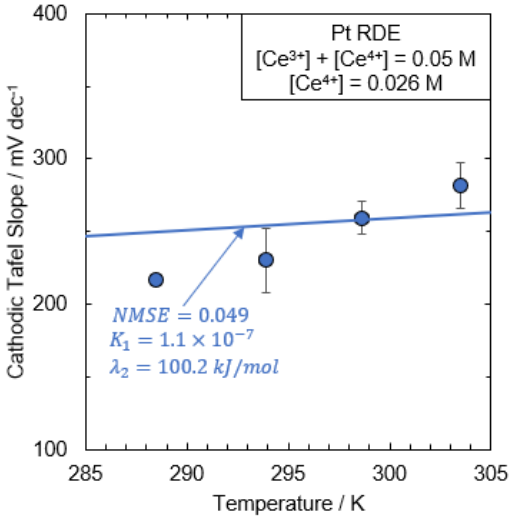

Figure D.4. Fit of Pt cathodic Tafel slope as a function of temperature with *CE*, *E* RDS rate law. Tafel slopes for the Pt RDE (blue circles) extracted from Tafel plots as a function temperature at Ce^{4+} concentration of 0.026 M and total Ce concentration of 0.05 M and fit using the *CE*, *E* RDS rate law (blue line). Reported values are averaged from three runs, with error bars representing one standard deviation from the average value in both horizontal and vertical directions. An Ag/AgCl reference electrode and graphite rod counter electrode were used. The solutions were sparged with nitrogen gas for at least 15 minutes before measurements were collected and blanketing with nitrogen was continued throughout the measurement collection. All data were collected at 2000 rpm of the RDE. The reorganization energy λ_2 and equilibrium constant K_1 were obtained through minimizing the NMSE of the Pt data (NMSE = 0.049).

The fit of the GC data to the *CE*, *E* RDS rate law is shown in **Fig. D.5**. Similar to the fit of the Pt data (**Fig. 5.8b–d**), the *CE*, *E* RDS rate law successfully predicts a maximum in exchange current density as a function of $[Ce^{4+}]$ at ~70% $[Ce^{4+}]$ (**Fig. D.5a**), an increase in exchange current density with temperature (**Fig. D.5b**), a decrease in cathodic Tafel slope with increasing $[Ce^{4+}]$,

(**Fig. D.5c**) and an increase in Tafel slope with temperature (**Fig. D.5d**). The optimal fitting parameters for the fit of the GC data to the *CE*, *E* RDS rate law are $K_1 = 6.5 \times 10^{-5}$, $\lambda_2 = 71.8$ kJ/mol, and $Z_2 = 8.64$. The differences between the fitted values for GC and Pt are discussed in the main text.

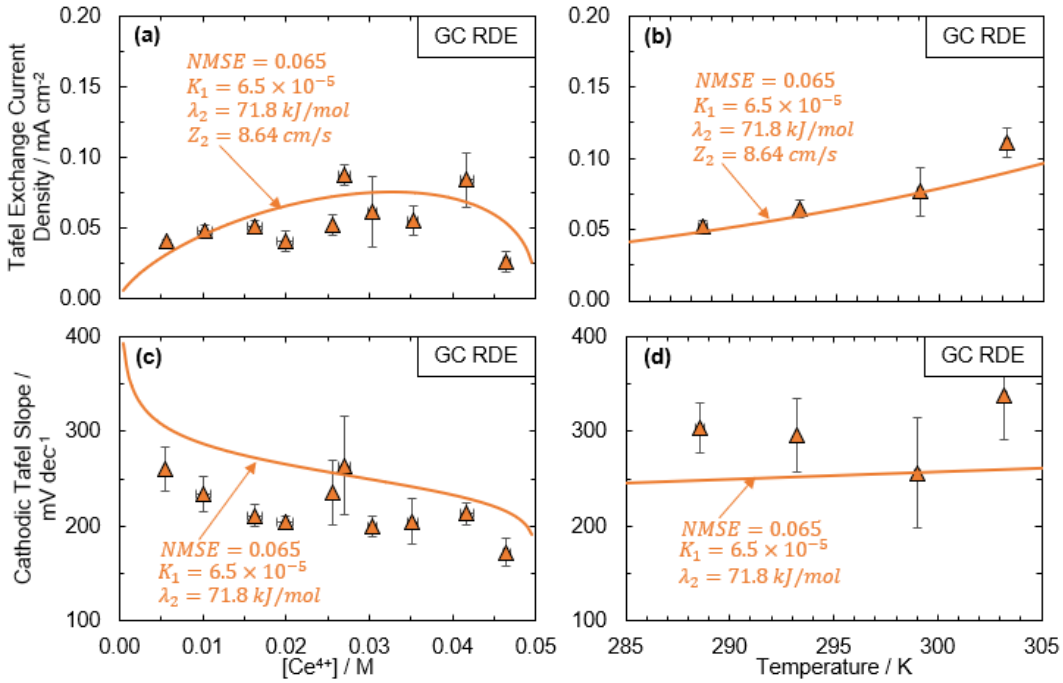

Figure D.5. Fit of GC data to *CE*, *E* RDS rate law. Fit of the *CE*, *E* RDS rate law to the experimental data for GC **(a)** exchange current densities as a function of [Ce^{4+}], **(b)** exchange current densities as a function of temperature, **(c)** cathodic Tafel slopes as a function of [Ce^{4+}], and **(d)** cathodic Tafel slopes as a function of temperature. Data in **(a)** and **(c)** collected at room temperature in 2 M H_2SO_4 at total cerium concentration of 0.05 M. Data in **(b)** and **(d)** collected at a total cerium concentration of 0.05 M with a Ce^{4+} concentration of 0.025 M. Solid orange lines are the fit to the data from the *CE*, *E* RDS rate law. The reorganization energy λ_2 and equilibrium constant K_1 were obtained through minimizing the NMSE of the GC data (NMSE = 0.065). Reported values are averaged from three runs, with error bars representing one standard deviation from the average value in both horizontal and vertical directions. An Ag/AgCl reference electrode and graphite rod counter electrode were used for all measurements. All measurements were collected at 2000 rpm of the RDE where mass transport is not limiting.

The fits of the *CE*, *C* RDS rate law to the Pt and GC data are shown in **Fig. D.6**. Although the rate law satisfies *Criterion 6*, which asserts that the exchange current density will increase with temperature, as shown in **Fig. D.6b** for Pt and **Fig. D.6f** for GC, it fails to capture the maximum in exchange current density at ~70% Ce^{4+} concentration (*Criterion 5*, **Fig. D.6a** for Pt and **Fig. D.6e** for GC). This is because the anodic and cathodic branches of the current expression (**Eq.**

D.36) are only dependent on either [Ce^{3+}] or [Ce^{4+}], and never are a factor of both. From **Eq. D.39**, the anodic current increases exponentially with positive overpotential, and the cathodic branch current is essentially constant with overpotential. As a result, Tafel slopes are unrealistically large at magnitudes of greater than 18,000 mV/decade, which is why they do not appear in **Fig. D.6c–d** for Pt or **Fig. D.6g–h** for GC (*Criteria 7–9*).

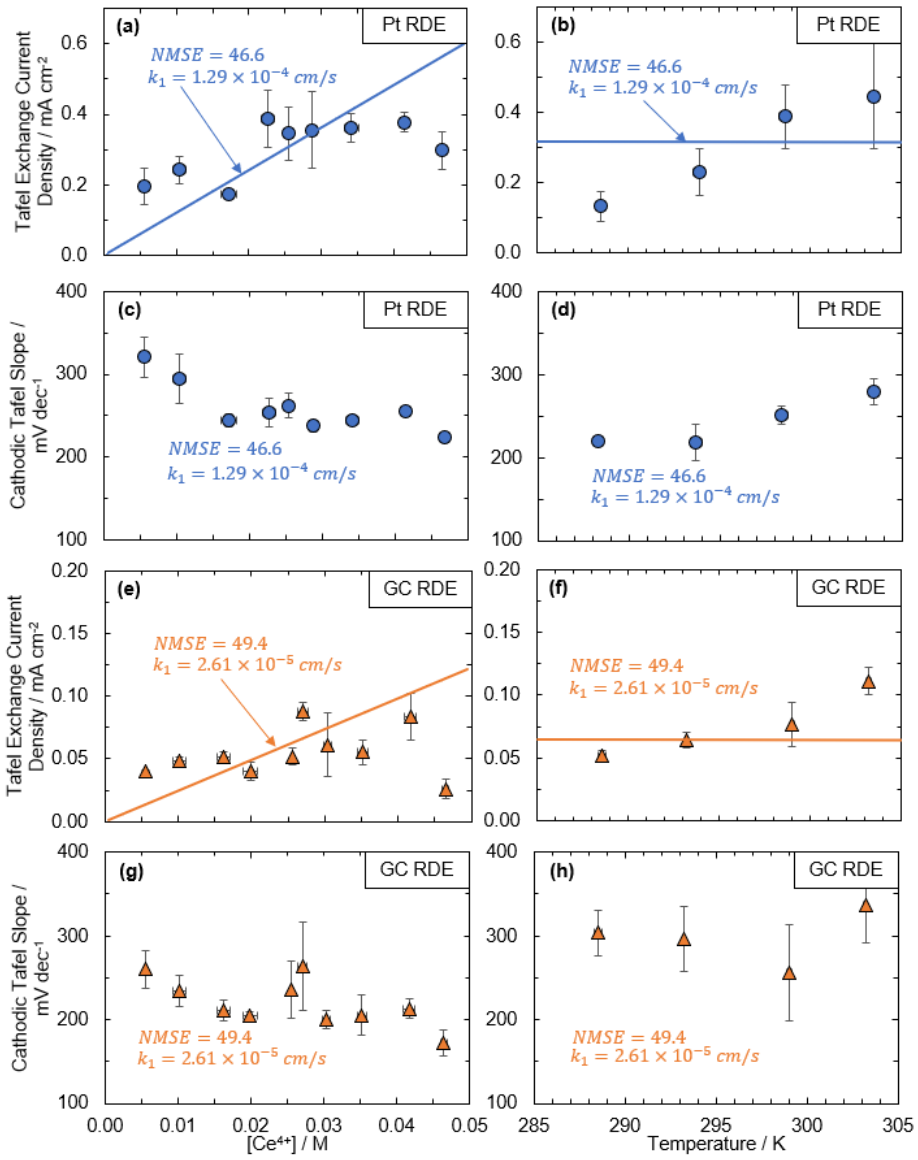

Figure D.6. Fit of Pt and GC data to *CE*, *C* RDS rate law. Fit of the *CE*, *C* RDS rate law to the experimental data for Pt **(a)** exchange current densities as a function of [Ce^{4+}], **(b)** exchange current densities as a function of temperature, **(c)** cathodic Tafel slopes as a function of [Ce^{4+}], and **(d)** cathodic Tafel slopes as a function of temperature. Data in **(a)** and **(c)** collected at room temperature in 2 M H_2SO_4 at total cerium concentration of 0.05 M. Data in **(b)** and **(d)** collected at a total cerium concentration of 0.05 M with a Ce^{4+} concentration of 0.026 M. Solid blue lines are the fit to the data from the *CE*, *C* RDS rate law. The *C* step forward rate constant k_1 in **(a)-(d)** was obtained through minimizing the NMSE of the Pt data (NMSE = 46.6). Fit of the *CE*, *C* RDS rate law to the experimental data for GC **(e)** exchange current densities as a function of [Ce^{4+}], **(f)** exchange current densities as a function of temperature, **(g)** cathodic Tafel slopes as a function of [Ce^{4+}], and **(h)** cathodic Tafel slopes as a function of temperature. Data in **(e)** and **(g)** collected at room temperature in 2 M H_2SO_4 at total cerium concentration of 0.05 M. Data in **(f)** and **(h)** collected at a total cerium concentration of 0.05 M with a Ce^{4+} concentration of 0.025 M. Solid orange lines are the fit to the data from the *CE*, *C* RDS rate law. The *C* step forward rate constant k_1 in **(e)-(h)** was obtained through minimizing the NMSE of the GC data (NMSE = 49.4). Reported values are averaged from three runs, with error bars representing one standard deviation from the average value in both horizontal and vertical directions. An Ag/AgCl reference electrode and graphite rod counter electrode were used for all measurements. All measurements were collected at 2000 rpm of the RDE where mass transport is not limiting.

Fig. D.7 shows the fits of the *EC*, *C* RDS rate law to the Pt and GC data. Similar to the *CE*, *C* RDS rate law discussed above, the kinetic current rate law (**Eq. D.57**) predicts a linear dependence of exchange current density with [Ce^{4+}], as shown in **Fig. D.7a** for Pt and **Fig. D.7e** for GC. The behavior of the Tafel slopes is not appropriately captured in the case of the *EC*, *C* RDS rate law (**Fig. D.7c–d** for Pt, and **Fig. D.7g–h** for GC) because the cathodic current is predicted to increase exponentially with negative overpotential, making Tafel slopes too small compared to experimentally reported Tafel slopes (failing *Criterion 7*) and essentially constant with changes in [Ce^{4+}] or temperature (failing *Criteria 8-9*).

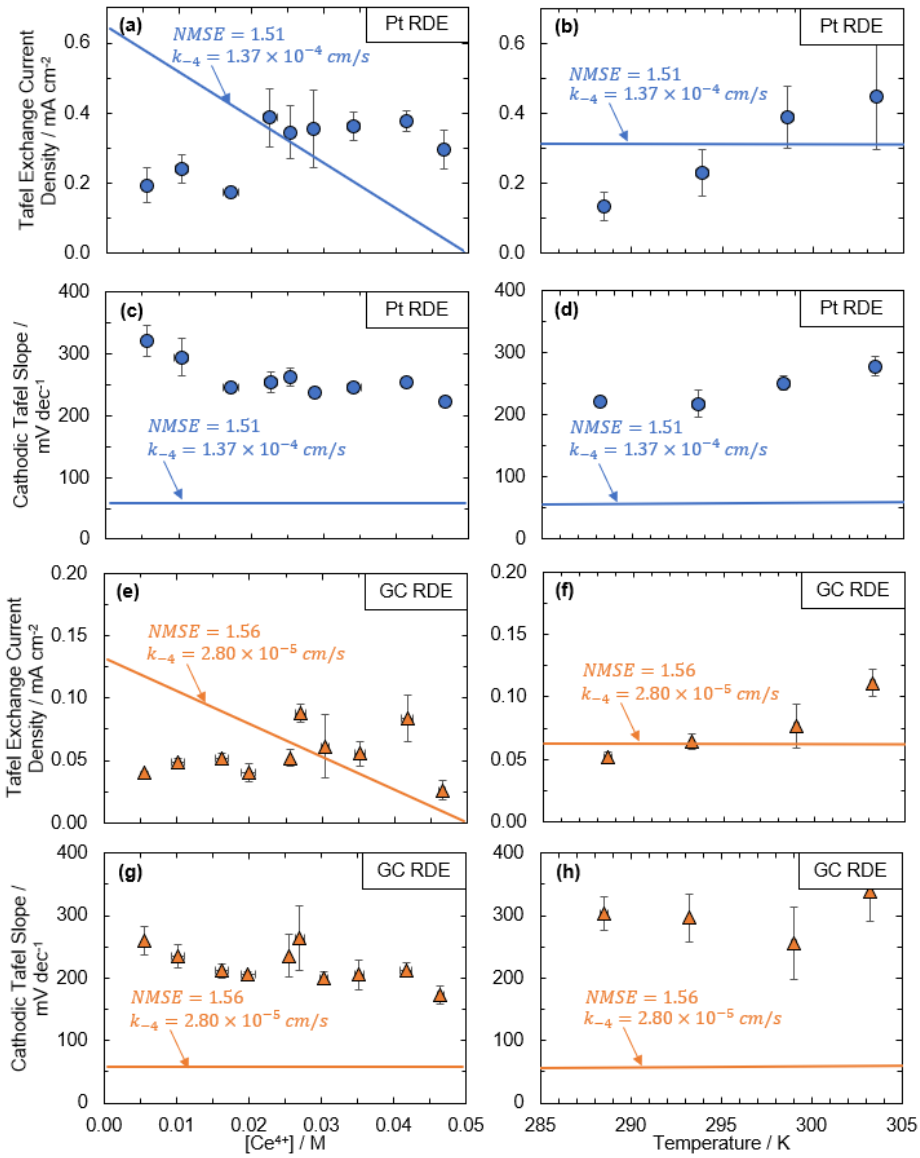

Figure D.7. Fit of Pt and GC data to *EC, C* RDS rate law. Fit of the *EC, C* RDS rate law to the experimental data for Pt **(a)** exchange current densities as a function of [Ce^{4+}], **(b)** exchange current densities as a function of temperature, **(c)** cathodic Tafel slopes as a function of [Ce^{4+}], and **(d)** cathodic Tafel slopes as a function of temperature. Data in **(a)** and **(c)** collected at room temperature in 2 M H_2SO_4 at total cerium concentration of 0.05 M. Data in **(b)** and **(d)** collected at a total cerium concentration of 0.05 M with a Ce^{4+} concentration of 0.026 M. Solid blue lines are the fit to the data from the *EC, C* RDS rate law. The *C* step backward rate constant k_{-4} in **(a)-(d)** was obtained through minimizing the NMSE of the Pt data (NSME = 1.51). Fit of the *EC, C* RDS rate law to the experimental data for GC **(e)** exchange current densities as a function of [Ce^{4+}], **(f)** exchange current densities as a function of temperature, **(g)** cathodic Tafel slopes as a function of [Ce^{4+}], and **(h)** cathodic Tafel slopes as a function of temperature. Data in **(e)** and **(g)** collected at room temperature in 2 M H_2SO_4 at total cerium concentration of 0.05 M. Data in **(f)** and **(h)** collected at a total cerium concentration of 0.05 M with a Ce^{4+} concentration of 0.025 M. Solid orange lines are the fit to the data from the *EC, C* RDS rate law. The *C* step backward rate constant k_{-4} in **(e)-(h)** was obtained through minimizing the NMSE of the GC data (NMSE = 1.56). Reported values are averaged from three runs, with error bars representing one standard deviation from the average value in both horizontal and vertical directions. An Ag/AgCl reference electrode and graphite rod counter electrode were used for all measurements. All measurements were collected at 2000 rpm of the RDE where mass transport is not limiting.

The fit of the *EC*, *E* RDS rate law to the Pt and GC data is included in **Fig. D.8**. While all kinetic behavior (*Criteria 5*–*9*) is technically met through the fit, some of the optimized fitting parameters for Pt were unreasonable, i.e., the reorganization energy was unreasonably large at 663 kJ/mol, and for both Pt and GC, the predicted equilibrium constant of the *C* step suggested that Ce^{3+} was preferentially complexed by sulfate, not coordinated by water. As discussed in the main text, our EXAFS results and DFT-predicted free energy of Ce^{3+} water coordination contradict this finding, and thus we can reject the *EC*, *E* RDS rate law. It can also be argued that while the cathodic Tafel slopes do decrease slightly with the increase in $[Ce^{4+}]$ for Pt (**Fig. D.8c**), the slope of the predicted behavior is not steep enough, possibly due to the unreasonably large, predicted, reorganization energy value.

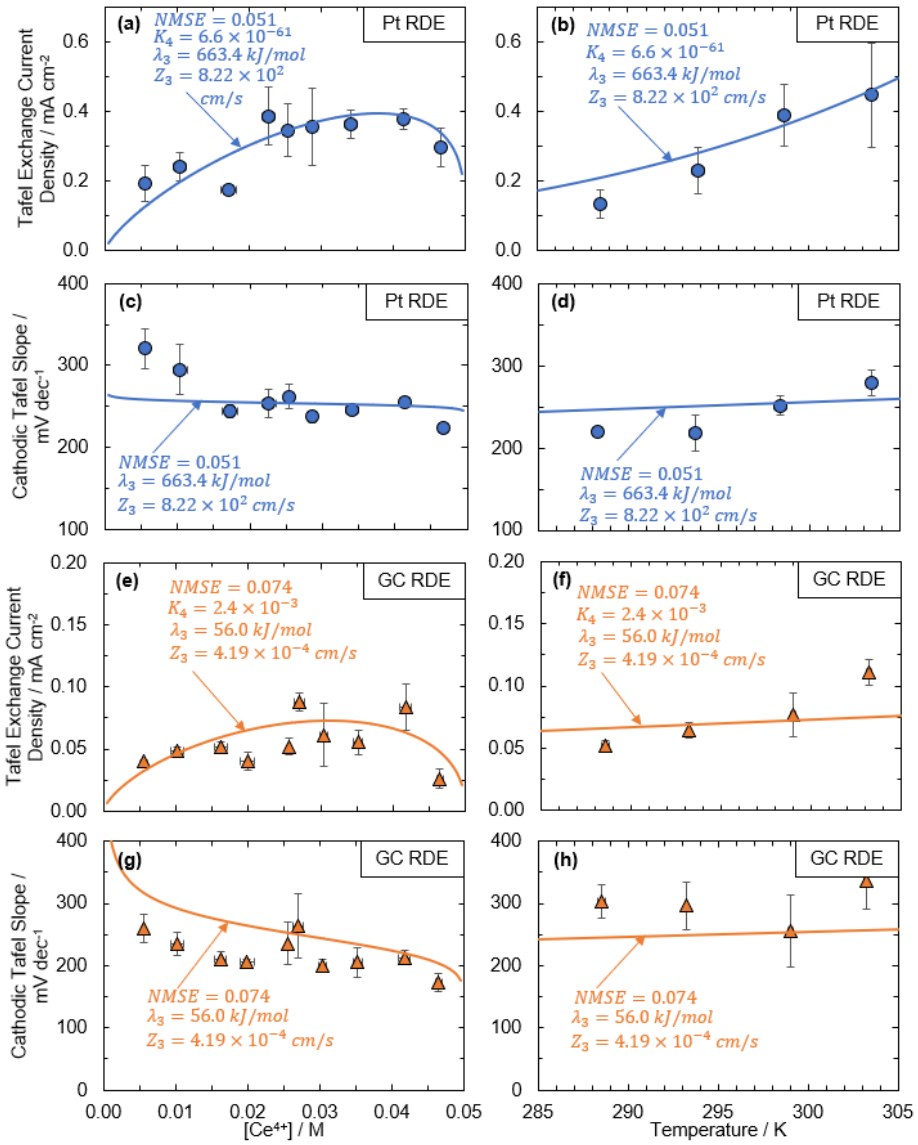

Figure D.8. Fit of Pt and GC data to *EC, E* RDS rate law. Fit of the *EC, E* RDS rate law to the experimental data for Pt **(a)** exchange current densities as a function of [Ce^{4+}], **(b)** exchange current densities as a function of temperature, **(c)** cathodic Tafel slopes as a function of [Ce^{4+}], and **(d)** cathodic Tafel slopes as a function of temperature. Data in **(a)** and **(c)** collected at room temperature in 2 M H_2SO_4 at total cerium concentration of 0.05 M. Data in **(b)** and **(d)** collected at a total cerium concentration of 0.05 M with a Ce^{4+} concentration of 0.026 M. Solid blue lines are the fit to the data from the *EC, E* RDS rate law. The reorganization energy λ_3, equilibrium constant K_4, and preexponential constant Z_3 were obtained through minimizing the NMSE of the Pt data (NMSE = 0.051). Fit of the *EC, E* RDS rate law to the experimental data for GC **(e)** exchange current densities as a function of [Ce^{4+}], **(f)** exchange current densities as a function of temperature, **(g)** cathodic Tafel slopes as a function of [Ce^{4+}], and **(h)** cathodic Tafel slopes as a function of temperature. Data in **(e)** and **(g)** collected at room temperature in 2 M H_2SO_4 at total cerium concentration of 0.05 M. Data in **(f)** and **(h)** collected at a total cerium concentration of 0.05 M with a Ce^{4+} concentration of 0.025 M. Solid orange lines are the fit to the data from the *EC, E* RDS rate law. The reorganization energy λ_3, equilibrium constant K_4, and preexponential constant Z_3 were obtained through minimizing the NMSE of the GC data (NMSE = 0.074). Reported values are averaged from three runs, with error bars representing one standard deviation from the average value in both horizontal and vertical directions. An Ag/AgCl reference electrode and graphite rod counter electrode were used for all measurements. All measurements were collected at 2000 rpm of the RDE where mass transport is not limiting.

D.3 References

1. Bard, A. J. & Faulkner, L. R. *Electrochemical Methods: Fundamentals and Applications*. (John Wiley & Sons, Inc., 2001). doi:10.1016/B978-0-08-098353-0.00003-8.